university of groningen

A Westerbork blind HI imaging survey of the Perseus-Pisces filament in the Zone of Avoidance

PhD thesis

to obtain the degree of PhD of the
University of Groningen
on the authority of the
Rector Magnificus Prof. E. Sterken
and in accordance with
the decision by the College of Deans.

and

to obtain the degree of PhD of the
University of Cape Town
on the authority of the
Vice-Chancellor Dr. M. Price
and in accordance with
the decision by the Doctoral Degrees Board.

Double PhD Degree

This thesis will be defended in public on
Tuesday 17 October 2017 at 11:00 hours

by

Mpati Analicia Ramatsoku

born on 16 August 1987
in Bethlehem, South Africa

Promotores
Prof. M.A.W. Verheijen
Prof. R.C. Kraan-Korteweg

Copromotor
Dr. W.J.G de Blok

Plagiarism Declaration

I, Mpati Ramatsoku, know the meaning of plagiarism and declare that all of the work in the document, save for that which is properly acknowledged, is my own.

Signature: Signed by candidate

Cover: A picture of the Westerbork telescope looking at the Milky Way.
ISBN: 978-94-6233-760-2
Printed by: Gildeprint

Abstract

In this thesis we study a structure associated with the Perseus-Pisces Supercluster (PPS; cz $\sim$ 6000 km s^{-1}), where it crosses the Zone of Avoidance (ZoA) at the Galactic longitude of $\ell \approx 160°$. This largely unexplored region contains the X-ray emitting 3C 129 cluster which hosts two strong radio sources with bent morphologies, thus indicative of a rich intra-cluster medium (ICM). Due to its low Galactic latitude of $b = 0.27$, where Galactic extinction is severe at optical wavelengths ($A_B = 1.8 - 8.0$), the details of its galaxy population and dynamics had not been investigated in detail before. Additionally, the diverse and dynamic cosmic environments of the PPS with the embedded galaxy cluster make this region an ideal laboratory to study the effects on these environments on the galaxy properties and galaxy transformation processes therein.

We used the Westerbork Synthesis Radio Telescope (WSRT) to blindly map this ZoA crossing of the PPS in the 21 cm H I-wavelength. This was conducted through 35 individual pointings observed for a total of 420 hours, covering a large area of about 9.6 sq.deg and a velocity range of approximately $cz \sim 2000-16000$ km s^{-1}, thus mapping the immediate surrounding regions to enable investigations of the various cosmic environmental effects on the H I properties of galaxies. With the resulting spectral line data cubes of an angular resolution of $23'' \times 16''$ and a velocity resolution of 16.5 km s^{-1} with a rms sensitivity of $\sim$ 0.4 mJy/beam, we detect 211 galaxies within the entire surveyed volume.

These new H I detections reveal a total of four distinct overdensities. Of these overdensities, the two major ones are located at the distance of the PPS at $cz \sim 4000 - 8000$ km s^{-1} and behind it at $cz \sim 8000 - 12000$ km s^{-1}. The galaxy overdensity associated with the PPS is used to demonstrate how this

supercluster connects across the ZoA and confirms earlier indications of a filamentary connection between Perseus, Pisces and the A569 clusters through this region of the sky. Galaxies in the background of the PPS seem to be part of the CID15 structure that had been earlier predicted in the reconstructed density and velocity maps from the 2MASS Redshift Survey.

We carry out a detailed census of the galaxy population in the 3C 129 cluster by combining the H I-data of the gas-rich galaxies with the near-infrared (NIR) images of the gas-poor galaxies. The NIR galaxies are identified from the high resolution ($0.2''$/pix, seeing $\sim 0.8''$) images of the UKIDSS Galactic Plane Survey. We obtain photometry in the J, H and K bands for about 9700 galaxies identified in the NIR images within the WSRT H I surveyed area. These measurements are used to derive the red-sequence of this cluster through the $(J-K)$ vs K colour-magnitude diagram to identify the gas-poor cluster member candidates. Within the spatial extent of the cluster of radius ~ 1.7 Mpc, a total of 261 galaxies are identified as cluster members, with 23 detected in H I. An assessment of the morphologies of these galaxy members reveals a clear morphological segregation, with E and E/S0 galaxies dominating the inner regions of the 3C 129 cluster and the late-type spirals found in the cluster outskirts.

We also examine the richness of the cluster by comparing it to two well-known clusters at similar redshifts. One being a massive cluster in the Great Attractor region, namely the Norma cluster, also located in the ZoA but in the South, and the other being the Coma cluster. The comparison shows that the 3C 129 cluster is quite rich as was suspected. The galaxy density in the core of the 3C 129 cluster is similar to that in the Norma cluster and slightly less than in the Coma cluster. Furthermore, an assessment of the spatial distribution of galaxies in the core shows a slight asymmetry aligned with the irregular distribution of the X-ray emission, thus consistent with the results from the X-ray analysis which surmised that the 3C 129 cluster seems to have undergone a merger and has not yet reached a dynamically relaxed state. In support of this we find a large substructure dominated by gas-rich galaxies North of the main cluster at a slightly higher recession velocity which could be falling into the cluster. All these findings seem to support a scenario where the 3C 129 cluster is still growing through accretion of galaxies from the PPS filament.

The wealth of H I data allows an analysis of the environmental effects on the galaxy properties within the WSRT surveyed volume. We first characterise the cosmic environments found within the two major overdensities as outlined by the H I-detected galaxies. This is conducted by perfoming tests to search for substructures. A total of four distinct substructures are found within the PPS ZoA overdensity ($cz \sim 4000 - 8000$ km s^{-1}) and three in the back-

ground galaxy overdensity ($cz \sim 8000 - 12000$ km s^{-1}). Our analysis of the H I properties of galaxies in these varying cosmic environments shows that highly disturbed H I-disks are found in larger and tightly bound groups, due to the higher incidence of tidal interactions between the galaxies. Furthermore, an indication of H I-gas deficiency is found in the core of the 3C 129 cluster. We assess the cause of this deficiency through models of the ICM of the 3C 129 cluster and find ram-pressure stripping to be the dominant gas removal process in this region. Additionally, highly H I-gas deficient galaxies are also found in the cluster outskirts. Most of these galaxies are located within galaxy groups where galaxy-galaxy interactions and mergers are prevalent, thus highlighting the importance of these processes in removing gas from galaxies in groups.

Contents

1 Introduction

1.1 The Zone of Avoidance

The Zone of Avoidance (ZoA) was first referred to by Proctor (1878) as the "Zone of a few Nebulae" because this part of the sky appeared to be "avoided" by nebulae in the General Catalogue of Nebulae (Herschel 1864). This was long before it became known that many of the "nebulae" were extragalactic objects. This region marks the band of the Milky Way where Galactic dust and stars make observing emission from external objects challenging due to confusion and extinction. Confusion results in the inefficiency to differentiate between emission from, for example, blended stars and galaxies (Jarrett et al. 2000) and extinction is due to absorption and scattering by dust particles which effectively reduce the amount of radiation received by the observer (Cardelli, Clayton & Mathis 1989). The extinction contour of $A_B \simeq 1.0$ mag was found by Kraan-Korteweg & Lahav (2000a) to delineate the area in the sky in which optical catalogues become highly incomplete. This area covers about 20% of the sky (Kraan-Korteweg 2005). A distribution of galaxies from optical observations in the Universe is shown in Fig. 1.1 where the effect of the ZoA on detecting galaxies behind the Galaxy is readily apparent.

The level of extinction decreases inversely proportional to the wavelength of observation and consequently, the Zone of Avoidance is significantly reduced at infrared wavelengths compared to optical wavelengths, although confusion remains a problem for photometric techniques. The Doppler-shifted 21 cm emission line from atomic neutral hydrogen (H I) in extragalactic objects on the other hand is not affected by extinction nor confusion when observed at recession velocities outside the velocity window where Galactic H I emission resides.

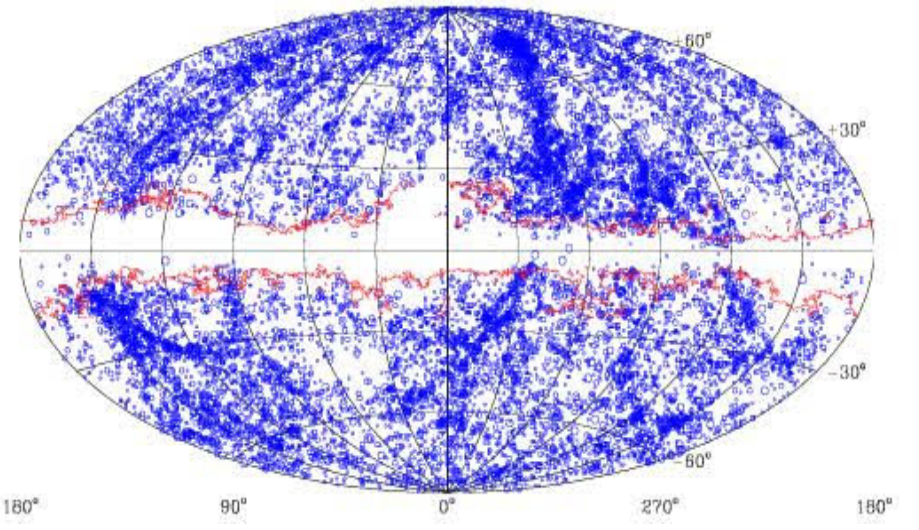

Figure 1.1 – An equal-area Aitoff projection of galaxies detected at optical wavelengths with diameters $D \geq 1.3'$. The extinction contour of $A_B = 1.0$ mag is shown to trace the ZoA (Figure from Kraan-Korteweg & Lahav 2000a).

1.1.1 Observations behind the Galaxy

At optical wavelengths the ZoA covers about 20% (Kraan-Korteweg & Lahav 2000a) of the sky. Even the most advanced and recent optical redshift surveys, such as the 6dF Galaxy Survey (6dFGS; Jones et al. 2009), avoid observing objects close to this region and limit their survey areas to Galactic latitudes of $|b| > 10°$.

The effect of extinction is reduced by several orders of magnitude in the near-infrared ($1.2-2.2\mu$m). For example, 10 magnitudes of extinction in the optical B-band (445 nm) is equivalent to 1 magnitude of extinction in the near-infrared K-band (2.2 μm). A distribution of galaxies observed in the near-infrared from the 2 Micron All Sky Survey Extended Sources Catalogue (2MASS XSC; Skrutskie et al. 2006) is shown in Fig. 1.2 (Jarrett 2004). In this case, the ZoA is mainly caused by confusion with stars from the Milky Way and is seen to be much smaller, covering about 10% of the sky compared to the ZoA at optical wavelengths. However, a follow-up survey of the 2MASS XSC, the 2MASS Redshift Survey (2MRS; Jarrett 2004, Huchra et al. 2012) exhibits a slightly larger ZoA because its galaxy redshifts were obtained with optical spectroscopy and avoid regions of $|b| < 5°$.

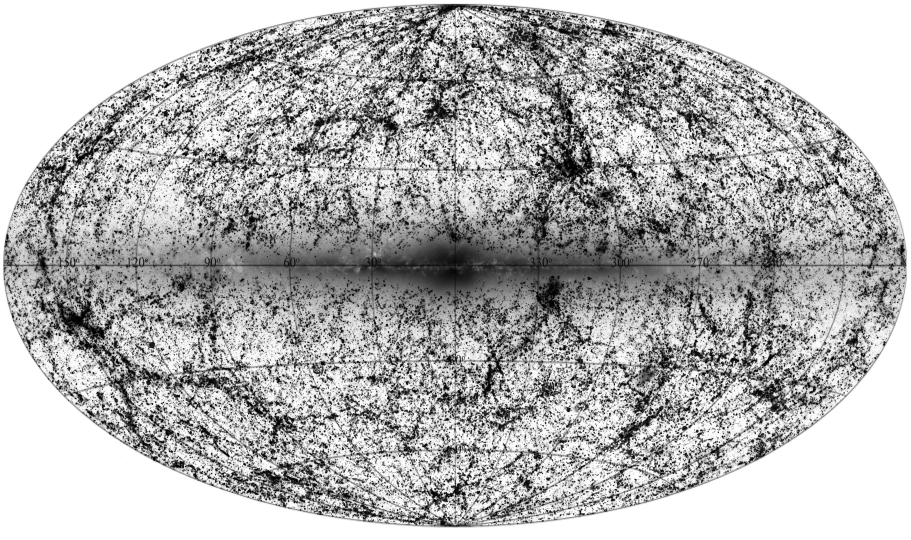

Figure 1.2 – A distribution of galaxies with photometric redshifts from the 2MASS XSCz. Galaxies have K-band magnitudes ≤ 11.75 mag. The 2MASS ZoA is shown as the dark band that is devoid of galaxies (Figure from Jarrett 2004).

At far-infrared (FIR; $12 - 100\mu$ m) wavelengths, the ZoA extinction effects are negligible but confusion with foreground objects in the Galaxy remains. A distribution of galaxies observed with the Infrared Astronomical Satellite (IRAS; Saunders et al. 2000a, Saunders et al. 2000b) is shown in Fig. 1.3. In this map the ZoA is shaded in grey and covers about 8% of the sky. The FIR observations tend to be biased against non-star forming and low-metallicity galaxies such as ellipticals and dwarf galaxies, but it is sensitive to normal spiral galaxies.

The Galactic dust is transparent at radio wavelengths (21 cm) because the typical dust grain is about 0.1μm in size and hence much too small to scatter or absorb the long 21 cm line emission from H I, thus observations at this radio wavelength have practically no Zone of Avoidance. To take advantage of this opportunity, numerous surveys have been conducted at the 21 cm wavelength in an effort to close the ZoA gap and achieve a truly full-sky redshift distribution of galaxies in the Local Universe. Examples of 21 cm surveys are the earlier studies which include a blind survey in the Northern ZoA using the 91-m Green Bank radio telescope (Kerr & Henning 1987) covering velocities out to 7500 km s^{-1} with a velocity resolution of 22 km s^{-1} and a beam size of $10.8'$. The other, systematic survey of the most obscured regions in the North is the Dwingeloo Obscured Galaxy Survey (DOGS; Kraan-Korteweg et al. 1994), which surveyed regions within $30° \leq \ell \leq 220°$, at $|b| < 5°$ to an rms limit of 40 mJy, out to 4000 kms^{-1} at a resolution of 40 km s^{-1} (Henning et al. 1998).

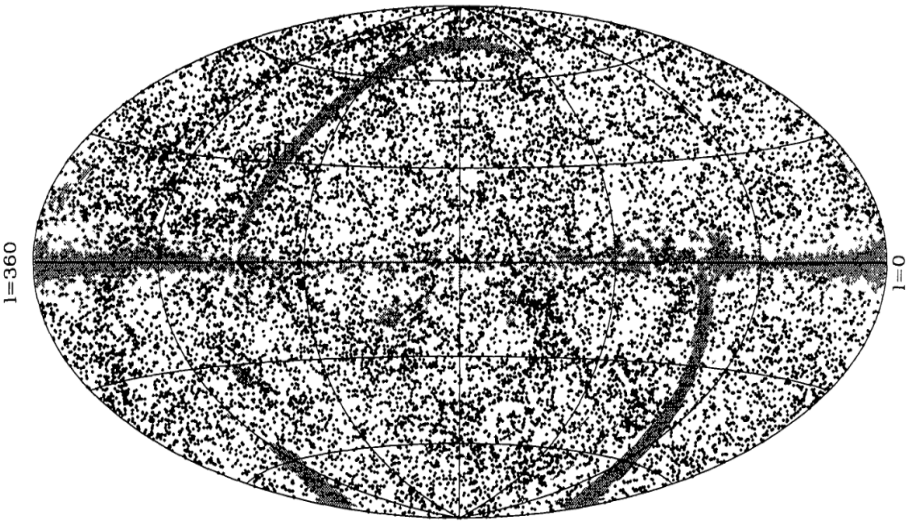

Figure 1.3 – An Aitoff projection centred on the Galactic Anticentre in Galactic coordinates of galaxies in the IRAS PSCz catalogue (Saunders et al. 2000b). The ZoA in the FIR is the grey patch of the sky without any objects.

Fairly recently, the southern ZoA has been mapped in H I by a systematic survey conducted with the Parkes multi-beam receiver; the HI Zone of Avoidance survey (HIZOA; rms $\approx$ 6 mJy beam^{-1}) which covered $52^\circ \leq \ell \leq 196^\circ$ (Henning et al. 2010) and extended to the northern ZoA at $36^\circ \leq l \leq 52^\circ$ and $196^\circ \leq \ell \leq 212^\circ$ (Donley et al. 2005). Both these surveys cover the redshift range of $cz = -1200 - 12700$ km s^{-1} with a resolution of 27 km s^{-1} and a beam of $15.5'$. A much deeper survey with a rms sensitivity of 1 mJy/beam and a beam size of $3.4'$ has been conducted in the Northern ZoA using the Arecibo L-Band Feed Array (ALFA ZoA; Henning et al. 2010). Because of the declination limits of Arecibo, this survey covers an area of about 300 deg^2 searching both the inner ZoA $30^\circ \leq \ell \leq 75^\circ$, $|b| < 2^\circ$ and its outer regions $175^\circ \leq \ell \leq 207^\circ$, $-2^\circ < b < 1^\circ$ out to velocities of about 18000 km s^{-1}.

The most recent blind HI survey for the northern sky ($\delta > -5^\circ$) out to a redshift of $cz \approx 20000$ km s^{-1} with a velocity resolution $\sim$1.3 km s^{-1} and a beam size of $10.8'$ and the same sensitivity as the H I Parkes All Sky Survey (HIPASS; Barnes et al. 2001), namely the Effelsberg-Bonn HI survey (EBHIS; Kerp et al. 2011), is currently ongoing with the first results already published (Winkel et al. 2016). It is surveying more than 8000 square degrees using the 100-m Effelsberg telescope.

These large H I surveys, and several other smaller ones not mentioned here, have demonstrated the effectiveness of searching for galaxies in the ZoA at the 21 cm wavelength. This resulted in a reduction of the ZoA as exemplified by the sky distribution of the 1000 H I brightest galaxies from HIPASS (Koribalski et al. 2004) shown in Fig. 1.4, where no ZoA is apparent.

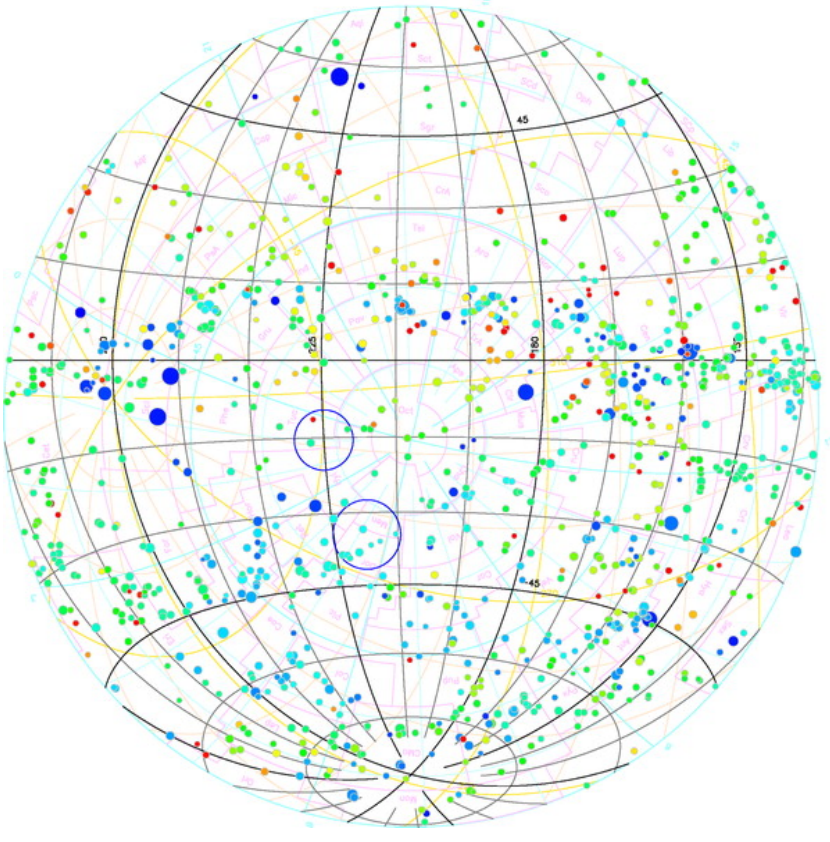

Figure 1.4 – The sky distribution of the 1000 HI brightest galaxies in zenithal equal area projection of the south celestial hemisphere. Galactic coordinates are shown by the grey lines. The lack of the ZoA in this map is clearly seen (Figure from Koribalski et al. 2004).

1.2 Why Study the ZoA?

1.2.1 The large-scale structures in the Local Universe

Galaxies in the Universe are distributed along filaments, sheets and in clusters, with large underdense volumes devoid of galaxies (Proust et al. 2006, Jones et al. 2009, Tempel et al. 2014). The scale of these features puts constraints on theories that explain the structure formation and dynamics of the large-scale structures in the Universe (Ouchi et al. 2005, Springel et al. 2005). Interestingly, the two dominant nearby superclusters that affect the dynamics of the Local Universe, namely the Great Attractor (Lynden-Bell et al. 1988) and the Perseus-Pisces Supercluster (Giovanelli et al. 1986, Haynes et al. 1988, Wegner, Haynes & Giovanelli 1993), are located at similar distances and on opposite sides on the sky and both are obscured by the Galaxy to a certain degree (Pomarède et al. 2015). Numerous concerted efforts have gone into mapping the large-scale structure (LSS) formed by galaxy clusters, sheets and filaments. This has been achieved through multi-wavelength redshift surveys including the Center for Astrophysics Redshift Survey (CfA; Huchra et al. 1983), the Two-degree-Field Galaxy Redshift Survey (2dFGRS; Colless et al. 2001), and the more recent 2MRS (Huchra et al. 2012) and Sloan Digital Sky Survey (SDSS; Alam et al. 2015). However, the ZoA obscuration persists over large areas of the sky. This has limited our knowledge of the true distribution and extent of cosmic structures behind the Milky Way. Many studies of the LSS often resort to predicting the LSS distribution by extrapolating the structures above and below the Galactic Plane (Kolatt, Dekel & Lahav 1995, Erdoğdu et al. 2006, Sorce, Hoffman & Gottlöber 2017). These density reconstruction methods might be based on incorrect assumptions regarding the distribution of objects in the ZoA and may result in misplaced or non-existing predicted structures. Mapping the real distribution of galaxies through redshift surveys is important to reduce the uncertainty in the LSS distribution. Redshift surveys in the ZoA in particular offer an opportunity to fully map the LSS distribution, to check the validity of the reconstructed density maps, and to understand the geometry of the voids behind the Galaxy which are useful for constraining the cosmological parameters (Lavaux et al. 2010).

1.2.2 The mass distribution in the Local Universe

The dipole anisotropy in the Cosmic Microwave Background (CMB) is explained by the peculiar motion of the Local Group (LG) towards the Galactic coordinates $\ell, b = 268°, 27°$ as a deviation from the uniform Hubble expansion in the frame of the CMB (Kogut et al. 1993). The peculiar motion of the LG is induced by the gravitational force of the distribution of mass in the Local Universe (Fixsen et al. 1996). The dipole pattern of the CMB from the Wilkinson Microwave Anisotropy Probe (WMAP; Bennett et al. 2003) is shown in Fig. 1.5. A fraction of about 35% of the motion of the LG is due to its acceleration towards the Local Supercluster (Shaya & Tully 2013). The other component is thought to originate from other unknown mass overdensities or voids at distances of about $100 - 200$ Mpc (Feldman, Watkins & Hudson 2010, Bilicki et al. 2011, Macaulay et al. 2011, Carrick et al. 2015). It is here that the lack of data in the ZoA presents a barrier for our understanding of the origin of the CMB dipole.

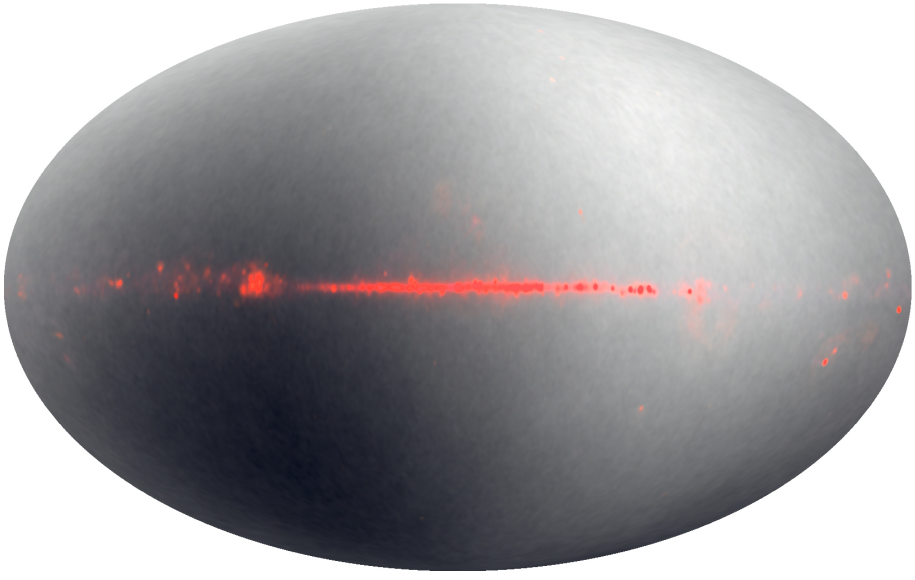

Figure 1.5 – The dipole anisotropy of the Cosmic Microwave Background in Galactic coordinates. One side is a plus or minus 0.00335 K variation with one pole hot and the other cold creating a dipole patten. Emission from the Milky Way is illustrated in red (Bennett et al. 2003).

The peculiar motion vector can be determined independent of the CMB observations through direct measurements of the local mass density distribution, thereby putting constraints on cosmological parameters such as the density and biasing parameters (Strauss & Willick 1995). While good agreement has been found in the amplitude of the mass density dipole with that of the CMB (Scrim-

geour et al. 2016), the direction of the vector is inconsistent, with a deviation of about $\lesssim 30°$ (Loeb & Narayan 2008). This remains the case even for the recent uniform "all-sky" surveys. The disagreement is about 15° for the IRAS Point Source Catalog Redshift survey (IRAS PSCz; Schmoldt et al. 1999) and 13° for the 2MASS Redshift survey (Erdoğdu et al. 2006). Similar disagreements in the peculiar motion vector have also been shown by Springob et al. (2016) with the latest data from the 2MASS Tully-Fisher survey (2MTF; Masters, Springob & Huchra 2008). The persistent discrepancies are caused to some degree by an incomplete mapping of the ZoA since it remains a contributor to the uncertainty in the mass density dipole measurements (Rowan-Robinson et al. 2000, Loeb & Narayan 2008, Springob et al. 2016).

It was suggested by Loeb & Narayan (2008) that an unknown mass of a few 10^{12} $M_\odot$ at 1 Mpc or 10^{15} $M_\odot$ at 20 Mpc behind the Galaxy could explain the discrepancy between the dipole as inferred from the gravitational acceleration exerted on the LG by the mass in the Local Universe and the CMB dipole. The former has been mostly ruled out since no galaxies with a mass of $\sim 10^{12}$ $M_\odot$ has been found at a distance of about 1 Mpc through various shallow H I redshift surveys in the ZoA (e.g., Kraan-Korteweg et al. 1994, Henning et al. 1998, Henning et al. 2000, McIntyre et al. 2015. However, an undiscovered galaxy cluster/overdensity of about 10^{15} $M_\odot$ at a distance of 20 Mpc or more might still be hiding in the ZoA. H I surveys that cover large areas of the ZoA and that reach deep enough in redshift to detect galaxies at these distances are still ongoing, or their data analysis is still in progress (e.g., EBHIS; Kerp et al. 2011, HIZOA; Staveley-Smith et al. 2016).

1.3 Galaxy clusters

Observations of galaxy clusters usually located at intersections of large-scale structures, have been instrumental in studies of the dynamics of the Local Universe since galaxy clusters contain most of the mass that provides gravitational attraction. For example, revealing the nature of the clusters in the ZoA that are associated with the Great Attractor (e.g., Norma cluster; Kraan-Korteweg et al. 1996) has been useful in improving our knowledge of the local cosmography (Willick 1990, Hudson et al. 2004, Mieske, Hilker & Infante 2005, Jones et al. 2009). On smaller scales galaxy clusters have been instrumental in enriching our knowledge on galaxy evolution.

Galaxy clusters are continually growing through accretion of galaxies and galaxy groups from the surrounding field and filaments (Ebeling, Barrett & Donovan 2004, Braglia, Pierini & Böhringer 2007, Fadda et al. 2008, Coppin et al. 2012). Studies have shown that galaxies start out as late-type and gas-rich in the field and by the time they reach the cluster core they are transformed

into gas-poor early-type galaxies (Dressler 1980). By determining where this transformation occurs, important information on the processes responsible for galaxy evolution can be attained. The environment is one of the main factors that influences this evolution. Examples of some of the environment-specific mechanisms that are responsible for the transformation of galaxies include ram-pressure stripping, harassment and galaxy mergers.

Ram-pressure stripping: This process occurs in rich galaxy clusters that contain hot, X-ray emitting gas, which makes up the intra-cluster medium (ICM). A galaxy falling into the cluster core encounters this ICM which exerts hydrodynamical pressure on the galaxy. If this pressure is high enough it can overcome the gravitational attractive force of the galaxy that is holding on to its gas, thus effectively stripping the galaxy of its star-forming fuel (Gunn & Gott 1972, Moran et al. 2007, Porter et al. 2008, Dressler et al. 2013, Jaffé et al. 2015).

Harassment: In some cases, galaxies often fly by each other as they move along their orbits during the transition into the cluster core, thus causing them to interact gravitationally. These interactions between neighbouring galaxies perturb the gas and stellar distribution. This harassment is often severe enough to affect the majority of the gas clouds and when this occurs a galaxy will undergo a sudden burst of star-formation, which consumes all the fuel for new star-formation (Moore et al. 1996, Duc & Bournaud 2008, Smith et al. 2015). In cases where harassment is less severe it only disrupts the diffuse gaseous haloes of galaxies which stops the gas from cooling and condensing, thereby "quenching" star formation in a galaxy (Dressler et al. 2013, Cattaneo 2015, Peng, Maiolino & Cochrane 2015, Jaffé et al. 2016). Both types of harassments effectively transform the morphology of the galaxy.

Mergers: In other cases, merger events take place when galaxies collide with each other. This particularly occurs when galaxies encounter each other at relatively low velocities (Toomre & Toomre 1972, Walker, Mihos & Hernquist 1996). Galaxy mergers often lead to the removal of gas from of a galaxy as it becomes gravitationally detached during the collision of funnelled to the nuclear regions where it gets consumed by star-formation or fuels an AGN (Baldry et al. 2004, Balogh et al. 2009).

It has been shown that ram-pressure stripping is an effective means to remove gas from an infalling galaxy, but only in the inner regions of a cluster where the ICM is dense enough, while infalling groups of galaxies are subjected more to mergers and harassment due to their close encounters with neighbouring galaxies, and the lack of a dense, intracluster medium in those environments.

A number of questions still remain open on the subject of environmental effects on galaxies. The first question concerns the origin of the red, non-star forming galaxies in the centres of galaxy clusters. Could gas removal mechanisms such as galaxy mergers and harassment be effective enough to remove gas completely from the infalling group galaxies or is ram-pressure stripping from the ICM within the cluster core acting alone in creating this population? Previous studies have shown evidence that galaxy "pre-preprocessing" does occur to a certain degree in low-mass groups prior to their infall into the cluster core (Zabludoff & Mulchaey 1998, Verdes-Montenegro et al. 2001, Ellingson et al. 2001, De Lucia et al. 2012). However, the relevance of pre-processing in the formation of gas-poor non star-forming galaxies is still debated (McGee et al. 2009, Vijayaraghavan & Ricker 2013).

The second question concerns the effects of the environment within large-scale structure filaments on the evolution of galaxies. Does pre-processing occur in these filaments? If this is the case, where in the filaments are galaxies losing their gas and which gas-removal process is at play? Studies on these questions have found evidence that filaments do have an effect on the gas content of the galaxies (Braglia, Pierini & Böhringer 2007). This effect is seen to be more dominant in low-mass dwarf galaxies as they travel along the filament but it is not yet clear which gas removal mechanisms are taking place (Fadda et al. 2008, Porter et al. 2008, Coppin et al. 2012).

Observing the emission from the H I-gas provides an opportunity to start addressing some of these questions. The environment leaves clear imprints on the delicate and diffuse H I-disks of galaxies thereby making H I an ideal tool for studying and understanding the mechanisms that affect galaxy evolution (Poggianti & van Gorkom 2001, Bravo-Alfaro et al. 2000a, Bravo-Alfaro et al. 2009, Chung et al. 2009, Gavazzi et al. 2013, Jaffé et al. 2015, Yoon et al. 2017). This task requires a comprehensive view of the different environments. This is achievable with H I surveys that cover large enough volumes to capture not just the densest environments (i.e., galaxy clusters) but also the filaments in which they are embedded.

1.4 This thesis

Recent targeted 21 cm observations of the 2MASX galaxies brighter than $K = 11.25$ mag were conducted in the ZoA over $80^\circ \leq \ell \leq 180^\circ$ and $|b| < 5^\circ$ with the 94m-class Nancay Radio Telescope (NRT) to a sensitivity of $rms \sim 3$ mJy and $cz \leq 12000$ km s^{-1}. Results from the NRT survey revealed hints of an overdense region crossing the Plane of the Galaxy at $\ell \approx 160^\circ$ and a redshift of $cz \sim 6500$ km s^{-1} (Ramatsoku et al. 2014). The location and redshift of this structure linked it to the expansive Perseus-Pisces Supercluster

(PPS; Giovanelli et al. 1986, Haynes et al. 1988). The existence of this filamentary connection of the PPS above and below the ZoA had been speculated in earlier studies (Focardi, Marano & Vettolani 1984, Chamaraux et al. 1990). This connection is quite prominent in the 2MASX all-sky distribution which includes photometric redshifts (Jarrett 2004) and was predicted by the 2MRS reconstructed density maps (Erdoğdu et al. 2006). However, it had never been confirmed spectroscopically due to the heavy obscuration of the galaxies at optical wavelengths which ranges from $A_B \approx 1.8-8.0$ mag (Schlafly & Finkbeiner 2011). Within this PPS filament, an X-ray galaxy cluster hosting two bright head-tail radio galaxies with bent morphologies, 3C 129 and 3C 129.1, is embedded (Spinrad 1975, Jaegers & de Grijp 1983, Lane et al. 2002, Lal & Rao 2004, Murgia et al. 2016). While this cluster has been studied extensively from its X-ray emission (Leahy & Yin 2000, Harris, Krawczynski & Taylor 2002, Krawczynski et al. 2003) very little was known about its galaxy populations despite it being a potentially massive and evolving constituent of the PPS.

Given the rich laboratory offered by galaxy clusters in enriching our understanding of the environmental effects on the nature of galaxies and the scarcity of rich nearby galaxy clusters, it remains useful to analyse clusters and their surroundings individually. This is useful particularly when these clusters appear to be nearby enough to be observed and analysed in great detail with our current instruments. The earlier NRT H I detections of galaxies were only sparsely distributed around the core of the cluster. This hinted at H I-deficiency signatures thereby already suggesting gas depletion in galaxies at the cluster core. Exploring this particular cluster in relation to its surroundings would provide more statistics in the ongoing quest to establish which mechanisms and which environments are most relevant for the transformation of galaxies. Furthermore, the location of this cluster in the ZoA region of the PPS allows for the determination of its mass contribution to the large-scale structure and offers an opportunity to study its relevance to the observed flow-fields in the PPS. This will add to the combined efforts to fully understand the dynamics of the Local Universe. The unknown nature of this particular region of the sky also presents a testbed for automated H I source calibration, finding, characterisation and visualisation efficiencies in a controlled but unbiased manner, particularly for more distant galaxies. Conducting these tests will be invaluable in preparing for the upcoming blind H I-imaging surveys that will be conducted with SKA pathfinders such as Apertif (Verheijen et al. 2008), ASKAP (Johnston, Feain & Gupta 2009) and MeerKAT (Booth & Jonas 2012).

In this thesis we have conducted a deep and blind H I-imaging survey with the Westerbork Synthesis Radio Telescope (WSRT) centred on the PPS ZoA overdense region covering an area of 9.6 deg^2 and radial velocities of $cz =$

$2000 - 16000$km s^{-1}. From this data set we have uncovered galaxies belonging to various structures located in the ZoA over the entire observed radial velocity range including the galaxy cluster in the PPS region. We have used this H I sample in combination with near-infrared imaging data from the UKIDSS Galactic Plane Survey (UKIDSS-GPS; Lucas et al. 2008) to conduct a census and determine the extent of the galaxy population of the 3C 129 cluster. We have also used these data to study the gas properties of the galaxies in various regions of the observed volume, including the cluster with the aim of investigating the variation of the galaxy properties with environment.

1.4.1 Thesis outline

This thesis is organised as follows: In chapter 2 the detailed description of the blind H I-imaging survey that provides the basis for this thesis is presented. A comprehensive description of the data reduction is provided and a compilation of the catalogue with an atlas of the derived H I products of the newly detected galaxies. In this chapter the previously predicted or otherwise unknown overdense regions over the observed redshift range in this hidden region of the Universe are also defined and characterised.

In chapter 3, the main focus is to compile a full census of the galaxy population in the 3C 129 cluster and its surroundings. This is conducted using a combination of galaxies detected in H I and galaxies that were identified from UKIDSS-GPS images using the near-infrared colour-magnitude relation. The data sets are complimentary in defining the cluster, particularly in the absence of optical spectroscopic redshifts, because the former is sensitive to gas-rich galaxies while the latter is able to outline the older population of gas-poor galaxies that tend to trace the core of clusters. The resulting near-infrared catalogue of the cluster galaxies is presented, including postage stamp images that give a visual impression of the type of galaxy population that forms the cluster. A further step is taken to identify substructure in the cluster as this indicates to a first approximation the dynamical state of this cluster's system.

Chapter 4 describes a definition and characterisation of substructures found within two selected major overdense regions. This is done using the spatial and velocity distribution of the H I-detections in combination with the near-infrared imaging data. The characterised substructures form regions within which the properties of galaxies are examined as a function of the environment in an effort to gain clues into the gas depletion mechanism at play.

In the first part of chapter 5 a summary of the main results from this thesis is presented. The second part of the chapter discusses future perspectives on further work to be done with the current presented, and future supplementary data.

2 The WSRT PP ZoA I. HI catalogue & atlas.

M. Ramatsoku[a,b,c], M.A.W Verheijen[a], R.C. Kraan-Korteweg[b], G.I.G. Józsa[d],W.J.G. de Blok[c,b,a], A.C. Schröder[e], T.H. Jarrett[b], E.C Elson[b], W. van Driel[f], P.A. Henning[g]

[a] Kapteyn Astronomical Institute, University of Groningen, Landleven 12, 9747 AV Groningen, The Netherlands
[b] Department of Astronomy, University of Cape Town, Private Bag X3, Rondebosch 7701, South Africa
[c] ASTRON, Netherlands Institute for Radio Astronomy, Postbus 2, 7990 AA Dwingeloo, The Netherlands
[d] SKA South Africa, Radio Astronomy Research Group, 3rd Floor, The Park, Park Road, Pinelands 7405, South Africa
[e] South African Astronomical Observatory (SAAO), PO Box 9, 7935 Observatory, Cape Town, South Africa
[f] GEPI, Observatoire de Paris, CNRS, Université Paris Diderot, 5 place Jules Janssen, 92190 Meudon, France
[g] Department of Physics and Astronomy, University of New Mexico, 1919 Lomas Blvd. NE, MSC07 4220, Albuquerque NM 87131-0001, USA

Submitted 24 November 2015, Accepted 23 April 2016
Published in Monthly Notices of the Royal Astronomical Society, volume 460, pages 923–941, 2016.

Abstract

We present results of a blind 21cm H I-line imaging survey of a galaxy overdensity located behind the Milky Way at $\ell, b \approx 160°$, 0.5°. The overdensity corresponds to a Zone-of-Avoidance crossing of the Perseus-Pisces Supercluster filament. Although it is known that this filament contains an X-ray galaxy cluster (3C 129) hosting two strong radio galaxies, little is known about galaxies associated with this potentially rich cluster because of the high Galactic dust extinction. We mapped a sky area of ∼9.6 sq.deg using the Westerbork Synthesis Radio Telescope in a hexagonal mosaic of 35 pointings observed for 12 hours each, in the radial velocity range $cz = 2400 - 16600$ km s^{-1}. The survey has a sensitivity of 0.36 mJy/beam rms at a velocity resolution of 16.5 km s^{-1}. We detected 211 galaxies, 62% of which have a near-infrared counterpart in the UKIDSS Galactic Plane Survey. We present a catalogue of the H I properties and an H I atlas containing total intensity maps, position-velocity diagrams, global H I profiles and UKIDSS counterpart images. For the resolved galaxies we also present H I velocity fields and radial H I surface density profiles. A brief analysis of the structures outlined by these galaxies finds that 87 of them lie at the distance of the Perseus-Pisces Supercluster ($cz \sim 4000 - 8000$ km s^{-1}) and seem to form part of the 3C 129 cluster. Further 72 detections trace an overdensity at a velocity of $cz \approx 10000$ km s^{-1} and seem to coincide with a structure predicted from mass density reconstructions in the first 2MASS Redshift Survey.

Keywords: galaxies: large scale structures: ZoA: surveys: galaxies: radio lines: galaxies: galaxy clusters (3C 129)

2.1 Introduction

Major steps forward have been achieved in mapping the large-scale distribution of galaxies forming the Cosmic Web, thanks to dedicated wide-field (on-sky), deep (in terms of redshift) galaxy redshift surveys such as the 2dF Galaxy Redshift Survey (2dFGRS; Colless et al. 2001), the 2MASS Redshift Survey (2MRS, Huchra et al. 2012), the Sloan Digital Sky Survey (SDSS; Eisenstein et al. 2011) and the 6dF Galaxy Survey (6dFGS; Jones et al. 2004). The largest areal coverage is provided by the 2MRS with 44000 galaxies. It is based on the brightest objects in the near-infrared 2MASS Extended Source Catalogue (2MASX; Jarrett et al. 2000) and has a relatively low median velocity of $cz_{\rm med} = 9000$ km s^{-1}. A version slightly deeper in velocity ($cz_{\rm med} = 15000$ km s^{-1}) is achieved through a combination of the 2MRS, SDSS and 6dFGS catalogues into the 2M++ galaxy compilation by Lavaux & Hudson (2011), however, it is not homogenous in sky coverage. Bilicki et al. (2014) have

therefore created a much deeper catalogue ($cz_{\rm med} \approx 60000$ km s^{-1}) based on photometric redshifts, (the 2MASS Photometric Redshift catalog; 2MPZ).

What all these 'all-sky' surveys have in common is the lack of information on galaxies hidden behind our own Milky Way due to dust extinction and confusion by high stellar densities. This is what creates the so called Zone of Avoidance (ZoA; for reviews see Kraan-Korteweg & Lahav 2000a and Kraan-Korteweg 2005). We still have a highly incomplete census of the galaxy distribution in the local Universe along the 360°-circle of the inner ZoA, i.e., for Galactic latitudes $|b| \leq 5°$, with a broader ZoA around the Galactic Bulge ($|b| \lesssim 10°$).

Uncovering galaxies in the ZoA is important for studying the kinematics of the Local Group (LG) and large-scale structures (LSS) in the local Universe. This includes understanding the origin of the dipole observed in the Cosmic Microwave Background (CMB; Fixsen & Kashlinsky 2011). Earlier studies focused on the significance of the Great Attractor (GA) at $45 - 50$ Mpc and the Perseus-Pisces Supercluster (PPS) at 57-114 Mpc as likely contributors (Dressler et al. 1987, Rowan-Robinson et al. 1990, Hudson 1993). More recent studies, however, suggest contributions to the dipole from more distant LSS at ∼200 Mpc like the Shapley Supercluster (Branchini & Plionis 1996, Plionis & Kolokotronis 1998, Kocevski & Ebeling 2006, Lavaux et al. 2010, Lavaux & Hudson 2011). It has been proposed that incomplete mapping of the ZoA is to a certain degree responsible for these uncertainties (Erdoğdu et al. 2006, Loeb & Narayan 2008).

Observing the 21 cm line emission of neutral hydrogen (H I) in gas-rich galaxies is an effective method of mapping the most obscured regions behind the Galactic Plane (GP). This is due to the transparency of foreground interstellar dust at this wavelength and the Doppler shift of the emission line. To take advantage of this, considerable efforts have been devoted to H I surveys to find galaxies in the ZoA and measure their redshifts.

Earlier H I surveys of the ZoA include the 91-m Green Bank radio telescope blind survey out to ∼7200 km s^{-1} (Kerr & Henning 1987) and the more systematic Dwingeloo Obscured Galaxy Survey (DOGS; Kraan-Korteweg et al. 1994), with an rms of 40 mJy at a channel width of 4 km s^{-1} out to 4000 km s^{-1}. The Parkes Multi-beam Receiver has been used to systematically map the ZoA in the southern hemisphere (HIZOA-S; Staveley-Smith et al. 2015) with an extension to the north (HIZOA-N; Donley et al. 2005) for the most obscured part of the ZoA ($|b| < 5°$). With an rms of ∼6 mJy and channel width of 13.2 km s^{-1} out to ∼12000 km s^{-1} these surveys together cover the ZoA from $\ell = 196°$ across the Galactic Bulge to $\ell = 52°$. Another recent and more sensitive survey is the Arecibo L-Band Feed Array Zone of Avoidance

Survey (ALFA ZoA; Henning et al. 2010, McIntyre et al. 2015) with an rms of 1 mJy at 9 km s^{-1} resolution which is mapping the ZoA accessible to the Arecibo telescope ($30° \lesssim \ell \lesssim 75°$ and $175° \lesssim \ell \lesssim 207°$). All of these surveys have contributed to uncovering gas rich galaxies and structures they belong to in the ZoA. However, they have so far left a major part of the northern ZoA mostly unexplored ($80° \lesssim \ell \lesssim 180°$).

For this reason a systematic H I follow-up pointed survey of 2MASX bright galaxy candidates in the ZoA without previous redshift information (∼1200 observed to date) was started with the 100m-class Nançay Radio Telescope (NRT)[1] to an rms of ∼3 mJy with a velocity resolution of 18 km s^{-1} out to $v \leq 12000$ km s^{-1} (van Driel et al. 2009, Ramatsoku et al. 2014, Kraan-Korteweg et al, in prep).

Among features uncovered by the 250 NRT detections was a filament crossing the Galactic plane at $\ell \approx 160°$ with a recession velocity range of $4000 - 7000$ km s^{-1} (see Fig. 1 in Ramatsoku et al. 2014). Its position and velocity suggest it to be part of the ZoA crossing of the PPS, which had been hypothesised to exist previously (Focardi, Marano & Vettolani 1984). This structure was earlier mapped with H I-observations of optically identified galaxies (e.g. Chamaraux et al. 1990) and tentative indicators for this filament were found, but it was sparsely sampled. This filament encompasses an X-ray galaxy cluster, 3C 129 at $\ell, b \approx 160.52°, 0.28°$ (Ebeling et al. 1998a, Leahy & Yin 2000). The X-ray cluster hosts two bright radio galaxies, a head-tail source (3C 129) and a double-lobed giant elliptical radio galaxy (3C 129.1), at $cz = 6236$ and 6655 km s^{-1}, respectively (Spinrad 1975). The presence of such radio sources usually implies a rich cluster environment. The cluster has a total X-ray luminosity of $L_{\rm X} = 1.89{\times}10^{44}$ h$_{50}^{-2}$erg s^{-1} as listed in the "Clusters In the ZoA" survey (CIZA; Ebeling et al. 1998a) from the ROentgen SATellite (ROSAT[2]; Truemper 1982). While not the most luminous ROSAT X-ray cluster listed, it should be noted that it might be more massive than suggested by its X-ray luminosity since the intervening high Galactic gas column density ($N_{\rm H} \approx 5.76 \times 10^{21}$ cm^{-2}; Stark et al. 1992) may well have reduced the X-ray flux in the ROSAT $0.2 - 2.4$ keV band by more than 30% (Leahy & Yin 2000).

Due to the high extinction layer of the Milky Way, most of the galaxies belonging to this cluster had not been observed before. Hence we decided to conduct a deep blind H I imaging survey with the Westerbork Synthesis Radio Telescope[3] (WSRT) of a mosaic covering a 9.6 sq.deg sky area which comprises the cluster and the surrounding filament within which the NRT survey showed

[1] http://www.nrt.obspm.fr/
[2] http://www.xray.mpe.mpg.de/cgi-bin/rosat/rosat-survey
[3] http://www.astron.nl/radio-observatory/

it to be embedded.

Our aims are to firstly investigate in detail the structure associated with the 3C 129 galaxy cluster. The H I data and accompanying near-infrared photometry will give distance estimates using the Tully-Fisher relation. These will be used to determine the cluster's relevance to flow fields around it and the larger Perseus-Pisces Complex, notably evident in the whole-sky 2MASS depictions of the large scale structure that appears to pierce the cluster as it crosses from the southern to northern Galactic hemispheres (Jarrett 2004). Moreover, these data will aid the 2MASS Tully-Fisher survey (2MTF; Masters, Springob & Huchra 2008) efforts, by complementing the inner $b \approx |5°|$ ZoA regions excluded from optical spectroscopy. Secondly, taking advantage of the wide areal coverage of our H I imaging survey of the cluster and its environments, we will be able to conduct an examination of environmental effects on the H I properties of these galaxies.

A further aspect of this project is to provide interferometric data cubes to assess data handling algorithms such as pipeline reduction, calibration, source finding and characterisation. Having a good handle on these algorithms will prove invaluable in the planning and preparation of the forthcoming H I surveys to be carried out with AperTIF at the WSRT (Verheijen et al. 2008, Oosterloo, Verheijen & van Cappellen 2010) and SKA precursor instrument H I surveys to be conducted with MeerKAT and ASKAP (de Blok 2011, Duffy et al. 2012, respectively). It is for this reason that our velocity search range ($2400 - 16600$ km s^{-1}), extends far beyond the mean velocity of the 3C 129 cluster.

In this first of a series of papers based on the WSRT imaging survey described above, we present the H I data of the galaxies unveiled in the ZoA, both as a catalogue containing H I parameters as well as an atlas of H I distributions and kinematics. We also include a discussion of the large-scale structures traced by the detected galaxies. Subsequent papers will focus in detail on the other aforementioned science goals.

This paper is organised as follows: in Sect. 2.2 we describe the observing strategy and WSRT data reduction. Section 2.3 provides a description of our source finding procedure. Methods used to determine the H I properties of detected galaxies are described in Sect. 2.4. The resulting H I atlas products are described in Sect. 2.5, while the full atlas is presented in Appendix A. Also in Sect. 2.5, the completeness of the survey and counterparts search are discussed. In Sect. 2.6 we discuss the measured H I parameters and their characteristics. Lastly, structures revealed by this survey are presented in Sect. 2.7.

We assume a Λ cold dark matter cosmology with $\Omega_{\rm M} = 0.3, \Lambda_\Omega = 0.7$ and a Hubble constant $\rm H_0 = 70$ km s^{-1} Mpc^{-1} throughout this paper.

2.2 Observations and Data Reduction

Observations were carried out using the WSRT between August and November 2012. We imaged a mosaic comprising 35 fields arranged in a hexagonal grid covering 9.6 sq.deg, each separated by $\Delta = 0.^{\circ}5$. This setup is similar to that of a single AperTIF phased array feed pointing, minus two fields. In Fig. 2.1, we present the layout of the mosaic with positions of galaxies from the literature shown in this field. We chose this particular mosaic grid to be able to cover the largest possible field of view with an acceptable noise variation of 20% between pointing centres. The total sky area covered is large enough to map the network between the PPS filament and the 3C129 cluster.

Each field was observed for a total on-source integration time of 2×6 hours, in between half-hour long pre- and post-calibrations. We obtained data in eight IF-bands per pointing, each 10 MHz wide, with 256 channels in dual polarisation mode, overlapping by 16% in frequency. This configuration covered a total effective bandwidth of 67 MHz with 1717 channels that are 39 kHz (8.25 km s^{-1}) wide at $z = 0$. We therefore cover a velocity range of $cz = 2400 - 16600$ km s^{-1} corresponding to a volume depth of about 214 Mpc. Therefore we map our main target with acceptable velocity resolution while still being able to survey the more distant universe. The total volume surveyed is 26300 Mpc^3.

The survey configuration allows the detection of galaxies with H I masses greater than $M_{HI} = 3.0 \times 10^8 M_{\odot}$ at the median distance of the PPS ($cz \approx$ 6000 km s^{-1}), assuming a line width of 150 km s^{-1} at the 6σ noise level such that we could attain acceptable statistics to map the cluster.

The observational parameters for the 35 pointings are summarised in Table 2.1. Column 1 gives the pointing number. Columns 2 & 3 and columns 4 & 5 are the central equatorial and Galactic coordinates of the pointings, respectively. The synthesised beam sizes and position angles are given in columns 6 and 7, respectively. In column 8 the average rms noise for each pointing is given. Column 9 gives the flux densities of the brightest continuum sources in each pointing.

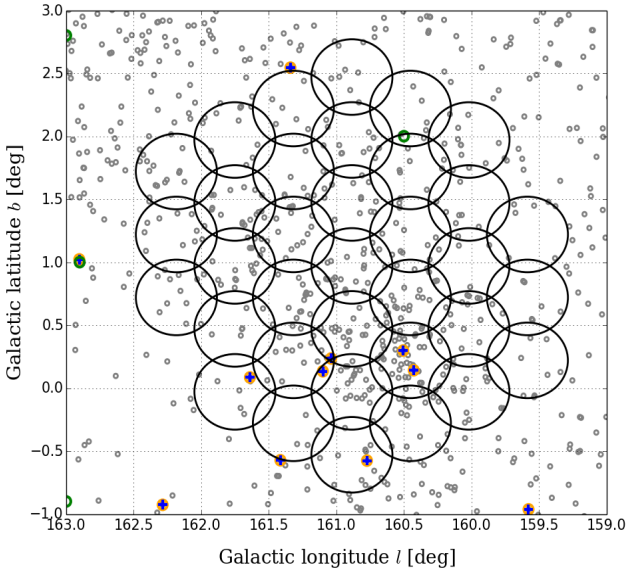

Figure 2.1 – The projected sky distribution of the observed hexagonal mosaic. The circles indicate the HPBW of the individual WSRT pointings. The small grey circles show the 2MASX near-infrared extended sources within this region, highlighting the 3C129 cluster centred at $\ell, b \approx 160.52°, 0.28°$. The orange open circles and blue crosses mark 7 galaxies within the observed area with redshifts listed in NED and HyperLEDA, respectively. Galaxies with HI detections from the NRT survey are shown in green open circles.

2.2.1 Data Processing

The uv-data were flagged, calibrated and Fourier transformed using the NRAO Astronomical Imaging Processing System package[1] (AIPS; van Moorsel, Kemball & Greisen 1996, Greisen 1990).

RFI flagging, Amplitude and Phase Calibration

Telescope-based gain and phase corrections were determined by observing the standard calibrators 3C 48 (J0137+331) with a flux density of 15.56 Jy and 3C 147 (J0542+498) with a flux density of 21.58 Jy. After loading the uv-data into AIPS, the system temperature (T_{sys}) was checked to assess the behaviour of antennae throughout the observation, followed by applying the time-dependent T_{sys} corrections. In all cases solar interference was excised from the observations by deleting visibilities from the short 9A, 9B and AB baselines

[1] http://www.aips.nrao.edu/index.shtml

Table 2.1 – Observing parameters of the WSRT PP ZoA survey.

Field	R.A (J2000)	Dec (J2000)	ℓ	b	Synth. beam	PA	rms noise	Cont. sources
	hh:mm:ss.ss	dd:dm:ds.ss	$^\circ$	$^\circ$	$'' \times ''$	$^\circ$	mJy/beam	mJy
(1)	(2)	(3)	(4)	(5)	(6)	(7)	(8)	(9)
01[a]	04:49:34.85	45:02:32.89	160.452	0.220	21.2 × 15.2	2.0	0.37	4001, 935
02[b]	04:47:25.35	44:43:13.83	160.452	−0.280	22.9 × 16.1	1.3	0.41	4001, 935
03[c]	04:46:54.93	45:12:44.14	160.019	−0.030	21.8 × 16.3	4.1	0.35	4001, 935
04	04:49:05.37	45:32:05.54	160.019	0.470	23.2 × 16.4	1.6	0.38	4001, 935, 703
05	04:51:45.83	45:21:42.96	160.452	0.720	23.4 × 16.4	4.7	0.41	4001, 935
06	04:52:13.84	44:52:07.62	160.885	0.470	23.8 × 16.3	0.0	0.36	4001, 935
07	04:50:03.82	44:32:59.77	160.885	−0.030	23.3 × 16.3	1.1	0.41	4001, 935, 414
08	04:54:25.33	45:11:06.33	160.885	0.970	23.4 × 16.6	1.1	0.38	
09	04:53:58.31	45:40:43.68	160.452	1.220	23.2 × 16.6	1.2	0.38	
10	04:54:51.88	44:41:28.59	161.318	0.720	24.3 × 16.7	1.7	0.39	426
11	04:57:03.82	45:00:15.90	161.318	1.220	24.3 × 16.7	1.6	0.40	703, 414
12	04:56:38.28	45:29:55.52	160.885	1.470	23.4 × 16.3	-0.1	0.38	426
13	04:59:17.21	45:18:53.53	161.318	1.720	23.5 × 16.3	0.1	0.38	426
14	04:52:41.37	44:22:31.99	161.318	0.220	22.8 × 17.3	12.6	0.38	414
15[d]	04:51:17.33	45:51:17.74	160.019	0.970	22.4 × 17.3	14.2	0.40	703
16	04:58:52.69	45:48:34.80	160.885	1.970	23.3 × 16.7	1.0	0.41	703
17	04:59:41.29	44:49:11.95	161.751	1.470	23.7 × 16.7	1.7	0.38	426
18	04:57:28.93	44:30:36.07	161.751	0.970	23.9 × 16.6	2.0	0.38	343
19	04:56:12.28	45:59:34.63	160.452	1.720	23.2 × 16.7	1.6	0.39	414
20	04:55:17.98	44:11:50.75	161.751	0.470	24.3 × 16.6	1.1	0.40	703
21	04:50:32.30	44:03:26.40	161.318	−0.280	24.1 × 16.6	2.1	0.40	426, 343
22[e]	04:48:35.38	46:01:37.44	159.586	0.720	21.7 × 17.0	5.5	0.45	
23	04:53:30.82	46:10:20.35	160.019	1.470	21.5 × 16.3	4.3	0.42	
24	04:47:55.26	44:13:43.16	160.885	−0.530	24.3 × 16.6	1.3	0.37	426
25	04:46:23.99	45:42:13.80	159.586	0.220	23.5 × 16.6	1.2	0.37	703, 414
26	04:58:27.75	46:18:15.45	160.452	2.220	23.6 × 17.1	3.6	0.40	426
27	05:01:32.02	45:37:21.12	161.318	2.220	23.9 × 17.0	3.1	0.39	426
28	05:01:55.06	45:07:38.02	161.751	1.970	23.7 × 16.7	1.9	0.38	414
29	05:00:04.97	44:19:30.33	162.184	1.220	24.0 × 16.6	1.7	0.37	703
30	04:57:53.61	44:00:56.31	162.184	0.720	24.2 × 16.6	0.9	0.40	703
31	04:53:08.43	43:52:56.36	161.751	−0.030	24.2 × 16.6	1.0	0.40	426
32	04:50:48.33	46:20:51.66	159.586	1.220	23.1 × 16.7	1.2	0.39	343
33	04:55:45.82	46:29:12.97	160.019	1.970	23.0 × 16.7	0.7	0.38	414
34	05:01:08.57	46:07:03.79	160.885	2.470	23.3 × 16.7	1.2	0.38	703
35	05:02:17.70	44:37:54.77	162.184	1.720	24.3 × 16.8	0.8	0.37	426, 343

[a] 3C 129 & 3C 129.1 (centred)
[b,c] 3C 129 & 3C 129.1 (off-centred)
[d,e] RFI on all short baselines

for time ranges during which the Sun was above the horizon. This measure is justified by the expected small sizes of our target sources. Additionally, Radio Frequency Interference (RFI) that affected flux and phase calibrators were flagged using the *clip* task which flags RFI by searching for amplitudes that are out of range. For the calibrators 3C 48 and 3C 147 we clipped amplitudes that were above 23 Jy and 29 Jy, respectively, after which we conducted an automated frequency dependent RFI flagging using *rflag*. In total, about 5% of all the uv-data was flagged. Gain and phase solutions were then determined and transferred to the visibility data of the science targets. The same calibrators

were used for bandpass corrections. Firstly, rough bandpass (BP) solutions were determined (task *bpass*) and examined. This was followed by further RFI flagging, if any, and the production of new BP solutions. The process was repeated, each time improving on the BP solutions. Once satisfied with the calibration results, we applied these to the uv-data of the science target. No self-calibration was performed.

Imaging Data Cubes

The calibrated uv-datasets were Fourier transformed into image cubes using the *imagr* task. For each pointing, eight data cubes were made as per the number of IF bands. The size of each image was 512 × 512 pixels with a pixel size of $6'' \times 6''$ and 256 channels. They were made using a *robust* weighting scheme set to 0.4, this being the best trade-off between the WSRT beam size and rms noise. Dirty beam image cubes corresponding to the antenna patterns were made for CLEANing purposes. They were 1024 × 1024 pixels in size, twice that of the image cubes. Since this is a blind survey, with the location of the H I emission not known beforehand, no CLEANing and continuum subtraction were done before or during the imaging process.

Continuum Subtraction

The removal of continuum sources as well as their instrumental responses from the data cubes was performed in the image plane for each of the eight IF bands in each cube using the Groningen Image Processing SYstem (GIPSY; van der Hulst et al. 1992). As an initial step the strongest continuum sources were masked and CLEANed. The initial CLEANing was conducted to mitigate the variability of their sidelobes from channel to channel, caused by the frequency dependent RFI flagging. This was followed by fitting a 0th-order polynomial baseline to the spectrum at each pixel including possible H I emission. After this initial baseline fit and subtraction, the rms noise per channel of each continuum-subtracted channel map was inspected. Data points above and below a chosen rms noise level were clipped and excluded from successive baseline fits. This procedure was repeated, each time increasing the baseline fit order until the 3rd order was reached, whilst gradually decreasing the rms noise clip levels down to $\pm 2\sigma$ so as to exclude the faint H I emission from the baseline fitting. The final 35 image cubes were produced by combining the eight IF bands for each pointing, excluding the first 5 and last 36 channels in each cube due to increased noise levels after the bandpass correction.

Figure 2.2 shows the rms noise as a function of velocity after continuum subtraction and Hanning smoothing in velocity. We achieved an average rms noise of 0.36 mJy/beam per channel, for a resolution of 16.5 km s^{-1}, with a

frequency dependent variation of less than 20% on average over the observed velocity range. This variation is due to RFI residuals as well as the bandpass roll-off at the edge of the IF bands and the 17 MHz standing wave ripple. Additionally 2 of the 35 pointings had severe residual RFI on all short baselines (i.e., less than 144m) which resulted in those baselines being completely flagged, hence increasing the noise in those cubes. Flagging all short baselines in these pointings decreased our inner UV coverage, which reduced the size of the largest structures to which our observations are sensitive. For instance in these fields we are sensitive to structures up to $7'$ in size, which is about $4\times$ smaller than what we would be sensitive to without RFI on the short baselines.

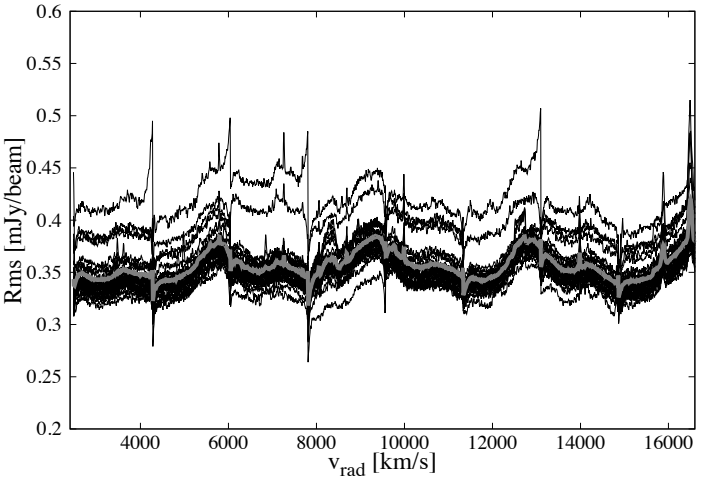

Figure 2.2 – The rms noise as a function of velocity in the 35 cubes after continuum subtraction and RFI flagging. The average noise level in each individual cube is mostly uniform at 0.36 mJy/beam over the whole observed velocity range. The average rms noise of all the individual cubes is illustrated by the thick grey line. Variations in the rms noise are frequency-dependent and caused by the bandpass roll-off in the overlapping regions of the eight IF bands, RFI residuals and the 17 MHz standing wave ripple. The increased rms noise in two of the fields is caused by severe RFI, which resulted in complete flagging of all their short baselines.

CLEANing and Mosaicking

To remove sidelobes of the synthesised beam, each of the 35 cubes were first CLEANed blindly to the 5σ noise level to remove the sidelobes from the brightest sources. The clean components were then restored with a Gaussian beam of $23'' \times 16''$ FWHM (PA $= 0°$). We then conducted a source finding procedure, as described in Sect. 2.3. The procedure resulted in defining those areas within the cube that contain only the identified H I signal in each channel. These areas were then used as masks to perform a new CLEAN image deconvolu-

tion down to the 0.33σ noise level. The final CLEANed cubes were combined into a mosaic to improve the sensitivity of the survey within the overlapping regions of the pointings. Mosaicking was conducted using the *flatn* task in AIPS which combines image cubes produced by *imagr*. Overlapping regions of images were averaged with a weighting scheme that accounts for the primary beam attenuation and the number of flagged visibilities.

An example of typical spatial noise variations in a mosaicked channel map, measured for each pixel over a range of 50 channels (nos. 411 to 460, i.e., the velocity range of 6903 to 7307 km s^{-1}) in the full primary-beam corrected mosaic is shown in Fig. 2.3. In these channels the average rms noise is $\sim$0.4 mJy beam^{-1} in the central region (black box in Fig. 2.3). It increases to 0.8 mJy beam^{-1} toward the edges due to the applied correction for primary-beam attenuation. Fig. 2.4 shows histograms of the spatial noise distribution for the primary-beam corrected mosaic (light grey) and the un-corrected mosaic (dark grey) in these channels as measured inside the area outlined by the black box. As expected, after applying the primary-beam correction, the peak of the distribution shifts to higher noise values while the distribution becomes broader.

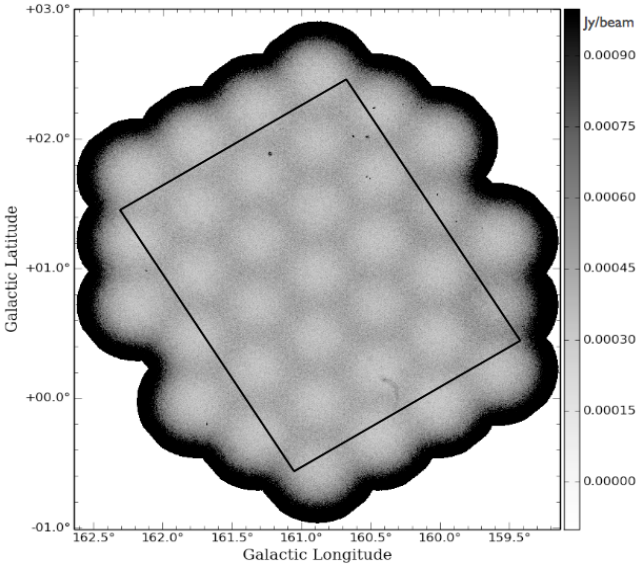

Figure 2.3 – An illustration of the spatial noise variation over 50 channels (nos. 411 to 460, or 6903 − 7307 km s^{-1} in radial velocity) out of the 1717 channels in our full, primary-beam corrected WSRT survey mosaic. Note the increase in the noise near the edges due to the applied correction for primary-beam attenuation. The black box outlines the inner region within which the spatial noise distributions, shown in Fig. 2.4, were calculated. The rms noise level values in Jy/beam are shown by the greyscale bar.

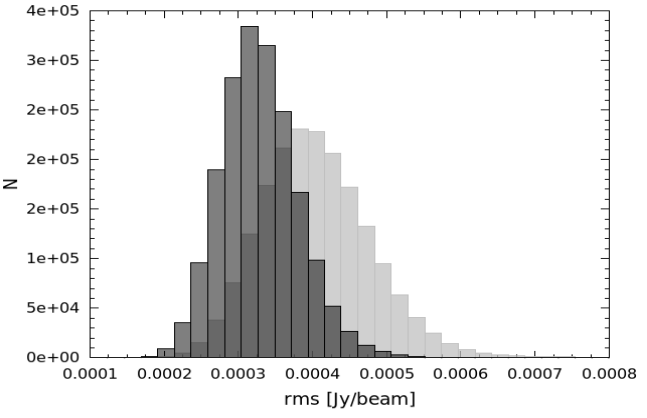

Figure 2.4 – An Illustration of the effect of the primary beam correction on the rms noise distribution. Histograms of the rms noise distribution measured over 50 channels within the inner regions (outlined by the black box in Fig. 2.3) of our full WSRT survey mosaic. The light grey distribution is measured from the primary-beam corrected mosaic and the dark grey from a mosaic without the primary-beam corrections.

2.3 Source Finding

Before compiling the list of sources detected, we investigated characteristics of the pixel value distribution in each of the 35 individual cubes without primary beam corrections so as to avoid spatial noise variations in the mosaicked cube, as illustrated by the light grey histogram in Fig. 2.4. We found four distinct trends in the distributions as illustrated in Fig. 2.5. The top panel displays the behaviour of the noise when there are neither imaging artefacts nor H I detections. Pixel values are then symmetrically distributed and near Gaussian. However, in cases where there are no imaging artefacts, but many H I detections (second panel), the pixel distribution is heavily skewed to positive pixels. Most sources detected in cubes with these characteristics are expected to be real. The third panel shows a negative and a more extended positive wing, representing cases where there are artefacts in the cube as well as real sources. The bottom panel shows a case with RFI residuals and imaging artefacts but no H I detections. In the latter two cases the wings are near symmetric and the positive peaks are unlikely to be due to real sources. Examples of representative imaging artefacts in the data cubes are shown in Fig. 2.6. The left panel shows gain calibration errors over only about 10 channels during half of the observation. The middle panel shows the effect of an imperfect bandpass after continuum subtraction. The right panel shows horizontal stripes due to remaining RFI. There was no one dominant source that caused these artefacts.

To find H I line emission from galaxies in the mosaicked cube, the spatial variation of the noise was largely removed by multiplying it by the weights cube given by $(1/\sigma^2)$, where σ is the weighted noise in each pointing. Source finding was then conducted in several steps using the GIPSY software. Firstly, the high resolution cube ($23'' \times 16''$) was smoothed to a beam size of $30'' \times 30''$ (bs30). Secondly, the high resolution and bs30 cubes were smoothed in velocity to four different resolutions, starting with Hanning smoothing (R2; 16.5 km s^{-1}) followed by a Gaussian smoothing kernel such that the FWHM of the resulting near-Gaussian spectral response function corresponds to four (R4; 33 km s^{-1}), six (R6; 49.5 km s^{-1}) and eight (R8; 66 km s^{-1}) channels, respectively. No down-sampling in spatial pixels or velocity channels was done after smoothing. Each of the 35 cubes was then searched at all eight different angular/velocity resolution combinations. Thirdly, for each resolution combination, channel maps were clipped at 8, 5, 4 and 3 times the rms noise level per channel. Lastly, a detection was accepted if it occurred at 8σ in a single velocity resolution element (i.e., in n-channels for Rn), at 5σ in 2 adjacent velocity resolution elements (2×n channels for Rn), at 4σ in 3 adjacent velocity resolution elements and at 3σ in 4 adjacent velocity resolution elements. All channels within a velocity resolution element had to be above the specified noise clip level. All the pixels containing the H I signal were combined into 3-dimensional masks. This automated source finding method resulted in 683 potential galaxy detection candidates.

A follow-up visual examination of all potential H I detections was conducted independently by two persons. This resulted in the rejection of a total of 235 as imaging artefacts due to residual RFI and side lobes of continuum sources (see Fig. 2.6 for examples). These artefacts occurred predominantly in the two pointings which had all short baselines removed due to RFI. As a result 90% of the automatically detected sources in these two pointings were rejected. This is not too severe because the two pointings with short baselines removed represent only a negligible fraction (0.1%) of all visibilities and (0.03%) of our total survey volume, while the affected data are still sensitive to structures up to $\sim 7'$ in size. The resulting list contained 448 remaining candidates. Visual inspection steps were taken to differentiate between real sources and those that resemble noise peaks in this list. We further removed 237 sources which were consistent with noise peaks or imaging artefacts based predominantly on their signal to local noise ratio. This led to a final detection list of 211 galaxies.

2.4 Data Products of Detected HI Sources

In this section we describe the methods used to determine the H I properties of galaxies detected. The structure of the H I catalogue and the atlas of the detections is discussed in Sect. 2.5.

2.4.1 The Global HI Profiles

The global H I profiles were made from the primary-beam corrected flux within the channel-dependent H I emission masks of the detected galaxies at the 16.5 km s^{-1} velocity resolution. Each profile was then partitioned into three velocity bins of equal width, referred to as the receding (r), the middle (m) and approaching (a) bins. We then determined the peak flux densities (F^p) in the three velocity bins as F^p_r, F^p_m and F^p_a, respectively. The three values were used to categorise the shape of the global profile as double-horned if $F^p_r > F^p_m < F^p_a$, Gaussian if $F^r_r < F^p_m > F^p_a$ and otherwise as asymmetric. For the double-horned profiles the peak flux densities on both the receding (r) and approaching (a) sides were considered separately for calculating their 20% and 50% levels. In the Gaussian and asymmetric cases only the absolute peak flux density was used. We then linearly interpolated between the data points from the profile centre outward to determine the velocities ($v_{r,20}$, $v_{a,20}$, $v_{r,50}$, $v_{a,50}$) corresponding to levels at 20% and 50% of the peak flux densities. It should be noted however, that for H I profiles with edges that are not consistently decreasing, this method tends to slightly underestimate the line widths.

The systemic velocity is determined according to;

$$v_{sys} = 0.25(v_{r,20} + v_{a,20} + v_{r,50} + v_{a,50}) \tag{2.1}$$

The profile line widths are measured using:

$$w_{20} = v_{r,20} - v_{a,20} \tag{2.2}$$

$$w_{50} = v_{r,50} - v_{a,50} \tag{2.3}$$

The total H I flux ($S_{\rm int}$) in Jy km s^{-1} was determined by integrating the global profiles according to;

$$S_{\rm int} = \Sigma S_\nu \Delta v \tag{2.4}$$

where S_ν is the H I flux density in Jy at each channel and Δv is the channel width in km s^{-1}.

For a particular galaxy, especially if it is spatially resolved, the size, shape and position of the H I clean mask changes from channel to channel due to the rotating H I disc. Thus the uncertainty in the flux also varies from channel to channel. To calculate the uncertainty in the flux of a global H I profile at each channel, we replicated the clean mask that encloses the H I emission and projected this at eight different line-free positions surrounding the detection. We then measured the signal in each of the eight projected masks and defined the uncertainty in the line flux from the galaxy as the rms scatter in the eight flux measurements in the projected masks.

2.4.2 Total HI maps

The total H I maps, showing the H I column density distributions were made using the CLEAN masks that define the H I emission from the CLEANed data cubes. These data cubes were corrected for primary beam attenuation. Pixels outside the CLEANed mask were set to zero and pixels inside the masks were summed up to build the H I maps. The advantage of this method is an attained higher signal-to-noise ratio at some pixels of the H I map. It does however, result in a non-uniform noise distribution across the map such that the 3σ column density level cannot be defined. We converted the pixel value of the H I map to column densities (in atoms cm^{-2}) using;

$$N_{\rm HI} = 1.82 \times 10^{18} \int T_{\rm b} dv \tag{2.5}$$

where T_b is the brightness temperature in Kelvin and dv is the channel width in km s^{-1} of the integrated H I emission line. For our survey, a typical $N_{\rm HI}$ sensitivity at the 3σ level is 5.3×10^{19} cm^{-2} where $dv = 16.5$ km s^{-1}.
The total H I mass of a galaxy (in M$_\odot$) was determined by calculating:

$$M_{\rm HI} = 2.36 \times 10^5 D^2 \int S_\nu dv \tag{2.6}$$

where D is the distance to the galaxy in Mpc measured according to:

$$D = \frac{v_{sys}}{H_0} \tag{2.7}$$

where H$_0$ is the Hubble constant and $\int S_\nu dv$ is the integrated global H I profile flux in Jy km s^{-1}.

We fitted a 2-dimensional Gaussian function to the H I map of each of the 211 detections. We then estimated the H I size ($D_{\rm HI}$) as defined by the fitted

Gaussian's major ($\Theta_{x,g}$) and minor ($\Theta_{y,g}$) axis FWHM in arcseconds such that $D_{\rm HI} = \sqrt{\Theta_{x,g} \times \Theta_{y,g}}$. The H I size ($D_{\rm HI}$) was then compared to that of the WSRT beam, $D_{\rm WSRT} = \sqrt{\Theta_x \times \Theta_y}$, where Θ_x and Θ_y are the beam FWHMs of 23″and 16″, respectively. An H I detection was defined as spatially resolved if $D_{\rm HI}$ exceeded $1.5 \times D_{\rm WSRT}$, otherwise it is considered marginally resolved. The resulting position angles of the fitted Gaussians were not corrected for the minimal effect of the slightly elongated synthesised beam which is oriented exactly North-South. The distribution of fitted position angles, however, does not show an excess of North-South orientations.

2.4.3 Radial Column Density Profiles

For the spatially resolved galaxies, the radial H I column density profiles were extracted from the total H I maps in which the pixel column density units were converted to $\rm M_\odot pc^{-2}$, by azimuthally averaging non-blank pixels in concentric elliptical annuli with radii along the semi-major axis of 5, 15, 25, 35,...,105″ with a width of 10″ and centred on the H I-centroid position of the galaxy. This position was defined as the centroid of the 2-dimensional Gaussian function fitted to the total H I map as described in Sect. 2.4.2. No corrections for beam smearing were applied. We averaged over the receding and approaching side separately to identify possible asymmetries. From the radial profiles, the H I radius ($\rm R_{HI}$) in kpc was measured as the radius where the mean surface density ($\Sigma_{\rm HI}$) drops to 1 $\rm M_\odot pc^{-2}$.

2.4.4 HI Velocity Fields

The velocity fields of the spatially resolved H I discs were produced by fitting a Gaussian to the R2.bs30 velocity profile at each pixel. The fitting algorithm used initial estimates for the amplitude, central velocity and velocity dispersion of the Gaussian function. The initial amplitude estimate simply is the peak flux density, whereas the initial estimates for the velocity centroid and dispersion are based on the flux-weighted first and second moment of the non-blank pixel profile, respectively. The advantage of fitting Gaussians instead of measuring the standard flux-weighted moments is that we can specify ranges within which the fitted parameters and their uncertainties must lie in order for a fit to be accepted. Fits were accepted only if 1) the central velocity lies within the H I mask, 2) the uncertainty in the velocity centroid is less than 10 km $\rm s^{-1}$, and 3) the velocity dispersion lies within the range of $5 - 50$ km $\rm s^{-1}$. This approach, however, does result in velocity fields that are patchy with holes where the signal-to-noise ratio is too low to obtain an acceptable fit.

2.4.5 Position-Velocity Diagrams

A position-velocity diagram (PVD) illustrates the shape of a projected rotation curve and the presence of a possible kinematic asymmetry of the rotating gas disc. Ideally, a PVD should be extracted along the kinematic major axis of an inclined rotating disc and centred on its dynamical centre. Usually, this geometry is derived from 2-dimensional velocity fields which are available only for the spatially resolved galaxies in our survey. Hence we followed different strategies for the resolved and marginally resolved galaxies.

For the PVDs of the resolved galaxies in our survey we estimated by eye the position angle of the receding side of the kinematic major axis by considering the direction perpendicular to the kinematic minor axis indicated by the green isovelocity contour of the velocity field depicted in the accompanying atlas. No detailed analysis of the velocity fields was carried out as this is planned for a forthcoming publication. The dynamical centres of the rotating gas discs were not derived from their 2-dimensional velocity fields but instead were assumed to coincide with the morphological centre of the UKIDSS image (see section 2.4.6). In those cases where an infrared counterpart could not be identified, the dynamical centre was assumed to coincide with the centroid of the Gaussian function fitted to the H I column density map.

For the PVDs of the marginally resolved galaxies we adopted the centroid and position angle of the 2-dimensional Gaussian fitted to the H I column density maps. In those cases where an infrared counterpart could be identified, we adopted the morphological centre of the UKIDSS image as the dynamical centre of the PVD. In case the UKIDSS image showed a clear elongation, we estimated by eye the position angle of the infrared image and adopted this as the kinematic major axis. For the marginally resolved galaxies, uncertainties in the exact position angle and dynamical centre have little effect on the PVD.

We extracted the PVDs from the Hanning smoothed cubes (R2) as well as from the cubes smoothed to 66 km s^{-1} resolution (R8), both at the $23'' \times 16''$ angular resolution

2.4.6 Counterparts

The sky area covered by our survey has a Galactic foreground extinction in the B-band of up to $A_B \sim 4.5$ mag. This makes optically identifying galaxies very difficult. However, the near-infrared wavelength opens a more transparent window since the extinction is less severe. We searched for NIR counterparts in the K-band images of the UKIRT Infrared Deep Sky Survey (UKIDSS; Hewett et al. 2006 Lawrence et al. 2007, Casali et al. 2007, Hambly et al. 2008). "UKIDSS uses the UKIRT Wide Field Camera (WFCAM; Casali et al.

2007 and a photometric system described in Hewett et al. 2006. The pipeline processing and science archive are described in Irwin et al (2008) and Hambly et al. 2008. We used data from the 10^{th} Galactic Plane Survey (GPS) data release, which is described in detail in Lucas et al. 2008"[1]. The WSRT PP ZoA survey overlaps with the UKIDSS GPS (Lucas et al. 2008) which has mapped 1800 deg^2 of the northern GP to a K-band depth of $K = 19.0$ mag (AB system).

The UKIDSS images were searched in two steps. Firstly, the UKIDSS GPS catalogue was searched for galaxy counterpart candidates that were within $1'$ radius of the H I positions. Only candidates closest to the H I positions were considered as likely counterparts. These were then verified by a visual inspection of UKIDSS GPS images within the search radius in the J, H and K bands (pixel size of $0.2''$). Secondly, to ensure that no potential counterparts were missed, the search radius was increased to $2'$. For this step, only those H I positions without a verified galaxy counterpart in the first step were cross-checked and verified by visual inspection as well. In some cases a UKIDSS image could not be used due to imaging artefacts. We then searched for 2MASS images instead, in the same manner as for UKIDSS.

Of all H I detected galaxies, 62% were found to have at least one near-infrared counterpart in the UKIDSS GPS catalogue, with an average offset of $2.6''$ from the H I position. The other 38% did not show any plausible counterpart close to the H I position.

Additionally, we also searched the Wide-field Infrared Survey Explorer (WISE; Wright et al. 2010) images for counterparts, by inspecting the W1 (3.4 μm), W2 (4.6 μm) and W3 (12 μm) colour composite images. For this search we examined images $3'\times\ 3'$ in size, specially constructed for the field using the method described in Jarrett et al. (2012). Only those galaxies closest to the H I position were considered and verified by eye as counterparts. In total 47% of the galaxies detected in H I were found to have a WISE counterpart.

In a further step, we investigated H I properties that might have affected the recovery of a UKIDSS counterpart. They are displayed in Fig. 2.7 where we plot the total H I mass of all detected galaxies as a function of velocity and their w_{50} line width as a function of H I mass. Detections with near-infrared counterparts are shown in red and those without a counterpart in blue. We find relatively more counterparts for H I-massive $\log(M_{\rm HI}/{\rm M}_\odot) = 9.5$ galaxies with large line widths ($w_{50} > 150$ km s^{-1}). We also note that most galaxies below $\log(M_{\rm HI}/{\rm M}_\odot) = 8.4$ do not have identifiable near-infrared counterparts. These low H I-mass detections are usually gas-rich, low surface brightness galaxies

[1] http://www.ukidss.org/

and are not easily detectable in the near-infrared.

In Fig. 2.8 we overlay the spatial distribution of the H I detections on a K-band Galactic extinction (A_K) map from the DIRBE/IRAS[1] data (Schlegel, Finkbeiner & Davis 1998, Schlafly & Finkbeiner 2011). Galaxies with near-infrared counterparts are indicated in red and those without in blue. The observed WSRT mosaic is outlined by the black dashed contour. The plot indicates that finding a galaxy counterpart at $\ell \approx 160°$ behind the GP does not seem to depend on Galactic extinction. The small group of H I detections without a near-infrared counterpart in the top left of the plot is due to poor UKIDSS imaging in that area.

2.5 The HI catalogue and atlas

2.5.1 The HI catalogue

The derived H I parameters of all detected galaxies are listed in tables presented. The first table (A1) lists the resolved galaxies and the second table (A2) the marginally resolved galaxies (see Sect. 2.4.2 for details on how sources were divided into these two categories). The first 10 entries of each of these tables are shown in Tables 2.2 and 2.3 to illustrate their structure. The column entries of the 211 H I detections are as follows:

Column (1): Galaxy designated identification based on the Right Ascension and Declination (J 2000.0) of the H I centroid.

Column (2)&(3): Galactic longitude and latitude in degrees.

Column (4): Systemic velocity in the barycentric-standard of rest (BSR) defined by the central velocity in km s^{-1} of the global H I profile.

Column (5) & (6): Observed H I profile line widths and their uncertainties (in km s^{-1}) measured at 20% and 50% level of the H I profile peak flux, respectively, determined at a velocity resolution of 16.5 km s^{-1}.

Column (7): The integrated H I flux ($S_{\rm int}$) corrected for primary beam attenuation, in Jy km s^{-1}.

Column (8): Luminosity distance D to the galaxy in Mpc derived from the systemic velocity measured in the BSR.

Column (9): The total H I mass in $M_\odot$.

[1] http://irsa.ipac.caltech.edu/applications/DUST/

Column (10): The H I radius measured at the $1\,M_{\odot}\,pc^{-2}$ surface density level (R_{HI}) in kpc, given for resolved sources only.

Column (11): Indication of an infrared counterpart, found in either UKIDSS (u), WISE (w) or 2MASS (m).

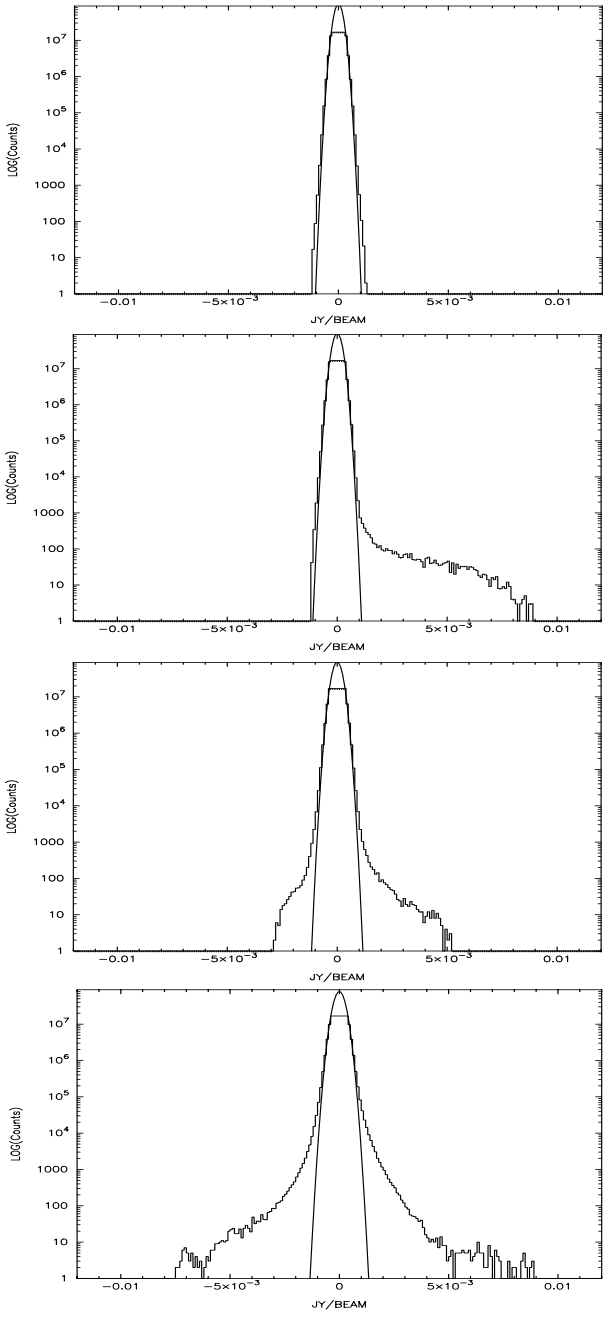

Figure 2.5 – Statistics of pixel values in individual cubes with a Gaussian curve overlaid, illustrating the four distinct characteristic cases identified. The top panel represents cases where there are neither imaging artefacts nor HI detections. In the second panel there are no imaging artefacts but many HI detections. The third panel illustrates cases in which there are imaging artefacts as well as HI detections. The bottom panel represents cases where there are no HI detections but many imaging artefacts and RFI residuals.

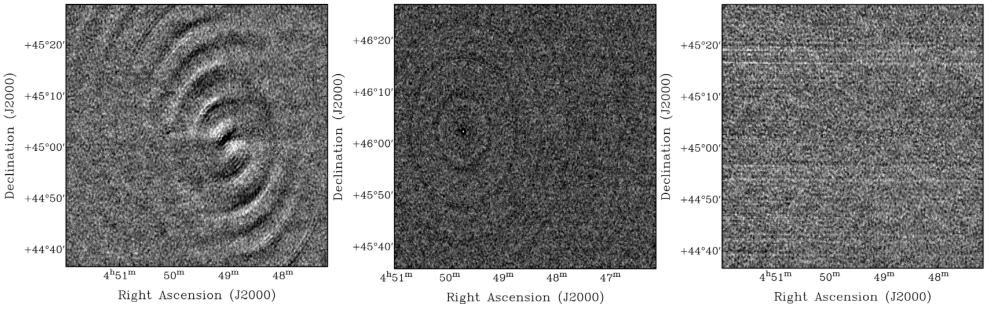

Figure 2.6 – Examples of various types of imaging artefacts in the data cubes. The left panel shows artefacts caused by gain calibration errors over a small number of channels during half of the observation of the respective pointing. The middle panel shows artefacts due to bandpass imperfections after continuum subtraction. The right panel shows stripes caused by remaining RFI.

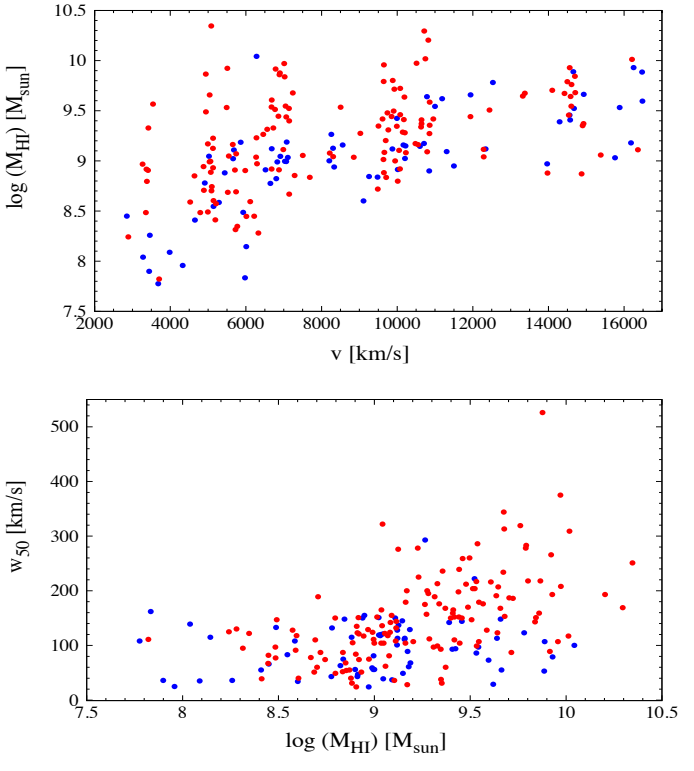

Figure 2.7 – A comparison between global HI properties of detected galaxies with near-infrared counterparts (red) and without (blue). The top panel shows the total HI mass as a function of radial velocity. The bottom panel shows the w_{50} line width as a function of total HI mass.

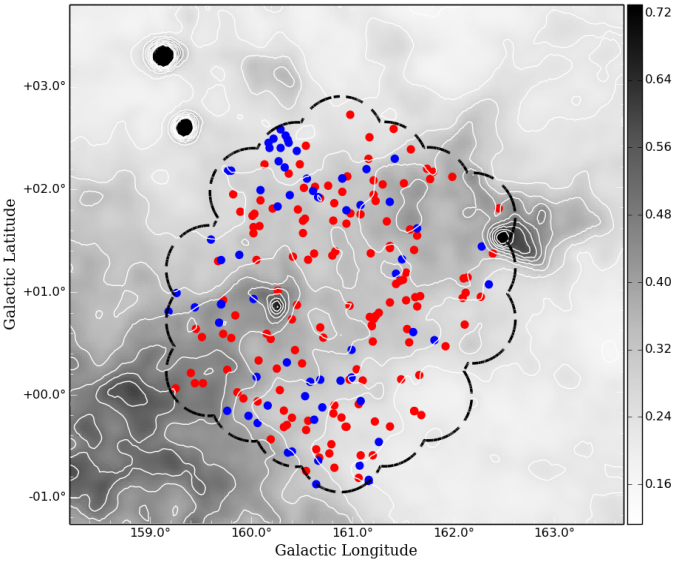

Figure 2.8 – The spatial distribution of galaxies detected in HI. Galaxies with a near-infrared counterpart are shown in red, those without a counterpart in blue. They are superimposed on a DIRBE/IRAS map of A_K Galactic extinction values in the NIR K band, ranging from 0.16 to 0.72 mag as shown on the greyscale bar. These correspond to $A_B = 1.8$ to 8.0 mag, respectively in the B band optical.

Table 2.2 – A sample table showing the structure of the catalogue for resolved galaxy detections. The full table is available in Appendix A1

ZoA	ℓ	b	v_{rad}	w_{20}	w_{50}	$S_{\rm int}$	D	$\log(M_{\rm HI})$	$R_{\rm HI}$	counterpart
	deg	deg	km s^{-1}	km s^{-1}	km s^{-1}	Jy km s^{-1}	Mpc	M$_\odot$	kpc	
(1)	(2)	(3)	(4)	(5)	(6)	(7)	(8)	(9)	(10)	(11)
J044427.17+455116.7	159.25	0.06	5506 ± 04	285 ± 14	266 ± 09	5.68 ± 0.41	79	9.9	24.2	u –
J044521.10+454432.8	159.44	0.11	5134 ± 03	290 ± 07	278 ± 07	1.34 ± 0.10	73	9.2	12.4	u –
J044542.87+442101.0	160.54	-0.75	10717 ± 01	198 ± 04	169 ± 03	3.57 ± 0.10	153	10.3	33.5	u –
J044602.33+443426.8	160.40	-0.56	6281 ± 03	117 ± 10	100 ± 06	5.78 ± 0.45	90	10.0	31.0	– –
J044632.27+452152.2	159.86	0.02	9740 ± 02	226 ± 06	212 ± 08	0.66 ± 0.05	139	9.5	17.4	u w
J044644.10+442004.0	160.67	-0.62	5654 ± 05	194 ± 13	179 ± 13	0.94 ± 0.09	81	9.2	12.7	u w
J044644.74+444734.7	160.32	-0.32	5709 ± 03	156 ± 09	135 ± 10	0.51 ± 0.05	82	8.9	9.9	u –
J044700.10+442439.7	160.64	-0.54	10747 ± 02	330 ± 07	309 ± 05	1.86 ± 0.09	154	10.0	35.8	u w
J044706.91+453449.0	159.76	0.24	4994 ± 03	216 ± 08	200 ± 06	1.24 ± 0.06	71	9.2	14.0	u w
J044727.30+445342.4	160.32	-0.16	5523 ± 02	69 ± 06	51 ± 06	0.33 ± 0.03	79	8.7	7.9	u –

Table 2.3 – A sample table for marginally resolved galaxy detections. The full table is available in Appendix A2.

ZoA	ℓ	b	v_{rad}	w_{20}	w_{50}	$S_{\rm int}$	D	$\log(M_{\rm HI})$	counterpart
	deg	deg	km s^{-1}	km s^{-1}	km s^{-1}	Jy km s^{-1}	Mpc	M$_\odot$	
(1)	(2)	(3)	(4)	(5)	(6)	(7)	(8)	(9)	(10)
J044524.14+451924.3	159.76	-0.16	6830 ± 06	108 ± 18	59 ± 16	0.43 ± 0.07	98	9.0	– –
J044533.70+441127.9	160.64	-0.88	2852 ± 01	90 ± 02	66 ± 03	0.71 ± 0.05	41	8.4	– –
J044540.97+454045.8	159.52	0.11	9660 ± 02	153 ± 06	142 ± 08	0.27 ± 0.03	138	9.1	u –
J044541.51+455022.6	159.40	0.21	14584 ± 03	217 ± 09	123 ± 07	0.43 ± 0.05	208	9.6	u –
J044546.04+444901.5	160.19	-0.44	5134 ± 05	94 ± 34	51 ± 10	0.68 ± 0.09	73	8.9	u –
J044550.59+443552.5	160.36	-0.57	16249 ± 05	95 ± 13	79 ± 16	0.67 ± 0.10	232	9.9	– –
J044556.60+450741.4	159.97	-0.21	6803 ± 03	82 ± 14	63 ± 08	0.30 ± 0.04	97	8.8	– –
J044559.91+450104.1	160.06	-0.28	12528 ± 05	171 ± 10	123 ± 42	0.80 ± 0.13	179	9.8	– –
J044630.07+451655.0	159.92	-0.04	10229 ± 05	170 ± 12	124 ± 18	0.24 ± 0.04	146	9.1	u w

2.5.2 The HI atlas

The HI data products described in Sect. 4 are presented here for all detected galaxies. They are shown in an HI atlas composed of two sections. The first section shows the resolved galaxies (one galaxy per page). The second provides maps of the marginally resolved galaxies (three per page). Schematics of the display panels are given in Figs. 2.9 and 2.10, respectively. An example page of the resolved and marginally resolved cases is presented in Figs. 2.11 and 2.12, respectively, the full atlas is available in Appendix. A. The panels presented in the respective atlases are:

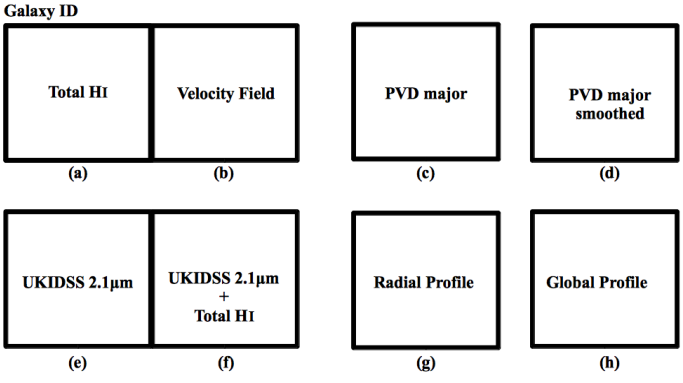

Figure 2.9 – Schematics of the panel arrangement of the derived HI data products for resolved galaxies.

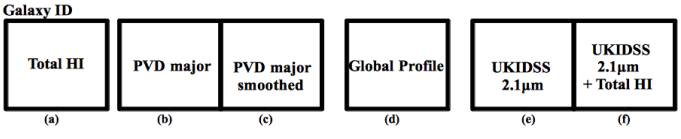

Figure 2.10 – Schematics of the panel arrangement of the derived HI data products for marginally resolved galaxies.

Total HI map: The total HI maps are presented at full angular resolution in panel (a) of Figs. 2.9 and 2.10. The HI column density contour levels are at 1, 2, 4, 8, 16, 32... $\times$ 10^{20} atoms/cm^2. The FWHM beam size is indicated by the hatched ellipse. The dashed line indicates the direction of the morphological major axis determined as the position angle of the fitted 2-dimensional Gaussian. The adopted HI centre position is indicated by a small white cross.

Velocity fields: In panel (b) of Fig. 2.9 the HI velocity fields are presented at an angular resolution of 30 arcseconds (not shown for marginally resolved galaxies in Fig. 2.10). Pixels shown in grey scales are where the radial velocity was measured. Lighter greyscales and blue contours show the approaching side, darker and red contours the receding side of the rotating HI disc. The systemic velocity as derived from the global HI profile (v_{sys}) is shown by the green contour. Contours are drawn from v_{sys} at intervals of 5, 10, 15, ..., 30, 35 km s^{-1} depending on the width of the global HI profile. The dashed line indicates the adopted kinematic major axis and the white circle indicates the location of the adopted dynamical centre. The FWHM beam size is indicated by the hatched circle.

Position velocity diagrams: Shown in panels (c) and (d) of Fig. 2.9 and (b) and (c) of Fig. 2.10 are the major-axis position-velocity diagrams (PVDs) at full angular resolution (23″and 16″). The panels show the PVD at a velocity resolution of 16.5 km s^{-1} (left) and 66 km s^{-1} (right), respectively. The position angle is indicated in the top left corner of each panel. The horizontal dashed line indicates the systemic velocity and the vertical dashed line the adopted centre of rotation. The red contour outlines the HI emission clean mask within which the integrated flux was determined. Contour levels are -3 (dashed), -1.5 (dashed), 1.5, 3, 4.5, 6, 9, 12, 15, 20, 25, 30 times the local rms noise level.

Near-Infrared images: Panels (e) of Fig. 2.9 and Fig. 2.10 respectively show the $1' \times 1'$ and $0.5' \times 0.5'$, near-infrared UKIDSS GPS K-band (2.1 μm) images (Lucas et al. 2008, Lawrence et al. 2007). For cases where an UKIDSS image was unavailable due to imaging artefacts, a 2MASX Ks-band (2.1 μm) image is shown instead. The white cross indicates the HI centre position. In panels (f) of Figs. 2.9 and Fig. 2.10, we overlaid the contours of the total HI map on a $2.5' \times 2.5'$ sized version of the near-infrared image, to show the extent of HI in comparison to the NIR component of the galaxy. For the resolved galaxies, the white cross and circle indicate the HI position and adopted dynamical centre respectively. For the marginally resolved galaxies, the dashed line, if present, indicates the position angle of the identified near-infrared counterpart.

Radial density profile: The radial HI column density profiles, corrected for a face-on orientation, are shown only for the resolved galaxies in panel (g) of Fig. 2.9. The red and blue points indicate the receding and approaching side respectively. The connected black points indicate the azimuthally averaged profile. The HI radius $R_{\rm HI}$ where the azimuthally averaged column density has dropped to 1 $M_{\odot}pc^{-2}$ is indicated by the vertical arrow. No correction for beam-smearing has been applied.

Global Profile: Figures. 2.9 and 2.10, panels (d) and (h), show the global HI profiles. The connected black dots give the primary-beam corrected integrated HI flux density in each channel at a velocity resolution of 16.5 km s^{-1}. The grey thick line is the HI profile derived from cubes that have been smoothed to 66 km s^{-1}. Indicated errors are derived as described in Sec. 2.4. The vertical arrow points to the systemic velocity.

2.5.3 Previous HI Detections

We cross-correlated our detections with HI detections reported in the literature. This was carried out using the NASA/IPAC Extragalactic Database (NED) and the Lyon/Meudon Extragalactic Database (HyperLeda). Using positional and velocity information, both databases were searched for galaxies previously detected in HI over our entire volume. We also made a comparison with the unpublished results of the NRT 2MASX HI follow-up survey (Kraan-Korteweg et al., in prep.). Three galaxies were found, all of which had been observed with the NRT. All three were also detected in our WSRT survey. It is not surprising that only three galaxies were found in these databases, given the paucity of previous observations and detections over our WSRT survey area. The two galaxies with published HI data were initially identified in optical searches by Weinberger (1980) and subsequently observed in HI (Chamaraux et al. 1990, Paturel et al. 2003). The third galaxy was detected in the NRT 2MASX HI follow-up survey.

The HI parameters measured by them and those of our survey are given in Table 2.4. The respective values of velocity and line widths of all three galaxies are in good agreement. The integrated fluxes ($S_{\rm int}$) of ZoA J045747.05+460717.5 and its literature counterpart are also in good agreement. However, our WSRT integrated flux measurement of ZoA J045132.28+442922.2 is six times lower than that of PGC 016173 as measured by Paturel et al. (2003). To investigate this discrepancy, the

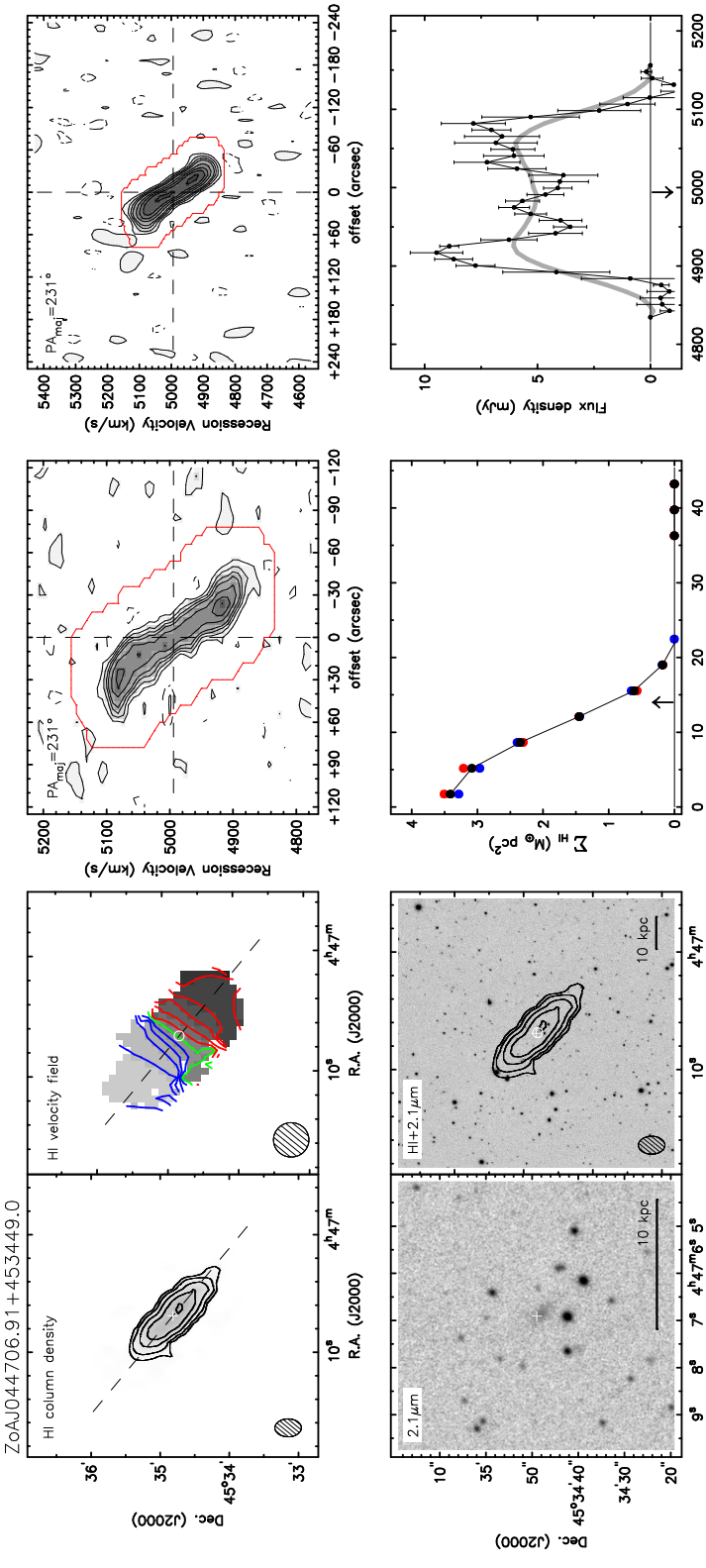

Figure 2.11 – A sample atlas page for resolved sources.

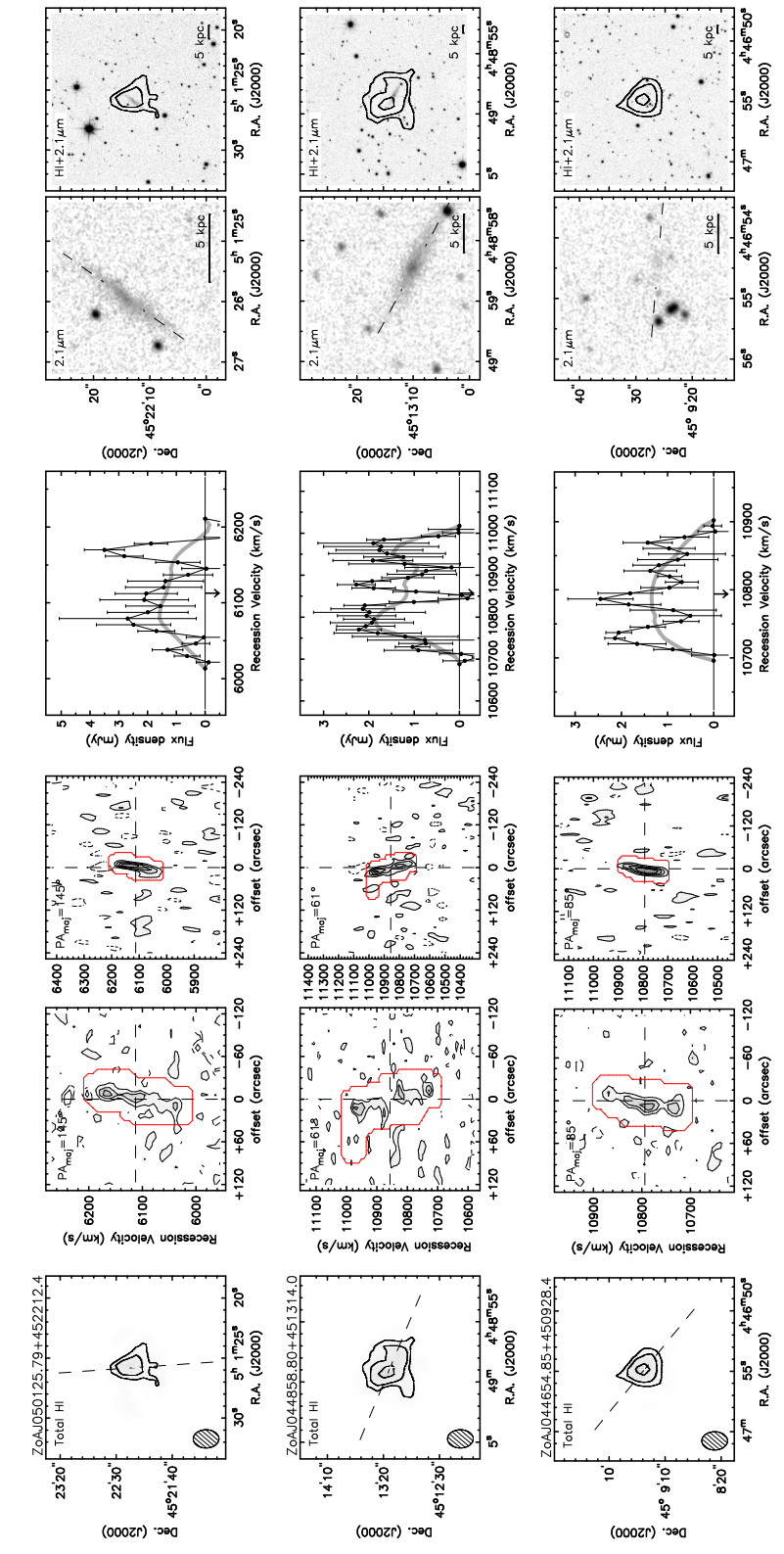

Figure 2.12 – A sample atlas page for marginally resolved sources.

relevant WSRT HI data cube was carefully examined by eye. No indication of any missed HI emission was found at that location. We then searched for a nearby, possibly confusing source within the large NRT beam (22′ FWHM in Declination). Its presence is indeed confirmed and illustrated in Fig. 2.13 which shows the HI column density map of the targeted galaxy in a larger field of view for the radial velocity range of $4752 - 5576$ km s^{-1} together with the respective NRT beams. In this total HI map our WSRT HI detection cross-identified with PGC 016173 corresponds to the southernmost galaxy in this group. It is obvious that the NRT beam picked up excess HI flux from the nearby HI-bright galaxy Wein 069 at top left, with an integrated flux as measured with the WSRT of 17.6 Jy km s^{-1}, explaining the higher NRT flux measurement.

For the third detection in common, ZoA J045145.44+443610.2 or Wein 069, we measured a slightly higher total integrated flux than Chamaraux et al (1990). This galaxy is in fact the large easternmost source in Fig. 2.13. Its HI diameter is large (72.8 kpc), resulting in an incomplete flux measurement for the narrow NRT beam.

We cannot provide any further statistical comparison with the literature, given the fact that only three previous detections were cross-identified with our detections.

Table 2.4 – A comparison of HI profile parameters with literature values.

ZoA	v km s^{-1}	w_{50} km s^{-1}	w_{20} km s^{-1}	$S_{\rm int}$ Jykm s^{-1}
(1)	(2)	(3)	(4)	(5)
PGC 016173 (Wein 072) [1]	5201	255	323	6.70
J045132.28+442922.2	5129±4	276±11	305±11	1.06±0.07
Wein 069 [2]	5178	–	285	14.60
J045145.44+443610.2	5086±1	251±2	269±1	17.63±0.32
04574731+4607167 [3]	7199±9	370	408	4.27±0.56
J045747.05+460717.5	7013±1	375±3	393±3	3.96±0.11

[1] Paturel et al. 2003
[2] Chamaraux et al. 1990
[3] Kraan-Korteweg et al, in prep.

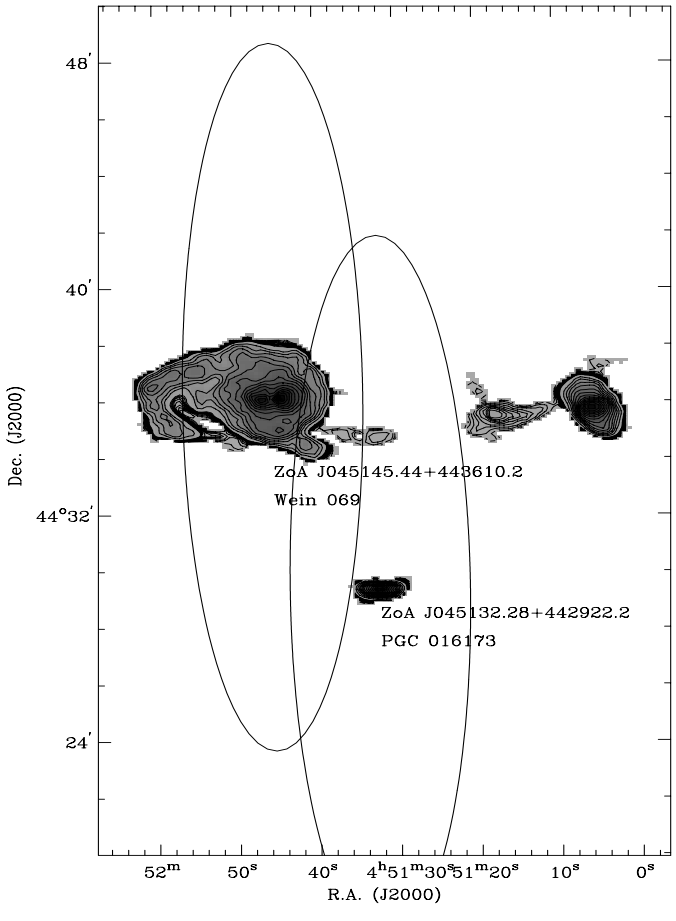

Figure 2.13 – An illustration to show why our measured WSRT flux of ZoA J045132.28+442922.2 is six times lower than the NRT value reported by Paturel et al. (2003). The WSRT total HI maps of ZoA J045145.44+443610.2 (Wein 069, on the left) and ZoA J045132.28+442922.2 (PGC 016173, at the bottom) with the NRT FWHM beam sizes of the reported literature detections overlaid. The NRT detection of the latter is confused by the former, which is much stronger. In addition, we detected ZoA J045105.4+443544.0 at a similar recession velocity on the right.

The completeness of our catalogue is defined as the fraction of sources detected by the survey from an underlying sample distribution. As a first estimate for this paper we use the integrated flux to estimate the completeness based on an empirical approach. Our method is based on inserting artificial sources throughout the surveyed volume and determining the rate at which they are recovered with our source finding scheme.

The artificial galaxies were based on simulations by Obreschkow et al. (2009a) who for about 3×10^7 galaxies evaluated the cosmic evolution of the atomic and molecular phases of the cold gas. Their simulations were based on the Semi-analytic Suite of SKA Simulated Skies (S^2-SAX; De Lucia & Blaizot 2007) and are built on physical models applied to the semi-analytical model of evolving galaxies for the Millennium simulations (Springel et al. 2005). They cover a redshift range of $z = 0 - 1.2$, a sky area field of 10 deg^2 and comprise galaxies with HI-peak flux $\geq 1\mu$Jy (Obreschkow et al. 2009b).

For our survey volume the simulations predict HI properties for 1183 galaxies spanning HI masses and integrated fluxes ranging from $\log(M_{HI}/M_\odot) = 6.05-10.26$ and $S_{int} = 0.001-4.149$ Jy km s^{-1}, respectively. The set of evaluated HI properties of each galaxy were used to build a detailed 3-dimensional model of the spatial and spectral distribution of the HI line emission. All of the 3-dimensional models were inserted in a single large synthetic cube matching our survey volume and the distribution of large-scale structures. This cube was then spatially smoothed to match the $23'' \times 16''$ beam of our WSRT observations. This final synthetic cube served as our noise-free sky model which was subsequently added to our observed data cube.

The data cube with the inserted artificial sources was then searched using the same procedure and detection criteria used to search for real galaxies as described in Sect. 2.3. No visual inspection of the artificial sources was done since their positions and redshifts were known a priori. The real sources were then removed from the list of detections such that only the detected artificial sources remained. A total of 101 artificial sources were recovered. The completeness for the whole WSRT survey was estimated by measuring the fraction of artificial sources recovered in given integrated flux and HI mass bins as represented Fig. 2.14.

From the detection rates of the simulated galaxies it follows that the WSRT PP ZoA survey is complete for objects with $\log(S_{int}/\text{Jy km s}^{-1}) > -0.45$ ($S_{int} = 0.35$ Jy km s^{-1}). The minimum integrated flux of an object to be detected by the WSRT PP ZoA survey is $\log(S_{int}/\text{Jy km s}^{-1}) > -0.98$ ($S_{int} = 0.1$ Jy km s^{-1}). From the bottom panel of Fig. 2.14 we show that our survey is complete for galaxies with HI masses of $\log(M_{HI}/M_\odot) > 9.5$.

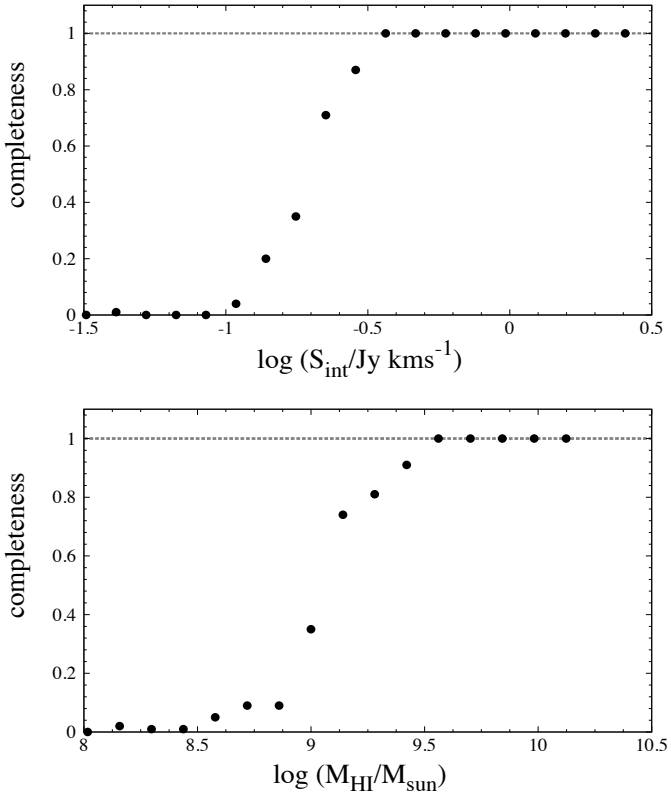

Figure 2.14 – Completeness of the WSRT PP ZoA survey as function of the integrated HI line flux (top panel) and the HI mass (bottom panel). Points represent the fraction of artificial objects recovered in each bin. The grey dotted horizontal line represent where the survey is complete.

We do however note that completeness is not just a measure of one parameter. A correction has to be made by integrating over another parameter such as the line width and peak flux as well as applying weighting to account for the relative source abundance in each parameter bin. In addition, given the depth of the survey, we expect the completeness to vary as a function of velocity. The completeness presented should therefore be regarded as a first approximation. In a forthcoming paper of this series we will provide a more robust verification and description.

2.6 The Distribution of HI Properties of Detected Galaxies

To investigate the H I properties of the 211 detected galaxies, we plot the distributions of a number of their measured global H I parameters in histograms (see Fig. 2.15): their radial velocities, w_{50} line widths, integrated line fluxes and total H I masses.

We have visually identified four main overdensities along the line of sight by assessing their velocity distribution in combination with their spatial distribution. Since these features are located in the Auriga (Aur) constellation, we name them accordingly Aur 1 to Aur 4. The nearest peak in redshift space is at 3000 km s^{-1} (Aur 1) and may be a galaxy group, whereas the most prominent and broadest overdensity extends over $4500 - 7500$ km s^{-1} (Aur 2), i.e., at the approximate PPS redshift range. This is followed by a further distinctive peak at $9500 - 11000$ km s^{-1} (Aur 3) and a narrower peak close to the high-end redshift range of our survey, at 15000 km s^{-1} (Aur 4). Of all the detections, 41% and 34% are associated with the two most prominent peaks Aur 2 and Aur 3, respectively. In between these peaks, regions nearly completely devoid of galaxies are evident, indicating a wide range of cosmic environments probed with this interferometric survey over a wide velocity range. Further details on these structures are given in Sect. 2.7.

In the w_{50} line widths histogram, the widths range from $24 - 526$ km s^{-1}, but most of the galaxies have $w_{50} < 225$ km s^{-1} and group around an average of 132 km s^{-1}. This is lower than the average w_{50} of 186 km s^{-1} of the $\alpha.40$ catalogue of the Arecibo Legacy Fast ALFA survey (ALFALFA $\alpha.40$; Haynes et al. 2011). This difference can be explained by the relatively large coverage ($\sim$2800 deg^2) and lower sensitivity of 2.2 mJy of the ALFALFA survey, which leads to a higher average H I mass of $\log(M_{\rm HI}\ /\ {\rm M}_\odot) = 9.5$ (see Fig. 2.16) and therefore a larger average line width (c.f., bottom panel of Fig. 2.7)

In the distribution of the integrated line fluxes, the average value is $\log(S_{\rm int}/{\rm Jy\,km\,s^{-1}}) = -0.32$, and the fluxes span the range from $\log(S_{\rm int}/{\rm Jy\,km\,s^{-1}}) = -1.40$ to 1.25, while the majority is restricted to a much tighter range of $\log(S_{\rm int}/{\rm Jy\,km\,s^{-1}}) = 0.6$ to 1.0 ($0.35 < S_{\rm int} < 1.0$ Jy km s^{-1}).

The H I mass distribution ranges from $\log(M_{\rm HI}/{\rm M}_\odot) = 7.7$ to 10.3. This is not excessively high compared to the most H I-massive galaxies known, which can reach 10.8 (e.g. Cluver et al. 2010). This is due to the relatively small volume surveyed. The overall galaxy distribution has a

mean HI mass of $\log(M_{\rm HI}/{\rm M}_\odot) = 9.1$, which is below that of ALFALFA of $\log(M_{\rm HI}/{\rm M}_\odot) = 9.5$. There is a non-negligible fraction of lower HI mass detections.

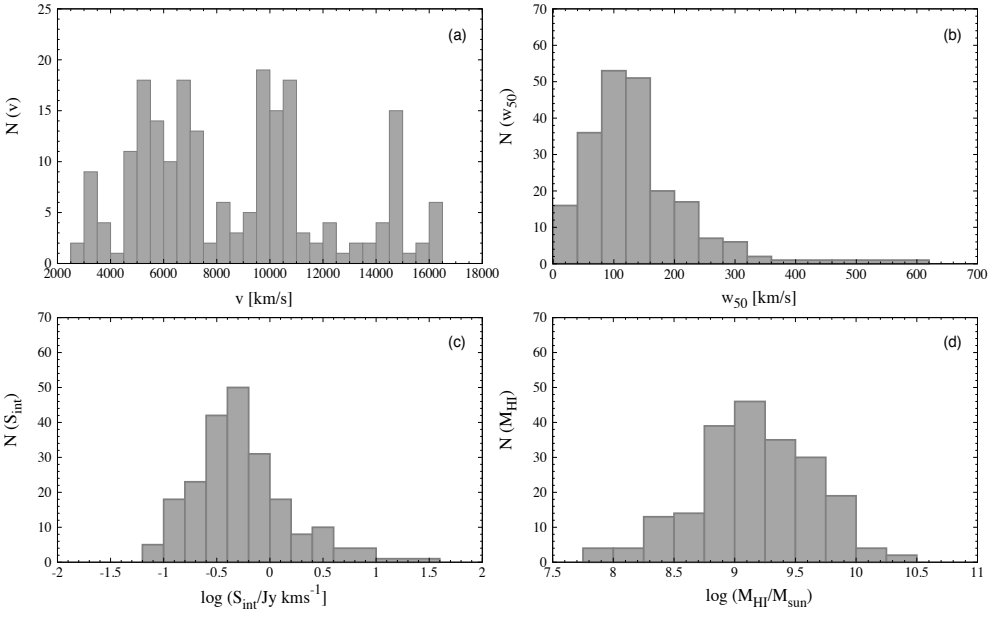

Figure 2.15 – Distributions of selected HI parameters of the WSRT ZoA PP detected galaxies. Top left: radial velocity (v). Top right: line width at the 50% peak flux level (w_{50}). Bottom left: logarithm of the integrated line flux ($\log S_{\rm int}/{\rm Jy\,km\ s^{-1}}$). Bottom right: logarithm of the total HI mass.

To assess where galaxies with different HI masses are found in redshift, we plot in Fig. 2.16 our HI masses as function of radial velocity. The black curve shows the predicted HI mass detection limit of our survey at the 3σ noise level for a galaxy with w_{50} of 150 km s^{-1}. The two prominent peaks indicating clustering at about 6000 and 10000 km s^{-1} are once again evident. Galaxies found at these distances have HI masses ranging from $\log({\rm M_{HI}}/{\rm M}_\odot) = 7.8 - 10.3$ and $8.6 - 10.3$, respectively. To gauge how the HI masses of our detections compare to those from other surveys, we also show HI masses from the ALFALFA survey in grey. In general we find objects with lower HI masses at all velocities which is consistent with the lower rms noise of $\sim$0.4 mJy of our WSRT survey compared to the 2.2 mJy of ALFALFA.

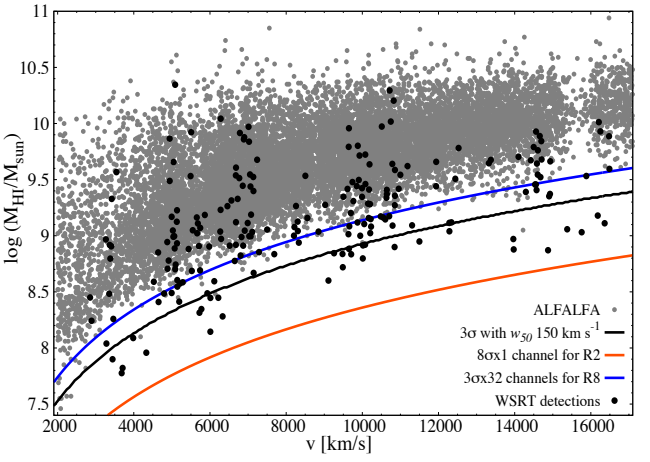

Figure 2.16 – Logarithm of total HI masses of galaxies detected in our survey (black dots) and the ALFALAFA survey (grey points) as a function of radial velocity. The black curve indicates the HI mass limit for the WSRT ZoA PP survey assuming a 3σ detection with a 150 km s^{-1} line width. In red we show the HI mass limit of a detection at $8\sigma\times1$ channel for a velocity resolution of 16.5 km s^{-1} (R2). The blue curve shows the HI mass limit of a detection at $3\sigma\times32$ channels for a velocity resolution of 66 km s^{-1} (R8).

2.7 Large Scale Structures Crossing the ZoA

Our survey does not have a large enough areal coverage to explore the angular distribution of the large scale structures (LSS) at the different redshift peaks. However, it is deep enough to explore prominent LSS that cross the Galactic Plane in radial velocity space. We have found galaxies over the full radial velocity range of $cz = 2400 - 16600$ km s^{-1}. Their velocity distribution is not homogenous, which is not unexpected given that we targeted a cluster and its environment at about 6000km s^{-1}. Interestingly, behind the targeted cluster we also find evidence for either a clustering, a cross-section of a filament or a wall at larger distances.

To explore the unveiled structures in the context of known LSS, we extracted galaxies with known redshifts from the literature (mainly the 2MRS) in the surroundings of our WSRT survey area. The 2MRS survey is homogenous and "all-sky" down to Galactic latitude $|b| = 5°$. However, it should be noted that it is NIR-selected and therefore favours early-type galaxies as opposed to the late-types typically detected in HI samples. Given the lack of other deep all-sky galaxy imaging or HI surveys, this remains the best data set to compare our results with and to study the connectivity of known LSS across this area of the ZoA. It

should be noted though that the peak sensitivity in redshift space of the 2MRS lies at about 12000 km s^{-1} and that it is very sparsely sampled above 15000 km s^{-1}.

In Fig. 2.17, the detected H I galaxies are plotted together with adjacent galaxies with known redshifts in an equal-area Aitoff sky projection for the Galactic coordinate range $80° < \ell < 200°$ and $-90° < b < 90°$, for four different radial velocity ranges. To clarify the effect of the new H I detections in the small WSRT region (9.6 deg^2), we provide a zoomed-in plot next to the large area map for each of the redshift intervals. The different panels or colours represent the four overdensity peaks identified in Fig. 2.15, namely in purple (Aur 1; $2000 - 4000$ km s^{-1}), blue (Aur 2; $4000 - 8000$ km s^{-1}), green (Aur 3; $8000 - 12000$ km s^{-1}) and red (Aur 4; $12000 - 16000$ km s^{-1}). The picture of the new ZoA crossing features becomes even clearer when assessing their positions in a redshift wedge (Fig. 2.18) which displays the Galactic longitude range of $155° - 165°$ for the latitude range $-30° < b < 30°$. The blue dashed lines outline our surveyed volume.

New features include a small number of nearby galaxies (Aur 1). The most prominent feature is Aur 2, around 6000 km s^{-1}, an overdensity associated with the 3C 129 X-ray cluster and the two strong radio sources, 3C 129 and 3C 129.1 (see Sect. 2.1). Further out in the $8000 - 12000$ km s^{-1} (green) redshift range a new striking feature peaking at 10000 km s^{-1} dominates. Additionally, we are seeing hints of the edge of another structure, C31, identified by Erdoğdu et al. (2006), at $14000 - 16000$ km s^{-1}. However, the number of detections at these higher radial velocities is relatively low because it lies close to the high-velocity limit of our survey where the H I mass sensitivity is reduced. In addition, the 2MRS has lost most of its sensitivity at ≥ 15000 km s^{-1}. Nevertheless, it clearly marks a high-density region, as demonstrated in Fig. 2.16 and 2.18. For these reasons, concrete conclusions regarding this most distant galaxy density peak, cannot be drawn at present.

The newly identified structures already pointed out in Sect. 2.6 are discussed in detail in the following subsections, starting with the two most prominent structures, Aur 2 and Aur 3, followed by a short overview of the minor structures Aur 1 and Aur 4.

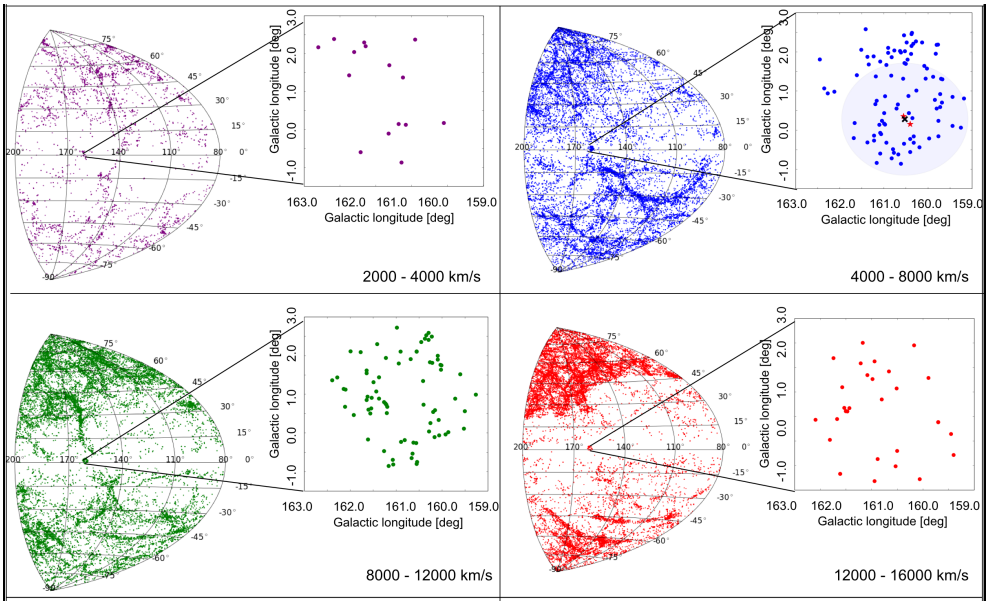

Figure 2.17 – Aitoff projections of the sky-distribution in Galactic coordinates for $80° < \ell < 200°$ and $-90° < b < 90°$. Galaxies with known redshifts from the literature and the 2MRS are shown as dots. The images at the top right corner of each panel show a zoomed-in on the spatial distributions of galaxies detected by the WSRT ZoA PP survey and point to their location within the context of the large-scale structures they reside in. The galaxy sky distributions are separated into four radial velocity bins. Top left: $2000 - 4000$ km s^{-1} (Aur 1), top right: $4000 - 8000$ km s^{-1} (Aur 2), the light shaded area indicates 1 Abell radius of $85'$ at this distance, centred on the 3C 129 cluster indicated by the black cross. Positions of the radio galaxies are indicated by red stars. Bottom left: $8000 - 12000$ km s^{-1} (Aur 3) and bottom right: $12000 - 16000$ km s^{-1} (Aur 4).

The Perseus-Pisces Supercluster Connection

The Perseus-Pisces Supercluster (PPS) is the most noticeable linear feature in the northern sky around $cz \approx 6000$ km s^{-1} (e.g. Giovanelli & Haynes 1985a, Giovanelli, Haynes & Chincarini 1986, Haynes et al. 1988, Wegner, Haynes & Giovanelli 1993). The main ridge of the PPS is a linear filamentary structure of about 45 Mpc in length (Seeberger, Huchtmeier & Weinberger 1994), bounded in ℓ between 80° and 180°. It comprises a rich chain of Abell clusters such as ACO 262, ACO 347 and ACO 426 (Gregory, Thompson & Tifft 1981, Wegner, Haynes & Giovanelli 1993).

In the top right panel of Fig. 2.17 the PPS can be traced from $\ell, b \approx 80°, 15°$, entering the ZoA at $\ell \approx 90°$ and emerging on the other side at $\ell, b \approx 90°, -5°$, the connection of which was confirmed to extend

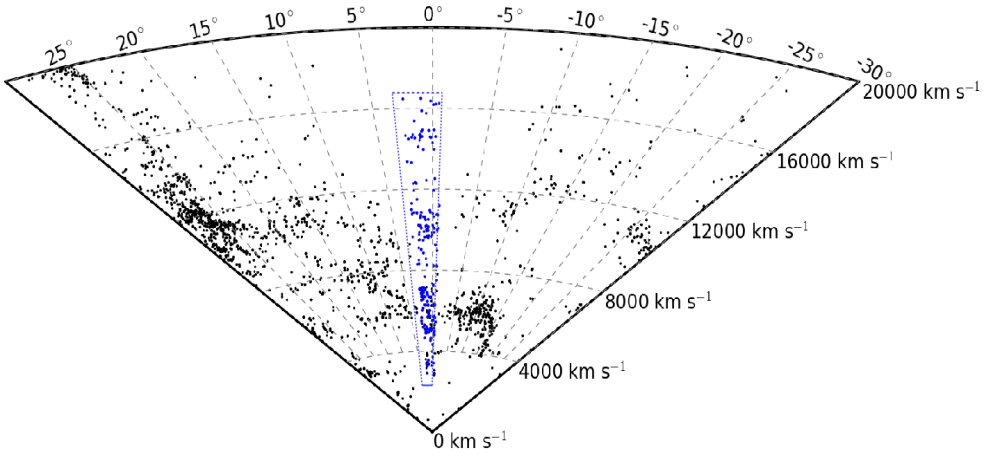

Figure 2.18 – Redshift wedge diagram for $155° < \ell < 165°$ and $-30° < b < 30°$. Galaxies with known redshifts from the literature and the 2MRS out to $cz \approx 20000$ km s^{-1} are plotted in black. The WSRT PP ZoA survey region (at about -1° $< b <$ 4°) is outlined by blue dashed lines and new detections are represented by blue dots.

across the Milky Way by the NRT ZoA survey (Kraan-Korteweg et al. in prep). The filament bends all the way to the south of the ZoA at $\ell, b \approx 120°, -30°$, where it connects to ACO 2634 ($\ell, b \approx 103°, -33°$) and ACO 2666 ($\ell, b \approx 107°, -33°$) at $cz \approx 8000$km s^{-1} (Merighi et al. 1986). It then bends at a slight angle, vanishing into the ZoA at $\ell \approx 160°$ and reappears aligned with the main ridge at $cz \approx 6000$km s^{-1}.

It is based on this observation that Focardi, Marano & Vettolani (1984) proposed an extension of the PPS across the ZoA towards a clump of galaxies associated with ACO 569 (see also Focardi, Marano & Vettolani 1986). This suggestion stemmed from a "conglomerate of galaxies" hinted at in Weinberger (1980) at $\ell \approx 160°$, where Spinrad (1975) had measured radial velocities of the two radio galaxies mentioned in Sect. 1. The lack of data in the obscured ZoA prompted further extensive studies (Focardi, Marano & Vettolani 1984, Focardi, Marano & Vettolani 1986, Chamaraux et al. 1990, Lu & Freudling 1995, Saurer, Seeberger & Weinberger 1997, Pantoja et al. 1997) ultimately confirming this link. It is clear now that our new observations not only substantiate this continuity, but also prove that this connection incorporates yet another major cluster that forms part of the PPS.

The HI detections in our survey are associated with the 3C 129 X-ray cluster with a mass of $M_X = 5 \times 10^{14} M_\odot$, centred at $\ell, b \approx 160.52°, 0.28°$ (Leahy & Yin 2000) which when added to the overall Perseus-Pisces

chain, makes the PPS one of the largest known structures in the local Universe. In fact, Chamaraux et al. (1990) showed that its dimension could be as large as $150 - 300$ Mpc, with the addition of other clusters in the south of the ZoA. Moreover, it has been postulated in the past that the PPS could be as densely populated as, or even more, than the Great Attractor (Saunders et al. 1991, Strauss & Willick 1995, Hudson et al. 1997). Adding this new mass overdensity to the overall mass of the PPS might lead to significant infall motions of galaxies in its immediate surroundings. A complete and detailed dynamical examination of this galaxy cluster, including flows associated with the structure, is one of the questions that will be addressed in a forthcoming paper of this series.

Behind the Perseus-Pisces Supercluster

The background of the PPS (see the bottom left panel of Fig. 2.17) comprises galaxies in the velocity range $8000 - 12000$ km s^{-1}. In this range, the most dominant filamentary structure is evident. The Aur 3 overdensity of galaxies is part of this structure, which can be traced from $\ell, b \approx 170°, 45°$ to the North of the ZoA, traversing the ZoA at $\ell \approx 160°$, emerging from the ZoA at $\ell \approx 150°$ to the South. It continues towards a cluster dominated by early type galaxies at $\ell, b, cz \approx 143°, -22°, 10720$ km s^{-1} (J7; Wegner et al. 1996). It then bends at a slight angle and diffuses into a sheet of galaxies at $\ell \gtrsim 143°$, $b \lesssim 40°$. The new HI detections in the ZoA at $\ell \approx 160°$ are not associated with any known cluster. However, they coincide with a structure, CID 15 predicted by Erdoğdu et al. (2006) in the 2MRS reconstructed density and velocity maps.

Additional ZoA Structures

Both the top left ($cz \approx 2000 - 4000$ km s^{-1}) and bottom right ($cz \approx 12000 - 16000$ km s^{-1}) panels of Fig. 2.17 indicate hints of galaxy overdensities. The nearer one, Aur 1, is too widely spread over the survey area to associate the detections with any large-scale structure in the vicinity. The more distant one, Aur 4 at the far edge of the survey volume does coincide with another structure, C31, predicted by Erdoğdu et al. (2006) (see their Fig. 10) at $cz \approx 14000 - 16000$ km s^{-1}, although the actual galaxy map (Fig. 2.17) does not give a clear hint of a connection to this feature. It seems to emerge from below the Galactic plane and ends in the ZoA without continuing into the northern Galactic hemisphere. There is not enough data for a quantitative analysis.

2.8 Summary

We have conducted a blind 21cm H I-line imaging survey with the WSRT of the area where the Perseus-Pisces Supercluster (PPS) crosses the Zone of Avoidance, centred at $\ell, b \approx 160°, 0.5°$. The survey comprises an effective area of $\sim$9.6 deg^2 observed at an angular resolution of $23'' \times 16''$ and a velocity resolution of 16.5 km s^{-1} with an average rms noise level of 0.36 mJy/beam over the radial velocity range of $cz = 2400 - 16600$ km s^{-1}. We detected 211 H I sources, of which only three had previously been detected in H I. We have presented the results as a data catalogue with derived H I-parameters and as an H I atlas with total H I maps and velocity fields, major axis position-velocity diagrams, global line profiles and overlays with near-infrared images. A total of 80 sources were resolved by the WSRT. We found near-infrared counterparts for 130 (62%) of our detections from UKIDSS and 100 (47%) mid-infrared counterparts from WISE. In cases where a UKIDSS image could not be found due to imaging artefacts we searched a 2MASS image at comparable wavelength to the UKIDSS K-band. The radial velocity distribution of our H I detections shows four overdensities crossing the Galactic Plane. The most prominent is a connection between the PPS above and below the ZoA and associated with the 3C 129 X-ray cluster. The new detections support previous claims that the PPS filament extends to the cluster A 569. Of particular interest is another ZoA structure behind the PPS at a radial velocity of 10000 km s^{-1}. While predicted previously, it has now been detected for the first time. It seems to belong to a prominent large scale filament at 10000 km s^{-1} which comprises one other known cluster, J7, residing just below the ZoA. The data presented here provide input for an upcoming detailed analysis of the 3C 129 cluster and the other overdensities detected, to be presented in forthcoming papers in this series.

Acknowledgments

MR acknowledges financial support from the Ubbo Emmius Fund of the University of Groningen. MR, RKK, ACS, TJ and EE acknowledge the research support provided by the South African National Research Foundation. The SA and NL authors of this collaboration all benefitted tremendously from collaborative exchanges support by the NRF/NWO bilateral agreement for Astronomy and Astronomy Enabling Technologies. MV acknowledges financial support from the DAGAL network for the People Programme (Marie Curie Actions) of the European UnionŌs Seventh Framework Programme FP7/2007-2013/ under REA grant agreement number PITNGA-2011-289313. MV acknowledges support by a Vici grant from the Innovational Research Incentives Scheme of the Netherlands Organisation for Scientific Research (NWO). MV also acknowledges the Leids Kerkhoven Bosscha Fonds (LKBF) for travel support. We would also like to thank K. Said, B. Frank, R. Juraszek, B. Koribalski, P. Serra, L. Fl'oer, L. Staveley-Smith and I. Wong for their various contributions to the project. The Westerbork Synthesis Radio Telescope is operated by the ASTRON (Netherlands Institute for Radio Astronomy) with support from the Netherlands Foundation for Scientific Research (NWO).

This publication makes use of data products from the Two Micron All Sky Survey, which is a joint project of the University of Massachusetts and the Infrared Processing and Analysis Center/California Institute of Technology, funded by the National Aeronautics and Space Administration and the National Science Foundation.

This research has also made use of the UKIRT Infrared Deep Sky Survey database.

This publication also makes use of data products from the Wide-field Infrared Survey Explorer, which is a joint project of the University of California, Los Angeles, and the Jet Propulsion Laboratory/-California Institute of Technology, funded by the National Aeronautics and Space Administration.

This research also makes use of the HyperLEDA database (http://leda.univ-lyon1.fr) and the NASA/IPAC Extragalactic Database (NED) which is operated by the Jet Propulsion Laboratory, California Institute of Technology, under contract with the National Aeronautics and Space Administration

2

Appendix

Appendix A: The HI Catalogue and Atlas

The derived HI parameters of the 211 detected galaxies are listed in tables presented in this section. The first table (A1) lists the resolved galaxies, and the second table (A2) the marginally resolved galaxies. The column entries of the 211 HI detections are as follows:

Column (1): Galaxy designated identification based on the Right Ascension and Declination (J 2000.0) of the HI centroid.

Column (2)&(3): Galactic longitude and latitude in degrees.

Column (4): Systemic velocity in the barycentric-standard of rest (BSR) defined by the central velocity in km s^{-1} of the global HI profile.

Column (5) & (6): Observed HI profile line widths and their uncertainties (in km s^{-1}) measured at 20% and 50% level of the HI profile peak flux, respectively, determined at a velocity resolution of 16.5 km s^{-1}.

Column (7): The total integrated HI flux ($S_{\rm int}$) in Jy km s^{-1}.

Column (8): Luminosity distance D to the galaxy in Mpc derived from the systemic velocity measured in the BSR.

Column (9): The total HI mass in $M_\odot$.

Column (10): The HI radius measured at the $1\,M_\odot\,pc^{-2}$ surface density level ($R_{\rm HI}$) in kpc, given for resolved sources only.

Column (11): Indication of an infrared counterpart, found in either UKIDSS (u), WISE (w) or 2MASS (m).

Table A1. A catalogue of resolved WSRT HI detections.

ZoA	ℓ	b	v_{rad}	w_{20}	w_{50}	$S_{\rm int}$	D	$\log(M_{\rm HI})$	$R_{\rm HI}$	counterpart
	deg	deg	km s^{-1}	km s^{-1}	km s^{-1}	Jy km s^{-1}	Mpc	M$_\odot$	kpc	
(1)	(2)	(3)	(4)	(5)	(6)	(7)	(8)	(9)	(10)	(11)
J044427.17+455116.7	159.25	0.06	5506 ± 04	285 ± 14	266 ± 09	5.68 ± 0.41	79	9.9	24.2	u –
J044521.10+454432.8	159.44	0.11	5134 ± 03	290 ± 07	278 ± 07	1.34 ± 0.10	73	9.2	12.4	u –
J044542.87+442101.0	160.54	-0.75	10717 ± 01	198 ± 04	169 ± 03	3.57 ± 0.10	153	10.3	33.5	u –
J044602.33+443426.8	160.40	-0.56	6281 ± 03	117 ± 10	100 ± 06	5.78 ± 0.45	90	10.0	31.0	u –
J044632.27+452152.2	159.86	0.02	9740 ± 02	226 ± 06	212 ± 08	0.66 ± 0.05	139	9.5	17.4	u w
J044644.10+442004.0	160.67	-0.62	5654 ± 05	194 ± 13	179 ± 13	0.94 ± 0.09	81	9.2	12.7	u w
J044644.74+444734.7	160.32	-0.32	5709 ± 03	156 ± 09	135 ± 10	0.51 ± 0.05	82	8.9	9.9	u –
J044700.10+442439.7	160.64	-0.54	10747 ± 02	330 ± 07	309 ± 05	1.86 ± 0.09	154	10.0	35.8	u w
J044706.91+453449.0	159.76	0.24	4994 ± 03	216 ± 08	200 ± 06	1.24 ± 0.06	71	9.2	14.0	u w
J044727.30+445342.4	160.32	-0.16	5523 ± 02	69 ± 06	51 ± 06	0.33 ± 0.03	79	8.7	7.9	– –
J044743.99+441946.5	160.79	-0.49	4878 ± 04	146 ± 10	117 ± 10	0.76 ± 0.05	70	8.9	9.9	u w
J044837.97+454508.0	159.80	0.55	5745 ± 02	136 ± 04	118 ± 10	0.74 ± 0.06	82	9.1	10.8	u w
J044840.48+452428.9	160.07	0.33	10956 ± 02	164 ± 07	152 ± 06	0.45 ± 0.05	157	9.4	17.6	u w
J044907.68+443018.3	160.81	-0.19	10644 ± 04	195 ± 08	168 ± 22	0.43 ± 0.04	152	9.4	16.4	u w
J044957.27+460315.1	159.72	0.92	4942 ± 01	185 ± 03	170 ± 02	2.59 ± 0.08	71	9.5	15.3	u w
J045002.21+452645.5	160.19	0.54	9611 ± 03	125 ± 07	110 ± 08	0.59 ± 0.06	137	9.4	16.9	– –
J045005.46+453021.9	160.15	0.59	9642 ± 03	307 ± 10	283 ± 08	1.38 ± 0.08	138	9.8	25.8	u w
J045013.10+440833.5	161.22	-0.27	5547 ± 02	124 ± 08	104 ± 06	0.76 ± 0.05	79	9.1	11.2	u w
J045022.07+442207.7	161.06	-0.10	5739 ± 02	125 ± 04	110 ± 14	0.31 ± 0.03	82	8.7	6.7	– –
J045026.43+451135.1	160.43	0.43	4639 ± 03	130 ± 06	68 ± 35	0.69 ± 0.05	66	8.9	7.9	u w
J045105.43+443544.0	160.97	0.14	5044 ± 01	187 ± 04	168 ± 03	3.71 ± 0.11	72	9.7	20.5	u –
J045132.28+442922.2	161.10	0.13	5129 ± 04	305 ± 11	276 ± 11	1.06 ± 0.07	73	9.1	11.1	u w
J045137.03+461912.8	159.70	1.31	7030 ± 04	134 ± 18	81 ± 08	0.42 ± 0.04	100	9.0	9.5	– –
J045145.44+443610.2	161.04	0.24	5086 ± 00	270 ± 01	251 ± 02	17.63 ± 0.32	73	10.3	36.4	u w
J045156.49+450320.0	160.71	0.55	4525 ± 03	188 ± 06	91 ± 20	0.39 ± 0.06	65	8.6	7.4	u w
J045208.67+434927.2	161.68	-0.21	7239 ± 01	330 ± 03	313 ± 04	1.90 ± 0.09	103	9.7	20.3	u w
J045220.74+454136.5	160.26	1.01	6458 ± 01	190 ± 03	175 ± 04	0.92 ± 0.06	92	9.3	14.5	u w
J045223.95+452744.1	160.45	0.87	5982 ± 02	97 ± 04	84 ± 06	0.47 ± 0.05	85	8.9	9.7	– –
J045227.46+444542.0	160.99	0.43	5144 ± 02	102 ± 04	83 ± 13	0.28 ± 0.03	73	8.6	6.0	– –
J045331.19+443916.6	161.20	0.51	10148 ± 02	125 ± 07	112 ± 06	0.39 ± 0.04	145	9.3	14.4	u w

Table A1 – Continued

ZoA	ℓ	b	v_{rad}	w_{20}	w_{50}	$S_{\rm int}$	D	$\log(M_{\rm HI})$	$R_{\rm HI}$	counterpart	
	deg	deg	km s^{-1}	km s^{-1}	km s^{-1}	Jy km s^{-1}	Mpc	M$_\odot$	kpc		
(1)	(2)	(3)	(4)	(5)	(6)	(7)	(8)	(9)	(10)	(11)	
J045408.61+444522.2	161.19	0.66	5063 ± 02	129 ± 06	111 ± 05	0.81 ± 0.05	72	9.0	9.9	–	–
J045414.22+461633.3	160.02	1.63	9024 ± 02	246 ± 09	200 ± 04	0.48 ± 0.05	129	9.3	15.4	u	w
J045414.90+450315.7	160.97	0.86	6269 ± 02	208 ± 05	165 ± 05	0.57 ± 0.05	90	9.0	8.7	u	w
J045420.49+454723.7	160.41	1.34	10856 ± 02	161 ± 06	128 ± 09	0.68 ± 0.05	155	9.6	19.7	u	w
J045426.94+444941.2	161.17	0.75	5072 ± 03	132 ± 08	105 ± 08	0.63 ± 0.04	72	8.9	8.9	u	w
J045430.27+461345.1	160.08	1.64	6726 ± 02	229 ± 07	213 ± 05	0.98 ± 0.06	96	9.3	14.5	u	w
J045442.75+462112.8	160.01	1.74	9881 ± 06	293 ± 11	218 ± 33	1.35 ± 0.09	141	9.8	25.6	u	w
J045443.51+444709.1	161.23	0.76	9926 ± 01	106 ± 03	87 ± 04	1.09 ± 0.05	142	9.7	23.5	u	w
J045445.29+453922.2	160.56	1.31	4941 ± 02	292 ± 06	218 ± 07	6.17 ± 0.10	71	9.9	22.9	u	w
J045446.73+442143.1	161.56	0.50	10510 ± 02	224 ± 04	208 ± 06	1.77 ± 0.07	150	10.0	27.2	u	w
J045514.42+453815.1	160.62	1.37	3355 ± 03	116 ± 07	97 ± 08	0.56 ± 0.05	48	8.5	5.9	u	w
J045546.73+444512.9	161.37	0.89	10177 ± 02	179 ± 03	165 ± 33	0.52 ± 0.05	145	9.4	16.0	–	–
J045604.55+452940.6	160.83	1.39	6684 ± 02	242 ± 08	216 ± 06	1.90 ± 0.06	95	9.6	16.9	u	w
J045616.24+455602.6	160.51	1.69	6990 ± 03	153 ± 12	132 ± 07	0.55 ± 0.04	100	9.1	11.4	u	w
J045626.80+455541.2	160.53	1.71	6901 ± 03	546 ± 06	526 ± 11	3.26 ± 0.12	99	9.9	25.6	u	w
J045635.00+460222.4	160.46	1.80	6679 ± 02	304 ± 07	286 ± 07	1.62 ± 0.08	95	9.5	20.5	u	w
J045714.03+451227.7	161.18	1.37	6279 ± 02	241 ± 04	225 ± 06	0.89 ± 0.06	90	9.2	13.7	u	w
J045721.12+454135.5	160.81	1.69	3420 ± 01	117 ± 02	99 ± 02	3.76 ± 0.10	49	9.3	13.6	u	w
J045723.71+463354.4	160.13	2.24	7064 ± 02	214 ± 07	198 ± 07	1.14 ± 0.09	101	9.4	16.3	u	w
J045726.29+440242.9	162.11	0.67	9698 ± 06	148 ± 18	107 ± 14	0.35 ± 0.04	139	9.2	12.5	u	w
J045735.72+444850.6	161.53	1.18	14422 ± 02	252 ± 04	234 ± 08	0.47 ± 0.05	206	9.7	21.2	m	w
J045742.65+453422.1	160.94	1.66	6293 ± 03	108 ± 07	75 ± 08	0.49 ± 0.03	90	9.0	10.1	u	w
J045747.05+460717.5	160.52	2.01	7013 ± 01	393 ± 03	375 ± 03	3.96 ± 0.11	100	10.0	30.7	u	w
J045750.73+461921.4	160.37	2.15	6861 ± 01	117 ± 05	104 ± 04	1.23 ± 0.07	98	9.4	17.3	u	w
J045752.30+455539.3	160.68	1.91	10822 ± 01	231 ± 09	193 ± 03	2.82 ± 0.10	155	10.2	33.7	u	w
J045800.33+462839.4	160.27	2.27	7079 ± 03	102 ± 07	68 ± 10	0.64 ± 0.06	101	9.2	12.1	–	–
J045808.63+450525.8	161.37	1.42	3543 ± 00	191 ± 01	176 ± 01	6.01 ± 0.10	51	9.6	16.9	u	w
J045809.05+454743.1	160.82	1.86	6562 ± 04	240 ± 17	189 ± 08	0.99 ± 0.06	94	9.3	13.4	u	–
J045810.84+460229.4	160.63	2.02	7137 ± 01	219 ± 03	204 ± 05	1.36 ± 0.07	102	9.5	18.3	u	w
J045828.65+441328.4	162.09	0.93	14608 ± 03	338 ± 07	319 ± 29	0.56 ± 0.05	209	9.8	24.6	u	w
J045830.71+463953.7	160.17	2.45	14658 ± 03	134 ± 14	107 ± 08	0.75 ± 0.13	209	9.9	31.8	–	–

Table A1 – Continued

ZoA	ℓ	b	v_{rad}	w_{20}	w_{50}	$S_{\rm int}$	D	$\log(M_{\rm HI})$	$R_{\rm HI}$	counterpart
	deg	deg	km s^{-1}	km s^{-1}	km s^{-1}	Jy km s^{-1}	Mpc	M$_\odot$	kpc	
(1)	(2)	(3)	(4)	(5)	(6)	(7)	(8)	(9)	(10)	(11)
J045835.03+453110.8	161.08	1.75	5037 ± 05	154 ± 23	124 ± 10	0.80 ± 0.06	72	9.0	9.0	u –
J045838.09+461747.7	160.48	2.24	7051 ± 02	200 ± 05	179 ± 07	1.46 ± 0.06	101	9.5	17.3	u w
J045843.03+455647.1	160.76	2.03	6770 ± 03	244 ± 06	204 ± 28	1.47 ± 0.07	97	9.5	16.9	u w
J045847.49+441350.2	162.12	0.98	6888 ± 01	190 ± 03	159 ± 06	3.19 ± 0.08	98	9.9	24.1	– –
J045855.81+454808.9	160.90	1.97	5098 ± 02	135 ± 05	74 ± 14	0.44 ± 0.03	73	8.7	7.5	u w
J045908.04+440500.0	162.27	0.94	6785 ± 01	116 ± 03	89 ± 02	3.71 ± 0.07	97	9.9	23.9	u w
J045909.87+451619.0	161.34	1.68	4888 ± 03	202 ± 08	189 ± 09	0.44 ± 0.04	70	8.7	7.5	u w
J045920.95+441945.4	162.10	1.12	10641 ± 03	194 ± 08	159 ± 07	0.47 ± 0.05	152	9.4	17.3	– –
J045936.64+445709.6	161.64	1.54	10190 ± 02	211 ± 04	191 ± 05	0.86 ± 0.06	146	9.6	21.5	u w
J045941.86+452913.7	161.23	1.88	7025 ± 01	156 ± 03	143 ± 02	2.92 ± 0.10	100	9.8	29.4	u w
J045946.93+455125.0	160.95	2.12	13320 ± 03	222 ± 09	207 ± 09	0.52 ± 0.05	190	9.6	21.0	u w
J045958.09+440554.1	162.35	1.06	5681 ± 05	188 ± 27	150 ± 10	0.83 ± 0.06	81	9.1	11.5	u w
J050007.95+452211.1	161.37	1.87	4914 ± 02	146 ± 05	132 ± 06	0.52 ± 0.04	70	8.8	7.6	u w
J050039.87+453120.2	161.30	2.04	3382 ± 03	216 ± 16	150 ± 06	1.15 ± 0.05	48	8.8	7.4	u w
J050117.24+454732.3	161.16	2.29	3368 ± 02	179 ± 06	151 ± 04	1.52 ± 0.07	48	8.9	8.7	u w
J050237.59+461133.0	160.98	2.72	9648 ± 01	122 ± 03	107 ± 02	2.02 ± 0.10	138	10.0	28.4	u w
J050251.93+451609.7	161.74	2.19	14499 ± 02	324 ± 06	278 ± 08	0.61 ± 0.05	207	9.8	23.9	u w
J050256.86+451230.4	161.80	2.16	3267 ± 02	146 ± 11	129 ± 05	1.78 ± 0.08	47	9.0	10.2	m –
J050320.82+450122.0	161.99	2.11	8504 ± 01	120 ± 03	99 ± 05	0.99 ± 0.05	121	9.5	17.9	u –

Table A2. A catalogue of the marginally resolved WSRT HI detections.

ZoA	ℓ	b	v_{rad}	w_{20}	w_{50}	$S_{\rm int}$	D	$\log(M_{\rm HI})$	counterpart
	deg	deg	km s^{-1}	km s^{-1}	km s^{-1}	Jy km s^{-1}	Mpc	$M_\odot$	
(1)	(2)	(3)	(4)	(5)	(6)	(7)	(8)	(9)	(10)
J044524.14+451924.3	159.76	-0.16	6830 ± 06	108 ± 18	59 ± 16	0.43 ± 0.07	98	9.0	u –
J044533.70+441127.9	160.64	-0.88	2852 ± 01	90 ± 02	66 ± 03	0.71 ± 0.05	41	8.4	– –
J044540.97+454045.8	159.52	0.11	9660 ± 02	153 ± 06	142 ± 08	0.27 ± 0.03	138	9.1	u –
J044541.51+455022.6	159.40	0.21	14584 ± 03	217 ± 09	123 ± 07	0.43 ± 0.05	208	9.6	u –
J044546.04+444901.5	160.19	-0.44	5134 ± 05	94 ± 34	51 ± 10	0.68 ± 0.09	73	8.9	u –
J044550.59+443552.5	160.36	-0.57	16249 ± 05	95 ± 13	79 ± 16	0.67 ± 0.10	232	9.9	– –
J044556.60+450741.4	159.97	-0.21	6803 ± 03	82 ± 14	63 ± 08	0.30 ± 0.04	97	8.8	u –
J044559.91+450104.1	160.06	-0.28	12528 ± 05	171 ± 10	123 ± 42	0.80 ± 0.13	179	9.8	– –
J044630.07+451655.0	159.92	-0.04	10229 ± 05	170 ± 12	124 ± 18	0.24 ± 0.04	146	9.1	u w
J044635.75+441909.5	160.66	-0.65	9992 ± 03	128 ± 11	94 ± 07	0.55 ± 0.07	143	9.4	u w
J044652.86+440859.1	160.82	-0.72	7501 ± 08	151 ± 24	122 ± 21	0.42 ± 0.07	107	9.1	– –
J044654.85+450928.4	160.06	-0.07	10794 ± 02	170 ± 06	155 ± 08	0.22 ± 0.02	154	9.1	u w
J044657.71+444649.5	160.35	-0.30	16209 ± 06	163 ± 29	117 ± 14	0.81 ± 0.08	232	10.0	– –
J044705.89+450301.9	160.16	-0.11	10165 ± 04	158 ± 09	111 ± 20	0.29 ± 0.03	145	9.2	u –
J044717.85+441654.2	160.77	-0.58	4993 ± 02	157 ± 05	147 ± 06	0.26 ± 0.03	71	8.5	u w
J044719.35+435436.2	161.06	-0.82	10077 ± 04	197 ± 13	186 ± 11	1.08 ± 0.17	144	9.7	u w
J044725.76+443638.5	160.54	-0.35	6219 ± 02	92 ± 06	82 ± 05	0.15 ± 0.02	89	8.5	– –
J044726.92+462337.0	159.18	0.81	5864 ± 02	149 ± 04	129 ± 09	0.92 ± 0.10	84	9.2	– –
J044727.96+444723.6	160.40	-0.23	7288 ± 04	90 ± 09	54 ± 12	0.28 ± 0.03	104	8.9	u w
J044731.28+434829.0	161.16	-0.86	11186 ± 02	54 ± 08	29 ± 06	0.69 ± 0.06	160	9.6	– –
J044735.05+455908.2	159.51	0.56	9945 ± 03	129 ± 14	104 ± 07	0.21 ± 0.03	142	9.0	– –
J044736.43+434854.0	161.16	-0.84	5440 ± 01	126 ± 05	115 ± 03	0.53 ± 0.05	78	8.9	– –
J044744.05+460456.5	159.45	0.64	12441 ± 02	159 ± 05	147 ± 06	0.43 ± 0.05	178	9.5	– –
J044752.21+451900.3	160.05	0.17	3280 ± 02	158 ± 05	139 ± 11	0.21 ± 0.02	47	8.0	– –
J044752.94+435840.2	161.07	-0.70	8204 ± 03	81 ± 10	56 ± 08	0.31 ± 0.03	117	9.0	u w
J044754.01+443847.3	160.56	-0.26	10074 ± 04	100 ± 12	74 ± 09	0.17 ± 0.02	144	8.9	– –
J044808.96+450326.3	160.28	0.04	9853 ± 04	259 ± 07	239 ± 30	0.59 ± 0.07	141	9.4	u w
J044809.24+443634.5	160.62	-0.25	9873 ± 04	120 ± 08	101 ± 15	0.28 ± 0.04	141	9.1	– –
J044819.38+440155.8	161.08	-0.60	4794 ± 03	92 ± 07	77 ± 09	0.28 ± 0.04	68	8.5	– –
J044830.74+455010.9	159.72	0.59	6012 ± 06	133 ± 15	67 ± 23	0.16 ± 0.04	86	8.4	– –

Table A2. – Continued

ZoA	ℓ	b	v_{rad}	w_{20}	w_{50}	$S_{\rm int}$	D	$\log(M_{\rm HI})$	counterpart
	deg	deg	km s^{-1}	km s^{-1}	km s^{-1}	Jy km s^{-1}	Mpc	M$_\odot$	
(1)	(2)	(3)	(4)	(5)	(6)	(7)	(8)	(9)	(10)
J044832.96+462704.2	159.26	0.99	8557 ± 06	128 ± 21	113 ± 14	0.41 ± 0.07	122	9.2	– –
J044837.47+461304.6	159.44	0.85	5930 ± 04	147 ± 12	133 ± 10	0.18 ± 0.04	85	8.5	– –
J044845.01+435610.4	161.20	-0.60	3410 ± 01	37 ± 04	24 ± 02	1.42 ± 0.09	49	8.9	– –
J044850.72+455649.4	159.68	0.70	5976 ± 03	168 ± 06	162 ± 11	0.04 ± 0.02	85	7.9	– –
J044850.94+444943.4	160.53	-0.02	14294 ± 02	163 ± 03	142 ± 12	0.25 ± 0.02	204	9.4	– –
J044857.72+443728.8	160.70	-0.13	16180 ± 03	77 ± 08	61 ± 10	0.12 ± 0.02	231	9.2	– –
J044858.80+451314.0	160.25	0.25	10857 ± 04	276 ± 08	236 ± 20	0.40 ± 0.04	155	9.4	u w
J044900.08+441936.1	160.93	-0.32	14604 ± 03	212 ± 07	107 ± 25	0.34 ± 0.04	209	9.5	u w
J044900.78+441902.8	160.94	-0.32	6332 ± 05	146 ± 21	130 ± 11	0.10 ± 0.03	90	8.3	– –
J044912.74+442451.3	160.89	-0.23	8216 ± 02	156 ± 05	81 ± 04	0.37 ± 0.04	117	9.1	– –
J044927.63+443253.7	160.82	-0.11	3707 ± 04	156 ± 11	111 ± 11	0.10 ± 0.02	53	7.8	u –
J044931.06+435844.3	161.26	-0.47	9257 ± 04	220 ± 13	148 ± 10	0.17 ± 0.03	132	8.8	– –
J044934.80+451030.3	160.35	0.31	6649 ± 02	84 ± 06	43 ± 07	0.28 ± 0.03	95	8.8	– –
J044935.92+445252.1	160.58	0.12	3985 ± 02	65 ± 05	35 ± 07	0.16 ± 0.02	57	8.1	– –
J044944.31+460225.7	159.70	0.88	14933 ± 02	77 ± 04	55 ± 12	0.43 ± 0.04	213	9.7	– –
J044945.15+460232.2	159.70	0.88	13964 ± 01	60 ± 03	24 ± 04	0.10 ± 0.02	199	9.0	u –
J044945.20+460234.8	159.70	0.88	15881 ± 03	106 ± 09	86 ± 10	0.28 ± 0.04	227	9.5	u w
J044945.25+460229.7	159.70	0.88	8258 ± 03	400 ± 07	293 ± 12	0.56 ± 0.05	118	9.3	u w
J044945.98+455144.8	159.84	0.77	5774 ± 02	129 ± 04	122 ± 05	0.14 ± 0.02	82	8.3	– –
J045002.27+444907.5	160.68	0.14	3461 ± 01	52 ± 04	36 ± 03	0.32 ± 0.02	49	8.3	– –
J045006.21+450306.5	160.50	0.30	14904 ± 02	69 ± 04	31 ± 07	0.21 ± 0.03	213	9.4	u w
J045034.24+435929.0	161.37	-0.32	5724 ± 06	137 ± 16	95 ± 16	0.13 ± 0.02	82	8.3	u w
J045035.09+442218.2	161.08	-0.07	4329 ± 01	43 ± 02	25 ± 04	0.10 ± 0.01	62	8.0	– –
J045045.12+443915.9	160.88	0.13	14558 ± 01	176 ± 03	144 ± 05	0.28 ± 0.03	208	9.5	– –
J045104.83+454944.1	160.02	0.93	16487 ± 07	93 ± 26	73 ± 15	0.30 ± 0.05	236	9.6	– –
J045117.24+443525.9	160.99	0.16	5026 ± 01	61 ± 04	39 ± 03	0.91 ± 0.05	72	9.0	– –
J045127.67+461953.7	159.67	1.30	5087 ± 05	118 ± 21	60 ± 10	0.40 ± 0.04	73	8.7	u w
J045136.02+452435.7	160.40	0.73	9648 ± 01	46 ± 03	31 ± 04	0.17 ± 0.02	138	8.9	u w
J045202.73+435400.5	161.61	-0.17	14928 ± 09	86 ± 33	60 ± 20	0.22 ± 0.04	213	9.4	u w
J045202.83+435359.9	161.61	-0.17	11938 ± 02	200 ± 04	152 ± 12	0.40 ± 0.05	171	9.4	u –
J045202.99+435400.5	161.61	-0.17	13974 ± 03	49 ± 06	40 ± 09	0.08 ± 0.02	200	8.9	u –

Table A2. – Continued

ZoA	ℓ	b	v_{rad}	w_{20}	w_{50}	$S_{\rm int}$	D	$\log(M_{\rm HI})$	counterpart	
	deg	deg	km s^{-1}	km s^{-1}	km s^{-1}	Jy km s^{-1}	Mpc	M$_\odot$		
(1)	(2)	(3)	(4)	(5)	(6)	(7)	(8)	(9)	(10)	
J045210.82+463120.9	159.60	1.51	10603 ± 03	158 ± 09	145 ± 10	0.26 ± 0.03	151	9.2	–	–
J045217.56+450844.6	160.68	0.65	6680 ± 04	147 ± 09	121 ± 33	0.39 ± 0.04	95	8.9	u	w
J045231.94+461230.3	159.88	1.36	7109 ± 03	133 ± 09	120 ± 07	0.44 ± 0.05	102	9.0	–	–
J045254.16+441202.2	161.48	0.14	16363 ± 04	162 ± 13	108 ± 12	0.10 ± 0.02	234	9.1	u	w
J045255.89+460258.8	160.05	1.31	7689 ± 02	99 ± 07	87 ± 08	0.24 ± 0.03	110	8.8	–	–
J045343.57+440459.8	161.66	0.18	5142 ± 02	92 ± 04	40 ± 08	0.32 ± 0.03	73	8.6	u	w
J045358.21+461405.5	160.02	1.57	7142 ± 02	165 ± 07	150 ± 05	1.02 ± 0.06	102	9.4	u	–
J045411.23+444554.1	161.19	0.67	9991 ± 03	112 ± 07	93 ± 14	0.46 ± 0.04	143	9.3	–	–
J045428.52+462803.0	159.89	1.78	14698 ± 03	186 ± 06	151 ± 16	0.67 ± 0.07	210	9.8	u	w
J045430.92+444645.3	161.21	0.73	10202 ± 04	221 ± 12	195 ± 11	0.38 ± 0.04	146	9.3	u	w
J045449.54+462052.1	160.03	1.76	9505 ± 01	78 ± 03	38 ± 06	0.51 ± 0.04	136	9.3	–	–
J045457.48+463735.6	159.82	1.95	6872 ± 05	169 ± 10	123 ± 33	0.36 ± 0.05	98	8.9	–	–
J045459.27+444700.0	161.26	0.79	10012 ± 02	62 ± 05	49 ± 06	0.13 ± 0.01	143	8.8	u	w
J045516.70+442734.8	161.54	0.63	10050 ± 02	105 ± 05	36 ± 04	0.26 ± 0.02	144	9.1	u	w
J045519.33+442356.6	161.60	0.60	10016 ± 02	63 ± 05	47 ± 07	0.17 ± 0.01	143	8.9	–	–
J045541.13+462255.5	160.09	1.89	9488 ± 02	98 ± 05	87 ± 17	0.12 ± 0.02	136	8.7	u	w
J045543.03+461423.6	160.21	1.81	9765 ± 02	201 ± 04	97 ± 14	0.44 ± 0.04	140	9.3	u	w
J045543.43+441116.9	161.81	0.52	15759 ± 04	135 ± 12	118 ± 14	0.09 ± 0.02	225	9.0	–	–
J045545.27+455110.8	160.51	1.57	15380 ± 02	73 ± 05	62 ± 08	0.10 ± 0.02	220	9.0	–	–
J045547.62+452909.9	160.80	1.35	14101 ± 04	213 ± 85	187 ± 08	0.53 ± 0.06	201	9.7	u	w
J045548.78+464858.3	159.77	2.18	4651 ± 04	77 ± 08	55 ± 20	0.25 ± 0.06	66	8.4	–	–
J045551.34+440335.6	161.92	0.46	9708 ± 02	67 ± 06	52 ± 09	0.15 ± 0.01	139	8.8	–	–
J045555.08+464704.8	159.80	2.18	6517 ± 04	75 ± 09	43 ± 16	0.40 ± 0.05	93	8.9	u	–
J045558.82+461234.1	160.26	1.83	10221 ± 02	119 ± 11	49 ± 06	0.28 ± 0.04	146	9.1	–	–
J045607.91+462638.4	160.09	1.99	9110 ± 04	91 ± 11	34 ± 14	0.10 ± 0.01	130	8.6	–	–
J045625.85+443832.0	161.53	0.91	10550 ± 03	165 ± 13	104 ± 07	0.27 ± 0.03	151	9.2	u	w
J045633.37+443124.4	161.64	0.85	10483 ± 01	61 ± 09	28 ± 02	0.28 ± 0.02	150	9.2	u	w
J045647.57+444925.8	161.43	1.07	9635 ± 02	164 ± 06	152 ± 06	0.23 ± 0.03	138	9.0	u	w
J045653.00+443516.6	161.62	0.94	10633 ± 03	296 ± 06	176 ± 474	0.40 ± 0.05	152	9.3	u	w
J045656.49+461134.0	160.38	1.94	6911 ± 02	138 ± 04	121 ± 06	0.48 ± 0.05	99	9.0	u	w
J045705.33+443341.0	161.67	0.95	14875 ± 02	67 ± 04	55 ± 06	0.07 ± 0.01	212	8.9	u	w

Table A2. – Continued

ZoA	ℓ	b	v_{rad}	w_{20}	w_{50}	$S_{\rm int}$	D	$\log(M_{\rm HI})$	counterpart
	deg	deg	km s^{-1}	km s^{-1}	km s^{-1}	Jy km s^{-1}	Mpc	M$_\odot$	
(1)	(2)	(3)	(4)	(5)	(6)	(7)	(8)	(9)	(10)
J045705.96+444834.3	161.47	1.10	14708 ± 04	189 ± 13	153 ± 10	0.46 ± 0.04	210	9.7	u –
J045711.02+444742.6	161.50	1.11	14561 ± 01	206 ± 03	193 ± 15	0.83 ± 0.04	208	9.9	u –
J045715.06+445255.8	161.43	1.17	14677 ± 03	246 ± 08	222 ± 11	0.32 ± 0.04	210	9.5	u w
J045751.11+455706.4	160.66	1.92	14574 ± 02	153 ± 05	93 ± 06	0.25 ± 0.03	208	9.4	– –
J045757.17+460156.9	160.61	1.98	5284 ± 02	149 ± 06	108 ± 08	0.29 ± 0.02	75	8.6	– –
J045757.30+462330.0	160.33	2.21	6009 ± 02	123 ± 06	115 ± 07	0.08 ± 0.03	86	8.1	– –
J045804.57+445518.5	161.49	1.31	9480 ± 06	152 ± 30	75 ± 13	0.16 ± 0.03	135	8.9	– –
J045811.77+450602.6	161.37	1.44	10081 ± 02	268 ± 03	259 ± 05	0.59 ± 0.06	144	9.5	u w
J045815.72+453936.1	160.94	1.79	11498 ± 04	167 ± 09	155 ± 34	0.14 ± 0.03	164	9.0	– –
J045816.80+463749.5	160.18	2.40	16477 ± 03	81 ± 06	53 ± 09	0.59 ± 0.09	235	9.9	– –
J045816.94+460925.8	160.55	2.10	8332 ± 04	195 ± 09	150 ± 25	0.26 ± 0.03	119	8.9	– –
J045816.96+453621.8	160.98	1.76	12287 ± 05	147 ± 18	136 ± 12	0.15 ± 0.03	176	9.0	– –
J045842.68+463243.4	160.29	2.40	8303 ± 02	150 ± 06	137 ± 07	0.40 ± 0.05	119	9.1	– –
J045852.18+463855.9	160.22	2.49	11306 ± 04	56 ± 10	37 ± 18	0.20 ± 0.04	162	9.1	u w
J045852.98+445329.6	161.61	1.40	5208 ± 03	147 ± 07	128 ± 20	0.29 ± 0.03	74	8.6	u w
J045900.14+453437.7	161.08	1.84	12338 ± 02	144 ± 07	128 ± 06	0.18 ± 0.02	176	9.1	– –
J045906.31+462358.9	160.45	2.37	3681 ± 03	117 ± 12	108 ± 07	0.09 ± 0.03	53	7.7	– –
J045913.88+463039.1	160.37	2.45	7068 ± 02	104 ± 05	56 ± 14	0.41 ± 0.05	101	9.0	– –
J045920.35+463222.8	160.36	2.48	5662 ± 04	224 ± 14	151 ± 10	0.68 ± 0.07	81	9.0	– –
J045926.99+463431.4	160.34	2.52	10788 ± 03	147 ± 08	113 ± 12	0.78 ± 0.10	154	9.6	– –
J045930.60+455248.7	160.90	2.10	6682 ± 04	270 ± 19	113 ± 08	0.62 ± 0.05	95	9.1	– –
J045930.82+455247.2	160.90	2.10	11940 ± 03	270 ± 24	148 ± 06	0.66 ± 0.04	171	9.7	u w
J045932.30+463928.6	160.29	2.58	10998 ± 03	122 ± 11	97 ± 07	0.60 ± 0.08	157	9.5	– –
J045932.66+441837.9	162.14	1.13	9908 ± 01	272 ± 04	260 ± 03	0.66 ± 0.05	142	9.5	u w
J045937.49+450218.9	161.57	1.60	14535 ± 05	183 ± 14	150 ± 14	0.28 ± 0.03	208	9.5	– –
J045940.69+462146.7	160.54	2.42	5193 ± 01	59 ± 03	39 ± 04	0.20 ± 0.02	74	8.4	u –
J045953.38+453145.6	161.21	1.94	10852 ± 03	172 ± 07	157 ± 09	0.33 ± 0.03	155	9.3	u w
J045955.96+445945.0	161.64	1.61	10208 ± 02	133 ± 06	119 ± 08	0.21 ± 0.03	146	9.0	– –
J050031.81+453733.6	161.21	2.08	12284 ± 02	153 ± 05	144 ± 05	0.18 ± 0.02	175	9.1	u w
J050045.76+454454.4	161.14	2.19	3442 ± 01	46 ± 02	36 ± 04	0.14 ± 0.01	49	7.9	u –
J050120.46+442255.1	162.28	1.43	10706 ± 02	133 ± 05	89 ± 15	0.27 ± 0.03	153	9.2	– –

Table A2. – Continued

ZoA	ℓ	b	v_{rad}	w_{20}	w_{50}	$S_{\rm int}$	D	$\log(M_{\rm HI})$	counterpart
	deg	deg	km s^{-1}	km s^{-1}	km s^{-1}	Jy km s^{-1}	Mpc	M$_\odot$	
(1)	(2)	(3)	(4)	(5)	(6)	(7)	(8)	(9)	(10)
J050124.98+441446.0	162.39	1.36	8849 ± 01	113 ± 03	104 ± 05	0.29 ± 0.03	126	9.0	– –
J050125.79+452212.4	161.51	2.05	6113 ± 02	153 ± 07	118 ± 07	0.22 ± 0.04	87	8.6	u w
J050212.15+453526.1	161.42	2.29	10847 ± 03	87 ± 06	56 ± 15	0.14 ± 0.02	155	8.9	– –
J050217.54+455441.1	161.17	2.50	13374 ± 01	371 ± 04	344 ± 04	0.55 ± 0.05	191	9.7	– –
J050231.16+451050.9	161.77	2.09	8306 ± 05	340 ± 18	322 ± 13	0.33 ± 0.04	119	9.0	m w
J050309.74+453102.6	161.58	2.38	2891 ± 02	165 ± 04	125 ± 12	0.44 ± 0.06	41	8.3	m –
J050329.24+454555.0	161.41	2.58	5490 ± 04	271 ± 09	217 ± 12	2.37 ± 0.19	78	9.5	u –
J050335.40+442816.5	162.45	1.80	7146 ± 04	88 ± 09	78 ± 12	0.19 ± 0.03	102	8.7	u –

The HI atlas

In this section we present the HI data products for all the detected galaxies. The HI atlas is displayed in two sections. The first (Figs. A1) presents the resolved galaxies, shown one per page. The second (Figs. A2) provides maps of the marginally resolved galaxies displayed three per page. The atlas contains total intensity maps, position-velocity diagrams, global HI profiles and UKIDSS or 2MASS counterpart images. For the resolved galaxies we also present HI velocity fields and radial HI surface density profiles.

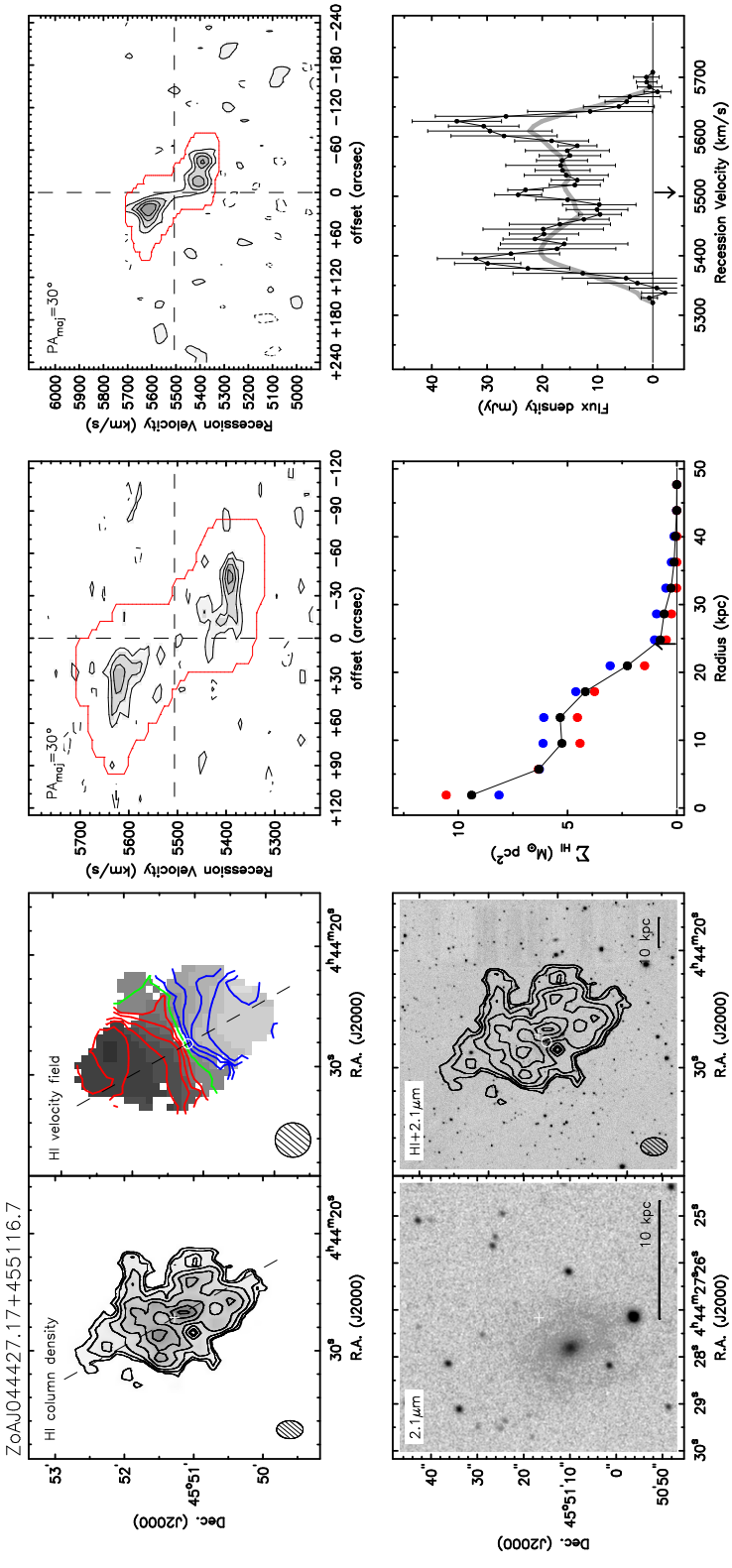

Figure A1. Resolved WSRT HI detections.

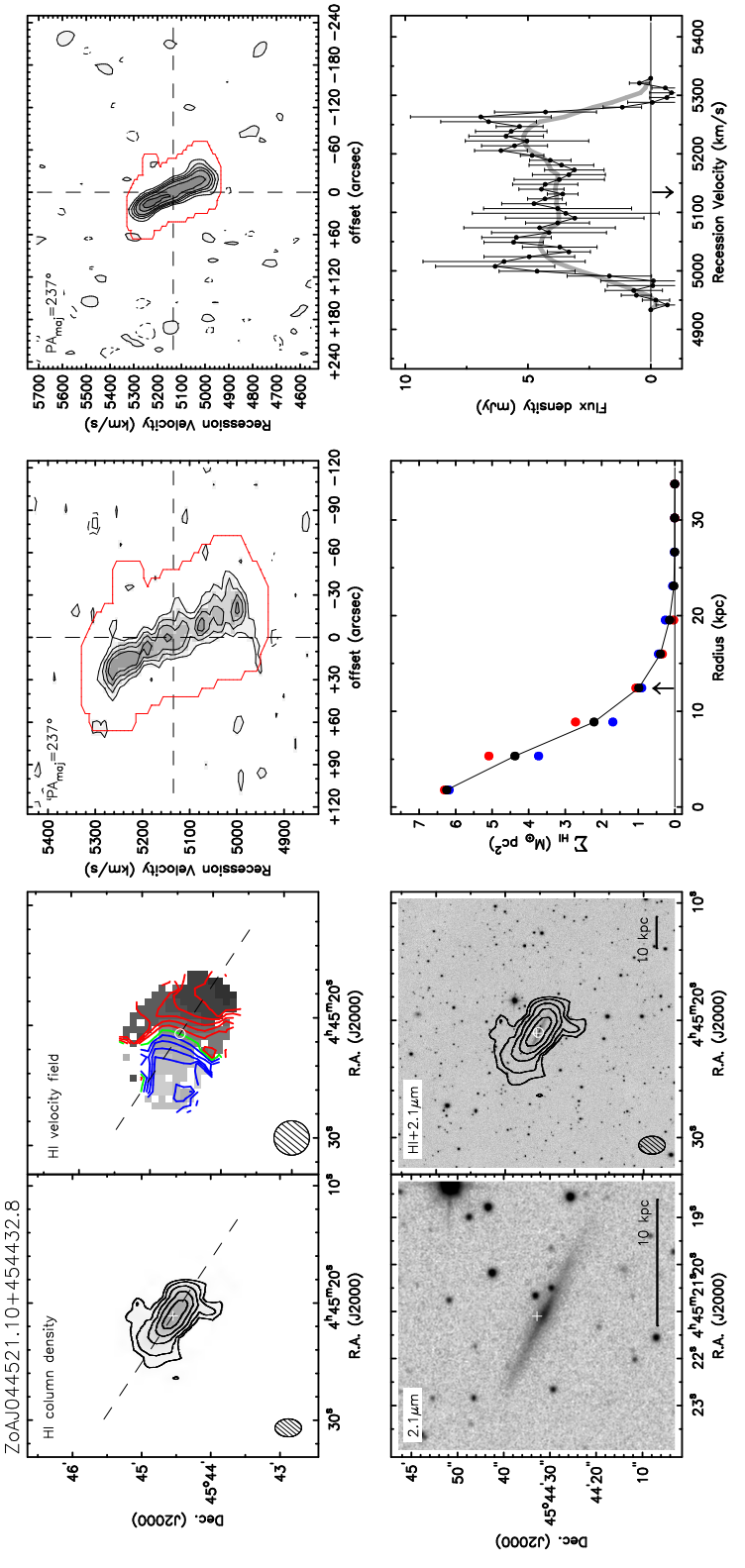

Figure A1. Resolved WSRT HI detections.

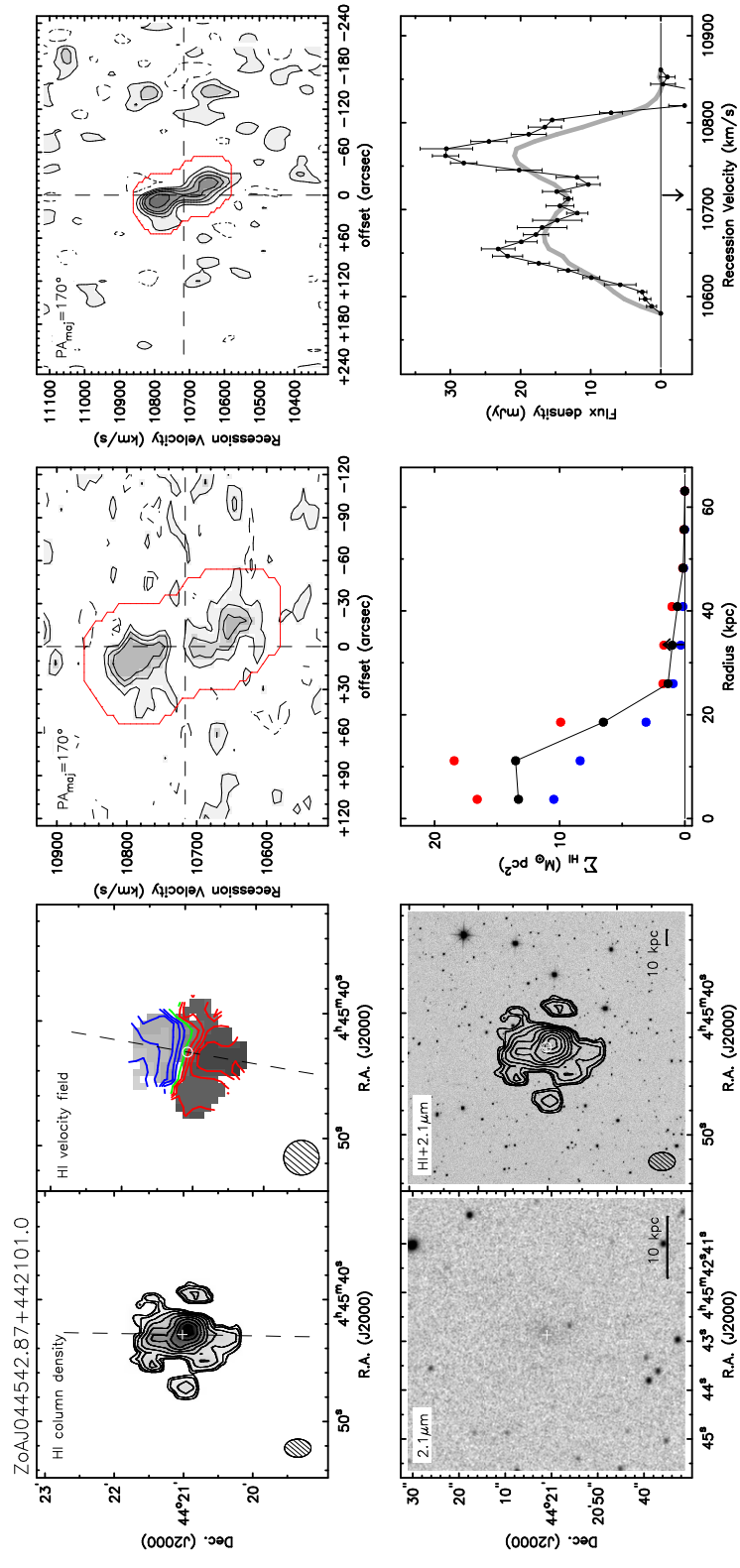

Figure A1. Resolved WSRT HI detections.

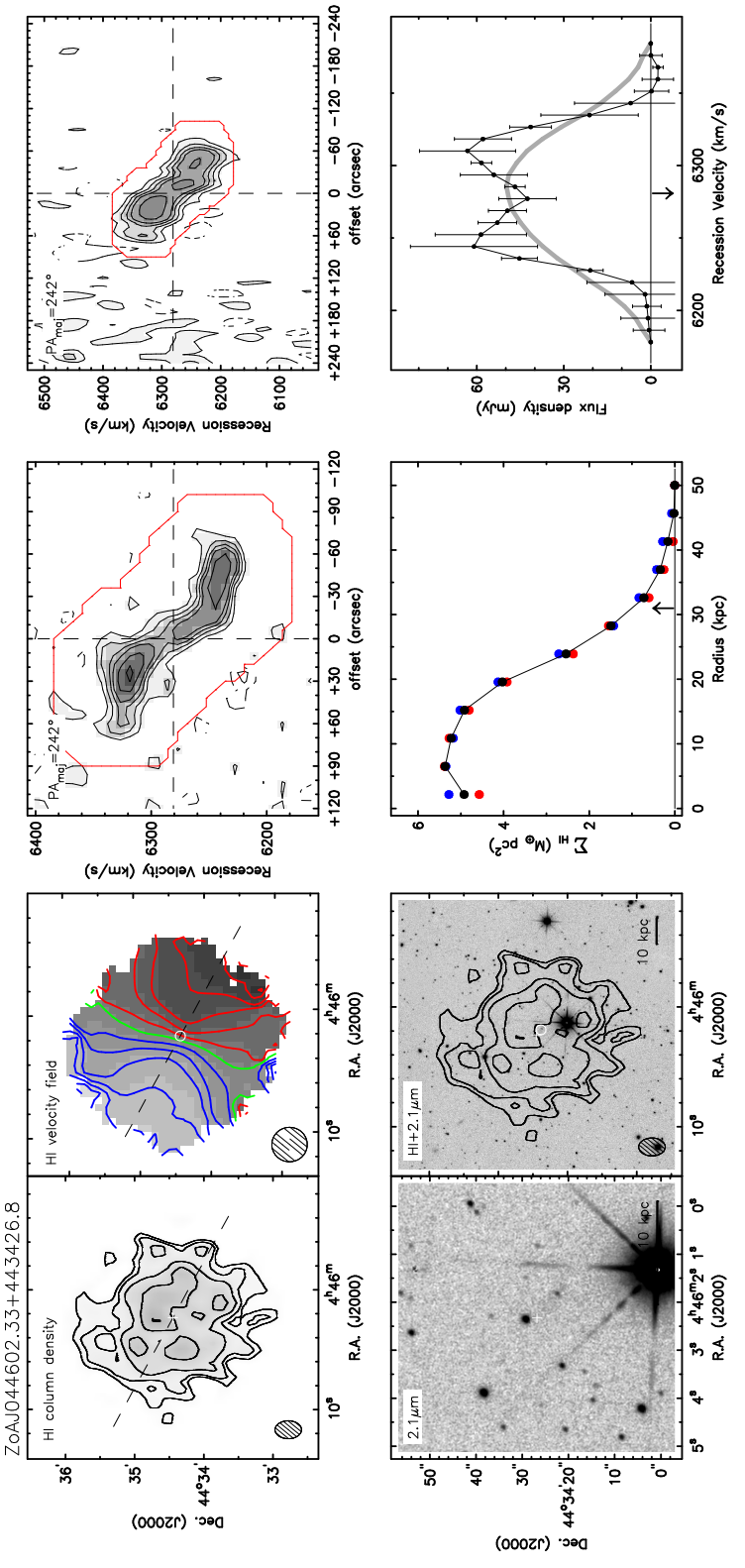

Figure A1. Resolved WSRT HI detections.

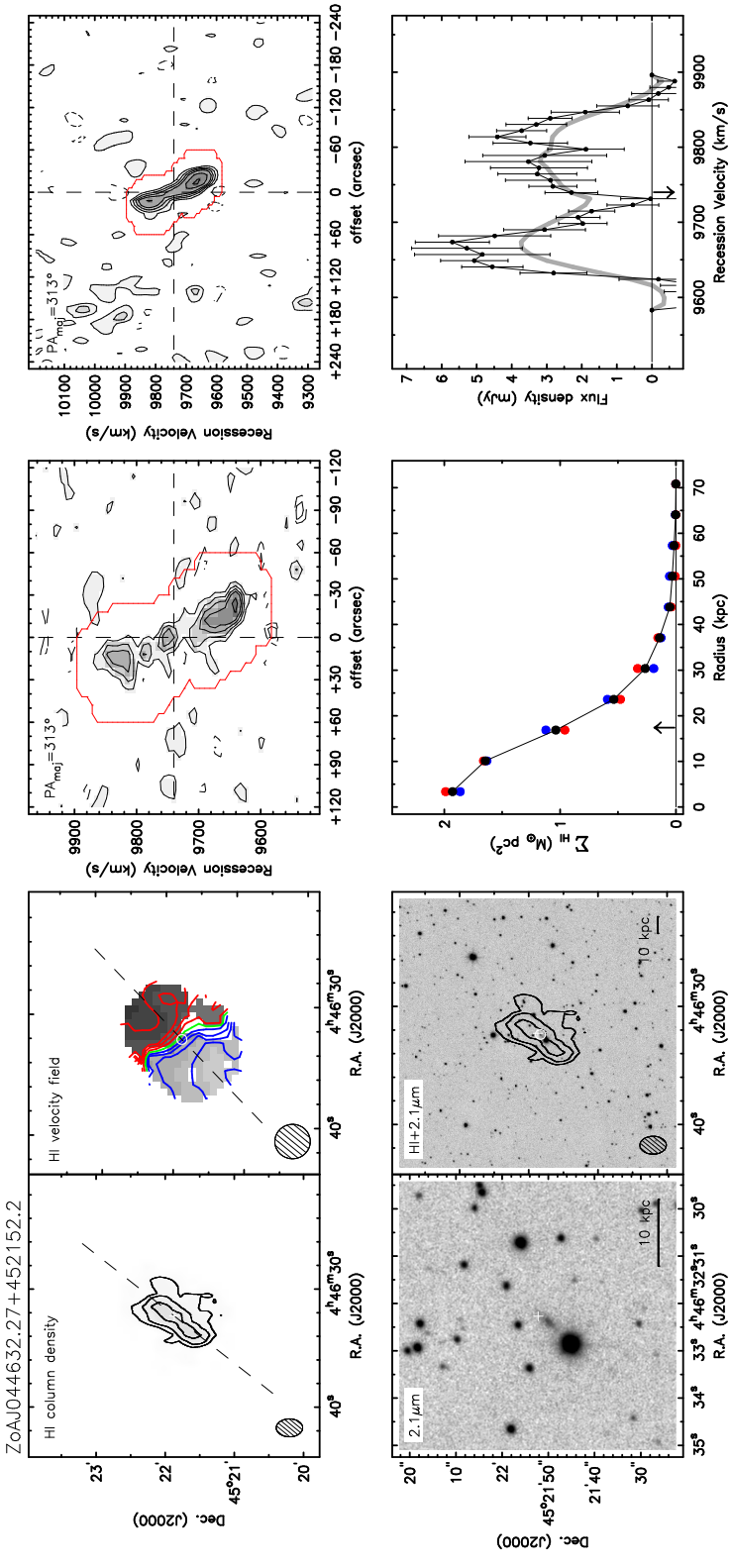

Figure A1. Resolved WSRT HI detections.

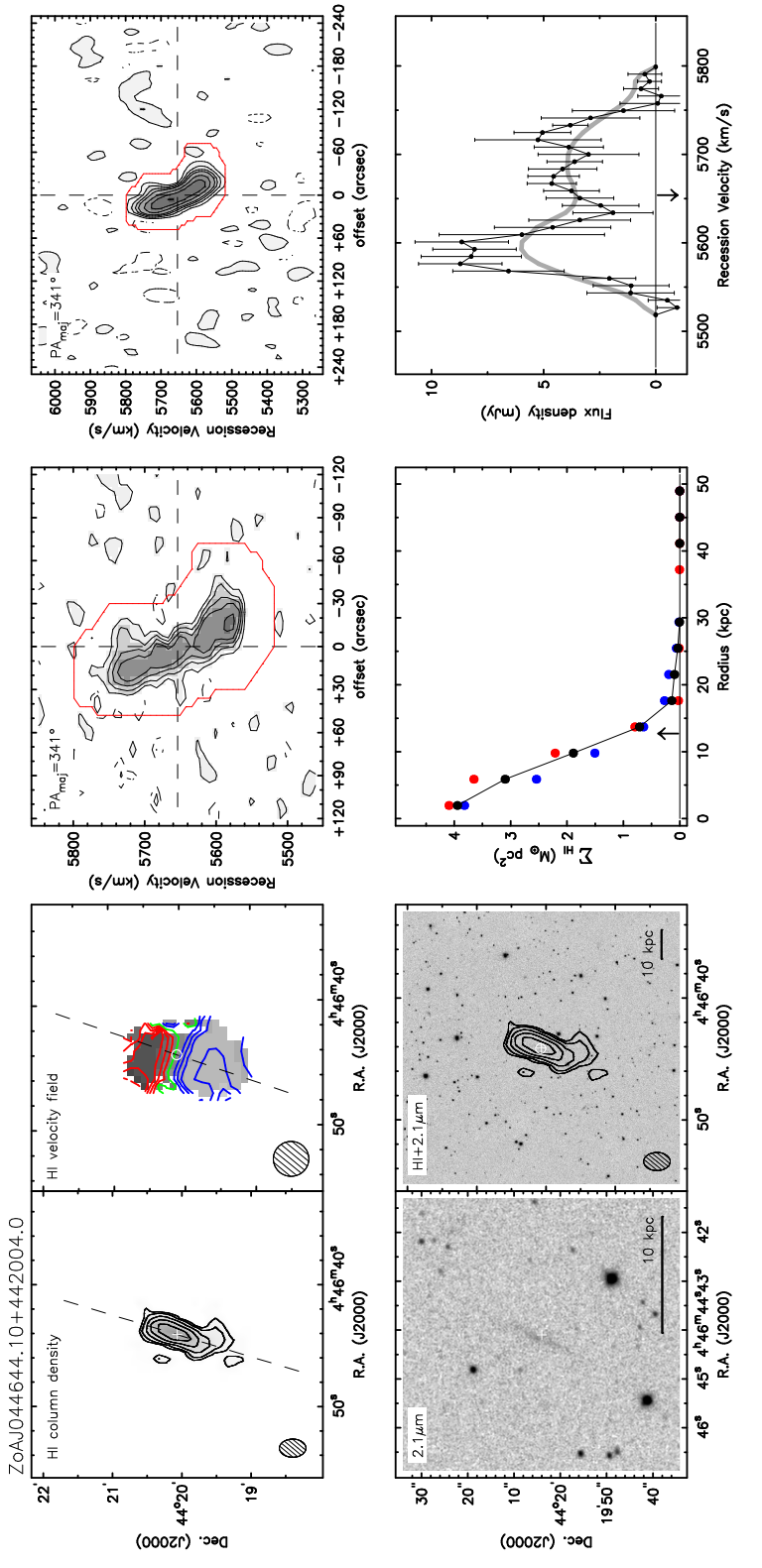

Figure A1. Resolved WSRT HI detections.

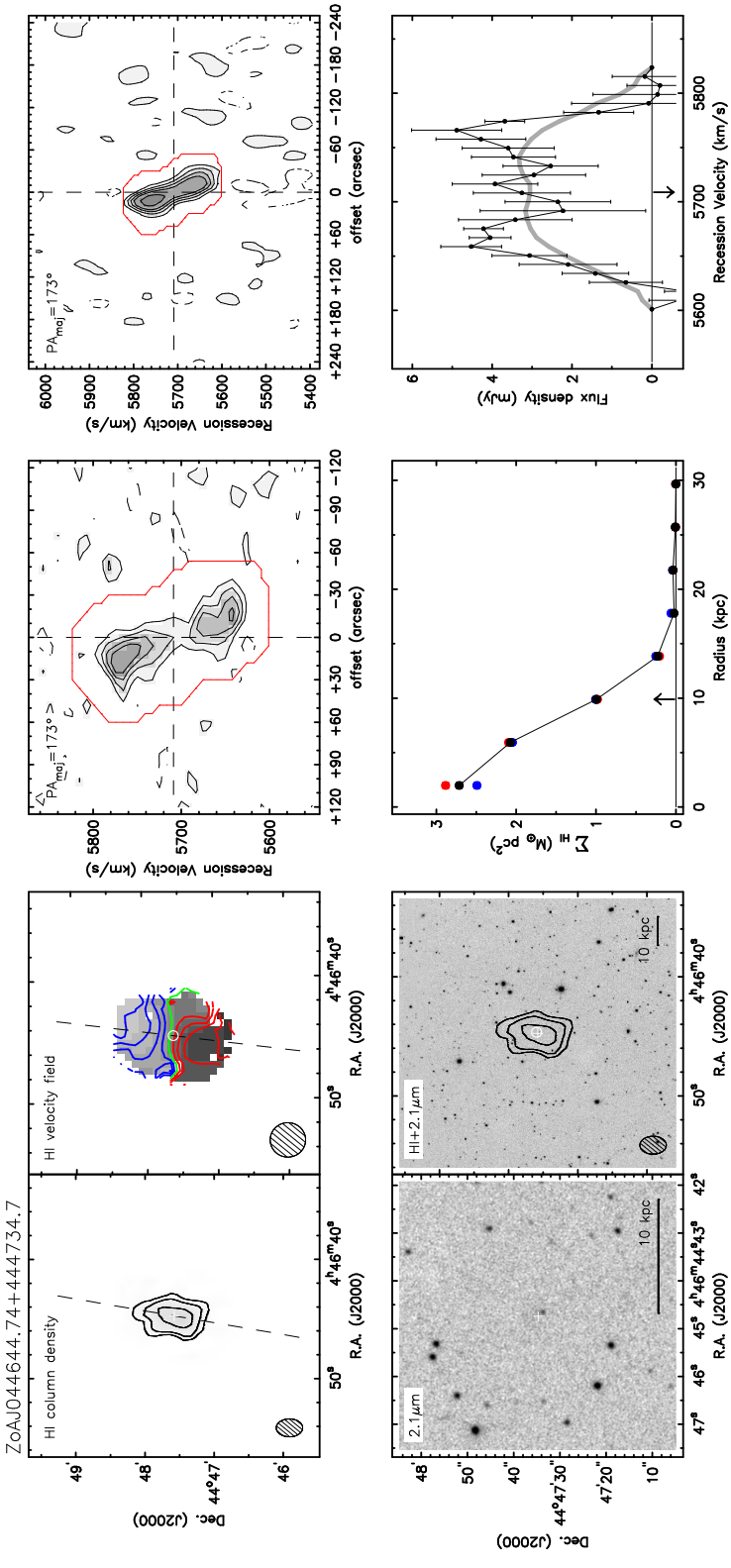

Figure A1. Resolved WSRT HI detections.

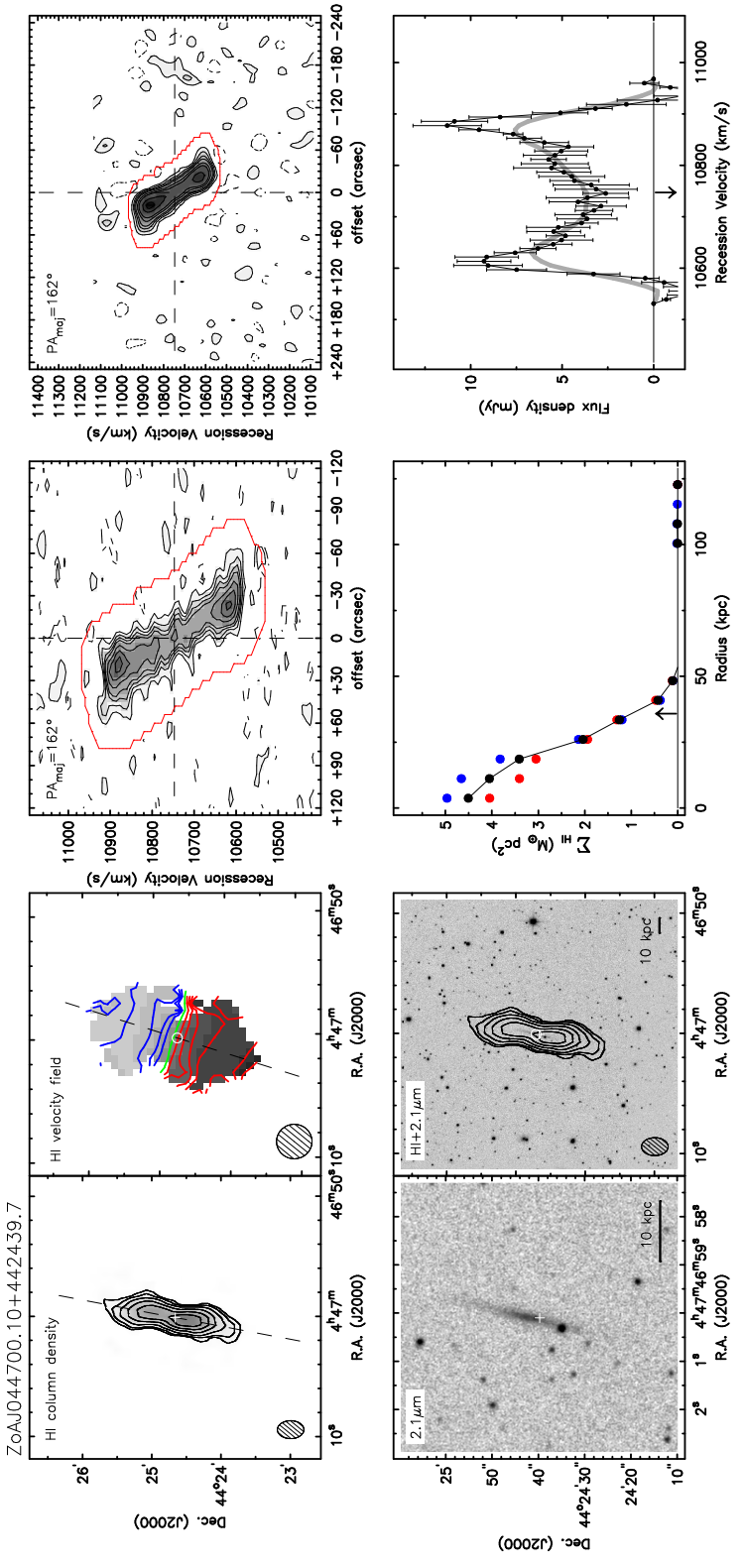

Figure A1. Resolved WSRT HI detections.

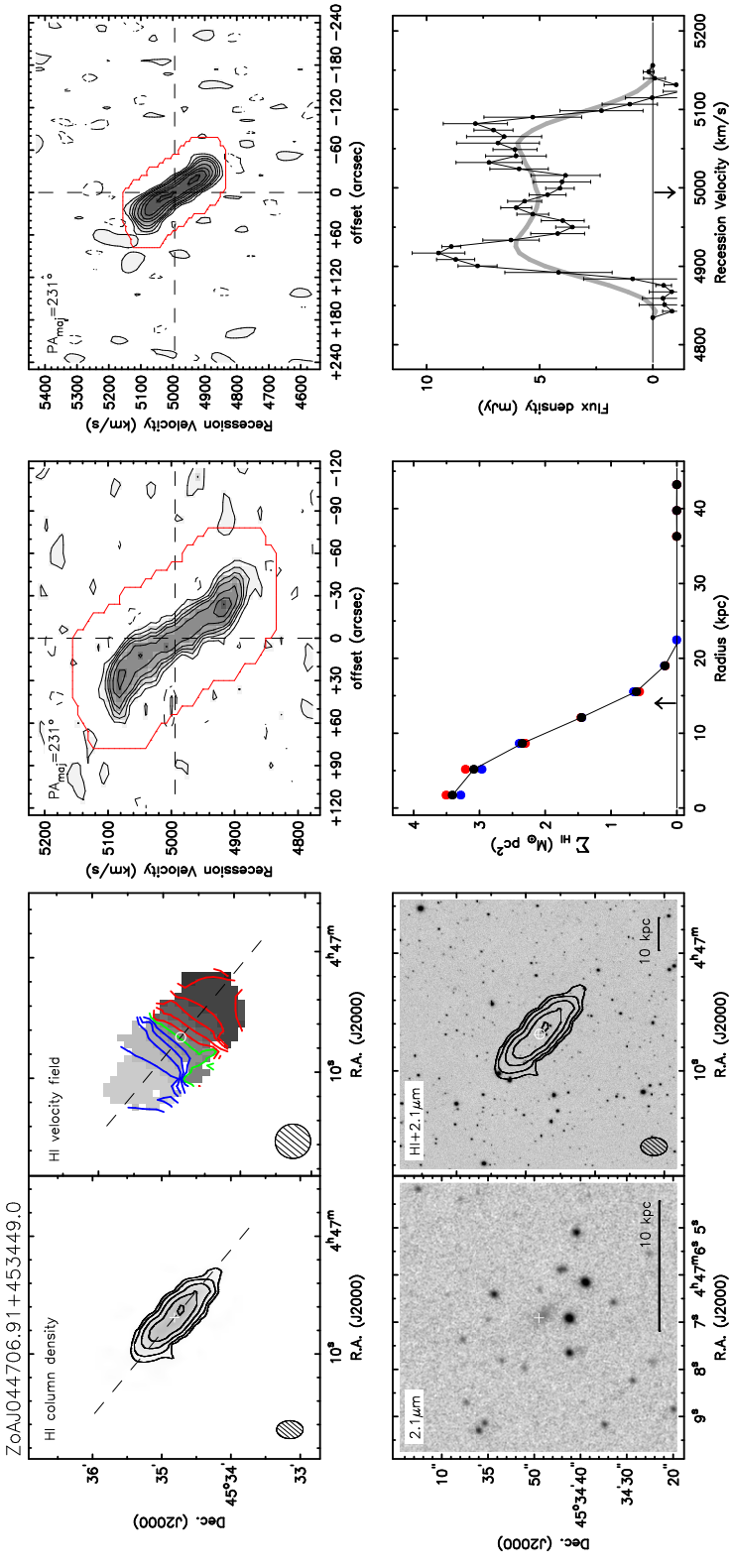

Figure A1. Resolved WSRT HI detections.

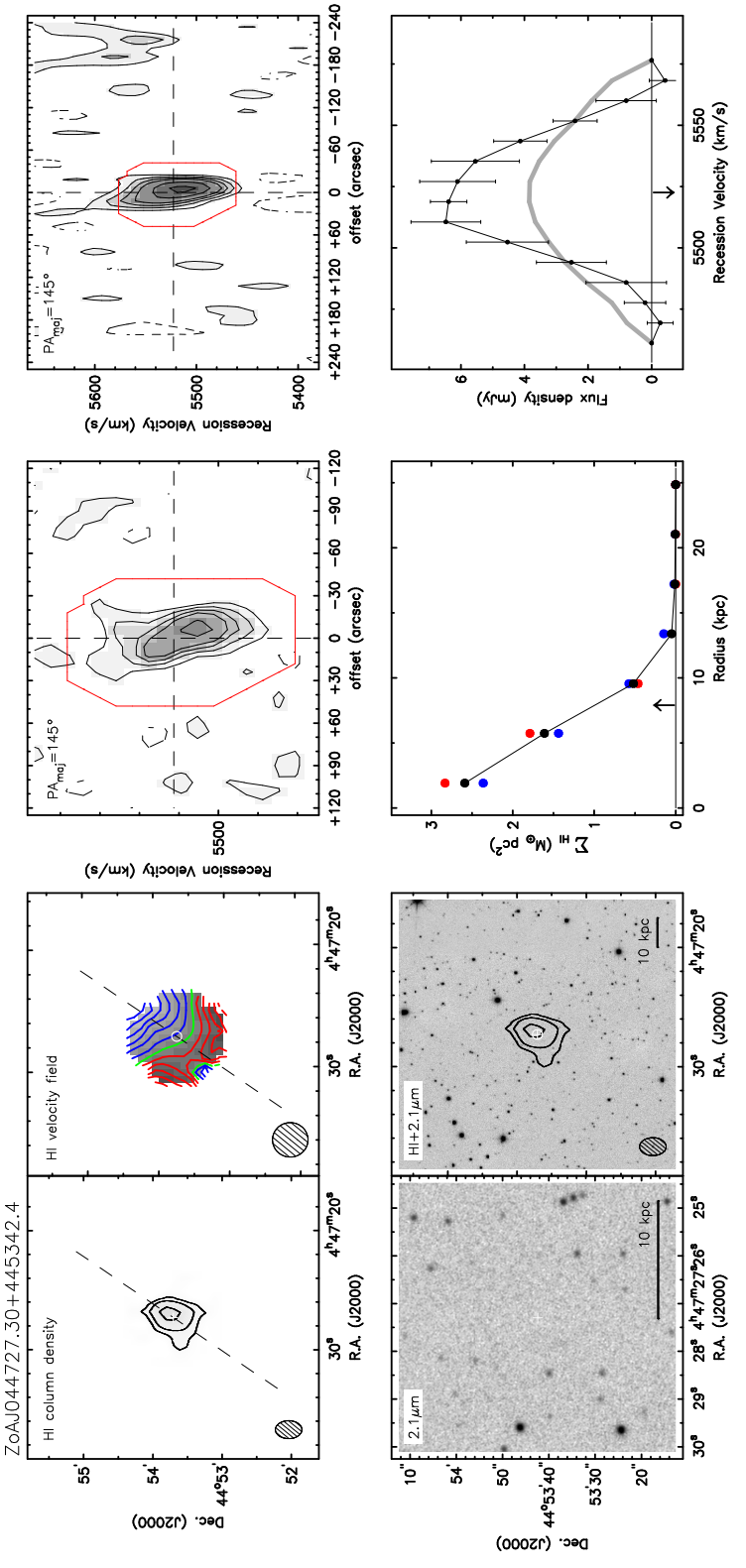

Figure A1. Resolved WSRT HI detections.

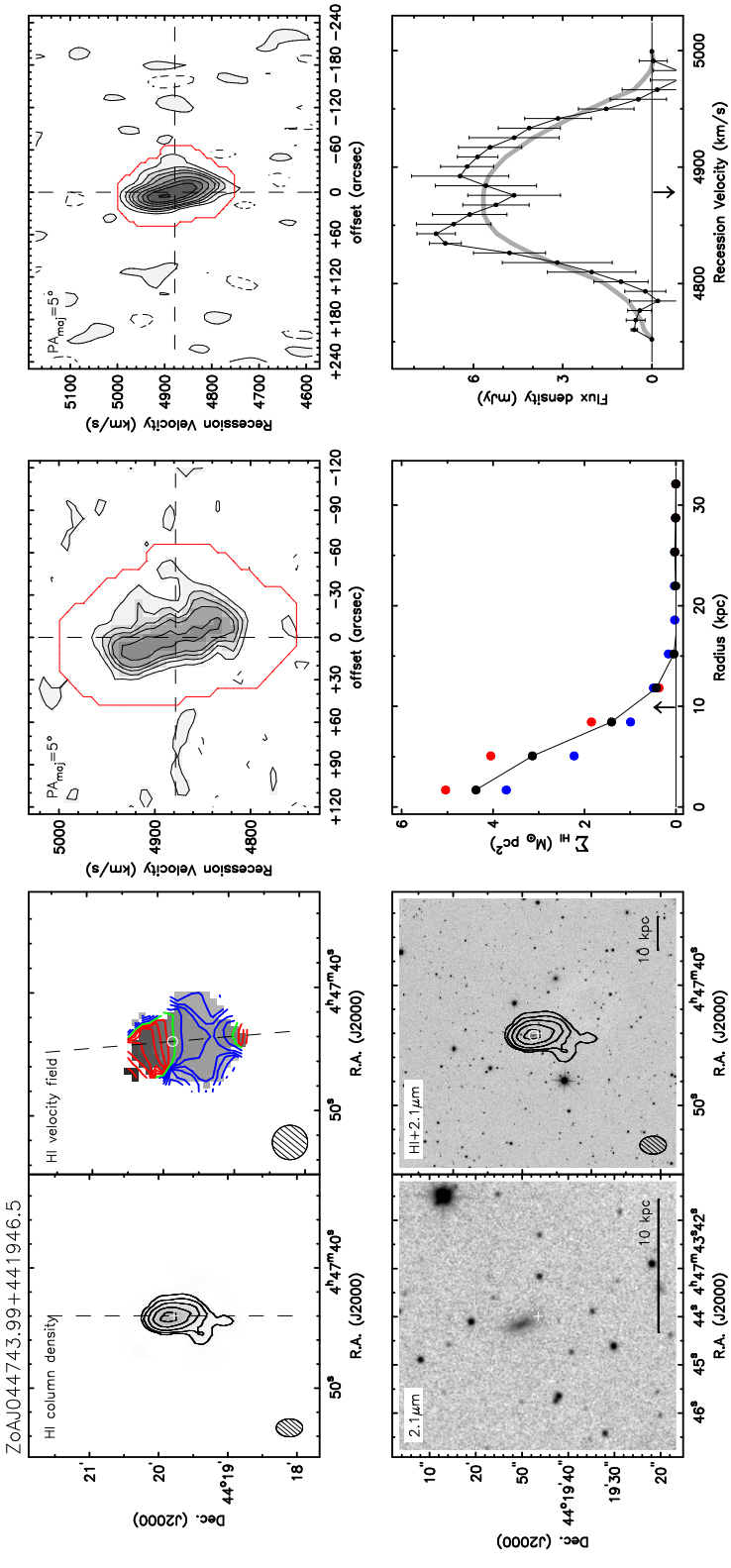

Figure A1. Resolved WSRT HI detections.

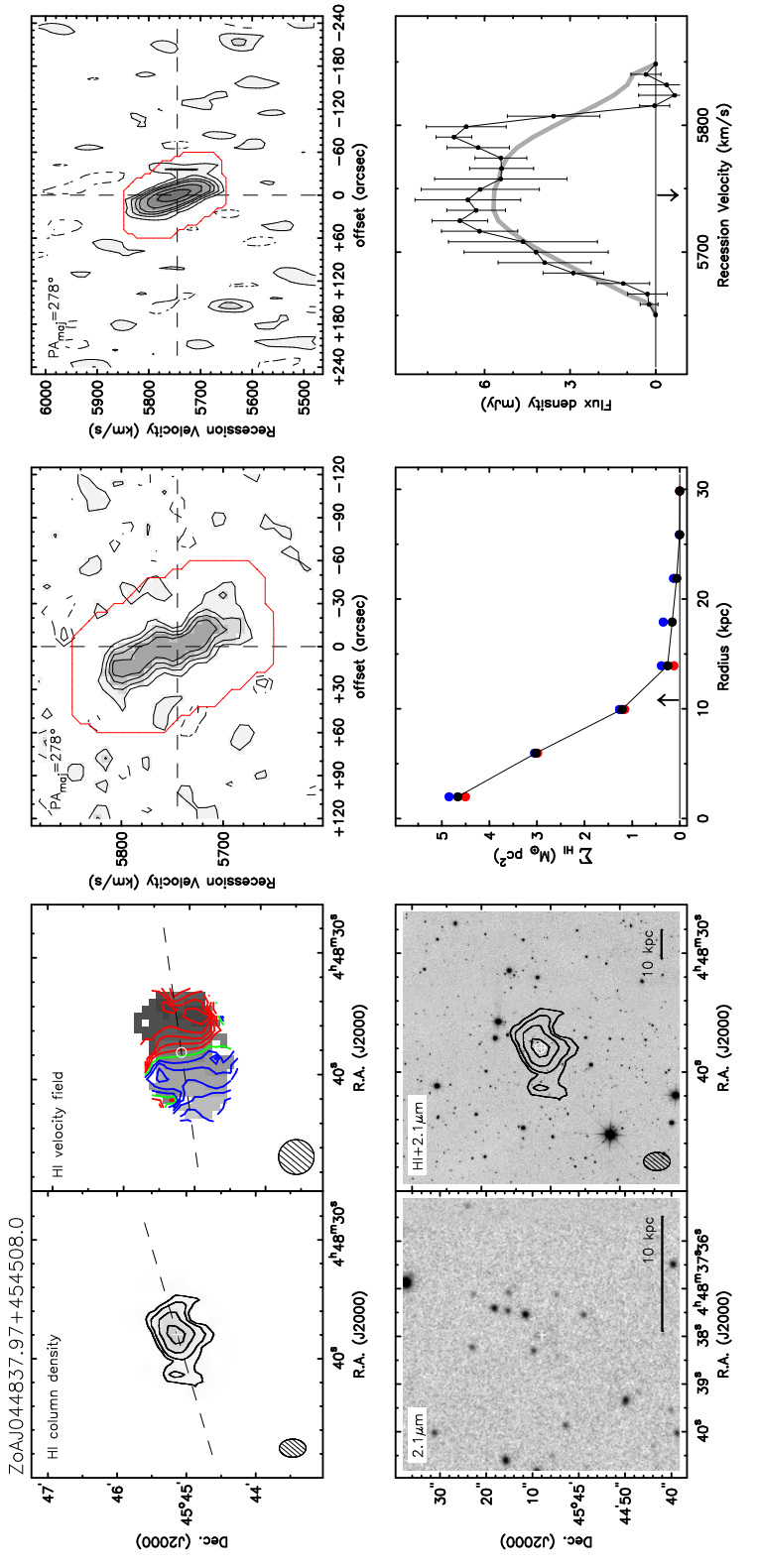

Figure A1. Resolved WSRT HI detections.

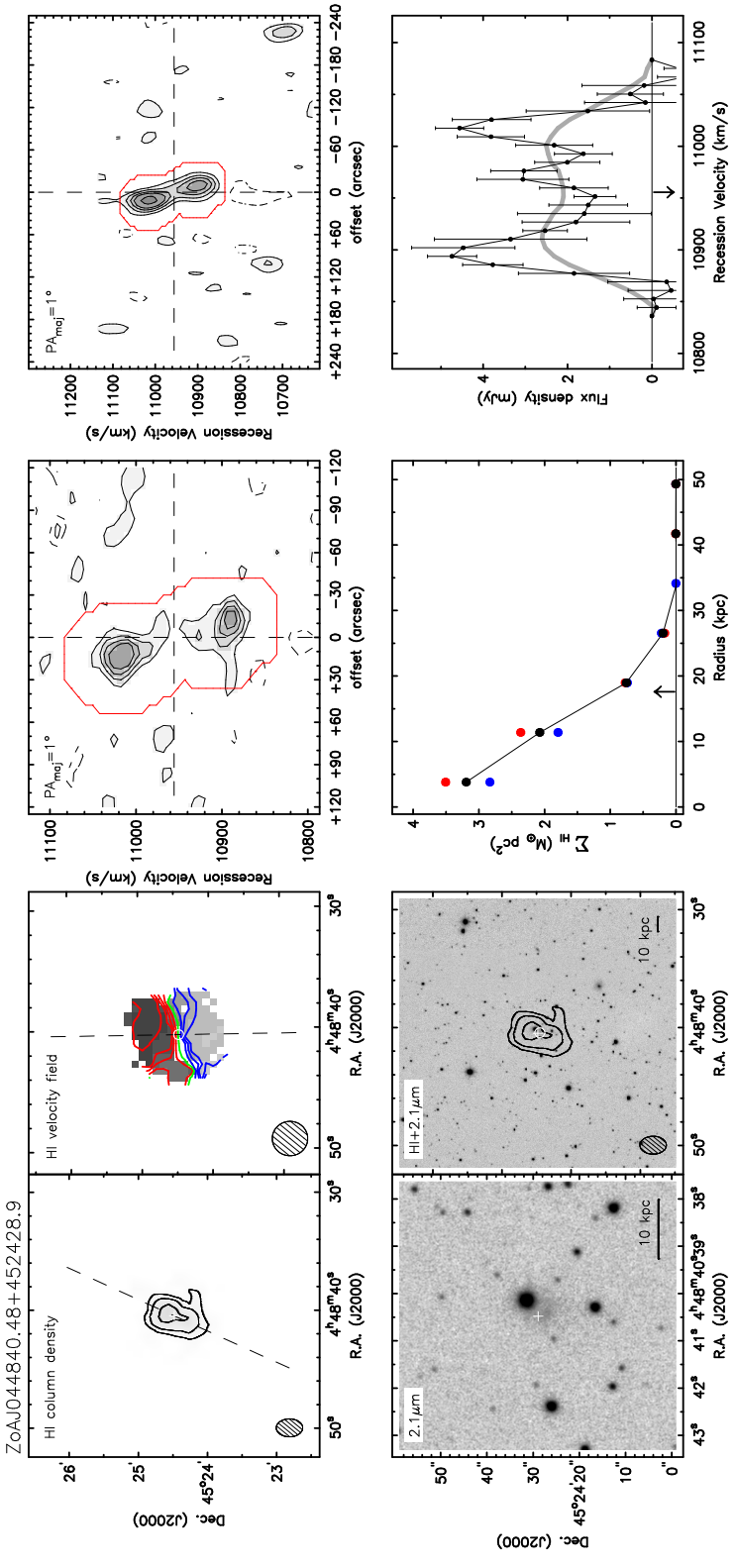

Figure A1. Resolved WSRT HI detections.

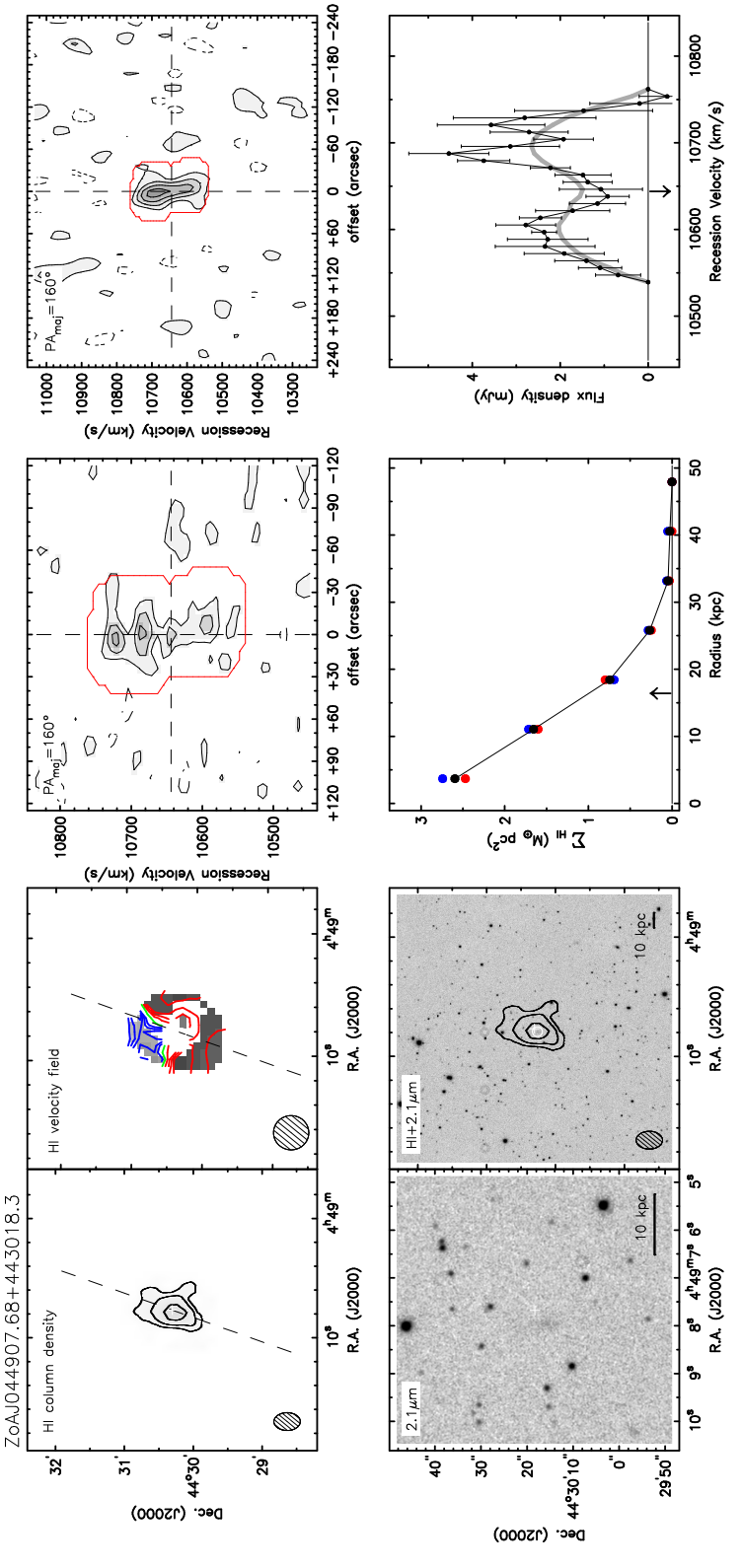

Figure A1. Resolved WSRT HI detections.

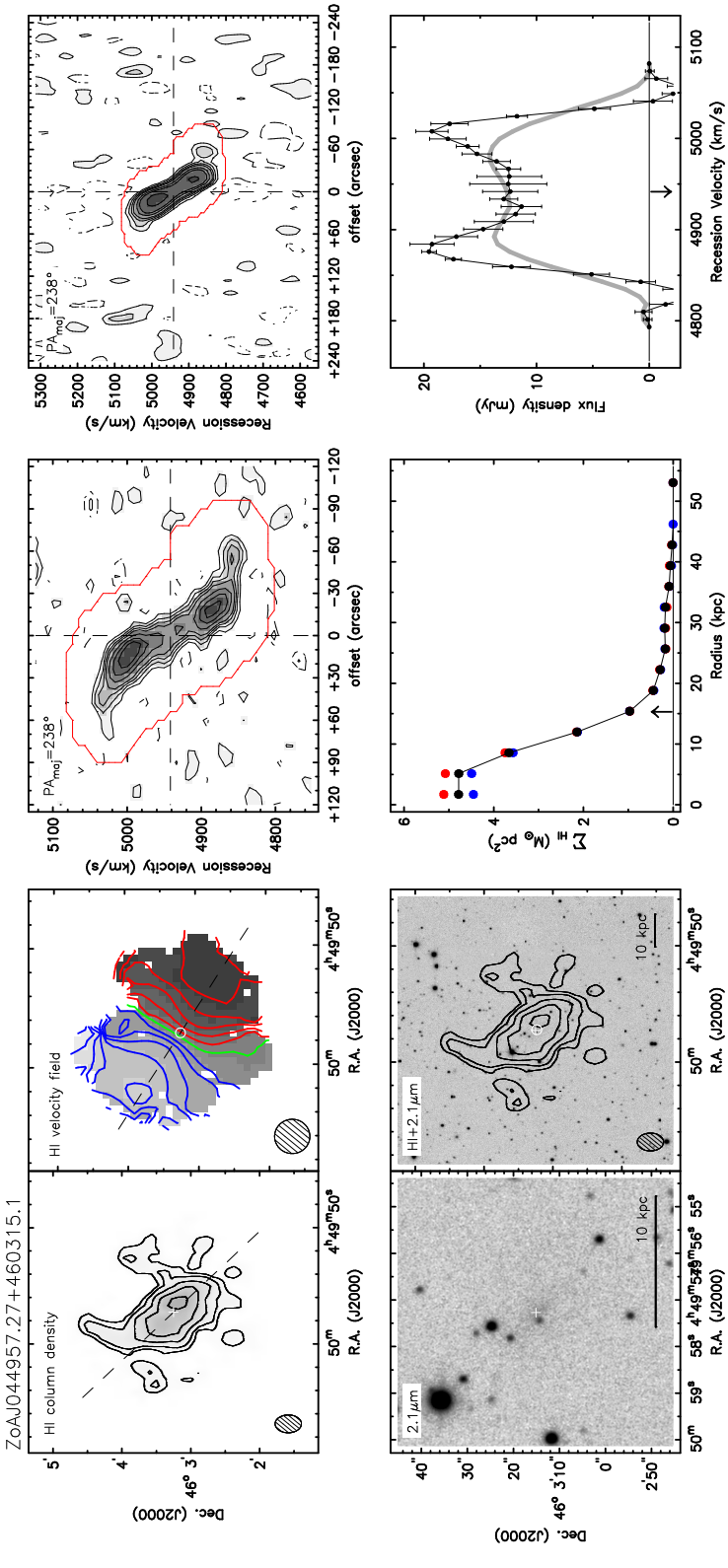

Figure A1. Resolved WSRT HI detections.

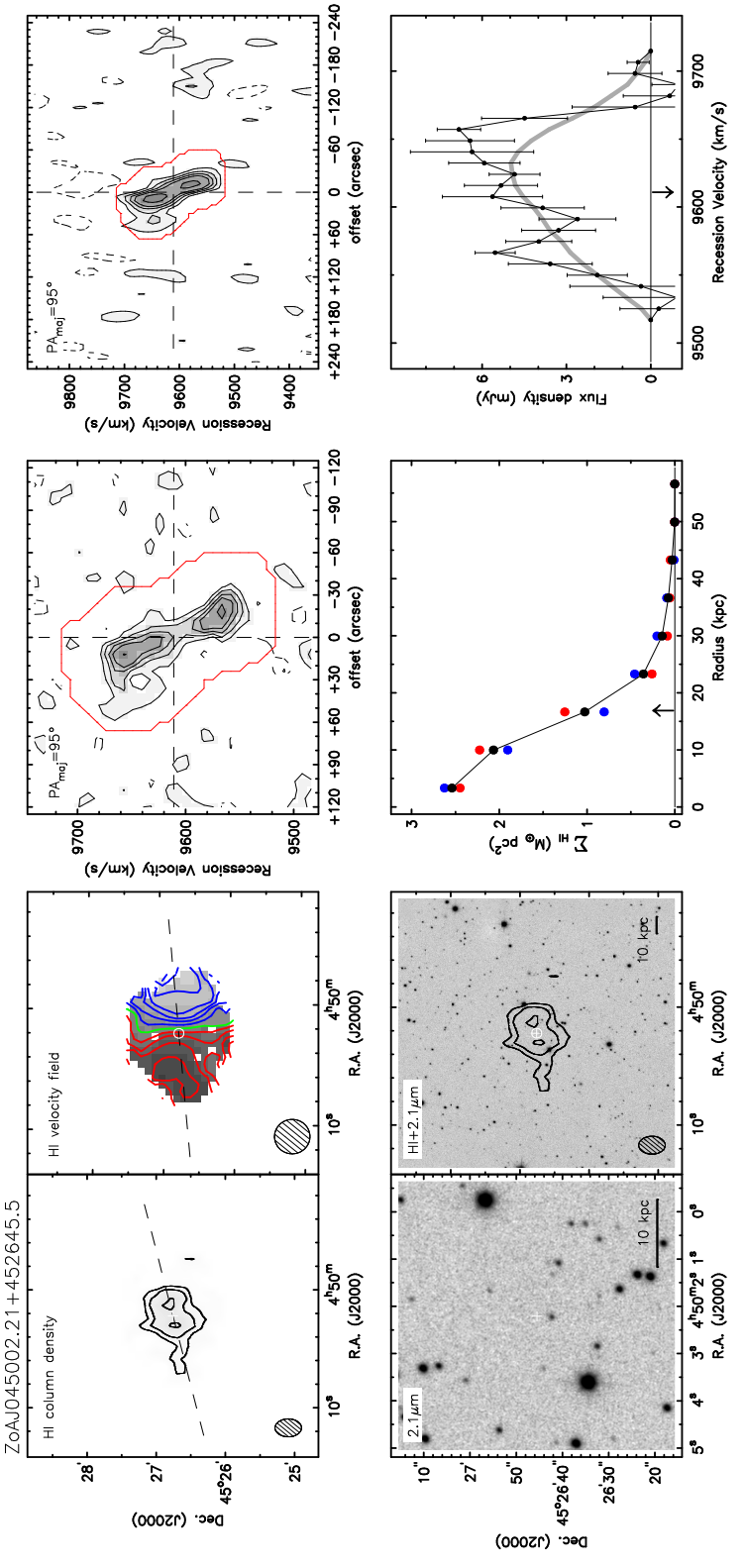

Figure A1. Resolved WSRT HI detections.

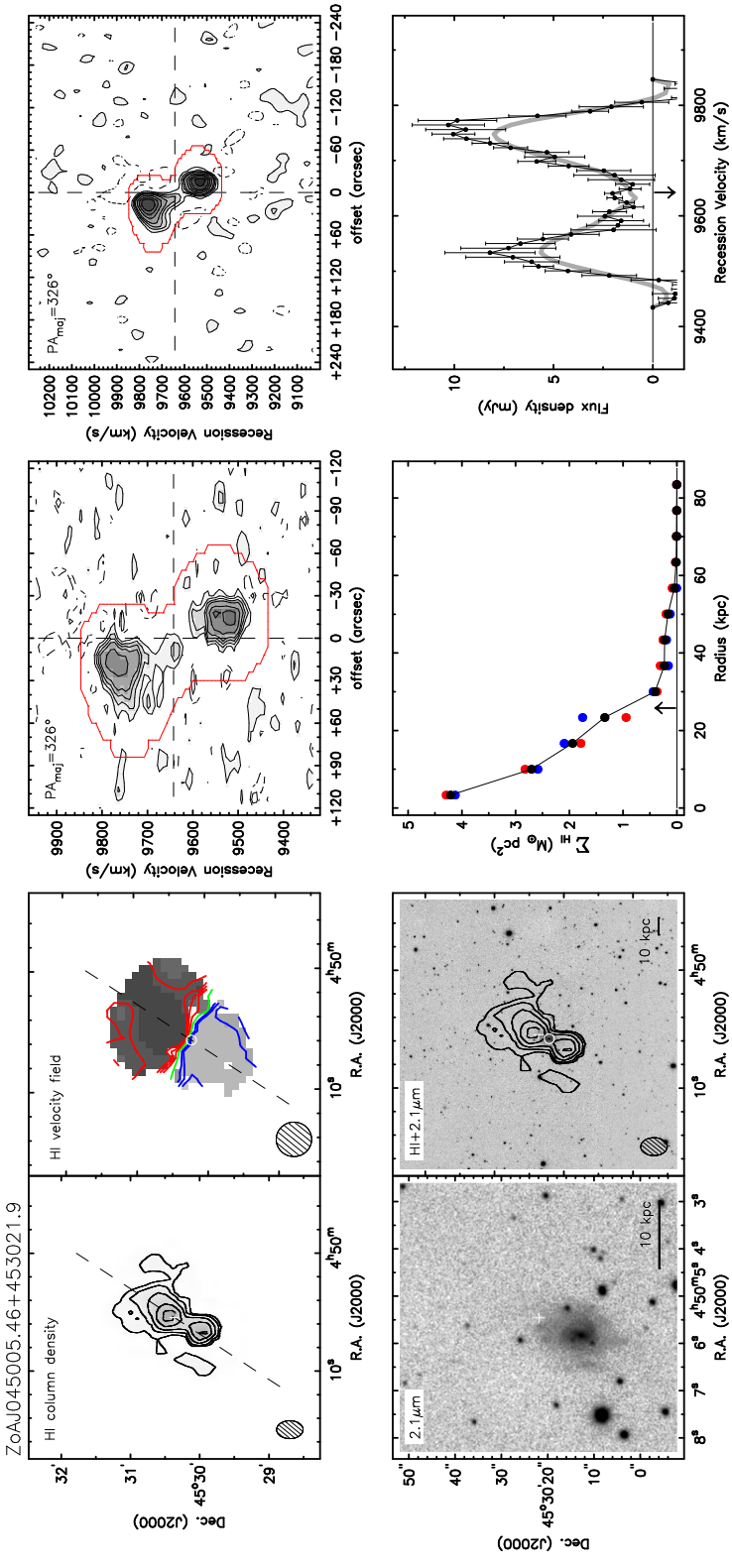

Figure A1. Resolved WSRT HI detections.

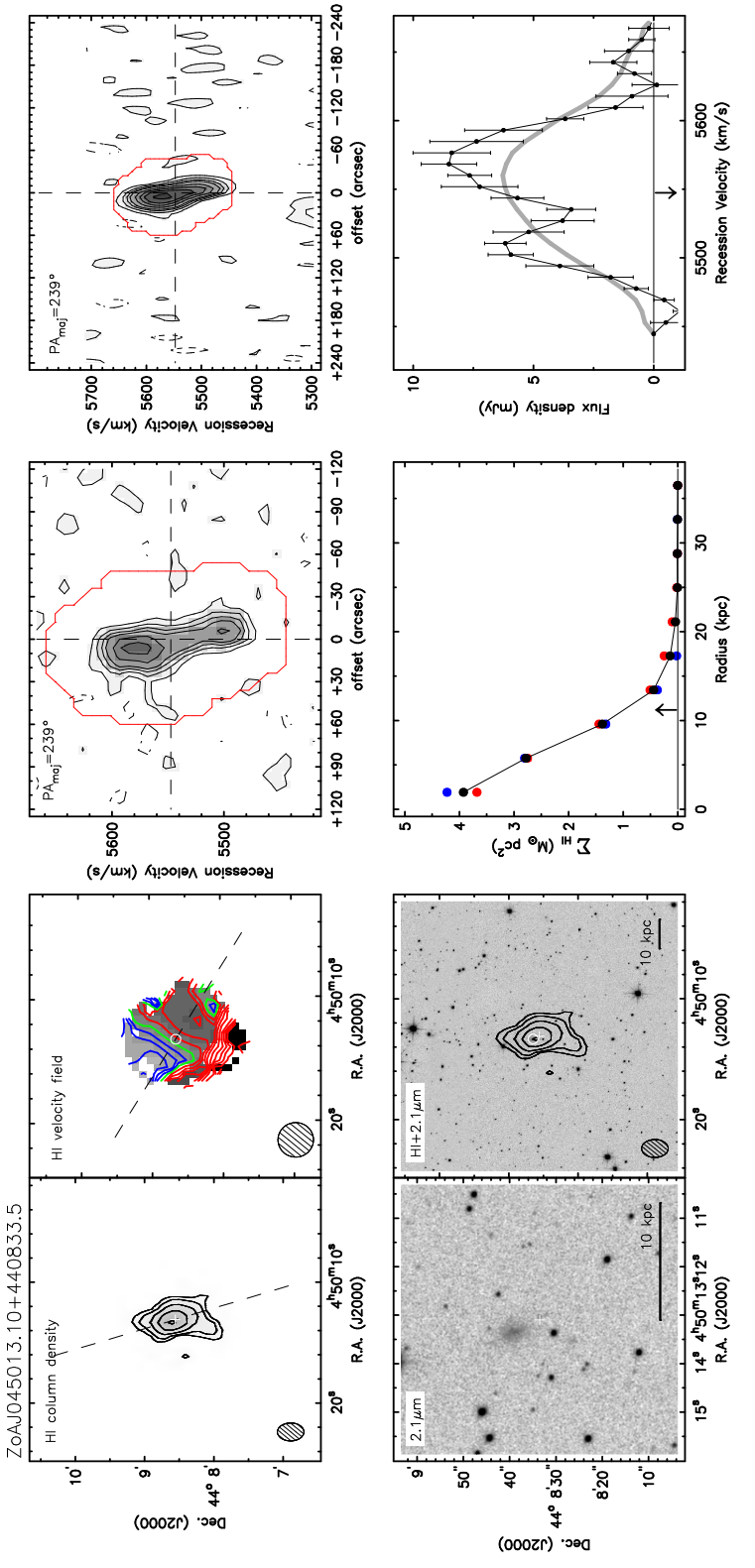

Figure A1. Resolved WSRT HI detections.

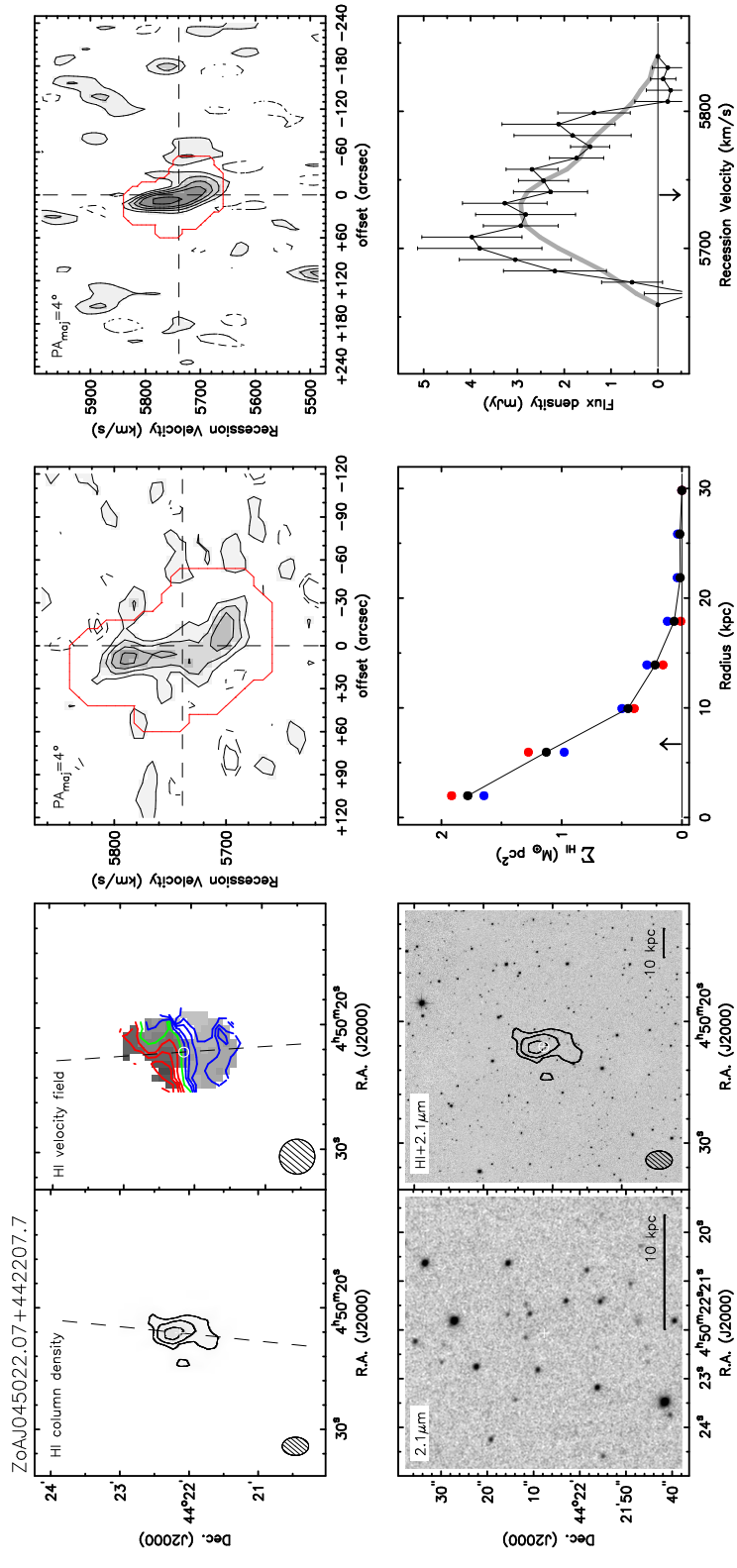

Figure A1. Resolved WSRT HI detections.

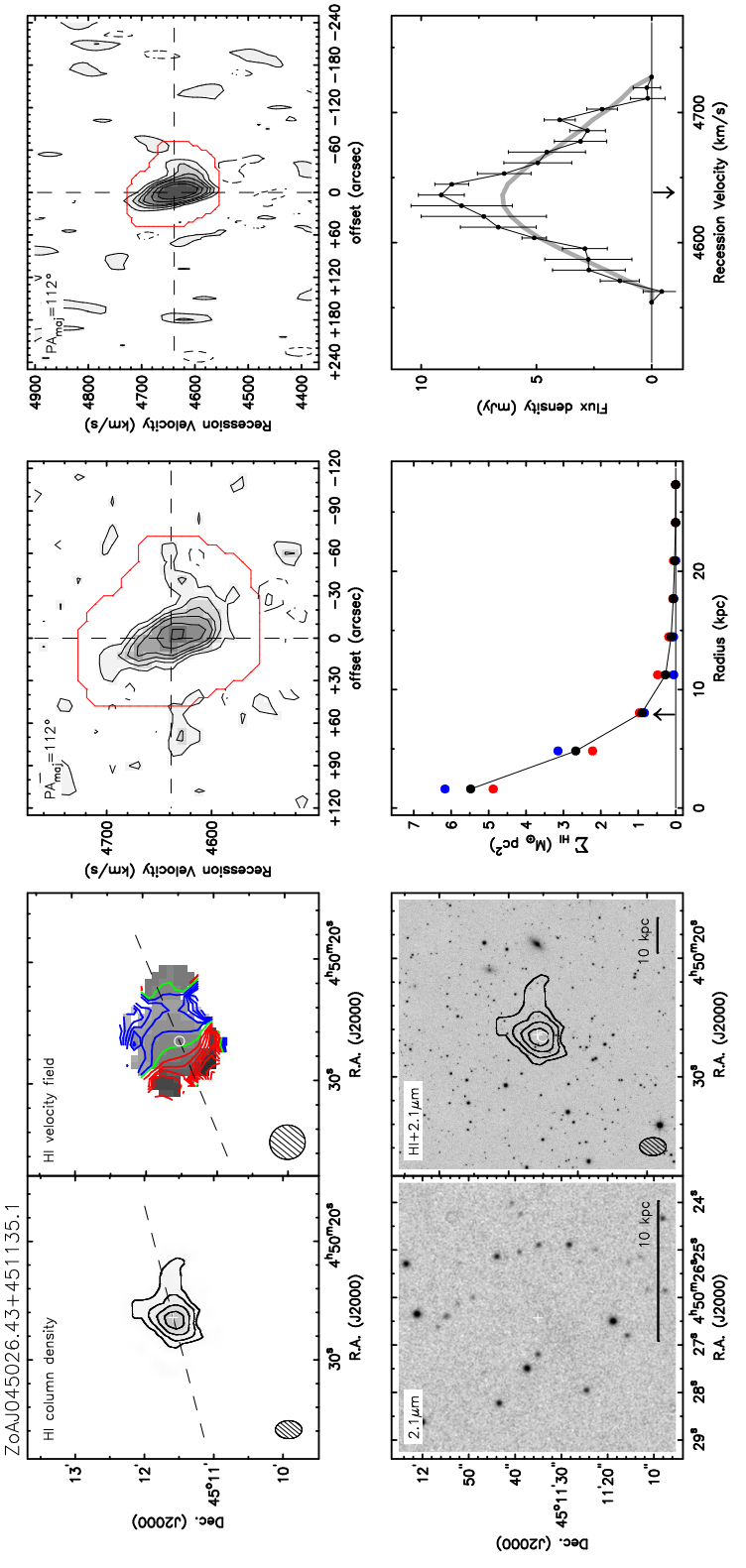

Figure A1. Resolved WSRT HI detections.

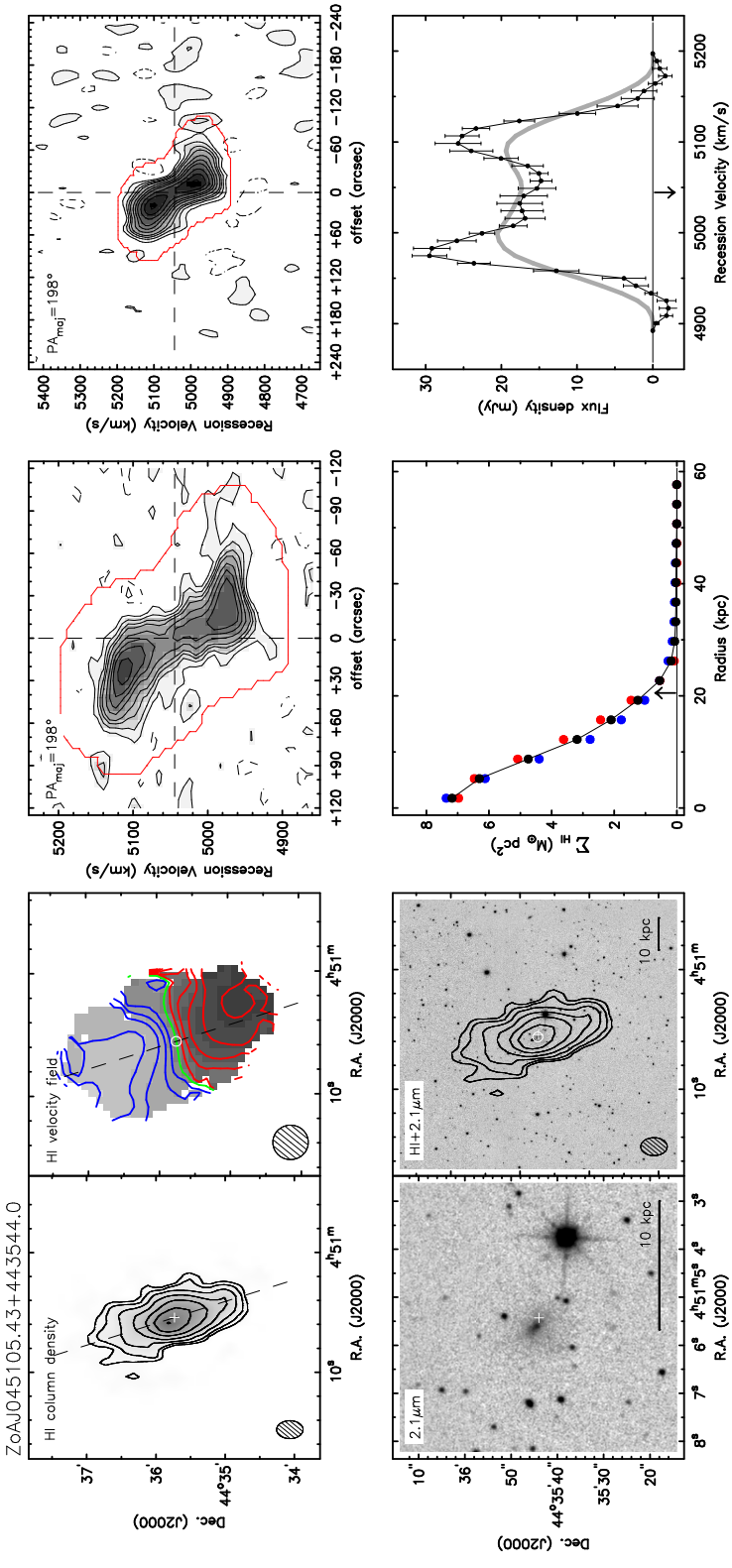

Figure A1. Resolved WSRT HI detections.

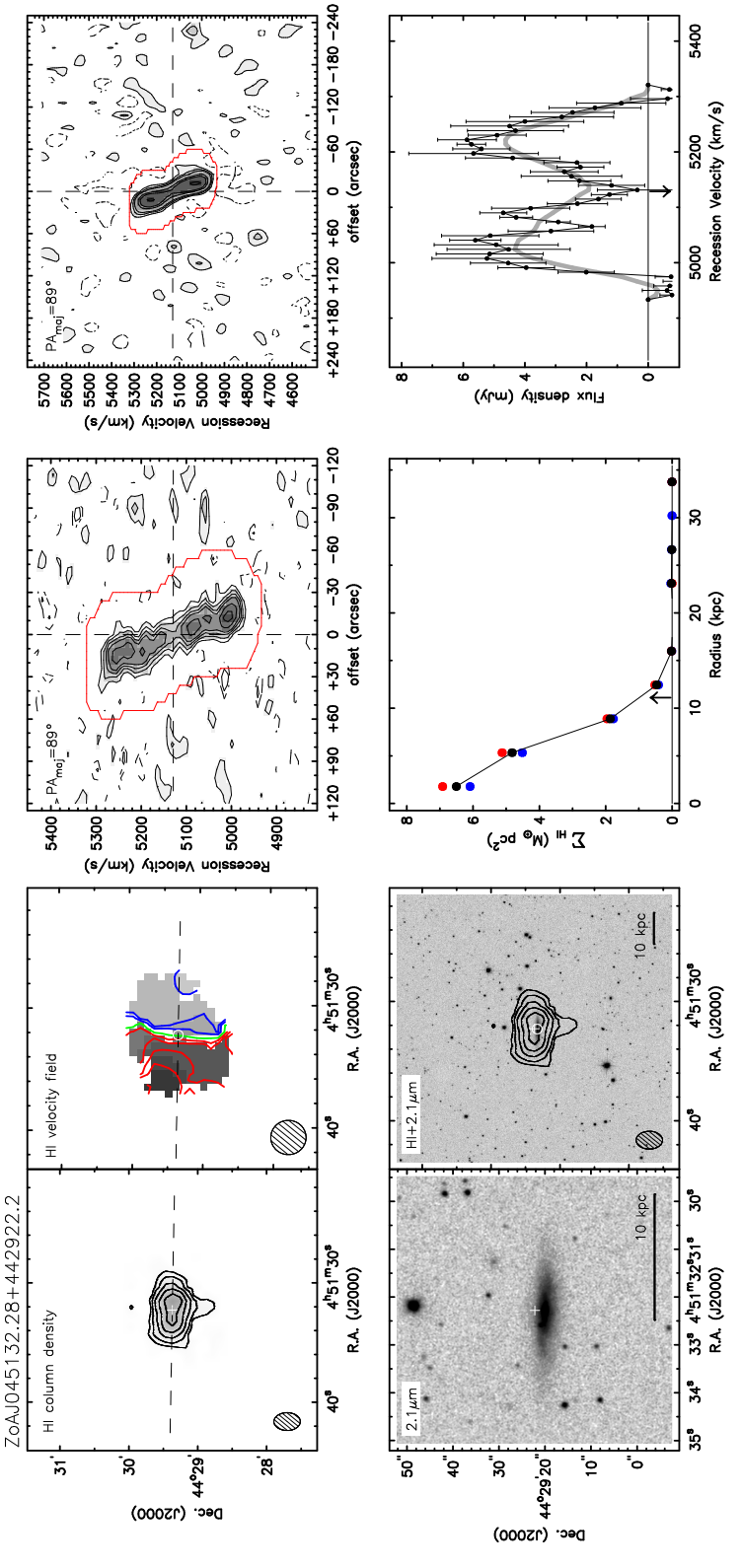

Figure A1. Resolved WSRT HI detections.

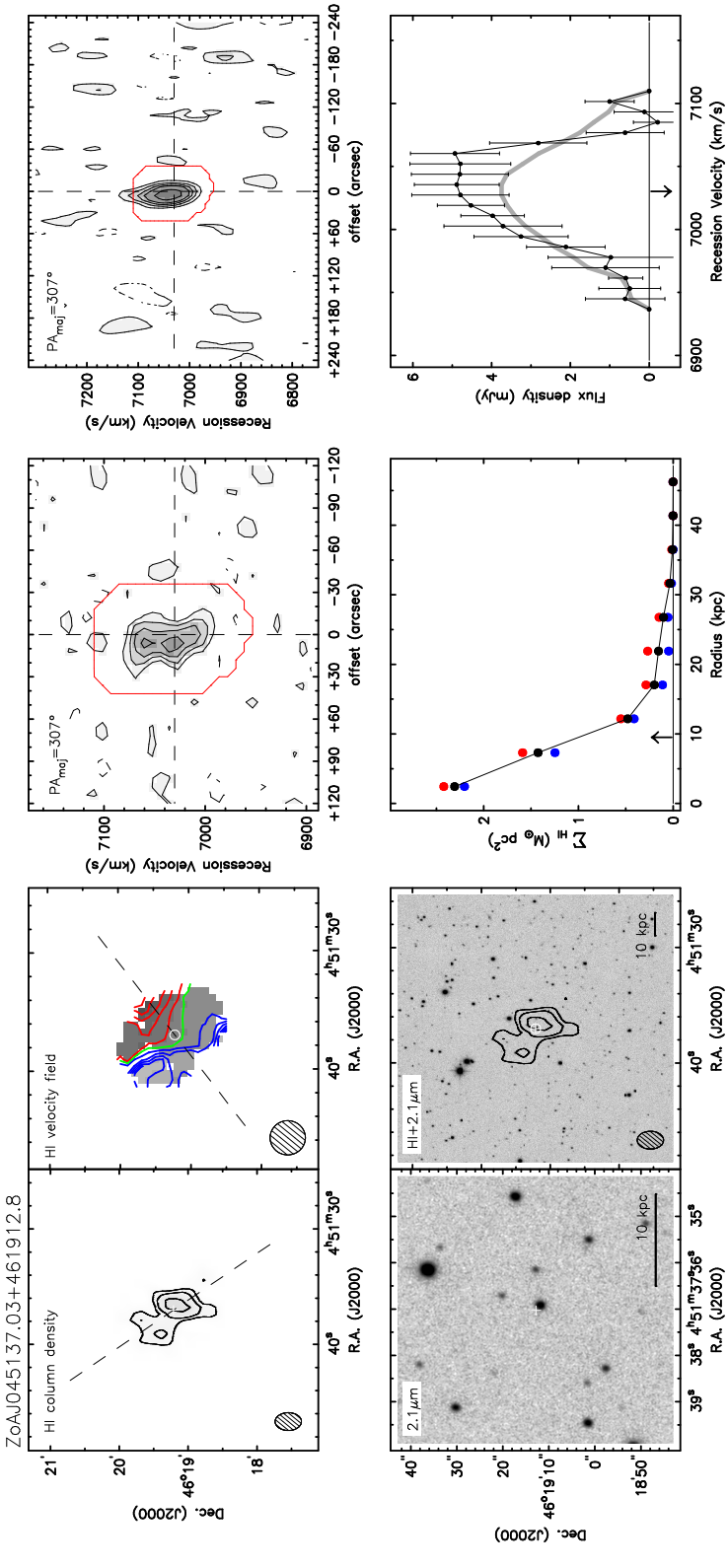

Figure A1. Resolved WSRT HI detections.

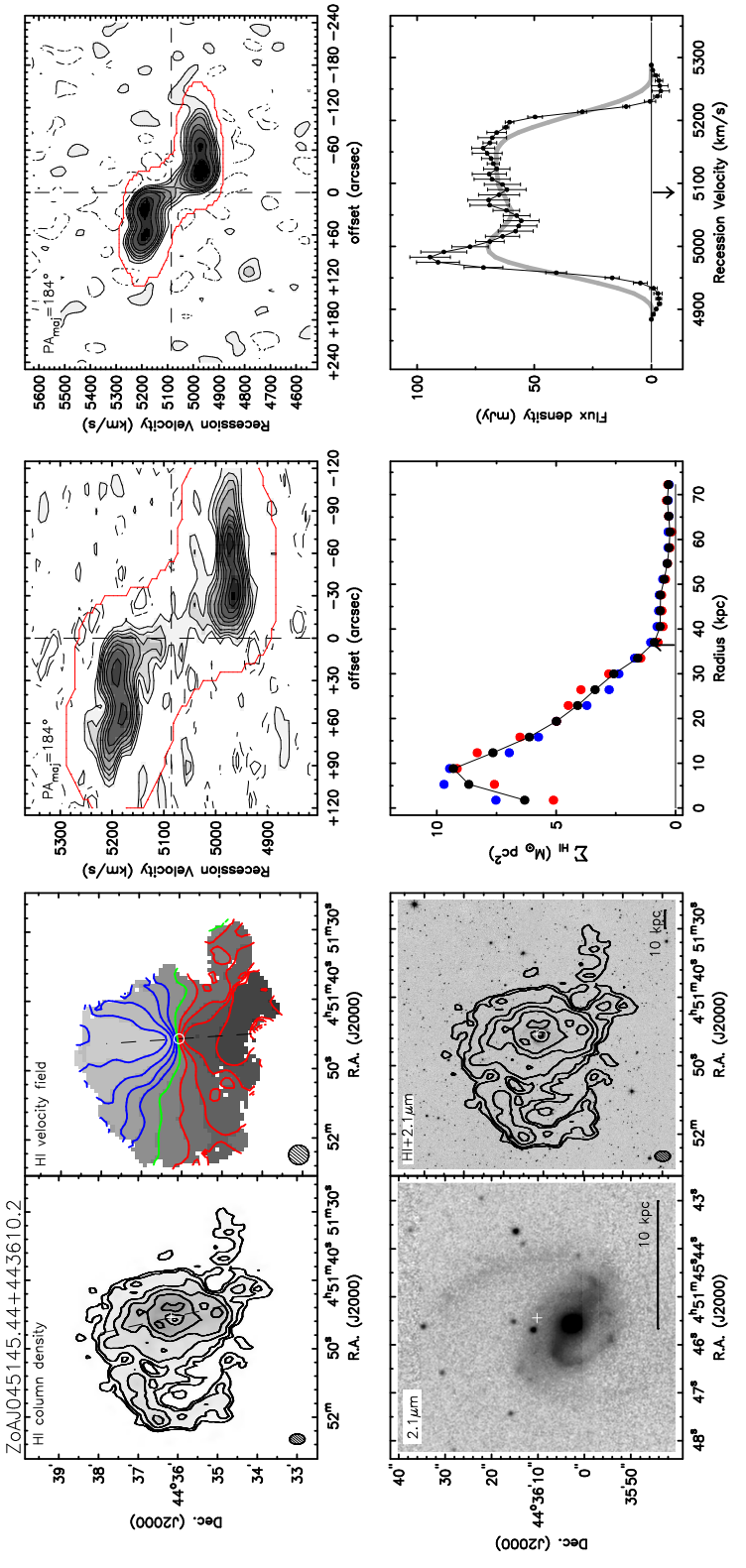

Figure A1. Resolved WSRT HI detections.

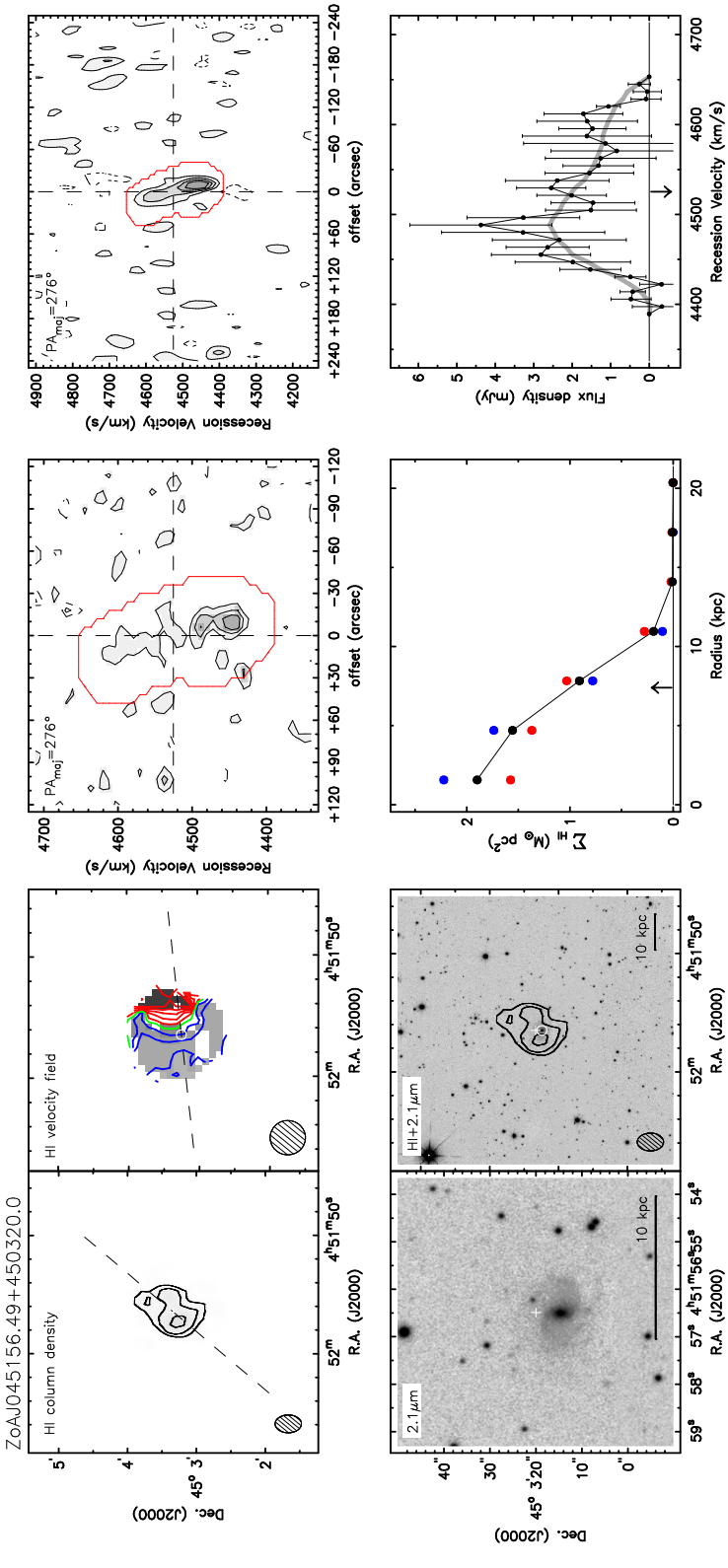

Figure A1. Resolved WSRT HI detections.

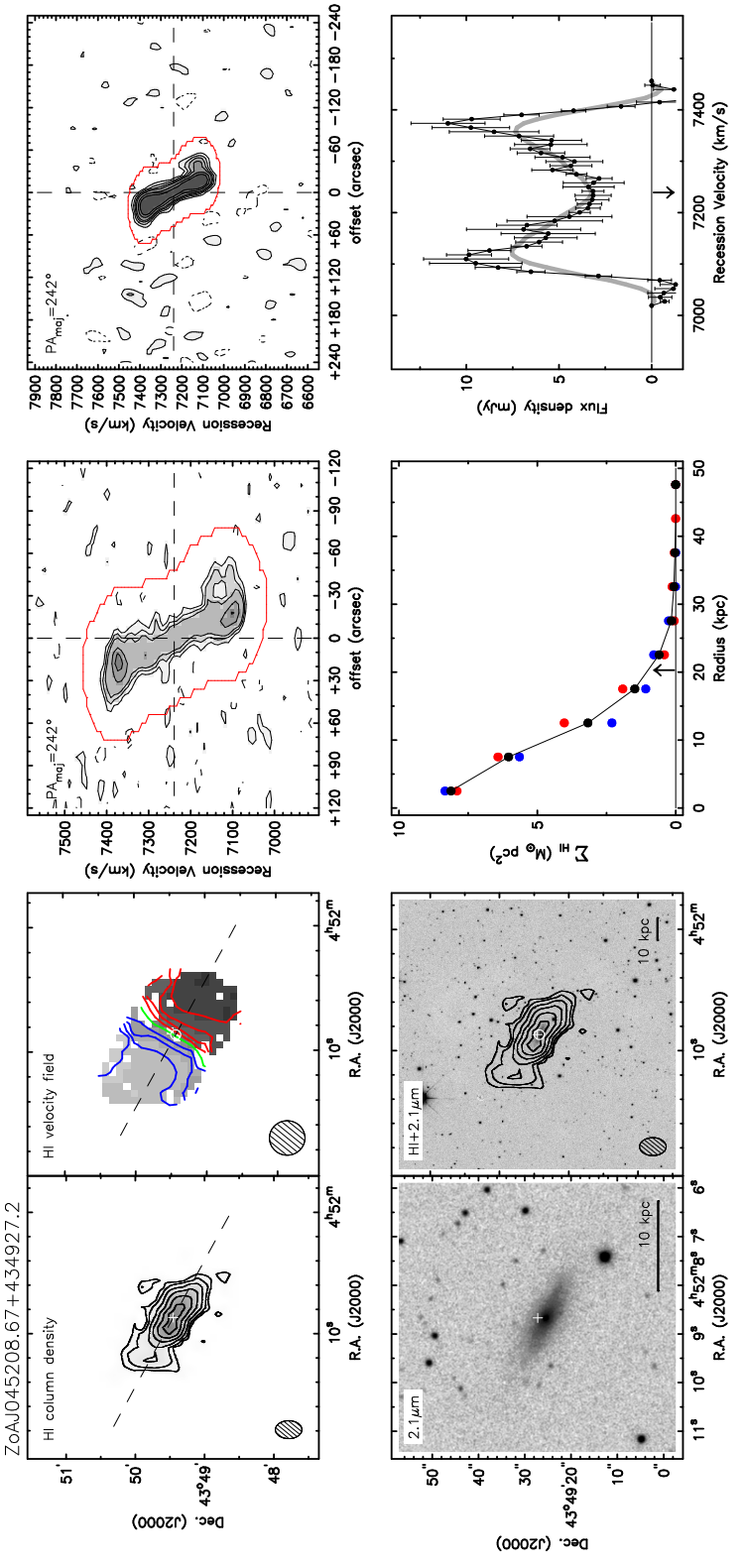

Figure A1. Resolved WSRT HI detections.

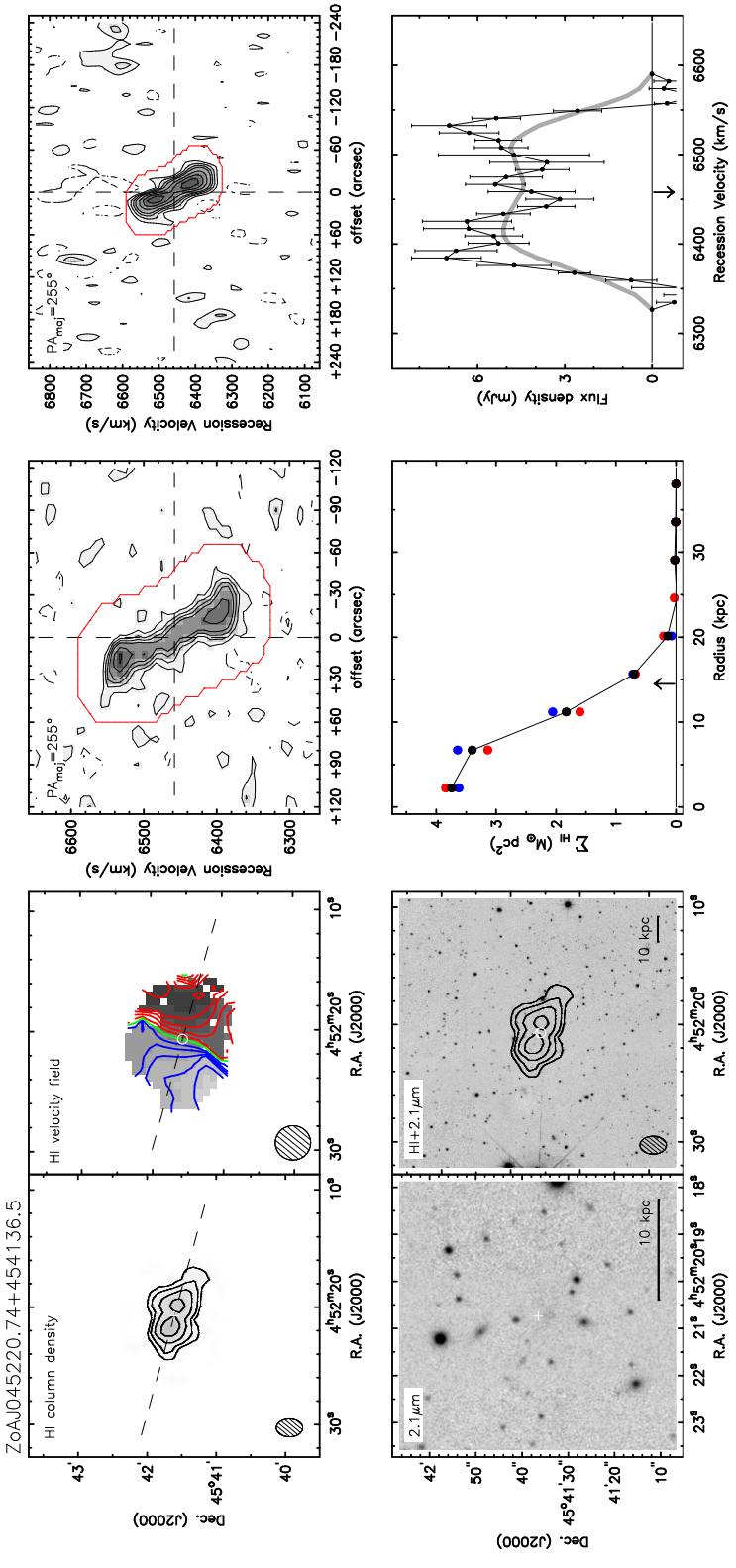

Figure A1. Resolved WSRT HI detections.

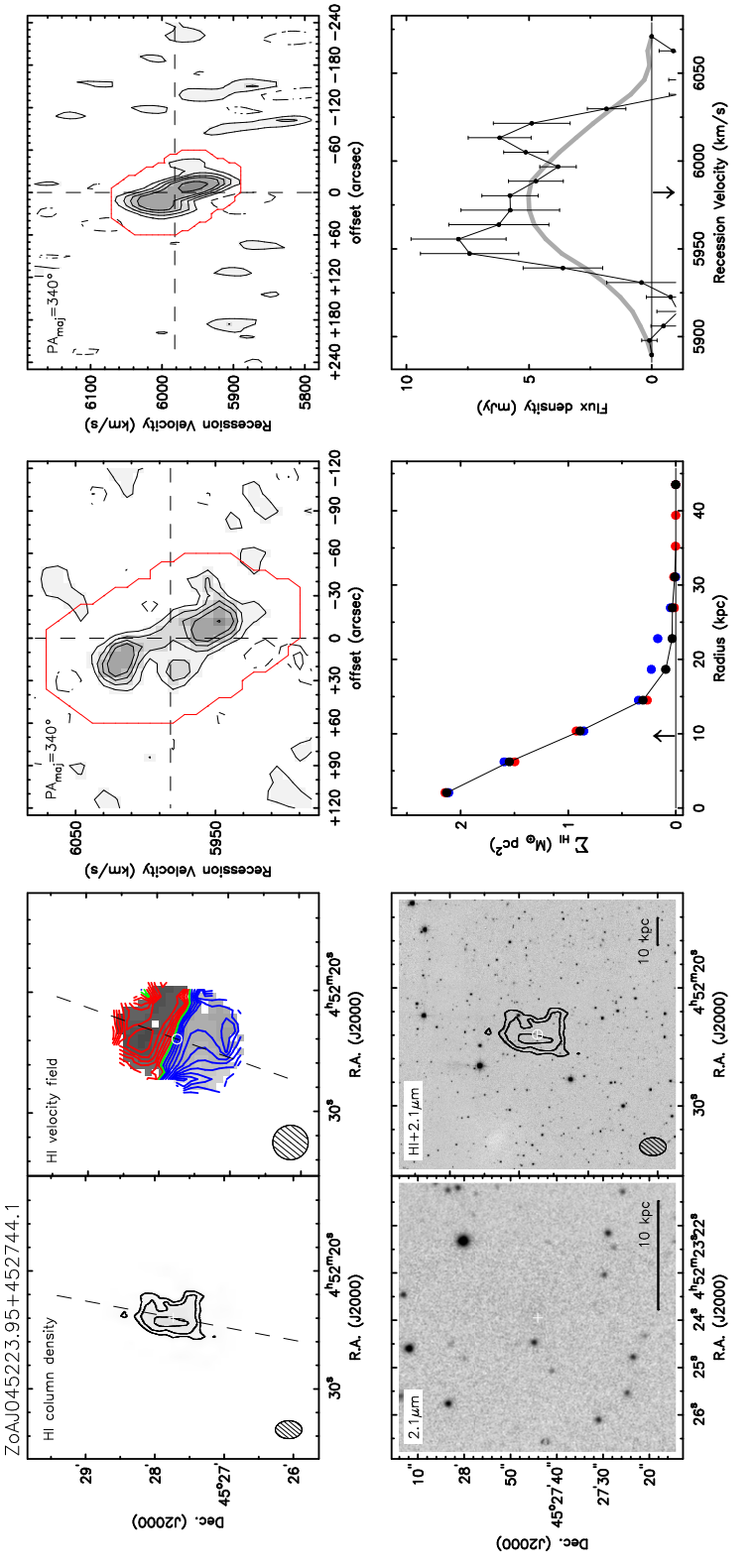

Figure A1. Resolved WSRT HI detections.

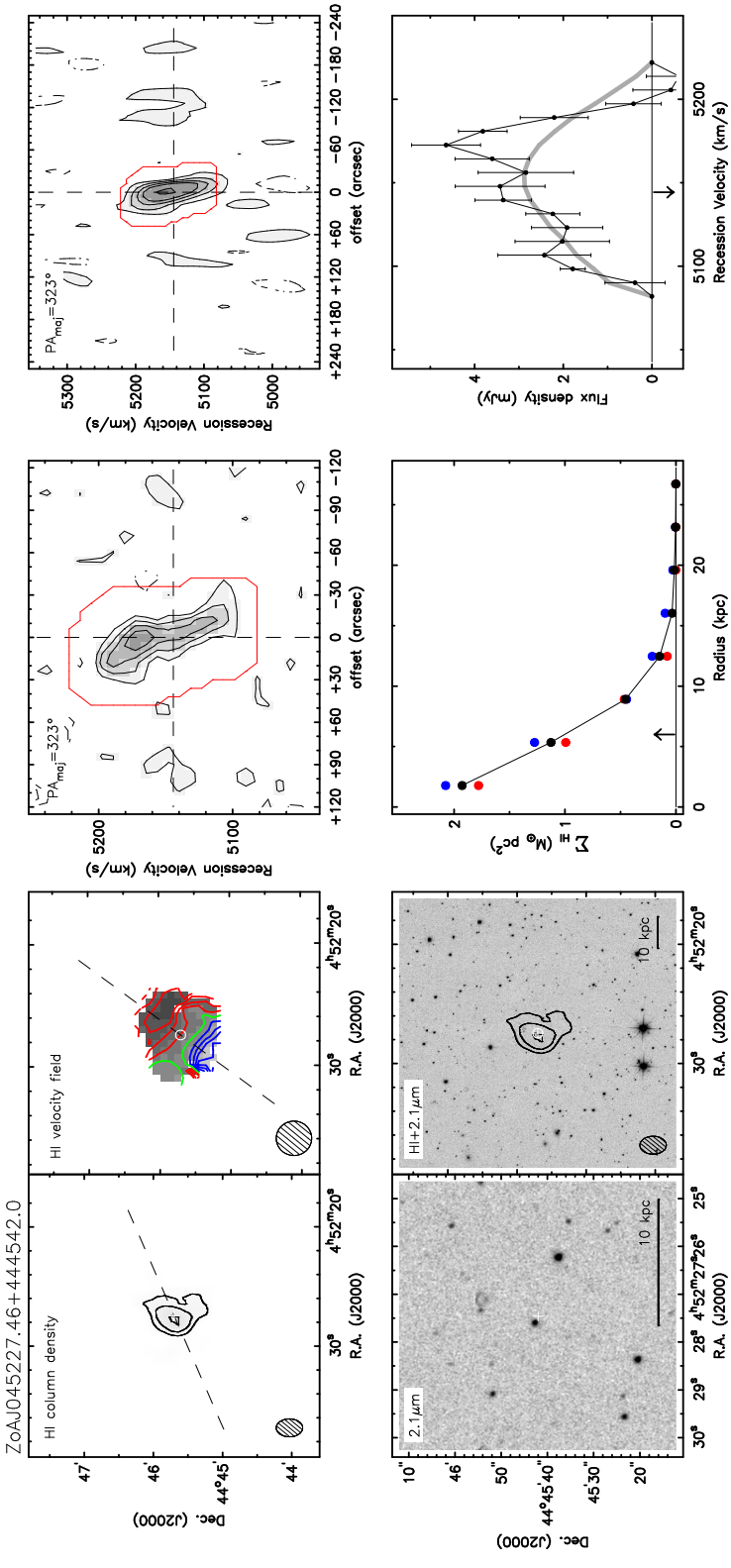

Figure A1. Resolved WSRT HI detections.

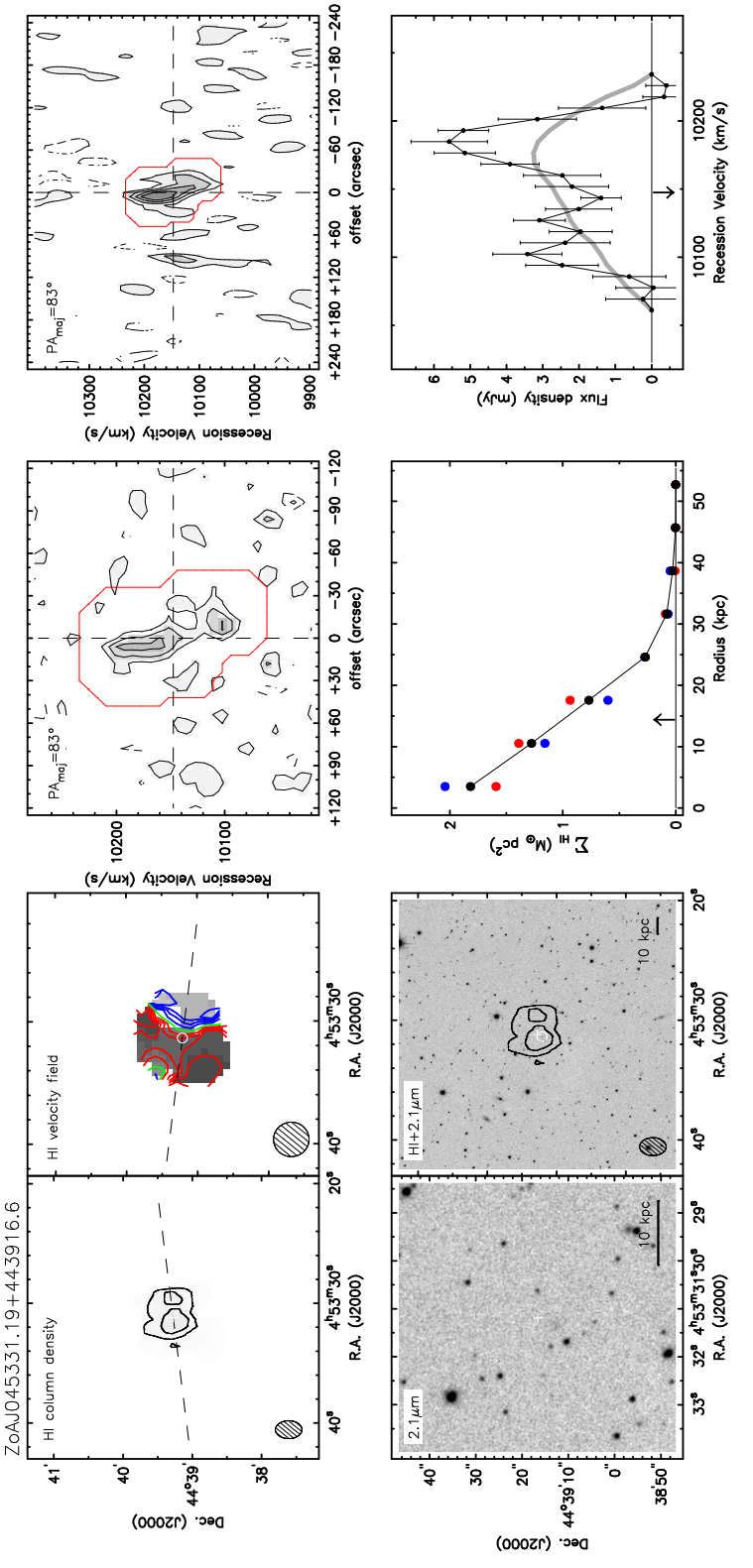

Figure A1. Resolved WSRT HI detections.

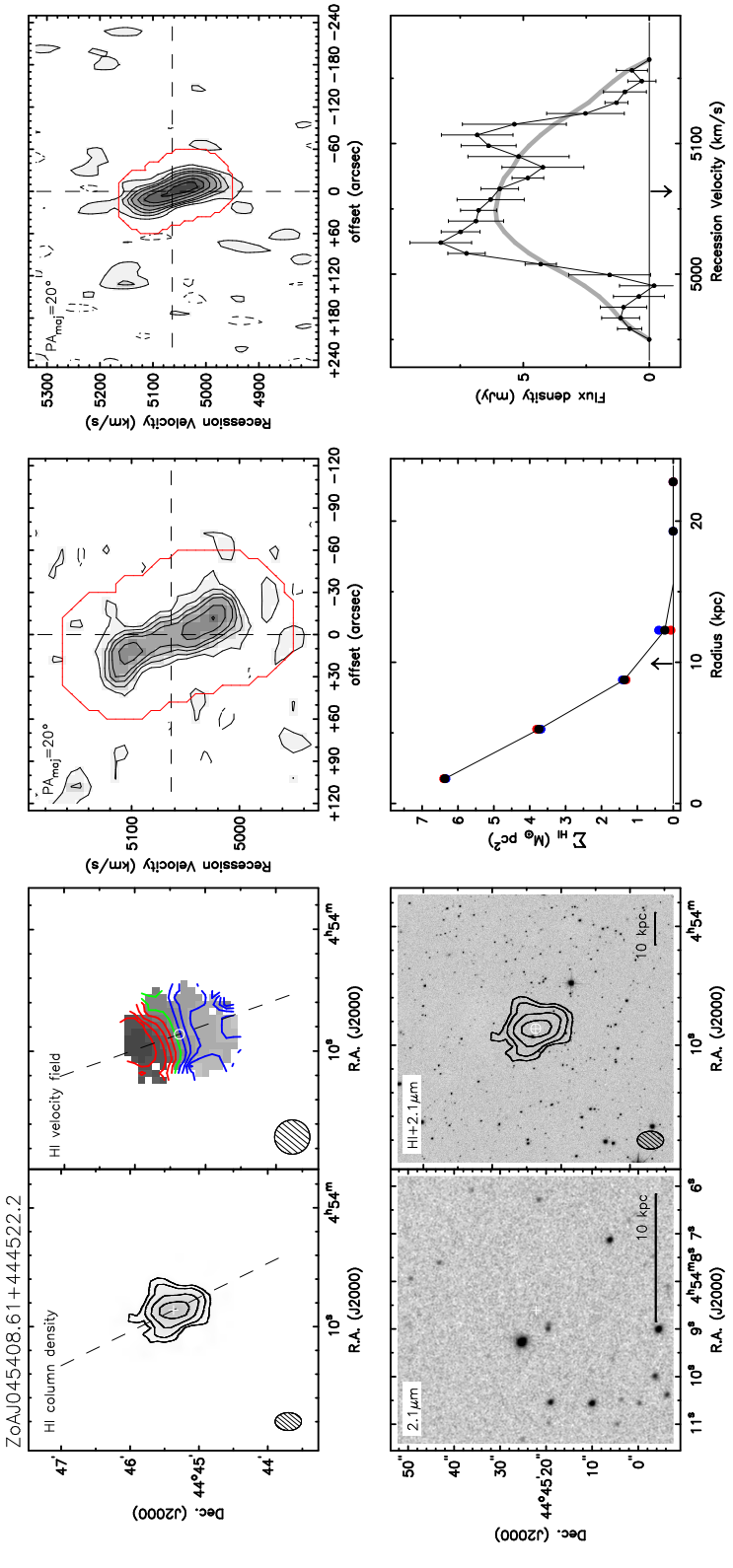

Figure A1. Resolved WSRT HI detections.

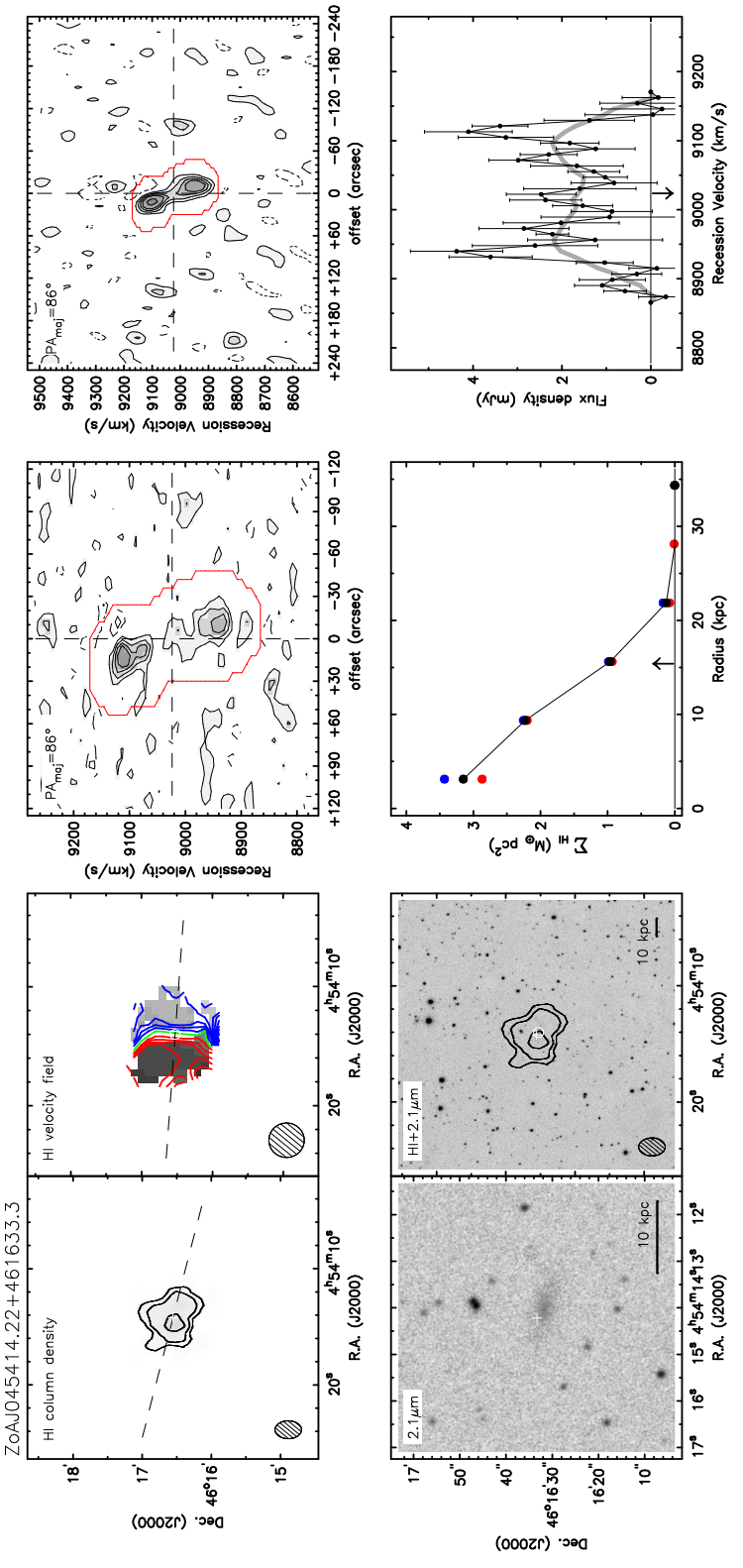

Figure A1. Resolved WSRT HI detections.

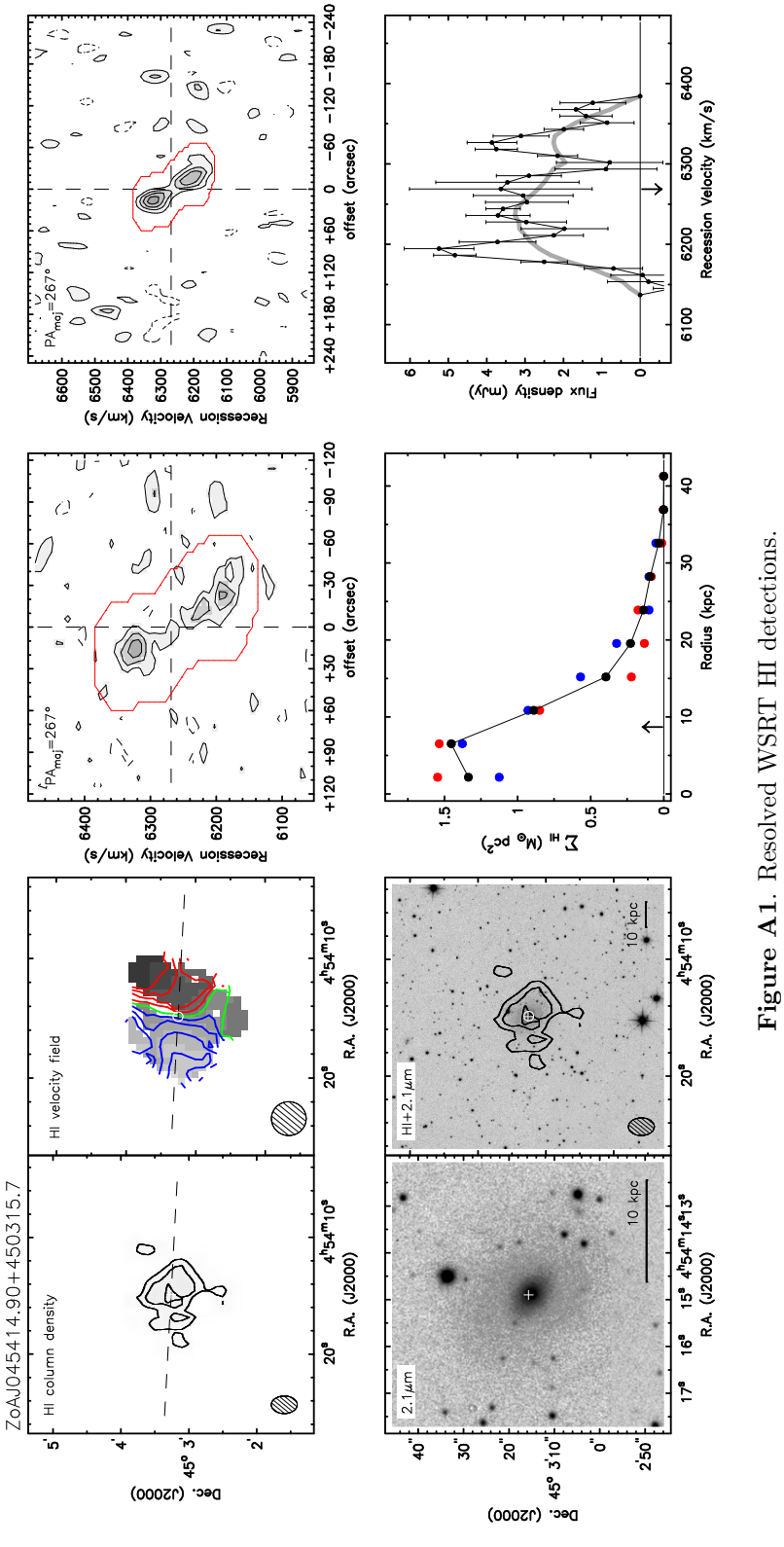

Figure A1. Resolved WSRT HI detections.

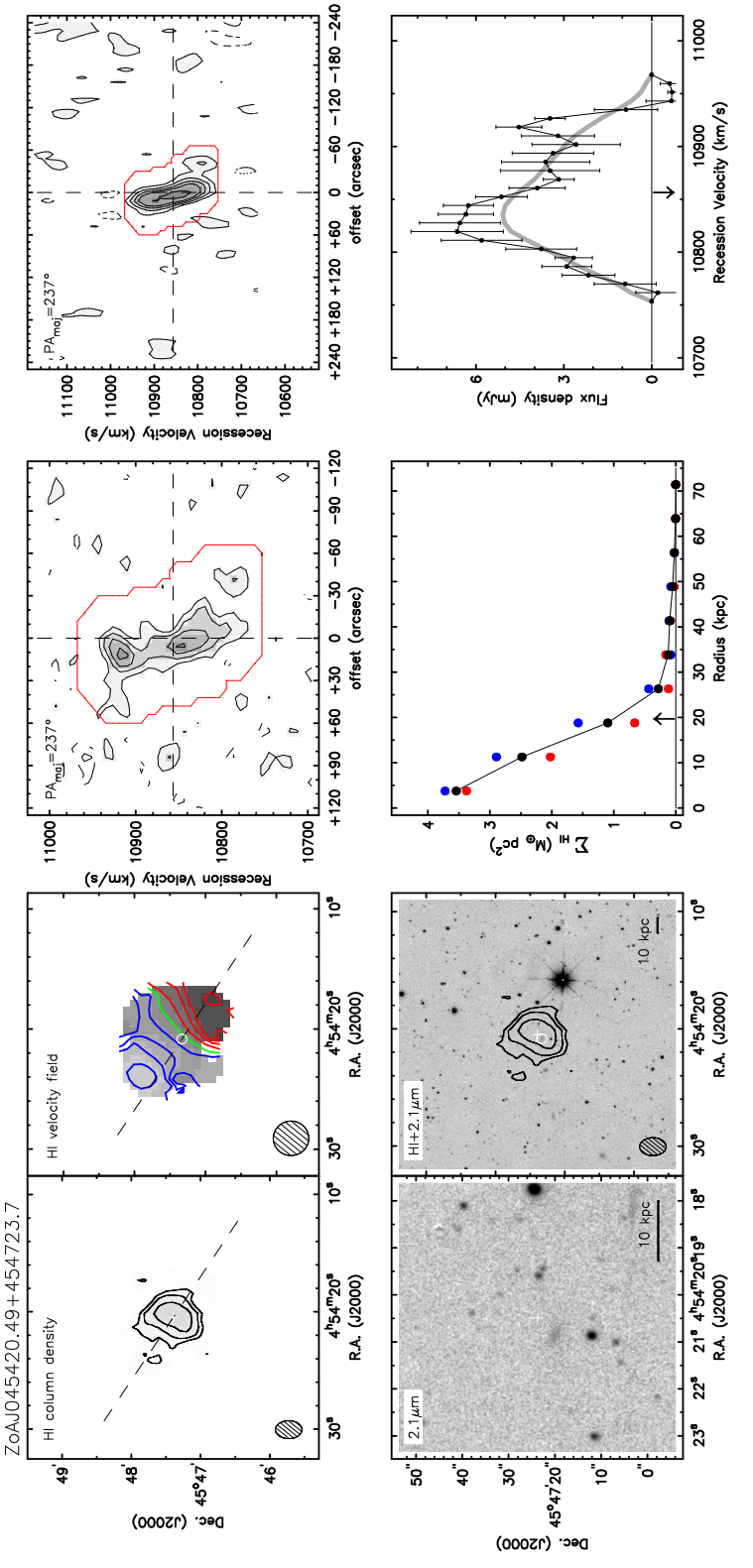

Figure A1. Resolved WSRT HI detections.

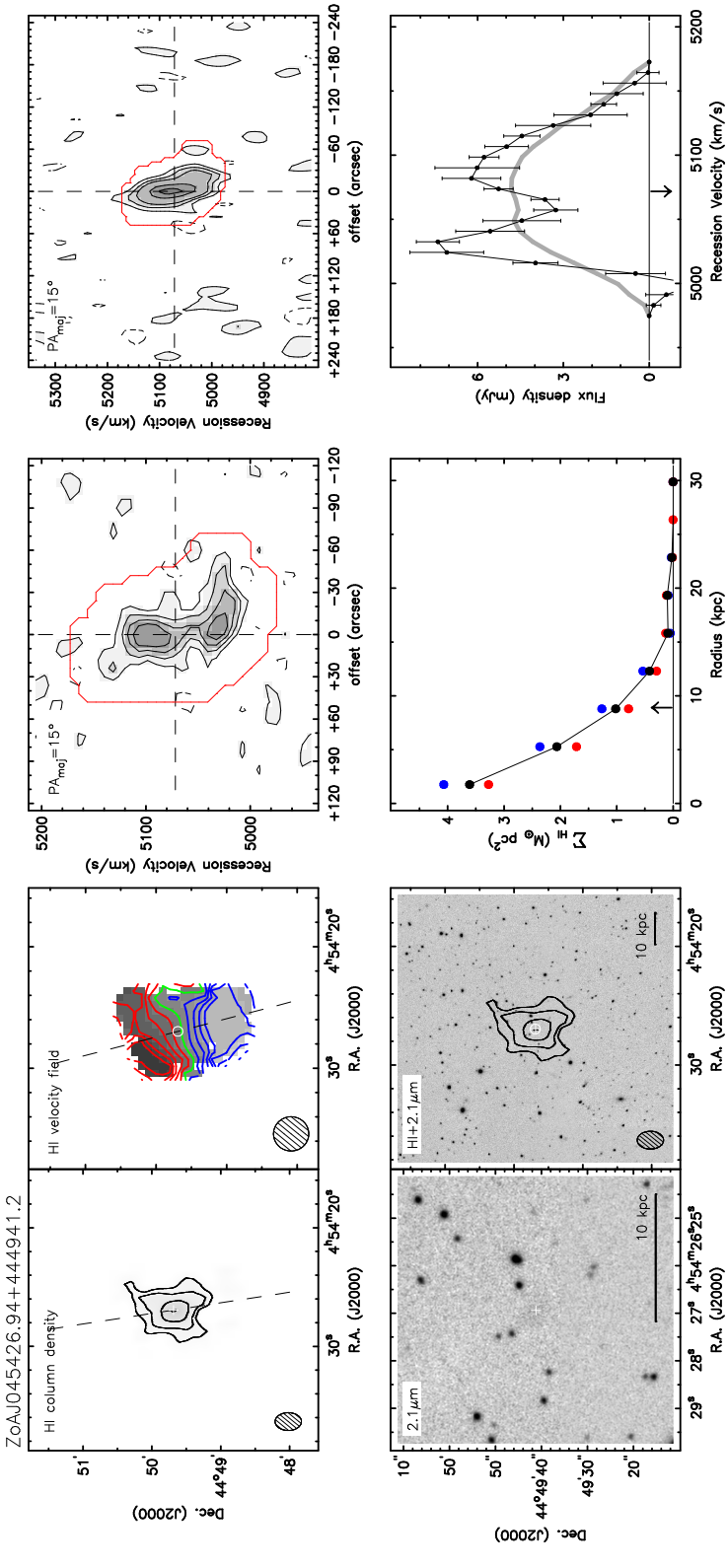

Figure A1. Resolved WSRT HI detections.

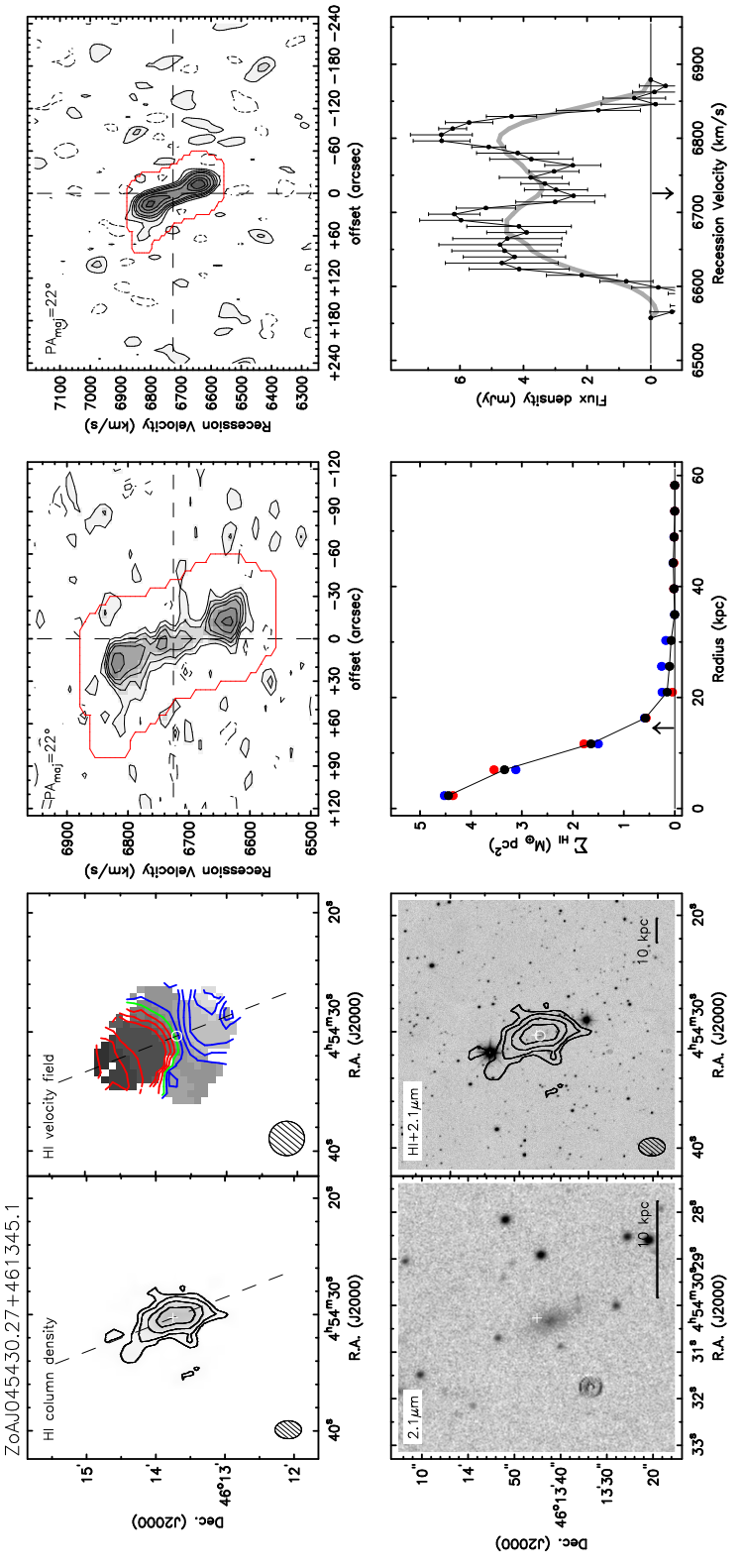

Figure A1. Resolved WSRT HI detections.

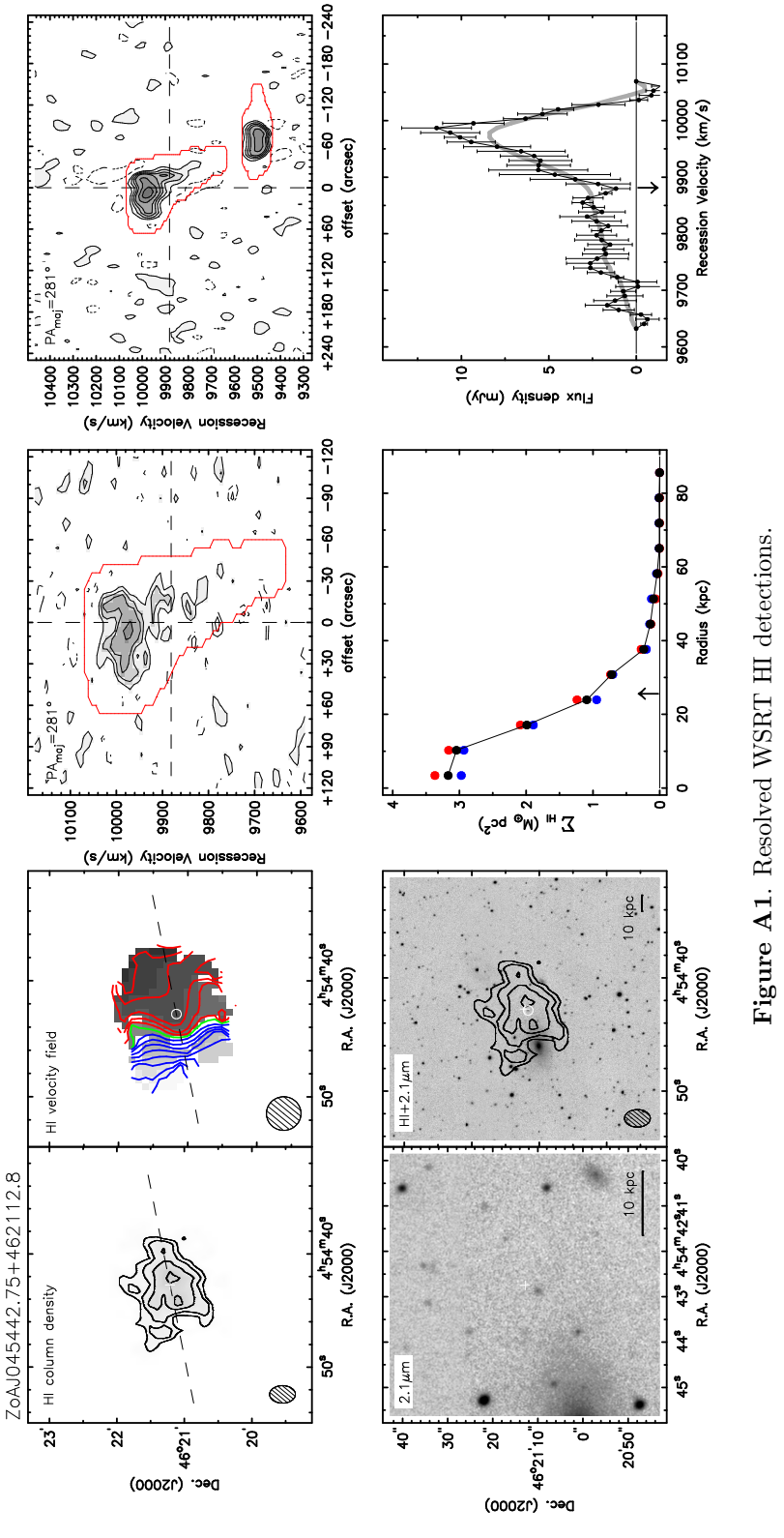

Figure A1. Resolved WSRT HI detections.

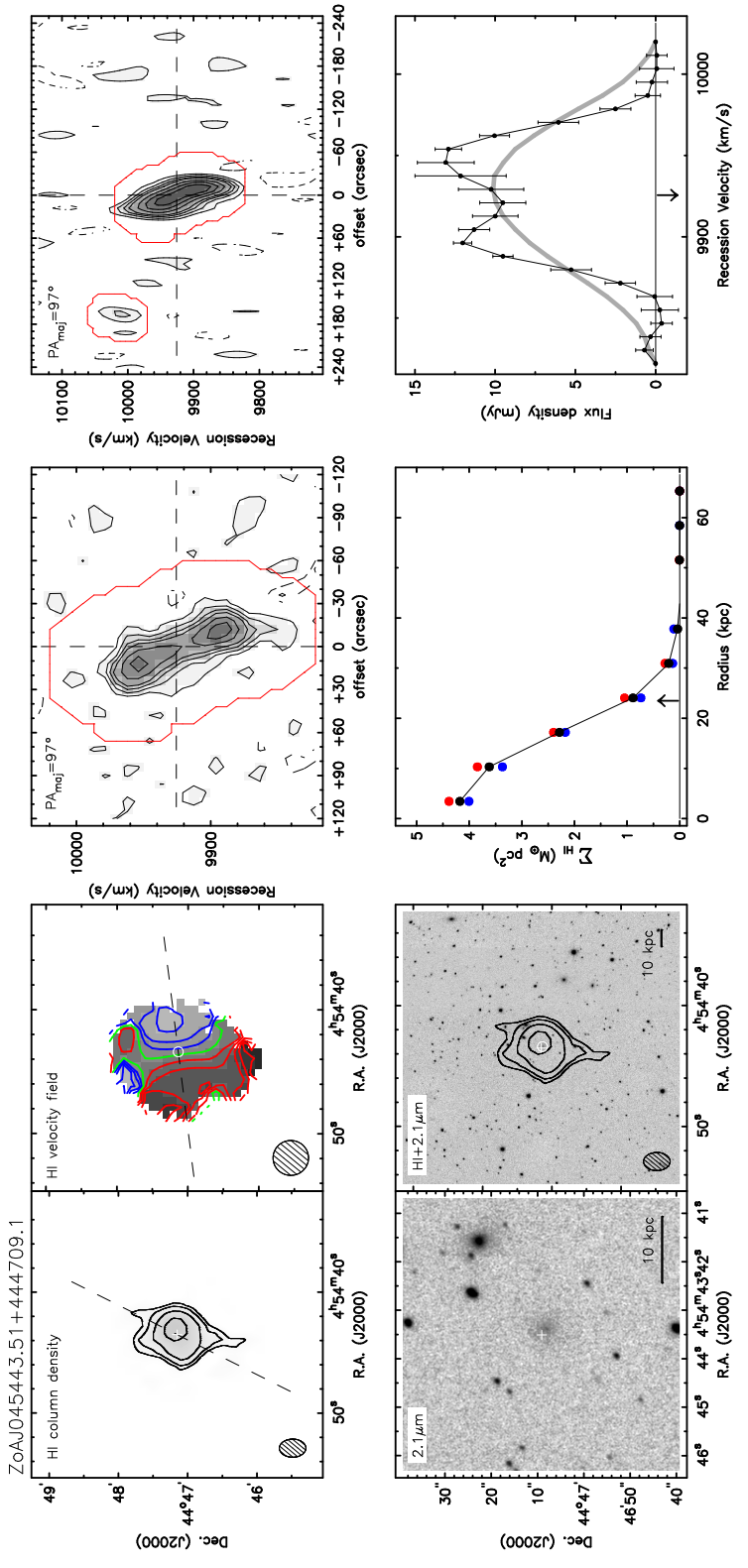

Figure A1. Resolved WSRT HI detections.

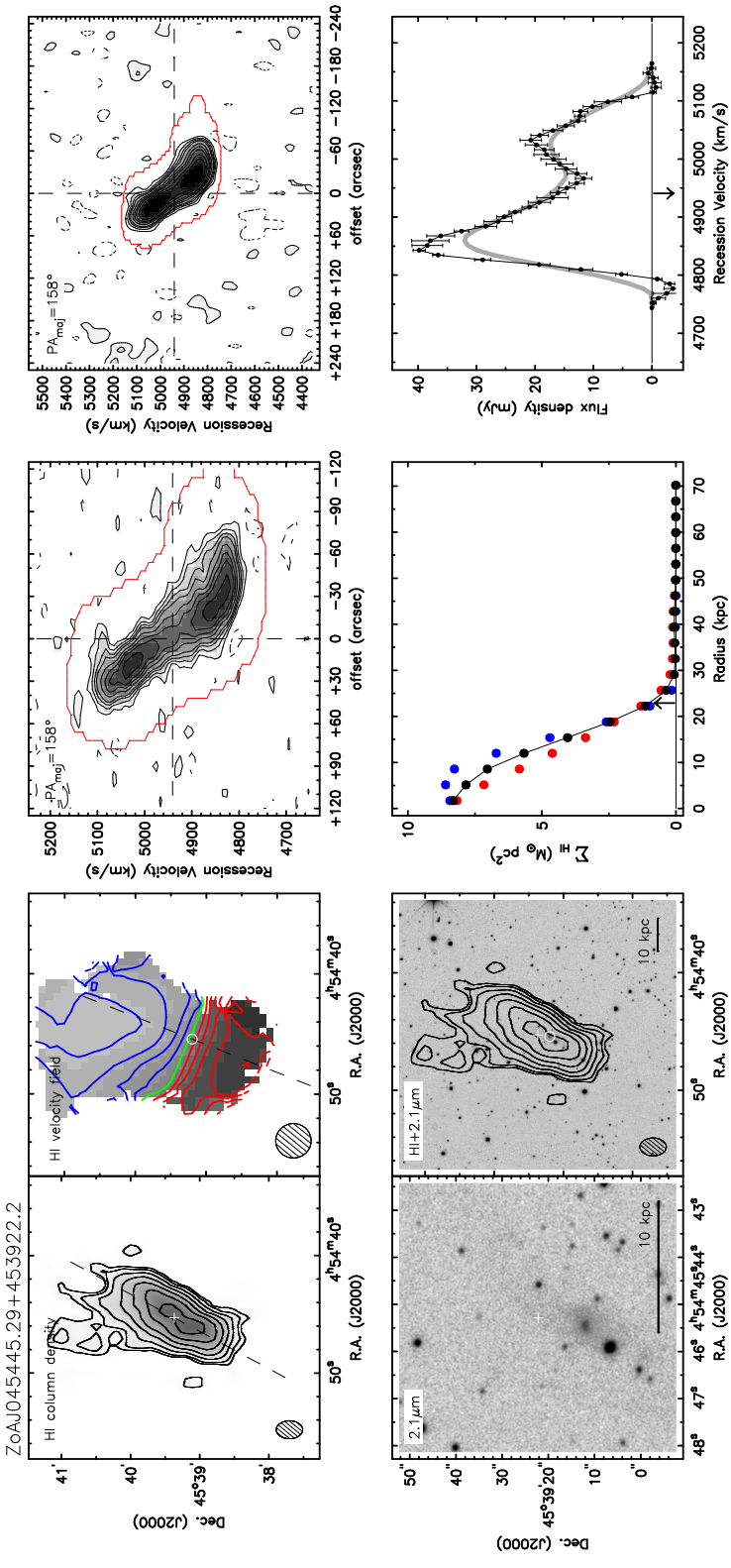

Figure A1. Resolved WSRT HI detections.

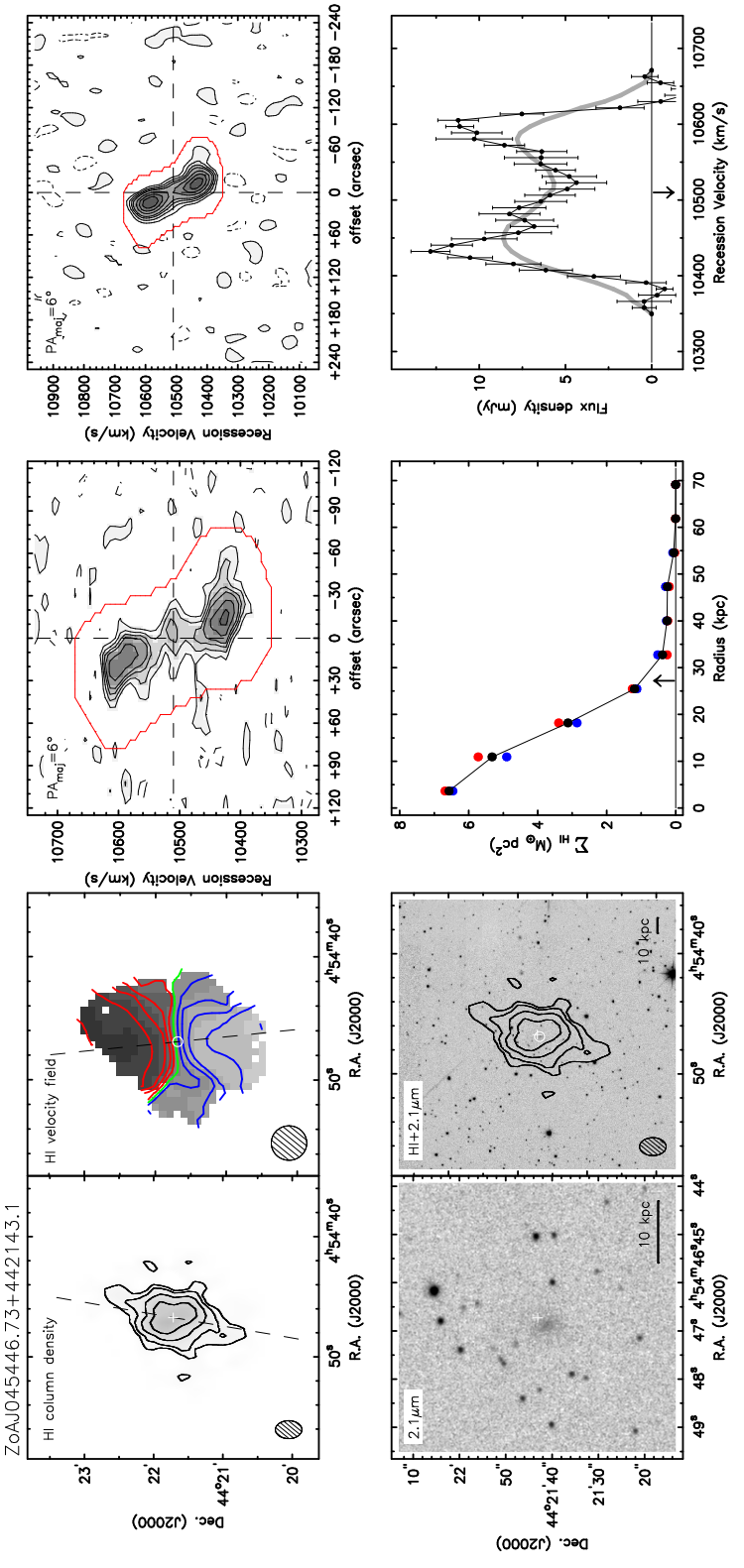

Figure A1. Resolved WSRT HI detections.

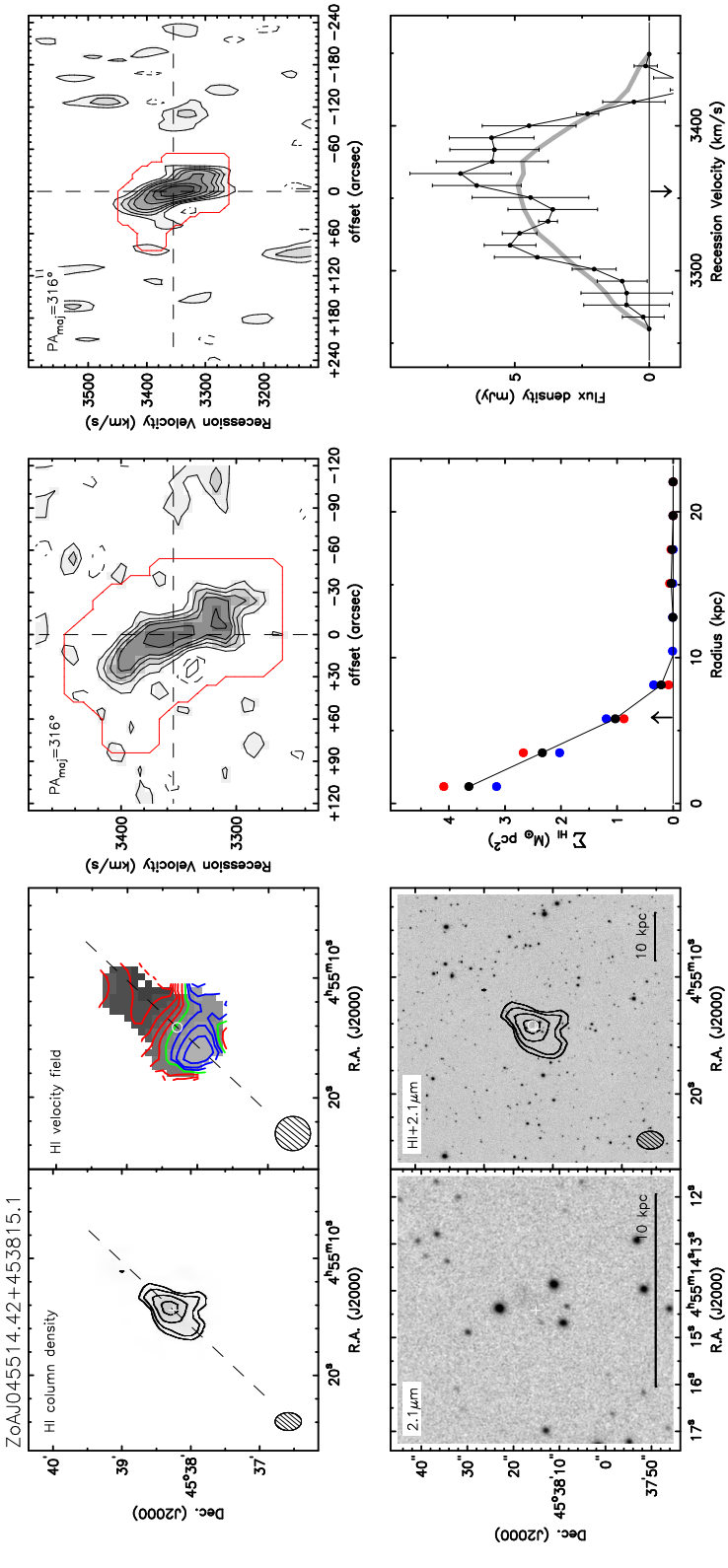

Figure A1. Resolved WSRT HI detections.

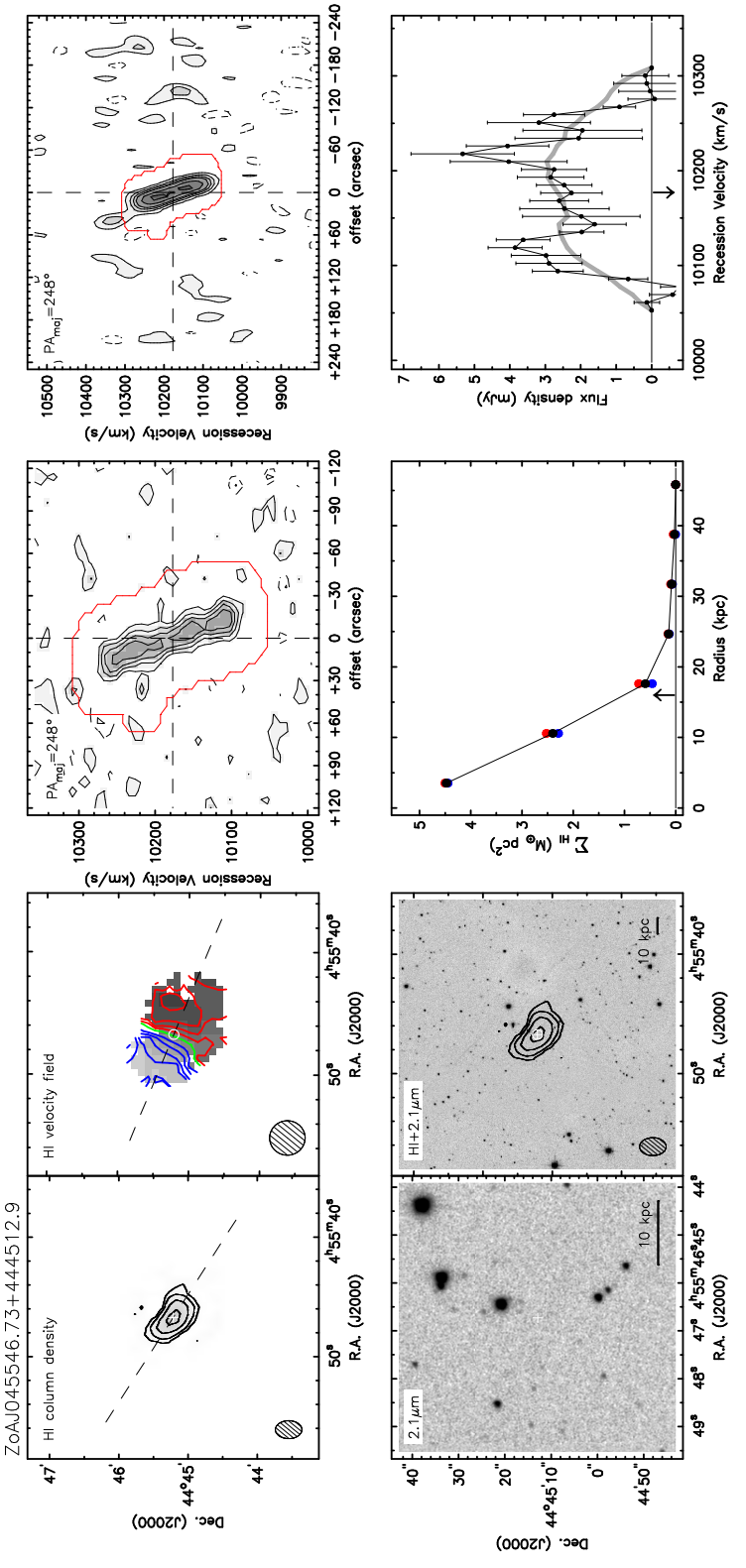

Figure A1. Resolved WSRT HI detections.

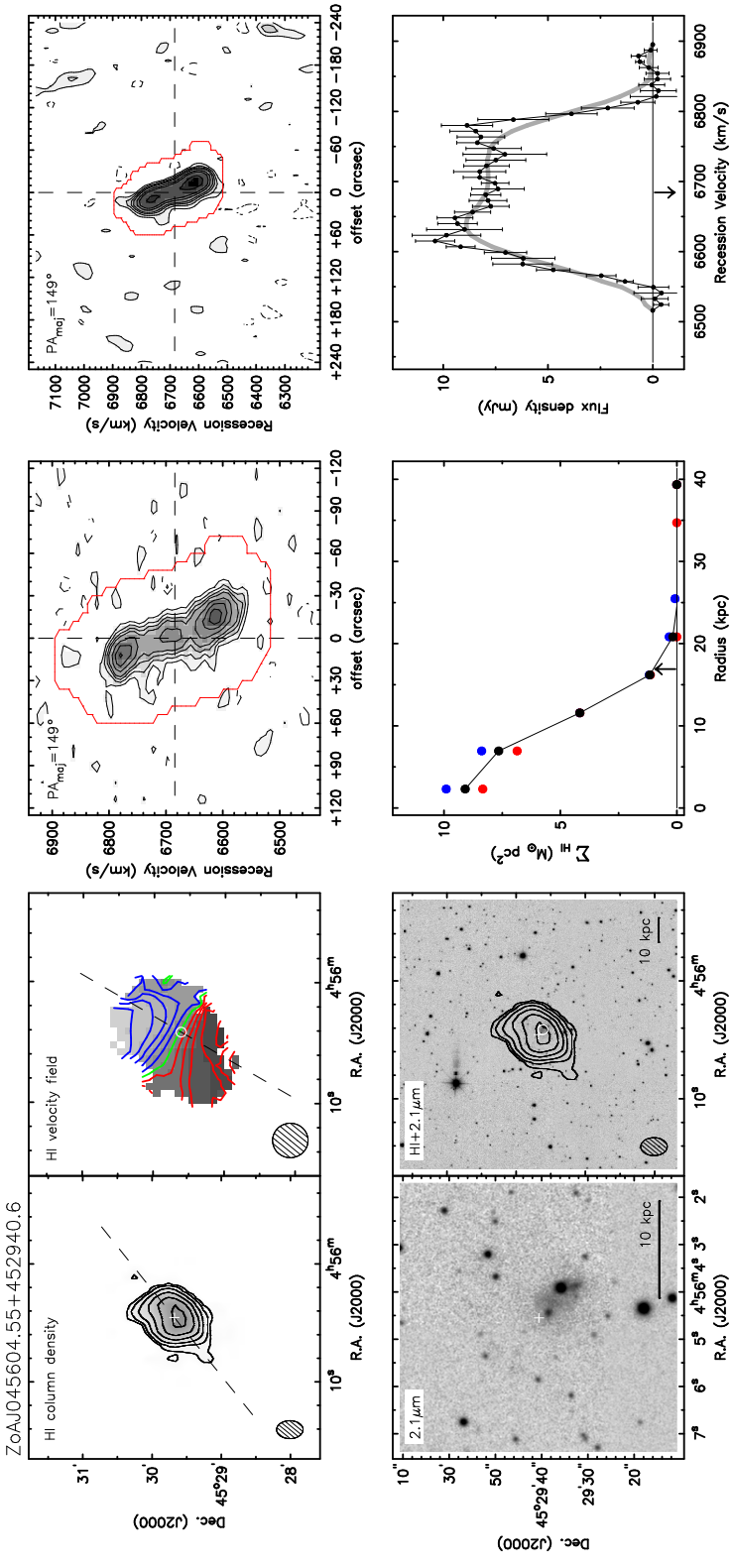

Figure A1. Resolved WSRT HI detections.

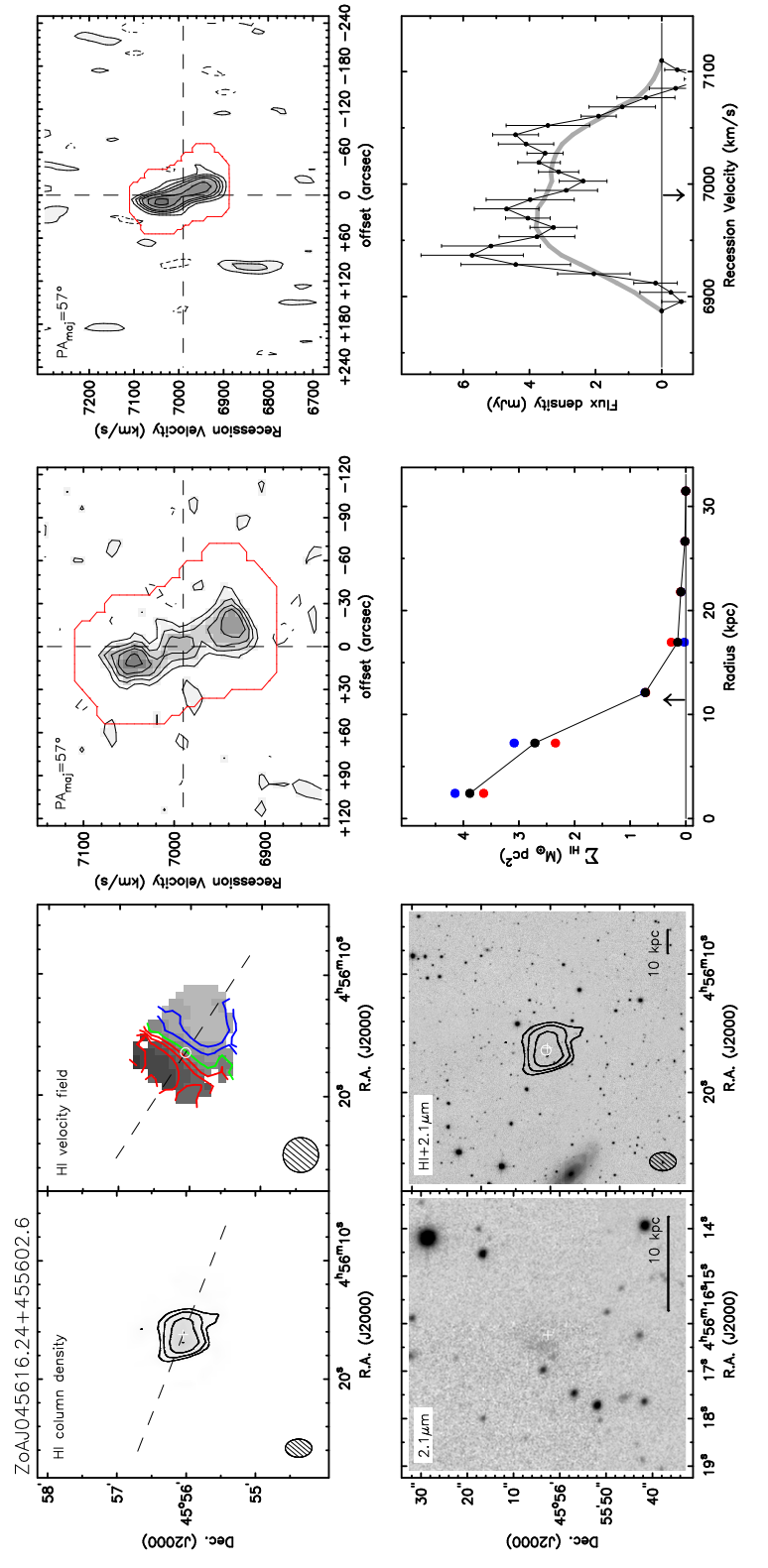

Figure A1. Resolved WSRT HI detections.

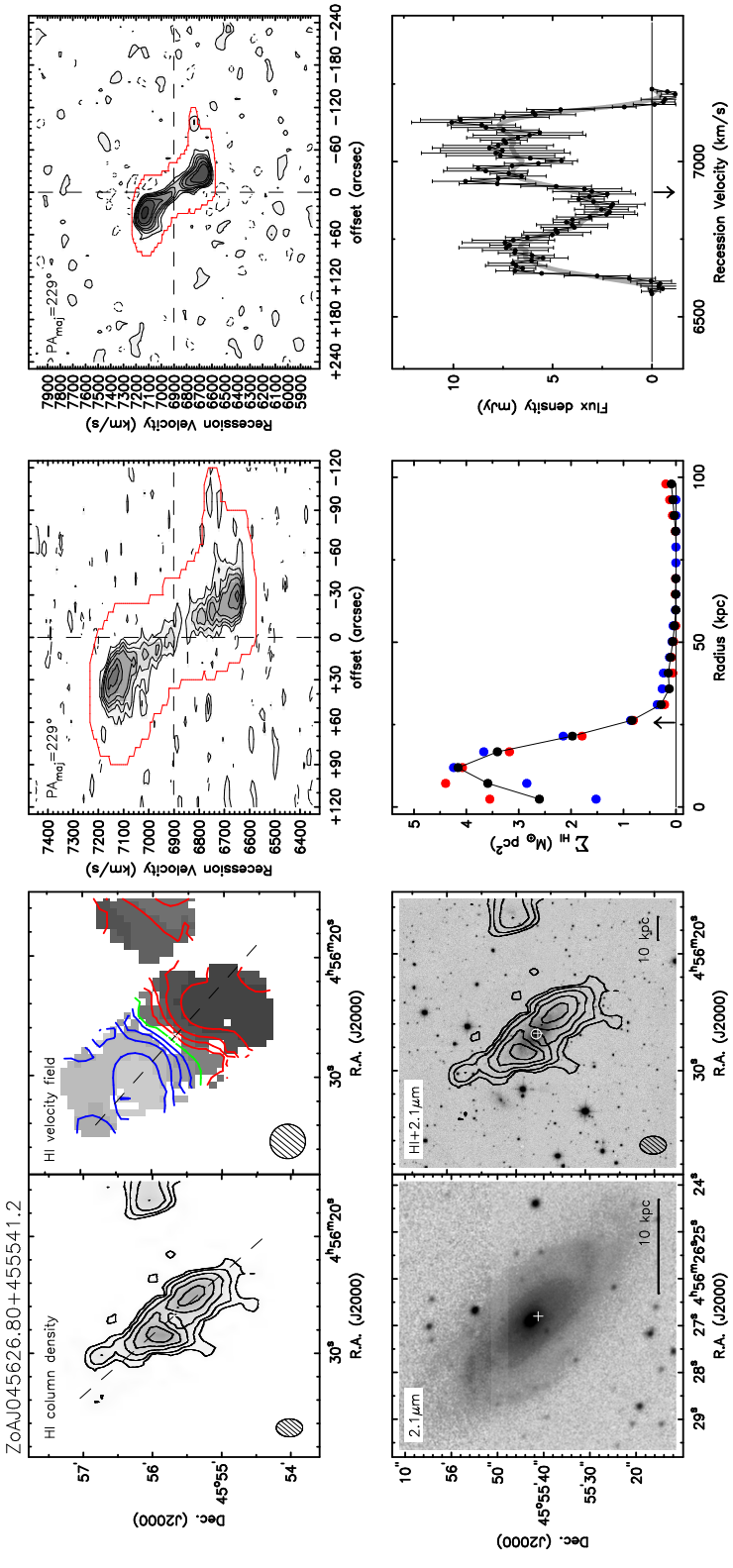

Figure A1. Resolved WSRT HI detections.

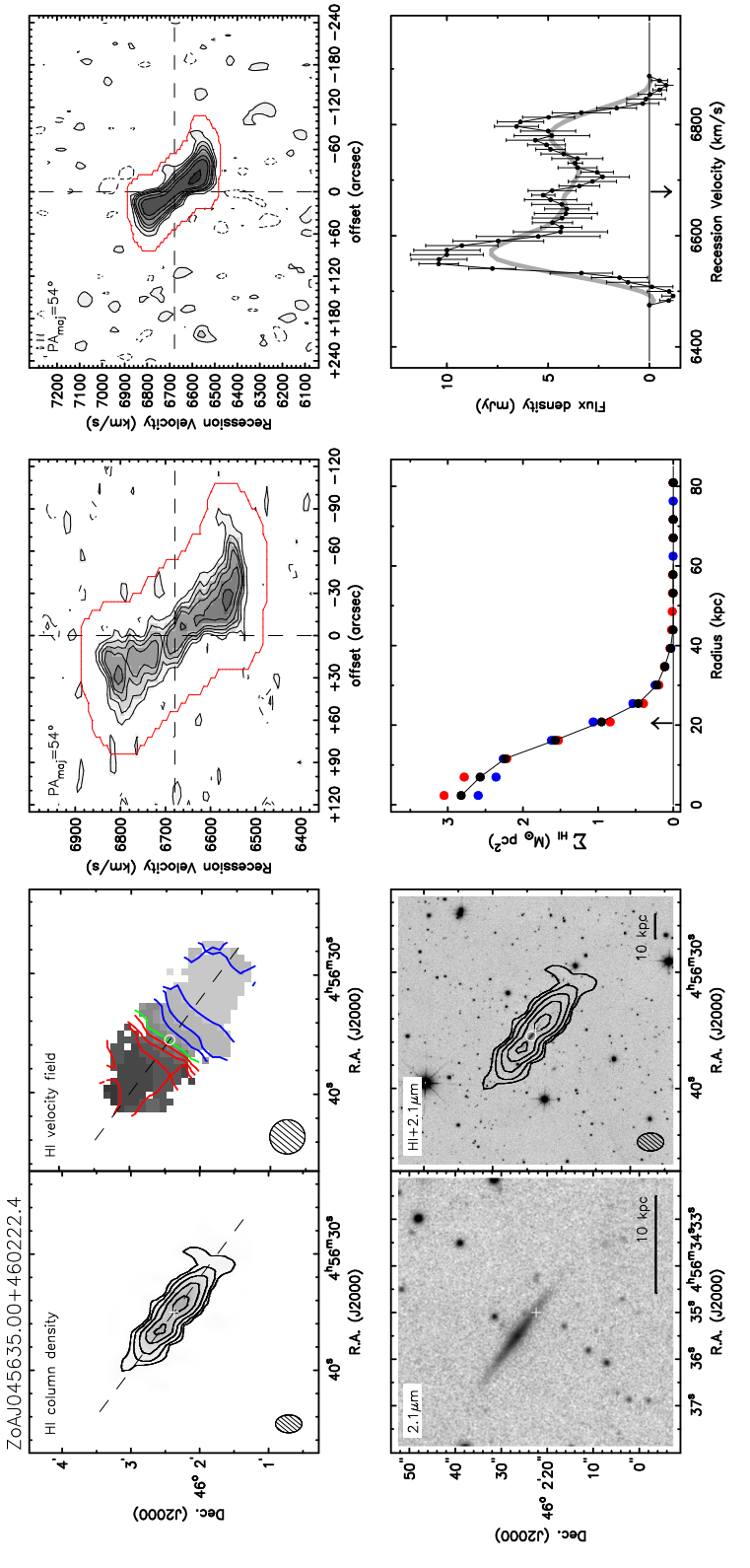

Figure A1. Resolved WSRT HI detections.

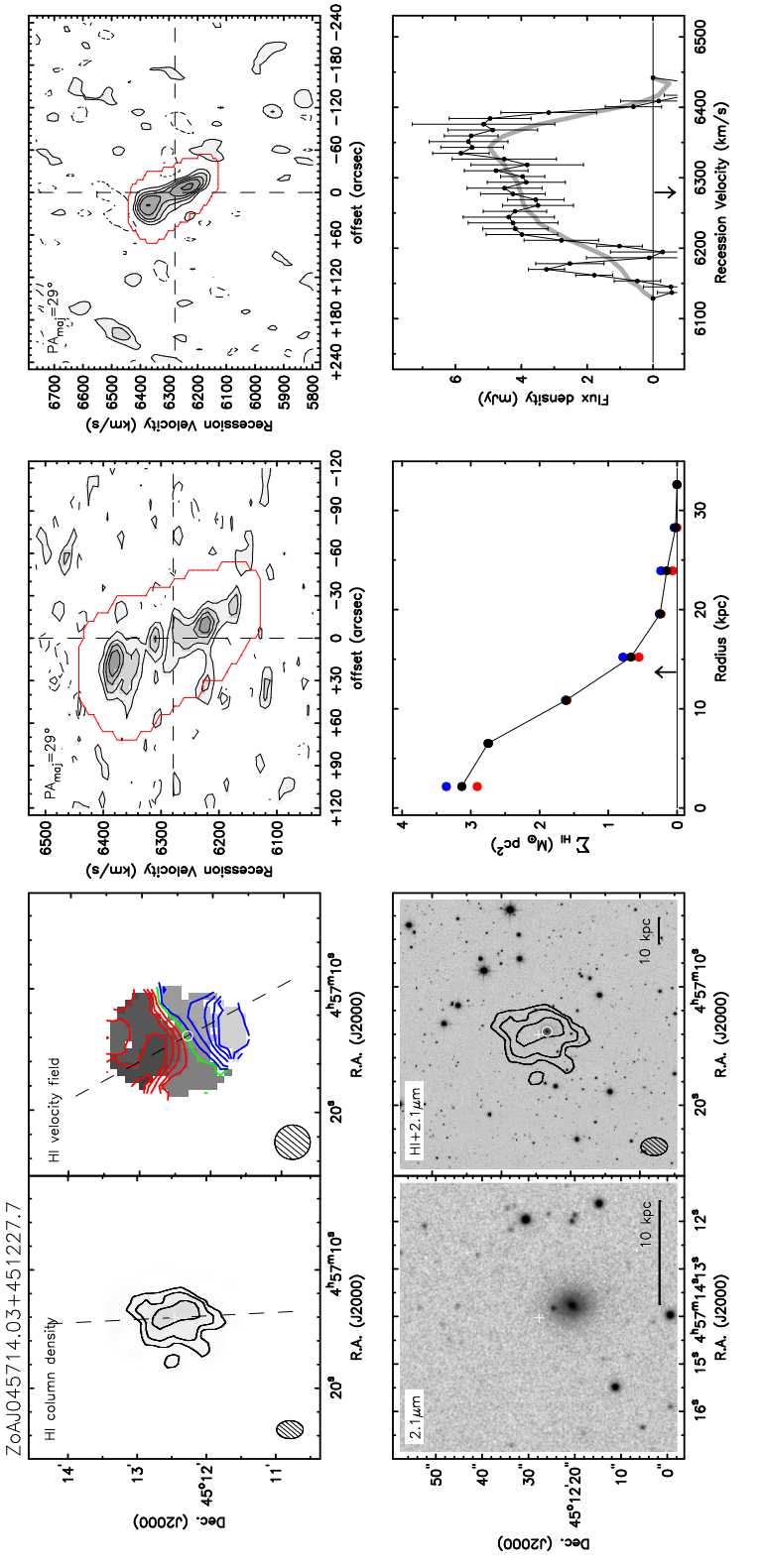

Figure A1. Resolved WSRT HI detections.

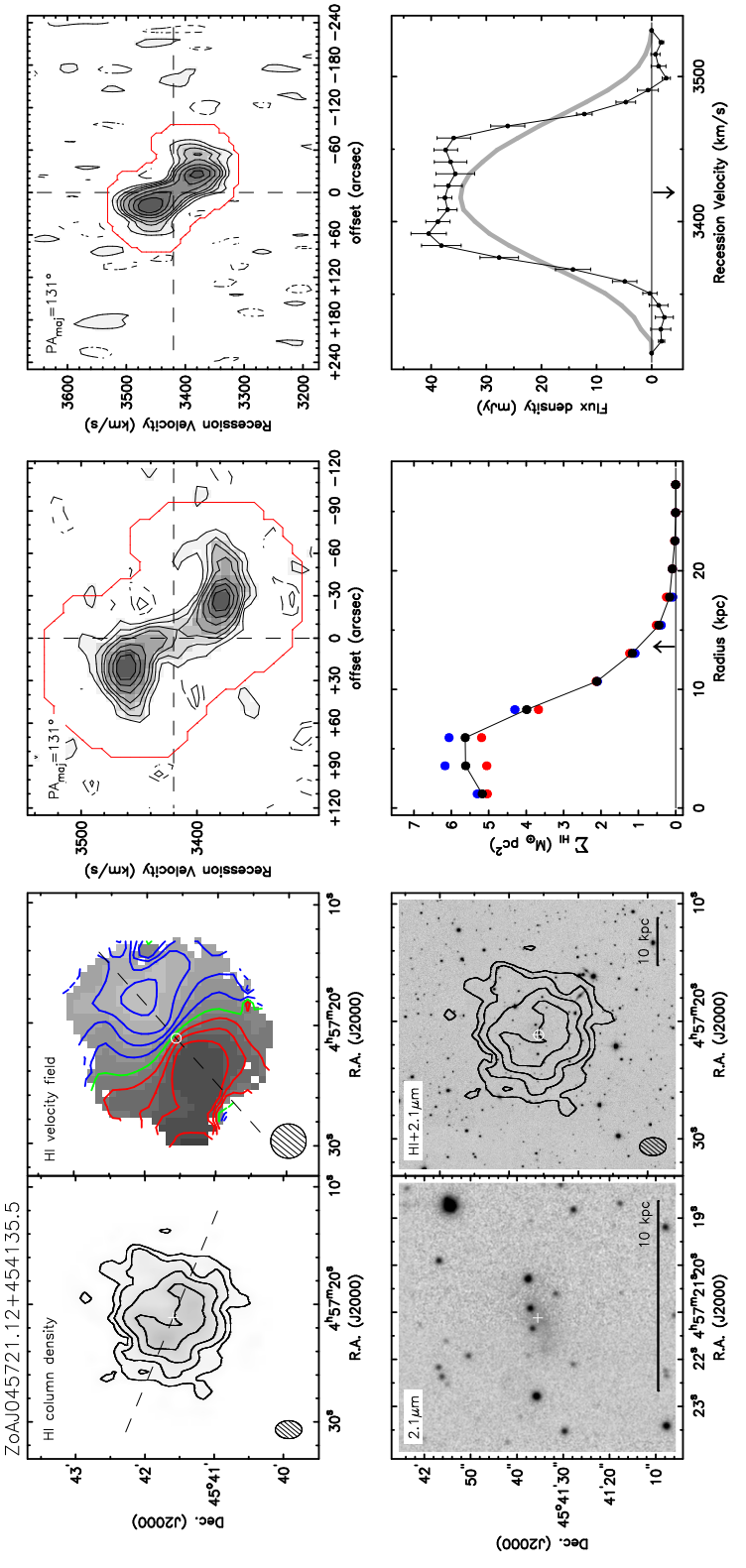

Figure A1. Resolved WSRT HI detections.

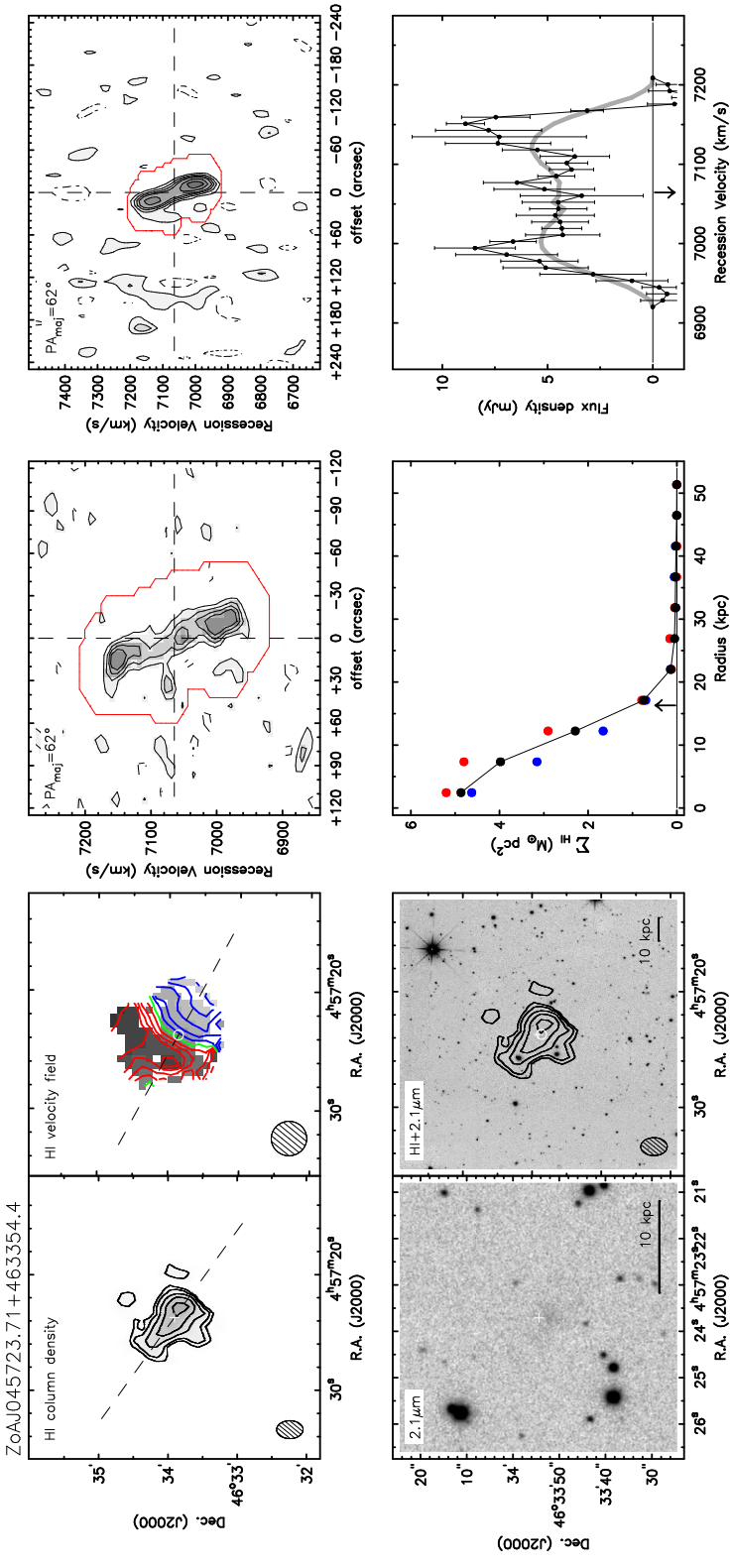

Figure A1. Resolved WSRT HI detections.

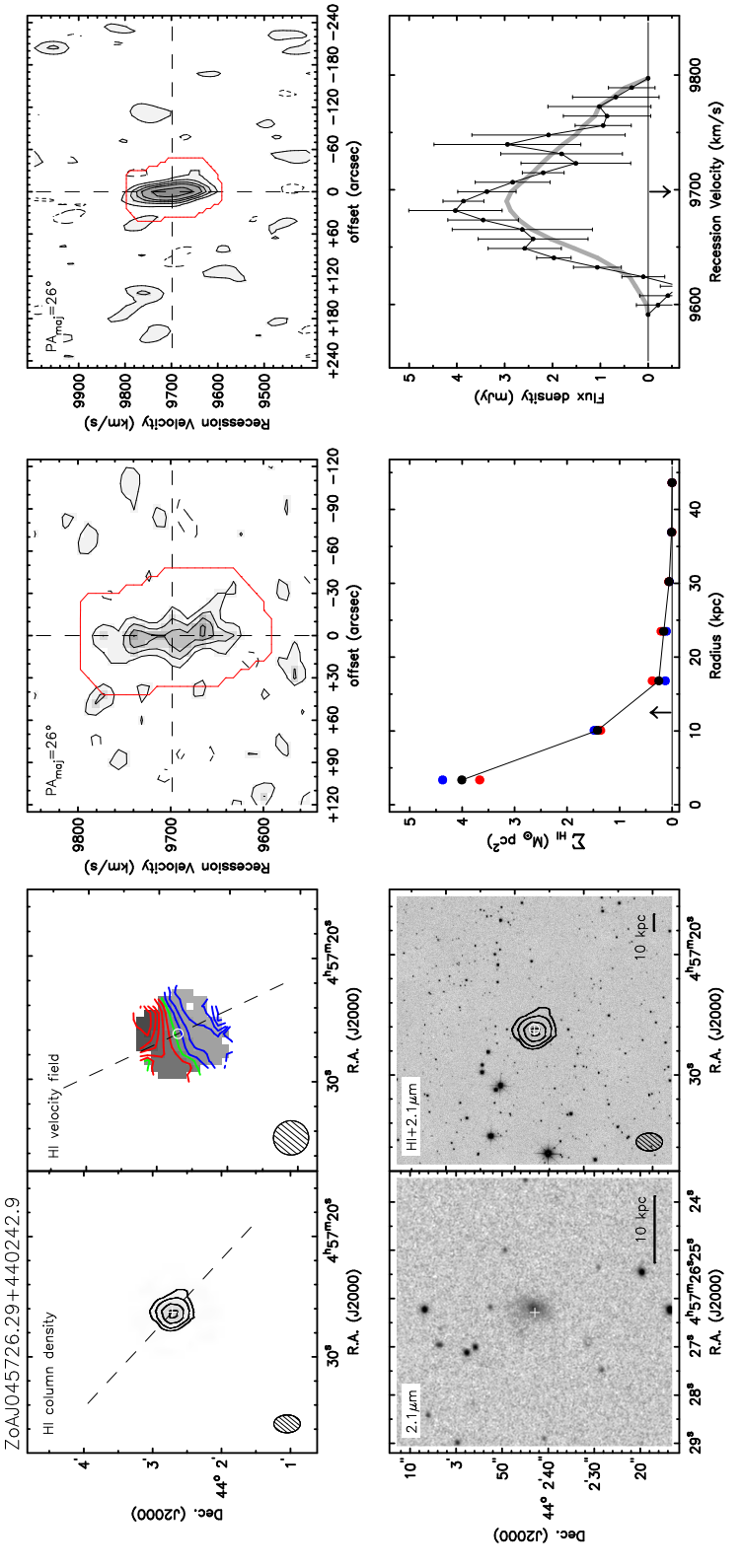

Figure A1. Resolved WSRT HI detections.

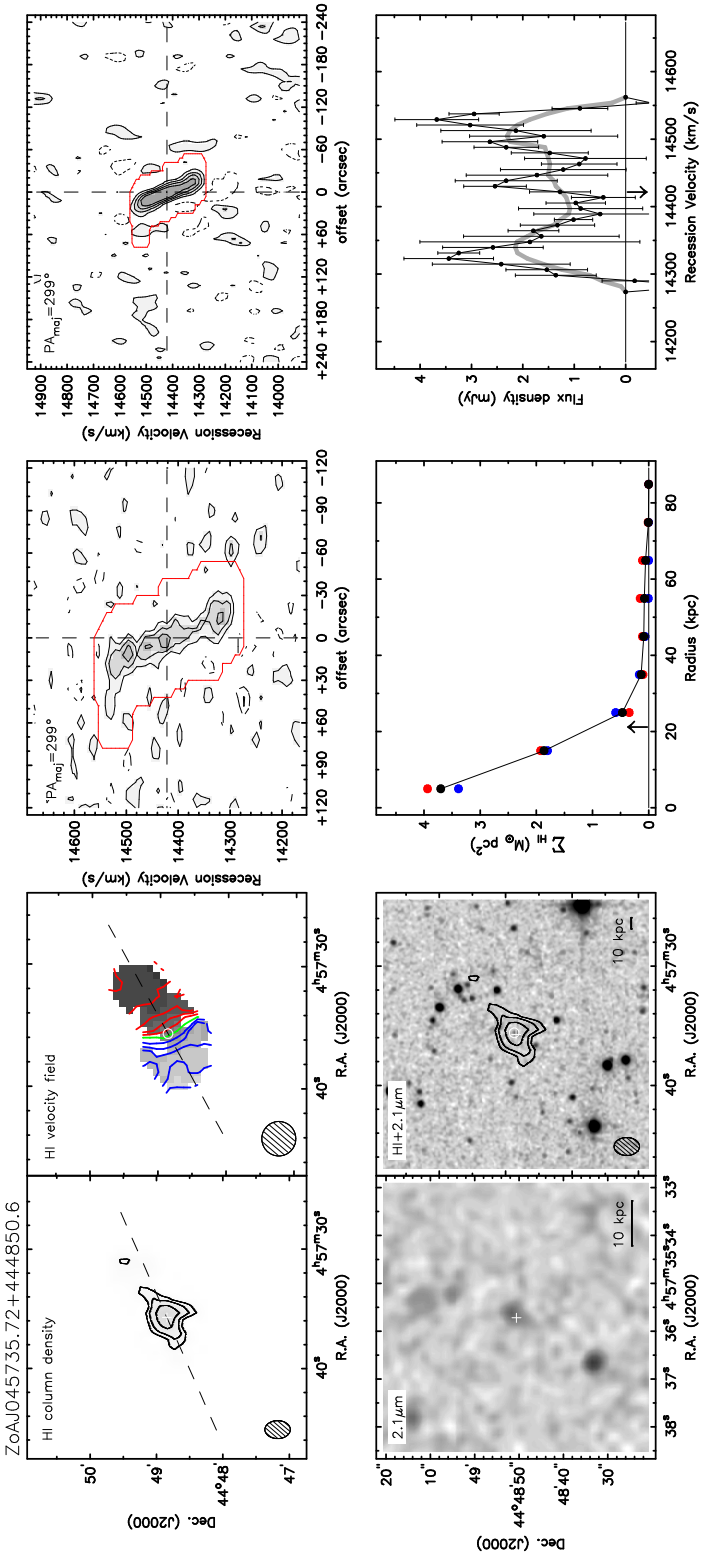

Figure A1. Resolved WSRT HI detections.

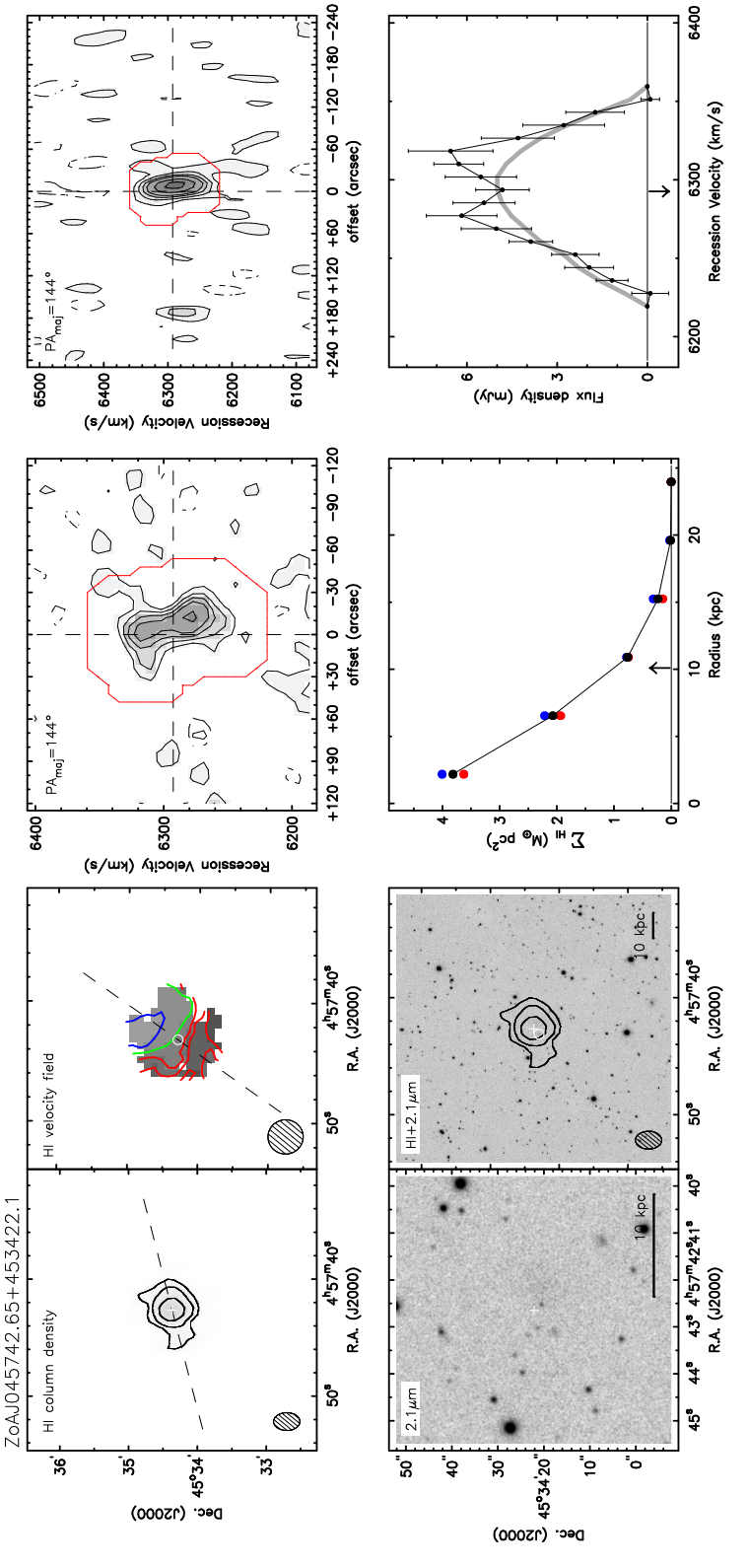

Figure A1. Resolved WSRT HI detections.

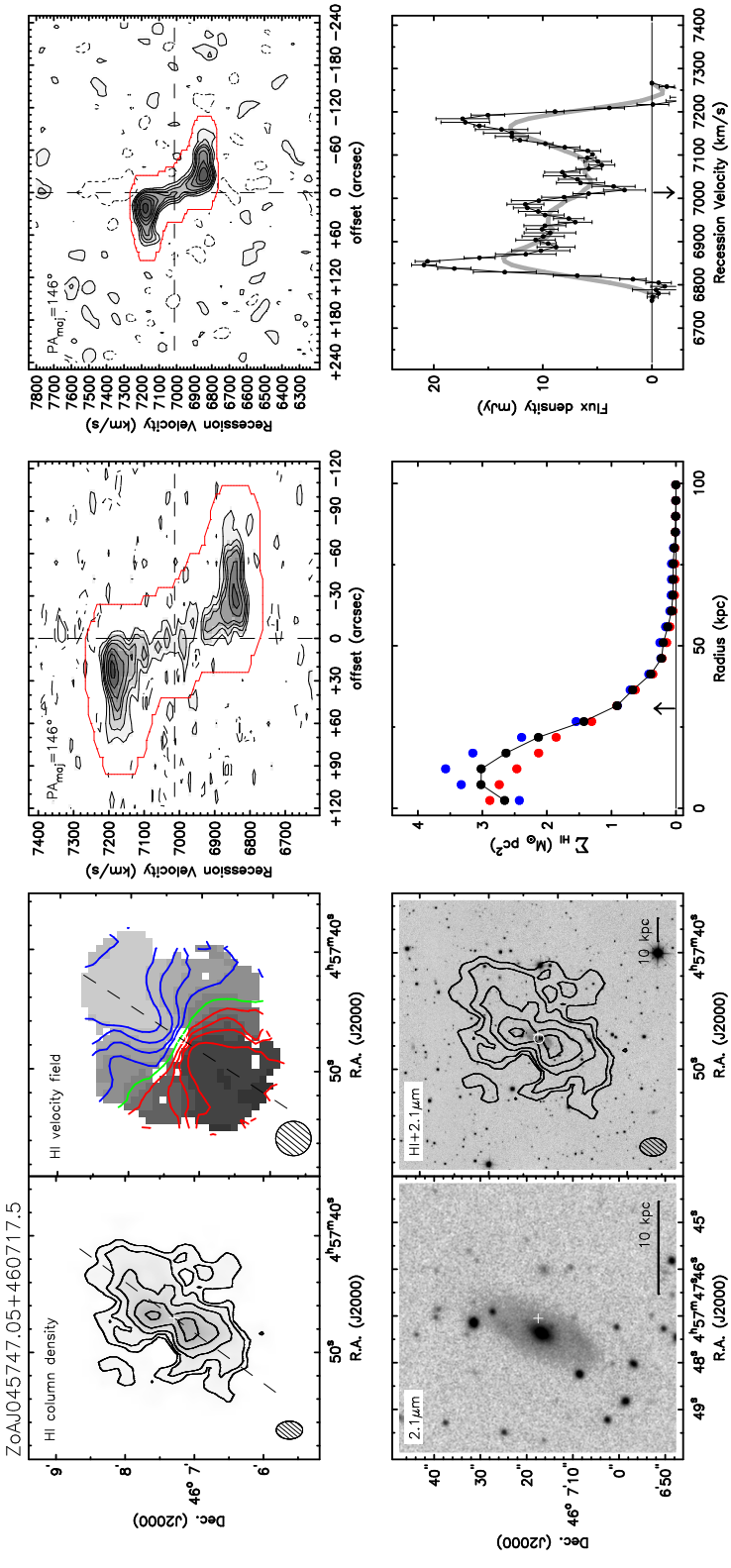

Figure A1. Resolved WSRT HI detections.

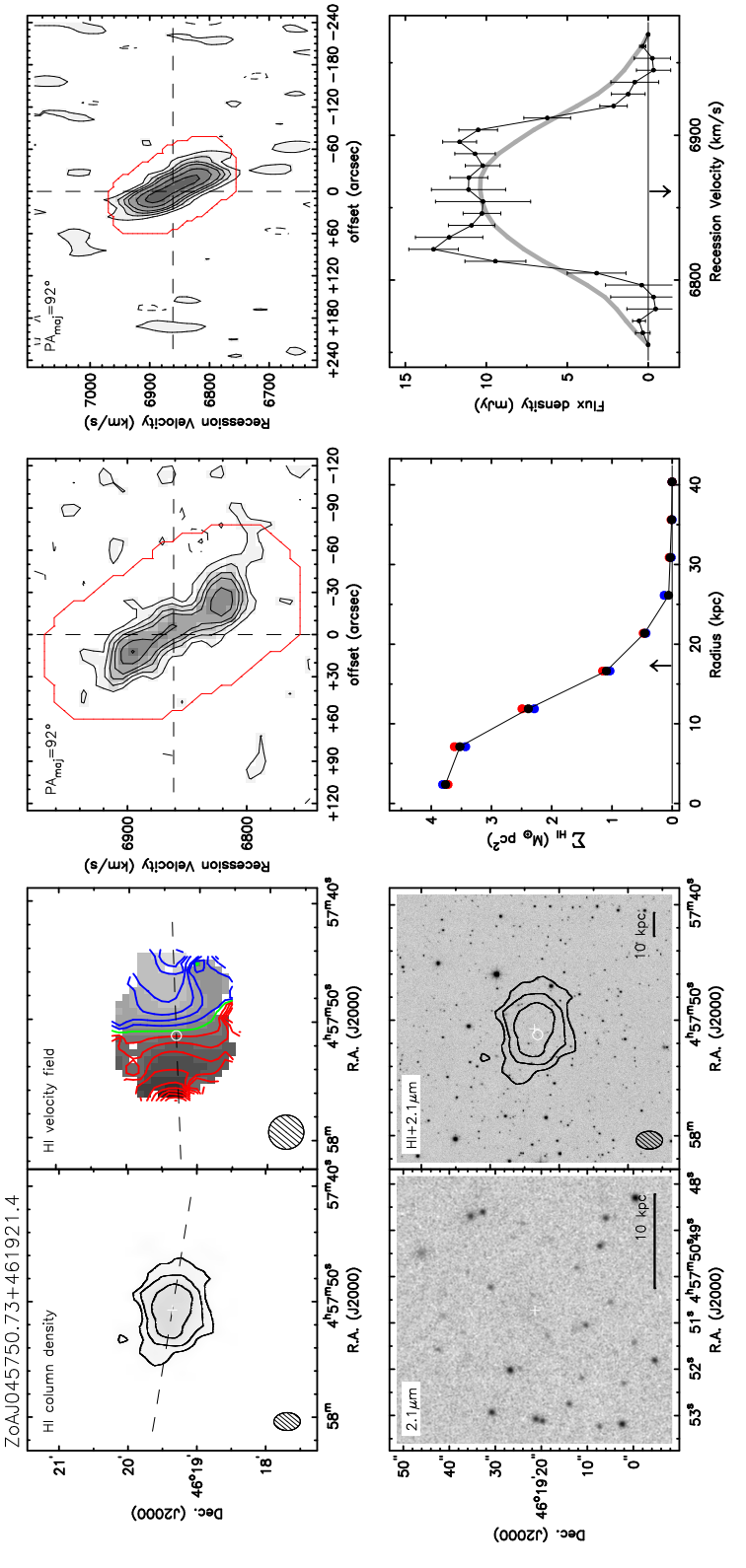

Figure A1. Resolved WSRT HI detections.

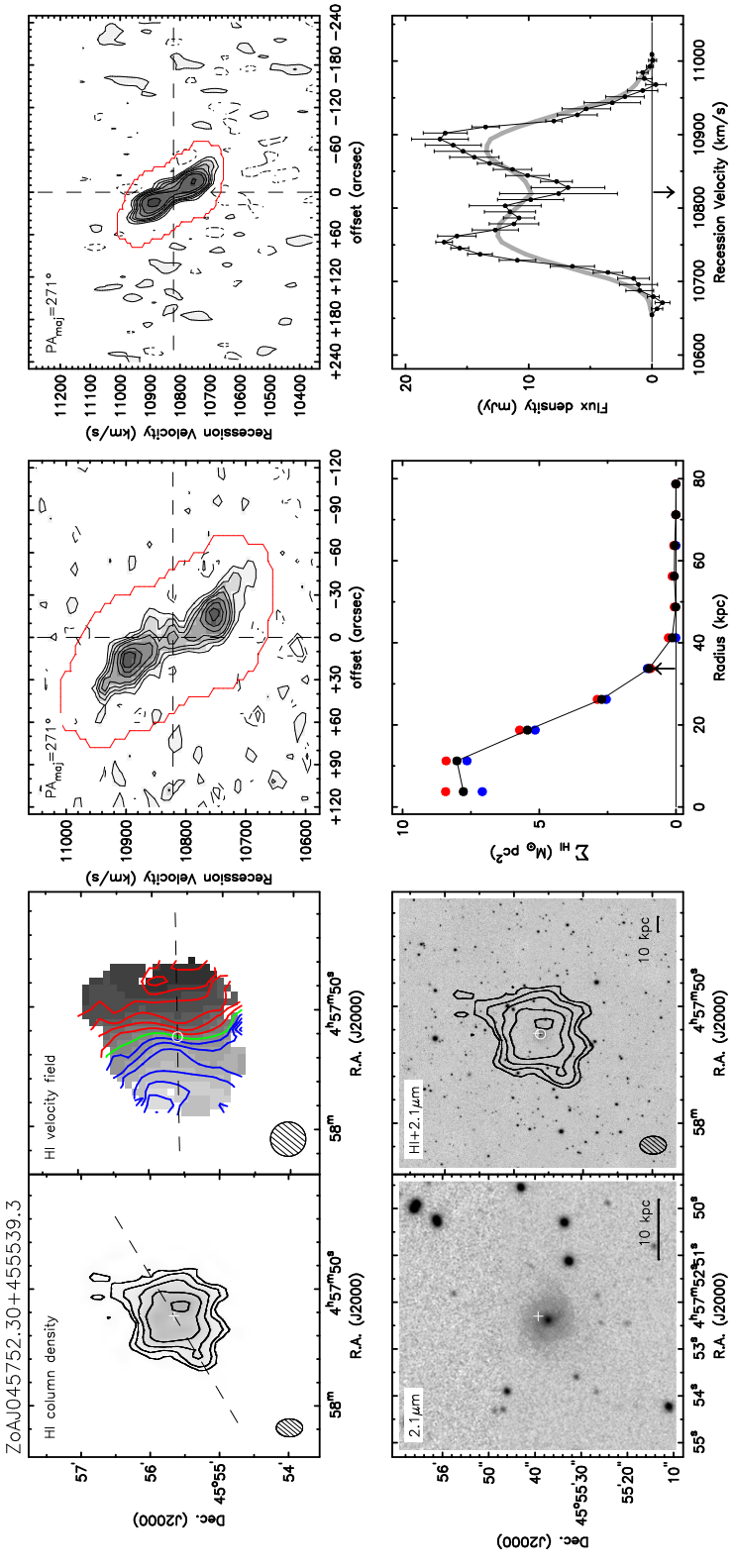

Figure A1. Resolved WSRT HI detections.

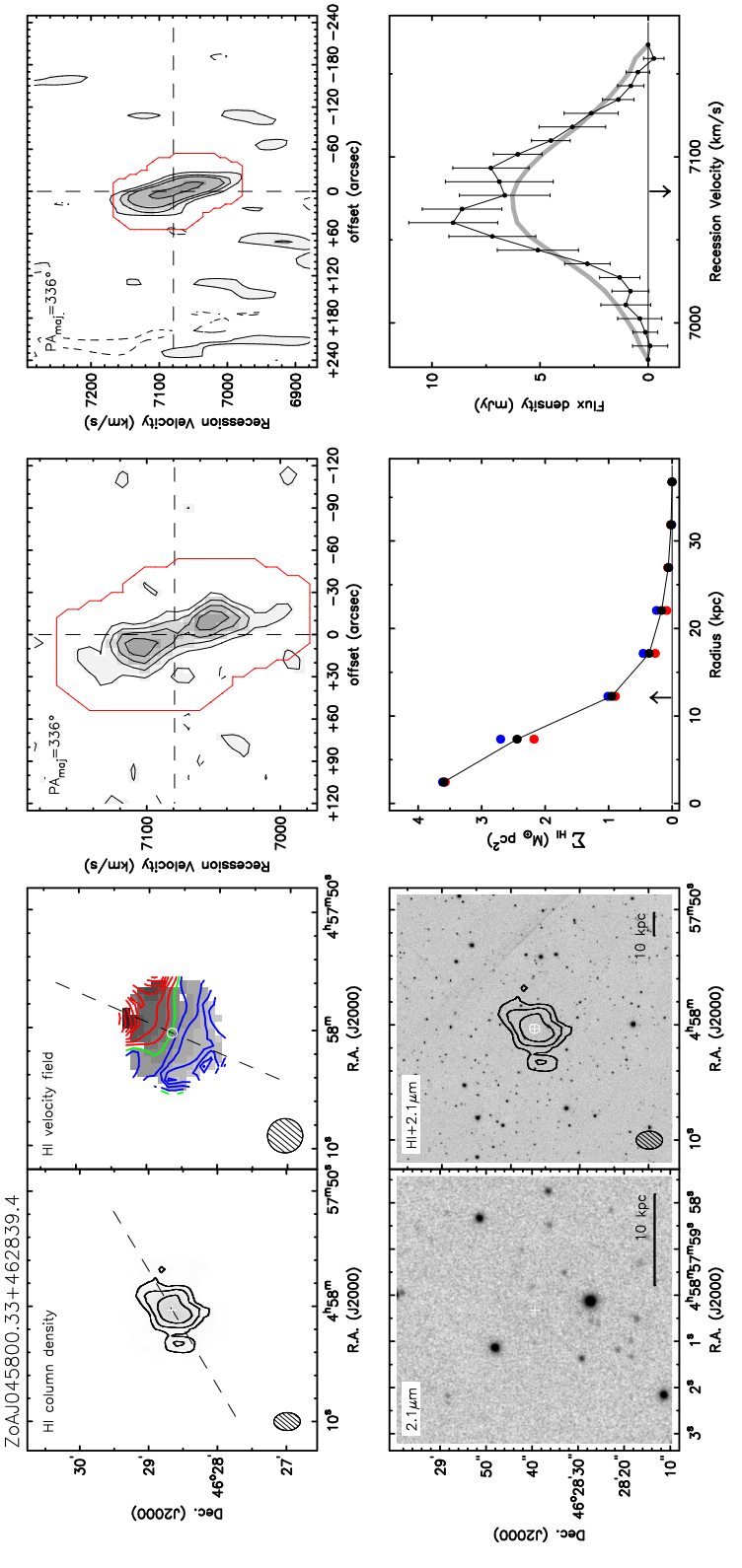

Figure A1. Resolved WSRT HI detections.

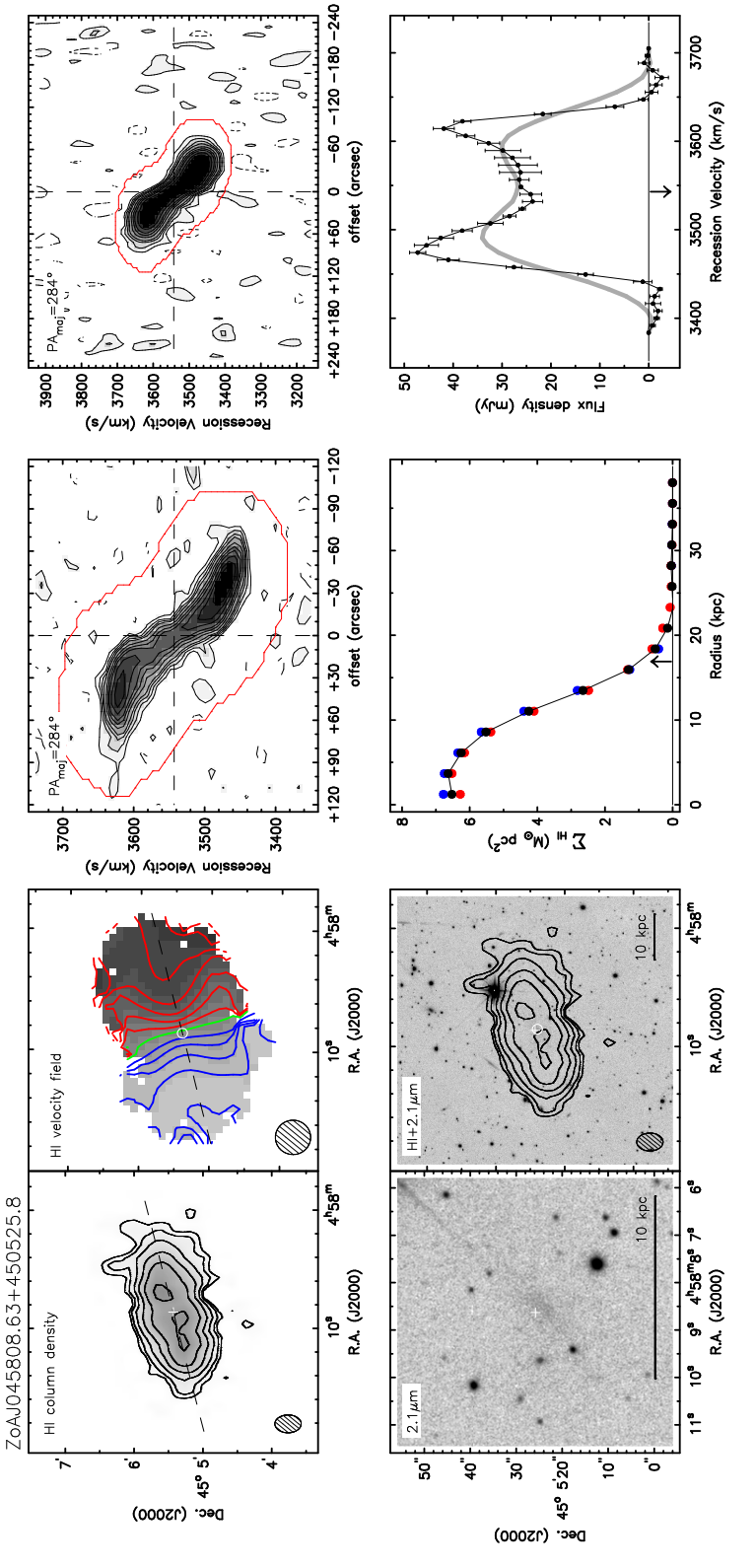

Figure A1. Resolved WSRT HI detections.

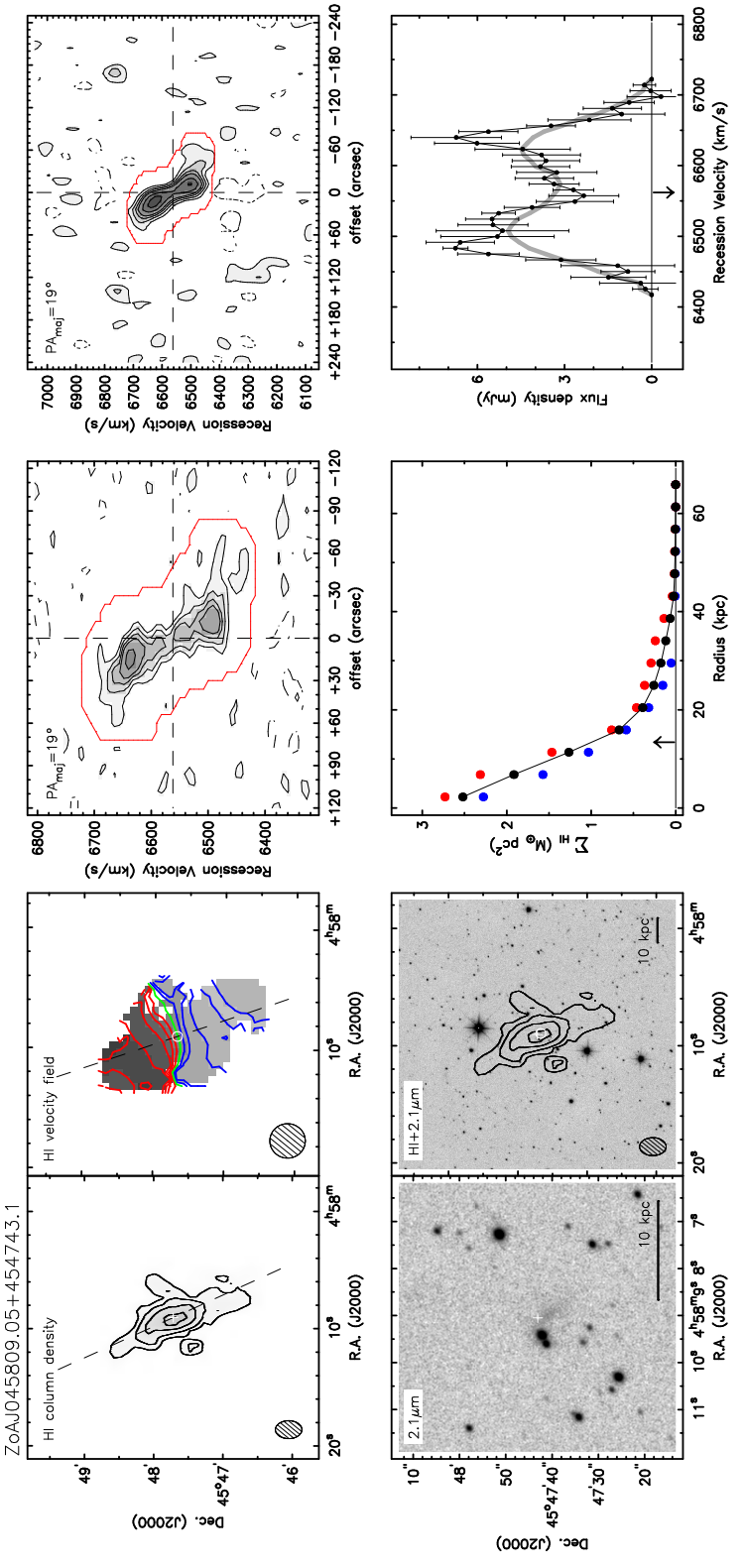

Figure A1. Resolved WSRT HI detections.

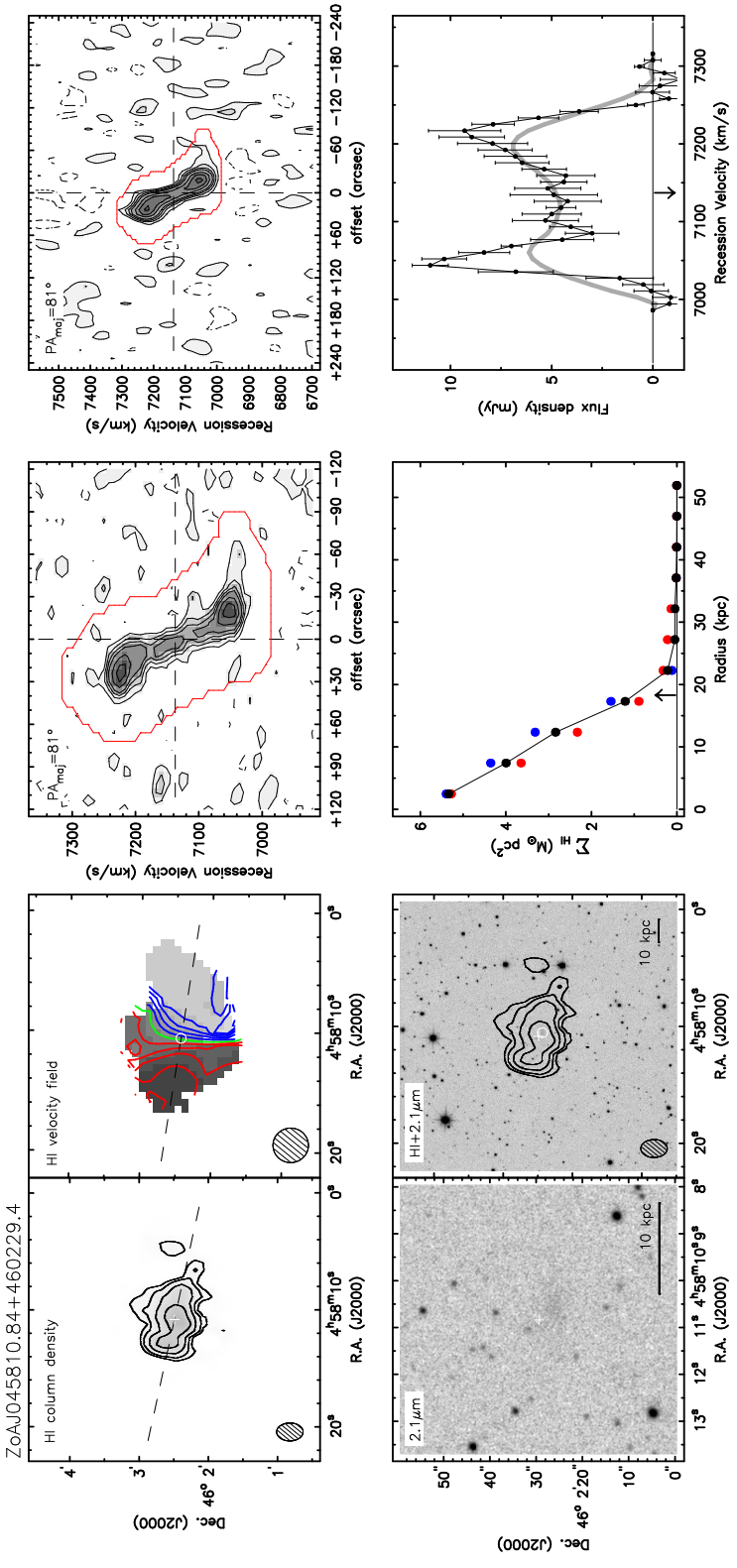

Figure A1. Resolved WSRT HI detections.

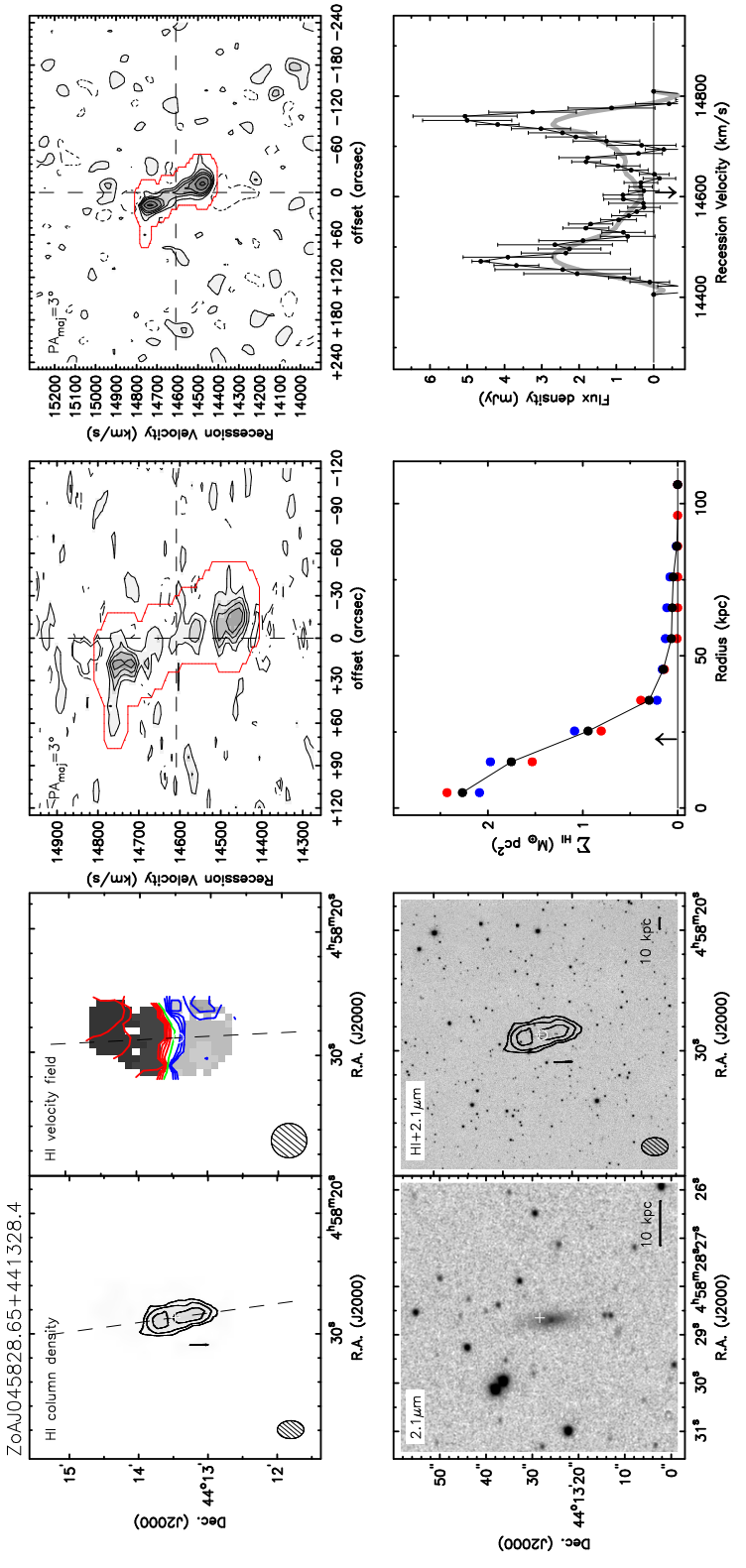

Figure A1. Resolved WSRT HI detections.

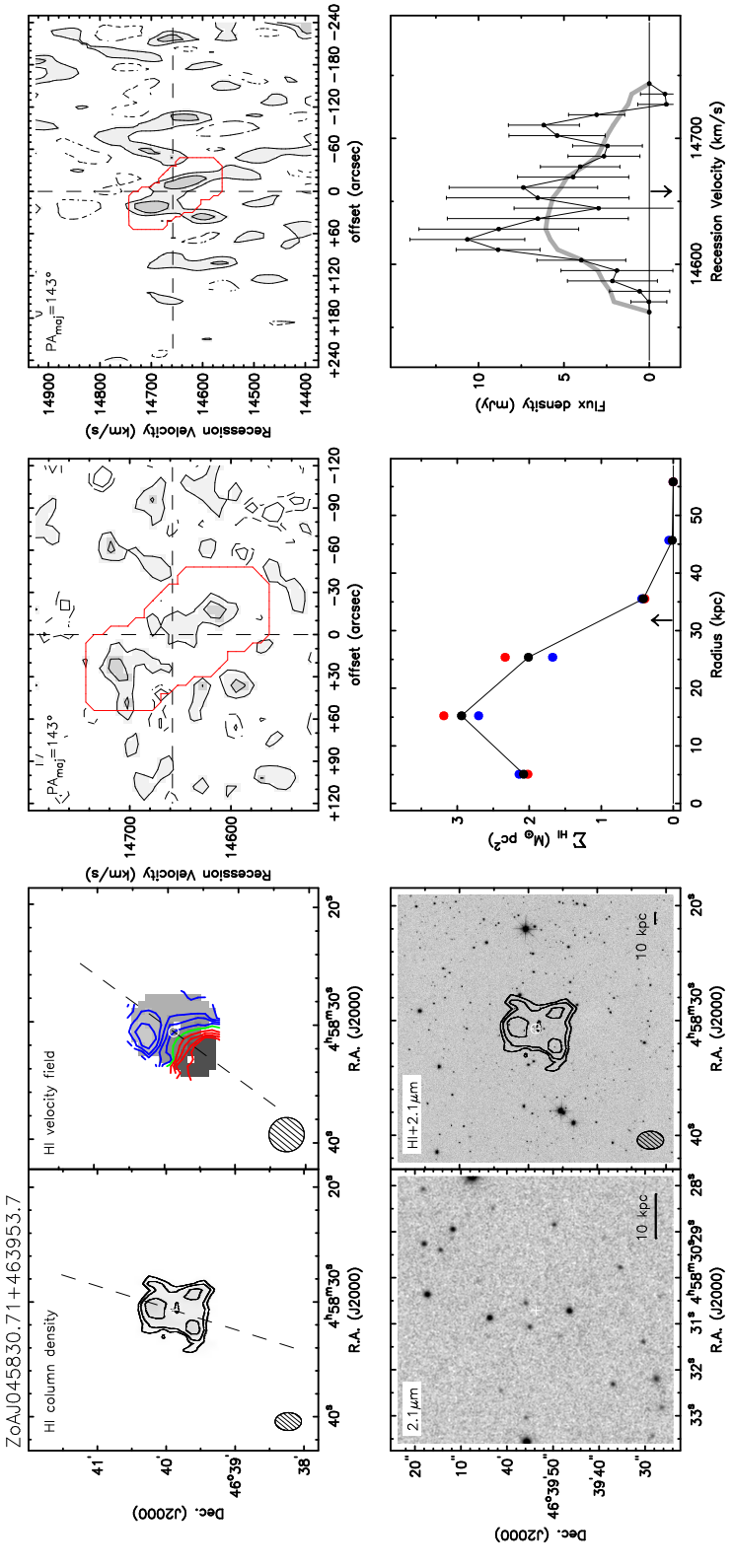

Figure A1. Resolved WSRT HI detections.

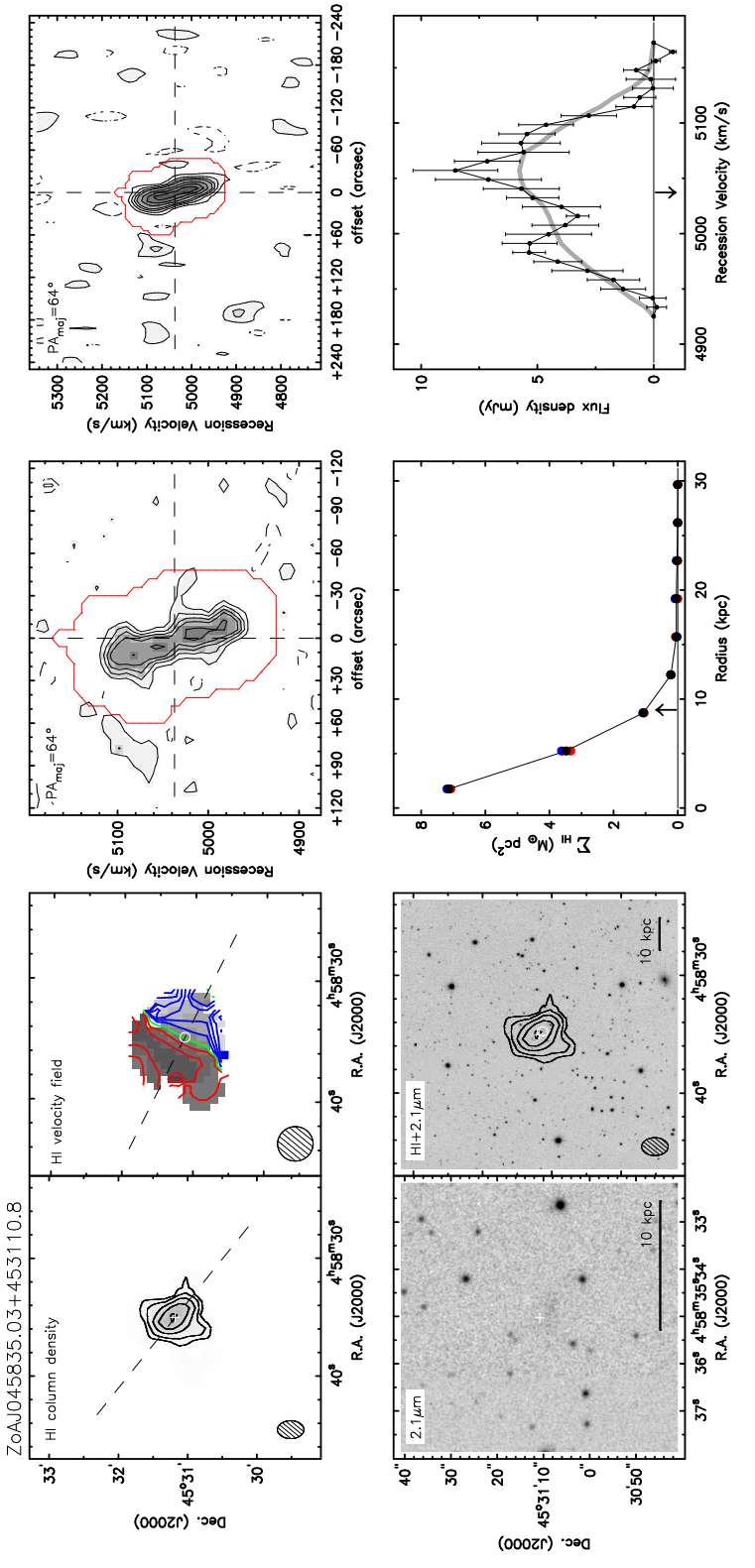

Figure A1. Resolved WSRT HI detections.

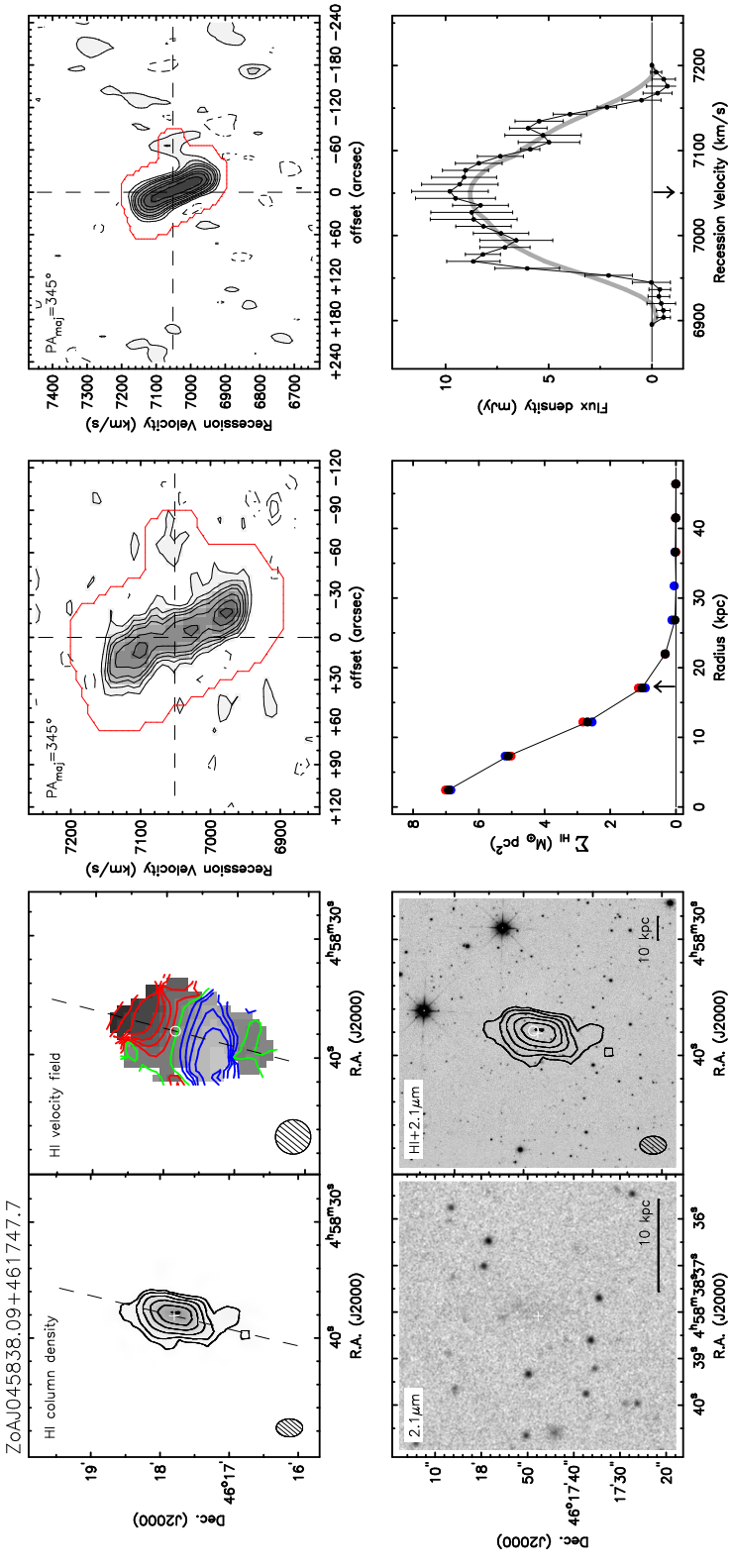

Figure A1. Resolved WSRT HI detections.

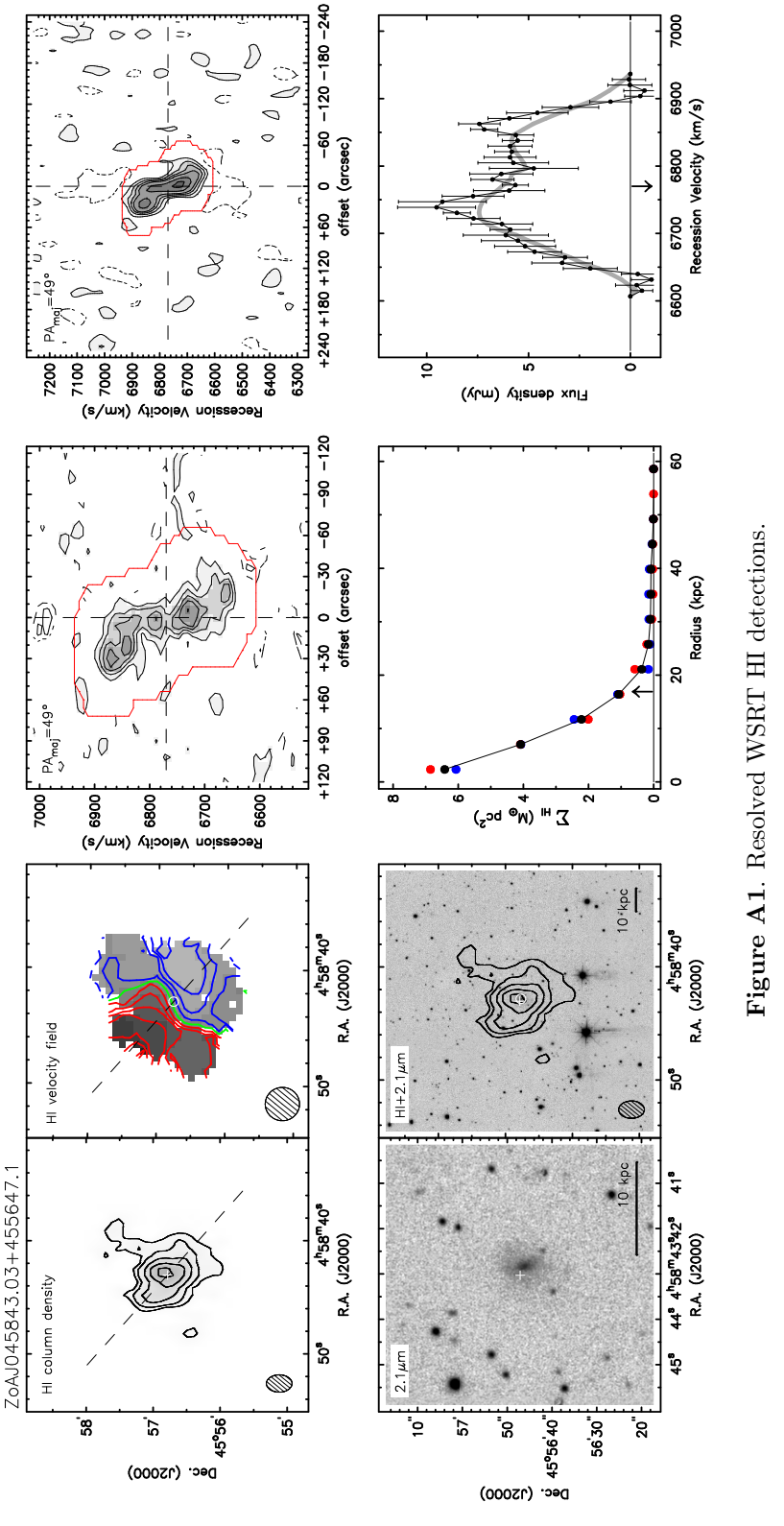

Figure A1. Resolved WSRT HI detections.

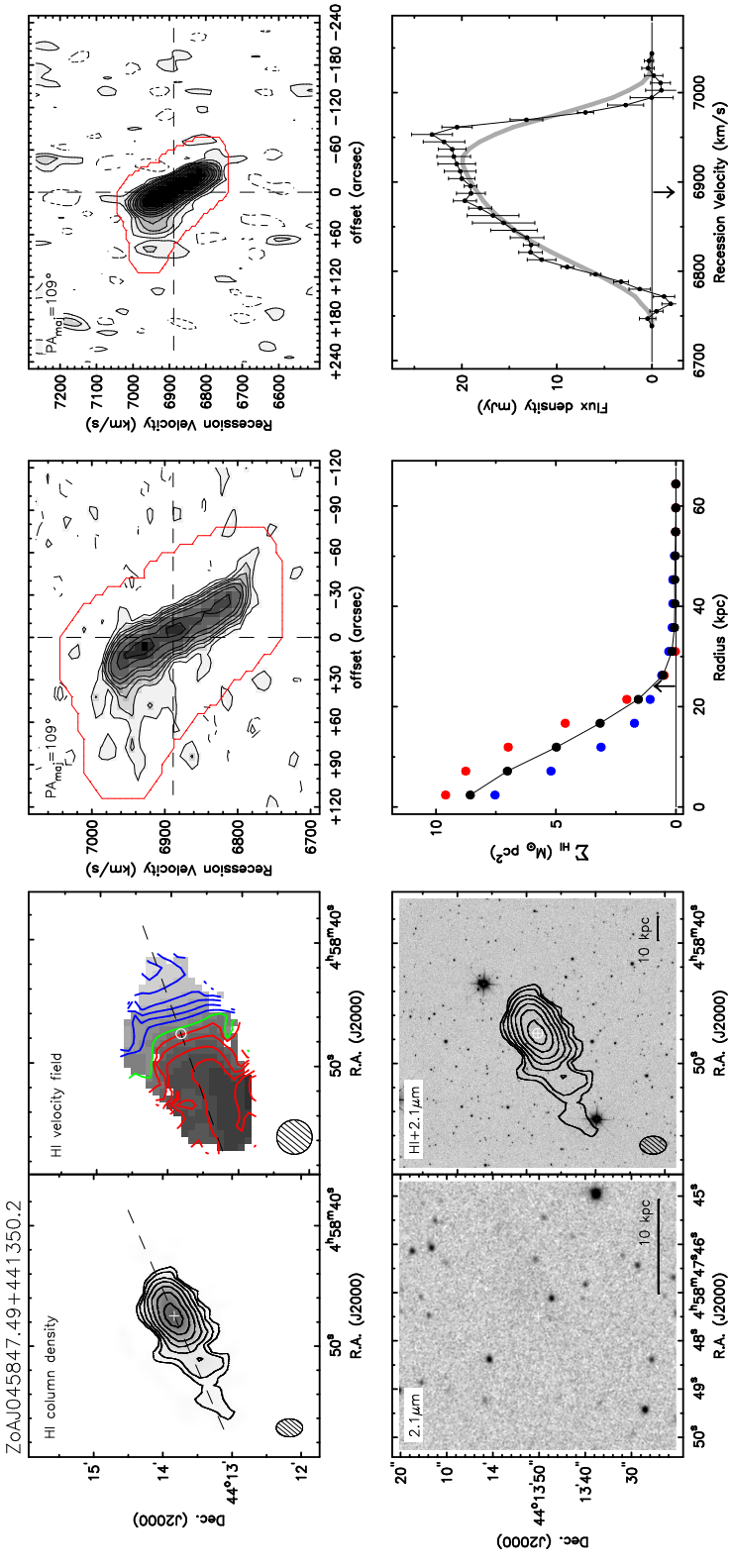

Figure A1. Resolved WSRT HI detections.

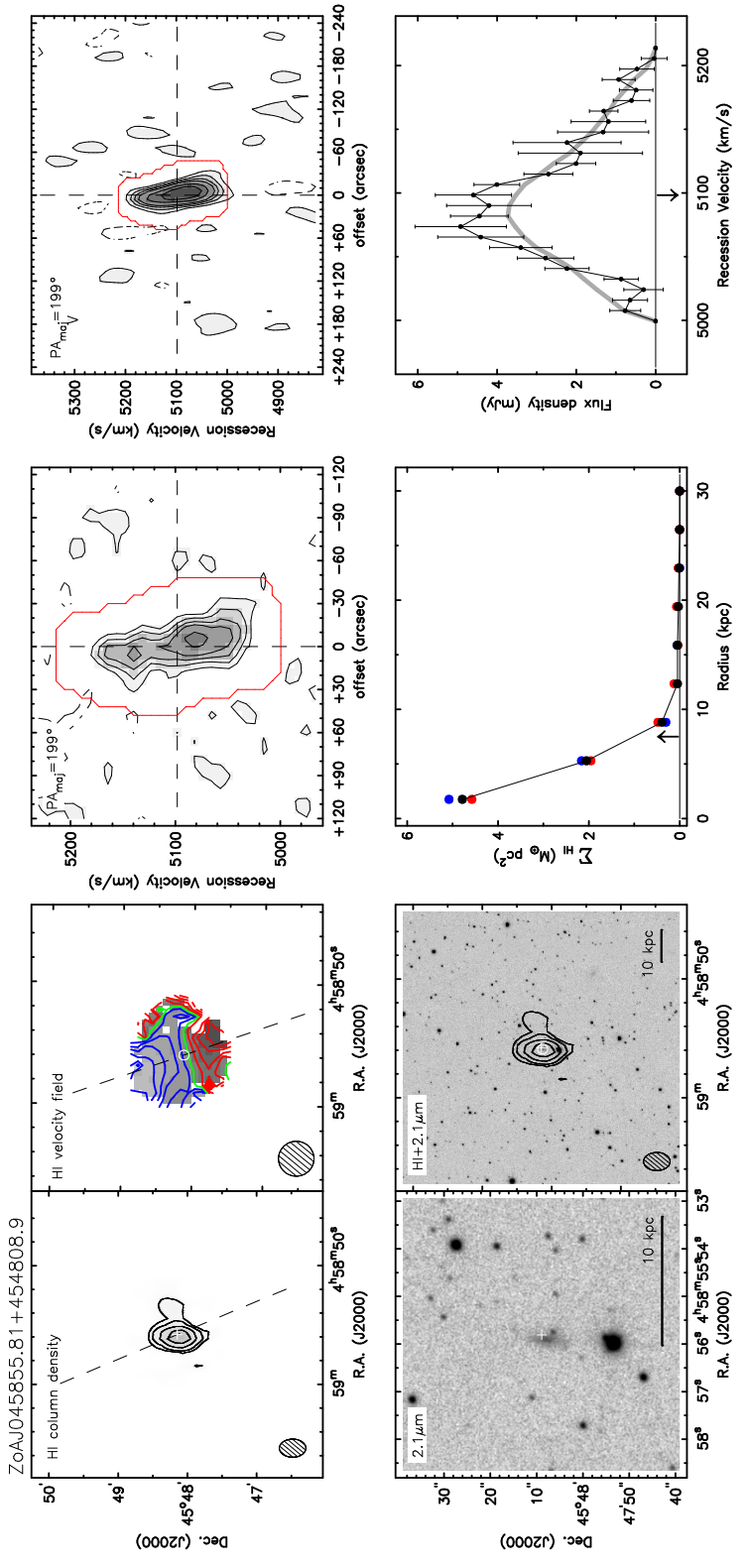

Figure A1. Resolved WSRT HI detections.

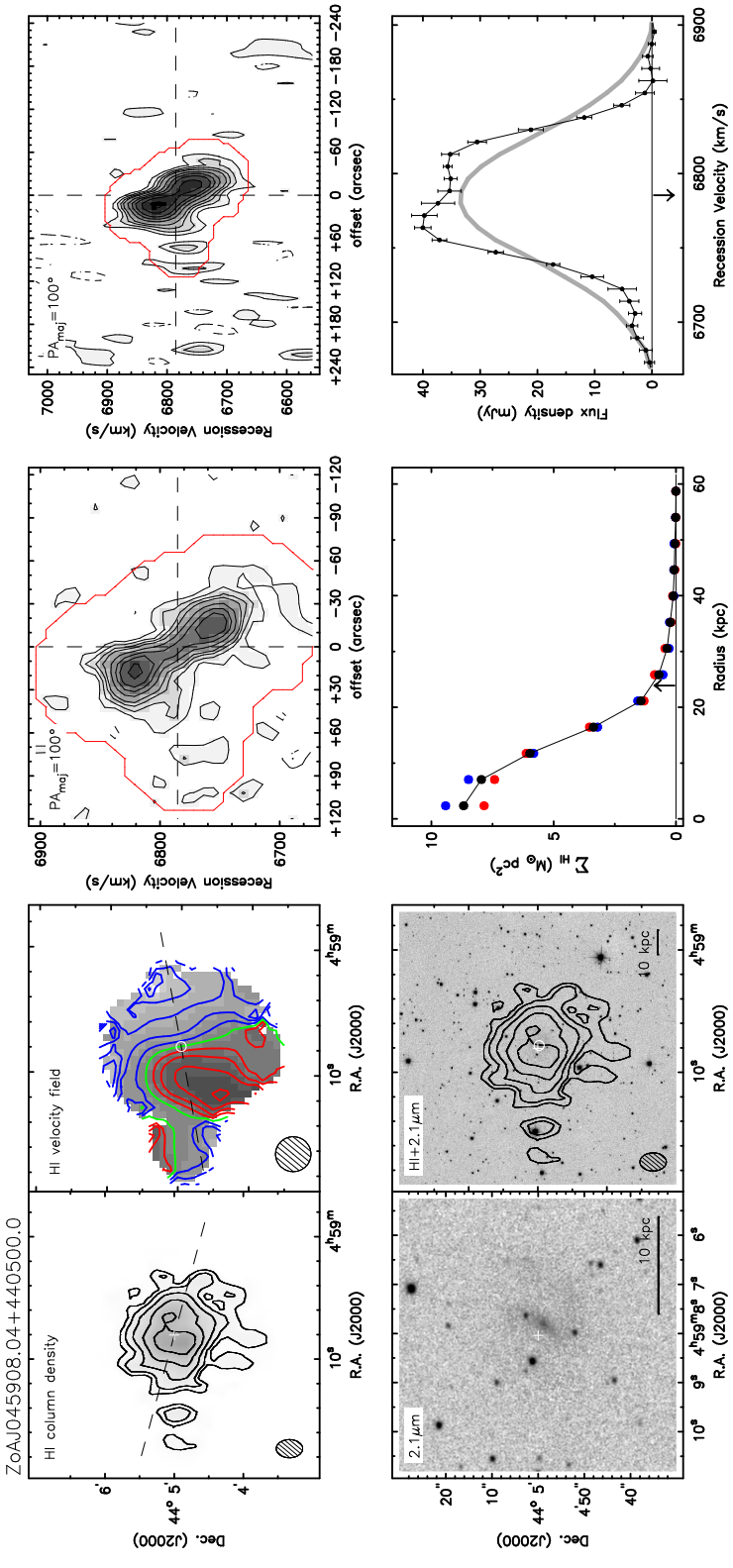

Figure A1. Resolved WSRT HI detections.

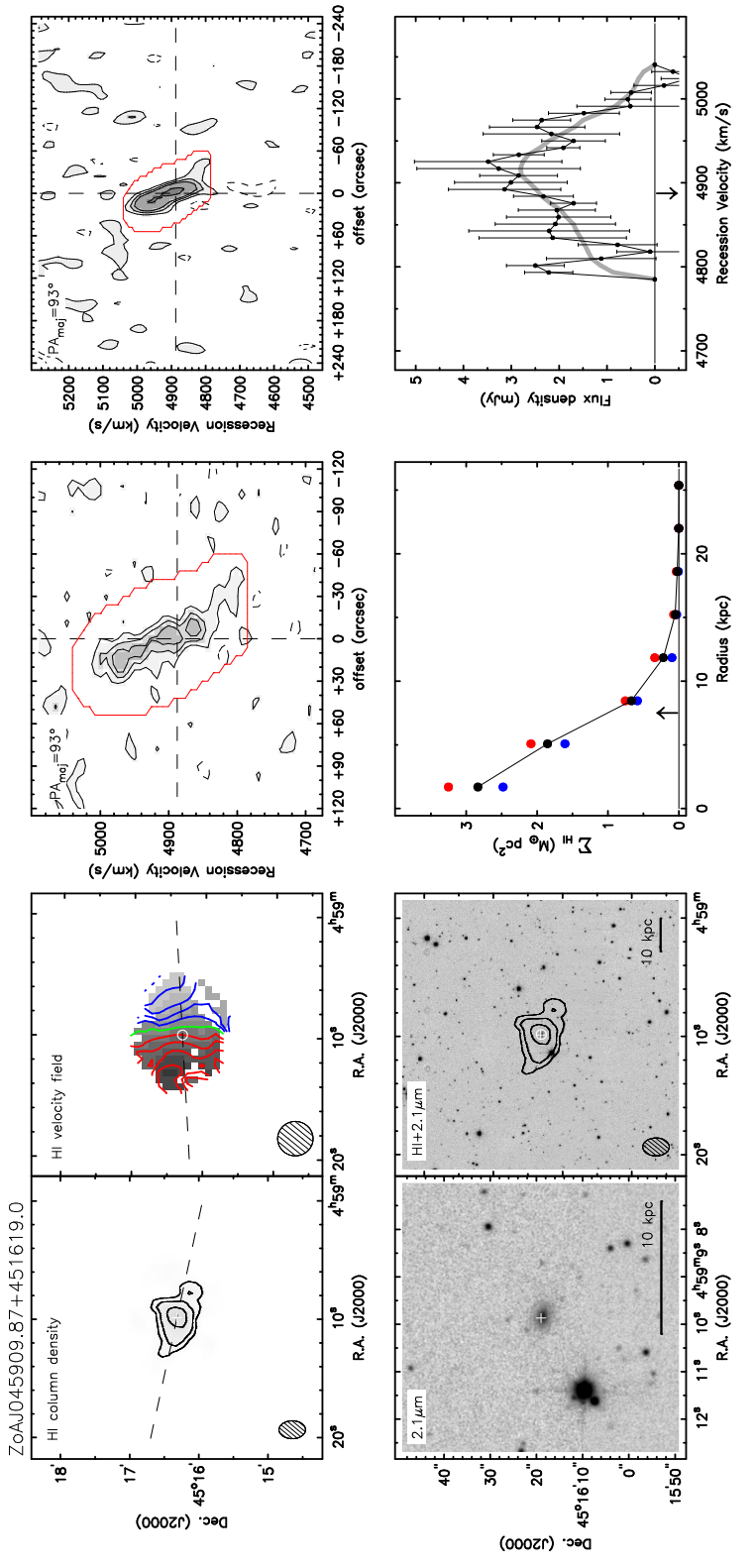

Figure A1. Resolved WSRT HI detections.

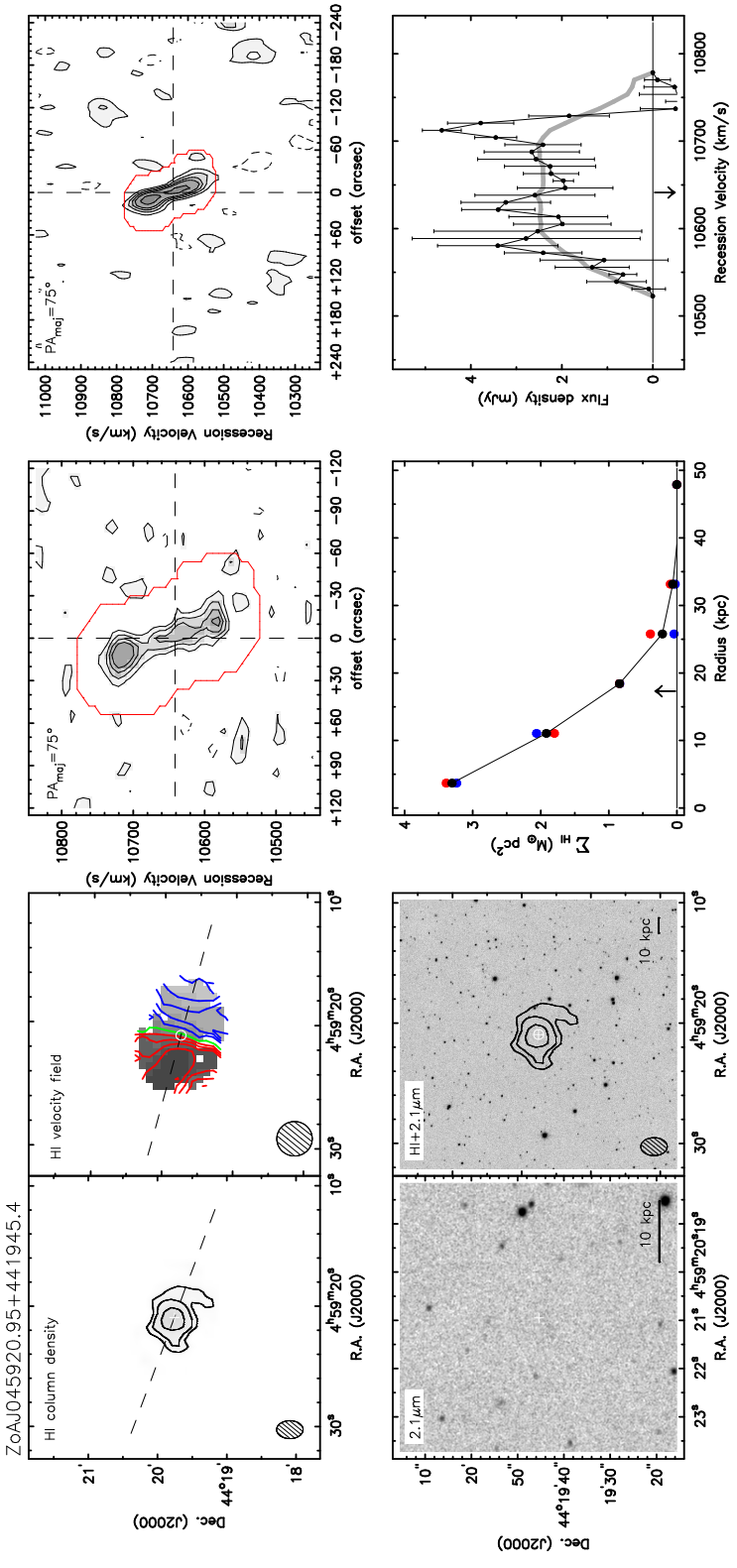

Figure A1. Resolved WSRT HI detections.

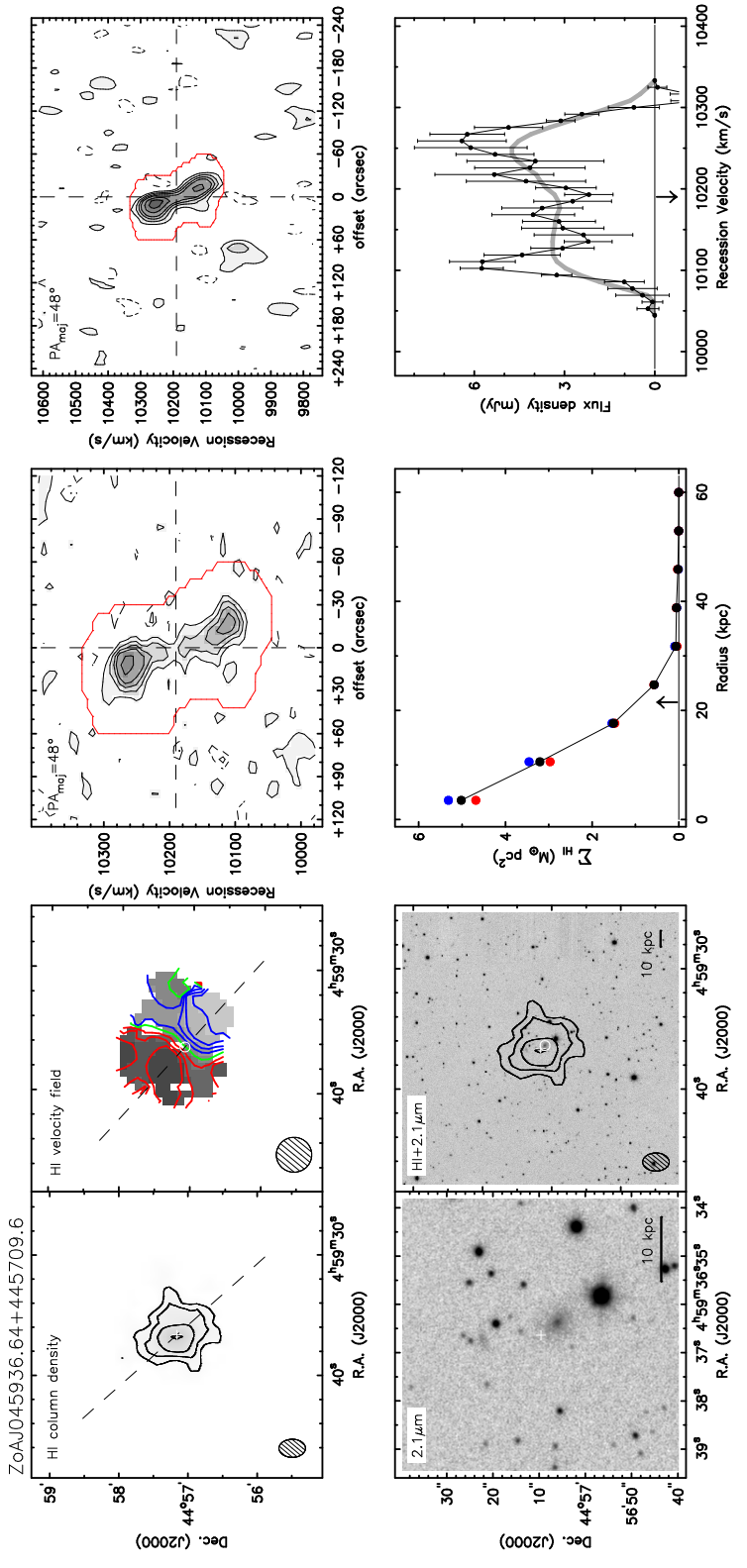

Figure A1. Resolved WSRT HI detections.

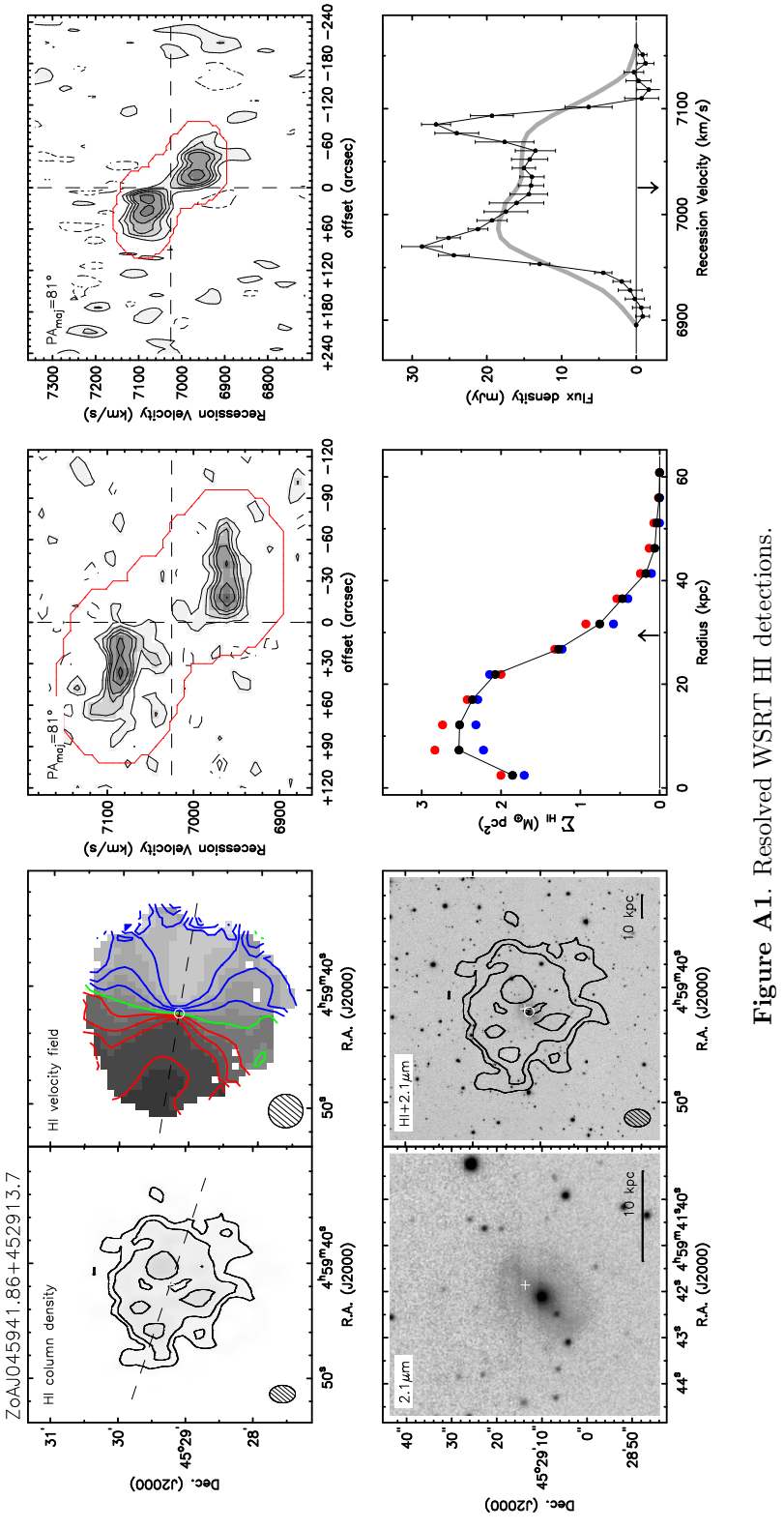

Figure A1. Resolved WSRT HI detections.

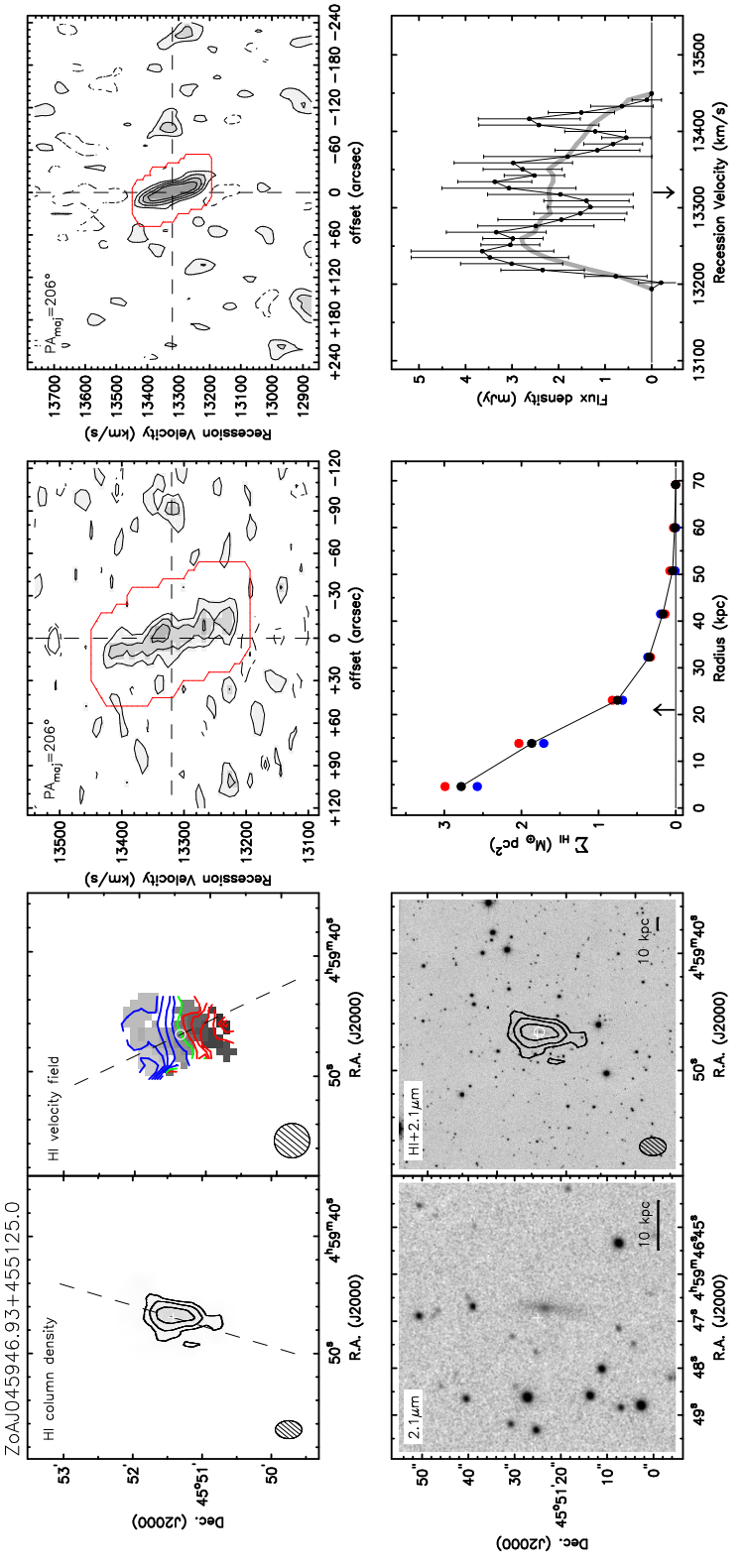

Figure A1. Resolved WSRT HI detections.

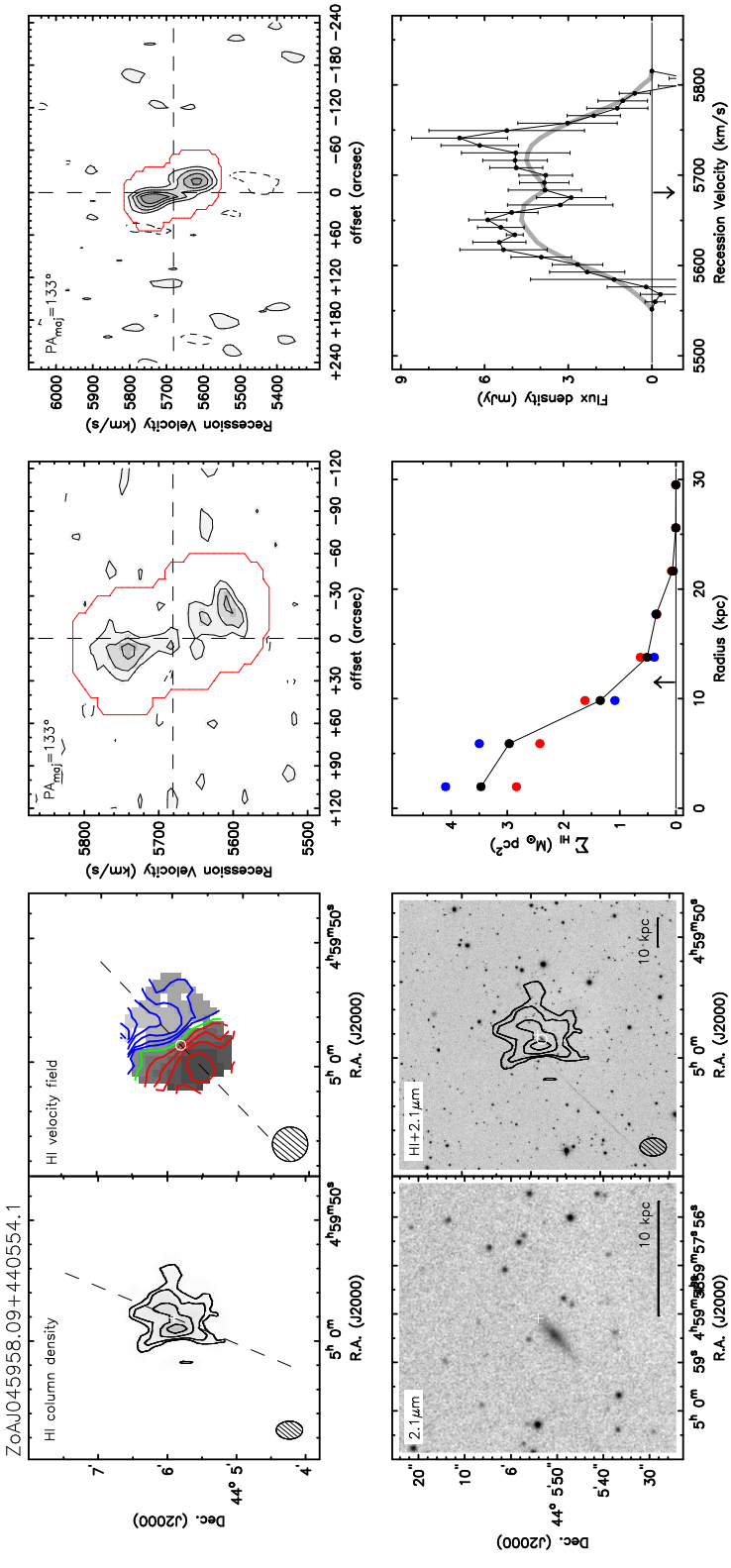

Figure A1. Resolved WSRT HI detections.

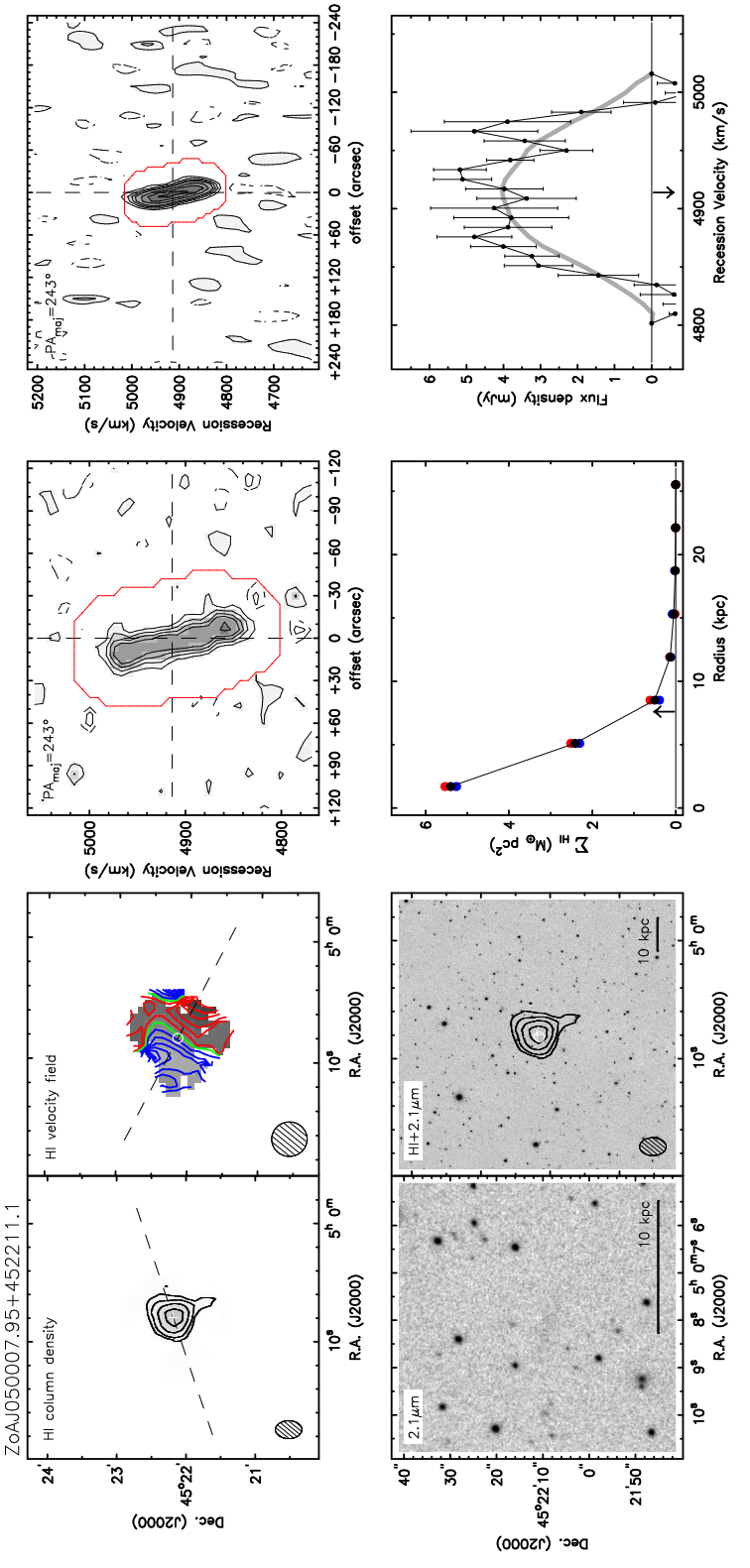

Figure A1. Resolved WSRT HI detections.

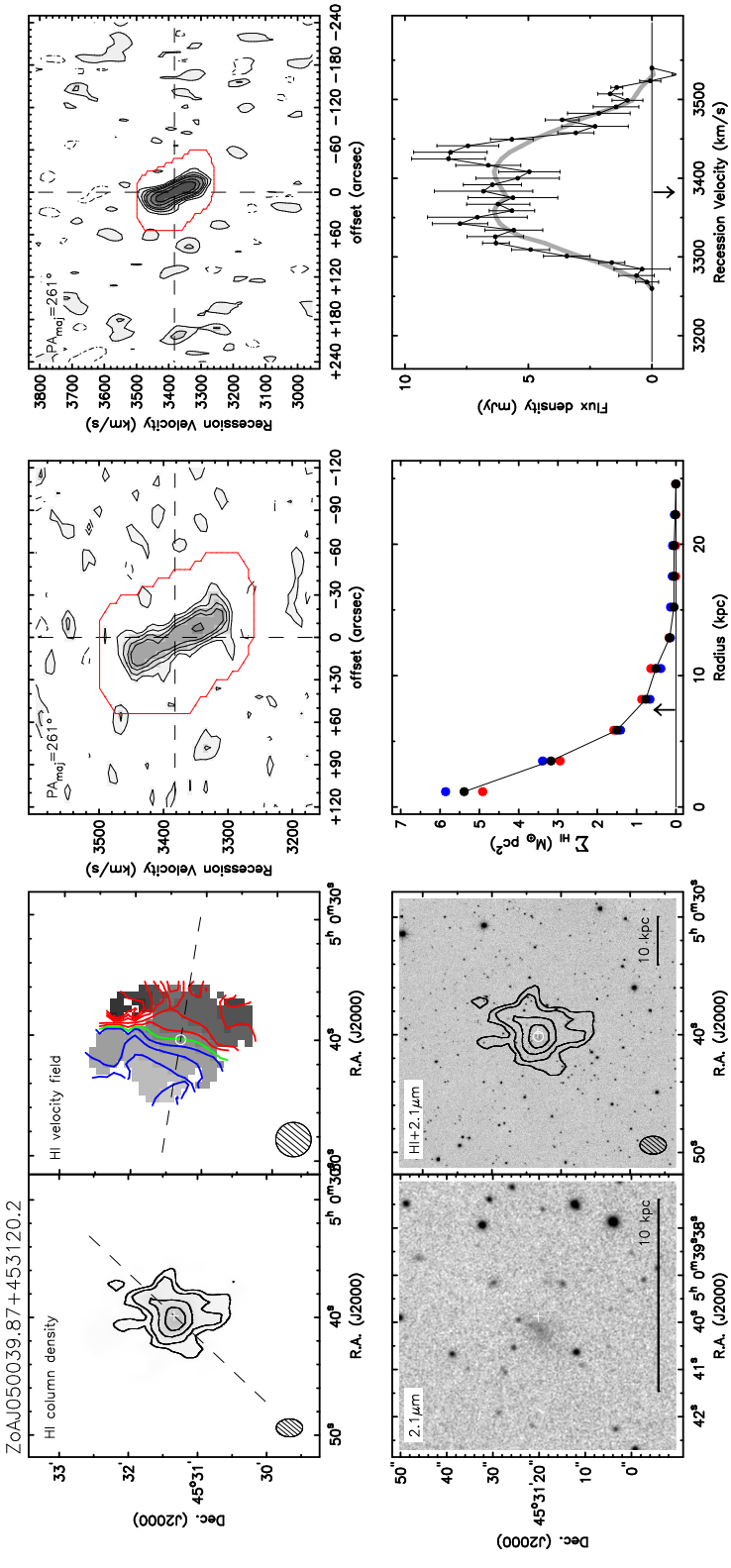

Figure A1. Resolved WSRT HI detections.

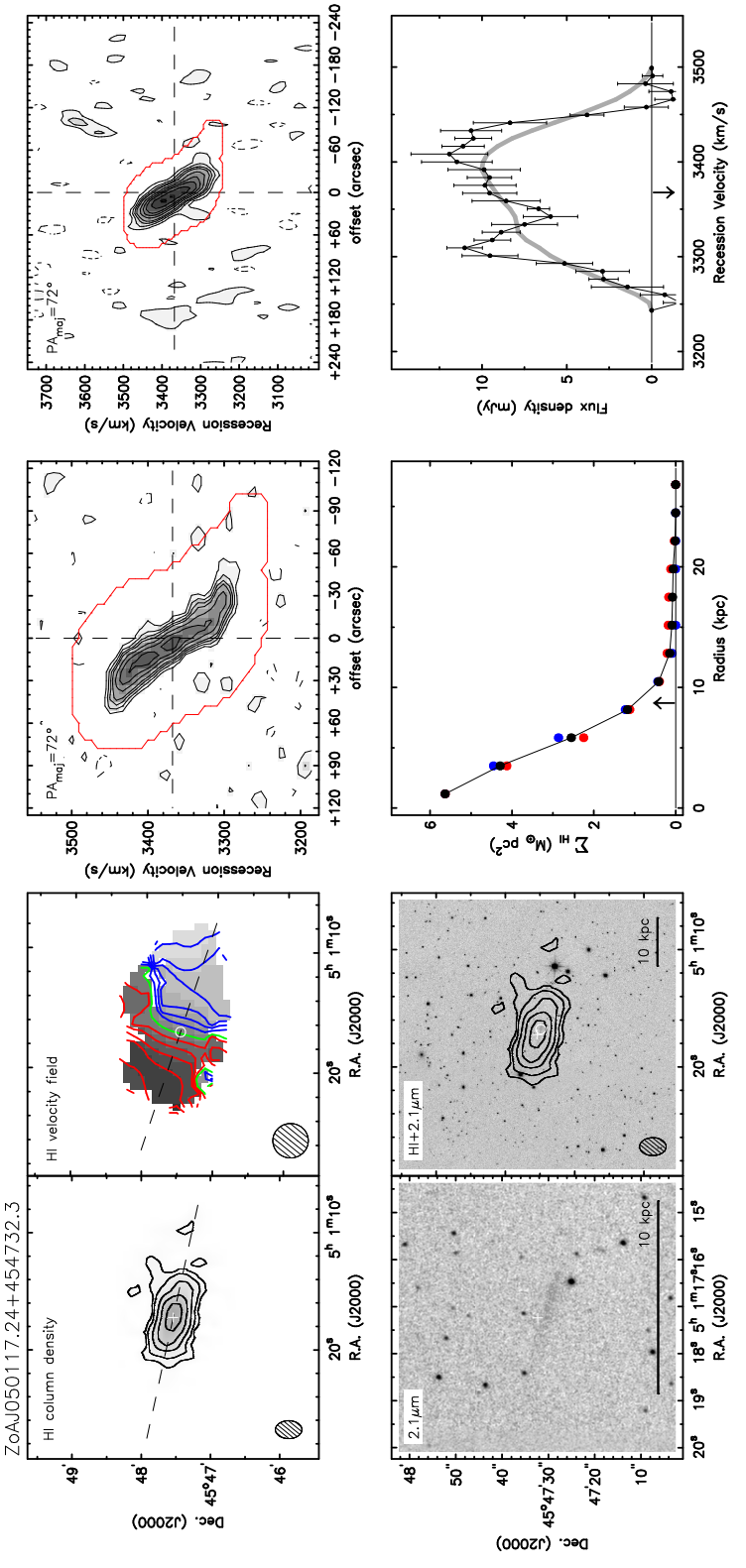

Figure A1. Resolved WSRT HI detections.

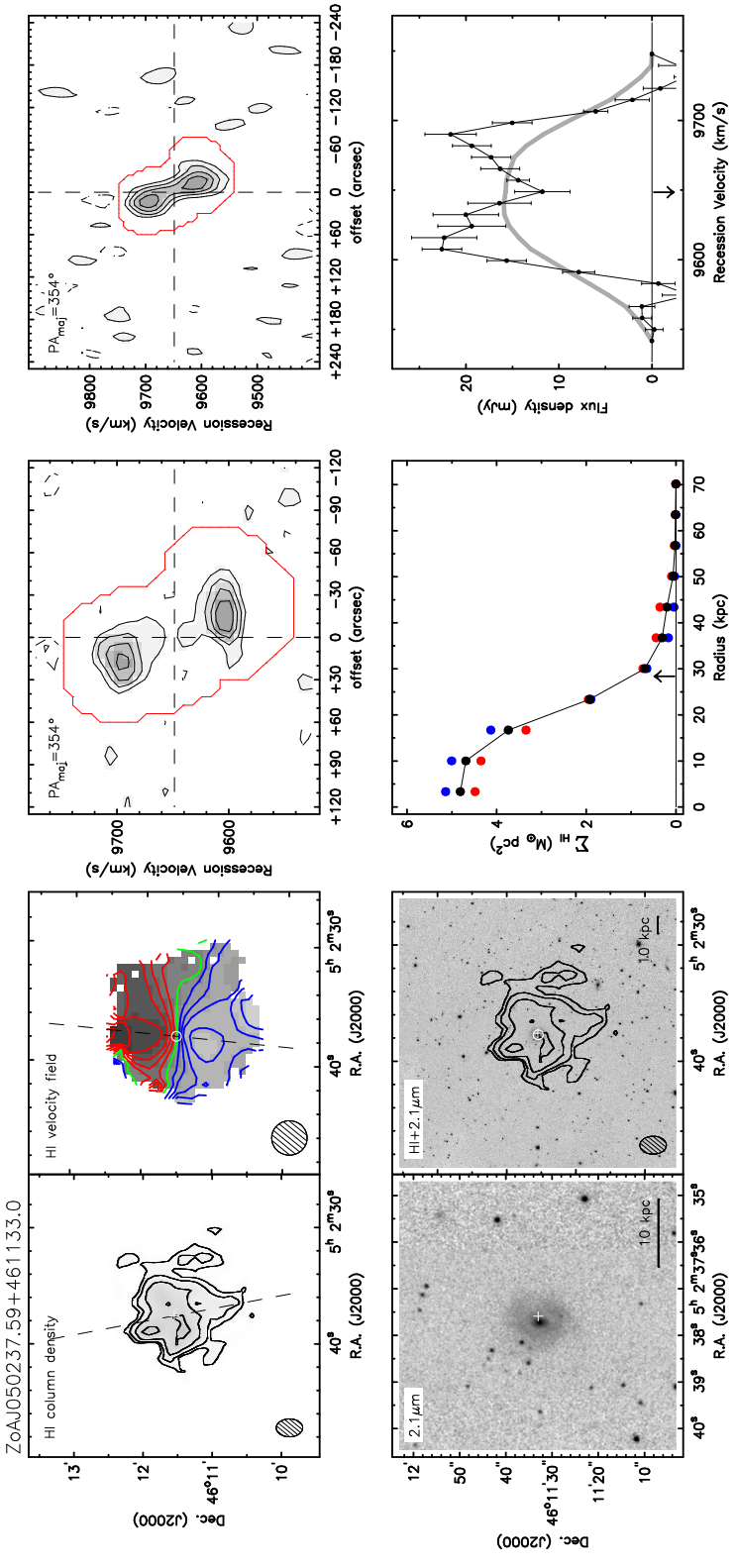

Figure A1. Resolved WSRT HI detections.

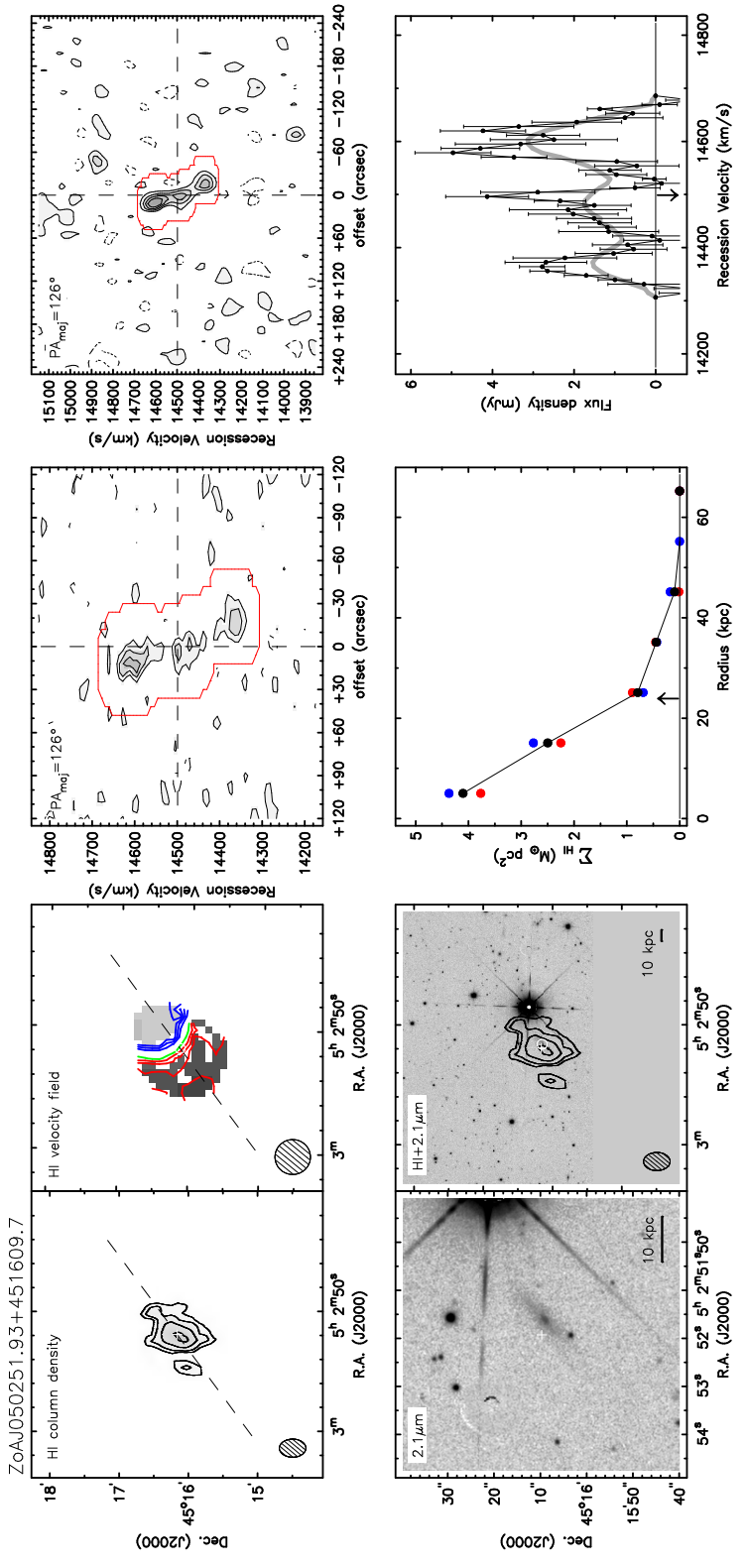

Figure A1. Resolved WSRT HI detections.

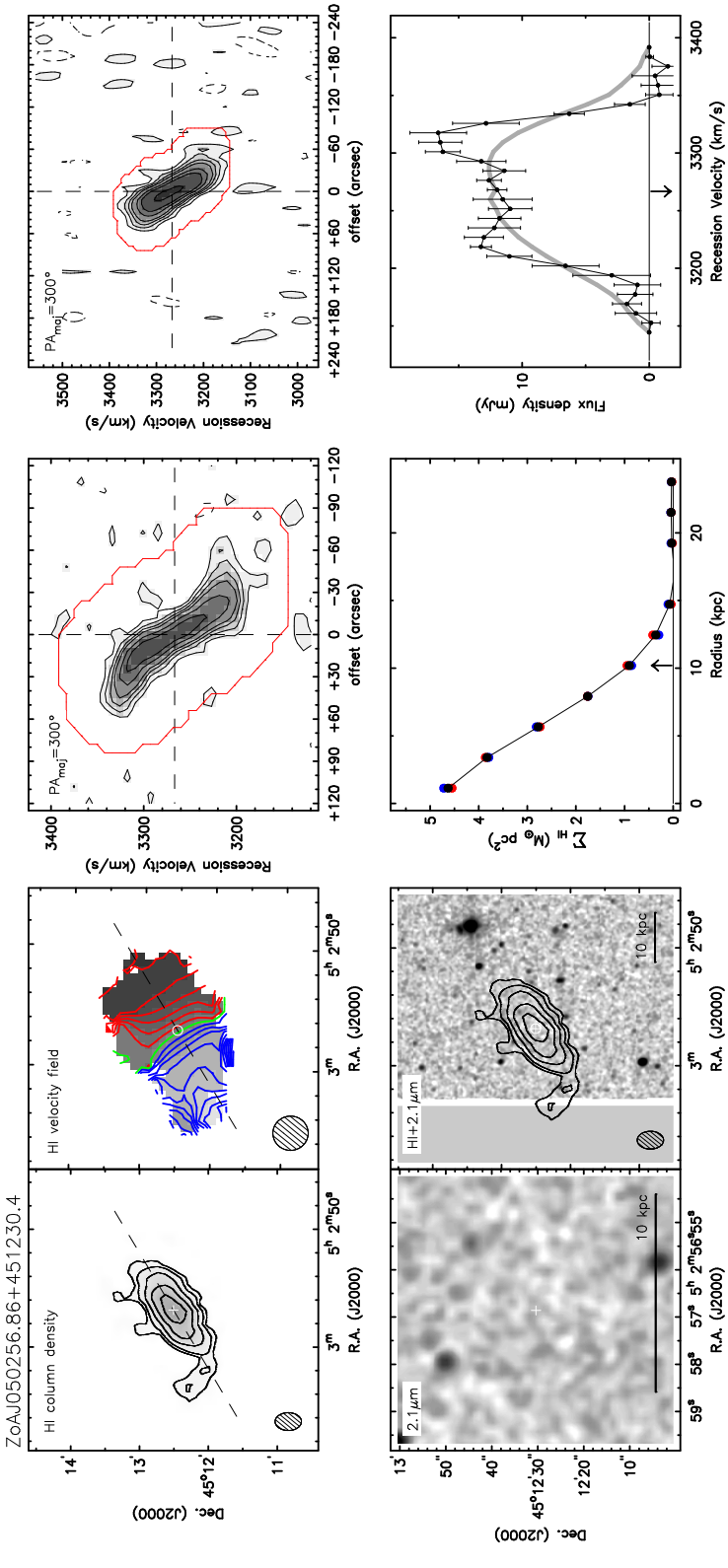

Figure A1. Resolved WSRT HI detections.

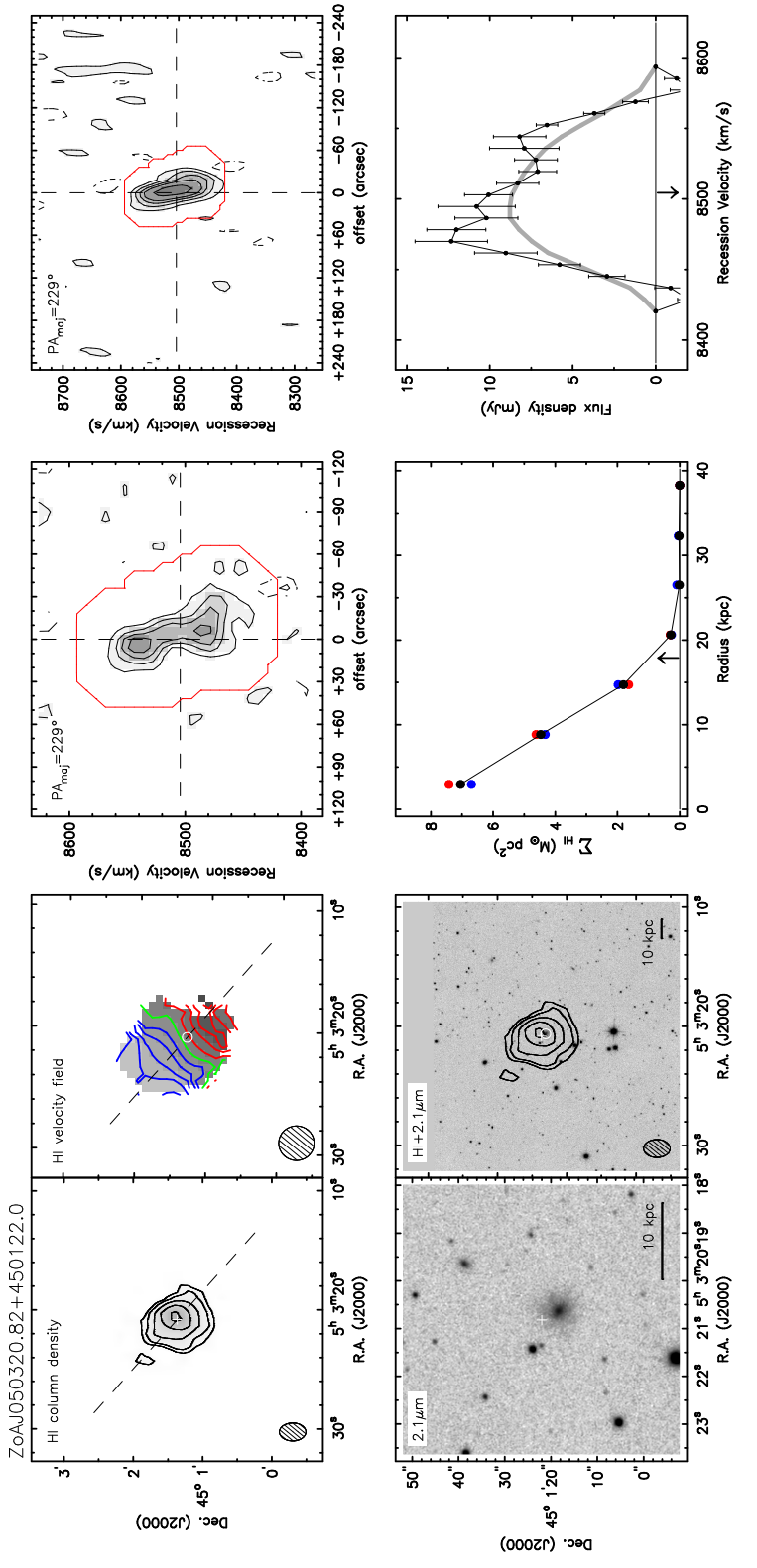

Figure A1. Resolved WSRT HI detections.

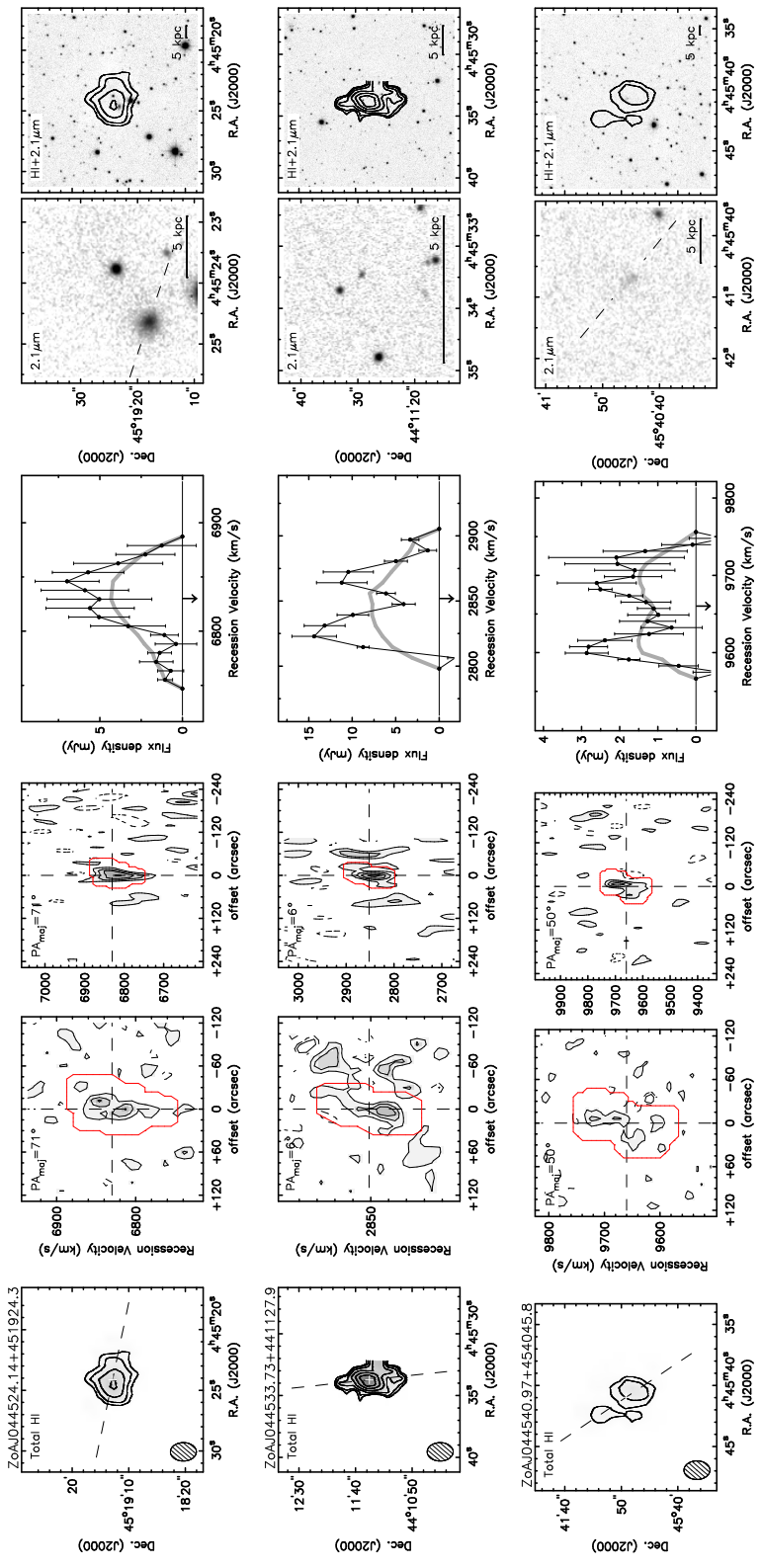

Figure A2. Marginally resolved WSRT HI detections.

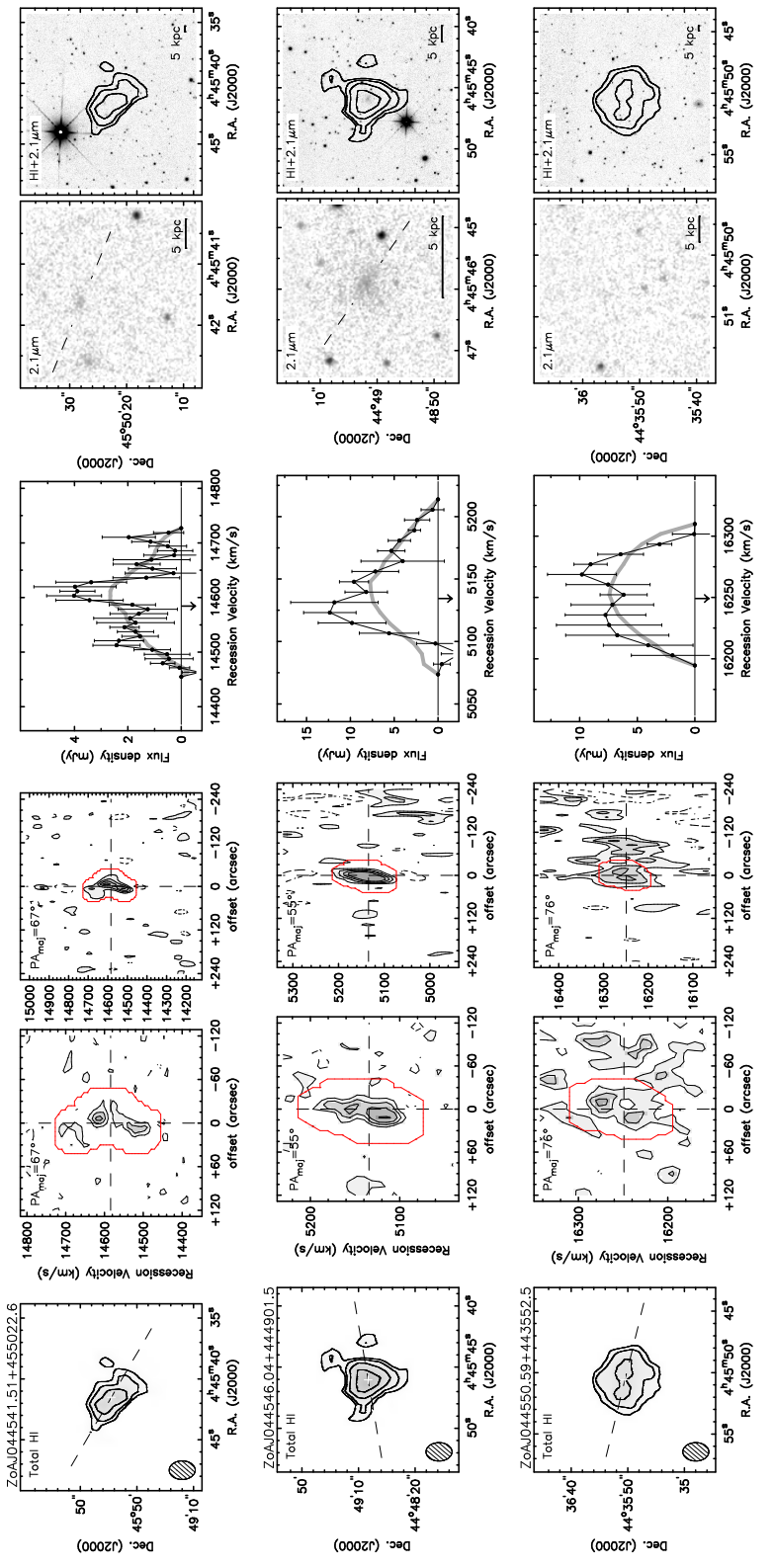

Figure A2. Marginally resolved WSRT HI detections.

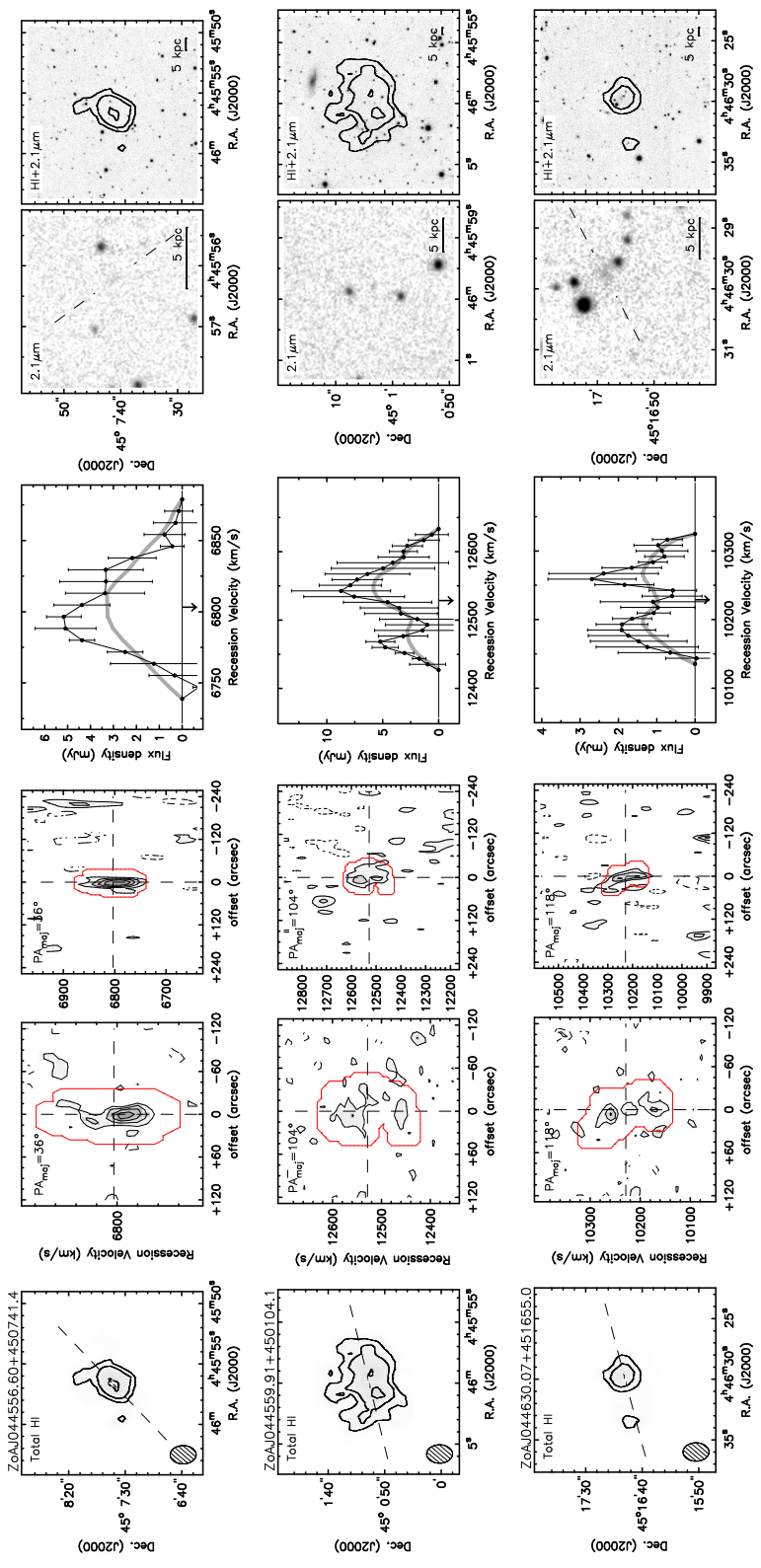

Figure A2. Marginally resolved WSRT HI detections.

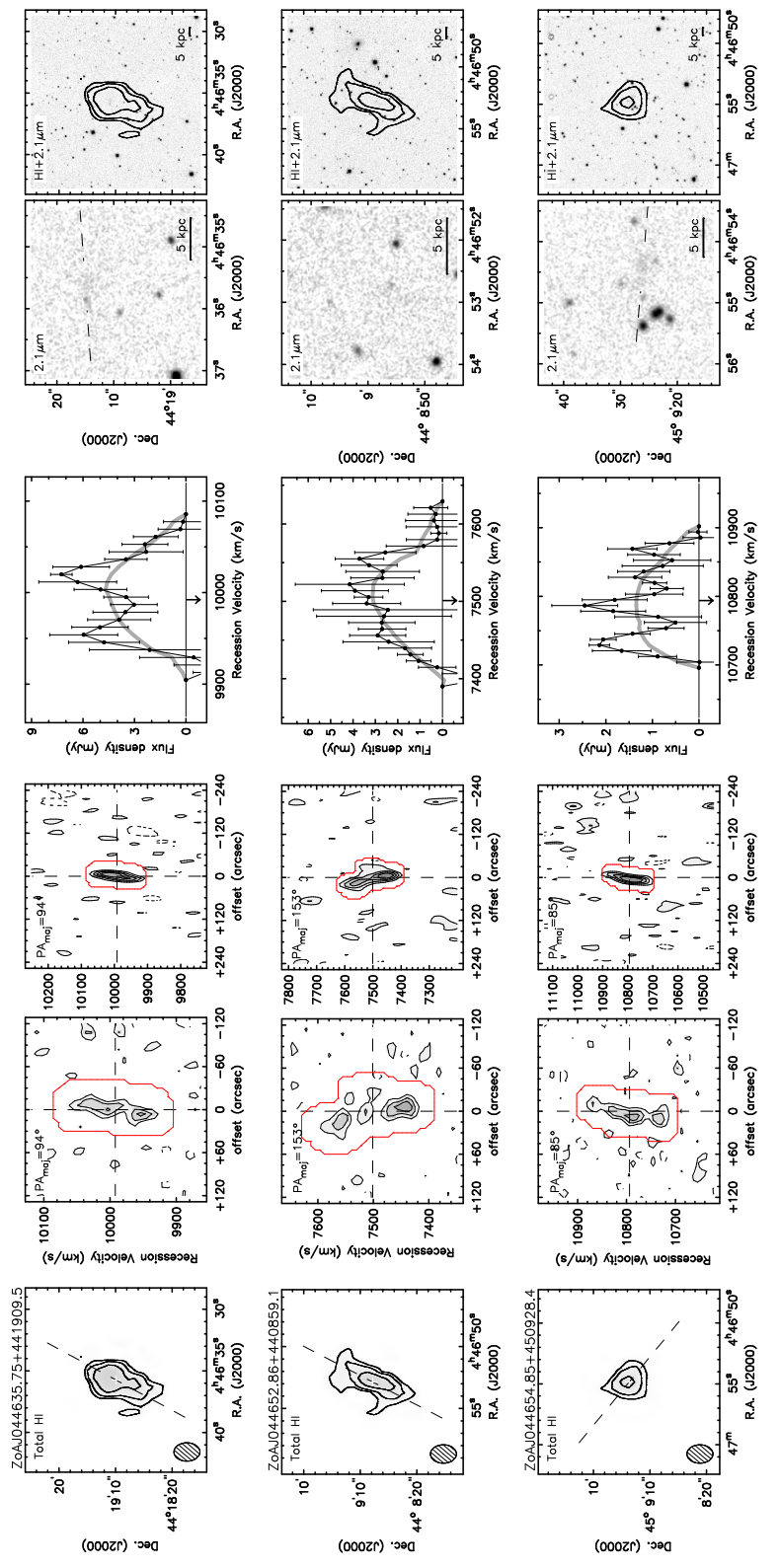

Figure A2. Marginally resolved WSRT HI detections.

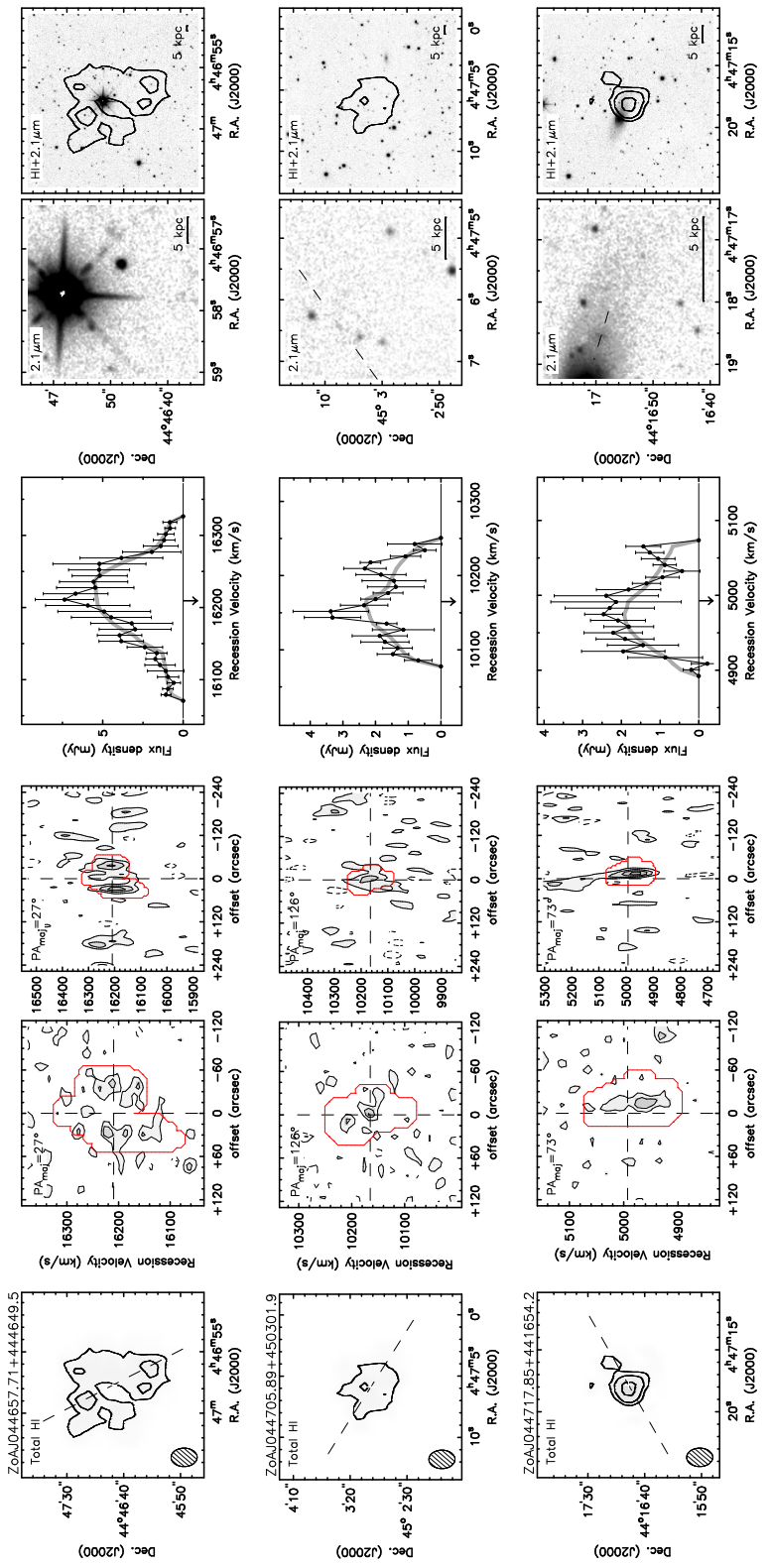

Figure A2. Marginally resolved WSRT HI detections.

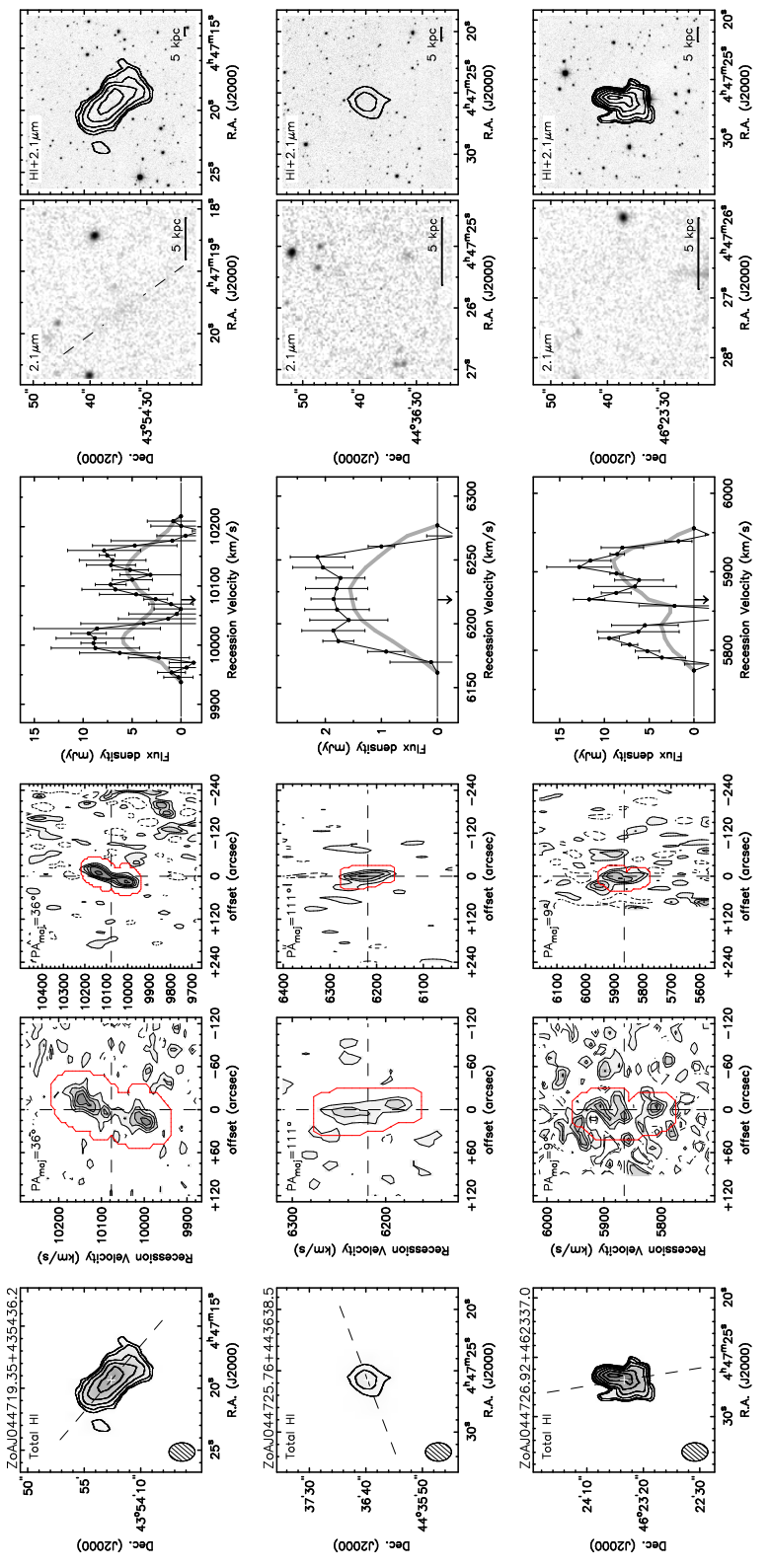

Figure A2. Marginally resolved WSRT HI detections.

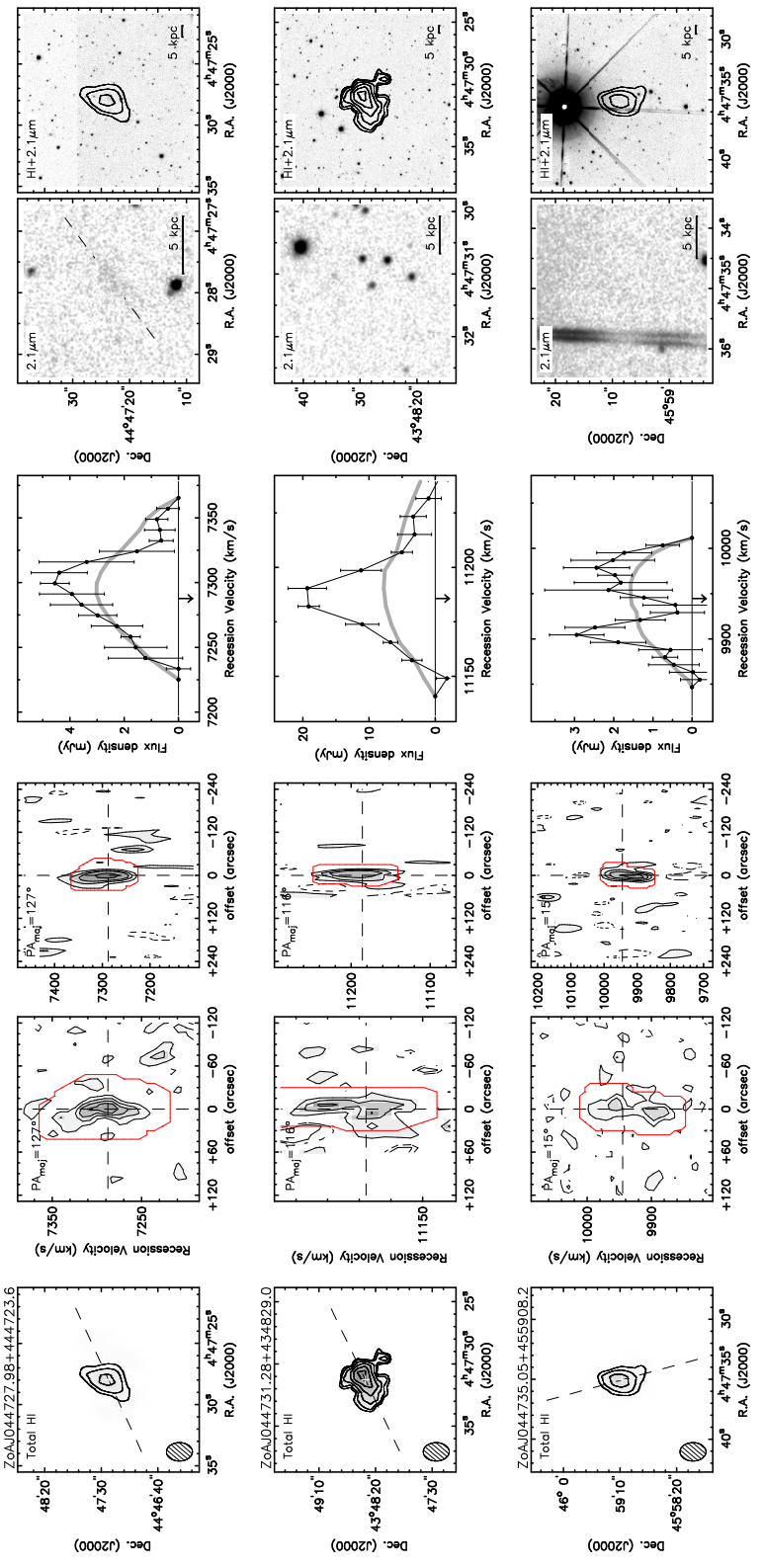

Figure A2. Marginally resolved WSRT HI detections.

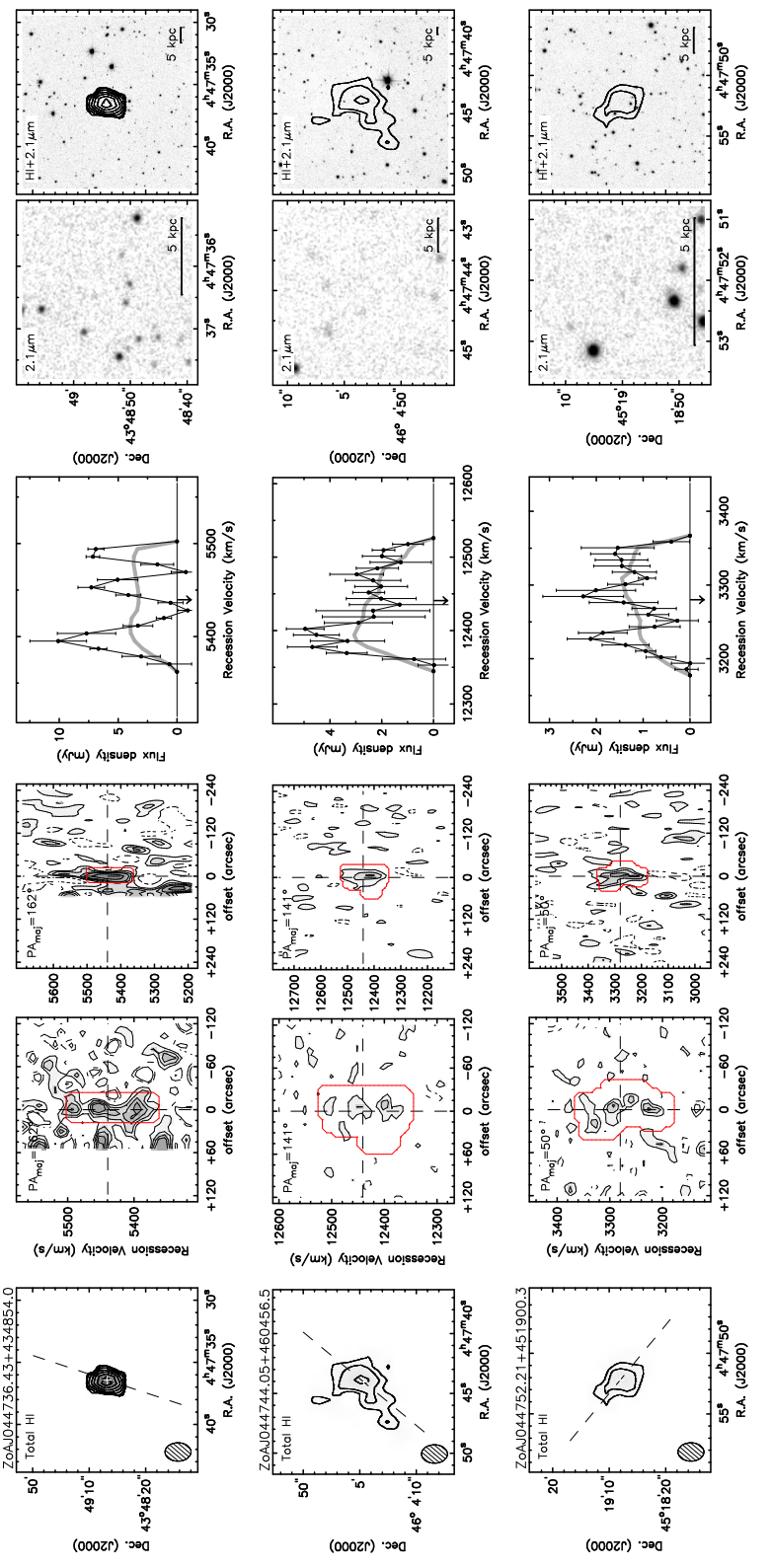

Figure A2. Marginally resolved WSRT HI detections.

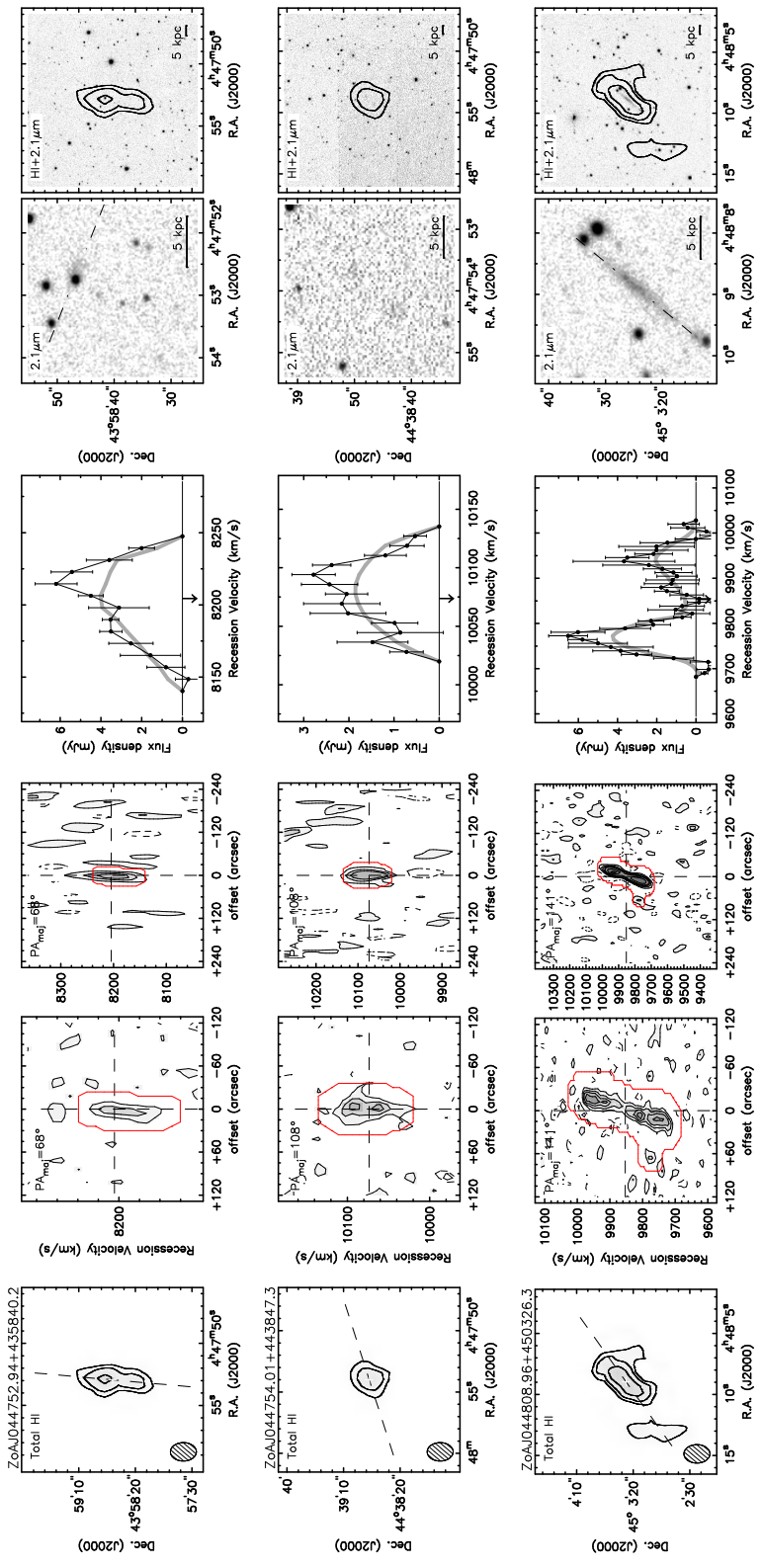

Figure A2. Marginally resolved WSRT HI detections.

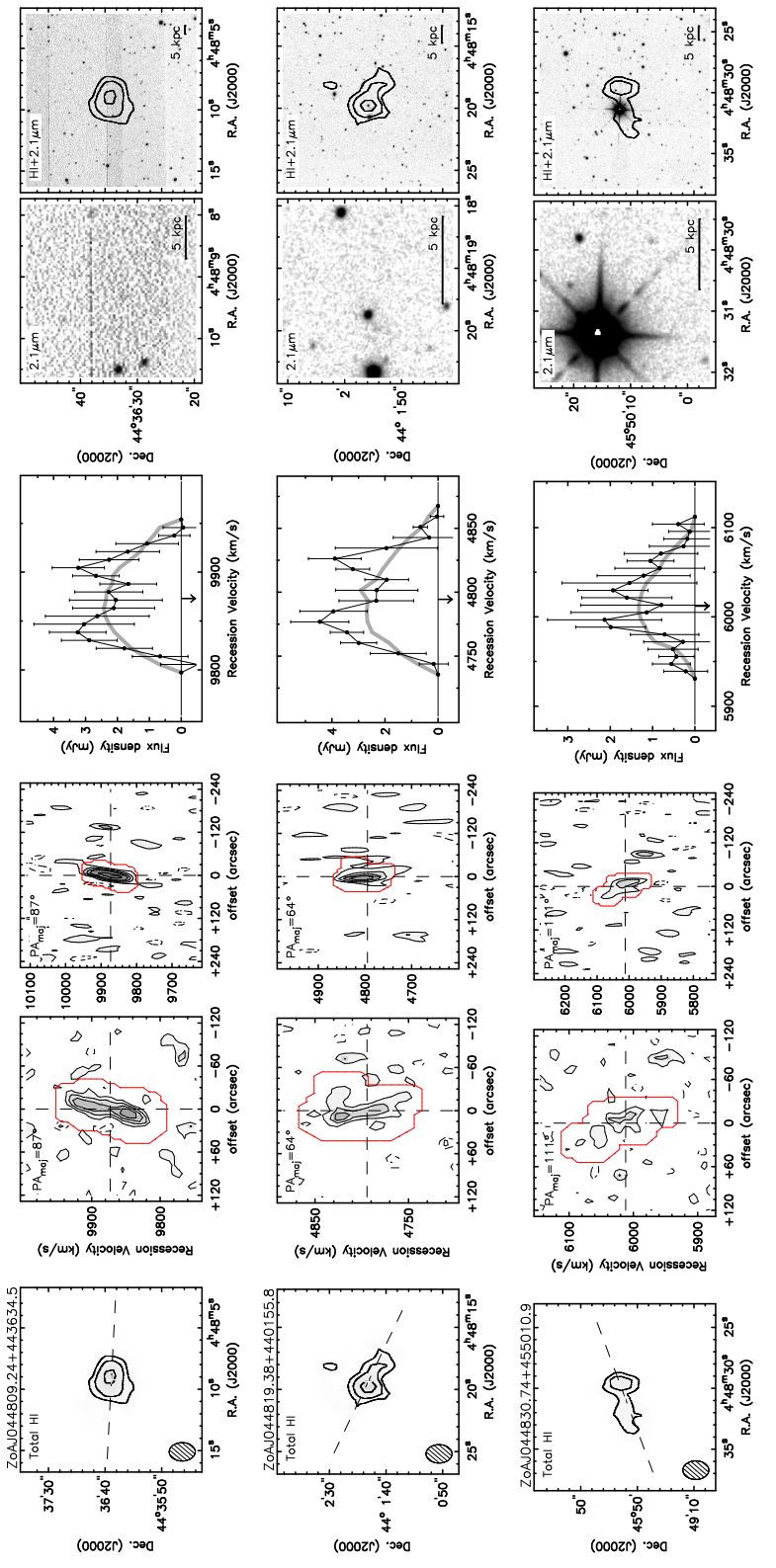

Figure A2. Marginally resolved WSRT HI detections.

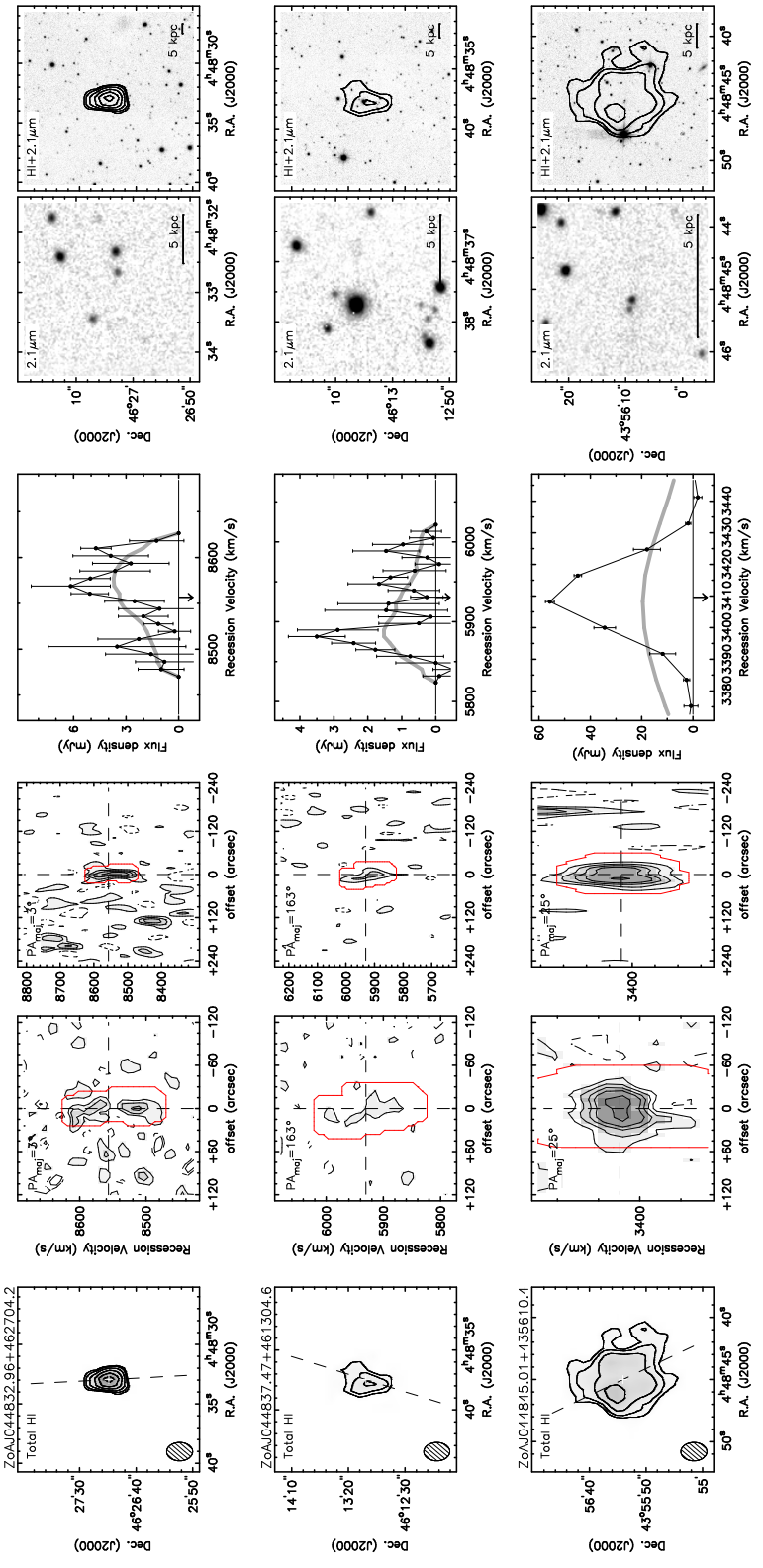

Figure A2. Marginally resolved WSRT HI detections.

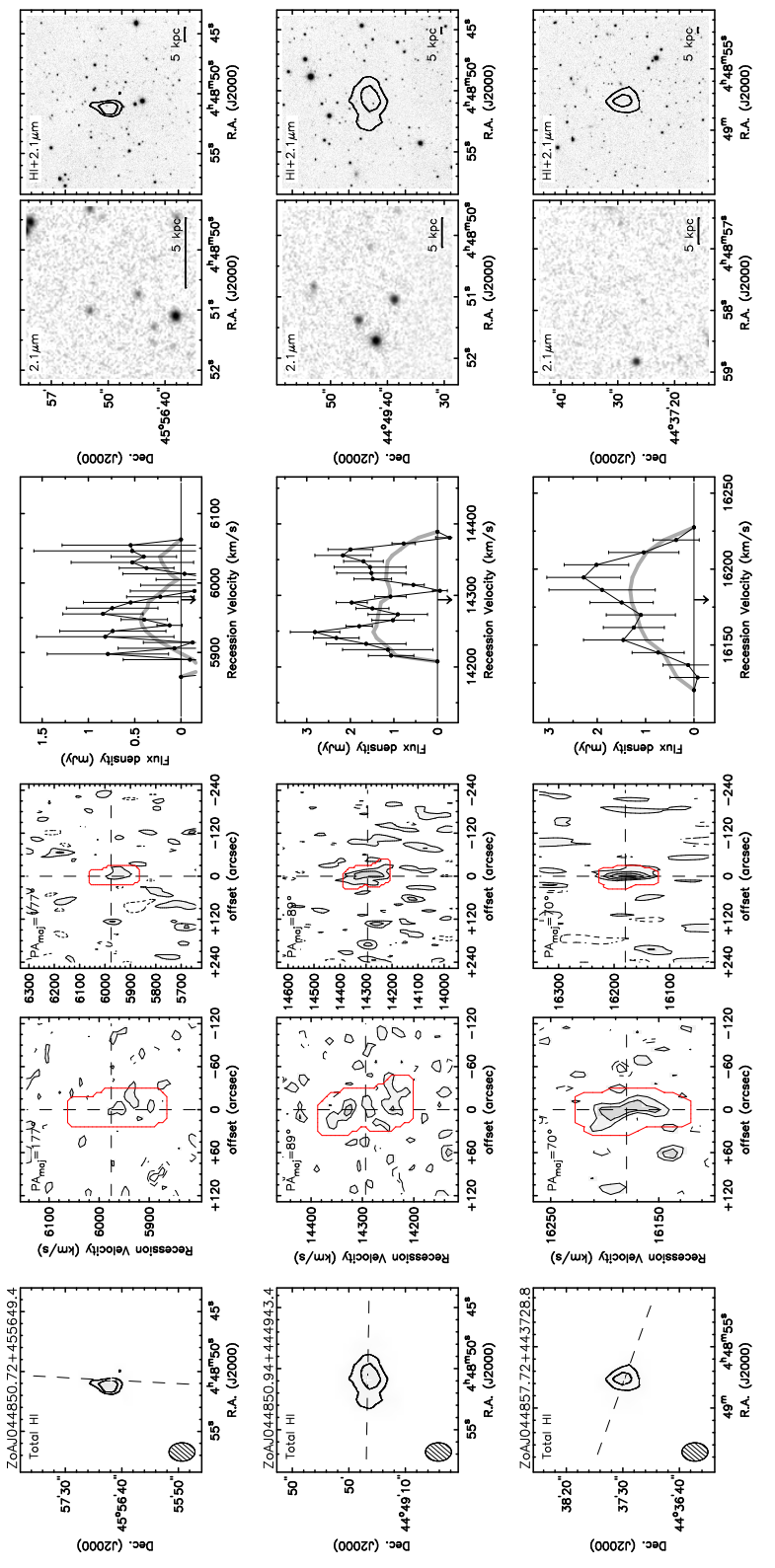

Figure A2. Marginally resolved WSRT HI detections.

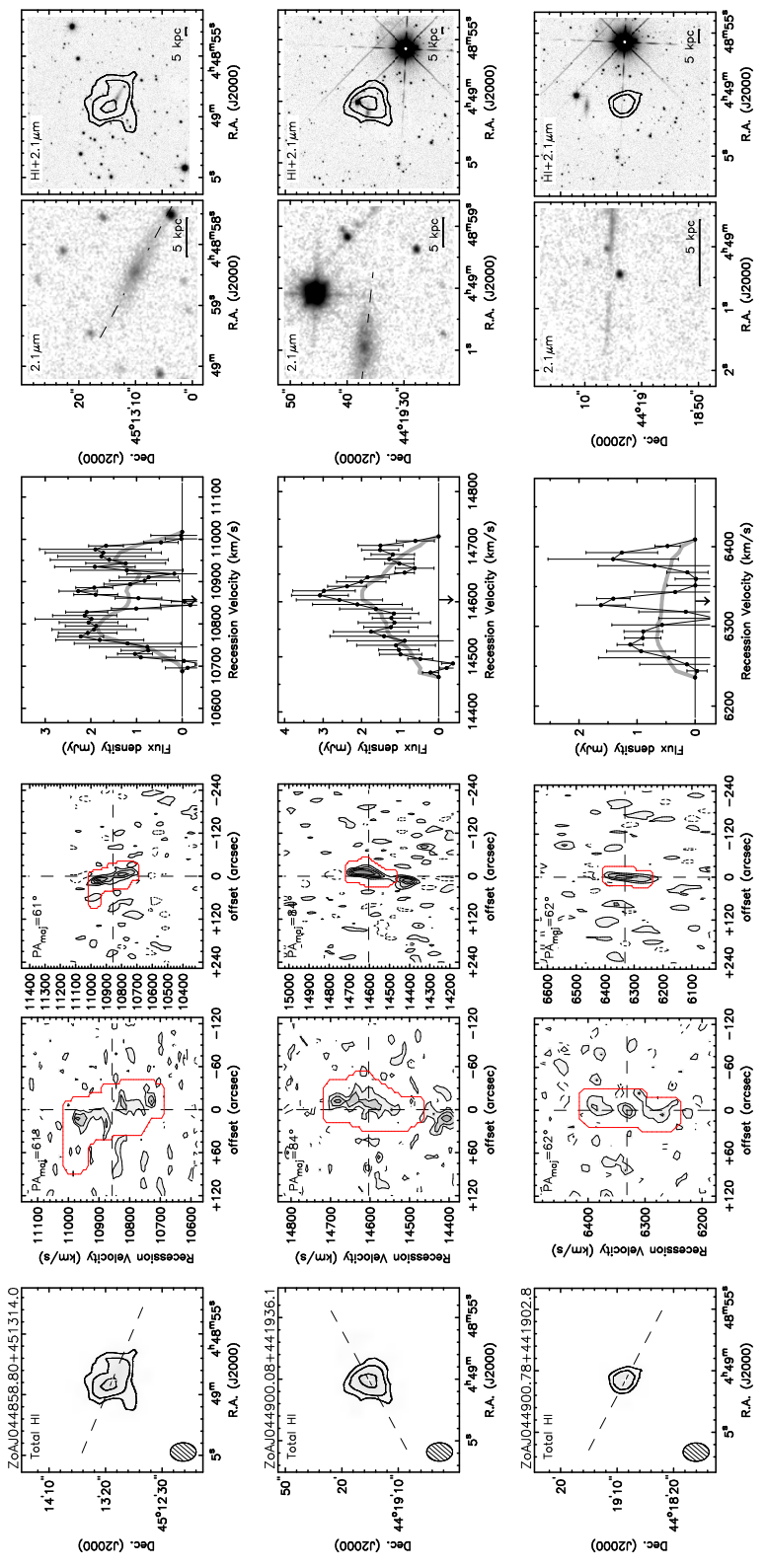

Figure A2. Marginally resolved WSRT HI detections.

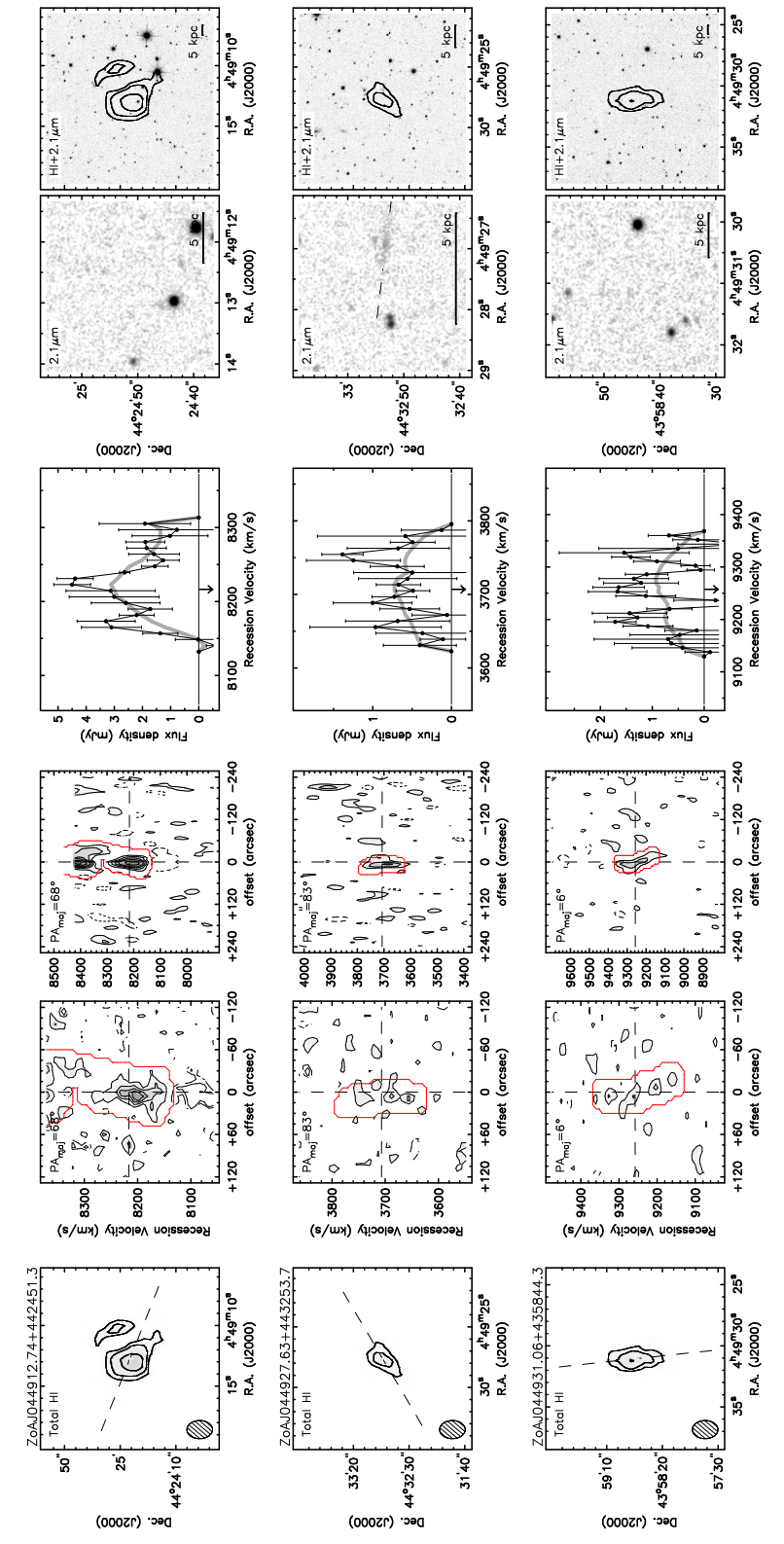

Figure A2. Marginally resolved WSRT HI detections.

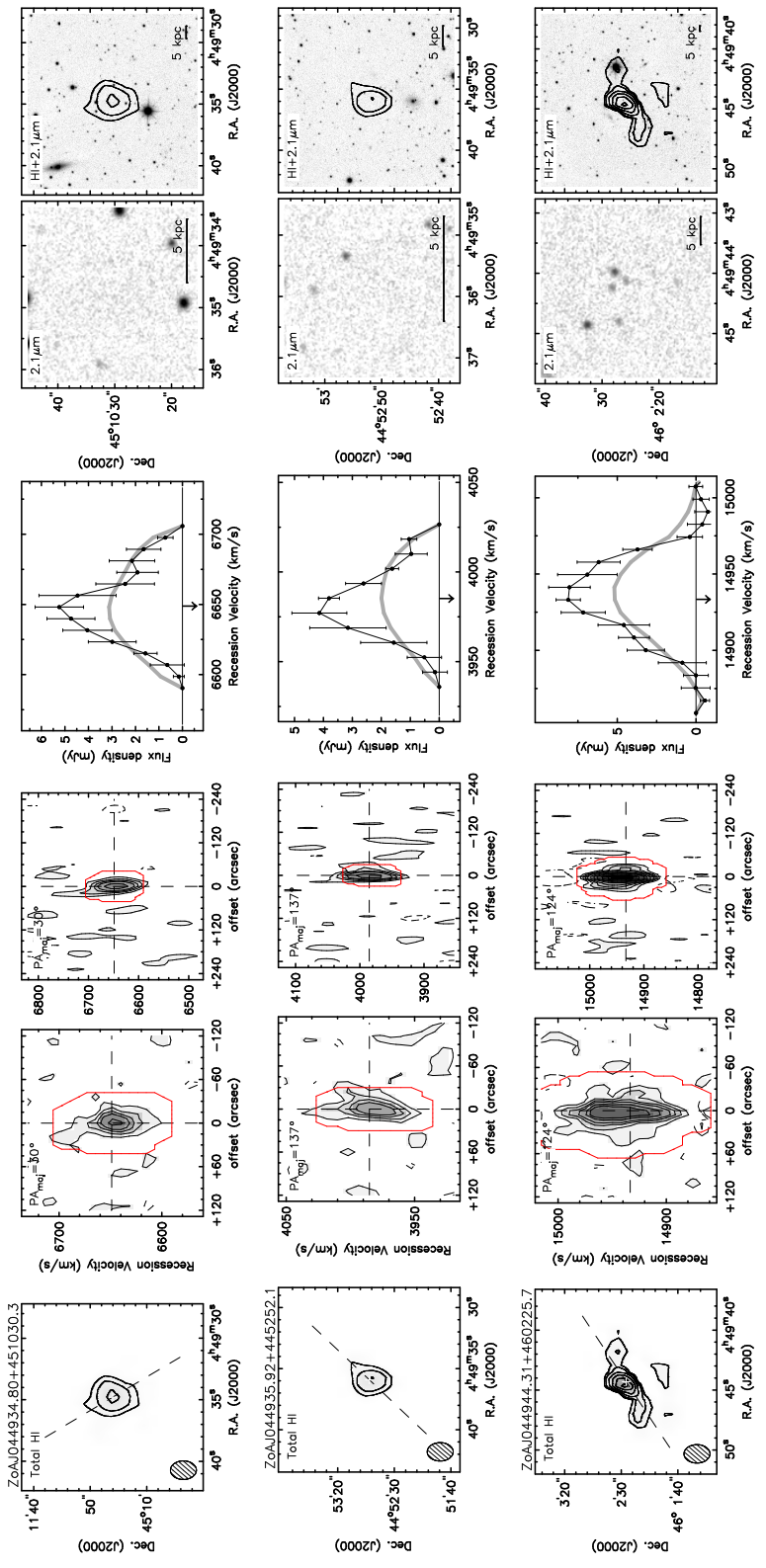

Figure A2. Marginally resolved WSRT HI detections.

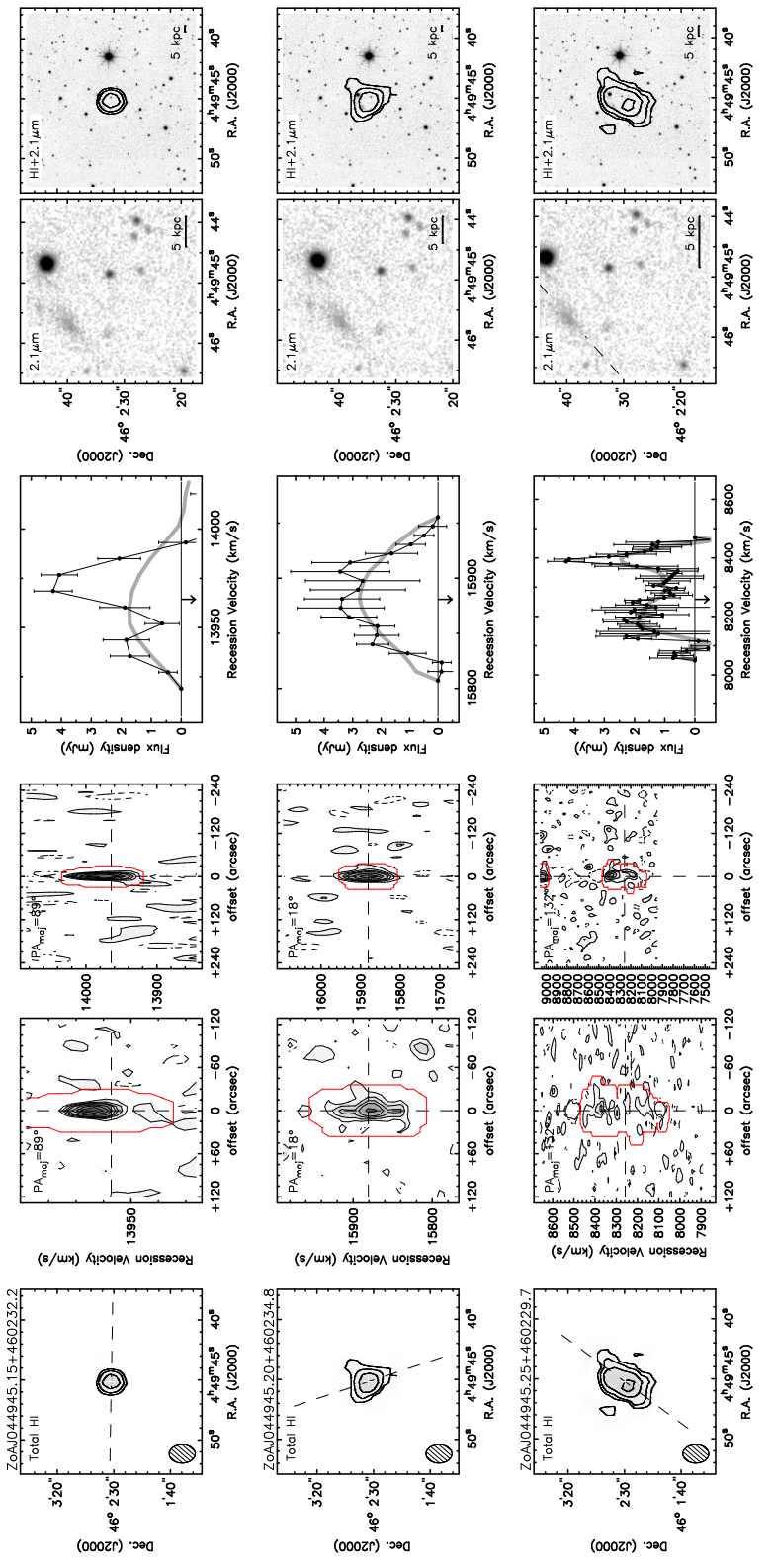

Figure A2. Marginally resolved WSRT HI detections.

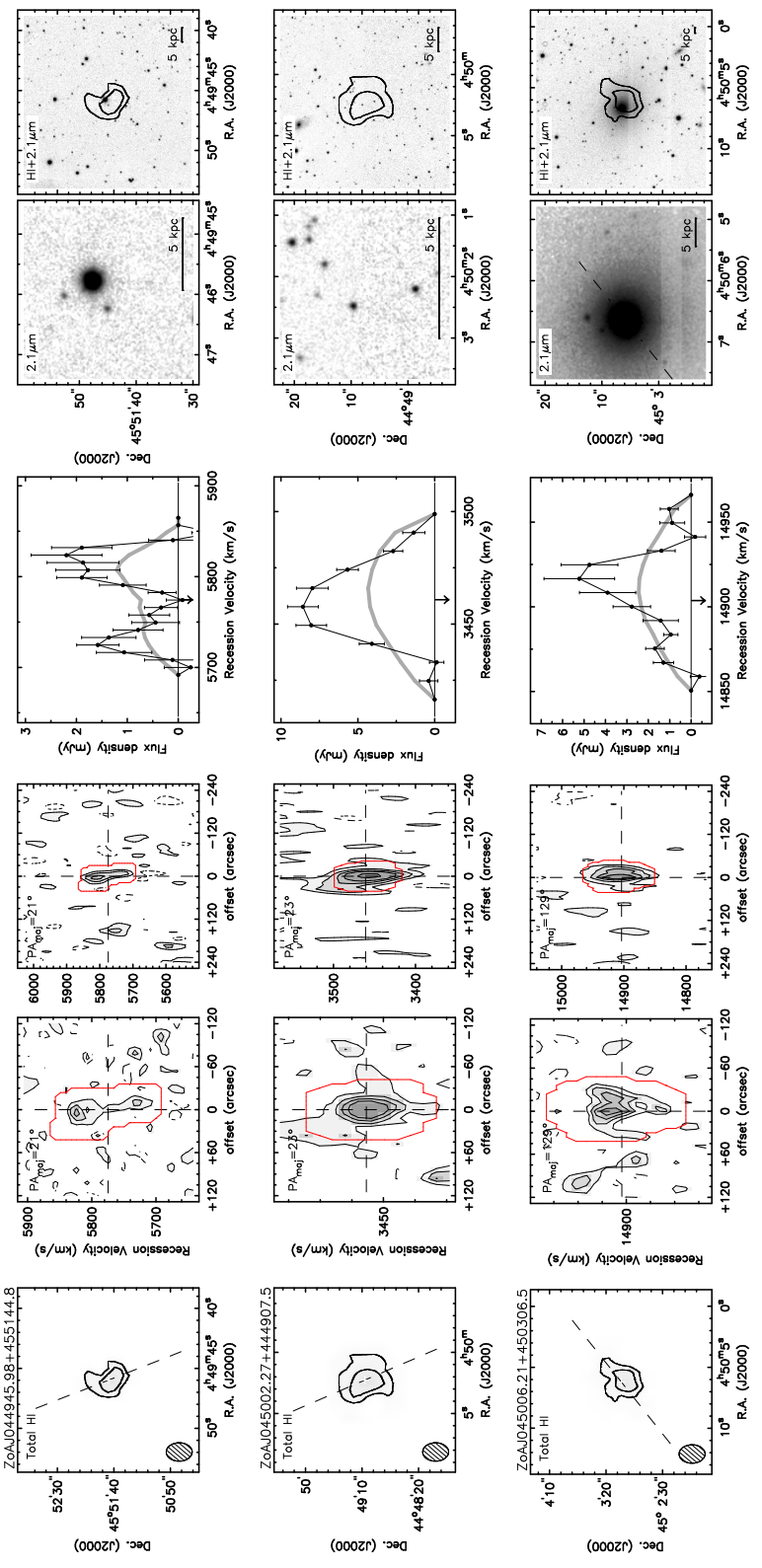

Figure A2. Marginally resolved WSRT HI detections.

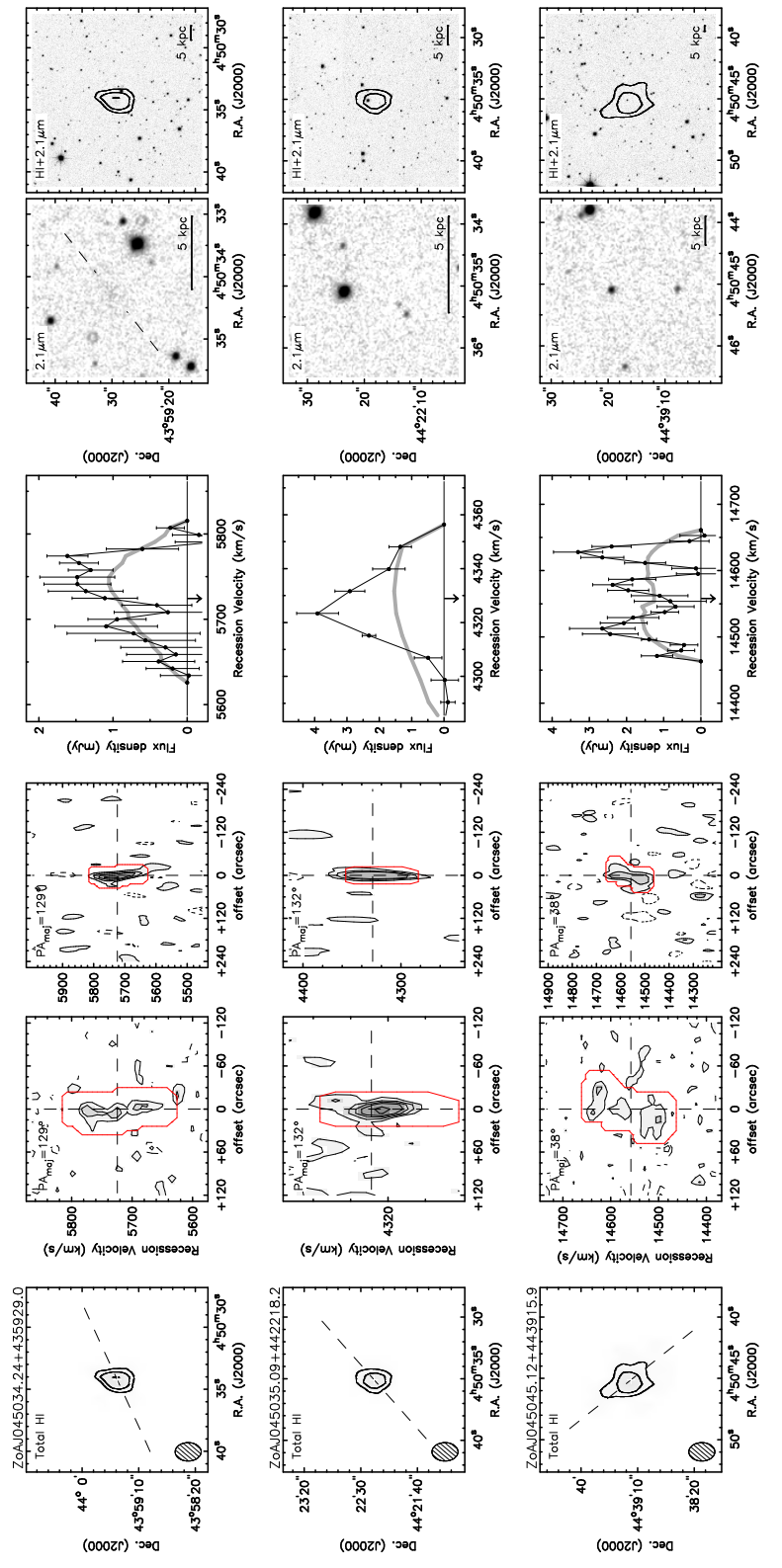

Figure A2. Marginally resolved WSRT HI detections.

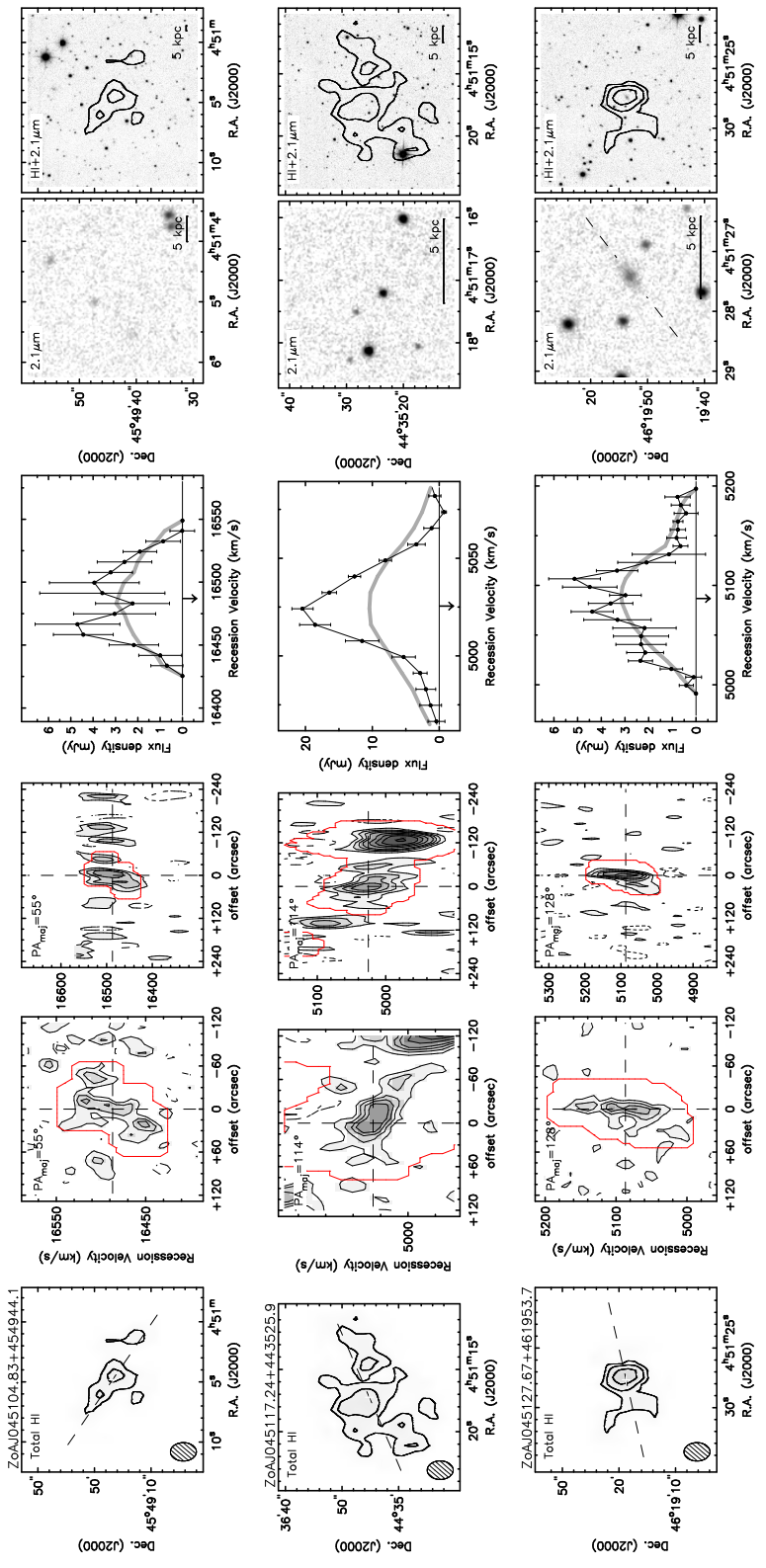

Figure A2. Marginally resolved WSRT HI detections.

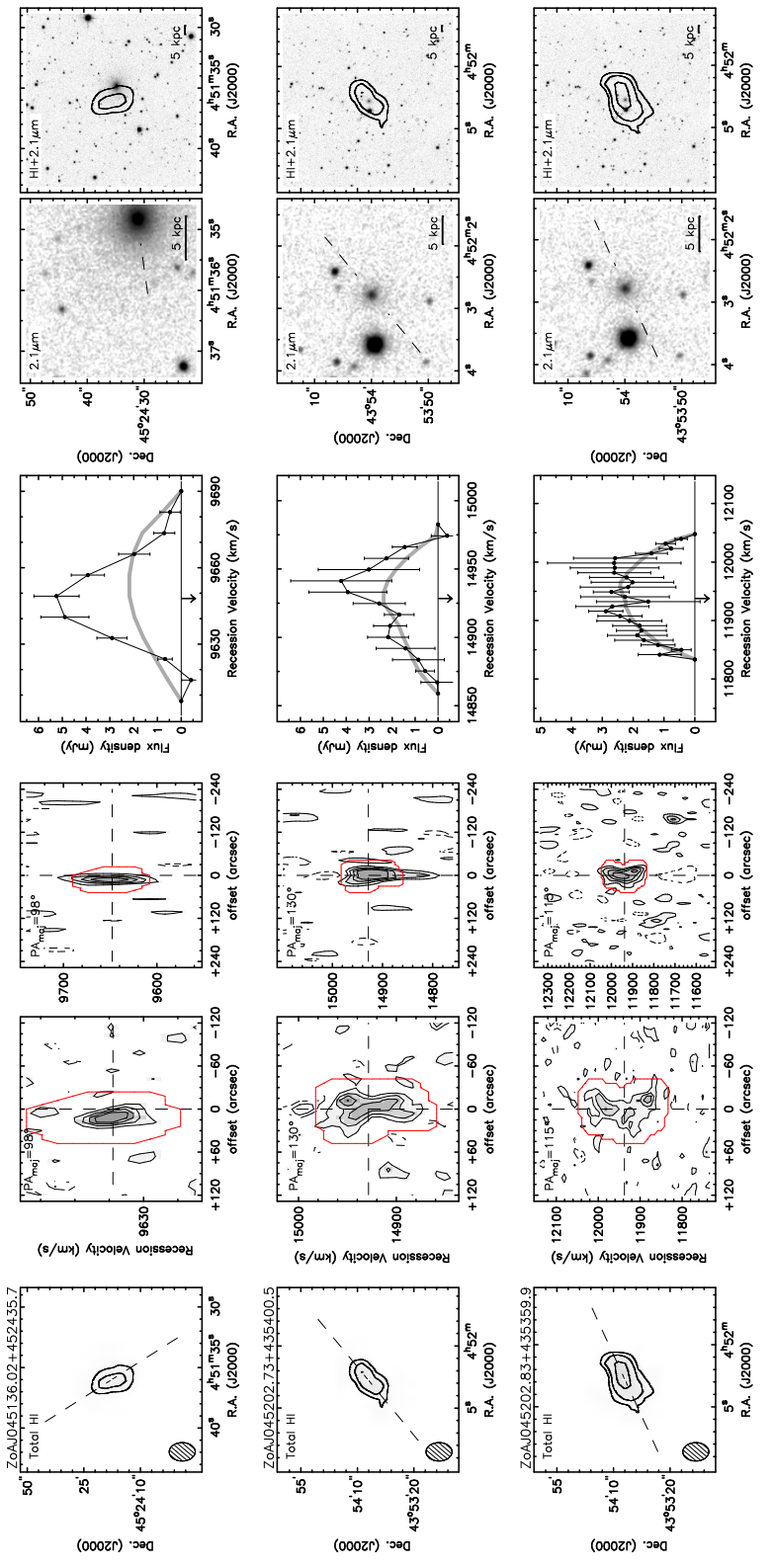

Figure A2. Marginally resolved WSRT HI detections.

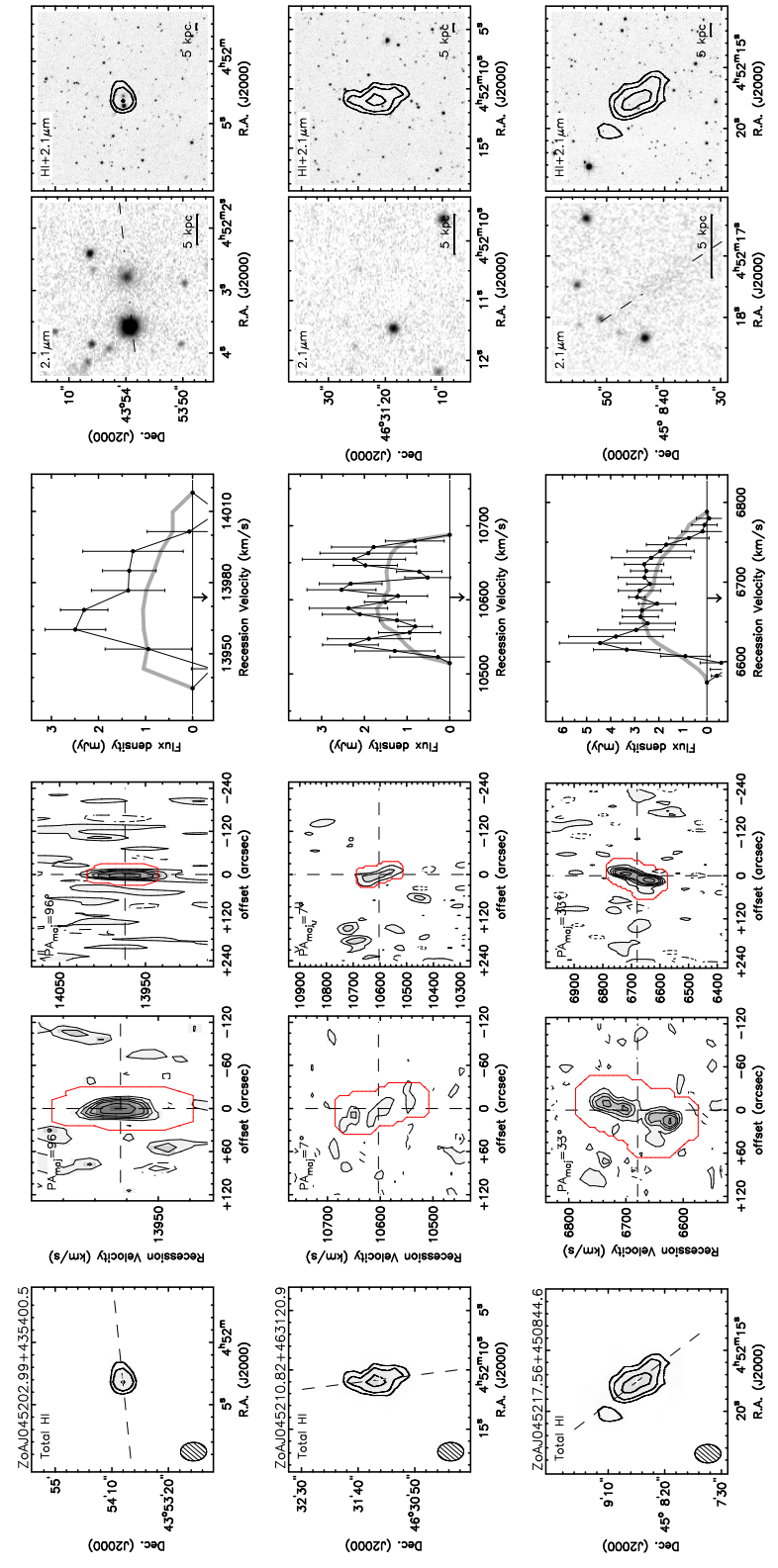

Figure A2. Marginally resolved WSRT HI detections.

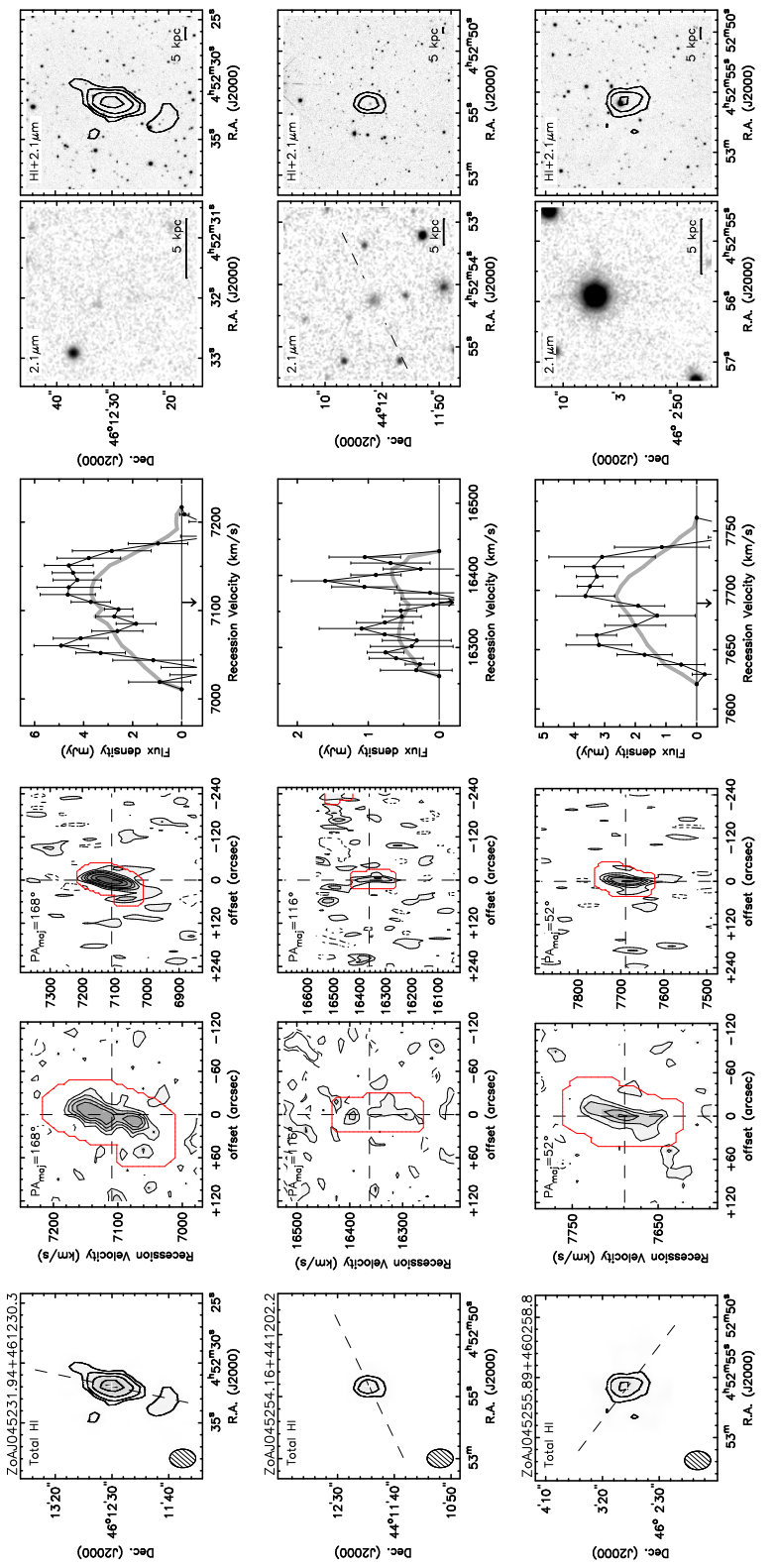

Figure A2. Marginally resolved WSRT HI detections.

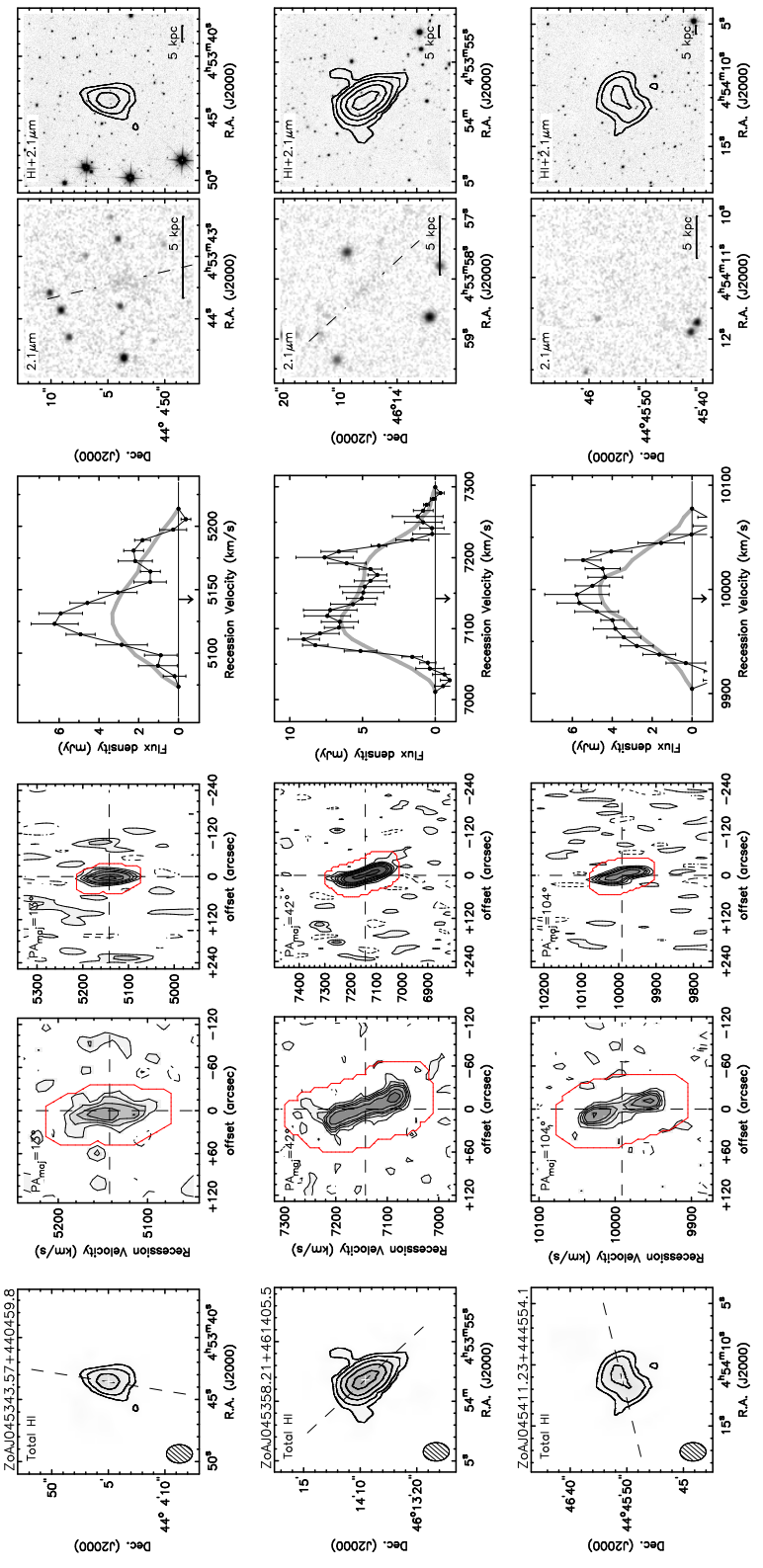

Figure A2. Marginally resolved WSRT HI detections.

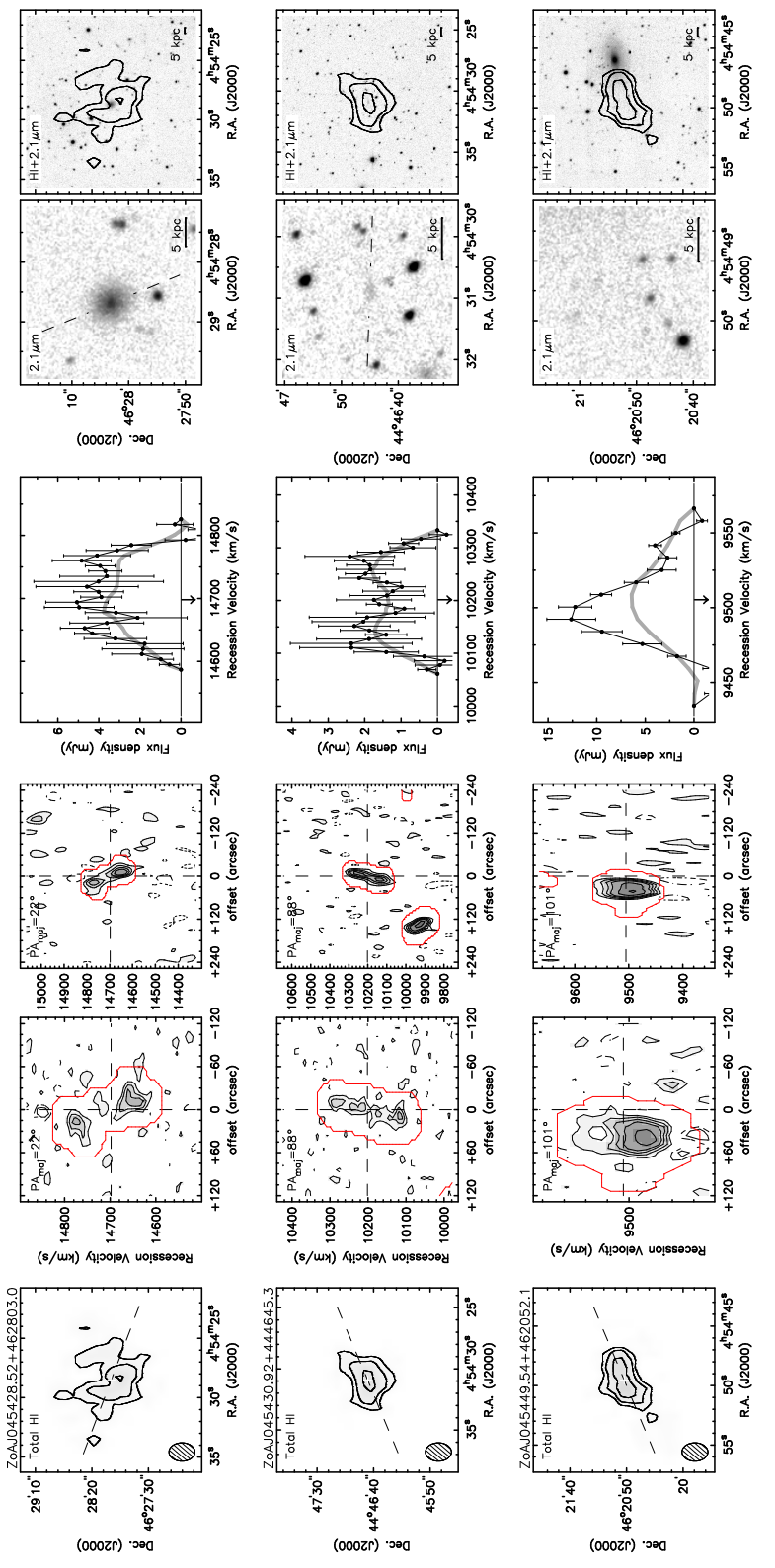

Figure A2. Marginally resolved WSRT HI detections.

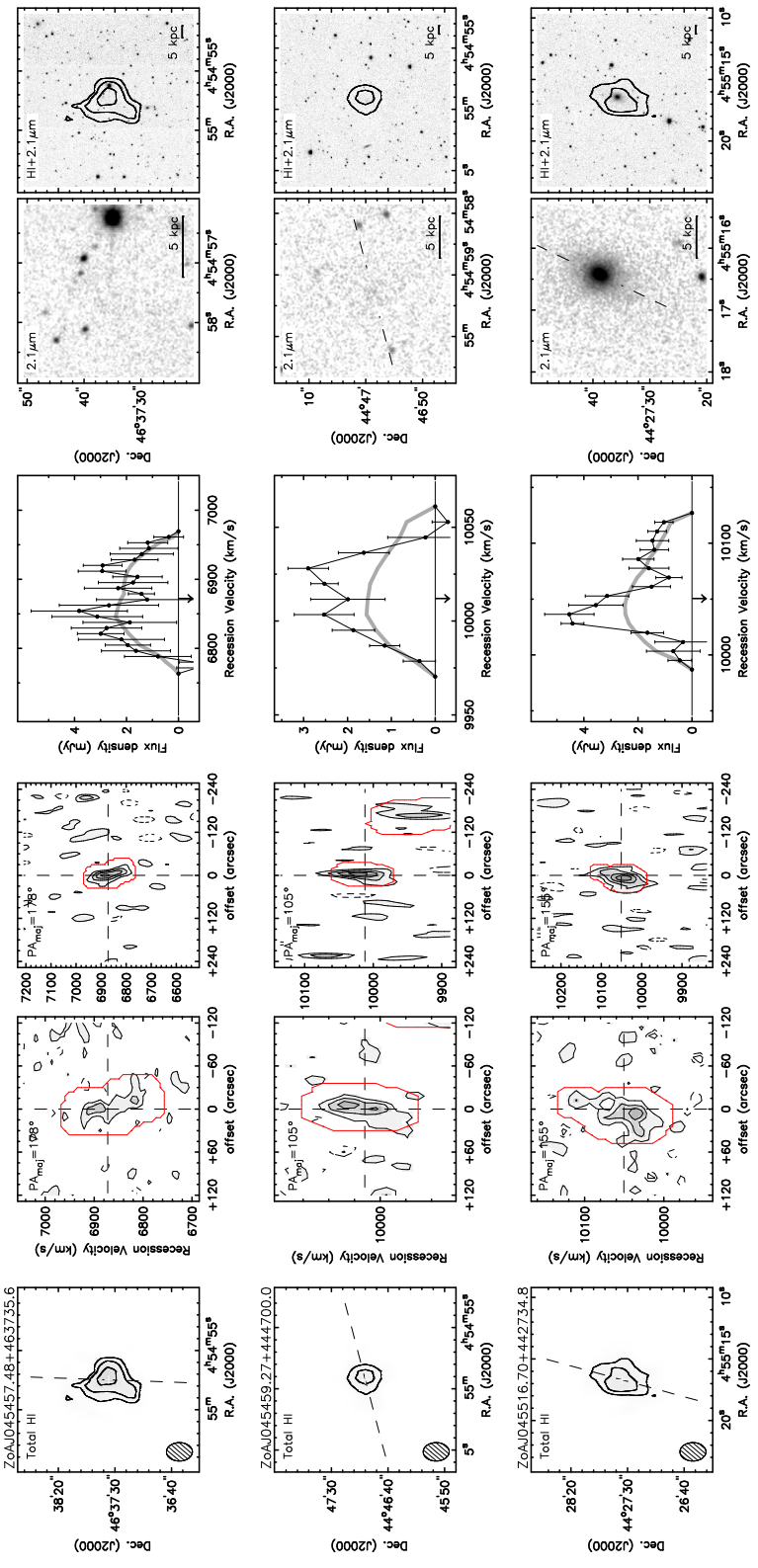

Figure A2. Marginally resolved WSRT HI detections.

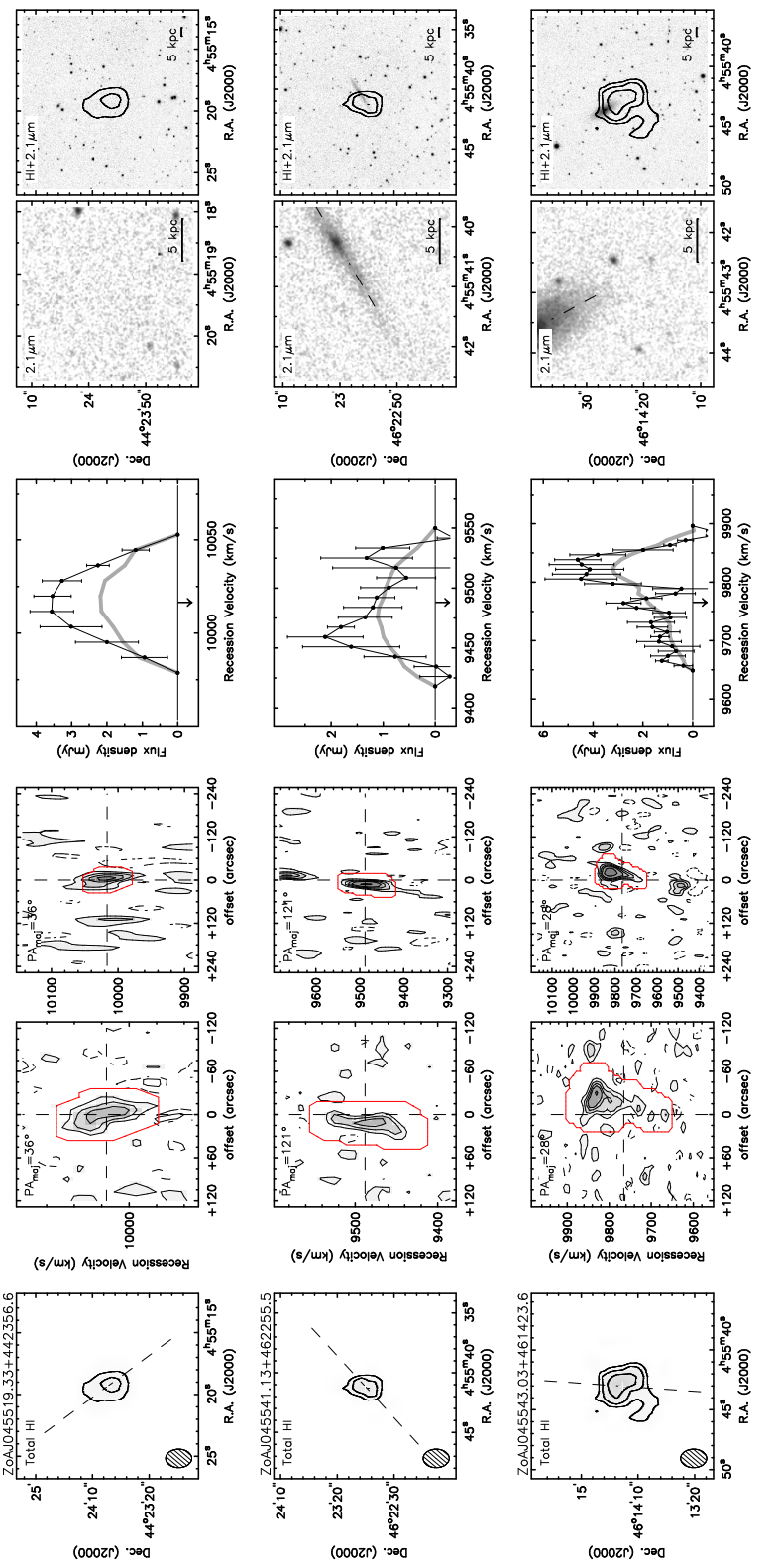

Figure A2. Marginally resolved WSRT HI detections.

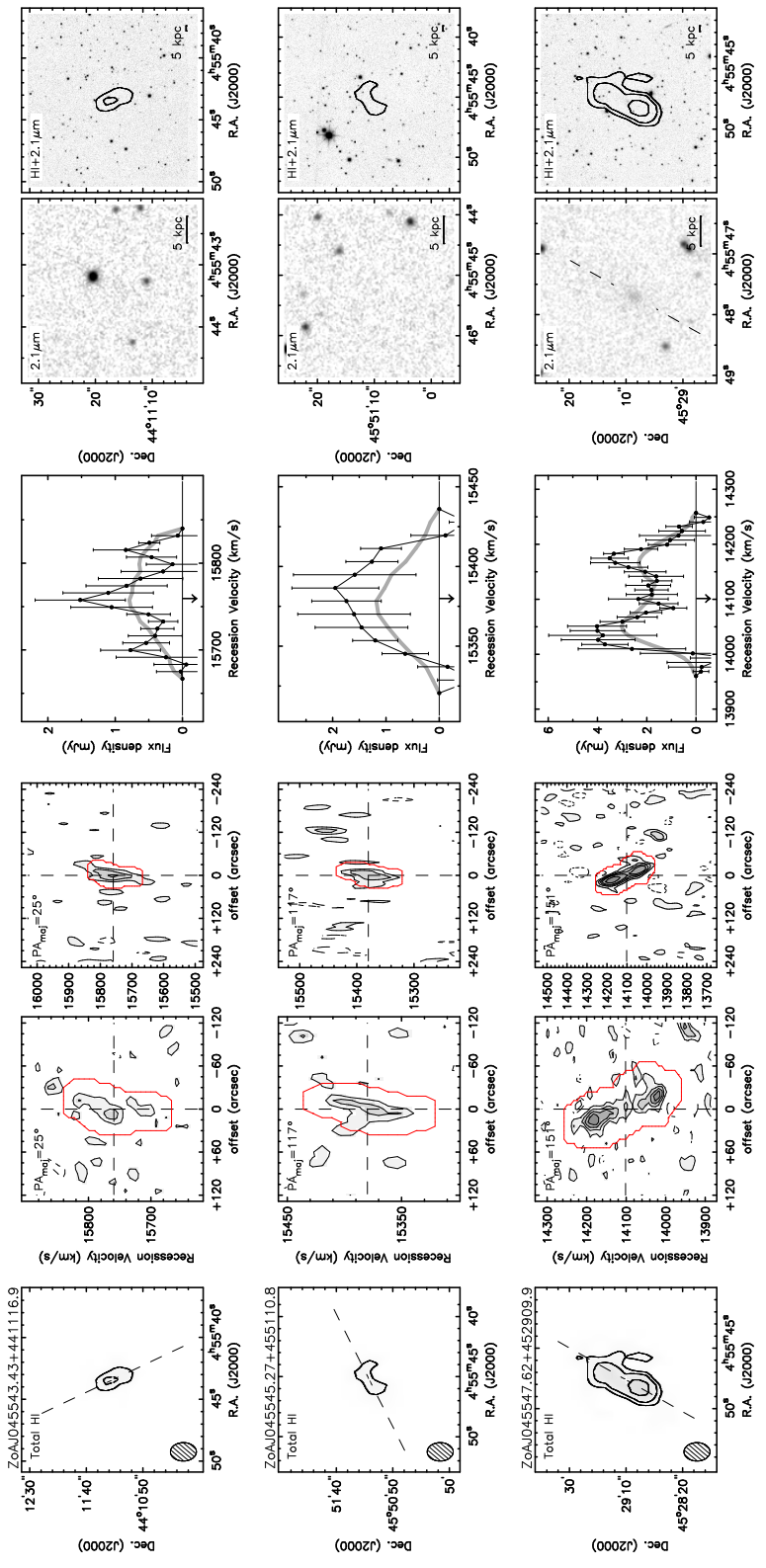

Figure A2. Marginally resolved WSRT HI detections.

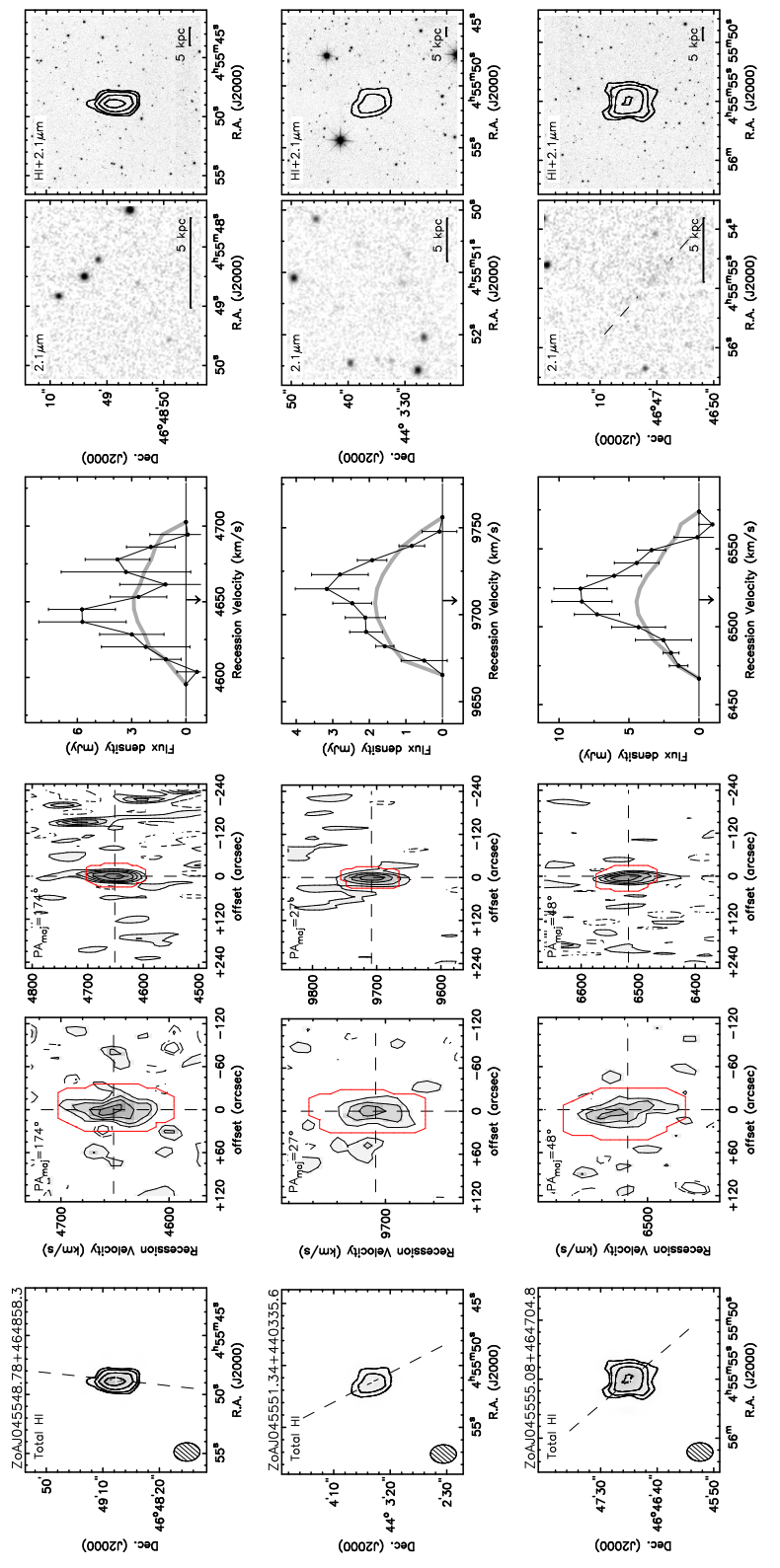

Figure A2. Marginally resolved WSRT HI detections.

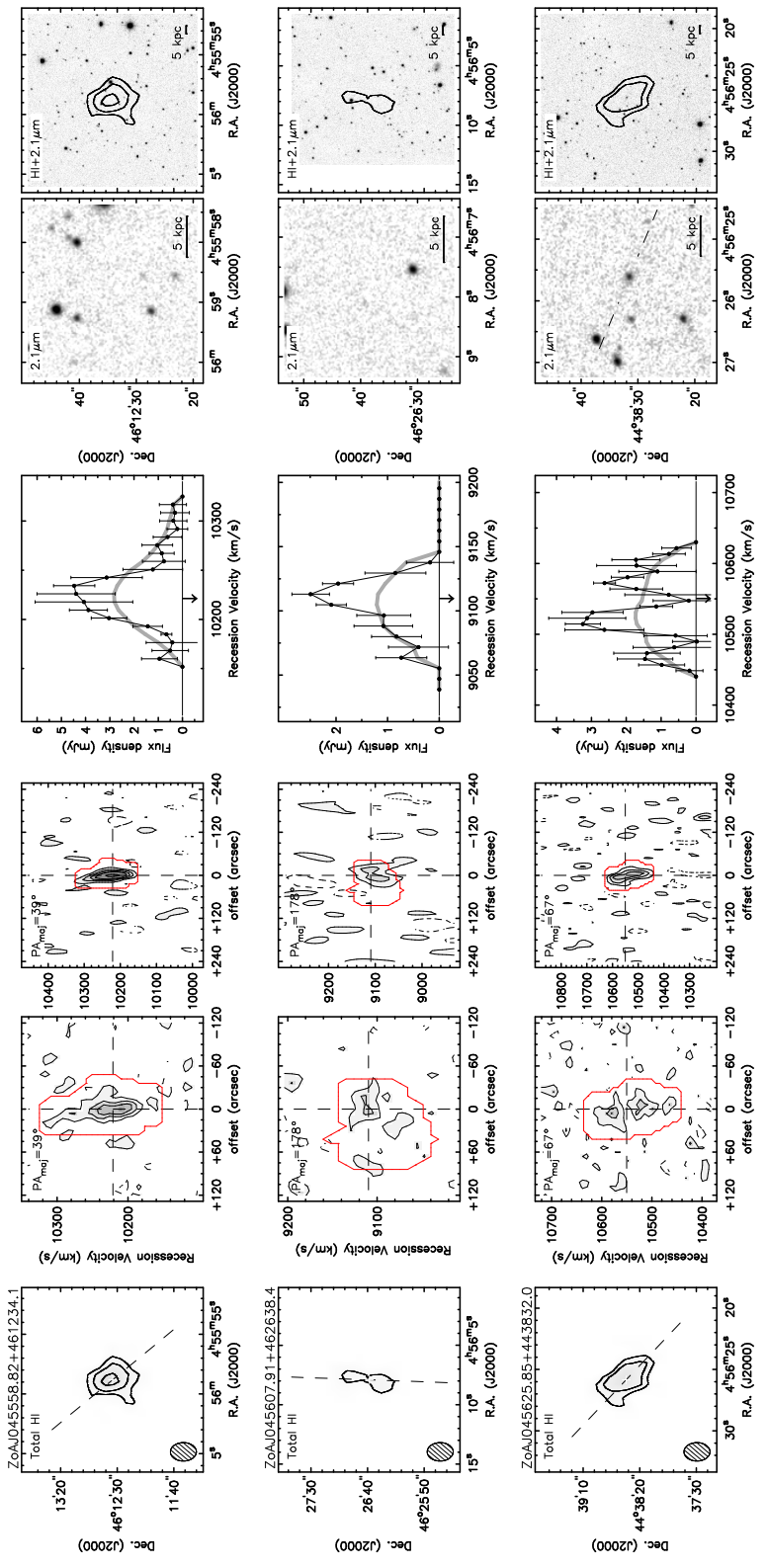

Figure A2. Marginally resolved WSRT HI detections.

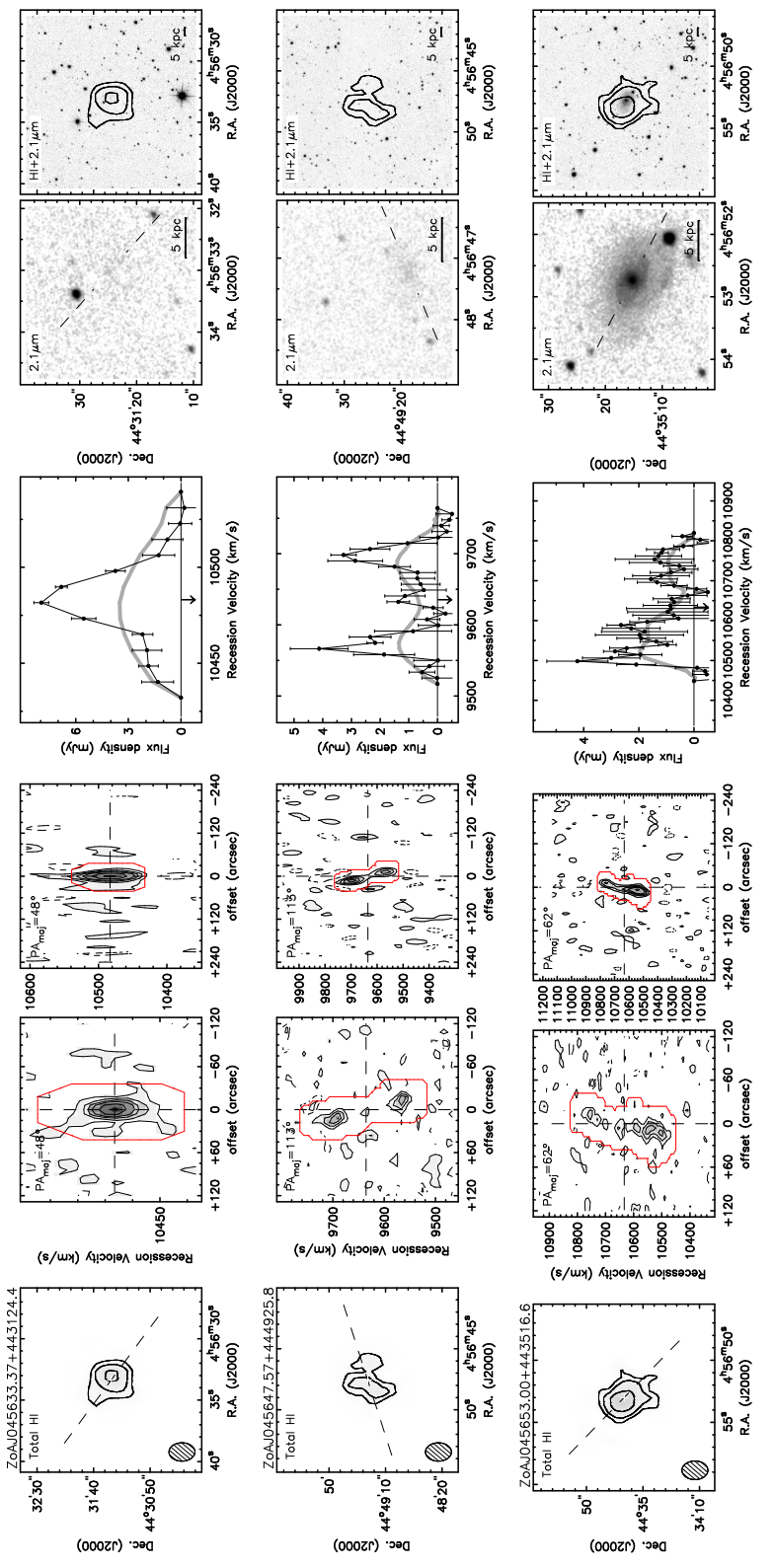

Figure A2. Marginally resolved WSRT HI detections.

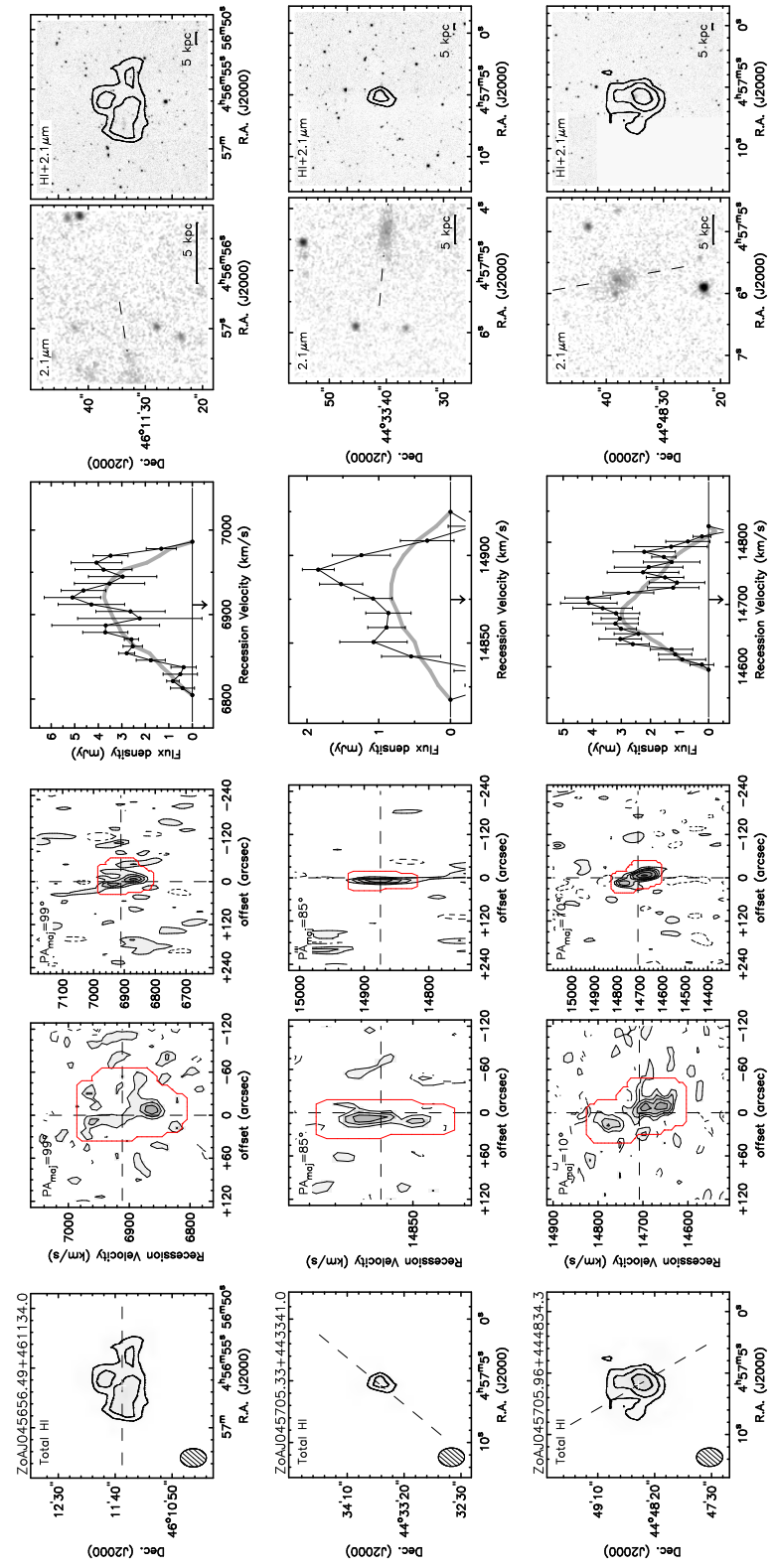

Figure A2. Marginally resolved WSRT HI detections.

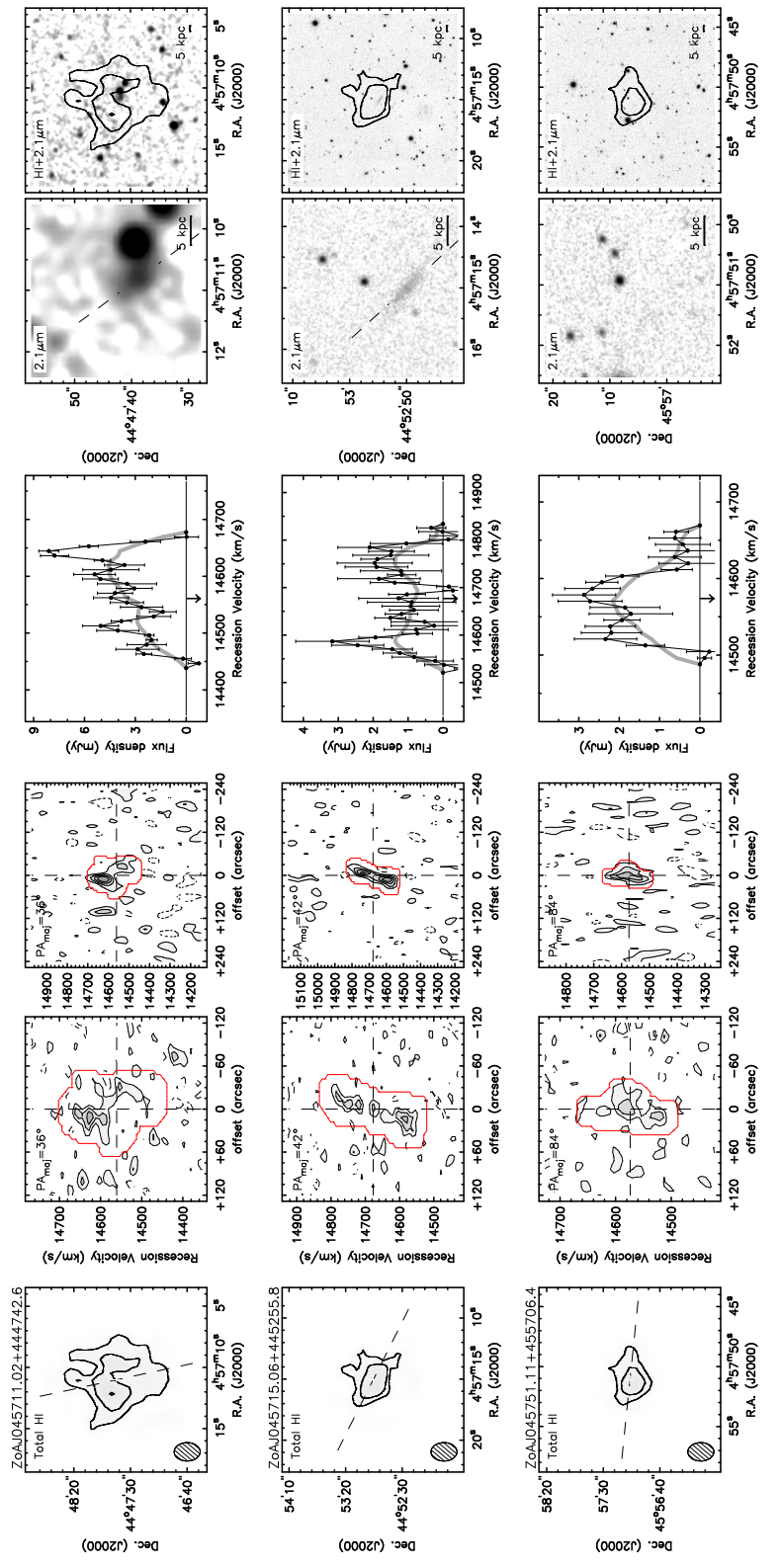

Figure A2. Marginally resolved WSRT HI detections.

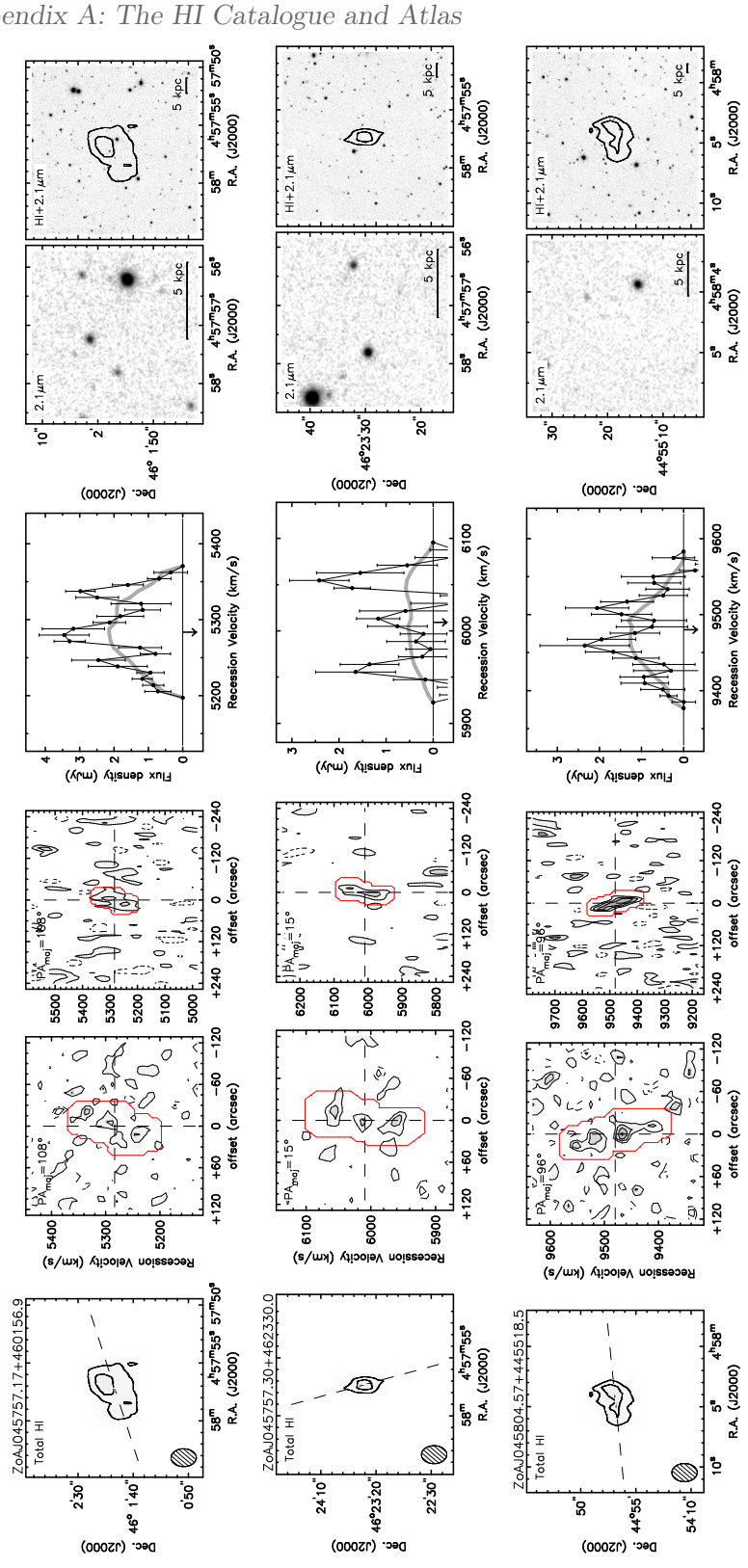

Figure A2. Marginally resolved WSRT HI detections.

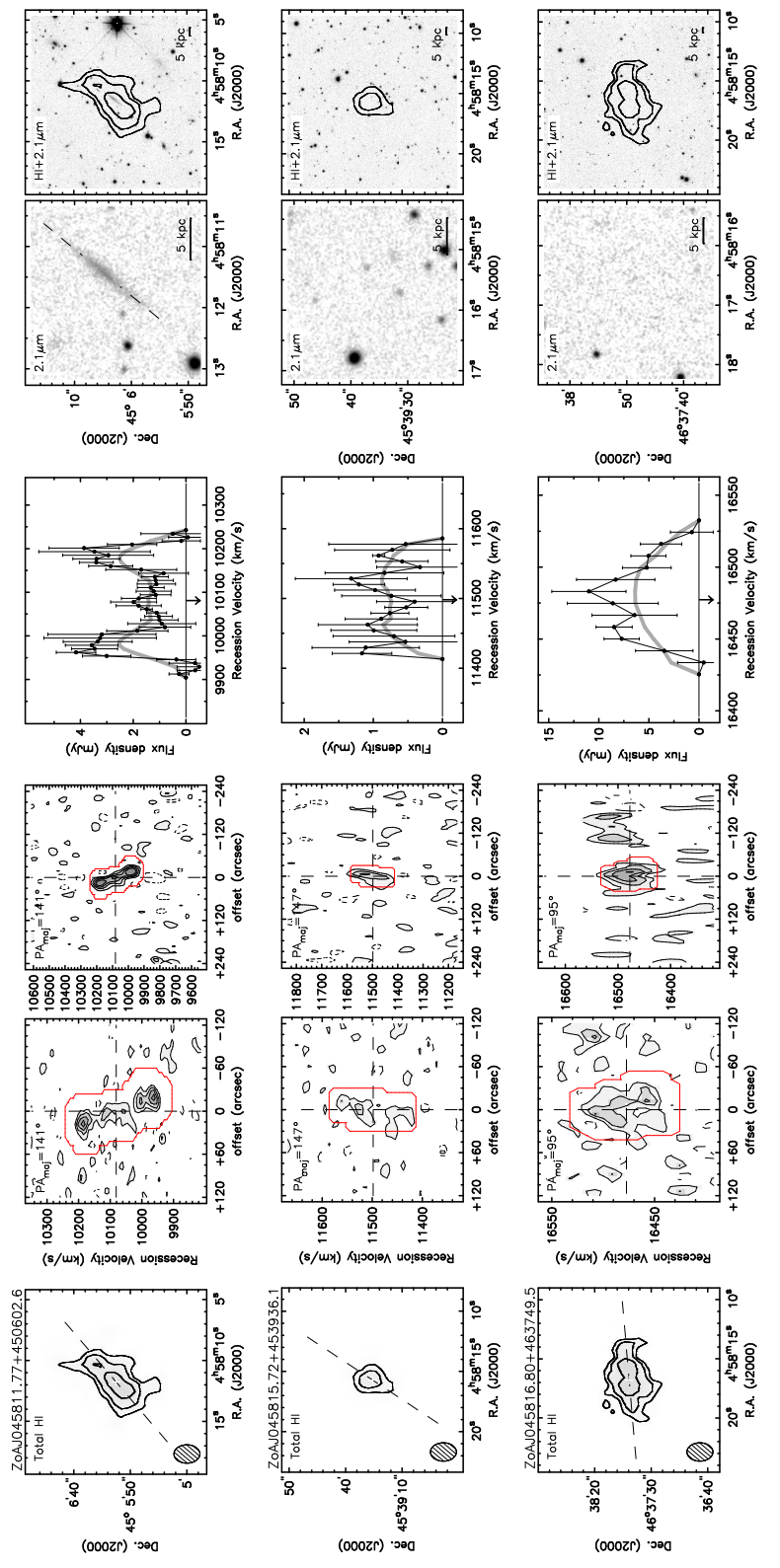

Figure A2. Marginally resolved WSRT HI detections.

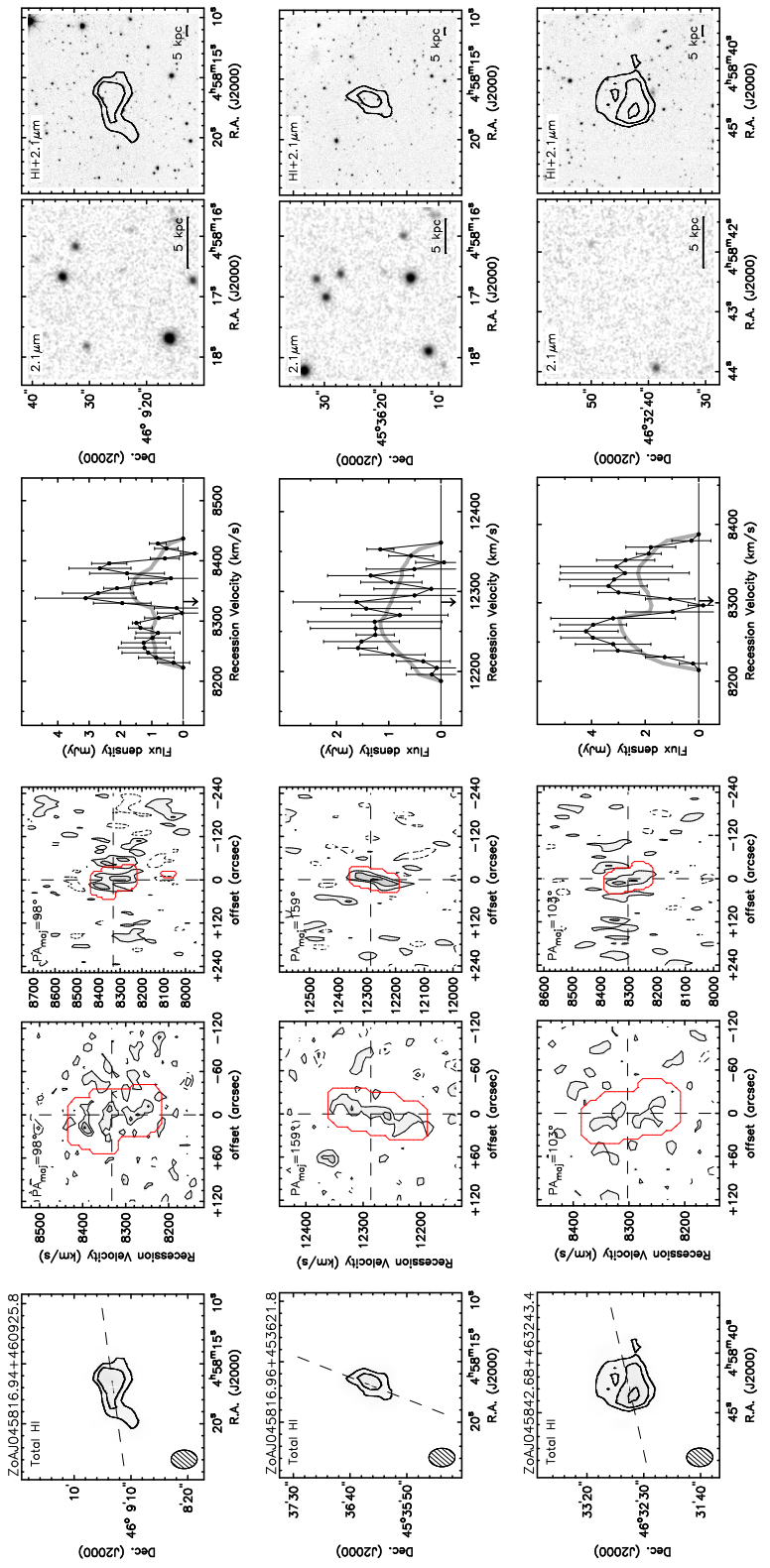

Figure A2. Marginally resolved WSRT HI detections.

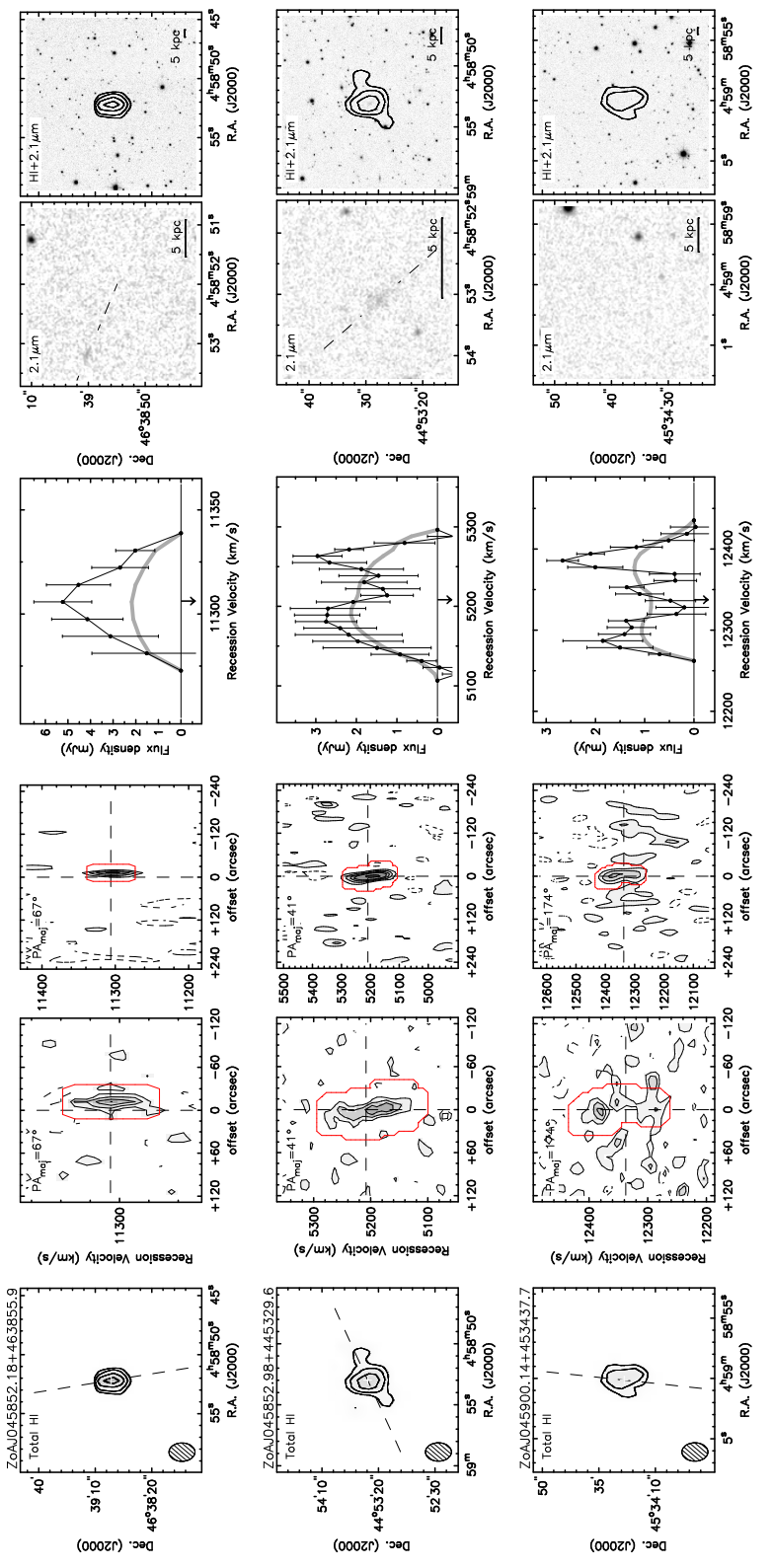

Figure A2. Marginally resolved WSRT HI detections.

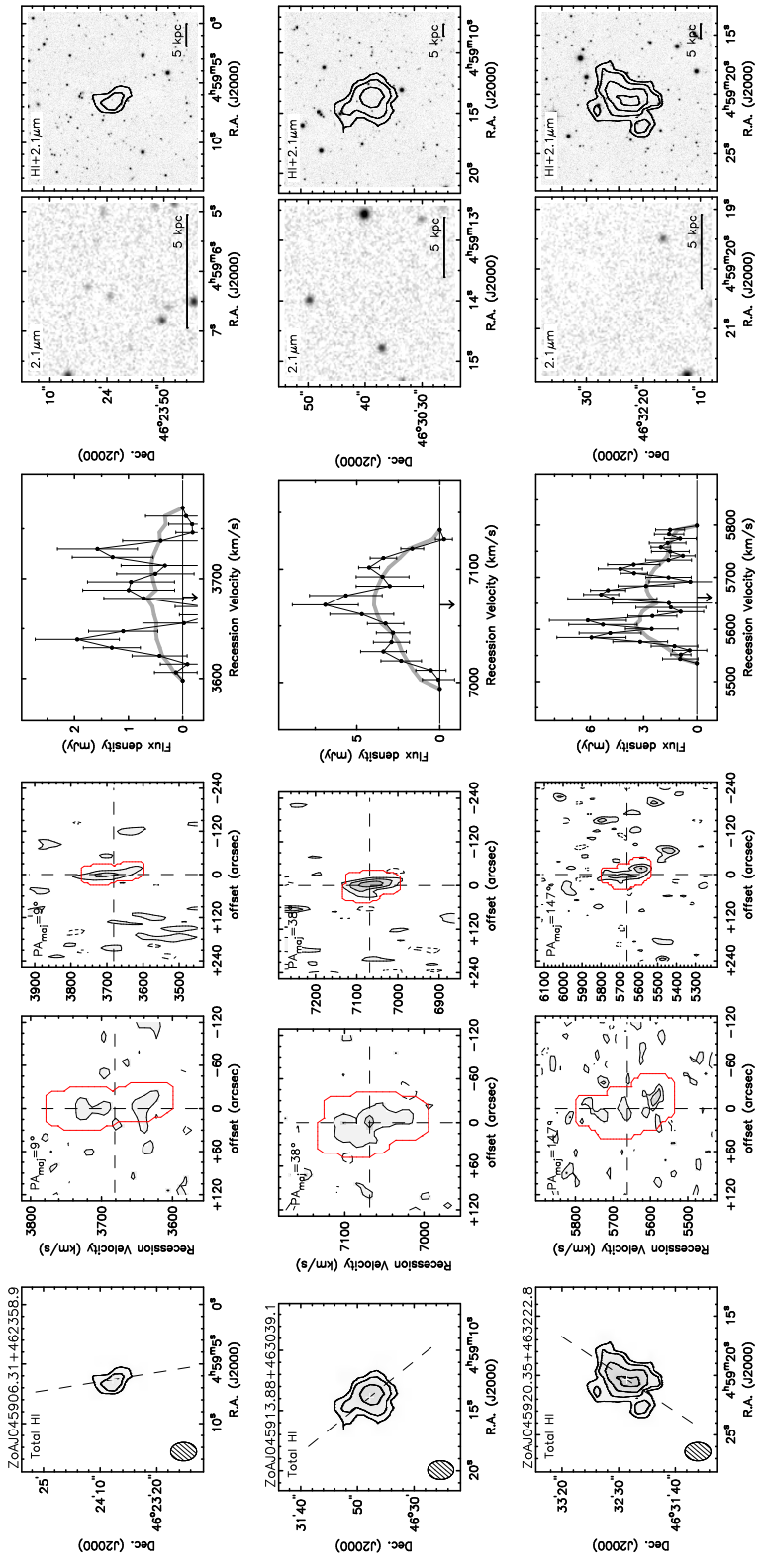

Figure A2. Marginally resolved WSRT HI detections.

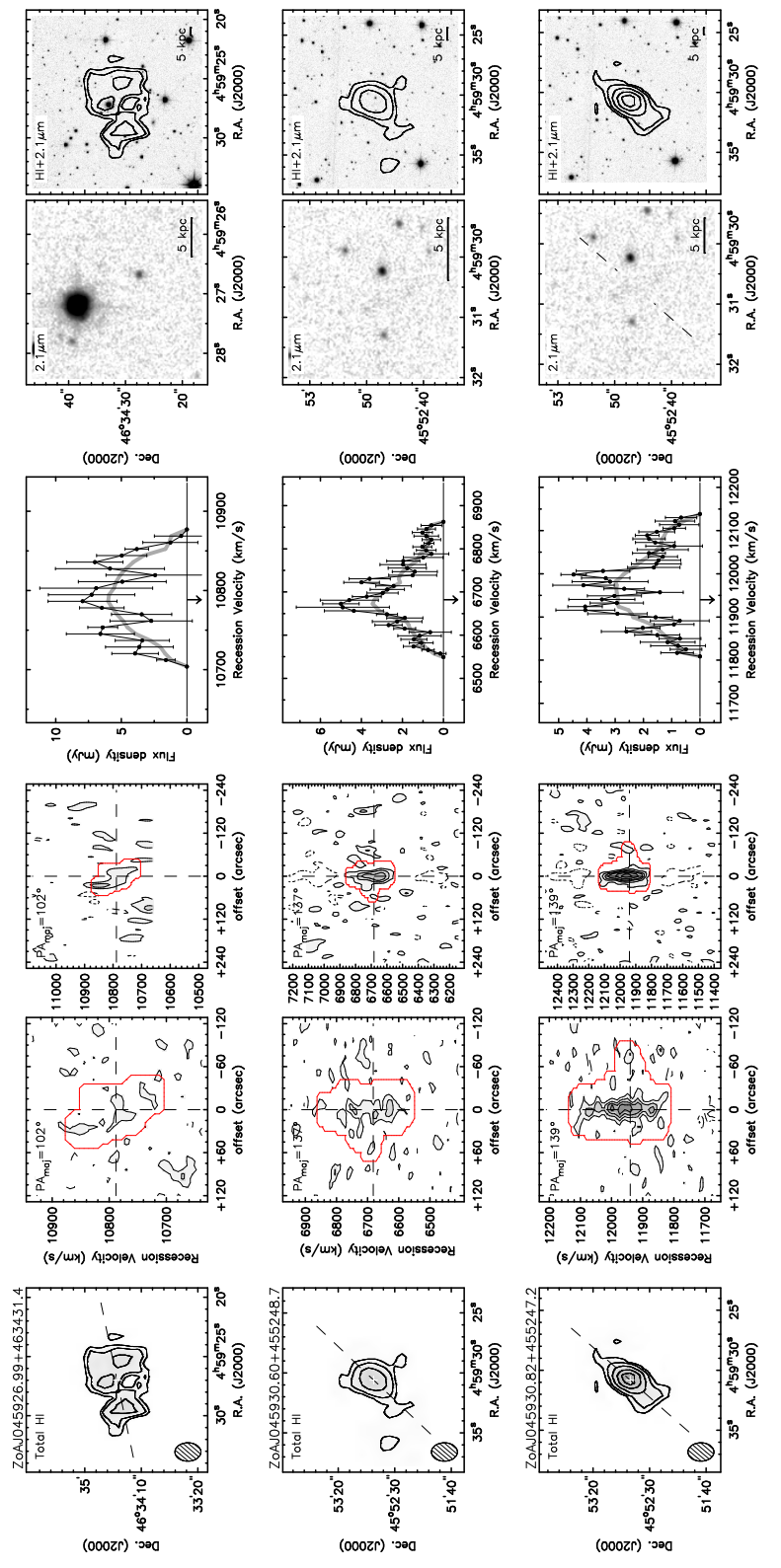

Figure A2. Marginally resolved WSRT HI detections.

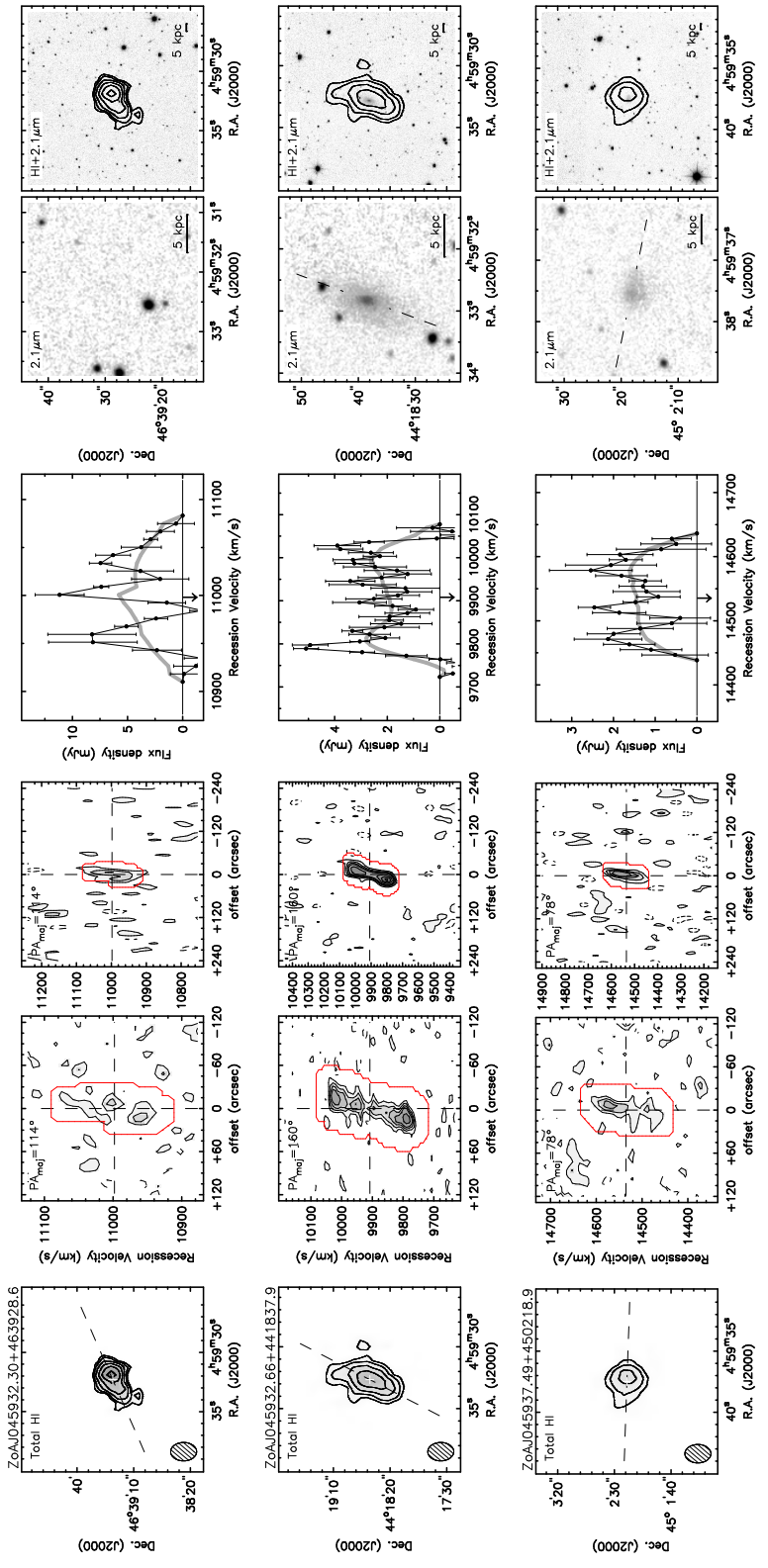

Figure A2. Marginally resolved WSRT HI detections.

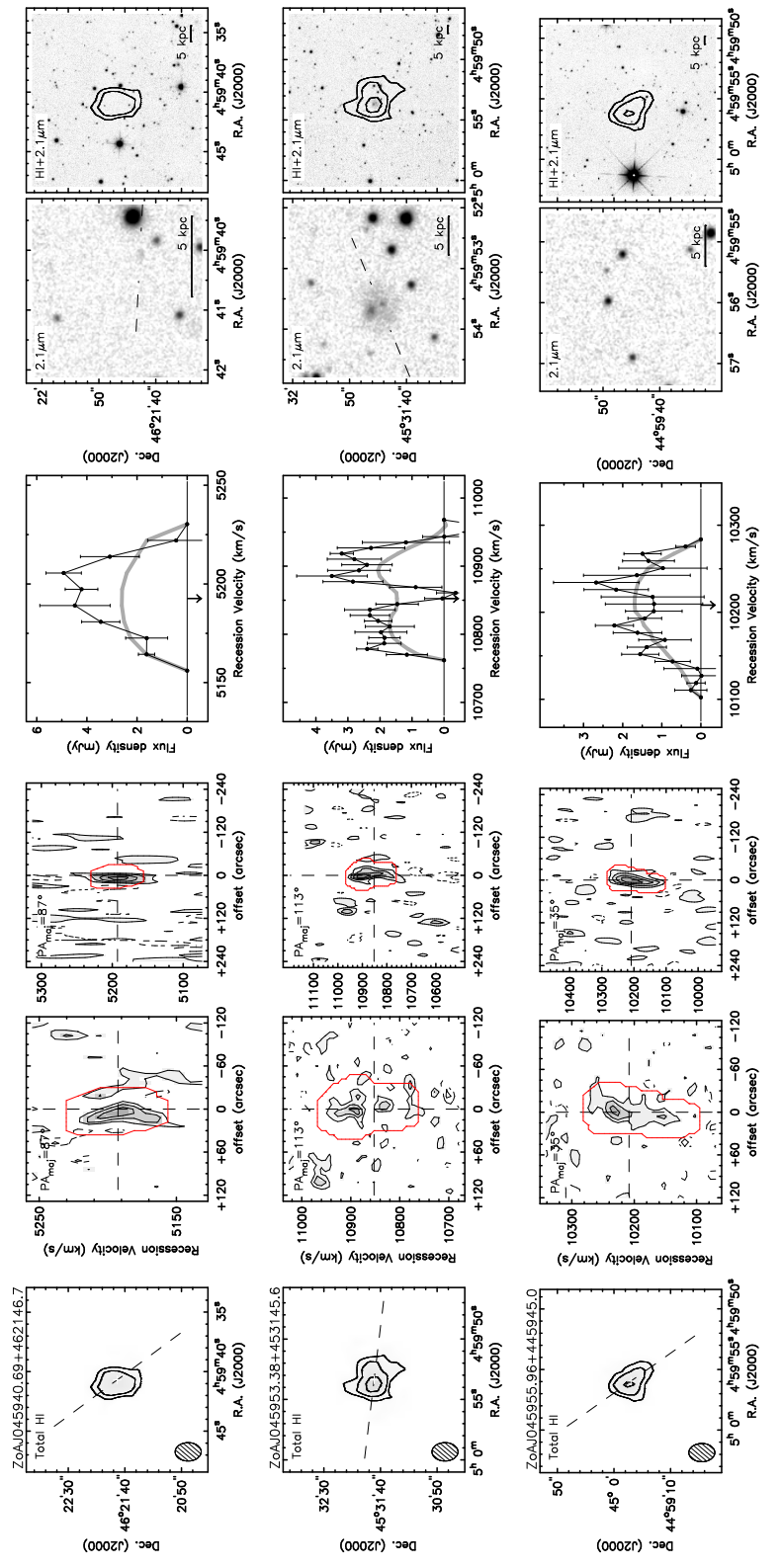

Figure A2. Marginally resolved WSRT HI detections.

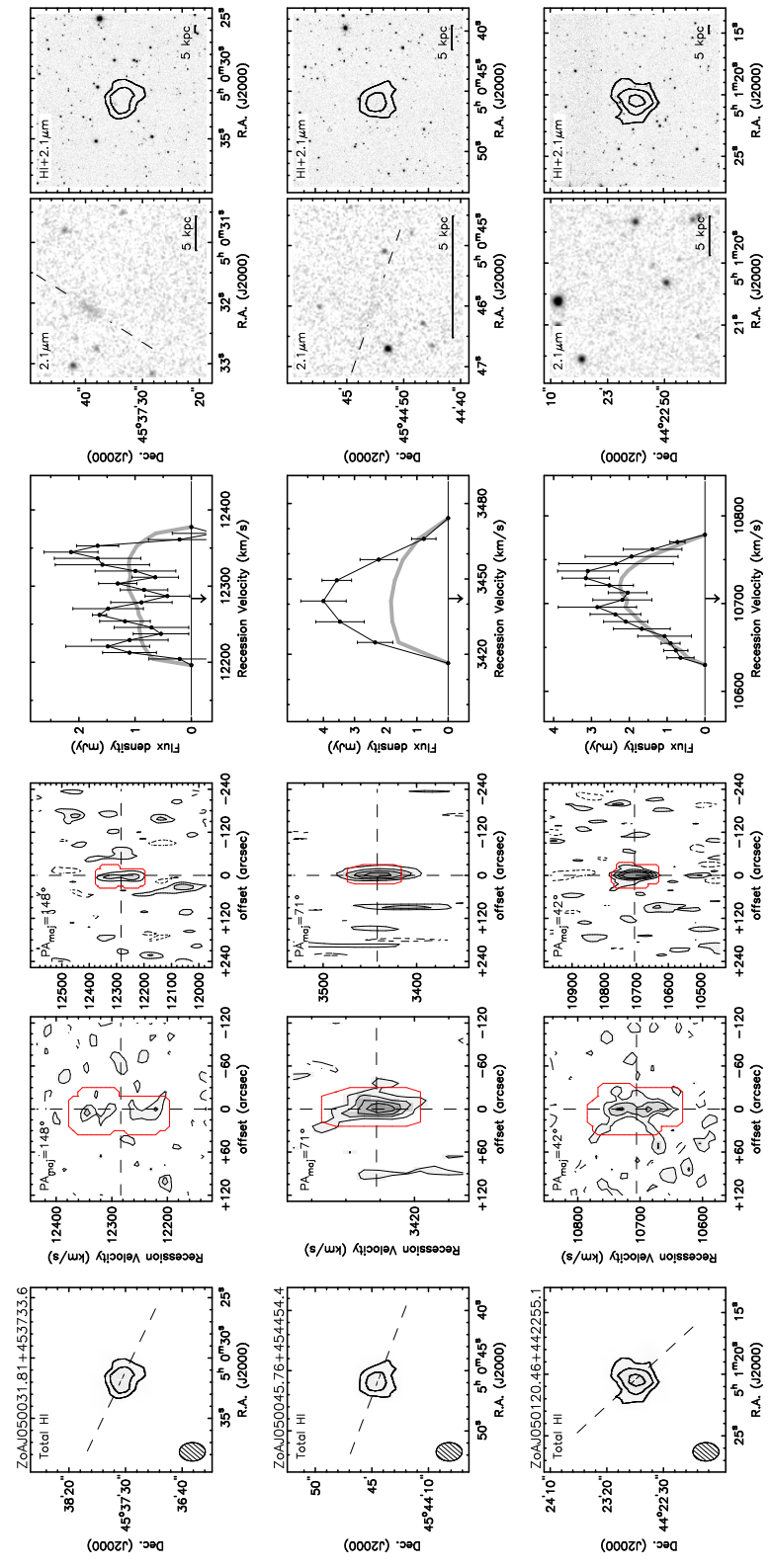

Figure A2. Marginally resolved WSRT HI detections.

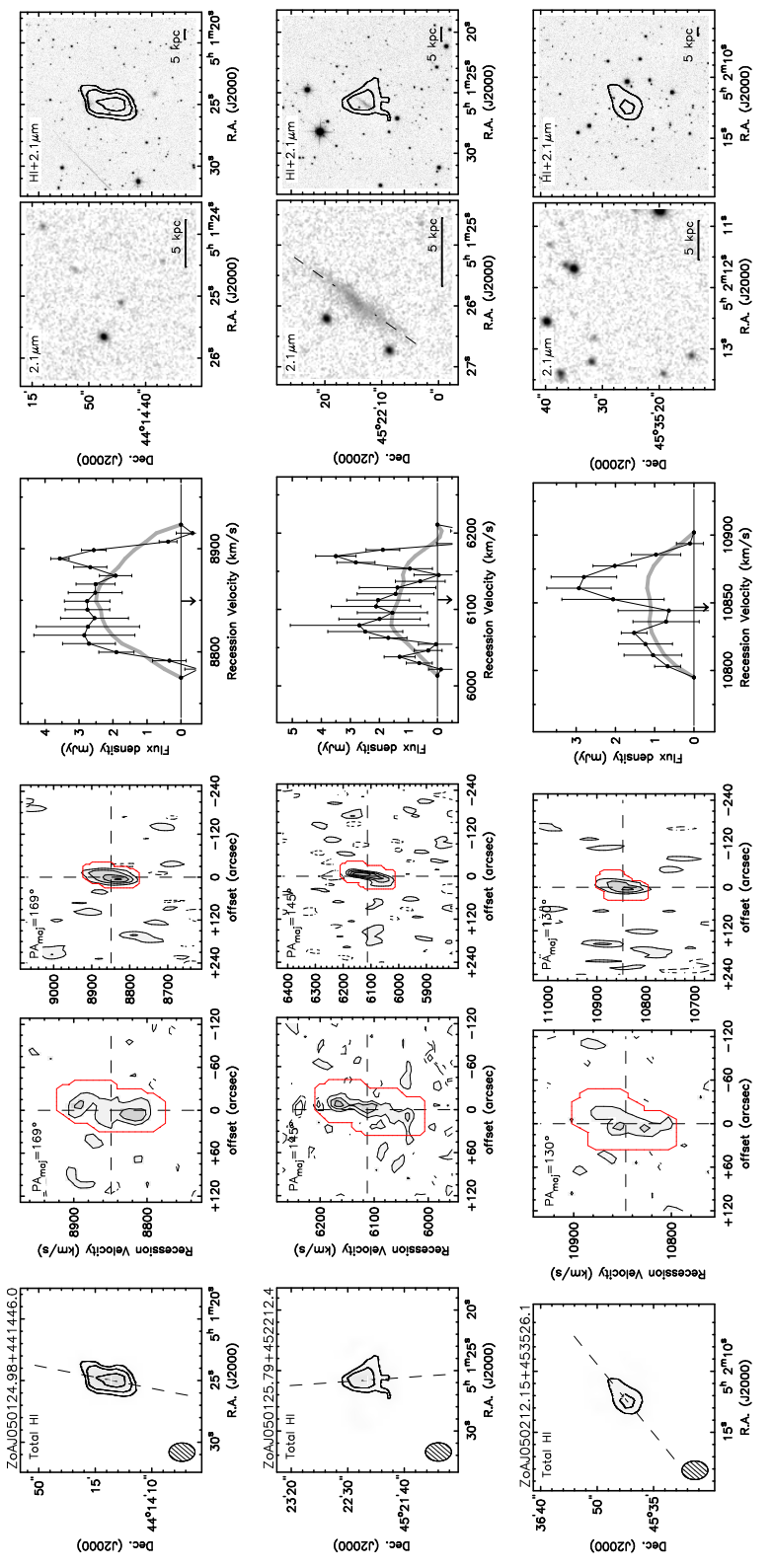

Figure A2. Marginally resolved WSRT HI detections.

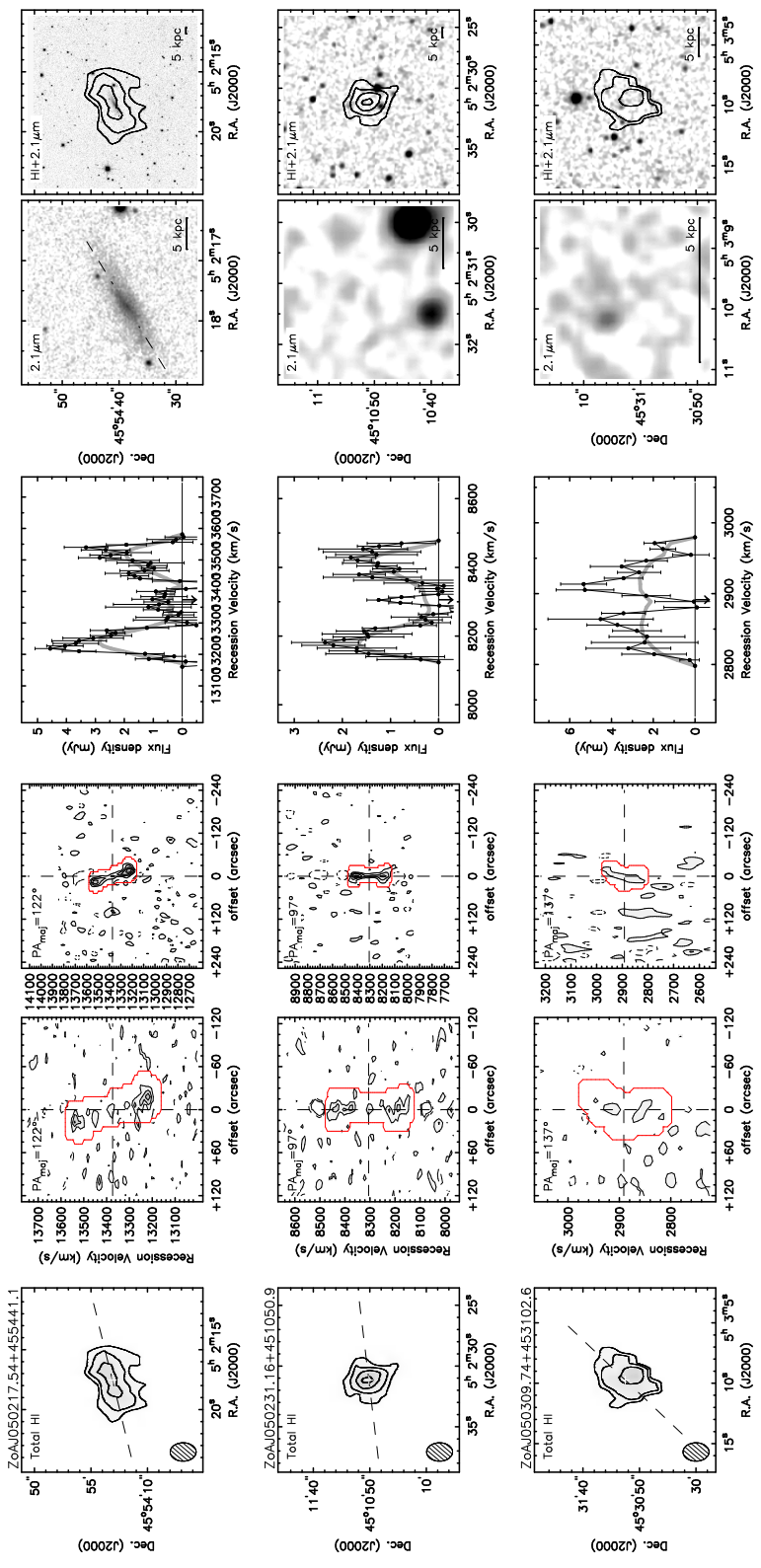

Figure A2. Marginally resolved WSRT HI detections.

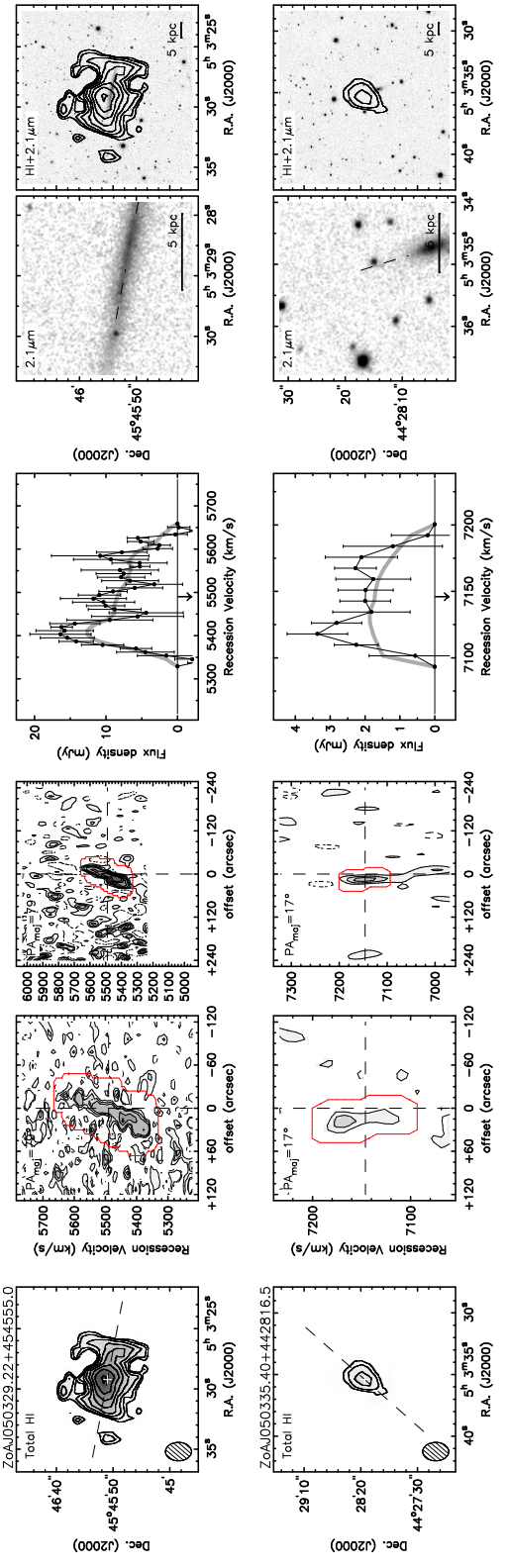

Figure A2. Marginally resolved WSRT HI detections.

3

The WSRT PP ZoA II. The 3C 129 cluster

M. Ramatsoku[a,b,c], M.A.W Verheijen[a], R.C. Kraan-Korteweg[b],T.H. Jarrett[b], K. Said[b], A.C. Schröder[d]

[a] Kapteyn Astronomical Institute, University of Groningen, Landleven 12, 9747 AV Groningen, The Netherlands

[b] Department of Astronomy, University of Cape Town, Private Bag X3, Rondebosch 7701, South Africa

[c] ASTRON, Netherlands Institute for Radio Astronomy, Postbus 2, 7990 AA Dwingeloo, The Netherlands

[d] South African Astronomical Observatory (SAAO), PO Box 9, 7935 Observatory, Cape Town, South Africa

Submitted to Monthly Notices of the Royal Astronomical Society, 09 May 2017.

Abstract

We present a catalogue of 261 galaxy members of the 3C 129 cluster. The cluster, located at $z \approx 0.02$, forms part of the Perseus-Pisces filament and is obscured in the optical due to its location in the Zone of Avoidance. Galaxies are identified in the near-infrared using the J and K band data provided by the UKIDSS Galactic Plane Survey within an area of radius of 1.1° centred on the X-ray emission of the cluster at $\ell, b \approx 160.52°, 0.27°$. Of these galaxies 26 have known redshifts, of which 23 from our HI observations and 3 from optical spectroscopy. A comparison of the 3C 129 cluster K-band luminosity function with those of well-known galaxy clusters at similar redshifts shows that the galaxy density in the core of the 3C 129 cluster is similar to that of the Norma cluster and slightly less than in the Coma cluster. This places the 3C 129 cluster among the richest galaxy clusters in the Perseus-Pisces filament. From an assessment of the spatial and velocity distributions of the 3C 129 cluster galaxies with redshifts, we measured a velocity of $cz = 5227 \pm 171$ km s^{-1} and $\sigma = 1097 \pm 252$ km s^{-1} for the main cluster, with a substructure in the cluster outskirts at $cz = 6923 \pm 71$ km s^{-1} with $\sigma = 422 \pm 100$ km s^{-1}. The presence of this substructure is consistent with previous claims based on the X-ray analysis that the cluster is not yet virialised and may have undergone a recent merger.

Keywords: galaxy clusters; photometry; 3C 129 cluster; near-infrared

3.1 Introduction

At the nodes of large filamentary structures in the Universe, clusters of galaxies are continually growing and evolving as they accrete matter from the surrounding large-scale structures (Ouchi et al. 2005, Springel et al. 2005, Muldrew, Hatch & Cooke 2015). Galaxy clusters are the largest gravitationally bound systems (Borgani et al. 2001, Allen et al. 2004, Vikhlinin et al. 2009, Mantz et al. 2010) and critical cosmological probes. Much of our present understanding on galaxy formation and evolution has been based on observing galaxies in cluster environments (Bell et al. 2004, Miller et al. 2009). Nearby galaxy clusters have particularly shaped our understanding because we are able to study them at a level of detail that would not be possible for clusters at high redshifts (eg., Drinkwater, Gregg & Colless 2001, Chung et al. 2009, Hammer et al. 2010, Karachentsev et al. 2014, Weinzirl et al. 2014).

Our attention was drawn to the nearby 3C 129 cluster when it was uncovered as an overdensity in our Nançay survey of 2MASX galaxies in the Zone of Avoidance (van Driel et al. 2009, Ramatsoku et al. 2014). It is part of the expansive Perseus-Pisces Supercluster (PPS) at a redshift of $z \approx 0.02$. Very little is known about this cluster's galaxy population despite being part of this well-studied filament (Giovanelli & Haynes 1985a, Haynes & Giovanelli 1986, Haynes et al. 1988, Hudson et al. 1997, Hanski et al. 2001). This is due to its location at extremely low Galactic latitudes, $\ell, b \approx 160.52°, 0.27°$ (Ebeling, Mullis & Tully 2002), where severe extinction ($A_B \geq 5$ mag) and stellar confusion in the plane of the Milky Way (MW) make locating even major overdensities in the galaxy distribution inherently difficult and unreliable (Kraan-Korteweg & Lahav 2000b, Roman, Iwata & Saitō 2000).

This galaxy cluster was first identified with the Uhuru satellite (Forman et al. 1978) in the 2−6 keV band as the X-ray source 4U 0446+44. It was subsequently observed with the ROentgen SATellite (ROSAT)[1], the European Space Agency X-ray Observatory (EXOSAT)[2] and the Einstein[3] satellite. It is also detected and listed in the CIZA catalogue as CIZA J0450.0+4501 (Ebeling, Mullis & Tully 2002). From analyses of these data, Leahy & Yin (2000) reported an X-ray temperature of kT=5.5 keV, a total luminosity of 2.7×10^{44} erg s^{-1} in the $0.2 - 10$ keV and a total cluster mass of 4.7×10^{14}M$_\odot$. For comparison, the Coma cluster has an X-ray temperature of 8.0 keV, a total luminosity of 7.26×10^{44} erg s^{-1} (Ebeling et al. 1998b) and a total cluster mass of $13 \pm 2 \times 10^{14}$M$_\odot$ (Hughes 1989).

The cluster contains two radio galaxies, 3C 129 and 3C 129.1 ($cz = 6236$ and 6655 km s^{-1}, respectively (Spinrad 1975)) with jets extending far into the intra-cluster medium (ICM). 3C 129 is a well-studied (Owen et al. 1979, Jaegers & de Grijp 1983, Taylor et al. 2001, Harris, Krawczynski & Taylor 2002, Lal & Rao 2004, Murgia et al. 2016) head-tail radio source with a curved tail that extends over 427 kpc (Krawczynski et al. 2003) and a total flux density of ~ 5.3 Jy at 1400 MHz (White & Becker 1992), while 3C 129.1 is a wide-angle tail radio source with a total flux density of ~ 1.9 Jy at 1400 MHz (Condon et al. 1998).

[1] https://heasarc.gsfc.nasa.gov/docs/rosat/rosat3.html
[2] https://heasarc.gsfc.nasa.gov/docs/exosat/exosat.html
[3] https://heasarc.gsfc.nasa.gov/docs/einstein/heao2_about.html

Due to the high extinction layer of the Milky Way, most of what is known about the cluster is from its X-ray and radio source properties since most of its constituent galaxies had not been observed before. For this reason we decided to perform a census of the galaxy population of this cluster by conducting a deep, blind, HI imaging survey with the Westerbork Synthesis Radio Telescope[1] (WSRT). This was done using a mosaic of about $3^\circ \times 3^\circ$ covering the cluster and its immediate surrounding regions of the PPS (Ramatsoku et al. 2016).

Our aims are to investigate the large-scale and sub-structure associated with the 3C 129 galaxy cluster and to determine its relevance to flow fields around it and the larger PPS. As evident in the 2MASS survey of extended sources, this large scale structure envelops the cluster as it crosses from the southern to northern Galactic hemispheres (Jarrett 2004) (see also Fig. 3.1). Our data will also aid in efforts by the 2MASS Tully-Fisher survey (2MTF; Masters, Springob & Huchra 2008) since they complement the inner ZoA regions ($b \approx |5^\circ|$) that are excluded from optical spectroscopy. Moreover, since we covered a wide area of the cluster with our HI imaging survey, we will be able to characterise the various environments in and around the cluster to study the environmental effects on the population of galaxies therein.

HI is an ideal diagnostic tool for studying processes in clusters because of its sensitivity to the environment. It has also proved most effective at detecting galaxies at low Galactic latitudes (Kraan-Korteweg et al. 1994, van Driel et al. 2009, Henning et al. 2010, McIntyre et al. 2015). However, it is unsuitable for tracing the dominant galaxy population of clusters which primarily comprises gas-poor, early-type galaxies. On the other hand, these early-type galaxies stand out at near-infrared wavelengths, particularly in the J and K bands. Combining the HI and NIR data provide a versatile and robust tool for conducting an inventory of the galaxy population in clusters, particularly behind the Galactic Plane (GP) where dust extinction primarily presents a challenge for optical wavelengths.

[1] http://www.astron.nl/radio-observatory/

In this paper we explore the NIR colour-magnitude properties of galaxies within the WSRT HI mosaic to identify cluster members of the 3C 129 cluster and to complement our HI detections at NIR wavelengths. This is achieved using data from the UKIDSS Galactic Plane Survey (Lucas et al. 2008).

The layout of the paper is as follows: In Section 3.2 we give a summary of the HI sample and discuss the near-infrared photometry of the UKIDSS images. The colour-magnitude relation and cluster membership selection are discussed in Sec. 3.3. A subset of the catalogue of the cluster galaxies and images are described and presented in Sec. 3.3.2, with the full catalogue and images given in Appendix B. The near-infrared properties and luminosity function of the cluster are discussed in Sec. 3.3.2. We describe the structure of the cluster in Sec. 3.4.1 and discuss along with a summary of the main results in Sec. 3.5.

We assume a Λ cold dark matter cosmology with $\Omega_{\rm M} = 0.3, \Lambda_{\Omega} = 0.7$ and a Hubble constant $\rm H_0 = 70$ km s^{-1} Mpc^{-1} throughout this paper.

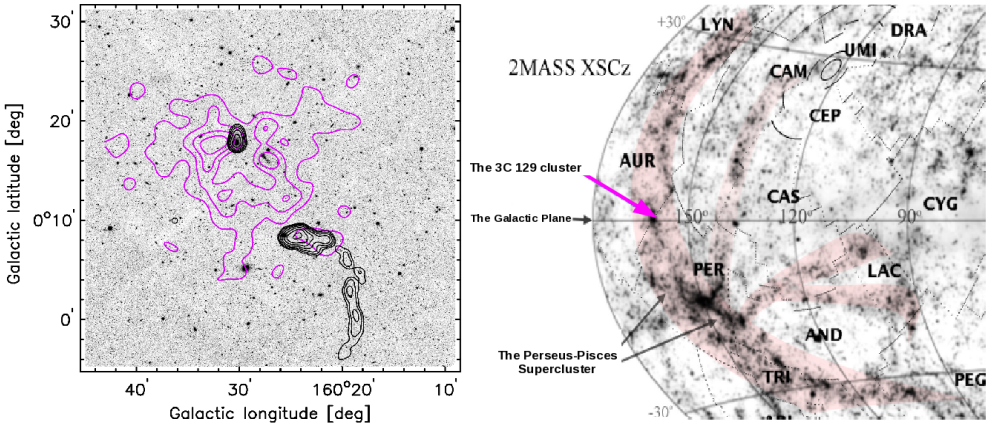

Figure 3.1 – Left panel: The central region of the 3C 129 cluster ($\sim 37' \times 37'$) showing the K-band UKIDSS image. The VLA 1424 MHz contours of the radio sources (NVSS; Condon et al. 1998) are overlaid in black. The 3C 129 is the head-tailed source with a curved tail on the right and the wide-angle tailed radio source on the left is 3C 129.1. The X-ray 0.1 - 2.4 keV emission from ROSAT is overlaid in magenta. Right panel: An Aitoff Galactic projection of the galaxy distribution extracted from the 2MASS Galaxy Catalog (XSCz) in the Local Universe shown from the northern hemisphere (Jarrett 2004). The image highlights the large filamentary structure of the PPS shaded in pink. The 3C 129 cluster lies in the GP crossing at $\ell \approx 161°$.

3.2 Data Samples

3.2.1 The HI data

We refer the reader to Ramatsoku et al. (2016) for a detailed description of the HI observations and data. Here, only a brief summary is provided:

The 21 cm HI-line imaging survey was conducted using the Westerbork Synthesis Radio Telescope (WSRT) comprising 35 pointings each with an integration time of 12 hours, in a hexagonal mosaic centred at $\ell, b \approx 160°, 0.5°$ which is where the Perseus-Pisces Supercluster crosses the Zone of Avoidance. The total sky area covered was $\sim$9.6 deg^2, with a survey rms sensitivity of 0.36 mJy/beam over the radial velocity range of $cz = 2400-16600$ km s^{-1}, with 16.5 km s^{-1} and $23'' \times 16''$ velocity and angular resolution respectively. A total of 214 HI galaxies in the HI mass range of $5 \times 10^7 - 2 \times 10^{10}$ M$_\odot$, with 80 galaxies spatially resolved, were detected over the entire radial velocity range. Of these galaxies, 87 were detected at a redshift of the 3C 129 cluster ($cz \sim 4000 - 8000$ km s^{-1}). The rest were found in the foreground and background of the cluster, at redshifts of, $cz = 2400-4000$ km s^{-1} and $cz \sim 10000-16600$ km s^{-1}, respectively. The footprint of our HI observations is shown in blue in Fig. 3.2.

3.2.2 The Near-Infrared Data

The cluster is prominent in the 2MASX catalogue as illustrated in the right panel of Fig. 3.1. However, we extracted our near-infrared sample of galaxies from images provided by the UKIRT Infrared Deep Sky Survey (UKIDSS: Lawrence et al. 2007) because of its improved depth and spatial resolution. We used Data Release 10 (DR10) of a sub-survey of UKIDSS, the Galactic Plane Survey (GPS), which covers an area of 1800 deg^2 to a 5σ $K(2.2\mu m)$-band depth of 18.8 mag (Vega)(Lucas et al. 2008).

The UKIDSS-GPS with a pixel scale of $0.2''$/pix (after microstepping) and an average seeing of $0.8''$ is highly successful at separating stars from galaxies further from the Galactic mid-plane ($|b| \gtrsim 5°$). However, it suffers from confusion at lower Galactic latitudes. At these regions visual inspection is still a superior method for identifying galaxies (Lucas et al. 2008). For this reason, prior to visual inspection, we opted to use the SExtractor software (SEXTRACTOR version 2.8.6; Bertin & Arnouts 1996) to extract sources from sixteen overlapping UKIDSS-GPS images of size $1° \times 1°$, supplemented by smaller images ($\sim 30' \times 30'$) which together cover the entire HI mosaic survey footprint of the WSRT (see Fig. 3.2).

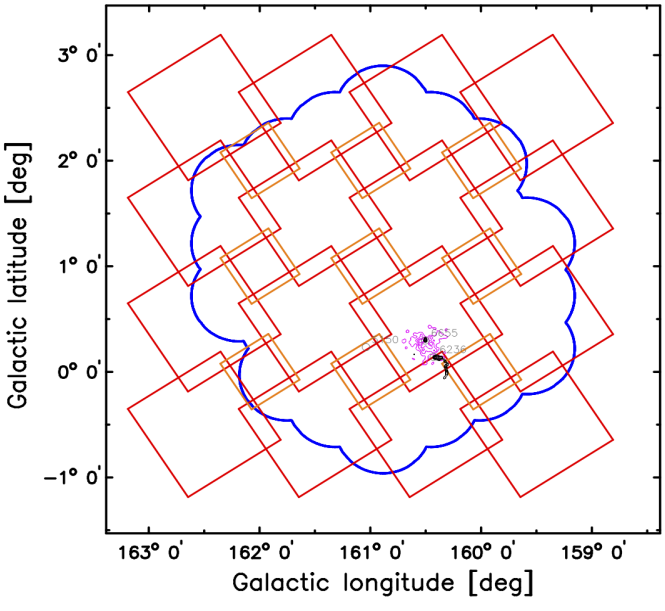

Figure 3.2 – The projected sky distribution of the observed WSRT hexagonal mosaic in blue. Coverage of the near-infrared tiles from the UKIDSS - GPS data is outlined in red. The X-ray emission is shown in magenta and the position of the contours of the radio sources 3C 129 and 3C 129.1 are shown in black.

For the purposes of source detection, the K-band was used. It is less affected by Galactic dust extinction and provides higher signal-to-noise ratios compared to the $J(1.2\mu m)$- or $H(1.6\mu m)$-bands.

The source detection performed by SEXTRACTOR uses an algorithm that registers a detection when a set number of pixels are connected as specified by the detection parameters, DETECT_MINAREA and DETECT_THRESH. An empirically two-fold approach was adopted to set these parameter values; for sources with pixel values above 9σ, a minimum of 10 adjacent pixels was required. Sources between $3\sigma - 9\sigma$ were only accepted, if they had a minimum of 50 adjacent pixels.

After identifying the sources, an analysis was conducted to deblend objects that are identified as connected on the sky based on the deblending parameters, DEBLEND_MINCONT and DEBLEND_NTHRESH which were chosen to be 0.001 and 32 respectively. These empirical values were selected after performing tests with a wide range of values and verifying results by visual inspection to ensure that spurious detections were minimised and no obvious sources were missed. We estimated the GLOBAL background noise with a small mesh set by, BACK_SIZE = 64. This size

was chosen to prevent an overestimation of the background due to wings of very bright sources. The set of SEXTRACTOR parameters adopted for detecting sources in the UKIDSS-GPS K-band images is given in Table. 3.1.

Table 3.1 – Parameters for SEXTRACTOR 2.8.6.

Parameter	Value
DETECT_MINAREA	50 (10 for sources above 9σ)
DETECT_THRESH	3 (9 for min. of 50 adjacent pixels)
ANALYSIS_THRESH	3
FILTER	Y
FILTER_NAME	default.conv
DEBLEND_NTHRESH	32
DEBLEND_MINCONT	0.001
CLEAN	Y
CLEAN_PARAM	1.0
MASK_TYPE	CORRECT
PHOT_APERTURES	5
PHOT_AUTOPARAMS	2.5, 3.5
PHOT_PETROPARAMS	2.0, 3.5
SATUR_LEVEL	422784/ADU
MAG_ZEROPOINT	24.105
GAIN	4.5/e-/ADU
GAIN_KEY	GAIN
PIXEL_SCALE	0.4/arcsec
SEEING_FWHM	0.8/arcsec
STARNNW_NAME	default.nnw
BACK_SIZE	64
BACK_FILTERSIZE	3
BACKPHOTO_TYPE	GLOBAL

3.2.3 Star-Galaxy Separation

SEXTRACTOR parameters described in section 3.2.2, were optimised to limit the number of stars and spurious detections. The optimal combination of threshold and minimum area was selected, relying on sources that appeared to be galaxies based on their visual inspection. However, the high stellar density in the GP resulted in many point-source detections (stars). In this section we present a step-by-step description of how the star-galaxy classification was performed.

(a) SEXTRACTOR stellarity index

A preliminary star-galaxy classification was conducted based on SEXTRACTOR's stellarity index (CLASS_STAR) which is a dimensionless parameter that characterises objects as point-like or extended. This classification parameter, CLASS_STAR, is based on the neural-network analysis approach that compares the point spread function to the object scale and then provides a confidence level estimate of the classification which ranges from 0 for galaxies to 1 for stars. Figure 3.3 shows the distribution of the CLASS_STAR values of $\sim$ 460,000 detected objects. Two clear populations with CLASS_STAR values of 0 and 1 are evident. The histogram for sources classified as galaxies decreases sharply for CLASS_STAR = 0.0 to 0.35, it then flattens and rises steeply from CLASS_STAR = 0.8 to 1.0. Based on the CLASS_STAR values, objects were initially classified in the following manner:

CLASS_STAR $\leq$ 0.35 (Galaxies),

0.35 $<$CLASS_STAR $<$ 0.8 (Stars or galaxies),

CLASS_STAR $\geq$ 0.8 (Stars),

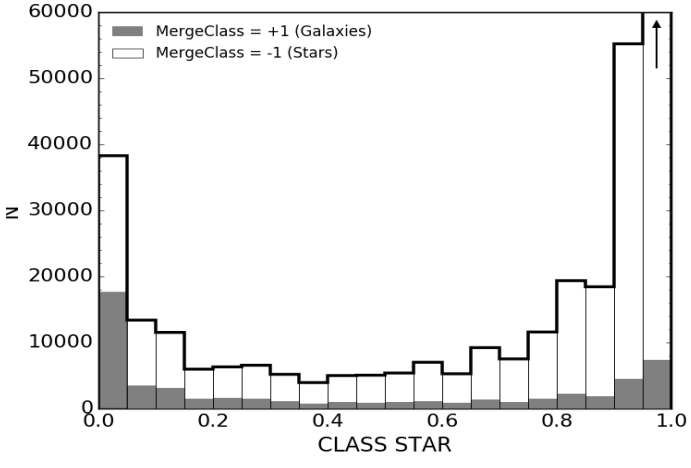

Figure 3.3 – The distribution of SEXTRACTOR stellarity index, CLASS_STAR of all objects found in the UKIDSS-GPS searched images. All objects with CLASS_STAR $>$ 0.8 are stars, those with CLASS_STAR $<$ 0.35, galaxies and 0.35 $<$CLASS_STAR $<$ 0.8 are ambiguous objects. The open histogram shows the distribution of objected labeled as stars in the UKIDSS catalogue (MERGECLASS=-1) and the filled histogram are those labelled as galaxies (MERGECLASS=+1). The horizontal arrow points to a higher number count of $\sim 10^5$ in that bin that is not shown in the plot.

(b) UKIDSS-GPS star-galaxy separator

To increase the reliability of objects classified as galaxies by CLASS_STAR, their classifications were cross-correlated with the UKIDSS-GPS catalogue which also provides a star-galaxy separation parameter, MERGEDCLASS. This parameter is based on quantitative measurements in the J, H and K passbands of the observed radial profiles by the UKIDSS data reduction pipeline (Dye et al. 2006). The profiles are characterised by the "mergeClassStat" parameter and identified as either point-like, resolved or an artifact. Resolved sources are assigned large "mergeClassStat" values and smaller values are associated with point-like sources. Additionally, the UKIDSS-GPS further separates galaxies from stars by making cuts based on the difference between the Petrosian (resolved) magnitude and the point source magnitude (Lucas et al. 2008). Galaxies are assigned parameter value of MERGECLASS$=+1$ and stars are assigned MERGECLASS$=-1$.

(c) Visual inspection

We found that the CLASS_STAR and MERGECLASS parameters are not reliable in all circumstances. For instance, out of all sources with CLASS_STAR $= 0.0$ only about 47% were classified as galaxies by MERGECLASS (see Fig. 3.3). As a result we needed to ensure that galaxies were not missed by only depending on the star galaxy classification based on these parameters, particularly in the ambiguous $0.35 <$ CLASS_STAR < 0.8 range. This necessitated a further step to improve the reliability of the classification of each object and to remove any spurious detections. For this task we conducted a visual inspection of all objects with CLASS_STAR < 0.8. Objects with CLASS_STAR > 0.8 were not inspected visually since only 0.05% of the objects in these bins had MERGECLASS $= +1$. This was performed using DS9 by inspecting the J, H and K bands three-colour (RGB) composite images. The extended nature of galaxies made them readily distinguishable in this manner.

After removing duplicate detections in overlapping regions of the UKIDSS images, artifacts and stars, the final sample consisted of 9737 unique galaxies over the full WSRT mosaic.

3.2.4 Star-Subtraction

The high stellar density affects images of galaxies at low Galactic latitudes. It is therefore important to take additional steps to remove stars superimposed on the galaxies to acquire accurate photometry. This was done by fitting a point spread function (PSF) to stars and subsequently removing them from the galaxy. For this purpose we used a four-step script based on the IRAF routine KILLALL (Buta & McCall 1999), which in turn is based on DAOPHOT tasks (Stetson 1987). The four steps were as follows: (a) We used IMSTAT to determine the rms and sky background in the image; (b) We modelled the galaxy using ELLIPSE and BMODEL, and removed this model from the image. It should however, be noted that galaxy structures such as spiral arms may be not be modelled fully and might result in residuals in the galaxy-subtracted image; (c) We used SEXTRACTOR to detect bright stars that are above 3.5σ in the image in which the galaxy has been subtracted. The PSF photometry of these sources was then determined using DAOPHOT (tasks ALLSTAR and PHOT) and removed from the image. This step was repeated for fainter stars above 1.8σ. To mitigate against misidentifying residual structures as stars, we required these stars to be detected by DAOFIND at the 2σ threshold; (d) The two lists with the bright and faint stars were combined and removed from the original image using the SUBSTAR task; (e) The residuals resulting from imperfect PSF fits to stars in the image were found and removed. We repeated steps (b) to (e) four times, each time improving the galaxy model, which resulted in a more reliable star removal.

Figure 3.4 shows example images for three galaxies in our sample before (left panel) and after (right panel) star-subtraction. It illustrates that this star removal procedure performs reasonably well. In fact, it has been shown by Woudt et al. (2005) and Mutabazi et al. (2014), through simulations of subtracting artificial stars added to non-crowded fields, that removing stars this way has a minimal effect (less than 0.01 mag on average) on the galaxy photometry.

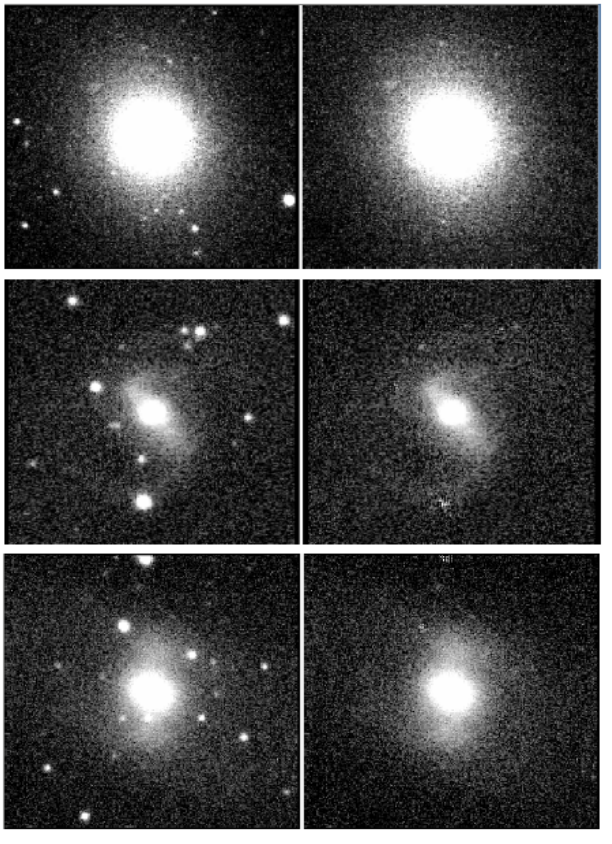

Figure 3.4 – Postage stamp examples of K-band images of galaxies before (left panels) and after star-subtraction (right panels).

3.2.5 The NIR Photometry

After subtracting all the stars we extracted the galaxy photometric parameters. Since UKIDSS photometric parameters are only measured within circular apertures which are inadequate for elongated galaxies, we used customised python scripts developed by K. Said[1] and W. Williams[2] based on a combination of SEXTRACTOR and IRAF tasks.

Astrometry of positions: First, the central positions of galaxies were determined by adding the three images from the J+H+K bands and measuring the intensity-weighted centroid. This method of determining positions is more accurate as it measures the centre of the galaxy from higher signal-to-noise images (Jarrett et al. 2000).

[1] khaled@ast.uct.ac.za
[2] w.williams5@herts.ac.uk

Ellipticities and geometries: Next, ellipticities and position angles were determined individually from the J, H and K band images. The IRAF task ELLIPSE was used to fit ellipses to the galaxy image. Ellipticities, $\epsilon = (1 - b/a)$ and position angles (ϕ; counter clockwise from North) were then fitted at semi-major axis intervals, while keeping the central coordinates, X and Y fixed. The ELLIPSE task produced tables containing the intensity (in counts) within the ellipse and the ellipticity and position angle at each semi-major axis interval including their errors. Then the galaxy's position angle and ellipticity were determined to be the average value in the outer disk between 1σ - 2σ isophotes, where σ is the sky background rms.

Magnitudes: Finally, the isophotal magnitudes were measured within elliptical apertures in all bands (J, H, K). The K-band surface brightness $\mu = 20$ mag arcsec^{-2} isophote was adopted to determine the isophotal radius ($r_{k_{20}}$). Fiducial magnitudes were measured within this same aperture of radius $r_{k_{20}}$ for the J, H, K-bands. All the magnitudes are based on the Vega calibration.

3.2.6 Photometric checks

To check our photometric consistency, we derived from the UKIDSS images galaxy magnitudes within a $7''$ radius circular aperture and compared these with their counterparts in the 2MASX catalogue (Jarrett et al. 2000) in the same $7''$ circular aperture. Sources in both catalogues were matched if they were separated by less than $1.5''$. We used this small correlation radius of $1.5''$ because the UKIDSS WFCAM astrometric calibration was derived from 2MASS (Hodgkin et al. 2009), which has a positional accuracy of about $0.5''$. Only galaxies with reliable photometry (as flagged in the 2MASX catalogue) were compared. We found 363 counterparts in the 2MASX catalogue.

In Fig. 3.5, we show a comparison of our UKIDSS photometry with that of the 2MASX. The comparison relation used is:

$$\Delta m = m_{2MASX} - m_{UKIDSS}. \tag{3.1}$$

By this equation, a positive Δm indicates that 2MASX magnitudes are fainter than our UKIDSS magnitudes. The offsets given in the top right corners of Fig. 3.5 indicate that the 2MASX galaxies are slightly brighter than their UKIDSS counterparts. These offsets can be attributed to the

higher resolution of the UKIDSS images with a seeing of $\sim 0.8''$ compared to 2MASS with a seeing of $\sim 3.0''$. The improved resolution of the UKIDSS allows for the detection and subtraction of fainter foregrounds stars that would otherwise contribute to the galaxy's brightness within the measurement aperture. It is also probable that the different filters used could have contributed to these slight offsets. The UKIDSS uses the Mauna Kea Observatory (MKO; Hodgkin et al. 2009) filter set which is slightly different from the 2MASS filter set (Cohen, Wheaton & Megeath 2003).

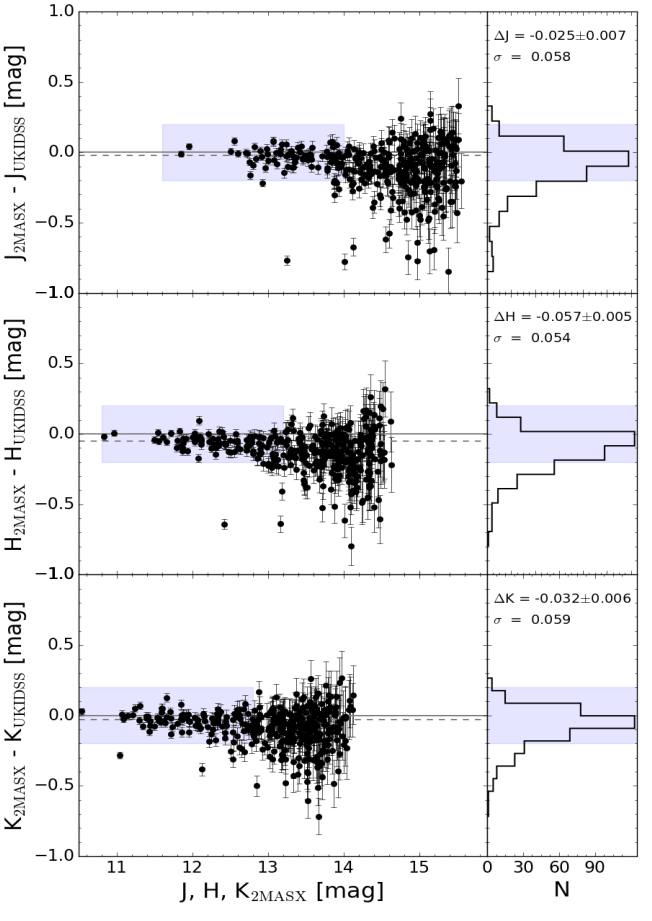

Figure 3.5 – Comparison between the 2MASX and UKIDSS circular aperture magnitudes measured within a $7''$ radius for the J (top), H (middle) and K (bottom) bands. The median offset between the two surveys is indicated by the dashed line and is printed in the top right legend. This median was determined within areas marked by the blue shades also marked in the histograms.

3.2.7 Extinction

Galaxies in the ZoA tend to have their brightness reduced due to the dust obscuration in the Milky Way. This effect is less prominent in the near-infrared compared to the optical, but it is nonetheless not negligible. Within our WSRT field the Galactic extinction values range from $A_K = 0.16 - 0.56$ mag (see Fig. 7 of Ramatsoku et al. 2016).

We correct for this effect using the extinction law;

$$\frac{A_\lambda}{E(B-V)} = R_\mathrm{v}, \tag{3.2}$$

where A_λ is the extinction in a given band and $E(B-V)$ is the colour reddening from Schlegel, Finkbeiner & Davis (1998) with the Schlafly & Finkbeiner (2011) correction factor of 0.86 applied. The value for $\mathrm{R_V} = 3.1$ is given by Schlegel, Finkbeiner & Davis (1998). Using the parametrisation by Fitzpatrick (1999) we derive the extinction in the J, H and K bands;

$$A_J = 0.741E(B-V), \tag{3.3}$$

$$A_H = 0.456E(B-V), \tag{3.4}$$

$$A_K = 0.310E(B-V). \tag{3.5}$$

The effect of extinction on our galaxies is low given that our field has a median extinction of $A_K = 0.29 \pm 0.05$ mag, however this is not negligible. This extinction also translates into a reduction of the isophotal radius of the galaxy due to the loss of the fainter, low surface brightness outer regions.

3.3 The Colour-Magnitude Relation

The colour-magnitude relation (CMR) has been shown to be a powerful technique for selecting galaxies in clusters since they form a distinct linear feature in the colour-magnitude diagram (Visvanathan & Sandage 1977). This feature, known as the red sequence, has a well-defined slope that evolves with redshift and a small (< 0.1 mag) intrinsic scatter (Bower, Lucey & Ellis 1992, Gladders et al. 1998, López-Cruz, Barkhouse & Yee 2004, Stott et al. 2009). In addition to the tight CMR, galaxies in regular clusters have a radial distribution that is typically centrally concentrated

(Dressler 1980). They also form the dominant population at the bright end of the galaxy luminosity function and create a high contrast against the background, thus making them easily recognisable in surveys (Gladders et al. 1998).

To find galaxy member candidates of the 3C 129 cluster, we use the CMR in the near-infrared to identify the red sequence feature as well as the angular on-sky projection distribution to detect clustering. The advantage of using this technique is that it is not affected by projection effects since any random distribution of galaxies will not form a coherent red sequence signature in the colour-magnitude diagram.

In Fig. 3.6 we present the NIR colour-magnitude diagram (CMD) of all 9737 galaxies within the observed WSRT mosaic (see Fig. 3.2). Colours were measured inside the $\mu_k = 20$ mag arcsec^{-2} fiducial isophotal aperture defined in the K-band and corrected for foreground extinction based on the DIRBE/IRAS maps as described in Sect. 3.2.7.

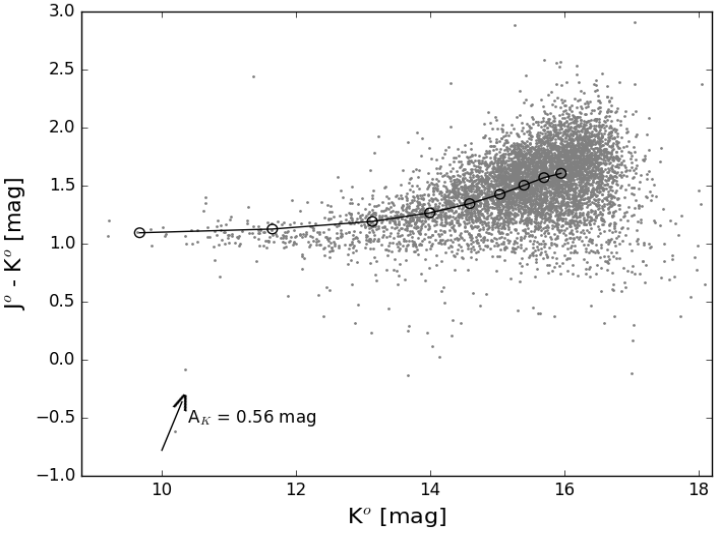

Figure 3.6 – The colour-magnitude diagram of 9737 sources from the UKIDSS-GPS within the WSRT mosaic (see Sect. 3.2.2). The reddening curve computed from redshift $z = 0.02$ to $z = 0.4$ is shown by black line with open circles representing the redshift bin and Galactic dust reddening vector for a K-band extinction of 0.56 mag is indicated with the arrow.

Two well-defined populations are apparent in this plot. The dominant population ($K^o < 12$ mag, $J^o - K^o \gtrsim 1.3$ mag) consists of redshifted background galaxies. The overlaid reddening curve[1] (Chilingarian, Melchior & Zolotukhin 2010) supports this claim. The other identifiable population is a slightly slanted band of galaxies that stretches between $8 \lesssim K \lesssim 16$ mag with colours, $J^o - K^o \approx 1.1$ mag. This second feature contains within it the red sequence of the 3C 129 cluster. Below the red sequence is a small population of blue outliers which were visually inspected and found to be close binary stars and/or artefacts that were missed during the star-galaxy separation process in the UKIDSS images (see Sect. 3.2.3).

3.3.1 The Red Sequence and Cluster Membership

To determine the galaxy cluster membership we used a three step process as follows:

Firstly, a region of the CMD containing the red sequence was selected and an estimate of the initial fit was made by visual inspection. All points deviating by more than 3σ from this initial fit were removed from the full sample. We then performed an iterative linear fit of the form, $J - K = \alpha K + c$ where the slope of the red sequence is denoted by α to points that were within $\pm 3\sigma$ of the initial fit. The final fit gives $(J - K)^o = -(0.023 \pm 0.002)K^o + 1.25$ with a 1σ dispersion of 0.039 mag. The slope matches that of the Coma cluster of $\alpha = -0.017 \pm 0.009$ (measured by Stott et al. 2009), which is at a similar redshift of $z \approx 0.02$ as the 3C 129 cluster. The $J - K$ colours of the red sequences are also comparable to that of galaxy clusters in the WIde-field Nearby Galaxy-cluster Survey (WINGS: Valentinuzzi et al. 2011). Galaxies within $\pm 3\sigma$ of the final fit formed the initial list of the cluster member candidates.

Secondly, we limited the relative background contamination in the initial sample list of red sequence galaxies by only selecting galaxies with $r_{k_{20}} > 3''$. This was motivated by the fact that the red sequence of the cluster becomes less well-defined for galaxies with $r_{k_{20}} < 3''$ which typically corresponds to magnitudes of $K^o \gtrsim 15.5$ mag; these are likely dwarf galaxies which are of no interest to this study.

[1] http://kcor.sai.msu.ru

Thirdly, we defined a radius r_{cl} of the cluster centred on the ROSAT X-ray emission. This cluster radius was chosen based on the spatial distribution (cf. Fig. 3.12) of the red sequence galaxies which have radii larger than $r_{k_{20}} > 3''$ out to where they became sparsely distributed. Assuming a redshift of $z = 0.02$ the radius was found to be $r_{cl} \approx 1.7$ Mpc ($\sim 0.8 r_A$[1]). It corresponds to about $1.34 R_{200}$, where R_{200} is the radius at which the average interior density of the cluster is $200 \times \rho_c$, where ρ_c is the critical density of the Universe. The R_{200} of the 3C 129 cluster is ~ 1.24 Mpc based on the $0.1 - 2.4$ keV band measurements by ROSAT (Piffaretti et al. 2011). We then only selected red sequence galaxies within $r_{cl} < 1.34 R_{200}$ as cluster members.

After applying the steps outlined above, we obtained a sample of 250 galaxy members of the 3C 129 cluster which lie on the red-sequence. Of these galaxies 13 were already previously detected in HI (Ramatsoku et al. 2016). The CMD of all galaxies on the red sequence is shown in Fig 3.7. In addition, we included 11 more galaxies with $r_{k_{20}} < 3''$ that were detected in HI within the velocity window and the defined radius of the cluster on the sky regardless of their location on the red-sequence. Thus the final sample of the 3C 129 cluster members comprises 261 galaxies.

We note that we cannot measure the contamination of the final sample by background galaxies without redshift measurements. However, it has been previously shown that this method of finding galaxy clusters members in both the infrared and optical wavelengths results in a background contamination of less than 5% (Gladders & Yee 2000).

3.3.2 Morphologies of the Cluster Members

Figure 3.8 shows the CMD of the cluster with galaxies separated into approximate morphologies based on a visual inspection and a subjective estimate of their bulge-to-disk ratios, their ellipticities and compactness. The morphological classification was independently conducted and adjudicated by co-authors. This classification is only meant to distinguish large-scale trends and to give a general description of galaxy morphologies in the cluster. Galaxies were classified into five broad groups of early-types (E/S0), early spirals (eS) such as Sa/Sb, medium spirals (mS) which were typically of Sc/Sd type, the late-type spirals (ℓS) which were

[1] r_A is the Abell radius

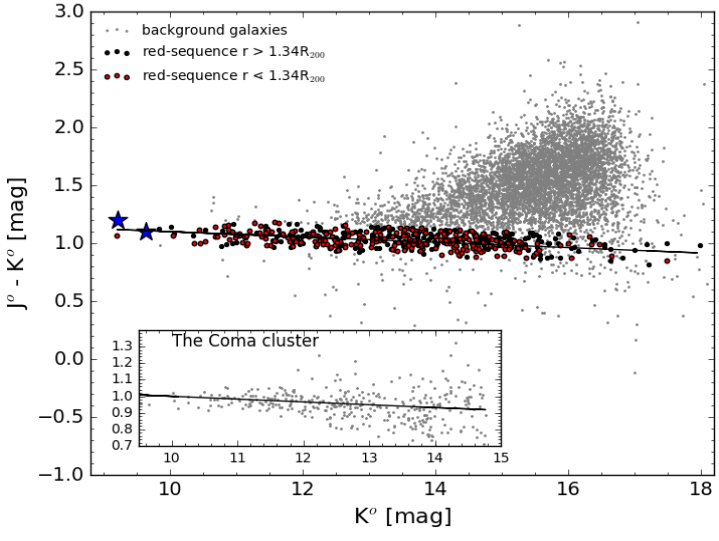

Figure 3.7 – The colour-magnitude diagram showing the red sequence signature of the 3C 129 cluster in red with the two blue stars identifying the bright radio sources, 3C 129 and 3C 129.1. The fitted slope, $\alpha = -0.023 \pm 0.002$ mag of the cluster is illustrated by the black solid line and compared to that of the Coma cluster using 2MASX data in the inserted CMD. Black points are galaxies outside the cluster radius of $r_{cl} < 1.34R_{200}$ and grey points are mostly background galaxies.

mostly Sdm, and Irregular (Irr) galaxies without any discernible structure. In Fig. 3.8 we also indicate with black squares, the galaxies detected in HI (with UKIDSS counterparts) within the velocity range and radius of the cluster.

Figure 3.8 shows early-type galaxies (E/S0) and the early-spirals to be mostly located on the bright end of the red sequence. This is to be expected given that we are evaluating a potentially rich cluster which tends to have more of these bright early-type galaxies than star forming late-type galaxies.

The mid-range spiral galaxies (mS) show no obvious trends in the CMD except that they are predominantly at magnitudes fainter than most of the early-type galaxies. There is a number of these type of galaxies ($\sim$ 23%) detected near the centre of the cluster (see also Figs. 3.12 and 3.13 in Sect. 3.4). Interestingly, they were not detected in HI, suggesting they might be stripped of their gas by ram-pressure from the ICM upon infall, thus resulting in HI deficiencies. Judging by their morphologies alone, these should have otherwise been detected in our HI observations.

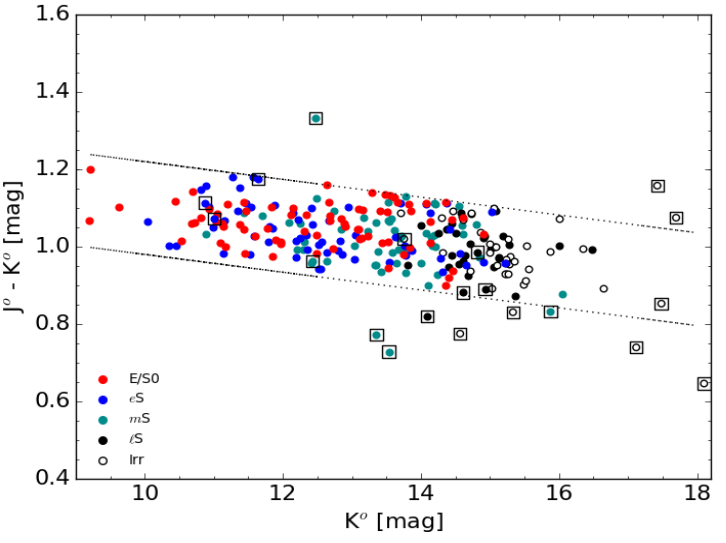

Figure 3.8 – The CMD of the 3C 129 cluster with members shown in red in Fig. 3.7 separated by morphologies defined in the colours in the legend. Circles are the red-sequence galaxies and those enclosed in squares are HI detected galaxies within the radius of the cluster and velocity range. The dotted lines show the $\pm 3\sigma$ rms dispersion (0.12 mag) from the fitted red sequence relation: $J - K = -0.023K + 1.25$. Magnitudes and colours are measured inside the K-band 20 mag arcsec^{-2} isophotal fiducial aperture and are corrected for Galactic extinction.

Late-type spirals and Irregular galaxies are mostly found at the fainter end of the CMD at $K^o \gtrsim 14$ mag. These are typically LSB galaxies which could have lost their gas through tidal stripping or interaction with the ICM (Conselice, Gallagher & Wyse 2003). On the other hand, most of the HI detected galaxies also populate this end of the CMD, but tend to be slightly bluer ($J^o - K^o \lesssim 1.0$) than their LSB counterparts. They are located in the cluster outskirts where we expect less interaction and where we expect galaxies to have retained their gas.

Analyses of these populations of galaxies as well as the effect of the various environments in which they reside, requires a more comprehensive analysis than presented in this paper. Here we only present a cursory description and we will study and discuss the detailed nature of these galaxies in a forthcoming paper.

The catalogue of cluster galaxies

A full catalogue of the 261 cluster members is presented in Appendix B, Table B. Galaxies are listed in ascending order of their K-band magnitudes (from the brightest to the faintest). For each galaxy a $1.2' \times 1.2'$ image in the J, H and K band was extracted. The false colour (RGB) postage stamps of these images are shown in Figure B in the same order as the catalogue. Galaxy morphologies are printed at the bottom of the images. The 24 galaxies that were detected in HI are framed in cyan. The first 30 entries of the catalogue and their corresponding images are shown in Table. 3.2 and Fig 3.9, respectively.

The columns are as follows:

Column 1 - The galaxy identifying number.

Column 2- Unique identifiers based on the Right Ascension (RA) and Declination (Dec) ZoAJhhmmss.ss±ddmmss.s.

Columns 3 & 4 - Equatorial coordinates, RA and Dec (J2000), respectively in degrees.

Columns 5 & 6 - Galactic longitude and latitude in degrees.

Column 7 - Ellipticity in the K-band at the 20 mag arcsec^{-2} isophote.

Column 8 - The K-band position angle in degrees, measured from celestial North to East.

Column 9 - The K_{20} isophotal major-axis radius in arcseconds.

Columns 10 & 11 & 12 - J, H and K band fiducial isophotal magnitudes (not corrected for foreground extinction).

Column 13 - The line of sight Galactic reddening in magnitudes.

Column 14 - $J - K$ colours, corrected for foreground extinction.

Column 15 - The estimated morphology of galaxies.

Column 16 - The radial velocities from the WSRT HI measurements plus optical velocities for the two galaxies 3C 129 and 3C 129.1.

Table 3.2 – Near−infrared parameters of the first 30 entries of 3C 129 cluster galaxies. The full catalogue is available in Appendix B

ID no.	Unique ID	RA	Dec	ℓ	b	ϵ_K	ϕ_K	r_{K20}	J_{K20}	H_{K20}	K_{20}	$E(B\text{-}V)$	J^o-K^o	Type	v_{rad}
	ZoA	deg	deg	deg	deg		deg	$''$	mag	mag	mag	mag	mag		km s^{-1}
(1)	(2)	(3)	(4)	(5)	(6)	(7)	(8)	(9)	(10)	(11)	(12)	(13)	(14)	(15)	(16)
1	J044908.26+445540.3	72.284	44.928	160.490	0.086	0.17	24.71	28.10	10.96 ± 0.02	9.94 ± 0.02	9.51 ± 0.02	0.89	1.07	E/S0	—
2	J045006.67+450305.8	72.528	45.052	160.505	0.298	0.20	65.00	37.30	11.21 ± 0.04	10.10 ± 0.04	9.59 ± 0.04	0.98	1.20	E/S0	6655*
3	J044909.06+450039.4	72.288	45.011	160.427	0.142	0.10	−60.00	25.60	11.50 ± 0.03	10.46 ± 0.04	10.00 ± 0.04	0.94	1.10	E/S0	6236$^{\times}$
4	J045145.56+443602.6	72.940	44.601	161.039	0.235	0.40	60.00	22.80	11.75 ± 0.03	10.82 ± 0.03	10.35 ± 0.04	0.79	1.07	*e*S	5086^{+}
5	J044939.78+440922.1	72.416	44.156	161.141	−0.337	0.09	−55.01	12.79	12.05 ± 0.02	11.16 ± 0.02	10.76 ± 0.02	0.65	1.01	E/S0	—
6	J044842.39+454818.5	72.177	45.805	159.769	0.593	0.40	−61.15	21.62	12.25 ± 0.02	11.23 ± 0.02	10.77 ± 0.02	1.12	1.00	*e*S	—
7	J045245.69+450106.2	73.190	45.018	160.829	0.638	0.44	85.11	19.63	12.31 ± 0.02	11.23 ± 0.02	10.78 ± 0.02	0.94	1.12	E/S0	—
8	J045219.88+451546.1	73.083	45.263	160.592	0.734	0.50	−60.00	25.90	12.23 ± 0.05	11.26 ± 0.05	10.83 ± 0.06	0.91	1.00	*e*S	—
9	J045326.75+441900.7	73.361	44.317	161.449	0.288	0.06	26.77	14.31	12.32 ± 0.02	11.38 ± 0.02	10.96 ± 0.02	0.69	1.06	E/S0	—
10	J045045.92+450659.7	72.691	45.117	160.529	0.428	0.27	0.36	13.39	12.62 ± 0.02	11.56 ± 0.02	11.05 ± 0.02	1.00	1.14	E/S0	—
11	J044719.31+441701.6	71.830	44.284	160.774	−0.576	0.47	−73.54	16.96	12.50 ± 0.02	11.56 ± 0.02	11.06 ± 0.02	0.69	1.15	*e*S	4993
12	J044843.25+445216.0	72.180	44.871	160.486	−0.007	0.11	32.33	9.98	12.54 ± 0.02	11.54 ± 0.02	11.11 ± 0.02	0.84	1.07	E/S0	—
13	J044459.45+453344.1	71.248	45.562	159.534	−0.059	0.30	−23.53	14.62	12.83 ± 0.02	11.73 ± 0.02	11.19 ± 0.02	1.35	1.06	E/S0	—
14	J044429.89+442914.8	71.125	44.487	160.291	−0.827	0.31	44.80	14.65	12.81 ± 0.02	11.78 ± 0.02	11.23 ± 0.02	0.98	1.16	*e*S	—
15	J044724.21+445928.3	71.851	44.991	160.244	−0.107	0.80	−35.00	31.50	12.64 ± 0.05	11.67 ± 0.05	11.25 ± 0.07	0.84	1.03	*m*S	—
16	J045414.90+450315.1	73.562	45.054	160.967	0.864	0.17	−41.28	19.00	12.79 ± 0.02	11.75 ± 0.02	11.29 ± 0.02	0.93	1.10	*e*S	6269
17	J045129.31+451852.0	72.872	45.314	160.458	0.652	0.57	−35.96	17.04	12.86 ± 0.02	11.84 ± 0.02	11.31 ± 0.02	1.04	1.10	E/S0	—
18	J045028.01+443407.6	72.617	44.569	160.916	0.037	0.70	−74.56	15.98	12.74 ± 0.02	11.79 ± 0.02	11.32 ± 0.02	0.80	1.07	E/S0	—
19	J045156.57+445815.0	72.986	44.971	160.774	0.496	0.47	−12.60	14.73	12.79 ± 0.02	11.79 ± 0.02	11.33 ± 0.02	0.94	1.05	*e*S	—
20	J045251.94+444122.5	73.216	44.690	161.095	0.443	0.56	63.37	16.94	12.90 ± 0.02	11.92 ± 0.02	11.47 ± 0.02	0.85	1.07	*e*S	—
21	J045018.46+454152.2	72.577	45.698	160.031	0.738	0.27	24.97	12.06	13.08 ± 0.02	11.99 ± 0.02	11.49 ± 0.02	1.17	1.08	E/S0	—
22	J045324.45+451127.6	73.352	45.191	160.768	0.835	0.40	29.03	12.08	12.97 ± 0.02	11.93 ± 0.02	11.50 ± 0.02	0.98	1.05	E/S0	—
23	J044753.50+443250.9	71.973	44.547	160.638	−0.328	0.10	25.00	13.10	12.88 ± 0.04	11.87 ± 0.05	11.52 ± 0.06	0.84	1.00	E/S0	—
24	J044734.77+452912.6	71.895	45.487	159.885	0.237	0.41	50.35	8.87	13.14 ± 0.02	12.05 ± 0.02	11.56 ± 0.02	1.19	1.06	E/S0	—
25	J045332.55+453232.6	73.386	45.542	160.510	1.076	0.39	−23.08	14.16	13.09 ± 0.02	12.03 ± 0.02	11.56 ± 0.02	0.98	1.11	E/S0	—
26	J044639.43+454052.2	71.664	45.681	159.633	0.240	0.41	85.72	12.30	13.12 ± 0.02	12.08 ± 0.02	11.57 ± 0.02	1.25	1.01	E/S0	—
27	J044730.43+454548.7	71.877	45.764	159.666	0.406	0.20	47.01	10.49	13.14 ± 0.02	12.11 ± 0.02	11.62 ± 0.02	1.25	0.98	*e*S	—

Table 3.2 – Continued

ID no.	Unique ID	RA	Dec	ℓ	b	ϵ_K	ϕ_K	r_{K20}	J_{K20}	H_{K20}	K_{K20}	$E(B\text{-}V)$	J^o-K^o	Type	v_{rad}
	ZoA	deg	deg	deg	deg		deg	$''$	mag	mag	mag	mag	mag		km s^{-1}
(1)	(2)	(3)	(4)	(5)	(6)	(7)	(8)	(9)	(10)	(11)	(12)	(13)	(14)	(15)	(16)
28	J044953.41+451613.5	72.473	45.270	160.312	0.408	0.60	−60.00	15.10	13.33 ± 0.05	12.16 ± 0.04	11.71 ± 0.06	1.01	1.18	*e*S	—
29	J045032.79+445411.7	72.637	44.903	160.668	0.262	0.29	−10.36	12.04	13.26 ± 0.02	12.21 ± 0.02	11.71 ± 0.02	0.92	1.15	*e*S	—
30	J044940.04+451119.0	72.417	45.189	160.350	0.325	0.62	−10.81	13.76	13.23 ± 0.02	12.22 ± 0.02	11.72 ± 0.02	0.98	1.09	*e*S	—

[*] v_{opt}: Spinrad 1975
[×] v_{opt}: Spinrad 1975
[+] v_{opt} = 5150 (Takata et al. 1994)

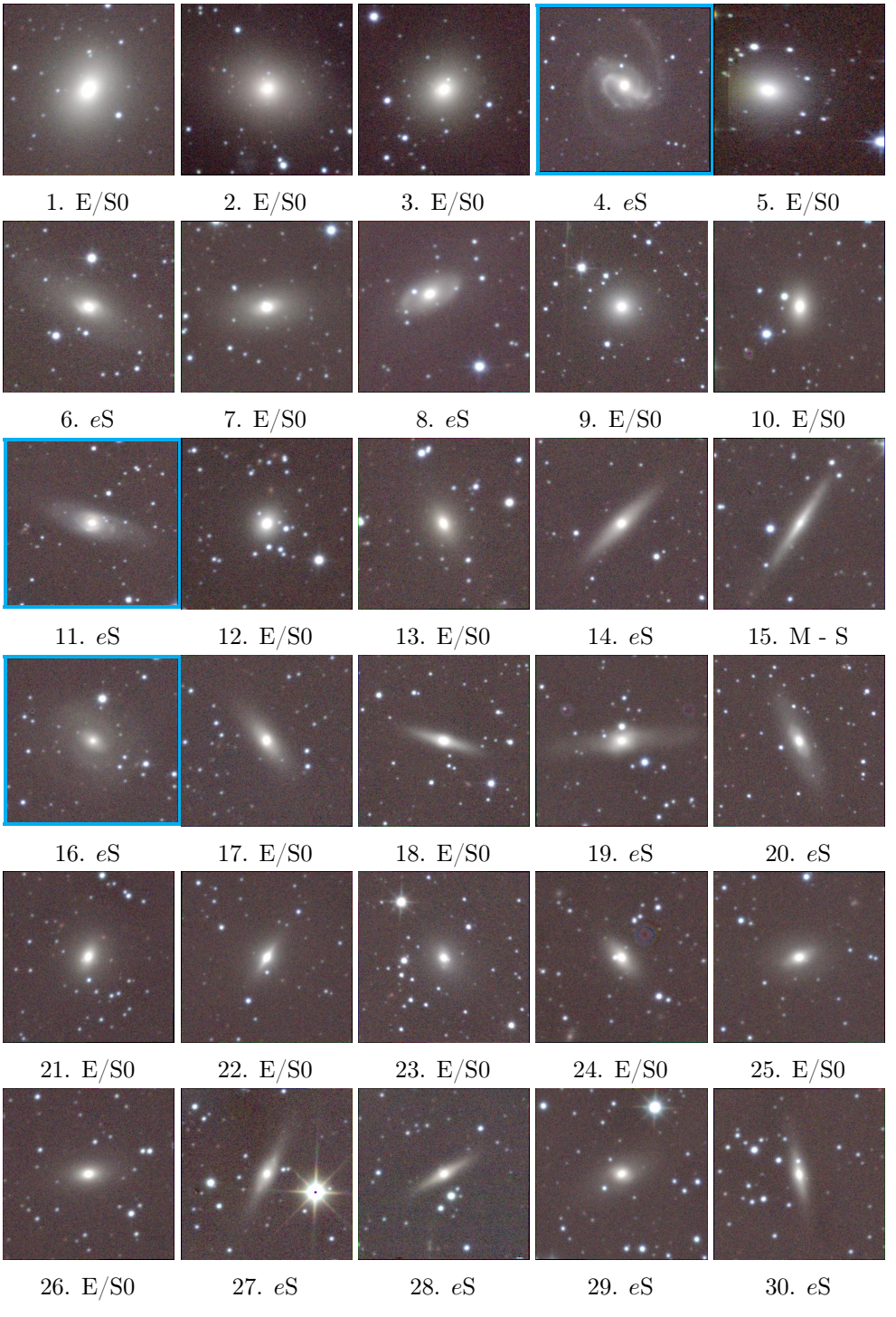

Figure 3.9 – The false-colour – J (blue), H (green) and K (red) representation ($1.2' \times 1.2'$) of the 30 brightest galaxies in the 3C 129 cluster. The cyan frames indicate HI detection in the WSRT HI-survey.

The 3C 129 cluster luminosity function

In this subsection we will assess the richness of the 3C 129 cluster based on the galaxy population identified in the UKIDSS-GPS images. We consider the 144 identified galaxies within the R_{500} radius of the cluster in order to make a fair comparison with the K-band luminosity functions (LF) of the well-studied, rich Coma and Norma galaxy clusters located at similar distances as the 3C 129 cluster. R_{500} is the radius at which the average interior density of the cluster is $500 \times \rho_c$, where ρ_c is the critical density of the Universe. For the 3C 129 cluster, $R_{500} = 0.87$ Mpc based on the ROSAT X-ray measurements in the $0.1 - 2.4$ keV bands (Piffaretti et al. 2011). We recall, however, that we lack spectroscopic redshifts for all but two of the early-type galaxies in the core of the 3C 129 cluster. Hence we cannot be certain that all galaxies we identify as cluster members are actually located in the cluster core.

We consider the fiducial, elliptical K-band aperture magnitudes, corrected for Galactic extinction. Figure 3.10 shows the distribution of these extinction corrected K^o-band magnitudes with a solid histogram while the dashed line shows the distribution of the non-corrected magnitudes. Based on our visual inspection of the UKIDSS-GPS images, we are confident that we have identified all galaxies brighter than $K \approx 15$ mag, corresponding to $K^o \approx 14.5$ mag. We refer to Table B and Fig. B for a visual impression of galaxies with these magnitudes.

The black symbols in Figure 3.11 show the inferred K^o-band LF of the 3C 129 cluster based on the number counts in 0.5 magnitude wide bins, normalised by the cluster's area within R_{500} (Mobasher et al. 2003). The error bars are derived from Poisson statistics while the open symbols indicate magnitude bins in which the number counts are estimated to be significantly affected by incompleteness. Given the severity and unknown small-scale patchiness of the Galactic extinction, we note that it is non-trivial to perform robust and quantitative completeness corrections. Therefore, we only consider the solid symbols in Figure 3.11 for our subsequent analysis.

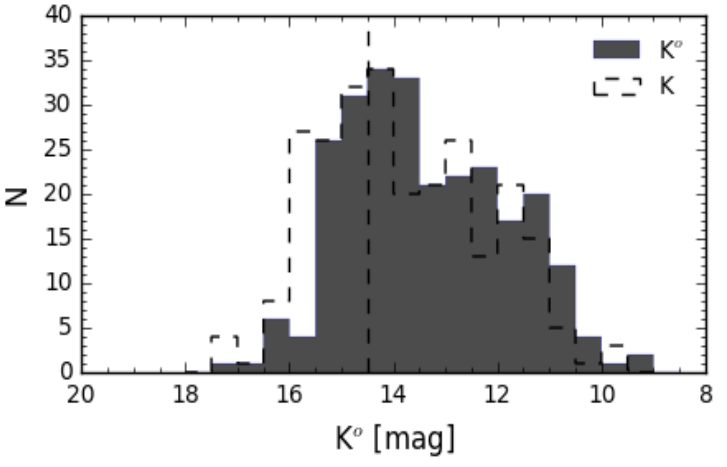

Figure 3.10 – Distribution of the fiducial isophotal magnitudes for the K-band. Histograms are plotted in 0.5 mag bins. The dashed histogram represents the observed magnitudes and the solid histogram the extinction-corrected magnitudes. The estimated completeness limit is shown by the vertical dashed line.

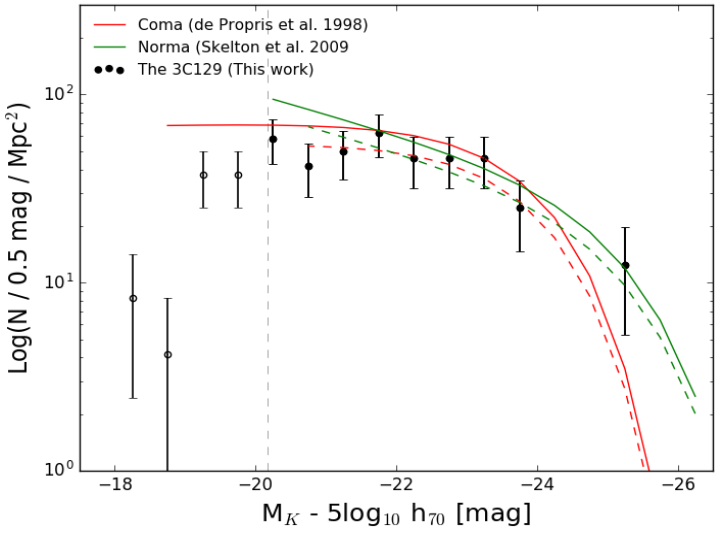

Figure 3.11 – Comparison of the K-band luminosity function per 0.5 mag bin of the 3C 129 cluster with two well known clusters at similar distances, the Norma (green) and Coma (red) clusters. The black points indicate the LF of the 3C 129 cluster out to an estimated completeness of $M_K \approx -20.2$ mag and open symbols are bins within which we expect to be incomplete. The dashed lines are the LF of the Coma (red) and Norma (green) clusters, normalised to the 3C 129 cluster.

The red solid line in Fig. 3.11 shows the K-band LF of the Coma cluster ($M_K^* = -24.0$ mag, $\alpha = -0.98$, $\phi^* = 76.0 \pm 3.0$ h$_{70}^2$ Mpc^{-2}) as derived by De Propris et al. (1998) while the green solid line indicates the K-band LF of the Norma cluster ($M_K^* = -25.4 \pm 0.8$ mag, $\alpha = -1.26 \pm 0.10$, $\phi^* = 27.8 \pm 2.4$ h$_{70}^2$ Mpc^{-2}) as derived by Skelton, Woudt & Kraan-Korteweg (2009). Note that the LF parameters of these two clusters are significantly different. We also refer to the result by De Propris (2017) who determined the average K-band LF for a sample of 24 galaxy clusters and found $M_K^* = -24.81 \pm 0.14$ mag and $\alpha = -1.41 \pm 0.10$, consistent with Skelton's result for the Norma cluster, while ϕ^* is not defined for this composite LF.

Here, we consider ϕ^* within R_{500} as a measure of a cluster's richness and a proxy for it's mass. We take the LF parameters for the Coma and Norma clusters, adopt and fix the corresponding values of M_K^* and α, and determine the value of ϕ^* by fitting these LFs to the solid black points in Fig.3.11. These fits are indicated by the dashed lines. This exercise resulted in values of $\phi^* = 59.4 \pm 6.3$ h$_{70}^2$ Mpc^{-2} for the Coma cluster and $\phi^* = 22.5 \pm 3.1$ h$_{70}^2$ Mpc^{-2} for the Norma cluster. This indicates that the galaxy density in the core of the 3C 129 cluster is similar to the central galaxy density in the Norma cluster and slightly less than in the Coma cluster. This finding is supported by the relative X-ray luminosities of the three clusters.

We did not conduct a detailed completeness analysis for the 3C 129 and are hampered by the lack of redshifts for the gas-poor galaxies. As a result no attempt was made to determine or fit a luminosity-function of the 3C 129 cluster.

Table 3.3 – A summary of parameters of comparison galaxy clusters.

Cluster	Distance	Lx$_{500}$	R$_{500}$	N	$M_{\rm Kcompl.}$
	Mpc	10^{44} erg s^{-1}	Mpc		mag
(1)	(2)	(3)	(4)	(5)	(6)
3C 129	89.1	0.9	0.87	144	-20.2 [1]
Norma	70.0	1.1	0.90	389	-19.5 [2]
Coma	98.9	3.4	1.14	649	-18.5 [3][1]

[1] This work
[2] Skelton, Woudt & Kraan-Korteweg 2009
[3] Eisenhardt et al. 2007

[1] This is an estimate, authors only list the H-band completeness limit

3.4 The Spatial Distribution of the 3C 129 Cluster Galaxies

The spatial distribution of all galaxies on our defined red-sequence is shown in Fig. 3.12. Members of the 3C 129 cluster are enclosed within the large dashed circle of radius of 1.7 Mpc centred on its X-ray emission ($\ell, b \approx 160.52°, 0.27°$). The smaller dotted circle encloses a prominent substructure to be discussed in Sect. 3.4.1. In this section we only discuss galaxies within the defined extent of the cluster (dashed circle).

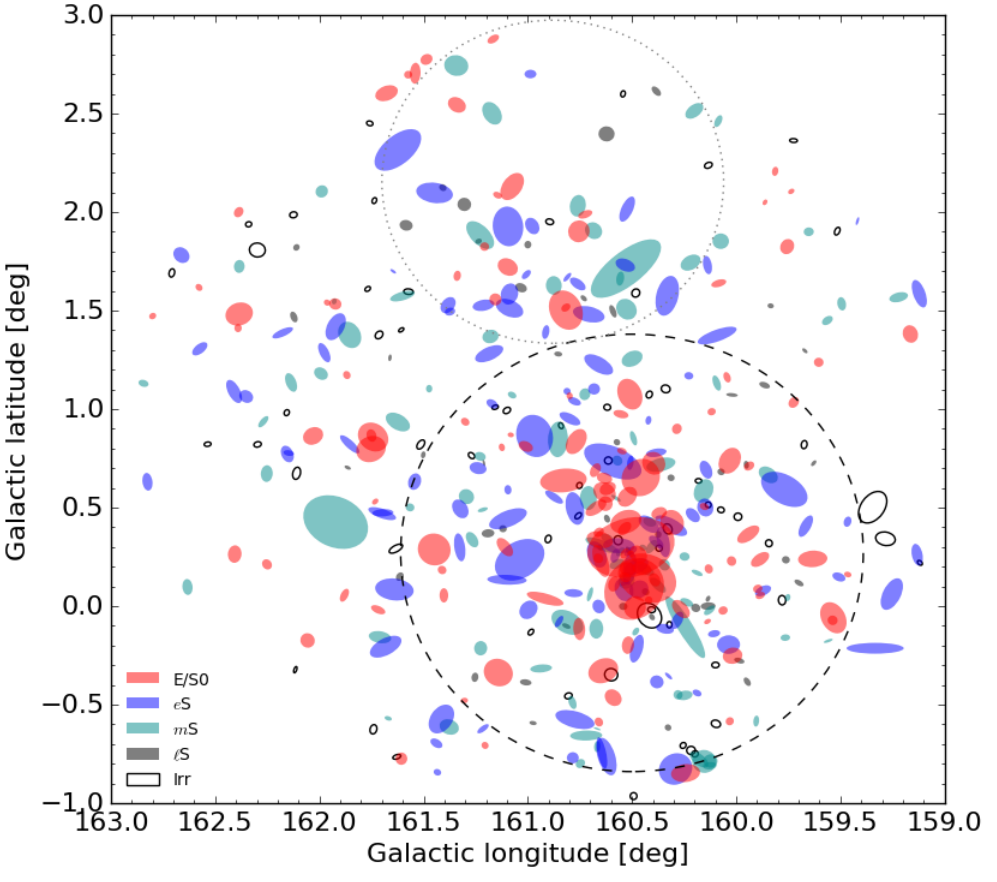

Figure 3.12 – The spatial distribution of galaxies on the red sequence. Points are shown relative to their radii, ellipticities and positions angles. The defined projected radius of the cluster, $r_{cl} = 1.7$ Mpc is shown by the black dashed line. The substructure of the cluster as described in Sect. 3.4.1 is denoted by the smaller dotted grey circle. The different colours illustrate the morphologies of the galaxies.

Galaxies within the inner region of the cluster of $r_{core} = 0.8$ Mpc, corresponding to its R_{500} (Piffaretti et al. 2011), are highly concentrated in the centre and are mostly early-type galaxies (E/S0). At larger projected radii the number of spirals (eS to Irr) increases steadily while the number of E/S0 galaxies decreases.

The spatial distribution in Fig. 3.12 is essentially a demonstration of the classical morphology-density relation (Dressler 1980). Most studies of the morphology-density (T - Σ) or morphology-radius (T - R) relation in galaxy clusters often use a composite of a large number of clusters to obtain an adequately high number of galaxies for each morphological type (Dressler 1980, Goto et al. 2003, Thomas & Katgert 2006). However, these composite (T - Σ) or (T - R) relations often lose information on the individual clusters. They also introduce large uncertainties given the large and sometimes inhomogeneous samples of clusters at different redshifts that are combined to make one cluster (Andreon 1996, van Dokkum et al. 2000).

To study the (T - R) relation specific to the 3C 129 cluster, we use a sample of all our classified galaxies (N=261). We show the results in Fig. 3.13 where the azimuthally averaged fractions of the morphological types are plotted as function of the projected distance from the core of the cluster to the outskirts. The fraction of E/S0 galaxies decreases from ∼36% in the core to almost 22% in the outskirts of the cluster. The early spirals (eS) fraction increases from 24% and peaks to 29% where the E/S0 population is lowest at $r_{cl} = 1.1$ Mpc and then decreases rapidly to 22% similar to the E/S0 fraction. On the other hand, ℓS and Irr galaxies show the opposite trend with an increasing fraction from the core towards the cluster outskirts. The morphology-radius relation of the 3C 129 cluster shows an obvious morphological segregation that is qualitatively consistent with those of the centrally concentrated rich clusters (Dressler et al. 1997).

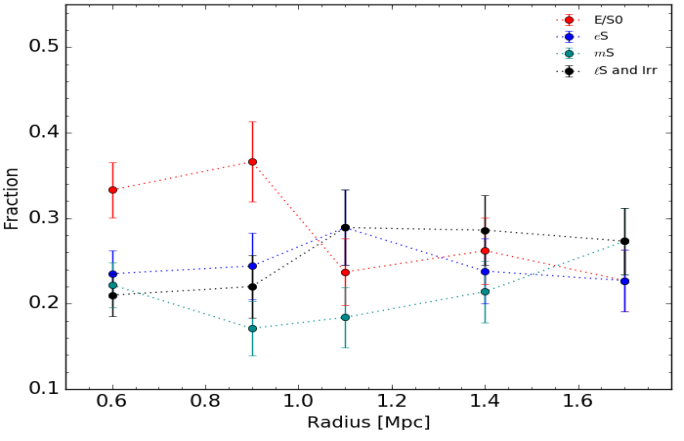

Figure 3.13 – The morphology-radius relation for the E/S0 (red), eS (blue), mS (darkcyan), ℓS & Irr (black) members of the cluster.

3.4.1 Substructure in the 3C 129 Cluster

Projected density distribution

To investigate the possible presence of substructure we analyse the projected galaxy number densities. Although this method ignores the redshift information it is optimal at identifying substructures with enhanced densities that are relatively large in separation (Pinkney et al. 1996). For the galaxies on the red sequence we study the projected galaxy number density using the bivariate kernel density estimator (Feigelson & Babu 2012),

$$f_{kern}(\mathbf{x},\mathbf{h}) = \frac{1}{n\prod_{j=1}^{p} h_j} \sum_{i=1}^{n} \left[\prod_{j=1}^{p} h_j Gk\left(\frac{\mathbf{x}_i - \mathbf{X}_{ij}}{h_{ij}}\right)\right] \tag{3.6}$$

where $p = 2$ is the number of variables, which are Galactic coordinates (ℓ, b) in our case represented by $\mathbf{X}_i = \mathbf{X}_{i1}, \mathbf{X}_{i2}$, with the smoothing length (bandwidth), $\mathbf{h} = (h_1, h_2)$. The number of galaxies is denoted by n and the bivariate Gaussian kernel function by Gk.

The resulting density map constructed with the red sequence galaxies is plotted in Fig. 3.14. It shows a distribution that is slightly elongated North-East to South-West in Galactic coordinates. This is possibly related to an intrinsically more elongated mass distribution of the large-scale filamentary structure (PPS) within which this cluster is embedded. Upon closer inspection two distinct structures become apparent. A dom-

inant density peak corresponds to the 3C 129 cluster centre, located at $(\ell, b) \approx (160.52°, 0.27°)$. The other, a more diffuse density peak about 2.9 Mpc (assuming $z = 0.02$) north from the cluster core located near $(\ell, b) \approx (160.88°, 2.20°)$, indicates a substructure, henceforth called the 3C129-A group.

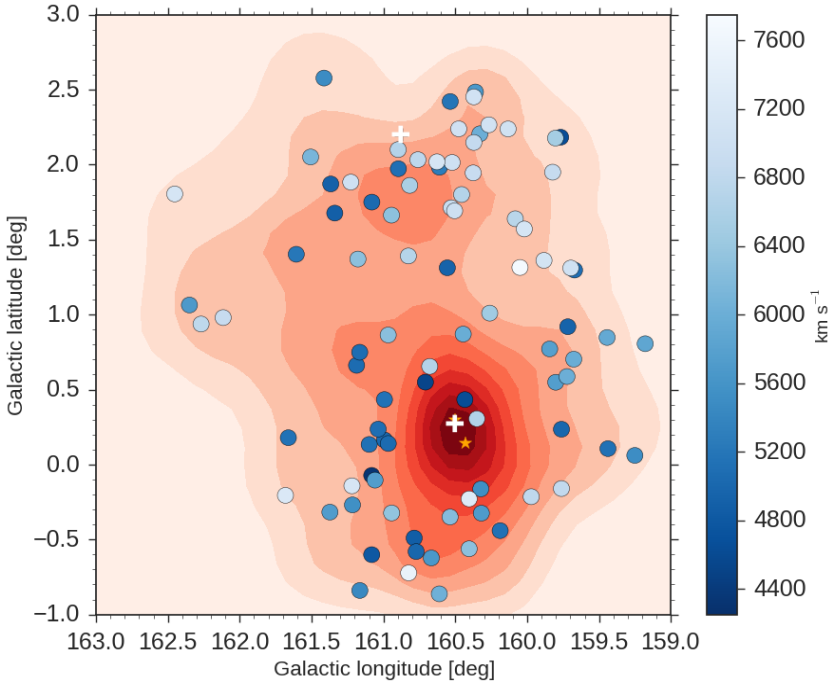

Figure 3.14 – The 2-dimensional kernel density map of galaxies on the red-sequence (red) in position space. Dots in gradient blues are galaxies detected in HI over the radial velocity range of the 3C 129 cluster (4000 - 8000 km s^{-1}). The displayed colour bar is the velocity range of the HI galaxies. The two white plus markers indicate the position of the X-ray emission over which the cluster is centred and the location near which the 3C129-A group lies.

A comparison with the X-ray emission map in Fig. 3.1 reveals that the core of the cluster is closely aligned with the X-ray gas emission. The X-ray contours are irregular and are not associated with any X-ray point source in the cluster. Thus supporting what was inferred by Leahy & Yin (2000) that 3C 129 cluster is under assembly through a merger and it is possibly growing along the filament.

Furthermore, we compared this galaxy projected density distribution with the spatial distribution of galaxies detected in H I in the velocity range of the cluster, marked by gradient blue dots. The latter shows the 3C129-A group to be more populated by H I-rich galaxies and also shows galaxies to have distinctly higher velocities than those around the core of the 3C 129 cluster. Furthermore, a relatively smaller number of H I detections was found in the core of the cluster, thus indicative of a gas removal mechanism taking place in this region. The implication of this is beyond the scope of this paper and will be discussed in detail in a paper that follows where we will be analysing the environmental effects on the H I properties of the galaxies.

Velocity Distribution

Having established the existence of the projected 3C129-A substructure in association with the 3C 129 cluster, we now investigate the radial velocity distribution of their constituent galaxies. We do this by using the 87 galaxies with measured H I radial velocities within the velocity range of the cluster's parent supercluster (PPS) of 4000 - 8000 km s^{-1} with and without a NIR-counterpart (Ramatsoku et al. 2016). A visual inspection of Fig. 3.14 indicates a bimodal velocity distribution of the H I detections. To check whether the velocity distribution is indeed statistically different from a Gaussian distribution we applied a Lilliefors test (see Feigelson & Babu 2012). The resulting p-value is $p < 0.01$ which indicates that the null hypothesis, which states that the full distribution is Gaussian, can be rejected, thus consistent with the presence of substructure in the radial velocity distribution.

We estimate the mean radial velocities of the two structures by selecting 43 H I-detected galaxies within a radius of 1.1° centred on the cluster's centre, and 44 within a radius of 0.8° centred on the 3C129-A group (see Fig. 3.12). The latter's radius was chosen to be as large as possible while maintaining mutual exclusivity with the 3C 129 cluster. The velocity distributions of the galaxies selected in the two structures are shown in Fig. 3.15. We fit two Gaussian profiles and obtained $cz = 5227 \pm 171$ km $s^{-1}$and $\sigma = 1097 \pm 252$ km s^{-1} for the 3C 129 cluster and $cz = 6923 \pm 71$ km s^{-1} and $\sigma = 422 \pm 100$ km s^{-1} for the 3C129-A group. We note that the velocity dispersion of the cluster is higher than that which was determined from the β-model of the cluster of $\sigma = 765$ km s^{-1} (Leahy & Yin 2000) but also note that our measurement is subject to large

uncertainties given the lack of optical spectroscopy for gas-poor galaxies in the cluster core.

Combining the results from the velocity and density distribution analysis we find a distinct substructure to the north of the 3C 129 cluster with higher velocity and more gas-rich spirals. Although the line-of-sight velocity difference of $cz_{gr} - cz_{cl} = 1696 \pm 185$ km s^{-1} is quite large, it is possible that the 3C129-A group is falling into the cluster. However, our sample is not large enough for a robust dynamical analysis to confirm this. A more detailed analysis can only be conducted with more redshifts of the gas-poor galaxies in the cluster and the immediate surrounding regions.

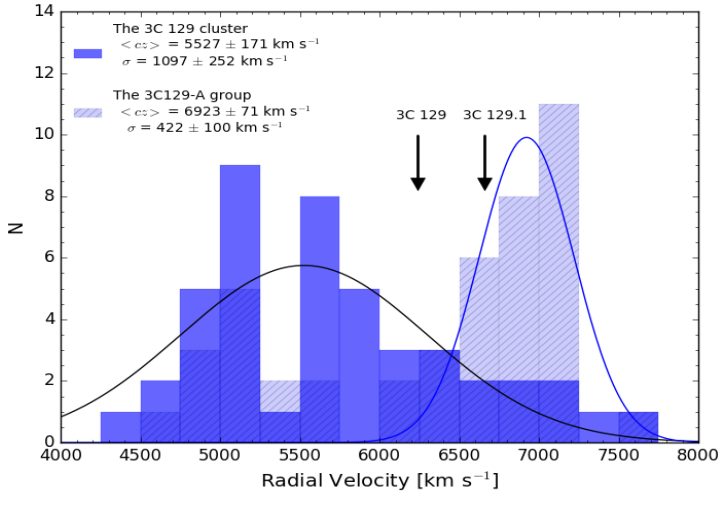

Figure 3.15 – The distribution of radial velocities of the 3C 129 cluster (dark blue) and its northern substructure; 3C 129-A (hatched light blue). Velocities bins are 250 km s^{-1} wide. The black line is a fitted Gaussian profile of the 3C 129 cluster and blue line for the 3C 129-A group. The radial velocities of the radio sources, 3C 129 and 3C 129.1 are indicated by arrows.

3.5 Summary and Discussions

We combined near-infrared images and colours from the UKIDSS Galactic Plane Survey with HI data from the Westerbork Synthesis Radio Telescope, in and around the 3C 129 cluster to identify its galaxy members. This was done by analysing the properties of the $J-K$ versus K magnitude of galaxies to define and fit the red-sequence of this cluster. The slope of its red sequence was found to be $\alpha = -0.023 \pm 0.002$ mag, similar to the Coma cluster ($\alpha = -0.017 \pm 0.009$). We determined the extent of the cluster, centred on the X-ray emission, out to a radius of 1.7 Mpc ($1.34R_{200}$). We obtained a sample of 261 identified 3C 129 cluster galaxies with $r_{k_{20}} > 3''$. Of these, 26 have redshift measurements, 23 from our WSRT HI observations and 3 from previous optical observations. A catalogue and colour images of the galaxy cluster members is presented.

The galaxies within the radius of 3C 129 cluster (1.7 Mpc) were used to present the cluster's luminosity function in the K-band. We compared this luminosity function with those of two well-known clusters at a similar redshift of $z \approx 0.02$, namely the Coma and Norma clusters. Results show that the galaxy density at the core of the 3C 129 cluster is comparable to that of the Norma cluster and slightly less than in the Coma cluster. This would place the 3C 129 cluster among the richest clusters in the Perseus-Pisces filament.

Using the high resolution ($0.8''$ seeing) UKIDSS images, we determined the broad morphologies of all the 261 cluster galaxies. We used the former to derive the morphology-radius relation of the cluster. A clear morphological segregation occurs at 0.6 - 0.9 Mpc from the cluster core, where the fraction of early-type galaxies increases inwards to more than 35%, while the fraction of late-type galaxies drops to about 16%. The segregation continues toward the cluster outskirts where the fraction of early-type galaxies drops to 22% and the fraction of late-types increases to almost 30%. A forthcoming study will assess how the environment may have affected the morphologies of these galaxies.

The spatial distribution of the galaxies in the 3C 129 cluster core shows a slight asymmetry and are aligned with the irregular X-ray emission that is not associated with any X-ray point source or any galaxy in the cluster. All these observations suggests that the system is non-Xray dominant (nXD) (Jones & Forman 1984). So the 3C 129 cluster could be

classified as an irregular nXD galaxy cluster. These features strengthen claims by Leahy & Yin (2000) that the cluster has undergone (or is undergoing) a merger and has not yet reached a dynamically relaxed state. This is supported by the identification of a substructure to the North of the main central region with a radial velocity distribution of $cz = 6923 \pm 71$ km s^{-1} and $\sigma = 422 \pm 100$ km s^{-1}, while the H I-detected galaxies around cluster core were measured to have, $cz = 5227 \pm 171$ km s^{-1} with $\sigma = 1097 \pm 252$ km s^{-1}. We suspect this substructure is infalling, which suggests the cluster is still growing by accreting from its parent large-scale structure that forms the Perseus-Pisces filament, which will have implications on the flow-fields around it and the larger PPS. However, this remains unconfirmed as more galaxy redshifts of the non H I-detected galaxies are required to conduct a detailed dynamical analysis of this cluster.

Acknowledgments

MR acknowledges financial support from the Ubbo Emmius Fund of the University of Groningen and the financial support provided by SKA South-Africa and the South African National Research Foundation. The SA and NL authors of this collaboration all benefitted tremendously from collaborative exchanges support by the NRF/NWO bilateral agreement for Astronomy and Astronomy Enabling Technologies. We would also like to thank W. Williams for the photometric contributions to the project. This research has also made use of the UKIRT Infrared Deep Sky Survey database. We acknowledge the UKIDSS support team, including M. Reads, S Hodgkin and P. Lucas for their various support on assessing the UKIDSS images. This work is part of MV's Vici research programme "The Panoramic Perspective on Gas and Galaxy Evolution" with project number 016.130.338, which is (partly) financed by the Netherlands Organisation for Scientific Research (NWO).

Appendix

3

Appendix B: The NIR Catalogue and Images

The near-infrared catalogue has the following columns:

Column 1 - The galaxy identifying number.

Column 2- Unique identifiers based on the Right Ascension (RA) and Declination (Dec) ZoAJhhmmss.ss±ddmmss.s.

Columns 3 & 4 - Equatorial coordinates, RA and Dec (J2000), respectively in degrees.

Columns 5 & 6 - Galactic longitude and latitude in degrees.

Column 7 - Ellipticity in the K-band at the 20 mag arcsec^{-2} isophote.

Column 8 - The K-band position angle in degrees, measured from celestial North to East.

Column 9 - The K_{20} isophotal major-axis radius in arcseconds.

Columns 10 & 11 & 12 - J, H and K band fiducial isophotal magnitudes (not corrected for foreground extinction).

Column 13 - The line of sight Galactic reddening in magnitudes.

Column 14 - $J - K$ colours, corrected for foreground extinction.

Column 15 - The estimated morphology of galaxies.

Column 16 - The radial velocities from the WSRT HI measurements plus optical velocities for the two galaxies 3C 129 and 3C 129.1.

Table B. Near−infrared parameters of the 3C 129 cluster galaxies.

ID no.	Unique ID	RA	Dec	ℓ	b	ϵ_K	ϕ_K	r_{K20}	J_{K20}	H_{K20}	K_{20}	$E(B\text{-}V)$	$J^o - K^o$	Type	v_{rad}
	ZoA	deg	deg	deg	deg		deg	$''$	mag	mag	mag	mag	mag		km s^{-1}
(1)	(2)	(3)	(4)	(5)	(6)	(7)	(8)	(9)	(10)	(11)	(12)	(13)	(14)	(15)	(16)
1	J044908.26+445540.3	72.284	44.928	160.490	0.086	0.17	24.71	28.10	10.96 ± 0.02	9.94 ± 0.02	9.51 ± 0.02	0.89	1.07	E/S0	—
2	J045006.67+450305.8	72.528	45.052	160.505	0.298	0.20	65.00	37.30	11.21 ± 0.04	10.10 ± 0.04	9.59 ± 0.04	0.98	1.20	E/S0	6655*
3	J044909.06+450039.4	72.288	45.011	160.427	0.142	0.10	−60.00	25.60	11.50 ± 0.03	10.46 ± 0.04	10.00 ± 0.04	0.94	1.10	E/S0	6236×
4	J045145.56+443602.6	72.940	44.601	161.039	0.235	0.40	60.00	22.80	11.75 ± 0.03	10.82 ± 0.03	10.35 ± 0.04	0.79	1.07	*e*S	5086+
5	J044939.78+440922.1	72.416	44.156	161.141	−0.337	0.09	−55.01	12.79	12.05 ± 0.02	11.16 ± 0.02	10.76 ± 0.02	0.65	1.01	E/S0	—
6	J044842.39+454818.5	72.177	45.805	159.769	0.593	0.40	−61.15	21.62	12.25 ± 0.02	11.23 ± 0.02	10.77 ± 0.02	1.12	1.00	*e*S	—
7	J045245.69+450106.2	73.190	45.018	160.829	0.638	0.44	85.11	19.63	12.31 ± 0.02	11.23 ± 0.02	10.78 ± 0.02	0.94	1.12	E/S0	—
8	J045219.88+451546.1	73.083	45.263	160.592	0.734	0.50	−60.00	25.90	12.23 ± 0.05	11.26 ± 0.05	10.83 ± 0.06	0.91	1.00	*e*S	—
9	J045326.75+441900.7	73.361	44.317	161.449	0.288	0.06	26.77	14.31	12.32 ± 0.02	11.38 ± 0.02	10.96 ± 0.02	0.69	1.06	E/S0	—
10	J045045.92+450659.7	72.691	45.117	160.529	0.428	0.27	0.36	13.39	12.62 ± 0.02	11.56 ± 0.02	11.05 ± 0.02	1.00	1.14	E/S0	—
11	J044719.31+441701.6	71.830	44.284	160.774	−0.576	0.47	−73.54	16.96	12.50 ± 0.02	11.56 ± 0.02	11.06 ± 0.02	0.69	1.15	*e*S	4993
12	J044843.25+445216.0	72.180	44.871	160.486	−0.007	0.11	32.33	9.98	12.54 ± 0.02	11.54 ± 0.02	11.11 ± 0.02	0.84	1.07	E/S0	—
13	J044459.45+453344.1	71.248	45.562	159.534	−0.059	0.30	−23.53	14.62	12.83 ± 0.02	11.73 ± 0.02	11.19 ± 0.02	1.35	1.06	E/S0	—
14	J044429.89+442914.8	71.125	44.487	160.291	−0.827	0.31	44.80	14.65	12.81 ± 0.02	11.78 ± 0.02	11.23 ± 0.02	0.98	1.16	*e*S	—
15	J044724.21+445928.3	71.851	44.991	160.244	−0.107	0.80	−35.00	31.50	12.64 ± 0.05	11.67 ± 0.05	11.25 ± 0.07	0.84	1.03	*m*S	—
16	J045414.90+450315.1	73.562	45.054	160.967	0.864	0.17	−41.28	19.00	12.79 ± 0.02	11.75 ± 0.02	11.29 ± 0.02	0.93	1.10	*e*S	6269
17	J045129.31+451852.0	72.872	45.314	160.458	0.652	0.57	−35.96	17.04	12.86 ± 0.02	11.84 ± 0.02	11.31 ± 0.02	1.04	1.10	E/S0	—
18	J045028.01+443407.6	72.617	44.569	160.916	0.037	0.70	−74.56	15.98	12.74 ± 0.02	11.79 ± 0.02	11.32 ± 0.02	0.80	1.07	E/S0	—
19	J045156.57+445815.0	72.986	44.971	160.774	0.496	0.47	−12.60	14.73	12.79 ± 0.02	11.79 ± 0.02	11.33 ± 0.02	0.94	1.05	*e*S	—
20	J045251.94+444122.5	73.216	44.690	161.095	0.443	0.56	63.37	16.94	12.90 ± 0.02	11.92 ± 0.02	11.47 ± 0.02	0.85	1.07	*e*S	—
21	J045018.46+454152.2	72.577	45.698	160.031	0.738	0.27	24.97	12.06	13.08 ± 0.02	11.99 ± 0.02	11.49 ± 0.02	1.17	1.08	E/S0	—
22	J045324.45+451127.6	73.352	45.191	160.768	0.835	0.40	29.03	12.08	12.97 ± 0.02	11.93 ± 0.02	11.50 ± 0.02	0.98	1.05	E/S0	—
23	J044753.50+443250.9	71.973	44.547	160.638	−0.328	0.10	25.00	13.10	12.88 ± 0.04	11.87 ± 0.05	11.52 ± 0.06	0.84	1.00	E/S0	—
24	J044734.77+452912.6	71.895	45.487	159.885	0.237	0.41	50.35	8.87	13.14 ± 0.02	12.05 ± 0.02	11.56 ± 0.02	1.19	1.06	E/S0	—
25	J045332.55+453232.6	73.386	45.542	160.510	1.076	0.39	−23.08	14.16	13.09 ± 0.02	12.03 ± 0.02	11.56 ± 0.02	0.98	1.11	E/S0	—

[*] v_{opt}: Spinrad 1975
[×] v_{opt}: Spinrad 1975
[+] v_{opt} = 5150 (Takata et al. 1994)

Table B – Continued

ID no.	Unique ID	RA	Dec	ℓ	b	ϵ_K	ϕ_K	r_{K20}	J_{K20}	H_{K20}	K_{K20}	$E(B\text{-}V)$	J^o-K^o	Type	v_{rad}
	ZoA	deg	deg	deg	deg		deg	$''$	mag	mag	mag	mag	mag		km s^{-1}
(1)	(2)	(3)	(4)	(5)	(6)	(7)	(8)	(9)	(10)	(11)	(12)	(13)	(14)	(15)	(16)
26	J044639.43+454052.2	71.664	45.681	159.633	0.240	0.41	85.72	12.30	13.12 ± 0.02	12.08 ± 0.02	11.57 ± 0.02	1.25	1.01	E/S0	—
27	J044730.43+454548.7	71.877	45.764	159.666	0.406	0.20	47.01	10.49	13.14 ± 0.02	12.11 ± 0.02	11.62 ± 0.02	1.25	0.98	eS	—
28	J044953.41+451613.5	72.473	45.270	160.312	0.408	0.60	−60.00	15.10	13.33 ± 0.05	12.16 ± 0.04	11.71 ± 0.06	1.01	1.18	eS	—
29	J045032.79+445411.7	72.637	44.903	160.668	0.262	0.29	−10.36	12.04	13.26 ± 0.02	12.21 ± 0.02	11.71 ± 0.02	0.92	1.15	eS	—
30	J044940.04+451119.0	72.417	45.189	160.350	0.325	0.62	−10.81	13.76	13.23 ± 0.02	12.22 ± 0.02	11.72 ± 0.02	0.98	1.09	eS	—
31	J045020.02+445348.1	72.583	44.897	160.649	0.229	0.58	−15.99	14.81	13.20 ± 0.02	12.22 ± 0.02	11.73 ± 0.02	0.95	1.06	E/S0	—
32	J045049.32+445742.3	72.706	44.962	160.655	0.337	0.36	−76.66	11.22	13.28 ± 0.02	12.26 ± 0.02	11.80 ± 0.02	0.91	1.09	E/S0	—
33	J045346.20+450747.8	73.443	45.130	160.855	0.846	0.41	7.89	15.79	13.31 ± 0.02	12.22 ± 0.02	11.80 ± 0.02	0.96	1.09	mS	—
34	J044414.05+443036.7	71.059	44.510	160.243	−0.848	0.39	28.13	12.21	13.30 ± 0.02	12.30 ± 0.02	11.81 ± 0.02	1.01	1.05	E/S0	—
35	J045147.22+450757.0	72.947	45.133	160.632	0.577	0.17	−44.96	10.23	13.21 ± 0.02	12.24 ± 0.02	11.81 ± 0.02	0.95	0.98	E/S0	—
36	J045117.73+451208.6	72.824	45.202	160.523	0.555	0.25	35.05	9.63	13.37 ± 0.02	12.35 ± 0.02	11.82 ± 0.02	1.01	1.12	E/S0	—
37	J045132.32+442920.1	72.885	44.489	161.100	0.133	0.73	−87.70	16.54	13.36 ± 0.02	12.43 ± 0.02	11.85 ± 0.02	0.76	1.18	eS	5129
38	J044918.07+445318.3	72.325	44.888	160.538	0.083	0.21	−18.37	10.40	13.23 ± 0.02	12.26 ± 0.02	11.86 ± 0.02	0.90	0.98	eS	—
39	J044941.69+452719.7	72.424	45.455	160.148	0.500	0.18	−13.54	8.04	13.42 ± 0.02	12.42 ± 0.02	11.86 ± 0.02	1.04	1.11	eS	—
40	J045021.54+450047.4	72.590	45.013	160.563	0.307	0.53	−84.10	13.27	13.43 ± 0.02	12.39 ± 0.02	11.90 ± 0.02	0.98	1.10	eS	—
41	J044558.57+441637.7	71.494	44.277	160.623	−0.764	0.55	−11.81	17.24	13.30 ± 0.02	12.31 ± 0.02	11.91 ± 0.02	0.85	1.03	eS	—
42	J045135.55+450302.9	72.898	45.051	160.673	0.499	0.50	54.65	10.20	13.39 ± 0.02	12.43 ± 0.02	11.95 ± 0.02	0.95	1.03	E/S0	—
43	J044913.04+443545.2	72.304	44.596	160.753	−0.116	0.48	4.20	9.99	13.45 ± 0.02	12.55 ± 0.02	12.14 ± 0.02	0.78	0.97	E/S0	—
44	J045005.82+453012.6	72.524	45.503	160.156	0.585	0.23	18.87	10.69	13.69 ± 0.02	12.72 ± 0.02	12.14 ± 0.02	1.09	1.08	mS	—
45	J044940.15+445844.4	72.417	44.979	160.511	0.191	0.64	7.97	14.62	13.63 ± 0.02	12.63 ± 0.02	12.17 ± 0.02	0.94	1.05	eS	—
46	J045134.83+452431.0	72.895	45.409	160.395	0.725	0.12	−70.79	10.37	13.68 ± 0.02	12.66 ± 0.02	12.18 ± 0.02	1.05	1.05	E/S0	—
47	J045217.59+443511.6	73.073	44.587	161.110	0.299	0.46	−36.63	9.46	13.53 ± 0.02	12.62 ± 0.02	12.19 ± 0.02	0.76	1.02	E/S0	—
48	J044747.17+444434.0	71.947	44.743	160.477	−0.216	0.50	10.00	12.70	13.59 ± 0.05	12.61 ± 0.06	12.20 ± 0.07	0.88	1.01	eS	—
49	J044935.63+450035.3	72.398	45.010	160.479	0.201	0.40	60.58	10.79	13.67 ± 0.02	12.65 ± 0.02	12.21 ± 0.02	0.95	1.05	eS	—
50	J044956.71+451705.5	72.486	45.285	160.307	0.425	0.17	56.59	11.24	13.81 ± 0.02	12.71 ± 0.02	12.26 ± 0.02	1.04	1.10	E/S0	—
51	J045018.81+451136.0	72.578	45.193	160.419	0.416	0.47	−47.84	10.04	13.83 ± 0.02	12.79 ± 0.02	12.28 ± 0.02	1.02	1.11	eS	—
52	J044557.04+450410.9	71.488	45.070	160.017	−0.252	0.09	−21.67	8.27	13.78 ± 0.02	12.78 ± 0.02	12.35 ± 0.02	0.98	1.01	E/S0	—
53	J044820.62+453134.0	72.086	45.526	159.942	0.364	0.51	53.15	10.89	13.84 ± 0.02	12.83 ± 0.02	12.38 ± 0.02	1.04	1.01	E/S0	—
54	J044608.05+441621.5	71.534	44.273	160.644	−0.745	0.75	−11.80	14.15	13.93 ± 0.02	12.96 ± 0.02	12.48 ± 0.02	0.84	1.09	eS	—
55	J045303.58+442506.5	73.265	44.418	161.327	0.298	0.68	−3.61	12.52	13.80 ± 0.02	12.92 ± 0.02	12.50 ± 0.02	0.78	0.97	eS	—
56	J044934.14+443426.7	72.392	44.574	160.810	−0.082	0.44	35.56	14.58	13.84 ± 0.02	12.91 ± 0.02	12.52 ± 0.02	0.76	0.99	mS	—

Table B – Continued

ID no.	Unique ID	RA	Dec	ℓ	b	ϵ_K	ϕ_K	r_{K20}	J_{K20}	H_{K20}	K_{K20}	$E(B\text{-}V)$	J^o-K^o	Type	v_{rad}
	ZoA	deg	deg	deg	deg		deg	$''$	mag	mag	mag	mag	mag		km s^{-1}
(1)	(2)	(3)	(4)	(5)	(6)	(7)	(8)	(9)	(10)	(11)	(12)	(13)	(14)	(15)	(16)
57	J045038.23+450521.6	72.659	45.089	160.535	0.393	0.36	47.90	6.84	14.07 ± 0.02	13.09 ± 0.02	12.54 ± 0.02	1.00	1.10	E/S0	—
58	J045125.48+452551.4	72.856	45.431	160.361	0.718	0.52	79.07	12.39	14.08 ± 0.02	13.04 ± 0.02	12.54 ± 0.02	1.09	1.06	mS	—
59	J044949.59+450319.7	72.457	45.055	160.470	0.262	0.20	−30.00	8.50	14.07 ± 0.07	13.03 ± 0.06	12.57 ± 0.08	0.96	1.08	E/S0	—
60	J045401.51+451426.6	73.506	45.241	160.798	0.951	0.55	−61.16	9.67	14.01 ± 0.02	13.01 ± 0.02	12.57 ± 0.02	0.98	1.02	eS	—
61	J045444.87+453116.6	73.687	45.521	160.660	1.226	0.50	51.50	13.71	13.94 ± 0.02	12.98 ± 0.02	12.57 ± 0.02	0.80	1.02	eS	—
62	J045233.08+445548.6	73.138	44.930	160.874	0.553	0.63	−57.68	8.91	14.06 ± 0.02	13.08 ± 0.02	12.59 ± 0.02	0.94	1.07	eS	—
63	J044646.93+441620.4	71.696	44.272	160.720	−0.657	0.61	−84.87	13.48	13.94 ± 0.02	12.99 ± 0.02	12.60 ± 0.02	0.74	1.01	mS	—
64	J044801.07+444319.3	72.004	44.722	160.519	−0.198	0.26	24.21	7.83	14.05 ± 0.02	13.08 ± 0.02	12.64 ± 0.02	0.86	1.04	E/S0	—
65	J045040.23+445701.0	72.668	44.950	160.646	0.309	0.70	−67.23	14.57	14.07 ± 0.02	13.09 ± 0.02	12.68 ± 0.02	0.92	0.99	mS	—
66	J044409.43+443700.4	71.039	44.617	160.153	−0.788	0.40	−51.65	10.30	14.22 ± 0.02	13.18 ± 0.02	12.70 ± 0.02	1.09	1.06	mS	—
67	J044902.91+445639.9	72.262	44.944	160.467	0.085	0.07	−89.11	8.41	14.11 ± 0.02	13.16 ± 0.02	12.70 ± 0.02	0.90	1.03	eS	—
68	J044927.08+450121.8	72.363	45.023	160.452	0.190	0.29	−83.90	7.96	14.22 ± 0.02	13.18 ± 0.02	12.73 ± 0.02	0.95	1.08	E/S0	—
69	J045429.83+444425.9	73.624	44.741	161.239	0.700	0.38	−74.39	7.18	14.23 ± 0.02	13.23 ± 0.02	12.75 ± 0.02	0.87	1.10	eS	—
70	J045156.51+450314.5	72.985	45.054	160.710	0.548	0.40	30.50	10.67	14.16 ± 0.02	13.23 ± 0.02	12.80 ± 0.02	0.94	0.96	mS	4523
71	J044642.74+444225.2	71.678	44.707	160.381	−0.385	0.02	−69.65	5.85	14.25 ± 0.02	13.26 ± 0.02	12.80 ± 0.02	0.92	1.06	eS	—
72	J045031.44+453451.2	72.631	45.581	160.145	0.692	0.43	−20.20	8.32	14.37 ± 0.02	13.35 ± 0.02	12.86 ± 0.02	1.20	0.99	eS	—
73	J044741.94+445903.4	71.925	44.984	160.282	−0.072	0.36	17.96	8.27	14.24 ± 0.02	13.30 ± 0.02	12.87 ± 0.02	0.86	1.01	eS	—
74	J045030.71+442816.0	72.628	44.471	160.997	−0.019	0.35	45.97	8.77	14.15 ± 0.02	13.25 ± 0.02	12.87 ± 0.02	0.79	0.94	eS	—
75	J045149.06+450924.8	72.954	45.157	160.616	0.597	0.22	44.85	7.22	14.29 ± 0.02	13.33 ± 0.02	12.87 ± 0.02	0.93	1.03	E/S0	—
76	J044615.88+450530.3	71.566	45.092	160.036	−0.195	0.65	62.54	9.64	14.26 ± 0.02	13.44 ± 0.02	12.91 ± 0.02	0.94	0.94	eS	—
77	J044752.80+450202.3	71.970	45.034	160.265	−0.015	0.40	−40.00	9.50	14.26 ± 0.08	13.35 ± 0.08	12.91 ± 0.09	0.86	0.98	E/S0	—
78	J045005.99+444129.8	72.525	44.692	160.780	0.066	0.57	−84.01	7.73	14.31 ± 0.02	13.41 ± 0.02	12.97 ± 0.02	0.82	0.98	eS	—
79	J044707.90+442944.4	71.783	44.496	160.590	−0.465	0.10	−69.40	7.97	14.43 ± 0.02	13.54 ± 0.02	12.98 ± 0.02	0.78	1.11	E/S0	—
80	J044918.88+454737.1	72.329	45.794	159.846	0.666	0.21	−51.00	9.01	14.60 ± 0.02	13.56 ± 0.02	12.98 ± 0.02	1.14	1.12	mS	—
81	J045418.02+453951.7	73.575	45.664	160.499	1.255	0.39	49.59	9.30	14.35 ± 0.02	13.41 ± 0.02	13.00 ± 0.02	0.88	0.96	mS	—
82	J045353.83+443238.8	73.474	44.544	161.324	0.494	0.37	37.88	8.88	14.45 ± 0.02	13.51 ± 0.02	13.02 ± 0.02	0.85	1.07	eS	—
83	J045146.37+452706.8	72.943	45.452	160.384	0.778	0.59	79.33	8.71	14.54 ± 0.02	13.53 ± 0.02	13.04 ± 0.02	1.13	1.01	eS	—
84	J044520.92+454430.7	71.337	45.742	159.440	0.110	0.77	24.83	14.61	14.94 ± 0.02	13.68 ± 0.02	13.05 ± 0.02	1.28	1.33	mS	5134
85	J045206.26+451041.6	73.026	45.178	160.632	0.649	0.23	−75.26	6.58	14.51 ± 0.02	13.48 ± 0.02	13.05 ± 0.02	0.90	1.07	E/S0	—
86	J044859.13+450201.1	72.246	45.034	160.391	0.134	0.22	−23.15	6.11	14.55 ± 0.02	13.54 ± 0.02	13.06 ± 0.02	0.93	1.08	E/S0	—
87	J045022.58+451600.9	72.594	45.267	160.370	0.472	0.26	65.62	6.78	14.66 ± 0.02	13.54 ± 0.02	13.06 ± 0.02	1.03	1.16	E/S0	—

Table B – Continued

ID no.	Unique ID	RA	Dec	ℓ	b	ϵ_K	ϕ_K	r_{K20}	J_{K20}	H_{K20}	K_{K20}	$E(B\text{-}V)$	$J^o{-}K^o$	Type	v_{rad}
	ZoA	deg	deg	deg	deg		deg	$''$	mag	mag	mag	mag	mag		km s^{-1}
(1)	(2)	(3)	(4)	(5)	(6)	(7)	(8)	(9)	(10)	(11)	(12)	(13)	(14)	(15)	(16)
88	J044848.38+450140.8	72.202	45.028	160.375	0.106	0.48	−43.50	8.56	14.60 ± 0.02	13.54 ± 0.02	13.11 ± 0.02	0.90	1.09	mS	—
89	J044941.44+445807.9	72.423	44.969	160.521	0.188	0.21	−34.30	6.52	14.52 ± 0.02	13.55 ± 0.02	13.12 ± 0.02	0.94	1.00	E/S0	—
90	J044922.34+444427.2	72.343	44.741	160.660	−0.002	0.08	−15.60	6.15	14.55 ± 0.02	13.59 ± 0.02	13.17 ± 0.02	0.84	1.01	eS	—
91	J044812.49+450920.1	72.052	45.156	160.210	0.107	0.24	−45.33	7.28	14.60 ± 0.02	13.61 ± 0.02	13.20 ± 0.02	0.94	0.99	eS	—
92	J044743.67+445439.8	71.932	44.911	160.342	−0.115	0.41	−69.81	7.60	14.56 ± 0.02	13.68 ± 0.02	13.21 ± 0.02	0.84	0.98	eS	—
93	J045131.32+450558.1	72.880	45.099	160.627	0.520	0.03	−16.62	6.54	14.74 ± 0.02	13.72 ± 0.02	13.25 ± 0.02	0.95	1.07	E/S0	—
94	J044944.65+452304.9	72.436	45.385	160.208	0.462	0.37	−41.69	7.31	14.70 ± 0.02	13.70 ± 0.02	13.26 ± 0.02	1.06	0.99	eS	—
95	J044933.20+445558.6	72.388	44.933	160.533	0.146	0.10	−56.04	4.90	14.75 ± 0.02	13.76 ± 0.02	13.28 ± 0.02	0.94	1.06	E/S0	—
96	J044935.99+445213.7	72.400	44.870	160.586	0.112	0.24	2.46	6.83	14.75 ± 0.02	13.73 ± 0.02	13.30 ± 0.02	0.93	1.05	E/S0	—
97	J044943.68+443245.1	72.432	44.546	160.850	−0.078	0.16	−59.70	5.72	14.63 ± 0.02	13.73 ± 0.02	13.35 ± 0.02	0.75	0.97	eS	—
98	J045216.50+441218.2	73.069	44.205	161.403	0.055	0.27	−3.60	6.37	14.72 ± 0.02	13.77 ± 0.02	13.35 ± 0.02	0.63	1.10	E/S0	—
99	J044947.45+450944.5	72.448	45.162	160.384	0.325	0.43	−44.49	7.29	14.89 ± 0.02	13.88 ± 0.02	13.37 ± 0.02	0.98	1.10	eS	—
100	J044417.15+443615.4	71.071	44.604	160.178	−0.779	0.50	−50.00	9.40	14.98 ± 0.11	13.80 ± 0.09	13.46 ± 0.12	1.09	1.04	mS	—
101	J045226.36+451011.7	73.110	45.170	160.676	0.690	0.39	21.47	6.53	14.89 ± 0.02	13.93 ± 0.02	13.47 ± 0.02	0.87	1.05	E/S0	—
102	J045216.79+455402.2	73.070	45.901	160.093	1.132	0.52	−17.24	7.05	14.93 ± 0.02	13.96 ± 0.02	13.49 ± 0.02	1.02	1.00	mS	—
103	J045301.01+442921.2	73.254	44.489	161.267	0.337	0.39	34.50	7.43	14.92 ± 0.02	13.97 ± 0.02	13.50 ± 0.02	0.80	1.08	mS	—
104	J045314.91+452642.6	73.312	45.445	160.553	0.974	0.49	−74.74	6.44	14.98 ± 0.02	13.98 ± 0.02	13.54 ± 0.02	0.98	1.02	E/S0	—
105	J044650.13+452342.0	71.709	45.395	159.871	0.078	0.45	65.44	7.23	15.07 ± 0.02	14.04 ± 0.02	13.55 ± 0.02	1.13	1.03	eS	—
106	J045004.69+450036.1	72.520	45.010	160.533	0.267	0.34	31.33	4.94	15.09 ± 0.02	14.08 ± 0.02	13.57 ± 0.02	0.97	1.10	E/S0	—
107	J045100.26+445855.4	72.751	44.982	160.659	0.375	0.24	36.21	4.72	15.04 ± 0.02	14.05 ± 0.02	13.62 ± 0.02	0.91	1.03	E/S0	—
108	J044959.35+445647.7	72.497	44.947	160.572	0.214	0.33	−53.30	6.69	15.11 ± 0.02	14.13 ± 0.02	13.65 ± 0.02	0.97	1.04	mS	—
109	J045432.63+451846.8	73.636	45.313	160.799	1.067	0.16	−0.60	3.03	15.19 ± 0.02	14.23 ± 0.02	13.67 ± 0.02	0.90	1.14	E/S0	—
110	J045445.42+453911.3	73.689	45.653	160.560	1.310	0.48	−39.85	9.48	14.87 ± 0.02	14.01 ± 0.02	13.73 ± 0.03	0.84	0.77	mS	4941
111	J045143.42+454722.1	72.931	45.789	160.118	0.987	0.26	−66.54	3.51	15.37 ± 0.02	14.40 ± 0.02	13.77 ± 0.02	1.34	1.02	E/S0	—
112	J044900.93+441937.0	72.254	44.327	160.936	−0.316	0.69	−85.32	9.15	15.20 ± 0.02	14.27 ± 0.02	13.81 ± 0.03	0.64	1.11	mS	6332
113	J044555.95+444549.4	71.483	44.764	160.248	−0.453	0.24	70.62	6.78	15.19 ± 0.02	14.23 ± 0.02	13.81 ± 0.03	0.99	0.95	mS	—
114	J045403.78+443621.7	73.516	44.606	161.294	0.556	0.49	−43.64	6.81	15.12 ± 0.02	14.20 ± 0.02	13.81 ± 0.02	0.87	0.94	mS	—
115	J044823.57+451244.2	72.098	45.212	160.187	0.169	0.03	41.98	5.03	15.23 ± 0.02	14.28 ± 0.02	13.82 ± 0.02	0.98	0.99	mS	—
116	J045105.62+443545.0	72.773	44.596	160.970	0.140	0.05	38.79	5.25	14.93 ± 0.02	14.18 ± 0.02	13.87 ± 0.03	0.77	0.73	mS	5044
117	J045156.82+453619.8	72.987	45.606	160.284	0.900	0.12	−0.68	4.67	15.62 ± 0.02	14.53 ± 0.02	13.88 ± 0.02	1.62	1.04	E/S0	—
118	J044920.79+450159.4	72.337	45.033	160.433	0.183	0.50	−60.00	7.60	15.25 ± 0.13	14.00 ± 0.09	13.89 ± 0.14	0.95	0.95	mS	—

Table B – Continued

ID no.	Unique ID	RA	Dec	ℓ	b	ϵ_K	ϕ_K	r_{K20}	J_{K20}	H_{K20}	K_{K20}	$E(B\text{-}V)$	J^o-K^o	Type	v_{rad}
	ZoA	deg	deg	deg	deg		deg	$''$	mag	mag	mag	mag	mag		km s^{-1}
(1)	(2)	(3)	(4)	(5)	(6)	(7)	(8)	(9)	(10)	(11)	(12)	(13)	(14)	(15)	(16)
119	J045029.63+441012.4	72.623	44.170	161.226	−0.214	0.15	2.40	6.40	15.15 ± 0.02	14.31 ± 0.02	13.92 ± 0.03	0.64	0.96	mS	—
120	J044706.52+451102.1	71.777	45.184	160.063	−0.022	0.07	−35.59	3.95	15.36 ± 0.02	14.40 ± 0.02	13.94 ± 0.02	0.94	1.01	E/S0	—
121	J044950.94+454506.7	72.462	45.752	159.938	0.711	0.14	−35.38	4.73	15.53 ± 0.02	14.48 ± 0.02	13.94 ± 0.02	1.15	1.09	E/S0	—
122	J044434.42+445034.2	71.143	44.843	160.031	−0.584	0.10	9.12	3.65	15.44 ± 0.02	14.40 ± 0.02	13.96 ± 0.02	1.11	1.01	E/S0	—
123	J044946.26+450747.6	72.443	45.130	160.406	0.302	0.49	24.10	6.81	15.45 ± 0.02	14.37 ± 0.02	13.97 ± 0.03	0.98	1.07	mS	—
124	J044658.40+452255.0	71.743	45.382	159.896	0.088	0.07	−35.86	4.02	15.61 ± 0.02	14.62 ± 0.02	13.99 ± 0.02	1.11	1.14	E/S0	—
125	J044816.56+451604.5	72.069	45.268	160.131	0.189	0.01	−39.80	4.12	15.38 ± 0.02	14.43 ± 0.02	14.00 ± 0.02	1.02	0.94	E/S0	—
126	J045042.89+445937.4	72.679	44.994	160.618	0.343	0.32	−63.47	5.81	15.48 ± 0.02	14.43 ± 0.02	14.00 ± 0.02	0.93	1.07	mS	—
127	J044403.24+443827.5	71.014	44.641	160.123	−0.786	0.00	90.00	5.90	15.56 ± 0.16	14.36 ± 0.13	14.02 ± 0.17	1.10	1.06	mS	—
128	J045021.00+451216.6	72.587	45.205	160.414	0.428	0.26	−72.94	5.67	15.53 ± 0.02	14.49 ± 0.02	14.02 ± 0.02	1.02	1.07	mS	—
129	J045029.29+460723.4	72.622	46.123	159.724	1.034	0.28	49.67	5.21	15.57 ± 0.02	14.62 ± 0.02	14.02 ± 0.02	0.99	1.13	E/S0	—
130	J044646.85+452209.9	71.695	45.369	159.884	0.054	0.09	−26.10	4.14	15.59 ± 0.02	14.60 ± 0.02	14.03 ± 0.02	1.10	1.09	E/S0	—
131	J045419.04+452229.0	73.579	45.375	160.726	1.075	0.20	72.14	5.28	15.48 ± 0.02	14.53 ± 0.02	14.03 ± 0.02	0.93	1.04	mS	—
132	J045416.62+452530.8	73.569	45.425	160.682	1.102	0.00	90.00	5.00	15.42 ± 0.14	14.49 ± 0.14	14.07 ± 0.16	0.90	0.96	eS	—
133	J044721.08+450806.7	71.838	45.135	160.128	−0.021	0.25	−58.10	5.70	15.47 ± 0.02	14.50 ± 0.02	14.09 ± 0.03	0.90	0.99	mS	—
134	J045002.01+450215.3	72.508	45.038	160.507	0.278	0.48	55.19	6.12	15.54 ± 0.02	14.54 ± 0.02	14.09 ± 0.02	0.98	1.03	eS	—
135	J045541.23+445953.2	73.922	44.998	161.171	1.026	0.33	−54.60	5.30	15.60 ± 0.02	14.64 ± 0.02	14.11 ± 0.02	0.90	1.11	eS	—
136	J044802.83+452237.9	72.012	45.377	160.022	0.229	0.17	22.56	4.32	15.71 ± 0.02	14.76 ± 0.02	14.12 ± 0.02	1.07	1.13	E/S0	—
137	J044524.63+451918.2	71.353	45.322	159.764	−0.160	0.02	−32.18	4.01	15.60 ± 0.02	14.71 ± 0.02	14.13 ± 0.03	1.14	0.98	mS	6830
138	J044908.53+450705.9	72.286	45.118	160.344	0.209	0.12	26.00	5.19	15.57 ± 0.02	14.58 ± 0.02	14.14 ± 0.03	0.96	1.02	mS	—
139	J044755.58+450438.2	71.982	45.077	160.237	0.019	0.43	−62.81	5.82	15.52 ± 0.02	14.55 ± 0.02	14.15 ± 0.03	0.88	1.00	mS	—
140	J045029.48+450139.1	72.623	45.028	160.567	0.334	0.15	−24.88	3.98	15.66 ± 0.02	14.65 ± 0.02	14.15 ± 0.02	0.97	1.09	Irr	—
141	J045026.25+445346.6	72.609	44.896	160.661	0.243	0.04	42.27	4.30	15.56 ± 0.02	14.64 ± 0.02	14.18 ± 0.02	0.93	0.98	E/S0	—
142	J044616.70+440932.4	71.570	44.159	160.748	−0.799	0.17	26.77	4.30	15.52 ± 0.02	14.62 ± 0.02	14.19 ± 0.03	0.79	0.99	mS	—
143	J044632.01+440858.6	71.633	44.150	160.784	−0.770	0.00	90.00	5.00	15.53 ± 0.14	14.43 ± 0.04	14.21 ± 0.17	0.75	1.00	eS	—
144	J044603.60+444430.9	71.515	44.742	160.279	−0.450	0.09	−5.20	4.19	15.61 ± 0.02	14.62 ± 0.02	14.24 ± 0.03	0.99	0.93	mS	—
145	J044357.81+443721.5	70.991	44.623	160.126	−0.810	0.48	81.34	5.71	15.74 ± 0.02	14.74 ± 0.02	14.25 ± 0.03	1.09	1.03	mS	—
146	J045159.93+451925.2	73.000	45.324	160.508	0.728	0.58	8.91	6.35	15.66 ± 0.02	14.69 ± 0.02	14.25 ± 0.03	0.99	0.98	eS	—
147	J045229.45+452451.7	73.123	45.414	160.493	0.852	0.59	−19.33	6.61	15.66 ± 0.02	14.72 ± 0.02	14.25 ± 0.02	0.98	0.99	mS	—
148	J044728.19+450836.8	71.867	45.144	160.135	0.000	0.49	88.14	6.20	15.63 ± 0.02	14.71 ± 0.02	14.26 ± 0.03	0.95	0.95	ℓS	—
149	J045409.86+445915.6	73.541	44.988	161.010	0.810	0.42	−78.78	6.35	15.66 ± 0.02	14.73 ± 0.02	14.28 ± 0.03	0.91	1.00	E/S0	—

Table B – Continued

ID no.	Unique ID	RA	Dec	ℓ	b	ϵ_K	ϕ_K	r_{K20}	J_{K20}	H_{K20}	K_{K20}	$E(B\text{-}V)$	J^o-K^o	Type	v_{rad}
	ZoA	deg	deg	deg	deg		deg	$''$	mag	mag	mag	mag	mag		km s^{-1}
(1)	(2)	(3)	(4)	(5)	(6)	(7)	(8)	(9)	(10)	(11)	(12)	(13)	(14)	(15)	(16)
150	J044944.04+452717.6	72.434	45.455	160.153	0.505	0.28	−69.33	3.95	15.88 ± 0.02	14.92 ± 0.02	14.32 ± 0.02	1.04	1.11	E/S0	—
151	J044456.88+453304.0	71.237	45.551	159.537	−0.072	0.04	−58.90	4.28	16.03 ± 0.03	14.95 ± 0.02	14.33 ± 0.03	1.35	1.12	E/S0	—
152	J045213.66+455728.1	73.057	45.958	160.043	1.161	0.38	−41.73	4.79	15.89 ± 0.02	14.96 ± 0.02	14.35 ± 0.03	1.04	1.09	E/S0	—
153	J045253.13+443406.9	73.221	44.569	161.191	0.369	0.36	78.70	5.33	15.76 ± 0.02	14.84 ± 0.02	14.36 ± 0.03	0.78	1.05	ℓS	—
154	J044744.15+441950.0	71.934	44.331	160.786	−0.489	0.60	−18.30	6.04	15.63 ± 0.02	14.83 ± 0.02	14.42 ± 0.03	0.70	0.90	ℓS	4878
155	J044434.53+452801.4	71.144	45.467	159.558	−0.176	0.19	−44.80	3.98	16.13 ± 0.02	15.09 ± 0.02	14.44 ± 0.03	1.30	1.13	mS	—
156	J045238.00+453139.1	73.158	45.528	160.421	0.943	0.30	16.90	3.91	15.94 ± 0.02	14.93 ± 0.02	14.44 ± 0.02	1.17	0.99	eS	—
157	J044926.79+445532.2	72.362	44.926	160.526	0.127	0.67	−51.10	7.25	15.81 ± 0.02	14.92 ± 0.02	14.45 ± 0.03	0.92	0.96	mS	—
158	J044651.22+442147.3	71.713	44.363	160.659	−0.588	0.06	−23.49	4.07	15.86 ± 0.03	15.03 ± 0.02	14.48 ± 0.03	0.73	1.07	E/S0	—
159	J045216.28+451657.3	73.068	45.283	160.570	0.738	0.20	34.80	4.58	15.96 ± 0.03	15.02 ± 0.02	14.52 ± 0.03	0.92	1.04	mS	—
160	J044858.75+441329.9	72.245	44.225	161.010	−0.387	0.47	−82.16	4.88	15.89 ± 0.02	14.98 ± 0.02	14.57 ± 0.03	0.67	1.03	ℓS	—
161	J044947.40+444454.6	72.447	44.749	160.701	0.060	0.67	16.72	6.49	15.96 ± 0.03	14.99 ± 0.02	14.59 ± 0.03	0.86	1.00	mS	—
162	J045224.39+451948.4	73.102	45.330	160.548	0.787	0.39	−64.60	4.15	16.01 ± 0.02	15.11 ± 0.02	14.60 ± 0.03	0.94	1.01	E/S0	—
163	J045012.16+445802.4	72.551	44.967	160.580	0.256	0.57	18.53	6.47	16.12 ± 0.03	15.08 ± 0.02	14.61 ± 0.03	0.97	1.09	eS	—
164	J044621.16+441634.4	71.588	44.276	160.667	−0.713	0.49	−5.56	4.98	15.90 ± 0.02	15.00 ± 0.02	14.62 ± 0.03	0.81	0.93	mS	—
165	J045532.82+450602.8	73.887	45.101	161.075	1.071	0.24	−51.61	3.82	16.05 ± 0.02	15.09 ± 0.02	14.63 ± 0.03	0.91	1.03	mS	—
166	J044858.41+451309.8	72.243	45.219	160.248	0.252	0.10	−46.62	4.23	16.21 ± 0.03	15.16 ± 0.02	14.69 ± 0.03	0.96	1.11	mS	—
167	J045011.73+445955.1	72.549	44.999	160.555	0.275	0.41	51.90	4.58	16.12 ± 0.02	15.12 ± 0.02	14.70 ± 0.03	0.98	1.00	mS	—
168	J044651.60+455551.6	71.715	45.931	159.465	0.428	0.30	−7.58	4.66	16.34 ± 0.03	15.33 ± 0.03	14.71 ± 0.03	1.22	1.11	eS	—
169	J044739.96+443348.7	71.917	44.564	160.600	−0.348	0.38	46.20	5.61	16.07 ± 0.03	15.09 ± 0.02	14.72 ± 0.03	0.84	0.98	Irr	—
170	J044406.51+445621.7	71.027	44.939	159.904	−0.584	0.33	10.47	4.93	16.27 ± 0.03	15.19 ± 0.02	14.75 ± 0.03	1.15	1.02	mS	—
171	J044541.16+454528.0	71.421	45.758	159.464	0.160	0.19	−38.51	3.12	16.40 ± 0.03	15.37 ± 0.02	14.75 ± 0.03	1.26	1.11	E/S0	—
172	J044645.56+450429.6	71.690	45.075	160.106	−0.140	0.36	84.91	5.14	16.07 ± 0.03	15.12 ± 0.02	14.76 ± 0.03	0.88	0.94	eS	—
173	J045255.84+454914.2	73.233	45.821	160.227	1.169	0.22	−59.55	3.79	16.14 ± 0.03	15.17 ± 0.02	14.76 ± 0.03	0.96	0.97	eS	—
174	J045251.64+441648.4	73.215	44.280	161.411	0.183	0.25	−14.71	3.83	15.99 ± 0.02	15.11 ± 0.02	14.77 ± 0.03	0.66	0.94	E/S0	—
175	J044708.49+450527.2	71.785	45.091	160.137	−0.078	0.09	75.04	3.10	16.07 ± 0.02	15.13 ± 0.02	14.79 ± 0.03	0.88	0.90	E/S0	—
176	J045433.21+445344.2	73.638	44.896	161.124	0.806	0.22	−27.96	3.42	16.30 ± 0.03	15.34 ± 0.02	14.80 ± 0.03	0.89	1.12	E/S0	—
177	J045441.39+451904.9	73.672	45.318	160.811	1.090	0.35	−37.70	3.06	16.31 ± 0.02	15.59 ± 0.02	14.81 ± 0.03	0.89	1.11	eS	—
178	J044838.24+445640.2	72.159	44.945	160.420	0.029	0.09	−68.89	3.45	16.11 ± 0.02	15.20 ± 0.02	14.82 ± 0.03	0.86	0.92	E/S0	—
179	J044614.90+452745.3	71.562	45.463	159.753	0.043	0.29	13.74	3.22	16.50 ± 0.03	15.47 ± 0.02	14.85 ± 0.03	1.23	1.11	mS	—
180	J045013.36+440839.0	72.556	44.144	161.210	−0.270	0.44	79.01	4.57	15.91 ± 0.02	15.21 ± 0.02	14.87 ± 0.03	0.63	0.78	Irr	5547

Table B – Continued

ID no.	Unique ID	RA	Dec	ℓ	b	ϵ_K	ϕ_K	r_{K20}	J_{K20}	H_{K20}	K_{K20}	$E(B\text{-}V)$	J^o-K^o	Type	v_{rad}
	ZoA	deg	deg	deg	deg		deg	$''$	mag	mag	mag	mag	mag		km s^{-1}
(1)	(2)	(3)	(4)	(5)	(6)	(7)	(8)	(9)	(10)	(11)	(12)	(13)	(14)	(15)	(16)
181	J044938.32+435622.7	72.410	43.940	161.305	−0.479	0.07	−73.58	3.12	16.23 ± 0.03	15.36 ± 0.03	14.89 ± 0.03	0.62	1.07	E/S0	—
182	J044953.62+450543.4	72.473	45.095	160.447	0.296	0.12	82.40	3.15	16.38 ± 0.02	15.38 ± 0.02	14.90 ± 0.03	0.99	1.05	mS	—
183	J045123.45+460416.4	72.848	46.071	159.863	1.121	0.47	−66.91	4.71	16.38 ± 0.03	15.37 ± 0.02	14.90 ± 0.03	1.02	1.04	ℓS	—
184	J045440.78+445807.9	73.670	44.969	161.082	0.869	0.23	80.85	2.66	16.37 ± 0.02	15.44 ± 0.02	14.90 ± 0.03	0.91	1.07	E/S0	—
185	J044921.23+460126.8	72.338	46.024	159.674	0.820	0.33	6.21	3.62	16.49 ± 0.03	15.39 ± 0.03	14.92 ± 0.03	1.17	1.07	Irr	—
186	J044738.78+450532.7	71.912	45.092	160.194	−0.009	0.21	−64.50	3.95	16.35 ± 0.03	15.35 ± 0.02	14.94 ± 0.03	0.87	1.03	ℓS	—
187	J044855.57+443933.7	72.232	44.659	160.671	−0.115	0.72	4.90	8.79	16.39 ± 0.03	15.49 ± 0.03	14.94 ± 0.04	0.80	1.10	mS	—
188	J044543.46+450440.7	71.431	45.078	159.985	−0.277	0.36	−80.84	4.44	16.34 ± 0.03	15.36 ± 0.02	14.95 ± 0.03	1.03	0.95	ℓS	—
189	J044952.70+451451.0	72.470	45.247	160.328	0.392	0.24	65.67	4.62	16.50 ± 0.03	15.57 ± 0.03	14.98 ± 0.03	1.00	1.09	Irr	—
190	J044957.62+440316.6	72.490	44.055	161.254	−0.361	0.33	11.46	4.17	16.18 ± 0.03	15.36 ± 0.02	14.98 ± 0.03	0.64	0.93	ℓS	—
191	J044810.67+444742.0	72.044	44.795	160.482	−0.129	0.38	32.80	3.89	16.40 ± 0.03	15.46 ± 0.03	14.99 ± 0.04	0.82	1.05	mS	—
192	J044856.82+444953.0	72.237	44.831	160.542	−0.002	0.09	75.80	3.55	16.35 ± 0.03	15.37 ± 0.03	15.03 ± 0.03	0.83	0.96	ℓS	—
193	J044507.40+450214.4	71.281	45.037	159.947	−0.384	0.34	−30.50	4.18	16.51 ± 0.03	15.52 ± 0.03	15.05 ± 0.03	1.12	0.98	ℓS	—
194	J045420.33+451848.0	73.585	45.313	160.776	1.039	0.61	53.91	5.80	16.43 ± 0.03	15.50 ± 0.02	15.05 ± 0.03	0.92	0.98	eS	—
195	J045443.36+444708.1	73.681	44.786	161.229	0.760	0.47	−58.34	4.83	16.47 ± 0.03	15.55 ± 0.03	15.05 ± 0.04	0.88	1.03	mS	—
196	J044955.20+451139.7	72.480	45.194	160.374	0.363	0.03	−6.91	3.08	16.45 ± 0.03	15.47 ± 0.02	15.07 ± 0.03	0.99	0.96	ℓS	—
197	J044737.90+451002.9	71.908	45.167	160.135	0.037	0.23	34.62	2.81	16.59 ± 0.03	15.85 ± 0.03	15.09 ± 0.03	0.94	1.09	ℓS	—
198	J044852.61+445740.8	72.219	44.961	160.434	0.073	0.23	−14.44	3.24	16.47 ± 0.03	15.51 ± 0.02	15.10 ± 0.03	0.89	0.98	ℓS	—
199	J044547.35+454302.2	71.447	45.717	159.507	0.148	0.61	43.30	5.75	16.72 ± 0.03	15.77 ± 0.03	15.12 ± 0.04	1.27	1.05	eS	—
200	J044622.17+453307.3	71.592	45.552	159.698	0.117	0.46	−73.56	4.31	16.77 ± 0.03	15.76 ± 0.03	15.16 ± 0.04	1.28	1.06	ℓS	—
201	J044545.92+444901.9	71.441	44.817	160.188	−0.441	0.11	67.60	4.00	16.62 ± 0.03	15.75 ± 0.03	15.21 ± 0.04	1.05	0.95	ℓS	5134
202	J045012.70+453746.5	72.553	45.630	160.072	0.681	0.21	−58.70	3.14	16.78 ± 0.03	15.76 ± 0.03	15.21 ± 0.03	1.14	1.08	ℓS	—
203	J045004.97+450154.3	72.521	45.032	160.517	0.281	0.34	−22.89	3.77	16.67 ± 0.03	15.69 ± 0.02	15.24 ± 0.03	0.97	1.01	ℓS	—
204	J044617.48+452600.3	71.573	45.433	159.780	0.030	0.23	−8.24	4.19	16.87 ± 0.04	15.83 ± 0.03	15.28 ± 0.04	1.20	1.07	Irr	—
205	J045311.77+453648.0	73.299	45.613	160.417	1.074	0.18	22.04	3.19	16.73 ± 0.03	15.73 ± 0.02	15.31 ± 0.03	1.10	0.94	Irr	—
206	J045329.73+443729.2	73.374	44.625	161.216	0.489	0.61	73.06	4.40	16.66 ± 0.03	15.71 ± 0.02	15.32 ± 0.04	0.85	0.97	mS	—
207	J044445.84+444702.1	71.191	44.784	160.097	−0.597	0.20	10.23	3.97	16.90 ± 0.04	15.94 ± 0.03	15.33 ± 0.05	1.11	1.09	Irr	—
208	J045127.65+450922.6	72.865	45.156	160.577	0.548	0.56	56.41	4.66	16.82 ± 0.03	15.88 ± 0.03	15.35 ± 0.03	0.97	1.06	mS	—
209	J044955.57+454444.8	72.482	45.746	159.951	0.717	0.47	17.14	3.51	17.00 ± 0.03	16.01 ± 0.03	15.42 ± 0.03	1.16	1.09	ℓS	—
210	J044437.62+443619.0	71.157	44.605	160.217	−0.732	0.28	25.70	3.64	16.93 ± 0.03	15.90 ± 0.03	15.44 ± 0.04	1.04	1.04	Irr	—
211	J045330.45+444657.0	73.377	44.783	161.095	0.590	0.53	0.35	4.16	16.82 ± 0.03	15.84 ± 0.03	15.44 ± 0.04	0.97	0.96	eS	—

Table B – Continued

ID no.	Unique ID	RA	Dec	ℓ	b	ϵ_K	ϕ_K	r_{K20}	J_{K20}	H_{K20}	K_{K20}	$E(B\text{-}V)$	J^o-K^o	Type	v_{rad}
	ZoA	deg	deg	deg	deg		deg	$''$	mag	mag	mag	mag	mag		km s^{-1}
(1)	(2)	(3)	(4)	(5)	(6)	(7)	(8)	(9)	(10)	(11)	(12)	(13)	(14)	(15)	(16)
212	J044756.88+442015.1	71.987	44.338	160.805	−0.456	0.20	66.40	3.21	16.75 ± 0.03	15.89 ± 0.03	15.45 ± 0.04	0.69	1.00	Irr	—
213	J044958.64+450152.9	72.494	45.031	160.505	0.267	0.31	−62.00	2.79	16.90 ± 0.03	15.87 ± 0.02	15.45 ± 0.03	0.96	1.03	E/S0	—
214	J045225.84+451456.9	73.108	45.249	160.614	0.739	0.00	−7.64	3.17	16.85 ± 0.03	15.87 ± 0.03	15.48 ± 0.04	0.90	0.99	Irr	—
215	J044531.48+443550.4	71.381	44.597	160.327	−0.617	0.12	−17.07	2.91	16.96 ± 0.03	15.98 ± 0.03	15.49 ± 0.04	1.04	1.02	ℓS	—
216	J044638.07+444609.2	71.659	44.769	160.324	−0.355	0.53	−89.04	4.01	17.01 ± 0.03	16.05 ± 0.03	15.53 ± 0.04	0.91	1.09	eS	—
217	J044744.40+445626.1	71.935	44.941	160.321	−0.095	0.18	−5.80	2.80	16.89 ± 0.03	15.99 ± 0.03	15.53 ± 0.04	0.85	1.00	Irr	—
218	J044922.06+453019.4	72.342	45.505	160.073	0.488	0.01	42.10	2.83	16.98 ± 0.03	16.04 ± 0.03	15.54 ± 0.04	0.99	1.01	Irr	—
219	J045057.35+452532.4	72.739	45.426	160.312	0.651	0.14	9.90	3.04	17.04 ± 0.03	15.98 ± 0.03	15.54 ± 0.04	1.08	1.03	ℓS	—
220	J044957.27+460315.1	72.489	46.054	159.720	0.920	0.44	19.55	4.28	16.93 ± 0.03	16.07 ± 0.03	15.56 ± 0.04	1.12	0.89	ℓS	4942
221	J045241.41+452024.6	73.173	45.340	160.572	0.832	0.05	−62.10	2.92	16.91 ± 0.03	16.01 ± 0.03	15.56 ± 0.04	0.93	0.95	ℓS	—
222	J044854.97+453243.7	72.229	45.545	159.991	0.454	0.06	−44.99	3.28	16.88 ± 0.03	16.01 ± 0.03	15.57 ± 0.04	0.97	0.89	Irr	—
223	J045243.81+443819.6	73.183	44.639	161.119	0.393	0.24	−26.00	3.20	16.89 ± 0.03	16.05 ± 0.03	15.57 ± 0.04	0.81	0.97	ℓS	—
224	J045338.36+452459.0	73.410	45.416	160.619	1.009	0.12	−50.48	2.87	17.07 ± 0.03	16.22 ± 0.03	15.57 ± 0.03	0.92	1.10	Irr	—
225	J044959.00+442427.5	72.496	44.408	160.985	−0.132	0.34	39.37	2.94	16.85 ± 0.03	16.17 ± 0.03	15.62 ± 0.05	0.69	0.93	Irr	—
226	J045143.42+445733.8	72.931	44.959	160.758	0.458	0.23	74.31	3.34	16.98 ± 0.03	16.10 ± 0.03	15.62 ± 0.04	0.94	0.95	Irr	—
227	J044812.83+445407.6	72.053	44.902	160.404	−0.055	0.14	32.10	3.16	17.03 ± 0.04	16.17 ± 0.03	15.64 ± 0.04	0.84	1.03	ℓS	—
228	J045038.65+445618.6	72.661	44.938	160.652	0.298	0.15	−86.90	2.79	17.02 ± 0.03	16.02 ± 0.03	15.65 ± 0.04	0.92	0.97	ℓS	—
229	J045453.21+444522.8	73.722	44.756	161.270	0.764	0.22	48.70	3.10	17.01 ± 0.04	16.09 ± 0.03	15.70 ± 0.05	0.89	0.93	Irr	—
230	J044822.79+445528.2	72.095	44.925	160.406	−0.018	0.17	46.87	3.19	17.10 ± 0.04	16.22 ± 0.03	15.72 ± 0.05	0.84	1.02	Irr	—
231	J045144.68+455508.4	72.936	45.919	160.020	1.072	0.63	0.58	4.87	17.34 ± 0.04	16.23 ± 0.03	15.74 ± 0.05	1.16	1.09	ℓS	—
232	J044706.85+453448.3	71.779	45.580	159.761	0.235	0.39	36.30	3.36	17.28 ± 0.04	16.31 ± 0.03	15.75 ± 0.04	1.25	0.99	ℓS	4994
233	J044926.38+445450.8	72.360	44.914	160.534	0.119	0.57	59.34	4.18	17.10 ± 0.03	16.21 ± 0.03	15.75 ± 0.04	0.92	0.96	eS	—
234	J044930.28+443329.0	72.376	44.558	160.815	−0.101	0.51	−64.84	3.81	16.99 ± 0.03	16.12 ± 0.03	15.79 ± 0.05	0.76	0.87	ℓS	—
235	J045109.62+450323.9	72.790	45.057	160.620	0.444	0.47	−35.74	3.64	17.15 ± 0.03	16.20 ± 0.03	15.79 ± 0.04	0.93	0.96	ℓS	—
236	J045517.43+450155.5	73.823	45.032	161.100	0.993	0.28	47.83	3.35	17.13 ± 0.03	16.17 ± 0.03	15.79 ± 0.04	0.90	0.96	Irr	—
237	J045401.45+451107.1	73.506	45.185	160.841	0.916	0.03	−22.56	2.69	17.14 ± 0.03	16.20 ± 0.03	15.80 ± 0.04	0.96	0.93	Irr	—
238	J044452.40+443535.1	71.218	44.593	160.255	−0.707	0.13	−44.30	2.75	17.23 ± 0.04	16.27 ± 0.03	15.83 ± 0.05	1.01	0.97	Irr	—
239	J044936.24+450910.5	72.401	45.153	160.370	0.294	0.16	−26.71	2.74	17.24 ± 0.04	16.27 ± 0.03	15.84 ± 0.04	0.97	0.97	Irr	—
240	J044727.80+444723.1	71.866	44.790	160.400	−0.230	0.68	−44.49	6.25	17.08 ± 0.04	16.32 ± 0.04	15.87 ± 0.07	0.88	0.83	Irr	7288
241	J044428.93+443630.5	71.121	44.608	160.197	−0.750	0.07	41.10	2.86	17.40 ± 0.04	16.46 ± 0.04	15.97 ± 0.06	1.06	0.96	Irr	—
242	J044746.91+453420.6	71.945	45.572	159.843	0.319	0.30	−41.46	3.09	17.48 ± 0.04	16.45 ± 0.03	15.99 ± 0.05	1.23	0.96	Irr	—

Table B – Continued

ID no.	Unique ID	RA	Dec	ℓ	b	ϵ_K	ϕ_K	r_{K20}	J_{K20}	H_{K20}	K_{K20}	$E(B\text{-}V)$	J^o-K^o	Type	v_{rad}
	ZoA	deg	deg	deg	deg		deg	$''$	mag	mag	mag	mag	mag		km s^{-1}
(1)	(2)	(3)	(4)	(5)	(6)	(7)	(8)	(9)	(10)	(11)	(12)	(13)	(14)	(15)	(16)
243	J045143.79+444623.9	72.932	44.773	160.902	0.341	0.45	43.24	3.42	17.32 ± 0.04	16.37 ± 0.03	16.02 ± 0.06	0.88	0.91	Irr	—
244	J044846.14+455955.0	72.192	45.999	159.628	0.725	0.34	29.77	3.04	17.61 ± 0.05	16.60 ± 0.04	16.10 ± 0.05	1.18	1.01	ℓS	—
245	J044942.24+452830.7	72.426	45.475	160.134	0.514	0.07	−32.30	2.56	17.45 ± 0.04	16.49 ± 0.03	16.10 ± 0.05	1.04	0.90	Irr	—
246	J045533.75+445954.9	73.891	44.999	161.157	1.009	0.20	−60.40	2.72	17.44 ± 0.04	16.50 ± 0.03	16.10 ± 0.05	0.91	0.94	Irr	—
247	J045024.44+453101.5	72.602	45.517	160.181	0.636	0.11	−61.08	2.70	17.78 ± 0.05	16.77 ± 0.04	16.28 ± 0.07	1.16	1.00	Irr	—
248	J044758.33+440708.0	71.993	44.119	160.975	−0.593	0.53	−81.40	3.07	17.66 ± 0.04	16.84 ± 0.04	16.38 ± 0.06	0.64	1.00	ℓS	—
249	J044644.16+442005.1	71.684	44.335	160.667	−0.623	0.56	−74.98	3.12	17.66 ± 0.04	16.81 ± 0.04	16.47 ± 0.07	0.73	0.88	mS	5654
250	J044602.99+445836.4	71.512	44.977	160.099	−0.299	0.33	−63.40	3.07	17.87 ± 0.05	17.24 ± 0.05	16.47 ± 0.07	0.96	0.99	Irr	—
251	J045222.42+450342.7	73.093	45.062	160.752	0.612	0.33	−74.00	2.64	18.03 ± 0.05	17.02 ± 0.04	16.57 ± 0.07	0.91	1.07	Irr	—
252	J045430.84+444644.9	73.628	44.779	161.211	0.727	0.68	5.66	2.85	18.45 ± 0.06	17.50 ± 0.05	17.08 ± 0.09	0.88	0.99	ℓS	—
253	J045302.36+454133.4	73.260	45.693	160.338	1.102	0.74	−73.61	3.78	18.56 ± 0.06	17.68 ± 0.05	17.09 ± 0.08	1.11	1.00	Irr	—
254	J044817.36+445352.2	72.072	44.898	160.416	−0.048	0.95	−33.50	11.71	18.42 ± 0.09	17.67 ± 0.09	17.17 ± 0.15	0.84	0.89	Irr	—
255	J045034.26+435930.6	72.643	43.992	161.370	−0.320	0.60	−48.07	2.10	19.24 ± 0.10	18.93 ± 0.13	17.81 ± 0.13	0.64	1.16	Irr	5724
256	J044602.10+443424.5	71.509	44.573	160.400	−0.560	0.05	68.79	1.51	19.00 ± 0.11	18.07 ± 0.09	17.85 ± 0.19	0.94	0.74	Irr	6281
257	J045426.93+444941.5	73.612	44.828	161.170	0.750	0.24	69.67	1.38	19.29 ± 0.09	18.44 ± 0.08	18.05 ± 0.15	0.89	0.85	Irr	5072
258	J045217.47+450839.9	73.073	45.144	160.680	0.650	0.56	43.93	1.78	19.72 ± 0.11	18.84 ± 0.09	18.27 ± 0.15	0.87	1.07	Irr	6680
259	J044644.76+444734.7	71.687	44.793	160.320	−0.320	0.19	75.89	0.94	19.83 ± 0.12	18.84 ± 0.09	18.80 ± 0.24	0.89	0.65	Irr	5709
260	J044838.16+454506.4	72.159	45.752	159.800	0.550	0.35	−77.10	1.07	21.83 ± 0.74	19.89 ± 0.27	18.96 ± 0.24	1.14	2.37	Irr	5745
261	J045026.76+451130.7	72.612	45.192	160.440	0.430	0.63	−53.75	0.73	21.77 ± 0.35	20.25 ± 0.17	20.07 ± 0.39	1.02	1.26	Irr	4639

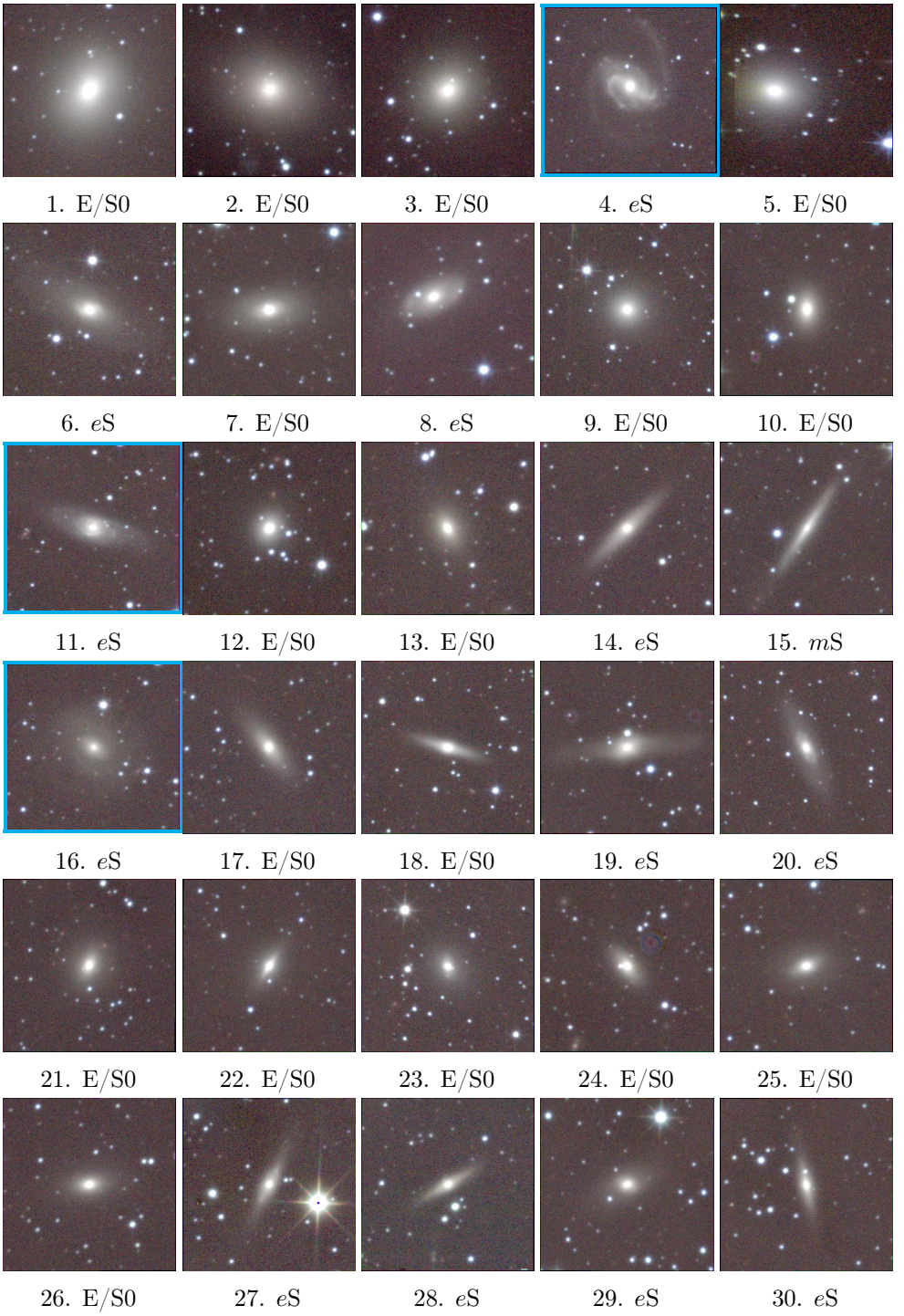

Figure B. The false-colour − J (blue), H (green) and K (red) representation ($1.2'$ × $1.2'$) of the 3C 129 cluster galaxies. The cyan frames indicate HI detection in the WSRT HI-survey.

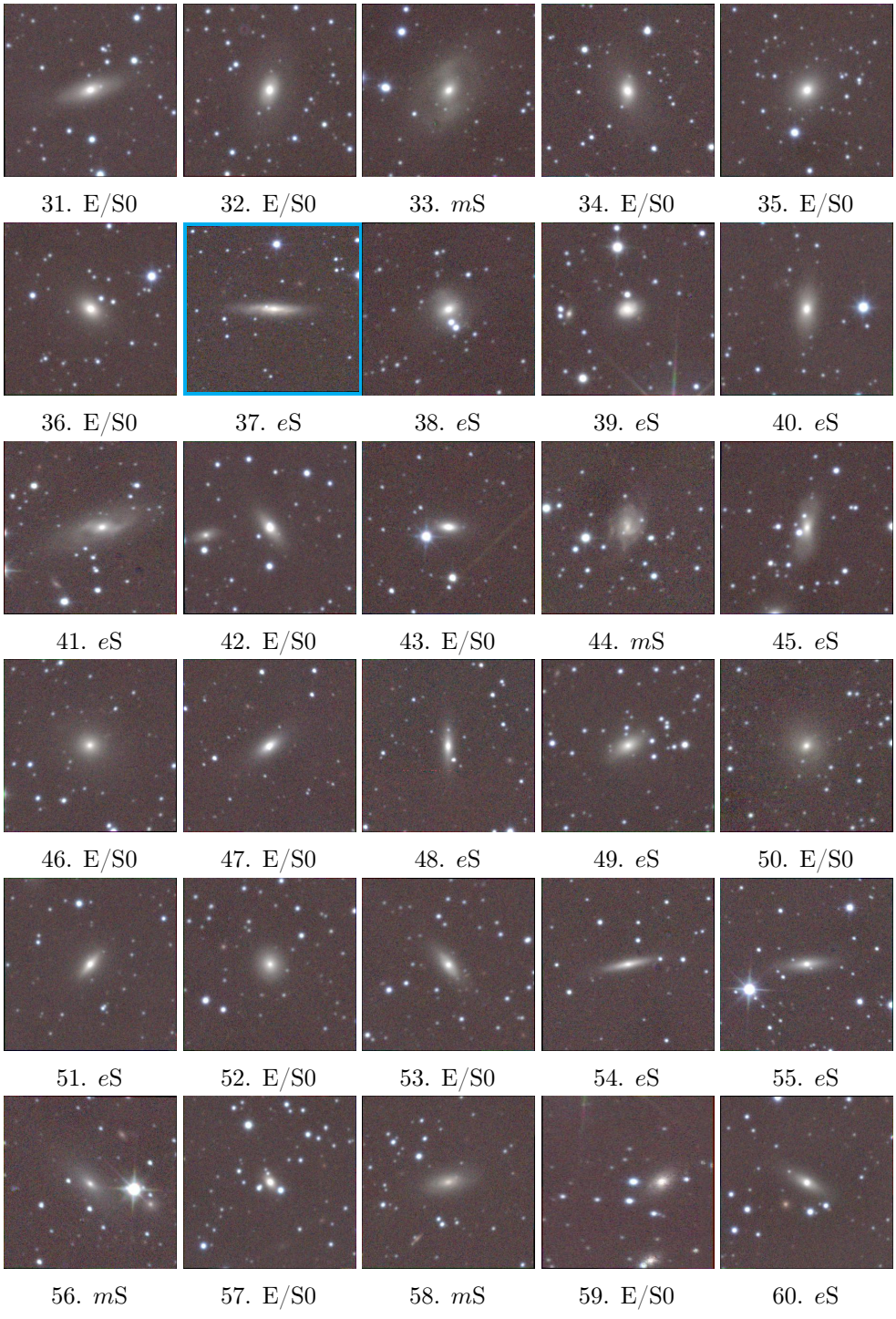

Figure B – Continued.

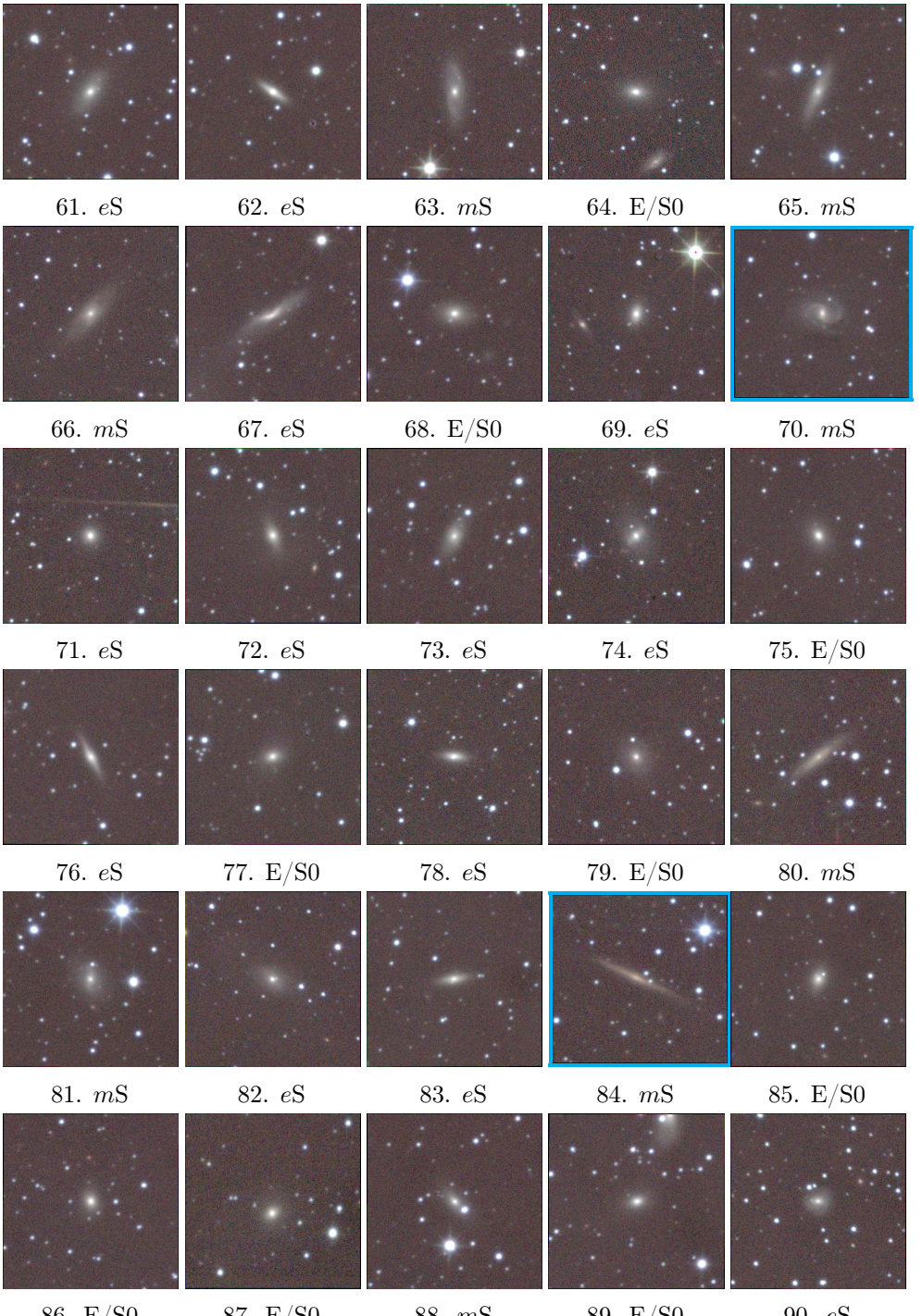

Figure B – Continued.

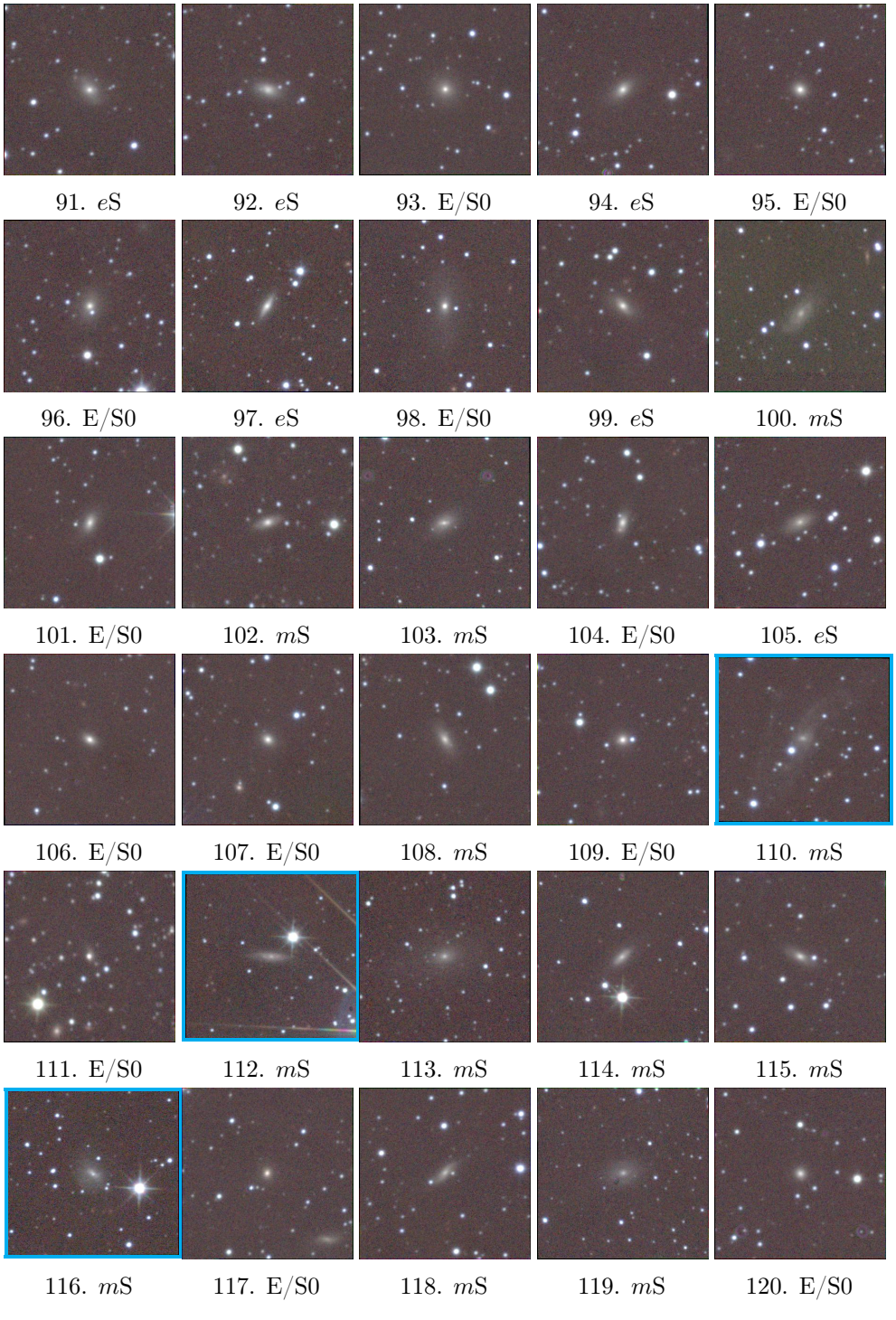

Figure B – Continued.

121. E/S0 122. E/S0 123. mS 124. E/S0 125. E/S0

126. mS 127. mS 128. mS 129. E/S0 130. E/S0

131. mS 132. eS 133. mS 134. eS 135. eS

136. E/S0 137. mS 138. mS 139. mS 140. Irr

141. E/S0 142. mS 143. eS 144. mS 145. mS

146. eS 147. mS 148. ℓS 149. E/S0 150. E/S0

Figure B – Continued.

151. E/S0 152. E/S0 153. ℓS 154. ℓS 155. mS

156. eS 157. mS 158. E/S0 159. mS 160. ℓS

161. mS 162. E/S0 163. eS 164. mS 165. mS

166. mS 167. mS 168. eS 169. Irr 170. mS

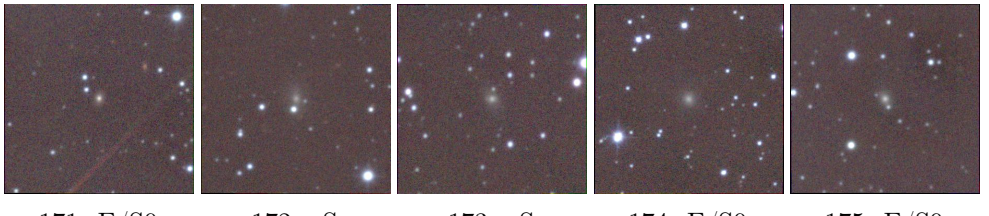

171. E/S0 172. eS 173. eS 174. E/S0 175. E/S0

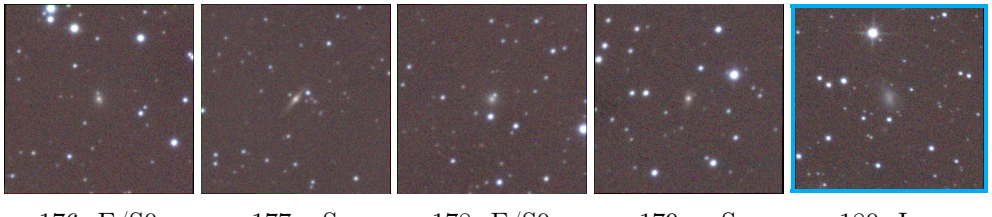

176. E/S0 177. eS 178. E/S0 179. mS 180. Irr

Figure B – Continued.

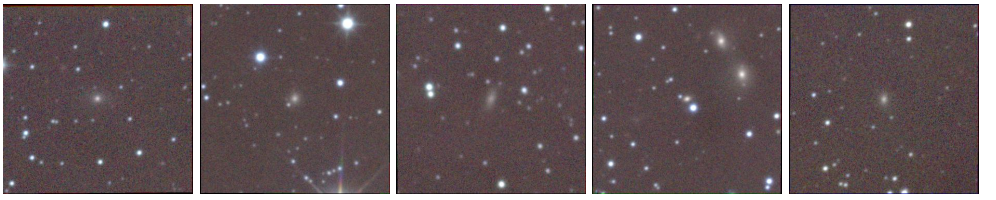

181. E/S0 182. mS 183. ℓS 184. E/S0 185. Irr

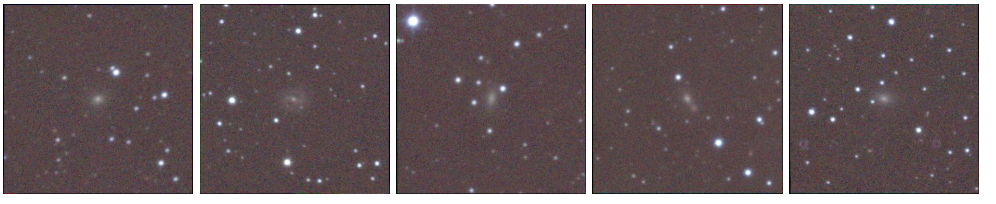

186. ℓS 187. mS 188. ℓS 189. Irr 190. ℓS

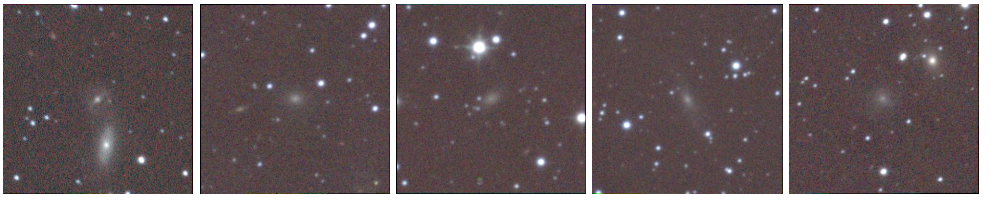

191. mS 192. ℓS 193. ℓS 194. eS 195. mS

196. ℓS 197. ℓS 198. ℓS 199. eS 200. ℓS

201. ℓS 202. ℓS 203. ℓS 204. Irr 205. Irr

206. mS 207. Irr 208. mS 209. ℓS 210. Irr

Figure B – Continued.

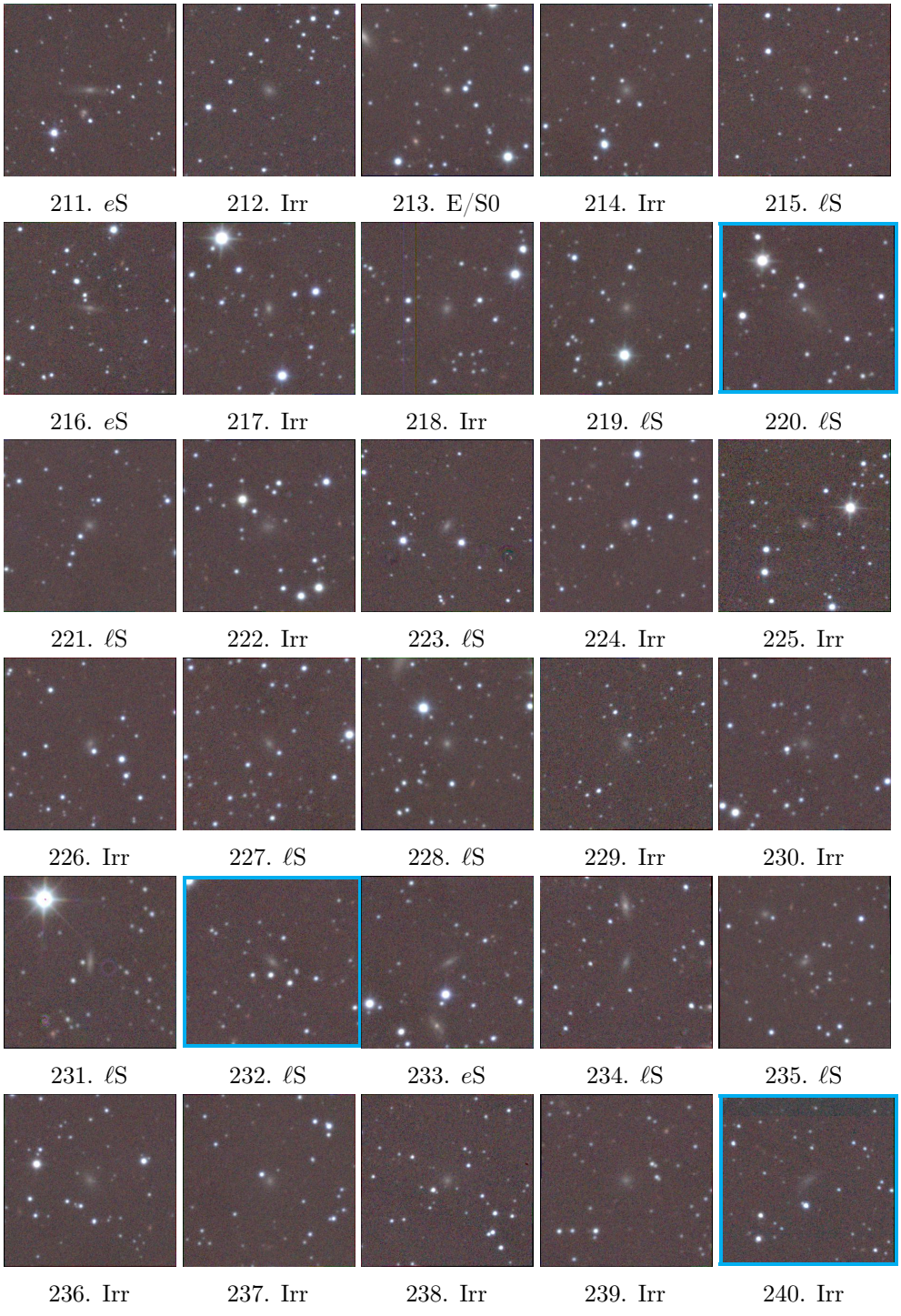

Figure B – Continued.

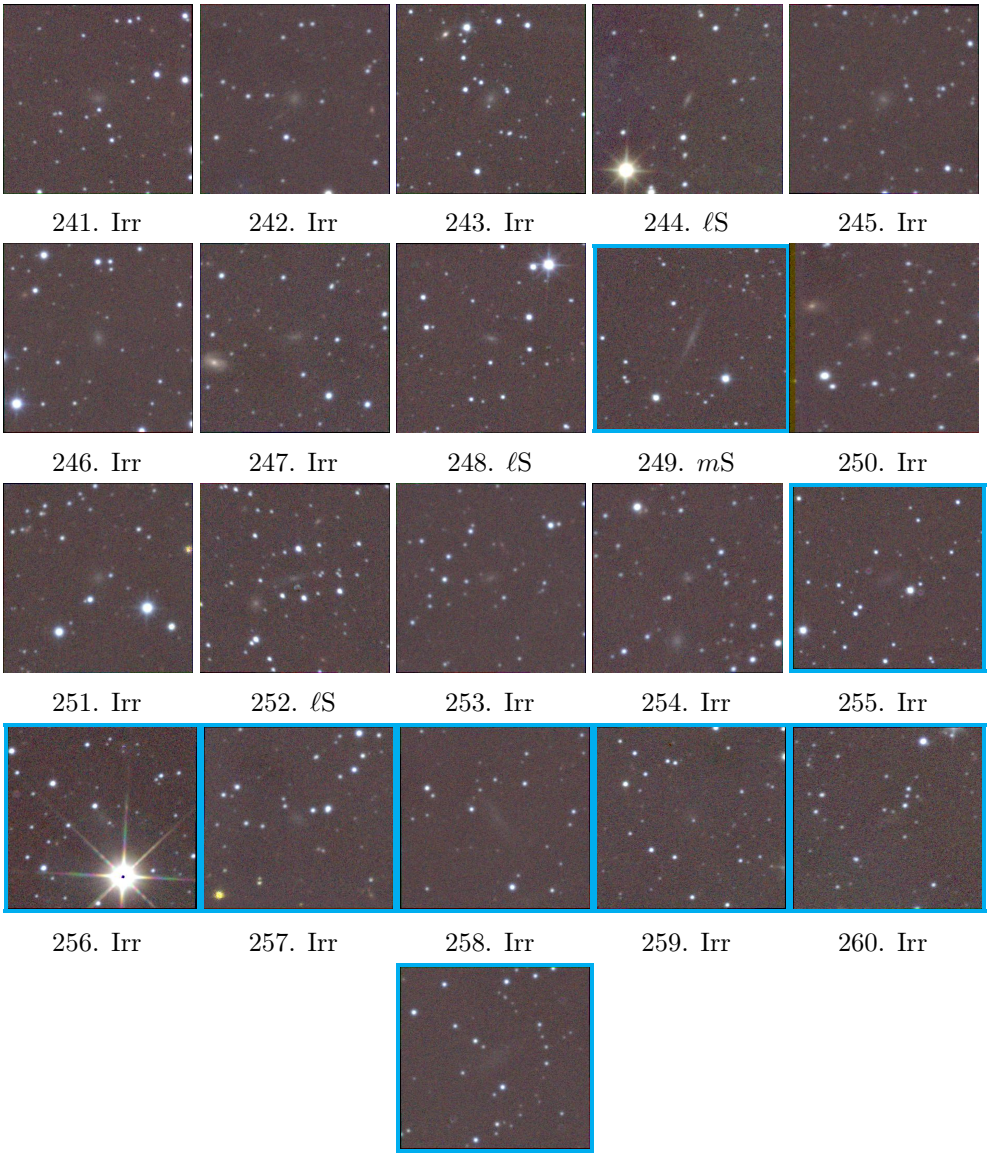

241. Irr 242. Irr 243. Irr 244. ℓS 245. Irr

246. Irr 247. Irr 248. ℓS 249. mS 250. Irr

251. Irr 252. ℓS 253. Irr 254. Irr 255. Irr

256. Irr 257. Irr 258. Irr 259. Irr 260. Irr

261. Irr

Figure B – Continued.

4

The WSRT PP ZoA III. Environmental Effects on HI

M. Ramatsoku[a,b,c], **M.A.W Verheijen**[a], **R.C. Kraan-Korteweg**[b]

[a] Kapteyn Astronomical Institute, University of Groningen, Landleven 12, 9747 AV Groningen, The Netherlands

[b] Department of Astronomy, University of Cape Town, Private Bag X3, Rondebosch 7701, South Africa

[c] ASTRON, Netherlands Institute for Radio Astronomy, Postbus 2, 7990 AA Dwingeloo, The Netherlands

Abstract

We exploit the large and blind H I-imaging data provided by the Westerbork Synthesis Radio Telescope of the Perseus-Pisces Supercluster in the Zone of Avoidance at $\ell = 160°$ in which the X-ray emitting 3C 129 cluster is embedded. The survey covered a sky-area of 9.6 sq.deg and the radial velocity range of $cz \approx 2000-16000$ km s^{-1}. We analyse the H I-properties in the range of environments found within the surveyed volume, focusing on a major galaxy overdensity containing the 3C 129 cluster and another overdensity in its background. We assess the H I morphologies of galaxies in these environments by examining asymmetries in their global H I profiles, kinematics and integrated H I-maps. Disturbed H I-morphologies are found in more than 60% of the galaxies that are located in densely populated groups and in ∼30% of the galaxies located in low density environments. This demonstrates the prominence of galaxy-galaxy interactions in dense environments in the disruption of the H I distribution in galaxies. We also measure the H I-content of the galaxies by computing the H I mass-to-light ratios and the gas-deficiency parameter values. An investigation of the H I-content as a function of the projected radial distance of the 3C 129 cluster revealed significant H I-deficiency in the core of the cluster. A simple analytical description of the ram-pressure stripping suggests that it is the dominant mechanism responsible for the dearth of H I in this inner region of the cluster. An analysis of the galaxies in the cluster outskirts shows galaxies with a low relative H I-content of $\log(M_{HI}/L_K) < -1.5$ $M_\odot/L_\odot$. Most of these galaxies are part of a potentially infalling group within the cluster radius. It seems likely that galaxy-galaxy interactions within subgroups are responsible for the relatively low H I content. The H I-content of galaxies within the cluster environment is also compared to that of galaxies located in groups for which no X-ray nor cluster association is found. We measure the H I-content for the late-type galaxies in these galaxies and find a median of $\log(M_{HI}/L_K) = -0.7 \pm 0.6$ $M_\odot/L_\odot$ and $Def_{HI} = 0.3 \pm 0.9$ for galaxies in the cluster population and $\log(M_{HI}/L_K) = -0.9 \pm 0.8$ $M_\odot/L_\odot$ and $Def_{HI} = 0.5 \pm 0.7$ for those in the galaxy groups. The similarities in the relative H I-content in these environments points to the importance of gas removal mechanisms occurring in galaxy groups and/or filaments that affect the transformation of galaxies.

Keywords: galaxies: large-scale structures: ZoA: surveys: galaxies: radio lines: galaxies: galaxy clusters (3C 129)

4.1 Introduction

Galaxy clusters located at the nodes of large-scale structures offer a unique laboratory to investigate the global and local environmental effects on the properties of galaxies. As evidenced by the morphology-density relation (Dressler 1980), late-type spiral galaxies are more frequent in low density regions while the early-type galaxies dominate regions with high galaxy densities. Surveys and studies of large-scale structure filaments, cluster outskirts and galaxy groups have found that the galaxy properties depend on the environment even where the galaxy density is lowest (Lewis et al. 2002, Treu et al. 2003, Porter et al. 2008, Roychowdhury et al. 2012). This has brought about the idea that galaxies may be undergoing pre-processing before falling into the higher density regions of clusters (Haines et al. 2007). However, it is not yet clear how or where this so called pre-processing occurs.

An important indicator of processes that affect galaxy evolution is the neutral atomic hydrogen gas (H I) which also provides a reservoir from which stars can be formed. The kinematically cold and extended H I disks make them a sensitive tracer of the different environmental processes such as ram-pressure stripping, tidal interactions and mergers. Observations have shown that the H I gas gets disturbed and truncated and eventually exhausted as galaxies transition into clusters (Vollmer 2003, Crowl et al. 2005, Chung et al. 2009, Abramson et al. 2011, Gavazzi et al. 2013). Simulations suggest that these effects are due to ram-pressure stripping and gravitational interactions (Roediger 2009, Tonnesen & Bryan 2009). The former is expected to be more prominent in galaxy clusters with masses of $M_{cl} \gtrsim 10^{14}$ $M_{\odot}$. This is due to the high intra-cluster medium (ICM) densities of these clusters and the increased orbital velocities of the galaxies as they fall into the cluster cores (Roediger & Brüggen 2007). Some evidence has shown that the H I gas can get completely removed after transiting through the cluster core (Kapferer et al. 2009, Jaffé et al. 2015). This has been supported by trends that show an increasing fraction of galaxies with asymmetric H I morphologies as a function of the projected distance from the cluster centre (Cayatte et al. 1990, Bravo-Alfaro et al. 2000b, Chung et al. 2009, Yoon et al. 2017). The scatter in this trend is quite large though, since highly disturbed galaxies are found in the cluster outskirts and groups as well. This has been attributed to the possible processing of galaxies in groups falling into the cluster or along the large-scale filamentary structures from which these galaxies transition (Verdes-Montenegro et al. 2001, Fujita 2004, De Lucia et al.

2012, Hess et al. 2017). The large scatter demands improved statistics on spatially resolved galaxies.

To understand the details of the H I properties of galaxies, it is important to probe not only the clusters comprising the galaxies but also the surrounding large-scale structure filaments within which they are embedded. The Perseus-Pisces Supercluster (PPS) is one of the largest filamentary structures nearby ($cz \approx 4000 - 8000$ km s^{-1}), comprising numerous rich clusters, thus making it an ideal region to study the effect of various environments on the H I properties of galaxies.

In Ramatsoku et al. (2016) we presented an H I survey with the Westerbork Synthesis Radio Telescope (WSRT) of galaxies in an overdensity located in the PPS filament behind the Milky-Way. Within this overdensity a lesser known galaxy cluster, namely the 3C 129 cluster, is embedded. The cluster is a massive structure ($\sim 10^{14}$M$_\odot$; Leahy & Yin 2000) containing two radio galaxies with jets extending into the ICM, one of which extending as far as $\sim$40′. It displays a significant X-ray emission of $\sim 10^{44}$ erg s^{-1} (Leahy & Yin 2000), thus making it an ideal environment to study the interplay between the ICM and galaxies falling in from the surrounding filament. Additionally, three more galaxy overdensities in the foreground and background of the PPS were found within the H I surveyed volume. We described how these overdensities connect with the filamentary large-scale structures on either side of the Galactic Plane. Overall, the H I detections of galaxies in the surveyed volume pointed to a diversity of cosmic environments, ranging from a high galaxy density cluster to galaxy overdensities with no known cluster association as well as empty voids. The distribution of the H I detections offers an unique opportunity to evaluate the H I gas content of galaxies in varying environments under uniform H I observing conditions.

In Ramatsoku et al. (2017, *submitted*) we studied the detailed distribution of galaxies in the 3C 129 cluster. The optical extinction at the location of the cluster ranges from $A_B = 1.8 - 8.0$ mag and as a result only three optical redshifts are available in the literature. This forced us to identify the gas-poor cluster galaxies in the near-infrared (NIR) using images from the UKIDSS Galactic Plane Survey (UKIDSS GPS; Lucas et al. 2008). We then carried out an analysis of the combined NIR and H I galaxies of the cluster. These data suggest that the cluster is in the process of assembling as evidenced by the presence of a possibly infalling substructure. Moreover, at the location of this substructure more gas-rich galaxies are found, while the core of the cluster is mainly dominated

by gas-poor galaxies, suggesting that by the time galaxies fall into the core the 3C 129 cluster, their H I content will be significantly reduced.

In this paper we aim to understand the environmental dependence of the mechanisms involved in transforming galaxies from gas-rich to gas-poor. We combine H I and NIR data in the entire WSRT surveyed volume to conduct an in-depth investigation of the relation between the H I properties of galaxies and their cosmic environment.

The paper is organised as follows: in Sect. 4.2 we provide a brief description of the H I-imaging observations conducted with the WSRT. Methods used to identify substructures within major overdensities in the surveyed volume are described in Sect. 4.3. Section 4.4 gives a description of the characteristics of the identified substructures. We present and discuss an analysis of the H I-content of galaxies located in the various environments in Sect. 4.5. This is followed by an assessment of the H I-morphologies of galaxies within the various substructures in Sect. 4.6. We then provide an analysis of the phase-space galaxy distribution of the 3C 129 cluster in Sect. 4.7. Lastly we discuss and summarise the main results in Sect. 4.8.

We assume a Λ cold dark matter cosmology with $\Omega_{\rm M} = 0.3, \Lambda_\Omega = 0.7$ and a Hubble constant $\rm H_0 = 70$ km s^{-1} Mpc^{-1} throughout this paper.

4.2 The WSRT PPZoA project

This study is based on data from the WSRT Persues-Pisces Zone of Avoidance (WSRT PPZoA) H I survey. Observations were carried out covering the radial velocity range of $cz = 2000 - 16000$ km s^{-1} with 16.5 km s^{-1} velocity resolution. With a volume depth of 214 Mpc we observed a hexagonal mosaic of 35 pointings leading to a total covered sky area of 9.6 deg^2 centred at $\ell, b \approx 160°, 0.5°$, which is where the Perseus-Pisces Supercluster (PPS) crosses the Zone of Avoidance. Each pointing was observed for 12 hours, reaching a survey sensitivity of rms = 0.36 mJy/beam and an angular resolution of $23'' \times 16''$. The survey configuration allowed the 6σ detection of galaxies with H I masses of $\log(\rm M_{HI}/M_\odot) = 8.5$ at the median distance of the PPS ($cz \approx 6000$ km s^{-1}), assuming a line width (w_{50}) of 150 km s^{-1}.

The observations yielded 211 galaxy detections over the entire radial velocity range with H I masses ranging from $\log(\rm M_{HI}/M_\odot) = 7.7 - 10.3$. Of these galaxies, 80 were spatially resolved with at least one and a half synthesised beams across. A total of 87 galaxies were detected in a prominent overdensity (Aur 2) at the redshift of the 3C 129 cluster of

$cz \sim 4000-8000$ km s^{-1}, and 72 are located at another major overdensity (Aur 3) behind the PPS at $cz \sim 8000-12000$ km s^{-1}. Galaxies found at these distances have H I masses ranging from $\log(M_{HI}/M_\odot) = 7.8-10.3$ ($w_{50} = 25-526$ km s^{-1}) and $8.6-10.3$ ($w_{50} = 28-322$ km s^{-1}), respectively.

The rest of the galaxies were located in minor overdensities in the foreground and background of the cluster, at the radial velocity ranges of, $cz = 2400-4000$ km s^{-1} and $cz \sim 12000-16000$ km s^{-1}, respectively. Using the deep UKIDSS-GPS images with a pixel scale of $0.2''$/pix and an average seeing of $0.8''$, counterparts were found for 62% of all the H I detections. Within the prominent Aur 2 and Aur 3 overdensities, NIR counterparts were found for 66% and 61% of the H I detections in those volumes. The other galaxies were either too obscured by the high levels of Galactic foreground extinction estimated between $A_K = 0.16$ to 0.72 mag, or were gas-rich, low surface-brightness galaxies that are not easily detectable in the near-infrared.

4.3 Identifying Substructures

The spatial and velocity distribution of galaxies in the Universe suggests ongoing accretion as groups and clusters of galaxies continue to assemble. This process results in substructures in these systems and demonstrates their dynamical nature. It is therefore important to quantify the incidence of substructure and take this into consideration when examining properties of galaxies as a function of their environment.

There are several methods of identifying substructures within large conglomerations of galaxies. One method is to search for the non-Gaussianity in the galaxy velocity distribution. This gives a first hint for the presence of substructure. This information alone, however, does not provide the details of substructures, such as galaxy density and the constituent galaxy population. It is essential to assess the clustering of galaxies in both the velocity and spatial distribution at the same time.

In this section we identify and assess environments within the two prominent overdensities in the WSRT PPZoA surveyed volume, namely the Aur 2 ($cz \sim 4000-8000$ km s^{-1}) and Aur 3 ($cz \sim 8000-12000$ km s^{-1}) regions. The velocity distributions of these systems are shown in panel (a) of Figs. 4.1 and 4.2. We searched for the presence of substructures

using the Dressler-Shectman (DS; Dressler & Shectman 1988) test and by taking into account the two-dimensional galaxy density distribution using the smooth particle hydrodynamics technique (SPH; Monaghan 2005). The identified substructures form the cosmic environments in which we will investigate the HI properties of their galaxy populations.

4.3.1 The Dressler-Shectman test

The DS test measures and compares the local (loc) kinematics of each galaxy and its nearest neighbours to the global (glo) kinematics of the entire structure (cluster/group). For the Aur 2 and Aur 3 systems, we computed for each galaxy (i) the mean velocity ($\bar{v}^i_{loc}$) and dispersion (σ^i_{loc}) of its N_{loc} nearest neighbours. These values were compared to the mean velocity ($\bar{v}_{glo}$) and dispersion (σ_{glo}) of the entire structure with N_{glo} members. The deviation of an individual galaxy from the whole structure was then calculated as:

$$\delta_i^2 = \left(\frac{N_{loc}+1}{\sigma^2_{glo}}\right)\left[(\bar{v}^i_{loc}-\bar{v}_{glo})^2+(\sigma^i_{loc}-\sigma_{glo})^2\right]. \quad (4.1)$$

For both systems we used $N_{loc} = \sqrt{N_{glo}}$ galaxy neighbours to ensure that kinematic deviations of a small number of neighbouring galaxies are not attenuated due to too many unassociated galaxies since this would lower the computed $\bar{v}^i_{loc}$ and σ^i_{loc} (Pinkney et al. 1996, Hou et al. 2012).

The DS test uses the Δ-value as the statistical test given by

$$\Delta = \sum_{i=1}^{N_{glo}} \delta_i. \quad (4.2)$$

This is the so-called "critical value" method. By this measurement, a global system is considered to have a kinematic substructure if $\Delta/N_{glo} > 1.0$ (Dressler & Shectman 1988).

For Aur 2 (N = 87, $\bar{v}$ = 6013 km s^{-1}, $\bar{\sigma}$ = 859 km s^{-1}) we measured $\Delta/N_{glo} = 1.5$ and for Aur 3 (N = 72, $\bar{v}$ = 9931 km s^{-1}, $\bar{\sigma}$ = 909 km s^{-1}) we find $\Delta/N_{glo} = 1.6$. Both these critical values point to the presence of substructures in these systems. The resulting "bubble plots" (Dressler & Shectman 1988) are displayed in Figs. 4.1 and 4.2 (panel c). The galaxy

positions are marked by circles with sizes relative to their kinematic deviations of $\exp(\delta_i)$ from their global structures. Using these plots we then considered galaxies to belong to the same substructure if they exhibit kinematic deviations of $\exp(\delta_i) > 5$, this value was chosen as it best resulted in substructures that were most coherent in both their spatial and velocity distributions. The galaxies that were assigned to the same substructure using these criteria as shown by a collections of circles with the same colours. Their velocity distributions are plotted separately in panels (d), (e) and (f) of Figs. 4.1 and 4.2. The velocity distribution of galaxies that are not associated with any substructure according to the criteria mentioned above are shown in panel (b) of Figs. 4.1 and 4.2.

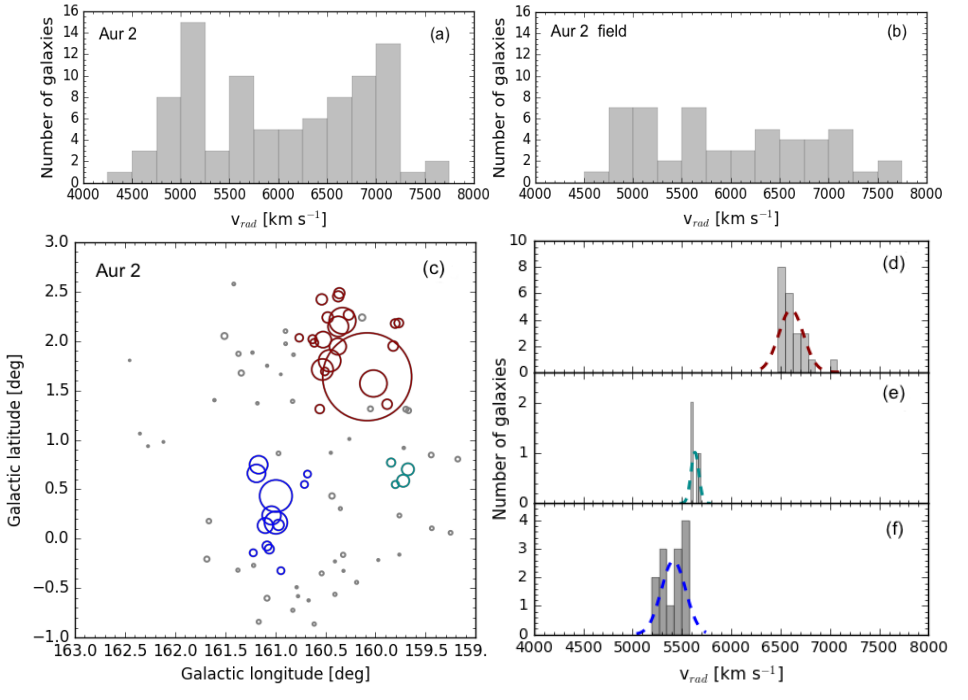

Figure 4.1 – Substructures identified in the Aur 2 overdensity ($cz \sim 4000 - 8000$ km s^{-1}). (a) The velocity distribution of galaxies detected in HI in the entire system. (b) The velocity distribution of galaxies unassociated with substructure. (c) The Dressler-Shectman "bubble plot" where the galaxy symbols are scaled with $\exp(\delta_i)$. The red, blue and cyan symbols denote galaxies which form substructures. Panels (d), (e) and (f) show the velocity distribution of the identified substructures where the dashed lines indicate the best-fitting Gaussian profile.

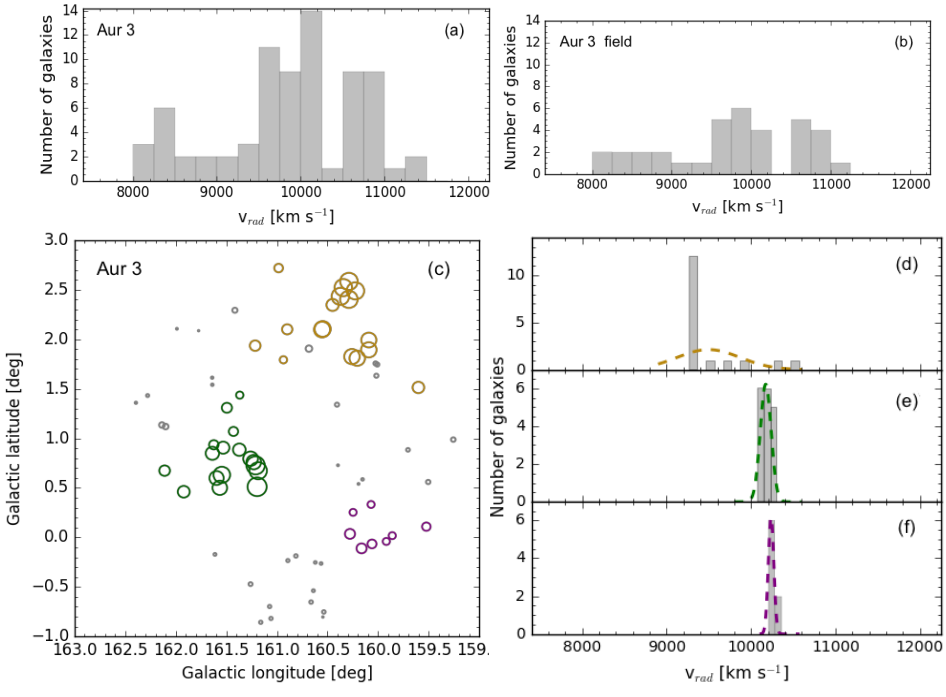

Figure 4.2 – Substructures identified in the Aur 3 overdensity $cz \sim 8000 - 12000$ km s^{-1}. (a) The velocity distribution of galaxies detected in the entire system. (b) The velocity distribution of galaxies unassociated with substructure. (c) The Dressler-Shectman "bubble plot" where the galaxy symbols are scaled with $\exp(\delta_i)$. The orange, green and purple symbols denote galaxies which form substructures. Panels (d), (e) and (f) show the velocity distribution of the identified substructures where the dashed lines indicate the best-fitting Gaussian profile.

4.3.2 The 2D-projection density

Given the low number of redshifts in these regions we also searched for spatial substructures on the sky by using the projected number density distribution of gas-poor galaxies identified in the near-infrared within the surveyed volume (see Chapter 3 for details). This was carried out by identifying galaxy neighbours following the SPH technique. This method calculates the density around a point by weighing each neighbour based on its distance from that point. From this definition the smoothed, projected galaxy density is given by

$$\rho = \sum_{i=1}^{n} W(r_i, d), \tag{4.3}$$

where n is the number of neighbours, r is the projected distance to each neighbour, d the distance to the n^{th} nearest neighbour and the weighting $W(r_i, d)$ is defined by Monaghan & Lattanzio (1985) as

$$W(r,d) = \frac{8}{\pi d^3} \begin{cases} 1 - 6\left(\frac{r}{d}\right)^2 + 6(\frac{r}{d})^3 & 0 \leq \frac{r}{d} \leq \frac{1}{2} \\ 2(1 - \frac{r}{d})^3 & \frac{1}{2} \leq \frac{r}{d} \leq 1 \\ 0 & \frac{r}{d} > 1. \end{cases} \tag{4.4}$$

This spline smoothing kernel is the standard in SPH and has better smoothing properties because it is centrally weighted with a finite tail unlike the TopHAT and Gaussian smoothing kernels. An important feature of an adaptive smoothing kernel is that it will not blur out filamentary structures into empty regions because it does not "oversmooth" dense regions. This is crucial as it has been shown from cosmological simulations that the transition between voids and filaments is significantly abrupt (van de Weygaert & Schaap 2009, Genel et al. 2014). Additionally, it preserves the distribution of galaxies better than a fixed smoothing kernel. We note that due to the adaptive nature of the smoothing kernel, the interpretation of the substructures could be complicated since the smoothing scale systematically changes with the environment, ranging from a small smoothing scale in overdense regions like clusters, to large smoothing scales in empty regions (e.g., voids).

We used an adaptive smoothing scale that included $n = 16$ neighbouring galaxies. The resulting two-dimensional (2D) projected density map is shown in greyscales in Fig. 4.3. Regions with a higher incidence of galaxies are seen darker.

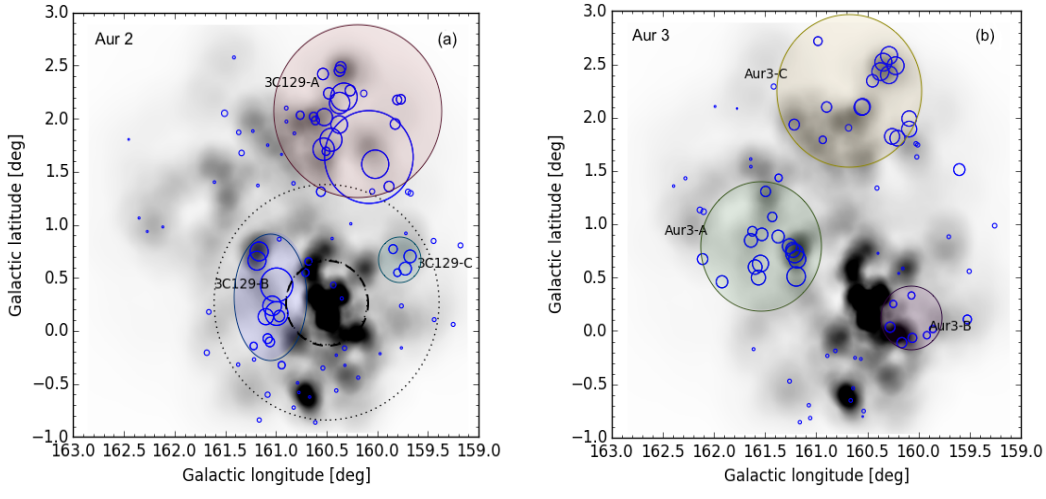

Figure 4.3 – The 2D-density projection map of galaxies on the red sequences shown by the grey contours. Overlaid in blue are the bubble plots of galaxies Aur 2 and Aur 3 based on the DS test. Identified substructures in both systems are marked and labeled. In panel (a) the radius of the 3C 129 cluster, r_{cl} = 1.7 Mpc = 1.34R_{200} ($R_{200} \sim 1.24$ Mpc ; Piffaretti et al. 2011) is illustrated by the large dotted circle and the core of the cluster, $R_{500} = \sim 0.8$ Mpc (Piffaretti et al. 2011) is shown by the smaller dashed circle.

We compared this map with the DS bubble-plots of the galaxies in the Aur 2 and Aur 3 environments as shown in panels (a) and (b), respectively. Based on this comparison we identified and labeled regions in the projected density map that are likely to coincide with substructures that were identified from the DS test bubble-plots. The sizes of these regions were chosen to be only large enough to include all the galaxies assigned to substructures based on these plots. The gas-poor galaxies within these regions were then assigned to these substructures. We do however, note that redshifts of the gas-poor galaxies are required to fully confirm these substructures, but given the high obscuration level, these are not easily obtainable.

4.4 Characterising environments

The presence of the substructures in the two major overdensities (Aur 2 and Aur 3) indicates a range of cosmic environments. In this section we discuss the main characteristics of the identified substructures.

4.4.1 Substructures in Aur 2 - The Perseus-Pisces ZoA Filament

We refer the reader to panel (a) of Fig. 4.3 for an illustration of the substructures discussed in this subsection.

The inner 3C 129 cluster is not identified with the DS test due to a lack of redshifts. The core radius of $r \sim 0.8$ Mpc, outlined by the smaller dashed circle in Fig. 4.3 is centred at $(\ell, b) \approx 160.5°, 0.27°$ and measured out to the characteristic radius R_{500}, being the radius of the cluster within which the mean overdensity is 500 times the critical density at the cluster redshift. It is the richest system in the surveyed volume which consist of 144 galaxies on the red-sequence and only 2 HI detected galaxies projected within its core. This is quite remarkable for the core of this X-ray cluster and is indicative of a gas depletion process, to be discussed in Sect. 4.5.1. It also comprises 2 spectroscopically confirmed members, the radio galaxies 3C 129 and 3C 129.1 with systemic velocities of 6236 km s^{-1} and 6655 km s^{-1} (Spinrad 1975), respectively. Within the cluster core, early-type galaxies make up 57% of the population. From its previous X-ray analysis in the 2.0 − 10 keV bands (Leahy & Yin 2000), it is estimated to have a total mass of $5 \times 10^{14} M_\odot$ and a total luminosity of 2.7×10^{44} erg.s^{-1}. The X-ray analysis also suggests that the cluster is not yet virialised as evidenced by the substructure in its X-ray morphology (see Leahy & Yin 2000). The galaxy distribution in the core of the cluster shows a fairly concentrated but elongated NW-SE spatial structure.

3C 129-A; Located North of the core of the cluster at $(\ell, b) \approx (160.19°, 2.07°)$, is the second largest substructure in the Aur 2 overdensity, containing 67 galaxies in total. It is the most HI-rich structure in this system with 22 galaxies (71% late-type) detected in HI and it has a large total fraction (60%) of late-type galaxies. We measured an average velocity of $\bar{v} = 6923$ km s^{-1} and a dispersion of $\sigma = 422$ km s^{-1} for this substructure. The HI

galaxies stand out with the largest deviations from the global kinematics of the Aur 2 population. The group is clearly separated in its velocity and spatial distribution from other substructures within the vicinity of the cluster core.

3C 129-B; Centred at $(\ell, b) \approx (161.05°, 0.33°)$ is a collection of about 51 galaxies, 13 detected in H I, 67% of which are late-type. Three of the H I detections are in an interacting system comprising one of the most H I massive galaxies in the volume with $\log(M_{HI}) = 10.3\ M_\odot$. In projection, the entire group is located closest to the core of the cluster with 58% of the galaxies being early-type in their morphology. It is quite tightly bound in velocity space with $\bar{v} = 5409$ km s^{-1} and $\sigma = 376$ km s^{-1}, and might be falling into the cluster centre.

3C 129-C; is the smallest substructure in the Aur 2 overdensity with $\bar{v} = 5877$ km s^{-1} and $\sigma = 126$ km s^{-1} centred at $(\ell, b) \approx (159.77°, 0.67°)$ with only 4 H I detected galaxies out of a total of 7. A small fraction (28%) of galaxies in this structure are early-type. The galaxies detected in H I are spatially coherent but their velocity offsets from the global population are only slightly above the set deviation threshold of $\exp(\delta_i) > 5$.

4.4.2 Substructures in Aur 3 - Behind the PPS ZoA Filament

The substructures discussed in this section are displayed in panel (b) of Fig. 4.3.

Aur 3-A; At $(\ell, b) \approx (161.54°, 0.80°)$ is the most prominent substructure in the Aur 3 system. No cluster is known near the spatial location and redshift of Aur 3-A but it coincides with the predicted CID 15 structure from the 2MRS reconstructed density maps (Erdoğdu et al. 2006). This substructure has a total of 71 galaxies, about 46% of which are early-types. A total of 17 galaxies are detected in H I with a velocity distribution that has an average of $\bar{v} = 10076$ km s^{-1} and a dispersion of $\sigma = 334$ km s^{-1}. The spatial distribution shows that, unlike the substructures in the Aur 2 system, the H I galaxies in Aur 3 coincide with the highest projected densities of galaxies identified in the near infrared.

Aur 3-B; is sparsely distributed spatially around $(\ell, b) \approx (160.15°, 0.1°)$, with only 8 H I-detected galaxies out of a total of 65, most ($\sim$66%) of which being late-type galaxies. The H I detected galaxies in this substructure have a mean radial velocity of $\bar{v} = 10281$ km s^{-1} and $\sigma = 524$ km s^{-1}. There is also a slight correlation in the spatial distribution of these H I detections and the near-infrared galaxies.

Aur 3-C; is the second largest substructure located at $(\ell, b) \approx (160.67°, 2.25°)$ comprising 54 galaxies. Half of the galaxies in this structure are early-types. We only detected 14 of these in H I. Most of these H I detections have a velocity of about 10203 km s^{-1} and also coincide with the near-infrared high density peak of galaxies in the North-West region in the spatial distribution of the galaxies. No known cluster is found in this region either.

Table 4.1 lists the number of galaxies, the velocity and the morphological type fractions for each of the substructures.

Table 4.1 – Characteristics of the identified substructures.

Main Structure	Substruc.	No. members HI (HI+NIR)	$< cz >$ km s^{-1}	σ km s^{-1}	$\frac{early}{late}$ HI+NIR	$\frac{early}{late}$ HI	Comments
Aur 2	The 3C 129 cl.	2 (144)	−−	−−	0.57	−−	Cluster core (R_{500}; $r = 0.8$ Mpc)
	3C 129-A	22 (67)	6923	422	0.40	0.21	
	3C 129-B	13 (51)	5409	376	0.55	0.33	
	3C 129-C	4 (7)	5877	126	0.28	−−	
Aur 2 field	—	46 –	5975	829	–	0.43	HI not associated with substructure
Aur 3	Aur 3-A	17 (71)	10076	334	0.46	0.20	
	Aur 3-B	8 (65)	10281	524	0.34	0.28	
	Aur 3-C	14 (54)	10203	375	0.50	0.25	
Aur 3 field	—	33 –	9837	928	–	0.31	HI not associated with substructure

4.5 The HI Gas Content in Various Environments

Observational and theoretical studies have shown that interactions between galaxies and their environments leave signatures on their fragile gas disks (Chung et al. 2009, Jaffé et al. 2011, Marasco et al. 2016). A well-known result of this is that galaxies in dense cosmic environments such as clusters and compact groups tend to be more gas-deficient compared to their isolated counterparts.

In this section we assess the HI gas-deficiency of galaxies within different environments in the WSRT PPZoA volume, in an effort to gain further insights into how and where galaxies lose their gas. This is conducted by examining their HI-mass relative to their K-band luminosity (M_{HI}/L_K) and their HI deficiency parameter Def_{HI} (Haynes, Giovanelli & Chincarini 1984, Solanes et al. 2001, Gavazzi et al. 2008). The latter defines the HI-deficiency as the logarithmic difference between the observed HI content and the expected value in isolated galaxies of the same linear size and morphology. We adopt the distance-independent approximation of Def_{HI} described by Solanes et al. (2002).

$$Def_{HI} = \left\langle \log\bar{\Sigma}_{HI}(T) \right\rangle - \log\bar{\Sigma}_{HI}, \tag{4.5}$$

where $\bar{\Sigma}_{HI}$ is the so-called mean "hybrid" HI surface density for a given morphological type T, computed within the optical disk as $\bar{\Sigma}_{HI} = S_{HI}/D^2_{opt}$ where S_{HI} is the total flux in Jy km s^{-1} and D_{opt} is the apparent optical diameter in arcmins. Given the high optical extinction in our survey area we are forced to use instead the extinction corrected (e.g., Riad, Kraan-Korteweg & Woudt 2010) diameter as measured in the NIR K-band at the 20 mag arcsec^{-2} isophote. We adjusted the NIR diameters to the expected optical diameters (D_{B25}) using the scaling factors provided by Jarrett (2000). We follow the prescription by Chung et al. (2009) and adopt the definition of Def_{HI} that is independent of morphological type by comparing all the morphologies to a mean hybrid HI surface density of $\log\left\langle \bar{\Sigma}_{HI}(T) \right\rangle = 0.37 \pm 0.07$ (Chung et al. 2009).

4.5.1 The HI-Content of the 3C129 Cluster Galaxies

The most striking behaviour of the H I-deficiency in galaxy clusters is its dramatic increase towards the cluster centre. This is particularly evident in rich Coma-like clusters that are characterised by high X-ray luminosities. In this case, ram-pressure stripping by the ICM is thought to be the dominant process for removing gas from galaxies (Giovanelli & Haynes 1985b, Bravo-Alfaro et al. 2000b, Schröder, Drinkwater & Richter 2001, Gavazzi et al. 2006, Dénes, Kilborn & Koribalski 2014). This cluster-centric increase of the H I-deficiency has been shown to also occur in less-rich and younger clusters such as the Virgo cluster, albeit in a less dramatic manner (Solanes et al. 2002, Safonova 2011). The X-ray luminosity of the 3C 129 cluster characterises it as a cluster that is more massive than the Virgo cluster, but not as massive and dynamically relaxed as the Coma cluster.

In this section we examine the projected radial behaviour of the H I-deficiency of galaxies in the relatively rich and dynamically non-relaxed 3C 129 cluster. The radial projected distance of galaxies is measured from the cluster centre at $(\ell, b) \approx (160.52°, 0.27°)$ as adopted from its X-ray emission, out to a maximum projected radius of $r_{cl} \approx 1.7$ Mpc. Within this volume 43 galaxies were detected in H I. However, for only 24 of these galaxies a NIR counterpart in the UKIDSS-GPS images could be identified. We used these 24 galaxies to calculate their relative H I-content as a function of the projected radial distance as shown in Fig. 4.4.

The inner regions: Within $r_{cl} < 0.5R_{200}$ ($R_{200} \sim 1.24$ Mpc) we find a single H I-detected galaxy. It is tempting to infer that this could be the result of a selection bias given that 19 out of the 43 galaxies that were detected in H I, could not be included in the construction of Fig. 4.4. We consider this possibility by inspecting the spatial distribution of all 43 galaxies detected in H I (with and without a NIR counterpart; e.g., left panel of Fig. 4.3). Only 2 out of 43 H I-detected galaxies are located within $r_{cl} < 0.5R_{200}$, with one of these two galaxies lacking a near-infrared counterpart. Thus the lack of H I detections within this inner projected radius is unlikely due to a sample selection bias.

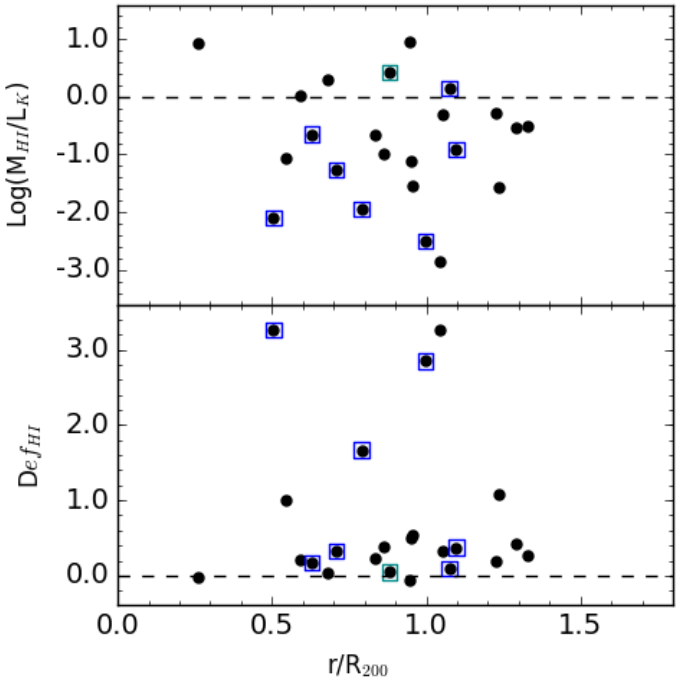

Figure 4.4 – The HI gas content of galaxies in the 3C 129 cluster as a function of their projected radial distance from the cluster centre. The upper panel shows the distribution of the $\log(M_{HI}/L_K)$ values and the bottom panel is the HI-deficiency parameter (Def_{HI}). Symbols enclosed in blue boxes denotes galaxies within the 3C129-B group.

The paucity of H I-detected galaxies within this inner projected radial distance can probably be attributed to the high ICM density of $\rho_0 = 6 \times 10^{-3}\mathrm{cm}^{-3}$ (Leahy & Yin 2000), which would strip the H I gas of galaxies through ram-pressure. This is supported by the X-ray maps of Leahy & Yin (2000) from ROSAT, which show that the X-ray emission of the 3C 129 cluster can be traced out to a radial distance of roughly $0.6R_{200}$, beyond which we start detecting galaxies in H I. As a result of this ram-pressure stripping, the measured H I-deficiency of galaxies is expected to increase toward the cluster centre to a level at which H I-depleted galaxies would not have been detected as they fall below our H I-mass detection limit. One might also be tempted to interpret this as just the classical morphology-density relation, but we note that more than 40% of the galaxies seen in projection against the centre of the cluster were estimated to be late-type galaxies, which are commonly known to be gas-rich (see Table 4.1).

The one galaxy within this region with $\log(M_{HI}/L_K) \approx 1.0$ $M_\odot/L_\odot$ and $Def_{HI} = -0.09$ displays a radial velocity of $cz \approx 4639$ km s^{-1}, while the line-of-sight velocity of the 3C 129 cluster is $cz = 5227$ km s^{-1} as measured from the H I detections (see Chapter 3), and $cz \sim 6295$ km s^{-1} when based on the two radio galaxies with optical redshifts (Spinrad 1975). It is possible that this one H I-detected galaxy is physically located further from the cluster core than it appears at its projected distance or infalling from behind.

The cluster outskirts: At larger projected distances from the cluster core we find eleven galaxies with a low relative H I-content of $\log(M_{HI}/L_K) < -1.0$ $M_\odot/L_\odot$, distributed over projected radial distances of $0.5R_{200}$ to $1.25R_{200}$. This low gas content is also demonstrated by the non-zero H I-deficiency parameter (Def_{HI}) measured over that projected radial distance range. We find that about 60% of galaxies that are substantially gas-poor with a relative H I-content of $\log(M_{HI}/L_K) < -1.5$ $M_\odot/L_\odot$ are actually located even further out from the centre of the cluster, at $r_{cl} > 0.75R_{200}$. We measured a mean of $<\log(M_{HI}/L_K)> = -0.89 \pm 0.06$ $M_\odot/L_\odot$ for these galaxies and a mean of $<\log(M_{HI}/L_K)> = -0.79 \pm 0.13$ $M_\odot/L_\odot$ for galaxies closer to the core of the cluster within $0.5R_{200} < r_{cl} < 0.75R_{200}$. These two means are not significantly different according to the student-t test which gives a p-value of 0.89. It therefore appears that galaxies relatively closer to the core of the cluster are not much more gas poor than those further out. This is not due to their intrinsic nature since ∼70% of the galaxies further from the cluster core were found to be late-type galaxies which are known to be usually gas-rich. It seems likely that another gas removal mechanism such as galaxy-galaxy interactions within subgroups maybe responsible for the relatively low measured H I content. We support this claim by noting that the spatial and velocity distributions of some of the gas-poorest galaxies with $\log(M_{HI}/L_K) < -1.5$ $M_\odot/L_\odot$ place them within the 3C 129-B group, which comprise 67% of late-type galaxies. Galaxies in this group are indicated by the blue boxes in Fig 4.4.

Our assessment of the H I-content of 24 galaxies in the cluster is hindered by low number statistics and our simple analysis does not point to any overall gas removal mechanism. We find that the ICM plays a role in depleting gas from the galaxies once they get within the vicinity of the X-ray emission, while galaxy-galaxy interactions within galaxy groups in the cluster outskirts are likely responsible for the removal of gas.

4.5.2 Comparison with other environments

In addition to the physical H I-gas removal mechanisms in the various environments, insights into the origin of the H I-content in galaxies can be inferred from evaluating its variation with the intrinsic properties of the galaxies such as their morphologies.

We examine the H I-content by measuring $\log(M_{HI}/L_K)$ and Def_{HI} of galaxies as a function of their morphology in the various cosmic environments found in the entire WSRT PPZoA volume. This is carried out by categorising all the H I galaxies with identified NIR counterparts into three environments. One environment is the X-ray emitting 3C 129 cluster which is formed by galaxies within the radius of the cluster of $r_{cl} \approx 1.7$ Mpc. This population includes galaxies in the 3C 129-B and 3C 129-C groups within this cluster radius. Galaxies in this cluster environment are likely affected by both ram-pressure stripping and tidal interactions. The other environment constitutes galaxies located in substructures/groups identified in Sect. 4.4 but excludes the aforementioned groups that lie within the radius of the 3C 129 cluster. These groups of galaxies have no known cluster association nor any X-ray emission at their locations. Galaxies in this group environment are likely not affected by ram-pressure stripping while tidal interactions are likely. The last environment is composed of the field galaxies which do not belong to any substructure nor cluster association in the entire survey volume ($cz \approx 2000 - 16000$ km s^{-1}). Galaxies in this field environments are not expected to be affected by gas removal processes. As a comparison sample we also consider the $\log(M_{HI}/L_K)$ and Def_{HI} values of the galaxies in the Virgo cluster as extracted from data provided by Chung et al. (2009).

For this analysis we adopt the estimated morphological types of the galaxies as defined from the NIR images, i.e. early-types (E/S0), early-spirals (eS), mid-range spirals (mS), late-spirals (ℓS) and everything else later than ℓS as Irregulars (Irr).

The relative H I gas content as a function of galaxy morphology is shown in Fig. 4.5. Galaxies in all three cosmic environments share a common pattern from late-type to early-type galaxies: A strong negative trend in $\log(M_{HI}/L_K)$ indicating a decreasing relative H I-content toward early-types, and a positive trend in Def_{HI} demonstrating an increasing H I-deficiency toward early-types.

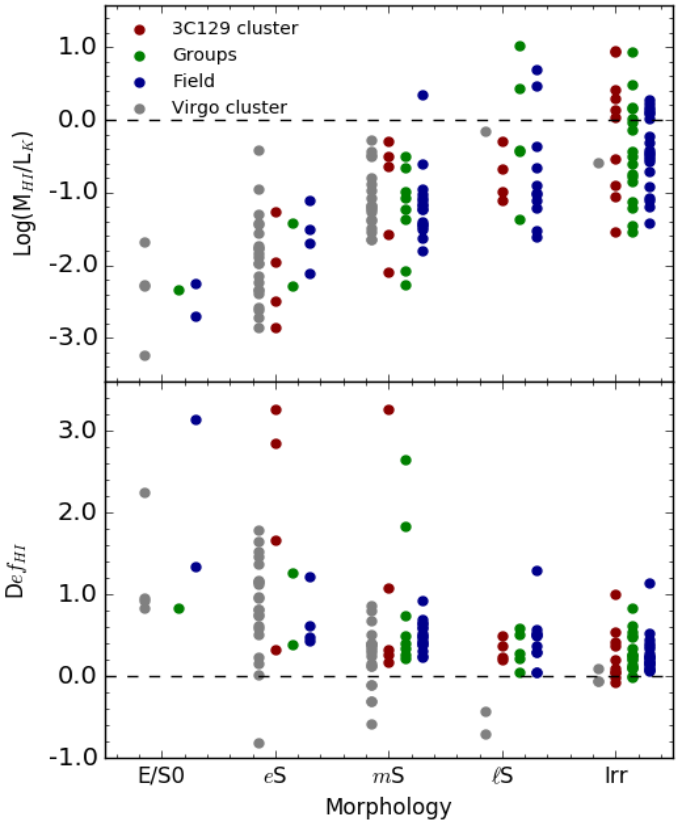

Figure 4.5 – The HI gas content as function of the galaxy morphology in the 3C 129 cluster shown in red symbols. The galaxy groups are represented by green symbols and field galaxies are shown in blue. The grey symbols are the Virgo cluster galaxies. The upper panel shows the distribution of the $\log(M_{HI}/L_K)$ and the bottom panel is the HI-deficiency parameter (Def_{HI}).

This is not surprising since early-type galaxies are known to be gas-poor. For the early-type galaxies (eS) in the cluster we measure a median of $\log(M_{HI}/L_K) = -2.2 \pm 0.6$ $M_\odot/L_\odot$ and $Def_{HI} = 2.3 \pm 1.1$. For the group population we find $\log(M_{HI}/L_K) = -1.8 \pm 0.42$ $M_\odot/L_\odot$ and $Def_{HI} = 0.8 \pm 0.4$. The early-type galaxies in the field have $\log(M_{HI}/L_K) = -1.6 \pm 0.5$ $M_\odot/L_\odot$ and $Def_{HI} = 0.5 \pm 0.3$. These measurements show that early-type galaxies in the cluster are slightly gas-poorer compared to early-type galaxies in the group and field environments. This is expected and is likely due to a combination of the nature of these galaxies and a gas removal mechanism in the cluster. This is supported by noting that E/S0 galaxies were only detected in the field and group environment and none were detected in the cluster.

The late-type population (mS, ℓS and Irr) exhibits a median of $\log(M_{HI}/L_K) = -0.7 \pm 0.6$ $M_\odot/L_\odot$ and $Def_{HI} = 0.3 \pm 0.9$ in the cluster, $\log(M_{HI}/L_K) = -0.9 \pm 0.8$ $M_\odot/L_\odot$ and $Def_{HI} = 0.5 \pm 0.7$ in galaxy groups, and $\log(M_{HI}/L_K) = -1.0 \pm 0.6$ $M_\odot/L_\odot$ and $Def_{HI} = 0.4 \pm 0.2$ in the field galaxy population. Based on these measurements, it is interesting to note that contrary to expectations there is no evidence suggesting a lower H I-content or a higher gas-deficiency in late-type galaxies located in the cluster compared to those in groups or in the field. However, it is worth noting that the field galaxies are not completely isolated but are part of large-scale filamentary structures within the WSRT volume (see Sect. 2.7) and may suffer from other gas-removal mechanisms as they travel through the filaments. The role played by these filamentary structures on the H I-gas is not yet clear. For comparison we note that the Virgo galaxies have median values of $\log(M_{HI}/L_K) = -1.2 \pm 1.2$ $M_\odot/L_\odot$ and $Def_{HI} = 0.2 \pm 0.4$ for the same late-type morphologies, thus indicating similar relative H I-content and gas deficiency as the 3C 129 cluster.

4.6 HI Morphologies

Peculiarities in the H I content, morphology and kinematics of galaxies have become an important tool in deciphering the effect of the environment on galaxies. By studying the various H I properties in relation to data from other wavelengths, crucial impacting mechanisms on the individual galaxies can be identified. Having characterised the various environments in the WSRT PPZoA volume we can now investigate the H I morphologies of the galaxies localised therein and gain hints on the possible processes taking place.

In this section we evaluate the range of H I morphologies in substructures outlined in Sect. 4.4. For this purpose we examine the H I-global profiles, integrated H I-maps and kinematics of galaxies in the substructures to identify disturbances in their H I distribution.

Asymmetries in the H I-global profiles are assessed by computing the ratio of the integrated flux ($S_{HIratio} = S_{HI,h}/S_{HI,l}$) where $S_{HI,h}$ is from the side (receding or approaching) of the H I-global profile with the highest integrated flux and $S_{HI,l}$ is from the lower side (Espada et al. 2011). Asymmetries in the integrated H I-maps are determined visually from the second lowest H I-column density contour in the maps. Kinematic lopsidedness is determined by visually inspecting the velocity fields and position velocity diagrams in a similar way as Swaters et al. (2002) have done. For galaxies with a UKIDSS counterpart we also measured offsets between the stellar and gas components. The necessary H I data used were extracted from the H I atlas and catalogue of Ramatsoku et al. (2016) and NIR coordinates were determined from co-added J+H+K band images. The UKIDSS-GPS has a nominal positional accuracy of $\sim 0.1'' - 0.3''$ (Lucas et al. 2008).

We note that determining H I morphologies by visually inspecting integrated H I-maps is prone to some subjectivity. Moreover the low signal-to-noise may result in artificial asymmetric H I distributions. In the future, using non-parametric methods such as those proposed by Giese et al. (2016) should provide a more homogenous and improved characterisation of the H I morphologies of galaxies since they will take these effects into account. These methods are however not available currently as they are still under development.

4.6.1 HI Morphologies in Aur 2

Figure. 4.6 shows a compilation of the integrated H I maps for all 87 galaxies located in the Aur 2 system. Individual galaxies are three times enlarged and placed at their proper positions on the sky. The X-ray emission contours of the 3C 129 cluster and the two radio sources located in this overdensity are also displayed, but at their actual size.

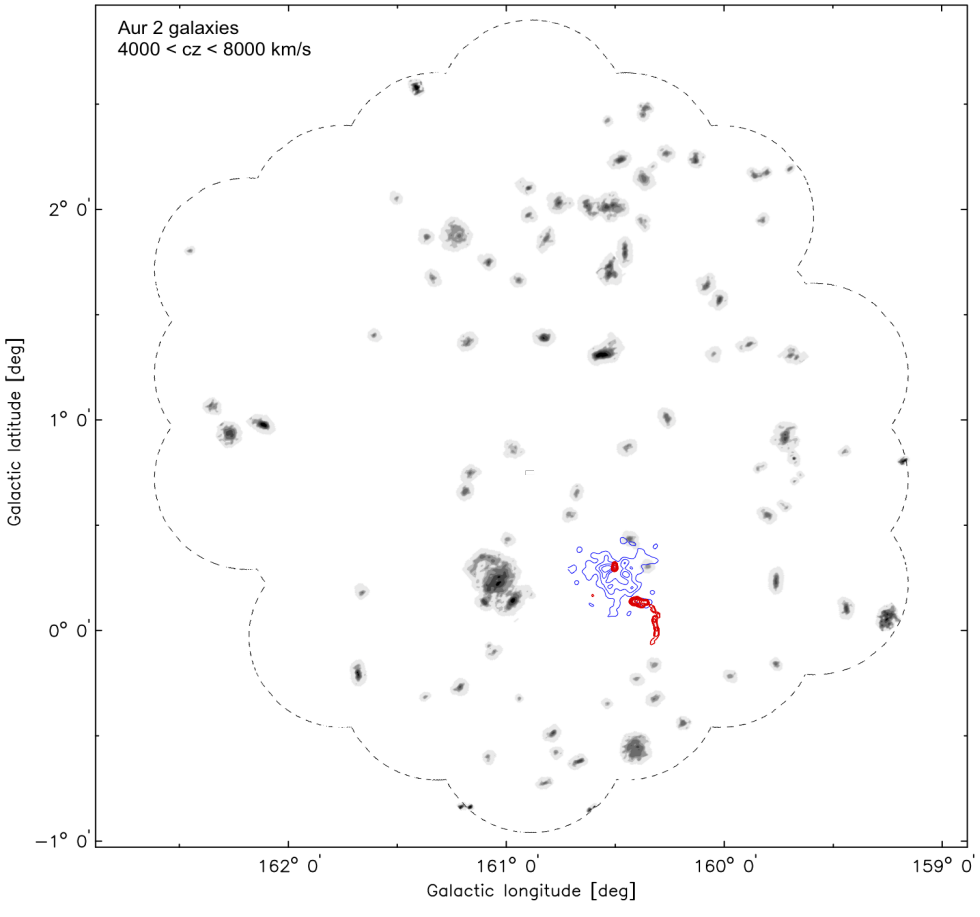

Figure 4.6 – The integrated HI maps with 23 × 16 arcsec angular resolution of all galaxies detected in HI in the Aur 2 overdensity. Galaxies are scaled up by a factor of 3. The X-ray emission of the 3C 129 cluster is shown in blue and the position of the contours of the radio sources 3C 129 and 3C 129.1 are shown in red. The dotted line outlines the WSRT PPZoA surveyed region.

3C 129-A: Figure 4.7 presents a close-up of the 3C 129-A group. Galaxies in this region are mostly characterised by a one-sided tail as evident from their integrated H I-maps (panel a). We identified asymmetries in H I-maps for ∼64% of galaxies located in this group. This asymmetry is also seen to some degree in their H I-global profiles (panel b) with 50% of the galaxies exhibiting $S_{HIratio} > 1.2$. The offsets between the H I and NIR centroids range from negligible offsets of ∼2″ to significant offsets as large as 20″ (see panel c).There is not preferred direction for the offsets of the gas disks with respect to the stellar disks. In the bottom part of Fig. 4.7 we show typical examples for the range of H I properties found in this structure. These galaxies are located at a projected distance of 2.9 Mpc from the core of the 3C 129 cluster thus ram-pressure stripping is unlikely responsible for the observed asymmetric morphologies. Instead, the H I asymmetries probably originate from gravitational interactions between the galaxies.

3C 129-B: This group of galaxies is located at a projected distance of 0.7 Mpc from the 3C 129 cluster core (panel (a) of Fig. 4.3). Galaxies in this region show a wide range of H I-morphologies. We find asymmetries in H I-maps for 54% of these galaxies. This is mostly due to the fact that the group comprises a tidally interacting triplet which results in asymmetric disks of those galaxies (e.g., panel (a) of Fig. 4.8). This interacting subgroup aside, the most common characteristic among the non-interacting galaxies is that the H I-disks do not show any distinct signs of asymmetries nor any significant offsets between the NIR and H I centres (5″ at most; panel b). There are also no obvious asymmetries inferred from the H I-global profiles. The lack of asymmetries is contrary to expectations since ram-pressure stripping from the X-ray emission, which would result in H I offsets from stellar components and in the presence of H I-tails, is supposed to be significant at these locations, given the vicinity of this group to the cluster centre. They do however exhibit smaller H I-radii compared to the stellar disk, with a median of $\frac{D_{HI}}{D_K} \sim 3.12$, with D_K measured from the K-band 20 mag arcsec^{-1} isophote. These kinds of galaxies with smaller relative H I-disks but without any morphological asymmetries, close to cluster centres are thought to result from gas depletion mechanisms such as thermal evaporation, starvation or viscous stripping, since these processes affect the entire disk on longer timescales compared to ram-pressure stripping (Nulsen et al. 1982, Cayatte et al. 1994).

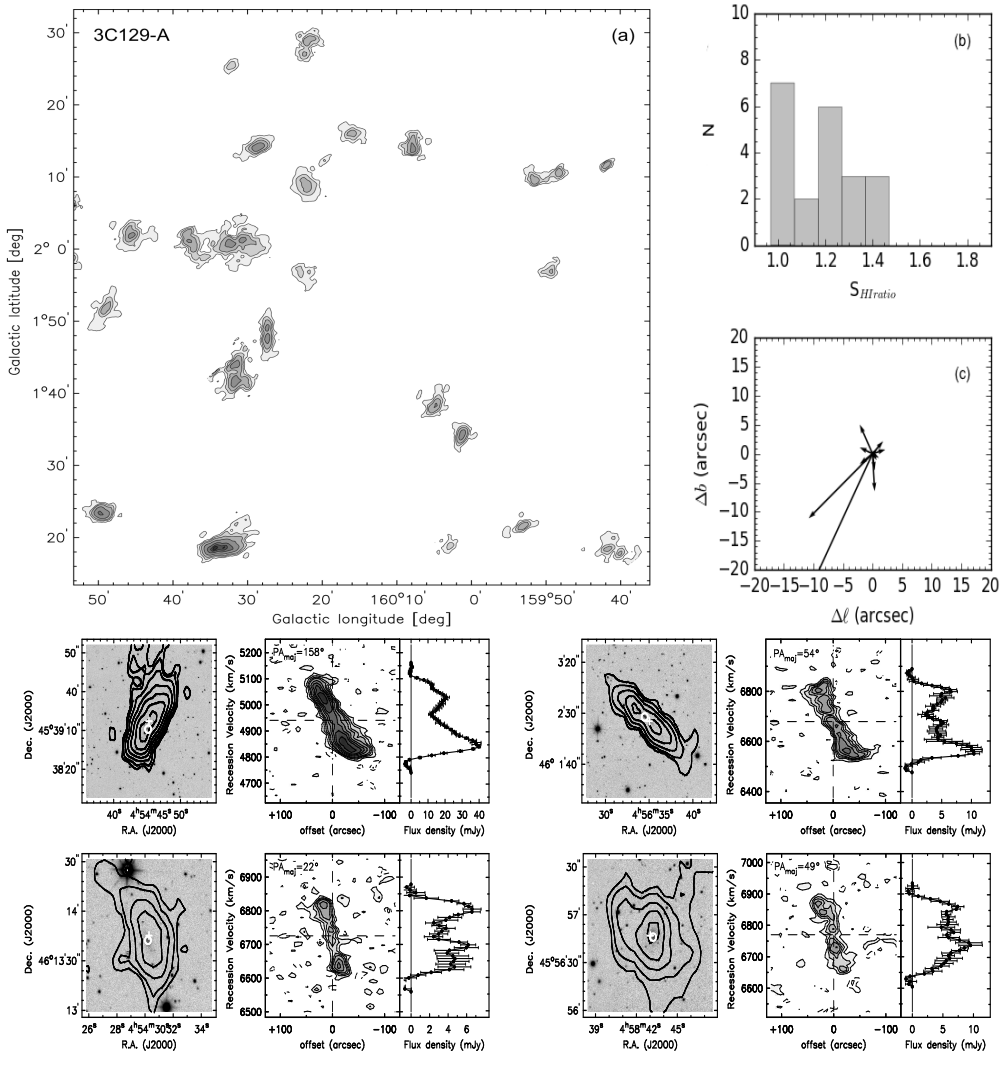

Figure 4.7 – The HI map of all the galaxies in the 3C129-A substructure is shown in panel (a). In panel (b) we show the integrated flux ratio, $S_{HIratio}$ distribution. The offsets between of the gas disks with respect to the stellar disks are shown in panel (c). The smaller images in the bottom panels are examples (selected at random) of the HI properties used to characterise galaxies in this structure. For each of the example galaxies we show in the left panel, the total HI maps at the $23'' \times 16''$ angular resolution overlaid over the K-band image. The HI column density contour levels are at 1, 2, 4, 8, 16, 32... $\times\ 10^{20}$ atoms/cm^2. The white cross and circle indicate the HI and NIR centroids, respectively. The middle panels show the major-axis position-velocity diagrams at a velocity resolution of 16.5 km s^{-1}. The global HI profiles are shown in the right panel where the connected black dots give the primary-beam corrected integrated HI flux density in each channel at a velocity resolution of 16.5 km s^{-1}.

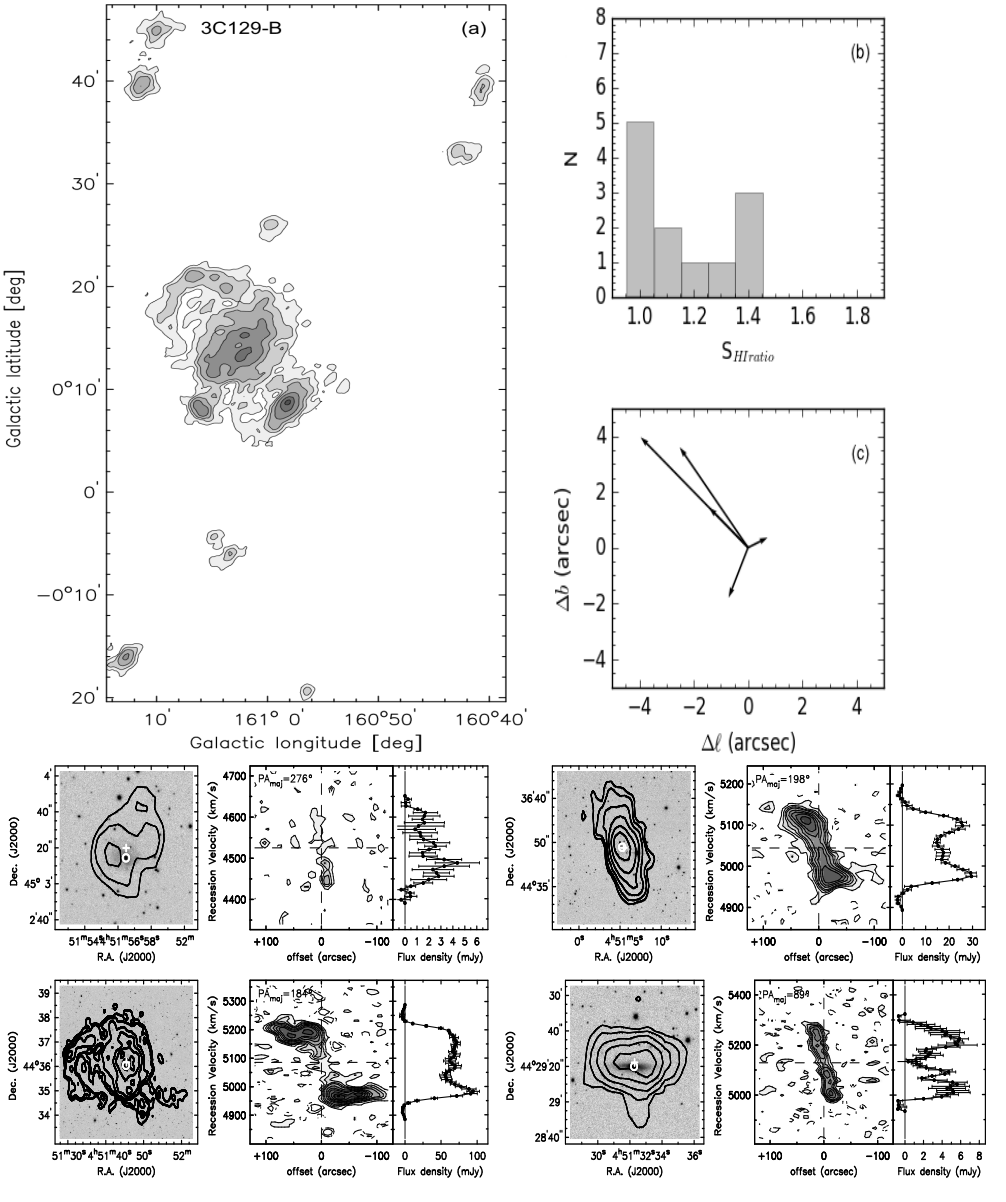

Figure 4.8 – Same as Fig. 4.7 but for the 3C129-B substructure.

3C 129-C: Galaxies in this small substructure do not show any signs of asymmetries in their H I-maps, global profiles or kinematics. The small number statistics does not allow for any further detailed analysis.

4.6.2 HI Morphologies in Aur 3

A composite image of the total H I maps for the 72 galaxies in the Aur 3 overdensity is shown in Fig. 4.6. The individual galaxies are located at their proper sky positions and enlarged three-fold, as in Fig. 4.6.

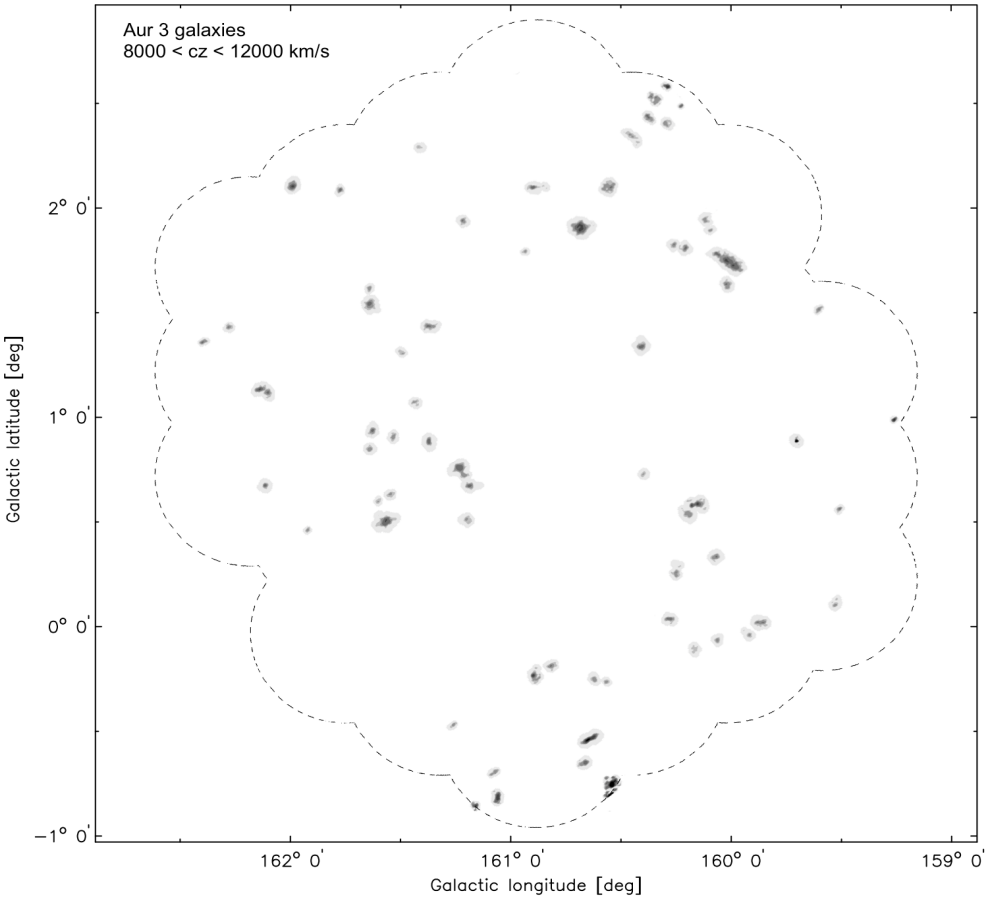

Figure 4.9 – The integrated HI maps with 23 × 16 arcsec angular resolution of all galaxies detected in HI in the Aur 3 overdensity, scaled up by a factor of 3.

Aur 3-A: This group comprises galaxies that show distortions in their global HI profiles with 63% of the galaxies exhibiting $S_{HIratio} > 1.15$ (panel (b) of Fig. 4.10). We also note asymmetries in their kinematics for 41% of the galaxies and in their integrated HI-maps for 53% of the galaxy population (panel a). About 83% of the galaxies with a near-infrared counterpart show offsets larger 5″ between the gas and stellar disks. Interestingly, all offsets are to the North. We previously mentioned that we are not aware of any cluster nor X-ray emission in or near the location of this substructure. The apparent offsets of the HI gas likely arise from a high incident of galaxy-galaxy interactions. This has a high probability given their tight spatial distribution and low velocity dispersion (e.g., Sect. 4.4.2), although the systematics in the offsets would better fit the notion of coherent ram-pressure stripping.

Aur 3-B: As illustrated in panel (b) of Fig. 4.11, only slight asymmetries in the global HI profiles are evident in galaxies located in this small HI group. Most of them (66%) are edge-on spiral galaxies as classified in the near-infrared K-band images. A fraction of 38% shows a slight compression on one side and a minor one-sided tail on the other side in their integrated HI map contours (see panel a). The low number count does not allow us to make concrete claims. However, given that their spatial distribution coincides with a high projected density of galaxies identified in the near-infrared we could speculate that it is possible that they are gravitationally interacting within this high density environment. For the galaxies in this group too, there seems to be a systematic offset of the HI disks.

Aur 3-C: As shown in Fig. 4.12, a relatively large fraction (57%) of galaxies in this group exhibits signs of asymmetries in their HI-global profile of $S_{HIratio} > 1.15$. We also find asymmetries in 64% of the galaxies as inferred from their HI integrated maps. A comparison of the integrated HI maps with their stellar disks for those with NIR counterparts shows offsets as large as ∼5″ (panel c). Galaxies in this group might be experiencing gravitational interaction within a high galaxy density environment. This claim is supported by the compact spatial distribution which coincides with the peak density of near-infrared galaxies as shown in panel (a) of Fig. 4.3.

Table C, in Appendix C, lists the HI and NIR properties of the galaxies used to assess the HI-morphologies and HI-content.

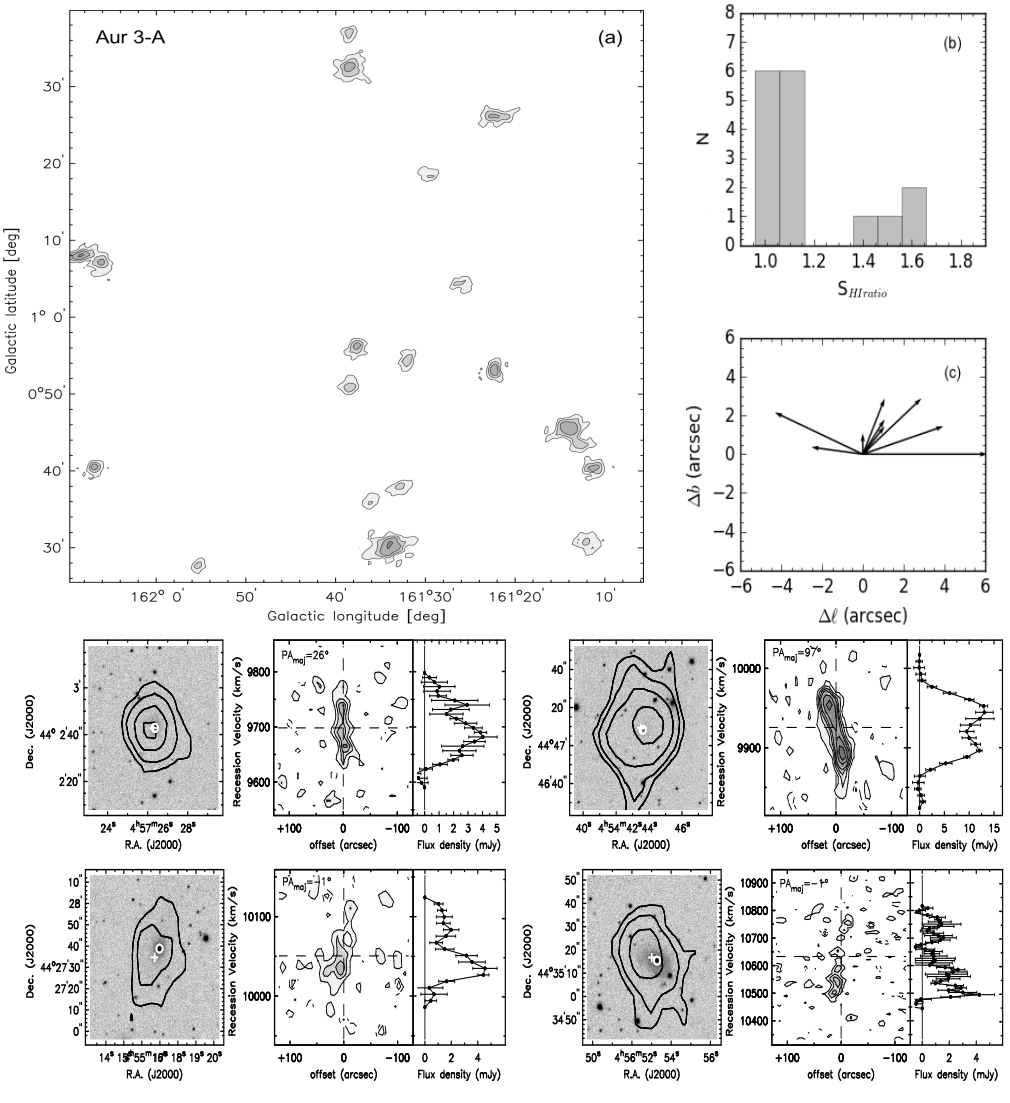

Figure 4.10 – Same as Fig. 4.7 but for the Aur 3-A substructure.

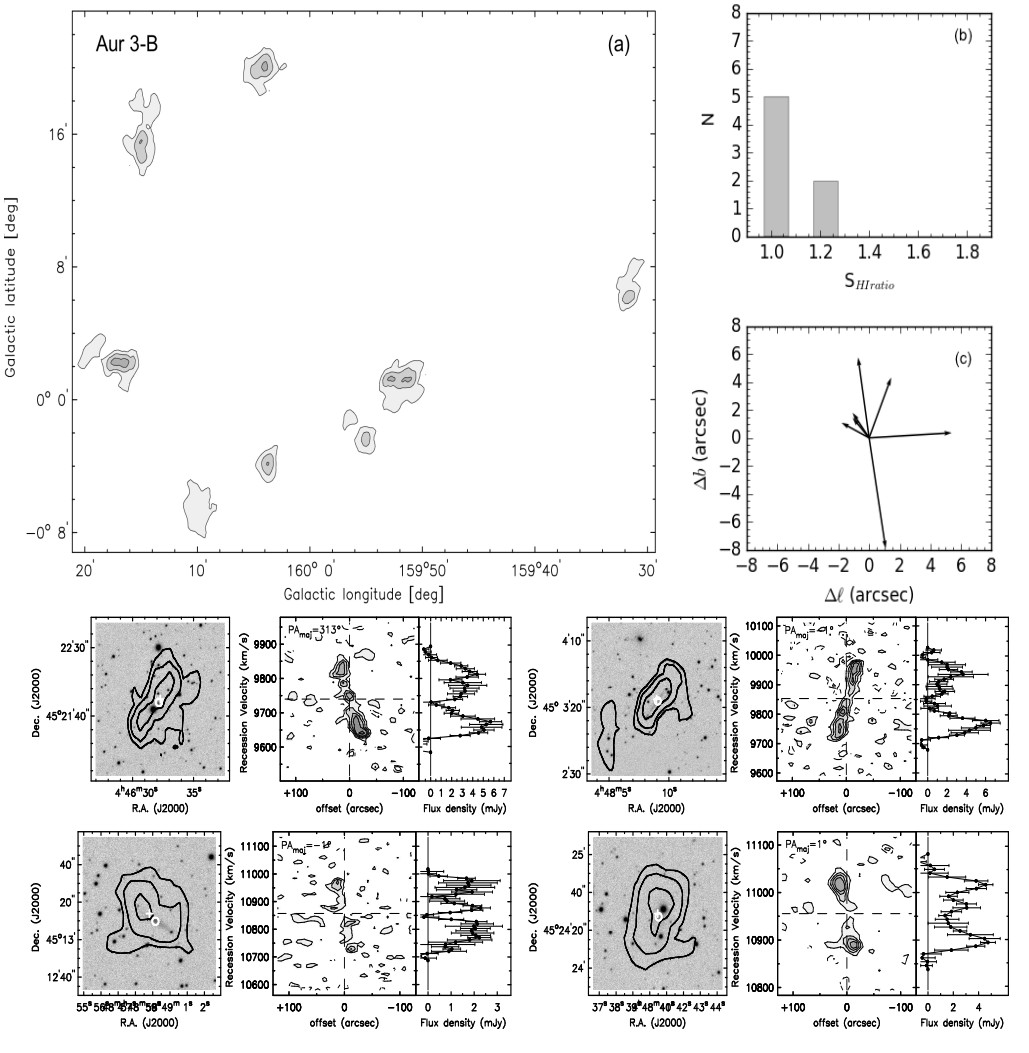

Figure 4.11 – Same as Fig. 4.7 but for the Aur 3-B subtructure.

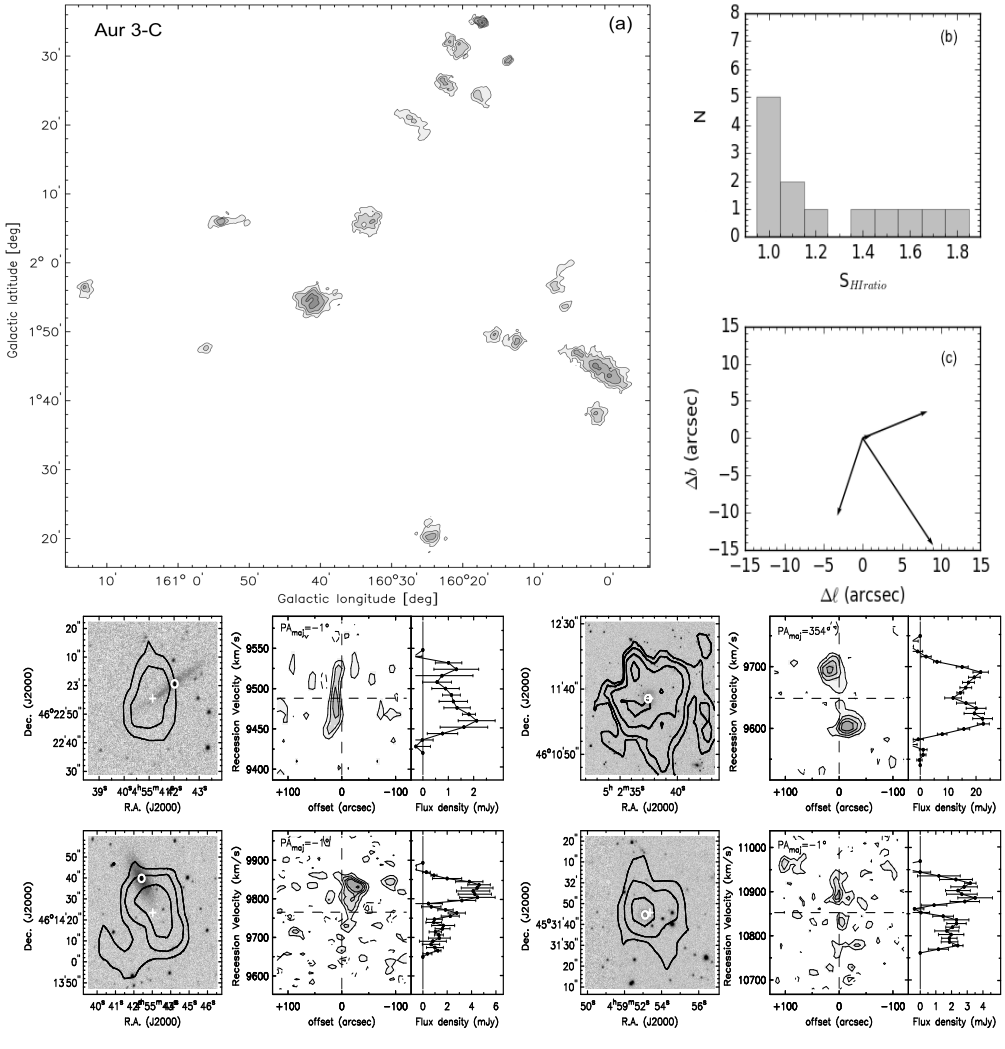

Figure 4.12 – Same as Fig. 4.7 but for the Aur 3-C subtructure.

4.7 A phase-space view of the 3C 129 cluster

In subsection 4.5.1 we focused on the HI content of galaxies as a function of the projected distance from the cluster centre. Galaxies appeared to be gas-deficient even at further distances from the cluster core where ram-pressure stripping is expected to be less effective. We attributed this pattern to galaxy-galaxy interactions within the subgroups. However, the other agent to consider for the observed HI-content of galaxies is their orbital histories. For example, a strong dependence on the galaxy gas deficiency was found in the Virgo cluster by Vollmer et al. (2001) who reported that the population of the most gas-deficient galaxies seem to have experienced at least one pericentric passage. It would thus be desirable to characterise the three-dimensional distribution of galaxies in a cluster and trace their orbital trajectories. This is a complex task because rich galaxy clusters have velocity dispersions of about 1000 km s^{-1}. As a result, the line-of-sight (l-o-s) distance of a given cluster member can only be measured with an accuracy no better than 15 Mpc (Hernández-Fernández et al. 2014).

Nevertheless, recent studies have shown that clues to the orbital histories of galaxies can be estimated by combining their projected positions with the kinematics of the galaxy distribution as a function of galaxy properties. An effective analysis method is to evaluate the cluster projected phase-space, defined by the projected radius and the l-o-s velocity of galaxies in the cluster-frame (Hernández-Fernández et al. 2014). Such a diagram displays lower limits on the three-dimensional distance to the cluster core and the l-o-s velocities of the cluster galaxies. This projected phase-space also makes it possible to statistically infer whether a galaxy is still falling into the cluster or is already within the virialised region of the cluster, or even whether it belongs to a population of so-called backsplash galaxies (Oman, Hudson & Behroozi 2013).

In this section we explore the location of HI-detected galaxies in the cluster projected phase-space in an attempt to gain further insights into how the inferred orbital histories of galaxies in the 3C 129 cluster could have shaped their current observed HI properties. For this purpose we selected all galaxies that were detected in HI within a projected distance from the cluster centre of $r_{cl} = 1.7$ Mpc. The l-o-s velocities normalised by the cluster velocity dispersion were determined by,

$$\frac{\Delta v}{\sigma_{cl}} = \frac{c(z - z_{cl})}{\sigma_{cl}(1 + z_{cl})}, \tag{4.6}$$

where c is the speed of light and z_{cl} and σ_{cl} are the estimated redshift and velocity dispersion of the cluster. We adopted a redshift of $z_{cl} = 0.02$ from the optical spectroscopy of the radio galaxies in the centre of the cluster and used $\sigma_{cl} = 765$ km s^{-1} as inferred from the β-model of the cluster by Leahy & Yin (2000). This dispersion is smaller than that measured from the H I-detections of $\sigma_{cl} = 1097$ km s^{-1}, but might better describe the cluster potential in the absence of optical spectroscopic redshifts.

Figure. 4.13 illustrates the galaxy distribution of the projected phase-space of the 3C 129 cluster. The diagram is basically a schematic representation of how the galaxy cluster assembles as galaxies approach into its gravitational potential. It demonstrates how galaxies fall in from larger radii and become members of the virialised population in the cluster centre. This virialised region is shown by the grey dashed lines based on Eqs. (2) and (3) by Mahajan, Mamon & Raychaudhury (2011). It is best approximated by a triangular shape, noting that within $r_{cl} < R_{200}$ a cluster is measured to have a dispersion of $\sigma_{cl} \approx 0.65\Delta v$ as predicted from hydrodynamical simulations by Mamon, Biviano & Murante (2010). The dotted grey lines represents the escape velocity assuming the cluster's total mass is distributed in accordance with a NFW potential (Navarro, Frenk & White 1996). The escape velocity was projected to the l-o-s velocity by applying the scaling factor of $v_{esc} \sim \sqrt{3\sigma_{cl}}$.

We first note that only a small fraction of about 18% of the H I detected galaxies that are confirmed members of the cluster, have velocities in excess of the escape velocity. Considering that the PPS resembles a filamentary sheet extending from $cz \sim 4000 - 8000$ km s^{-1} (Giovanelli & Haynes 1985a, Giovanelli et al. 1986, Seeberger, Huchtmeier & Weinberger 1994), these galaxies are likely members of subgroups that are falling into the 3C 129 cluster from the PPS filament. However, it is also important to note that the NFW model assumes a spherical potential. Most clusters, however, do not have spherical halos. This is likely the case with the 3C 129 cluster given that it shows hints of being in the process of accreting substructures as discussed in Chapter 3. Consequently, the lines in Fig. 4.13 should merely be considered as indicative.

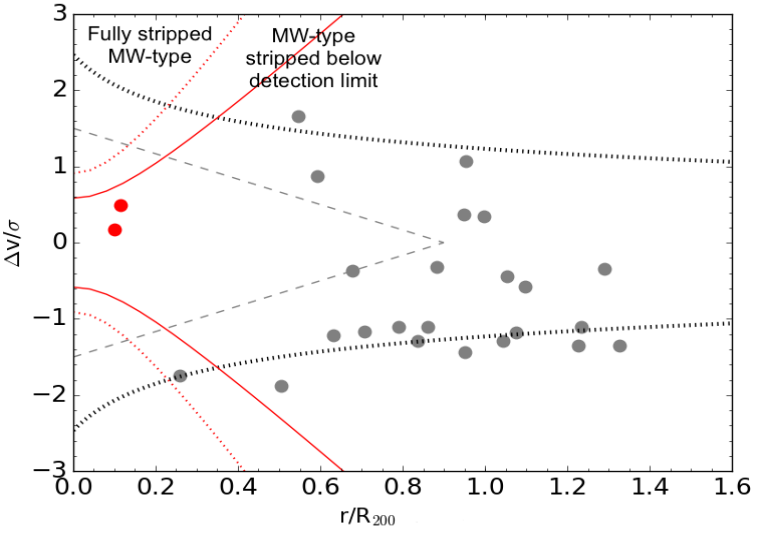

Figure 4.13 – The projected phase-space distribution for the 3C 129 cluster. All HI detected galaxies in the cluster with and without a NIR counterpart are shown in grey. The black dotted line is the escape velocity assuming an NFW potential for the cluster. The grey cone represents the virialised region. The red circles are the 3C 129 and 3C 129.1 galaxy radio sources in the core of the cluster. The solid red lines outline the regions where a modelled Milky Way-like galaxy is expected to be gas stripped to an HI-mass below our detection limit (red-solid line). The red dashed line is where this galaxy is expected to be completely gas stripped.

Secondly, and more meaningful, very few H I-detected galaxies are found within the virialised region. The highest incidence of H I-detected galaxies are located outside this estimated virialised region. We attribute this to the possible effects of ram-pressure stripping by the cluster's ICM. Hints of this effect could already be surmised from the curved head-tail morphologies of the two radio sources in the centre of the cluster, evident in the NVSS 1400 MHz maps shown in Fig. 4.6. In the next section we examine the influence of ram-pressure stripping as manifested by the distribution of galaxies in projected phase-space.

4.7.1 HI Stripping

According to prescriptions by Hernández-Fernández et al. (2014) the effectiveness with which the ICM pushes gas out of galaxies ($\eta = P_{ram}/\prod_{gal}$) can be computed as the ram-pressure (P_{ram}) exerted over the anchoring gas pressure of a galaxy as a result of its own gravity ($\prod_{gal}$; Gunn & Gott 1972). The ram-pressure exerted on a galaxy is defined as,

$$P_{ram} = \rho_{ICM} v_{gal}^2, \tag{4.7}$$

where, v_{gal} is the velocity of the galaxy, projected onto the line-of-sight by scaling it with a factor of $\sqrt{3}$, and ρ_{ICM} is the ICM gas density based on the standard β-model profile (Cavaliere & Fusco-Femiano 1976) described by,

$$\rho_{ICM}(r) = \rho_0 \left[1 + \left(\frac{r_{cl}}{r_0}\right)^2\right]^{-3/2\beta}, \tag{4.8}$$

In this equation ρ_0 is the central ICM density, r_0 is the core radius of the cluster from the β-profile and r_{cl} is its three-dimensional radius, scaled statistically to the projected radius r_p by $r_{cl} = (\pi/2) r_p$.

The adopted parameters from the β-model of the 3C 129 cluster are $\rho_0 = 1.0 \times 10^{-26}$ g cm^{-3}, $r_0 = 11' \pm 1'$ and $\beta = 0.7 \pm 0.2$ (Leahy & Yin 2000).

The restoring gravitational force per unit area of a galaxy ($\prod_{gal}$) was determined following derivations by Jaffé et al. (2015),

$$\prod_{gal} = 2\pi G \Sigma_g \Sigma_s, \tag{4.9}$$

where G is the gravitational constant, Σ_g and Σ_s are the gas and stellar surface densities assuming an exponential profile of $\Sigma = \Sigma_0 e^{-r_t/R_d}$ where r_t is the radial distance from the galaxy centre and R_d is the scale-length of the stellar disk.

We have not measured stellar masses for our HI-galaxy sample but we use a Milky Way (MW) type model galaxy (see Jaffé et al. 2015) to estimate the region in the phase-space diagram where we expect the gas disk of this type of galaxy to be completely stripped within the 3C 129 cluster (i.e., $r_t = 0$). This region is to the left of the red dotted lines in Fig. 4.13. The HI detection limit at the distance of the cluster is $M_{HI} = 3 \times 10^8 M_\odot$. As a result, the gas disk of the galaxies does not have to be stripped down to $r_t = 0$ to fall below our detection limit. We estimated the radius r_t at which the remaining gas mass fraction ($f = \frac{M_{HI,lim}}{M_{gas,tot}}$) of a MW-type galaxy would fall below our survey HI detection limit. This radius was measured to be $r_t \approx 1.20$ kpc using Eq. 2 in Jaffé et al. (2015). A MW-type galaxy within the 3C 129 cluster is expected to have been gas-stripped to an HI mass below that of our survey limits when it is left of the red solid lines. Our HI detections are consistent with this crude approximation. Only one galaxy is found within the predicted HI-limit stripped region and none are found in the "completely" stripped region. We stress the approximations and assumptions that are used for our arguments as imposed by the limited observational data.

4.7.2 Orbital Trajectories of the Galaxies

Recently, attempts were made to use a phase-space analysis to better understand the origin of the HI properties of galaxies that are embedded in clusters. For example, in a study of the Virgo cluster, Yoon et al. (2017) showed that it is possible to trace the orbital trajectories of HI stripped galaxies in the phase-space diagram.

The trajectories of the galaxies in projected phase-space is expected to be as follows: A galaxy transitioning from the cluster's surrounding regions will fall into the cluster from larger distances at velocities that are close to the escape velocities. As it moves closer to the cluster core, its orbital velocity will increase to its maximum velocity as it passes close to the cluster centre. After this first crossing of the cluster, it will move out of the cluster centre back to the outskirts where it will turn around and fall in again. It will oscillate back and forth in this manner until it settles into the virialised region of the cluster. A schematic overview of how an infalling galaxy settles into the virialised region is shown traced by arrows in Fig. 4.14. This orbital sequence is also illustrated in Fig. 4 by Jaffé et al. (2015) based on cosmological simulations in phase-space.

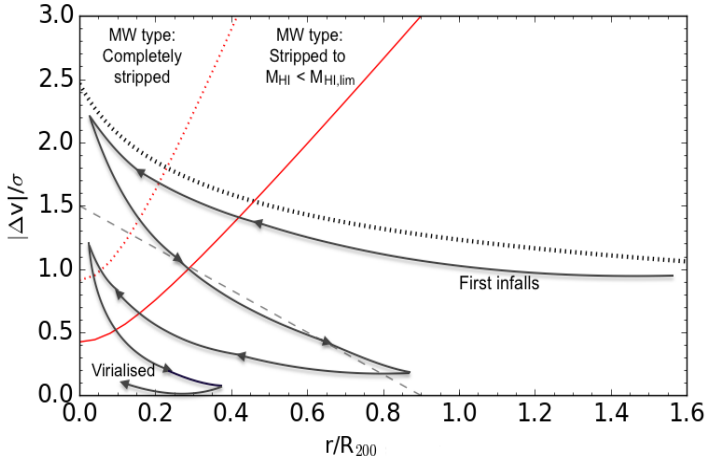

Figure 4.14 – A schematic snapshot of the orbital trajectory of an infalling galaxy in phase-space. The predicted orbital progression is traced by lines and arrows. The black dotted line is the escape velocity assuming an NFW potential for the cluster. The grey cone represents the virialised region. The solid red lines outline the regions where a modelled Milky Way-like galaxy is expected to be gas stripped to an HI-mass below our detection limit (red-solid line). The red dashed line is where this galaxy is expected to be completely gas stripped.

Most of our H I detected galaxies appear to be localised within the region of first infall. Their radial velocities are expected to be increasing as they move in from the outskirts and experience an increasing ICM density closer to the core. They would only start losing gas as they move closer to the stripping region (leftward of the red lines). This effect is seen in the relative H I-content of the galaxies shown in Fig. 4.15. Galaxies with the highest velocities $|\Delta v|/\sigma > 1.0$ at radii less than $0.8R_{200}$ have a slightly lower H I content of $\log(\mathrm{M_{HI}/L_K}) < -1.0$ $\mathrm{M_\odot/L_\odot}$ compared to those at $r_{cl} > 0.8R_{200}$.

The relative H I content of the galaxies in the 3C 129 cluster seems to suggest that they are on their way to the cluster for the first time. About 26% of these galaxies are located in the 3C 129-B subgroup. They are outlined by black boxes in Fig. 4.15 and already show signs of high gas deficiencies, possibly due to tidal interactions while also falling into the cluster core. An accurate assessment of the timescales for orbital trajectories is not trivial, however a rough approximation of the crossing time can be made.

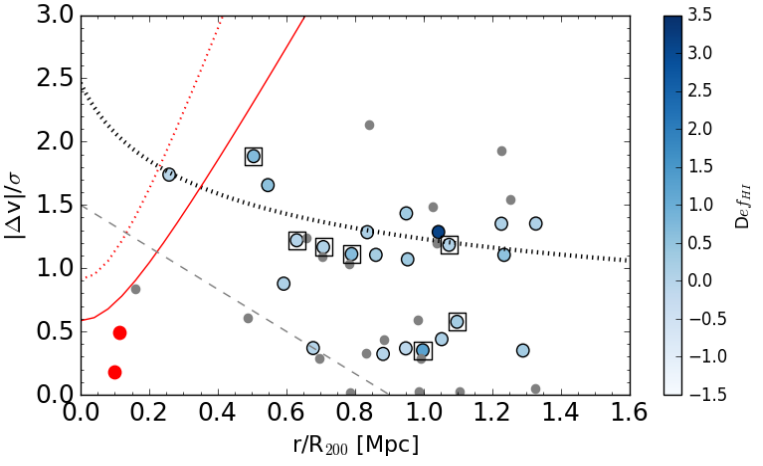

Figure 4.15 – The projected phase-space distribution for the 3C 129 cluster. Galaxies detected in HI with a NIR counterpart are illustrated by gradient-blue points which represent their relative HI content $\log(M_{HI}/L_K)$. HI detections without a NIR counterpart are represented by grey symbols. Galaxies outlined by black boxes are located in the 3C 129-B subgroup. The black dashed line and the grey cone are the same as in Fig. 4.13. Similarly, the solid and dashed red lines. Radio sources, 3C 129 and 3C 129.1 are shown by red dots.

If we assume that a galaxy (e.g. MW-type) moving within the potential of the 3C 129 cluster in the infall region has a velocity of $1.1\sigma_{cl}$, it would take ∼1.65 Gyr to cross from the outskirts of the cluster at $r_{cl} = 1.34R_{200}$ into the region in which it will be completely stripped ($r_{cl} < 0.2R_{200}$) and ∼1.0 Gyr assuming an increased velocity of $1.6\sigma_{cl}$. For this galaxy to experience enough stripping to fall below our HI detection limit at ($r_{cl} < 0.4R_{200}$), the crossing time is about 1.3 Gyr at a velocity of $1.1\sigma_{cl}$ and 0.9 Gyr with velocity of $1.6\sigma_{cl}$. Tonnesen, Bryan & van Gorkom (2007) reported from cosmological simulations that the timescale for complete gas removal is around ≥ 1 Gyr. Therefore it seems that galaxies within the 3C 129 cluster will pass through the centre of the cluster only once, before their HI-gas is completely stripped.

Caution should be taken when interpreting the galaxy distribution in phase-space since projection effects could cause the observed velocity to be lower than the true orbital velocity. Similarly, the true three-dimensional radius could be larger than the observed projected radius. However, when multiple objects are found in the same location in phase-space the probability that they have similar orbits is significantly increased (Oman, Hudson & Behroozi 2013).

4.8 Discussion and Summary

We used data from the WSRT PPZoA blind H I-imaging survey of a dynamic region associated with a largely unexplored filament of the Perseus-Pisces Supercluster (PPS; $cz \sim 6000$ km s^{-1}) located in the Zone of Avoidance (ZoA). The H I-detected galaxies from this survey revealed a myriad of diverse cosmic environments from galaxy voids to several major overdensities in redshift space that had previously remained hidden behind the Milky-Way. One of the revealed major overdensities (Aur 2) contains the massive, X-ray emitting 3C 129 cluster embedded in the filament of the PPS. Another major overdensity behind the PPS has no known cluster association nor X-ray emission detected in its vicinity. The unique characteristics of these regions offered a range of cosmic environments from which we could study their effects on the observed H I-properties of galaxies.

We performed tests to search for the presence of substructures in the two major overdensities Aur 2 and Aur 3, and found a high degree of substructure in both. Within the Aur 2 system, two substructures are found inside the radius of the cluster of $r_{cl} = 1.7$ Mpc and one substructure is found at larger projected radii. The existence of these substructures suggests that the cluster is still assembling by actively accreting galaxies and galaxy groups from the PPS. Three substructures were found within the Aur 3 system. The galaxy populations within the identified substructures in Aur 2 and Aur 3 demonstrate the variety of these cosmic environments. About 52% of the galaxies in substructures located within Aur 2 are early-type galaxies, while the Aur 3 system contains a somewhat lower fraction (43%) of early-type galaxies and is dominated by gas-rich late-type galaxies.

We assessed the H I-morphologies of galaxies within the various environments by examining asymmetries in the global H I profiles, integrated H I-maps and position-velocity diagrams. We find that asymmetries are common in the two major substructures within the Aur 2 system. A fraction of about 63% of these galaxies show these asymmetries in the global H I profiles and 60% in their integrated H I-maps. Similar fractions of asymmetries are also found in the global H I profiles of galaxies located in large substructures in the Aur 3 system. When we compare with galaxies in smaller groups, we find slight peculiarities in only ∼33% of their H I-maps. We conclude that the disrupted H I-morphologies are

likely the result of tidal interactions in densely populated groups.

When examining the H I galaxy distribution within the 3C 129 cluster we find a paucity of H I-detections in the core of the cluster within $r_{cl} = 0.5R_{200}$. Only 2 of the H I-detections in the cluster are located in this region. The majority (∼94%) of galaxies detected in H I are located in the outskirts at projected distances of $r_{cl} > 0.5R_{200}$. This segregation points to a high gas deficiency in the core of this cluster resulting from effects of ram-pressure stripping due to the dense ICM of the 3C 129 cluster of $\rho_0 = 6 \times 10^{-3}\mathrm{cm}^{-3}$. We support this claim by analysing the projected phase-space diagram. We modelled the ICM density profile and predicted regions in this diagram where galaxies are likely to experience ram-pressure stripping. Our H I-galaxy distribution in this phase-space projection coincides well with the estimated ram-pressure stripping locations with almost all of the H I-detected galaxies found outside the predicted estimated gas-stripping regions in phase-space.

We evaluate the H I-content in various environments by combining near-infrared imaging data from the UKIDSS GPS with the H I data. We start by measuring the H I-content as a function of the projected distance from the 3C 129 cluster core. There is no statistically significant trend found of a decreasing H I-content from the cluster outskirt to distances closer to the core, contrary to expectations for a rich cluster. Instead, galaxies with a significantly lower relative H I-content of log $(\mathrm{M_{HI}/L_K}) < -1.0$ $\mathrm{M_\odot/L_\odot}$ and exhibiting H I-deficiencies of $Def_{\mathrm{HI}} > 1.0$, are located in the cluster outskirts at projected radii of $0.5R_{200} < r_{cl} < 1.1R_{200}$. We suggest that this is due to galaxy interactions during mergers within groups that are falling into the cluster. This is supported by noting that ∼50% of these galaxies are located in a group that shows a clear galaxy merger located within the projected radius of the cluster of $r_{cl} = 1.34R_{200}$. We further affirm this claim by comparing the H I-content of galaxies associated with the 3C 129 cluster with those unassociated with any cluster nor X-ray emission in our surveyed volume, but are located in galaxy groups. Similar fractions of galaxies with a significantly lower H I-content are found within this "non-cluster" population.

The picture of environmentally driven gas removal processes remains complex. It is still not clear which mechanism is dominant in removing gas from galaxies. We found that the incidence of H I-detections correlates with environment in that no detections are found in the dense core of the 3C 129 cluster, where ram-pressure is expected to be most effective. However, we also find galaxies with a significantly lower relative H I-content in lower density groups far from the cluster centre. This suggests that galaxy-galaxy interactions plays a role in removing gas from galaxies before they enter the cluster. By the time groups of galaxies fall into the cluster they might already be gas-poor or even completely H I-depleted.

Appendix

Appendix C: The HI and near-infrared in various environments

The HI and near-infrared properties of galaxies identified within the various cosmic environments in the WSRT PPZoA survey volume.

Column (1) - Unique identifiers based on the Right Ascension (RA) and Declination (Dec) ZoAJhhmmss.ss±ddmmss.s (J2000).

Column (2 & 3) - Galactic longitude and latitude of the HI centroid in degrees.

Column (3 & 4) - Galactic longitude and latitude of the NIR centroid in degrees for HI galaxies with counterparts only.

Column (5) - The radial velocities from the WSRT HI measurements.

Column (6) - The total integrated HI-flux in Jy km s^{-1}

Column (7) - The HI radius in kpc measured at the $1Mpc^{-2}$ surface density level given for resolved sources only.

Column (8) -The K_{20} isophotal major-axis radius in kpc.

Column (9) - K-band fiducial isophotal magnitudes (not corrected for foreground extinction).

Column (10) - The line of sight Galactic reddening in magnitudes.

Column (11) - The estimated morphology of galaxies from the NIR images.

Column (12) - The flux ratios between the side of the HI-global profile with the highest integrated flux to the side with the lowest integrated flux.

Column (13 & 14) - Indicates asymmetries in the integrated HI-maps and the galaxy kinematics, respectively. A "y" represents cases with asymmetries, the "n" are cases in which no obvious asymmetries were identified.

Column (15) - The galaxy substructure membership.

Table C. The HI and NIR properties of galaxies in various environments

Unique ID	$\ell_{\rm HI}$	$b_{\rm HI}$	$\ell_{\rm NIR}$	$b_{\rm NIR}$	v_{rad}	$S_{\rm HI}$	$r_{\rm HI}$	r_{K20}	K_{20}	$E(B\text{-}V)$	Morph	–	HI Asymmetry	–	Subgroup
	deg	deg	deg	deg	km/s	Jy km/s	kpc	kpc	kpc	mag		$S_{HIratio}$	HI-map	PVD	
(1)	(2)	(3)	(4)	(5)	(6)	(7)	(8)	(9)	(10)	(11)	(12)	(13)	(14)	(15)	(16)
J044427.17+455116.7	159.2509	0.0607	159.2534	0.0607	5506	5.68	24.2	5.1	12.19	1.40	mS	1.11	y	y	–
J044521.10+454432.8	159.4381	0.1061	159.4381	0.1053	5134	1.34	12.4	5.2	12.66	1.28	mS	1.06	y	y	–
J044524.14+451924.3	159.7618	-0.1601	159.7638	-0.1598	6830	0.43	–	2.2	13.95	1.14	Irr	1.03	n	n	–
J044533.70+441127.9	160.6396	-0.8759	–	–	2851	0.71	–	–	–	–	–	1.30	n	n	–
J044540.97+454045.8	159.5236	0.1090	–	–	9660	0.27	–	–	–	–	–	1.09	y	n	Aur 3-B
J044541.51+455022.6	159.4030	0.2145	159.4017	0.2157	14584	0.43	–	1.6	17.28	1.27	Irr	1.64	y	n	–
J044542.87+442101.0	160.5366	-0.7515	160.5363	-0.7518	10717	3.57	33.5	3.3	15.50	0.88	Irr	1.03	y	y	–
J044546.04+444901.5	160.1881	-0.4407	160.1879	-0.4411	5134	0.68	8.5	1.4	14.85	1.05	ℓS	1.20	y	n	–
J044550.59+443552.5	160.3634	-0.5730	–	–	16249	0.67	–	–	–	–	–	1.20	n	n	–
J044556.60+450741.4	159.9720	-0.2148	–	–	6803	0.30	–	–	–	–	–	1.01	y	y	–
J044559.91+450104.1	160.0622	-0.2791	–	–	12528	0.80	25.5	–	–	–	–	1.66	y	n	–
J044602.33+443426.8	160.4041	-0.5620	160.4041	-0.5630	6281	5.78	31.0	0.7	17.56	0.94	Irr	1.01	n	n	–
J044630.07+451655.0	159.9190	-0.0402	159.9175	-0.0403	10229	0.24	–	2.1	15.68	1.01	Irr	1.04	y	n	Aur 3-B
J044632.27+452152.2	159.8603	0.0183	159.8608	0.0180	9740	0.66	17.4	5.6	13.73	1.10	Irr	1.04	y	y	Aur 3-B
J044635.75+441909.5	160.6625	-0.6518	160.6611	-0.6514	9992	0.55	–	0.9	17.81	0.77	Irr	1.51	y	n	–
J044644.10+442004.0	160.6672	-0.6231	160.6666	-0.6226	5654	0.94	12.7	1.8	16.08	0.73	mS	1.38	y	y	–
J044644.74+444734.7	160.3191	-0.3244	160.3191	-0.3244	5709	0.51	9.9	0.4	18.52	0.89	Irr	1.03	n	n	–
J044652.86+440859.1	160.8247	-0.7228	–	–	7501	0.42	10.9	–	–	–	–	1.36	y	n	–
J044654.85+450928.4	160.0605	-0.0653	160.0601	-0.0665	10794	0.22	–	2.6	17.64	0.91	ℓS	1.27	n	n	Aur 3-B
J044657.71+444649.5	160.3536	-0.3033	–	–	16209	0.81	–	–	–	–	–	1.26	n	n	–
J044700.10+442439.7	160.6397	-0.5372	160.6389	-0.5366	10747	1.86	35.8	7.1	13.76	0.74	ℓS	1.17	y	n	–
J044705.89+450301.9	160.1634	-0.1101	160.1631	-0.1079	10165	0.29	–	0.7	18.58	0.87	Irr	1.25	n	n	Aur 3-B
J044706.91+453449.0	159.7615	0.2352	161.3677	1.8708	4994	1.24	14.0	1.2	15.16	1.25	ℓS	1.06	n	n	–
J044717.85+441654.2	160.7725	-0.5805	160.7737	-0.5763	4993	0.30	–	5.6	10.91	0.69	eS	1.65	n	y	–
J044719.35+435436.2	161.0588	-0.8175	161.0597	-0.8171	10077	1.08	–	1.8	17.32	0.61	Irr	1.15	n	n	–
J044725.76+443638.5	160.5367	-0.3498	–	–	6219	0.15	–	–	–	–	–	1.28	n	n	–
J044726.92+462337.0	159.1788	0.8055	–	–	5864	0.92	–	–	–	–	–	3.13	y	n	–
J044727.30+445342.4	160.3227	-0.1624	–	–	5523	0.33	7.9	–	–	–	–	1.11	y	y	–
J044727.96+444723.6	160.4042	-0.2290	160.4040	-0.2295	7288	0.28	8.0	3.2	15.59	0.88	Irr	1.51	n	y	–
J044731.28+434829.0	161.1598	-0.8561	–	–	11186	0.69	–	–	–	–	–	1.10	y	y	–

Table C – Continued

Unique ID	$\ell_{\rm HI}$	$b_{\rm HI}$	$\ell_{\rm NIR}$	$b_{\rm NIR}$	v_{rad}	$S_{\rm HI}$	$r_{\rm HI}$	r_{K20}	K_{20}	$E(B\text{-}V)$	Morph	–	HI Asymmetry	–	Subgroup
	deg	deg	deg	deg	km/s	Jy km/s	kpc	kpc	kpc	mag		$S_{HIratio}$	HI-map	PVD	
(1)	(2)	(3)	(4)	(5)	(6)	(7)	(8)	(9)	(10)	(11)	(12)	(13)	(14)	(15)	(16)
J044735.05+455908.2	159.5052	0.5597	–	–	9945	0.21	–	–	–	–	–	1.29	n	n	–
J044736.43+434854.0	161.1645	-0.8398	–	–	5440	0.53	–	–	–	–	–	1.03	n	n	–
J044743.99+441946.5	160.7863	-0.4901	160.5583	1.3103	4878	0.76	9.9	2.1	14.20	0.70	ℓS	1.19	y	y	–
J044744.05+460456.5	159.4482	0.6421	–	–	12441	0.43	–	–	–	–	–	1.50	y	n	–
J044752.21+451900.3	160.0481	0.1659	–	–	3280	0.21	–	–	–	–	–	1.28	n	n	–
J044752.94+435840.2	161.0722	-0.6968	161.0700	-0.6967	8204	0.31	–	1.2	16.55	0.60	Irr	1.47	n	n	–
J044754.01+443847.3	160.5635	-0.2628	–	–	10074	0.17	–	–	–	–	–	1.48	n	n	–
J044808.96+450326.3	160.2781	0.0360	160.2784	0.0356	9853	0.59	–	2.6	14.87	0.88	mS	1.62	n	n	Aur 3-B
J044809.24+443634.5	160.6209	-0.2520	–	–	9873	0.28	–	–	–	–	–	1.19	n	n	–
J044819.38+440155.8	161.0818	-0.6011	–	–	4794	0.28	5.0	–	–	–	–	1.31	y	n	–
J044830.74+455010.9	159.7234	0.5868	–	–	6012	0.16	–	–	–	–	–	1.34	y	n	3C 129-C
J044832.96+462704.2	159.2571	0.9876	–	–	8557	0.41	–	–	–	–	–	2.01	n	n	–
J044837.47+461304.6	159.4440	0.8473	–	–	5931	0.18	–	–	–	–	–	2.01	n	n	–
J044837.97+454508.0	159.8014	0.5487	159.8020	0.5488	5745	0.74	10.8	0.4	18.61	1.14	Irr	1.05	n	n	3C 129-C
J044840.48+452428.9	160.0695	0.3327	160.0698	0.3322	10956	0.45	17.6	3.3	14.67	0.99	Irr	1.04	n	n	Aur 3-B
J044845.01+435610.4	161.2047	-0.6042	–	–	3410	1.42	9.1	–	–	–	–	1.71	n	n	–
J044850.72+455649.4	159.6760	0.7024	–	–	5976	0.04	–	–	–	–	–	1.83	n	n	3C 129-C
J044850.94+444943.4	160.5328	-0.0165	–	–	14294	0.25	–	–	–	–	–	1.30	n	n	–
J044857.72+443728.8	160.7019	-0.1323	–	–	16180	0.12	–	–	–	–	–	1.25	n	n	–
J044858.80+451314.0	160.2475	0.2533	160.2477	0.2517	10857	0.40	–	3.2	14.42	0.96	ℓS	1.02	n	n	Aur 3-B
J044900.08+441936.1	160.9346	-0.3185	160.9362	-0.3164	14604	0.34	–	8.5	13.75	0.64	ℓS	1.14	n	n	–
J044900.78+441902.8	160.9431	-0.3229	–	–	6332	0.10	–	–	–	–	–	1.12	n	n	3C 129-B
J044907.68+443018.3	160.8125	-0.1865	160.8135	-0.1864	10644	0.43	16.4	1.9	16.82	0.72	ℓS	1.41	n	y	–
J044912.74+442451.3	160.8918	-0.2333	–	–	8216	0.37	–	–	–	–	–	1.18	n	n	–
J044927.63+443253.7	160.8174	-0.1134	160.8160	-0.1153	3707	0.10	–	1.1	16.58	0.74	Irr	1.30	n	n	–
J044931.06+435844.3	161.2606	-0.4708	–	–	9257	0.17	–	–	–	–	–	1.01	n	n	–
J044934.80+451030.3	160.3503	0.3051	–	–	6649	0.28	–	–	–	–	–	1.46	y	n	–
J044935.92+445252.1	160.5780	0.1190	–	–	3985	0.16	–	–	–	–	–	1.06	n	n	–
J044944.31+460225.7	159.7040	0.8813	–	–	14933	0.43	21.4	–	–	–	–	1.62	y	n	–
J044945.15+460232.2	159.7042	0.8843	159.7035	0.8868	13964	0.10	–	3.4	15.43	1.14	mS	1.18	n	n	–
J044945.20+460234.8	159.7037	0.8849	–	–	15881	0.28	–	–	–	–	–	1.33	y	y	–

Table C – Continued

Unique ID	$\ell_{\rm HI}$	$b_{\rm HI}$	$\ell_{\rm NIR}$	$b_{\rm NIR}$	v_{rad}	$S_{\rm HI}$	$r_{\rm HI}$	r_{K20}	K_{20}	$E(B\text{-}V)$	Morph	–	HI Asymmetry	–	Subgroup
	deg	deg	deg	deg	km/s	Jy km/s	kpc	kpc	kpc	mag		$S_{HIratio}$	HI-map	PVD	
(1)	(2)	(3)	(4)	(5)	(6)	(7)	(8)	(9)	(10)	(11)	(12)	(13)	(14)	(15)	(16)
J044945.25+460229.7	159.7049	0.8841	–	–	8258	0.56	–	–	–	–	–	1.21	y	y	–
J044945.98+455144.8	159.8438	0.7709	–	–	5775	0.14	–	–	–	–	–	1.76	n	n	3C 129-C
J044957.27+460315.1	159.7175	0.9188	161.3387	1.6764	4942	2.59	15.3	1.5	15.21	1.12	ℓS	1.09	y	n	–
J045002.21+452645.5	160.1938	0.5404	–	–	9611	0.59	16.9	–	–	–	–	1.36	y	y	–
J045002.27+444907.5	160.6757	0.1389	–	–	3461	0.32	4.3	–	–	–	–	1.19	n	n	–
J045005.46+453021.9	160.1538	0.5862	160.1561	0.5855	9642	1.38	25.8	6.5	11.95	1.09	mS	1.46	y	y	–
J045006.21+450306.5	160.5041	0.2970	–	–	14904	0.21	–	–	–	–	–	2.21	y	n	–
J045013.10+440833.5	161.2157	-0.2693	161.2149	-0.2678	5547	0.76	11.2	1.8	14.67	0.63	Irr	1.61	y	y	–
J045022.07+442207.7	161.0590	-0.1040	–	–	5739	0.31	6.7	–	–	–	–	1.44	n	y	3C 129-B
J045026.43+451135.1	160.4336	0.4330	160.4351	0.4329	4639	0.69	7.9	0.2	19.76	1.02	Irr	1.24	y	n	–
J045034.24+435929.0	161.3724	-0.3174	161.3721	-0.3171	5724	0.13	–	0.8	17.61	0.64	Irr	2.02	y	y	–
J045035.09+442218.2	161.0816	-0.0724	–	–	4329	0.10	–	–	–	–	–	1.10	n	n	3C 129-B
J045045.12+443915.9	160.8831	0.1312	–	–	14558	0.28	–	–	–	–	–	1.17	n	n	–
J045046.67+433751.7	161.2193	-0.1418	–	–	7152	0.32	–	–	–	–	–	3.01	y	y	3C 129-B
J045104.83+454944.1	160.0159	0.9254	–	–	16487	0.30	–	–	–	–	–	1.14	n	n	–
J045105.43+443544.0	160.9668	0.1400	160.9670	0.1405	5044	3.71	20.5	1.8	13.63	0.77	mS	1.09	y	y	3C 129-B
J045117.24+443525.9	160.9931	0.1637	–	–	5026	0.91	–	–	–	–	–	1.37	y	y	3C 129-B
J045127.67+461953.7	159.6706	1.2967	159.6701	1.2959	5087	0.40	–	1.1	15.28	0.85	ℓS	1.01	y	y	–
J045132.28+442922.2	161.0994	0.1338	161.0998	0.1334	5129	1.06	11.1	6.7	11.69	0.76	eS	1.00	n	n	3C 129-B
J045136.02+452435.7	160.3968	0.7284	160.3953	0.7251	9648	0.17	–	6.4	11.92	1.05	E	1.52	n	n	–
J045137.03+461912.8	159.6965	1.3102	–	–	7030	0.42	9.5	–	–	–	–	1.10	y	n	–
J045145.44+443610.2	161.0369	0.2361	159.7616	0.2349	5086	17.63	36.4	8.0	10.35	0.79	eS	1.09	y	y	3C 129-B
J045156.49+450320.0	160.7083	0.5493	160.7094	0.5482	4525	0.39	7.4	3.3	12.52	0.94	mS	1.48	n	y	3C 129-B
J045202.73+435400.5	161.6120	-0.1710	161.6121	-0.1709	14928	0.22	–	3.6	14.67	0.55	Irr	1.27	n	n	–
J045202.83+435359.9	161.6123	-0.1709	161.6122	-0.1713	11938	0.40	17.8	3.2	14.63	0.55	mS	1.18	y	y	–
J045208.67+434927.2	161.6819	-0.2055	161.6822	-0.2059	7239	1.90	20.3	7.1	12.10	0.56	eS	1.05	y	y	–
J045210.82+463120.9	159.6020	1.5137	–	–	10603	0.26	–	–	–	–	–	1.08	n	n	Aur 3-C
J045217.56+450844.6	160.6782	0.6544	160.6789	0.6534	6680	0.39	–	0.8	18.00	0.87	Irr	1.04	y	y	3C 129-B
J045220.74+454136.5	160.2608	1.0094	–	–	6458	0.92	14.5	–	–	–	–	1.02	n	y	–
J045223.95+452744.1	160.4454	0.8699	–	–	5982	0.47	9.7	–	–	–	–	1.64	y	y	–
J045227.46+444542.0	160.9934	0.4332	–	–	5144	0.28	6.0	–	–	–	–	1.41	n	y	3C 129-B

Table C – Continued

Unique ID	$\ell_{\rm HI}$	$b_{\rm HI}$	$\ell_{\rm NIR}$	$b_{\rm NIR}$	v_{rad}	$S_{\rm HI}$	$r_{\rm HI}$	r_{K20}	K_{20}	$E(B\text{-}V)$	Morph	–	HI Asymmetry	–	Subgroup
	deg	deg	deg	deg	km/s	Jy km/s	kpc	kpc	kpc	mag		$S_{HIratio}$	HI-map	PVD	
(1)	(2)	(3)	(4)	(5)	(6)	(7)	(8)	(9)	(10)	(11)	(12)	(13)	(14)	(15)	(16)
J045231.94+461230.3	159.8834	1.3613	–	–	7109	0.44	–	–	–	–	–	1.30	y	y	3C 129-A
J045254.16+441202.2	161.4776	0.1387	161.4778	0.1386	16363	0.10	–	1.9	16.29	0.62	Irr	1.19	n	n	–
J045255.89+460258.8	160.0500	1.3142	–	–	7689	0.24	–	–	–	–	–	1.13	y	y	–
J045331.19+443916.6	161.1958	0.5114	161.1970	0.5108	10148	0.39	14.4	0.8	18.48	0.90	Irr	1.61	y	y	Aur 3-A
J045343.57+440459.8	161.6618	0.1789	161.6620	0.1781	5142	0.32	6.7	0.7	16.68	0.62	Irr	2.22	n	y	–
J045358.21+461405.5	160.0202	1.5706	160.0200	1.5704	7143	1.02	–	0.7	18.06	0.85	ℓS	1.33	y	n	3C 129-A
J045408.61+444522.2	161.1870	0.6615	–	–	5063	0.81	9.9	–	–	–	–	1.17	y	n	3C 129-B
J045411.23+444554.1	161.1851	0.6730	–	–	9991	0.46	15.7	–	–	–	–	1.18	n	n	Aur 3-A
J045414.22+461633.3	160.0175	1.6323	160.0174	1.6316	9024	0.48	15.4	3.0	15.02	0.83	ℓS	1.14	y	y	–
J045414.90+450315.7	160.9673	0.8639	160.9672	0.8637	6269	0.57	8.7	8.1	11.07	0.93	eS	1.42	y	n	–
J045420.49+454723.7	160.4064	1.3402	160.4077	1.3404	10856	0.68	19.7	2.8	15.96	0.92	Irr	1.62	n	y	–
J045426.94+444941.2	161.1654	0.7489	161.1652	0.7488	5072	0.63	8.9	0.5	17.78	0.89	Irr	1.24	y	y	3C 129-B
J045428.52+462803.0	159.8945	1.7849	159.8947	1.7855	14698	0.67	–	5.7	13.39	0.74	mS	1.03	y	y	–
J045430.27+461345.1	160.0829	1.6388	160.0835	1.6385	6726	0.98	14.5	3.2	14.08	0.84	mS	1.06	y	y	3C 129-A
J045430.92+444645.3	161.2106	0.7272	161.2106	0.7269	10202	0.38	–	1.3	16.96	0.88	ℓS	1.14	n	n	Aur 3-A
J045442.75+462112.8	160.0088	1.7450	160.0173	1.7500	9881	1.35	25.6	14.9	10.70	0.86	E	2.49	n	n	–
J045443.51+444709.1	161.2290	0.7603	161.2287	0.7598	9926	1.09	23.5	2.6	14.74	0.88	Irr	1.12	y	y	Aur 3-A
J045445.29+453922.2	160.5557	1.3120	160.4351	0.4329	4941	6.17	22.9	3.2	13.47	0.84	mS	1.45	y	y	3C 129-A
J045446.73+442143.1	161.5644	0.5010	161.5651	0.5009	10510	1.77	27.2	2.9	14.90	0.82	Irr	1.18	y	y	Aur 3-A
J045449.54+462052.1	160.0256	1.7565	–	–	9505	0.51	15.9	–	–	–	–	1.26	y	y	–
J045457.48+463735.6	159.8230	1.9495	–	–	6872	0.36	–	–	–	–	–	1.27	y	n	3C 129-A
J045459.27+444700.0	161.2603	0.7949	161.2602	0.7948	10012	0.13	–	0.7	18.79	0.89	Irr	1.13	n	y	Aur 3-A
J045514.42+453815.1	160.6236	1.3663	160.6226	1.3660	3355	0.56	5.9	0.4	17.75	0.85	Irr	1.16	y	y	–
J045516.70+442734.8	161.5446	0.6318	161.5429	0.6318	10051	0.26	–	5.0	12.33	0.86	E	1.09	n	n	Aur 3-A
J045519.33+442356.6	161.5966	0.5998	–	–	10017	0.17	–	–	–	–	–	1.08	n	n	Aur 3-A
J045541.13+462255.5	160.0921	1.8936	160.0898	1.8926	9488	0.12	–	4.5	13.87	0.86	mS	1.62	y	y	Aur 3-C
J045543.03+461423.6	160.2064	1.8087	160.2039	1.8127	9765	0.44	–	7.4	11.86	0.85	eS	1.87	y	y	Aur 3-C
J045543.43+441116.9	161.8061	0.5233	–	–	15759	0.09	–	–	–	–	–	1.16	n	n	–
J045545.27+455110.8	160.5120	1.5713	–	–	15380	0.10	–	–	–	–	–	1.09	n	n	–
J045546.73+444512.9	161.3716	0.8856	–	–	10177	0.52	16.0	–	–	–	–	1.15	n	n	Aur 3-A
J045547.62+452909.9	160.8023	1.3467	160.8027	1.3467	14101	0.53	–	1.7	16.84	0.89	Irr	1.09	y	n	–

Table C – Continued

Unique ID	$\ell_{\rm HI}$	$b_{\rm HI}$	$\ell_{\rm NIR}$	$b_{\rm NIR}$	v_{rad}	$S_{\rm HI}$	$r_{\rm HI}$	r_{K20}	K_{20}	$E(B\text{-}V)$	Morph	–	HI Asymmetry	–	Subgroup
	deg	deg	deg	deg	km/s	Jy km/s	kpc	kpc	kpc	mag		$S_{HIratio}$	HI-map	PVD	
(1)	(2)	(3)	(4)	(5)	(6)	(7)	(8)	(9)	(10)	(11)	(12)	(13)	(14)	(15)	(16)
J045548.78+464858.3	159.7672	2.1826	–	–	4651	0.25	–	–	–	–	–	1.35	n	n	3C 129-A
J045551.34+440335.6	161.9207	0.4614	–	–	9708	0.15	–	–	–	–	–	1.01	n	n	Aur 3-A
J045555.08+464704.8	159.8030	2.1768	159.8036	2.1754	6517	0.40	–	0.6	18.29	0.77	Irr	1.21	n	n	3C 129-A
J045558.82+461234.1	160.2586	1.8252	–	–	10221	0.28	–	–	–	–	–	1.19	y	y	Aur 3-C
J045604.55+452940.6	160.8267	1.3906	160.8267	1.3889	6684	1.90	16.9	3.2	13.30	0.92	Irr	1.06	n	y	–
J045607.91+462638.4	160.0920	1.9923	–	–	9110	0.10	–	–	–	–	–	1.13	n	n	Aur 3-C
J045616.24+455602.6	160.5050	1.6921	160.5049	1.6929	6990	0.55	11.4	1.3	15.99	0.88	Irr	1.26	n	n	3C 129-A
J045625.85+443832.0	161.5306	0.9059	–	–	10551	0.27	–	–	–	–	–	1.42	y	n	Aur 3-A
J045626.80+455541.2	160.5289	1.7123	160.5286	1.7125	6901	3.26	25.6	15.5	10.06	0.90	mS	1.43	y	y	3C 129-A
J045633.37+443124.4	161.6377	0.8493	161.6369	0.8485	10483	0.28	–	0.9	18.18	0.84	Irr	1.66	y	n	Aur 3-A
J045635.00+460222.4	160.4566	1.8004	160.4565	1.8022	6679	1.62	20.5	6.1	12.76	0.88	mS	1.46	y	y	3C 129-A
J045647.57+444925.8	161.4294	1.0698	–	–	9635	0.23	–	–	–	–	–	1.05	y	y	Aur 3-A
J045653.00+443516.6	161.6237	0.9351	161.6234	0.9343	10633	0.40	–	8.2	12.04	0.90	mS	2.18	y	y	Aur 3-A
J045656.49+461134.0	160.3756	1.9446	160.3786	1.9477	6911	0.48	–	2.4	15.80	0.84	Irr	1.38	y	y	3C 129-A
J045705.33+443341.0	161.6673	0.9472	161.6656	0.9449	14875	0.07	–	5.1	15.18	0.88	ℓS	2.59	n	n	–
J045705.96+444834.3	161.4745	1.1034	–	–	14708	0.46	–	–	–	–	–	1.47	y	y	–
J045711.02+444742.6	161.4950	1.1061	–	–	14561	0.83	–	–	–	–	–	1.86	n	n	–
J045714.03+451227.7	161.1780	1.3703	161.1789	1.3684	6279	0.89	13.7	3.1	12.59	0.90	eS	1.46	n	y	–
J045715.06+445255.8	161.4344	1.1698	161.4354	1.1687	14677	0.32	–	3.8	15.72	0.95	mS	1.03	n	n	–
J045721.12+454135.5	160.8110	1.6890	160.8112	1.6892	3420	3.76	13.6	1.5	14.14	0.87	Irr	1.06	n	y	–
J045723.71+463354.4	160.1330	2.2377	160.1335	2.2372	7064	1.14	16.3	1.3	16.03	0.74	Irr	1.09	y	y	–
J045726.29+440242.9	162.1098	0.6743	162.1095	0.6739	9698	0.35	12.5	3.4	13.93	0.72	Irr	1.01	y	y	Aur 3-A
J045735.72+444850.6	161.5257	1.1750	–	–	14422	0.47	21.2	–	–	–	–	1.20	n	y	–
J045742.65+453422.1	160.9443	1.6631	160.9439	1.6616	6293	0.49	10.1	0.5	18.27	0.89	Irr	1.23	n	n	–
J045747.05+460717.5	160.5223	2.0143	160.5229	2.0148	7013	3.96	30.7	6.1	11.61	0.81	eS	1.31	y	y	3C 129-A
J045750.73+461921.4	160.3713	2.1477	160.3711	2.1480	6861	1.23	17.3	0.5	18.94	0.70	Irr	1.08	n	n	3C 129-A
J045751.11+455706.4	160.6627	1.9181	–	–	14574	0.25	–	–	–	–	–	1.20	n	n	–
J045752.30+455539.3	160.6838	1.9057	160.6842	1.9053	10822	2.82	33.7	5.8	12.98	0.77	mS	1.05	y	y	–
J045757.17+460156.9	160.6103	1.9819	–	–	5284	0.29	–	–	–	–	–	1.05	n	n	3C 129-A
J045757.30+462330.0	160.3289	2.2054	–	–	6009	0.08	–	–	–	–	–	1.73	n	n	3C 129-A
J045800.33+462839.4	160.2669	2.2656	–	–	7079	0.64	12.1	–	–	–	–	1.30	n	n	3C 129-A

Table C – Continued

Unique ID	$\ell_{\rm HI}$	$b_{\rm HI}$	$\ell_{\rm NIR}$	$b_{\rm NIR}$	v_{rad}	$S_{\rm HI}$	$r_{\rm HI}$	r_{K20}	K_{20}	$E(B\text{-}V)$	Morph	–	HI Asymmetry	–	Subgroup
	deg	deg	deg	deg	km/s	Jy km/s	kpc	kpc	kpc	mag		$S_{HIratio}$	HI-map	PVD	
(1)	(2)	(3)	(4)	(5)	(6)	(7)	(8)	(9)	(10)	(11)	(12)	(13)	(14)	(15)	(16)
J045804.57+445518.5	161.4944	1.3087	–	–	9480	0.16	–	–	–	–	–	1.54	n	n	Aur 3-A
J045808.63+450525.8	161.3696	1.4229	161.3697	1.4223	3543	6.01	16.9	0.9	15.32	0.90	Irr	1.13	n	n	–
J045809.05+454743.1	160.8177	1.8616	160.8180	1.8609	6562	0.99	13.4	1.5	15.65	0.80	Irr	1.11	y	y	–
J045810.84+460229.4	160.6278	2.0185	–	–	7137	1.36	18.3	–	–	–	–	1.03	y	y	3C 129-A
J045811.77+450602.6	161.3673	1.4365	161.3662	1.4361	10081	0.59	–	1.7	15.77	0.91	mS	1.04	y	n	Aur 3-A
J045815.72+453936.1	160.9359	1.7928	–	–	11498	0.14	–	–	–	–	–	1.00	n	n	Aur 3-C
J045816.80+463749.5	160.1763	2.3974	–	–	16477	0.59	–	–	–	–	–	1.00	y	n	–
J045816.94+460925.8	160.5480	2.1042	–	–	8332	0.26	–	–	–	–	–	1.43	y	n	Aur 3-C
J045816.96+453621.8	160.9804	1.7622	–	–	12287	0.15	–	–	–	–	–	2.35	n	n	–
J045828.65+441328.4	162.0854	0.9318	162.0860	0.9312	14608	0.56	24.6	7.4	13.71	0.80	mS	1.08	n	y	–
J045830.71+463953.7	160.1739	2.4500	–	–	14658	0.75	31.8	–	–	–	–	1.57	n	n	–
J045835.03+453110.8	161.0809	1.7500	161.0812	1.7491	5037	0.80	9.0	0.5	17.55	0.94	Irr	1.31	n	n	–
J045838.09+461747.7	160.4764	2.2384	160.4758	2.2382	7051	1.46	17.3	2.3	18.88	0.71	ℓS	1.02	n	y	3C 129-A
J045842.68+463243.4	160.2890	2.4029	–	–	8303	0.40	–	–	–	–	–	1.03	y	n	Aur 3-C
J045843.03+455647.1	160.7603	2.0326	160.7598	2.0320	6770	1.47	16.9	3.3	13.21	0.85	mS	1.03	y	n	3C 129-A
J045847.49+441350.2	162.1156	0.9797	–	–	6889	3.19	24.1	–	–	–	–	1.23	y	y	–
J045852.18+463855.9	160.2245	2.4883	160.2254	2.4912	11306	0.20	–	1.2	17.66	0.69	Irr	1.51	n	n	Aur 3-C
J045852.98+445329.6	161.6067	1.4021	161.6071	1.4020	5208	0.29	–	0.8	16.68	1.01	ℓS	1.20	y	y	–
J045855.81+454808.9	160.8963	1.9726	160.8965	1.9726	5098	0.44	7.5	1.8	14.66	0.87	ℓS	1.22	y	y	–
J045900.14+453437.7	161.0813	1.8430	–	–	12338	0.18	–	–	–	–	–	1.30	n	n	–
J045906.31+462358.9	160.4456	2.3660	–	–	3681	0.09	–	–	–	–	–	1.22	n	n	–
J045908.04+440500.0	162.2693	0.9367	162.2688	0.9360	6785	3.71	23.9	3.3	13.78	0.78	mS	1.08	y	y	–
J045909.87+451619.0	161.3387	1.6765	160.7858	-0.4893	4888	0.44	7.5	1.5	13.93	1.02	ℓS	1.46	y	n	–
J045913.88+463039.1	160.3715	2.4518	–	–	7069	0.41	–	–	–	–	–	1.27	y	n	3C 129-A
J045920.35+463222.8	160.3604	2.4842	–	–	5662	0.68	–	–	–	–	–	1.12	y	n	3C 129-A
J045920.95+441945.4	162.0998	1.1192	–	–	10641	0.47	17.3	–	–	–	–	1.05	n	n	–
J045926.99+463431.4	160.3440	2.5212	–	–	10788	0.78	–	–	–	–	–	1.03	y	n	Aur 3-C
J045930.60+455248.7	160.8977	2.1000	–	–	6682	0.62	–	–	–	–	–	1.02	y	n	–
J045930.82+455247.2	160.8984	2.1003	160.8981	2.1002	11940	0.66	21.9	0.7	18.71	0.90	Irr	1.80	y	y	Aur 3-C
J045932.30+463928.6	160.2885	2.5841	–	–	10998	0.60	–	–	–	–	–	2.07	n	n	Aur 3-C
J045932.66+441837.9	162.1362	1.1350	162.1364	1.1355	9908	0.66	–	3.9	13.69	0.93	mS	1.01	y	n	–

Table C – Continued

Unique ID	$\ell_{\rm HI}$	$b_{\rm HI}$	$\ell_{\rm NIR}$	$b_{\rm NIR}$	v_{rad}	$S_{\rm HI}$	$r_{\rm HI}$	r_{K20}	K_{20}	$E(B\text{-}V)$	Morph	–	HI Asymmetry	–	Subgroup
	deg	deg	deg	deg	km/s	Jy km/s	kpc	kpc	kpc	mag		$S_{HIratio}$	HI-map	PVD	
(1)	(2)	(3)	(4)	(5)	(6)	(7)	(8)	(9)	(10)	(11)	(12)	(13)	(14)	(15)	(16)
J045936.64+445709.6	161.6384	1.5411	161.6385	1.5397	10190	0.86	21.5	3.5	14.20	0.99	mS	1.20	y	y	–
J045937.49+450218.9	161.5724	1.5961	–	–	14535	0.28	–	–	–	–	–	1.07	y	n	–
J045940.69+462146.7	160.5356	2.4210	160.5397	2.4301	5193	0.20	–	0.8	16.37	0.65	Irr	1.13	y	n	3C 129-A
J045941.86+452913.7	161.2273	1.8831	161.2288	1.8829	7025	2.92	29.4	7.2	11.80	0.95	mS	1.15	y	y	–
J045946.93+455125.0	160.9453	2.1229	160.9450	2.1222	13320	0.52	21.0	4.9	14.83	0.90	mS	1.20	n	n	–
J045953.38+453145.6	161.2149	1.9356	–	–	10853	0.33	–	–	–	–	–	1.01	y	y	Aur 3-C
J045955.96+445945.0	161.6397	1.6125	–	–	10208	0.21	–	–	–	–	–	1.14	n	n	–
J045958.09+440554.1	162.3500	1.0637	162.3514	1.0638	5681	0.83	11.5	2.6	14.07	0.69	eS	1.04	y	y	–
J050007.95+452211.1	161.3668	1.8708	159.7174	0.9188	4914	0.52	7.6	0.3	19.49	1.00	ℓS	1.10	n	n	–
J050031.81+453733.6	161.2077	2.0834	161.2069	2.0851	12284	0.18	–	2.1	16.53	0.91	Irr	1.08	n	n	–
J050039.87+453120.2	161.3040	2.0382	161.3047	2.0387	3382	1.15	7.4	0.8	14.97	1.03	Irr	1.22	y	y	–
J050045.76+454454.4	161.1362	2.1908	161.1361	2.1916	3442	0.14	–	0.1	20.26	0.83	ℓS	1.48	n	n	–
J050117.24+454732.3	161.1577	2.2899	161.1578	2.2892	3368	1.52	8.7	1.0	17.21	0.77	mS	1.10	y	y	–
J050120.46+442255.1	162.2778	1.4321	–	–	10706	0.27	–	–	–	–	–	1.19	n	y	–
J050124.98+441446.0	162.3933	1.3593	–	–	8849	0.29	–	–	–	–	–	1.22	y	y	–
J050125.79+452212.4	161.5067	2.0507	161.5068	2.0514	6113	0.22	–	4.1	14.17	1.03	mS	1.87	y	y	–
J050212.15+453526.1	161.4152	2.2928	–	–	10847	0.14	–	–	–	–	–	1.88	y	y	–
J050217.54+455441.1	161.1707	2.5012	–	–	13374	0.55	–	–	–	–	–	1.31	n	y	–
J050231.16+451050.9	161.7739	2.0864	–	–	8306	0.33	–	–	–	–	–	1.10	n	n	–
J050237.59+461133.0	160.9832	2.7187	–	–	9649	2.02	28.4	–	–	–	–	1.27	y	y	Aur 3-C
J050251.93+451609.7	161.7409	2.1888	161.7406	2.1878	14499	0.61	23.9	7.0	14.26	0.92	mS	1.25	y	n	–
J050256.86+451230.4	161.7981	2.1631	–	–	3267	1.78	–	–	–	–	–	1.18	y	n	–
J050309.74+453102.6	161.5759	2.3813	–	–	2891	0.44	–	–	–	–	–	1.16	y	n	–
J050320.82+450122.0	161.9884	2.1059	161.9887	2.1046	8504	0.99	17.9	3.2	13.22	1.06	mS	1.49	y	y	–
J050329.24+454555.0	161.4136	2.5772	161.4132	2.5750	5490	2.37	–	5.6	12.59	0.65	mS	1.53	y	y	–
J050335.40+442816.5	162.4525	1.8045	162.4539	1.8007	7146	0.19	–	3.3	13.37	1.08	eS	1.35	y	n	–

5 Summary and Future Work

Abstract

The main results from the study that has been carried out in this thesis are summarised in this chapter. In the first part a brief statement on the motivation behind this work and outline of the main goals is provided and the main results summarised. The second part contains a discussion on the future prospects and planned studies to be carried out that are directly related to the work conducted in this thesis.

5.1 Introduction

This project was started with the main goal of mapping a major overdensity of the Perseus-Pisces Supercluster (PPS) that had remained largely unexplored to date. The interest in this overdensity was motivated by hints of the potentially rich X-ray emitting 3C 129 cluster embedded therein, which also hosts two strong radio sources (Spinrad 1975). Due to its low Galactic latitude the galaxy composition of this cluster had not been investigated in detail despite it being a component of the expansive PPS filament. The high extinction levels in this region of the sky make finding galaxies at optical wavelength ineffective. The only way to investigate the galaxy distribution in this overdensity is through 21 cm line emission H I observations. The required H I-survey was conducted with the Westerbork Synthesis Radio Telescope (WSRT). With these radio observations we aimed to,

- construct a spectral data cube from which the H I properties of the galaxies in and around the 3C 129 cluster and its immediate surrounding regions in the PPS could be extracted,
- map the distribution of the galaxies on the sky and in redshift, and investigate how the large-scale structure of the PPS filament connects across the Zone of Avoidance,
- analyse the galaxy population of the 3C 129 cluster and study its properties in detail,
- characterise the cosmic environments within the surveyed volume and investigate the link between the galaxy properties and their environments.

In addition to these scientific goals, the project was also designed in such a way that it could be used as a pilot study for the upcoming H I-surveys to be conducted with Apertif. For this purpose, it provides data with which calibration, visualisation, source finding and characterisation techniques can be tested on real H I data cubes. It is absolutely vital to have a good handle on these issues before the large datasets from these forthcoming surveys start streaming in.

5.1.1 The WSRT H I-imaging of the Perseus-Pisces Supercluster in the Zone of Avoidance

A blind H I-imaging survey was performed targeting a wall-like structure that encompasses a potentially rich cluster. This cluster, known mostly from its X-ray emission as the 3C 129 cluster, is part of the Perseus-Pisces Supercluster filament that crosses the Zone of Avoidance (ZoA) around $(\ell, b, v) \approx (160.5°, 0.27°, 6000 \text{ km s}^{-1})$. Observations were carried out using the WSRT, comprising 35 individual pointings each observed for 12 hours. The pointings were arranged in a hexagonal mosaic similar to a single Apertif pointing. It covered an area of about 9.6 sq.deg centred at $(\ell, b) \approx (160.8°, 0.9°)$ and a radial velocity range of approximately $cz \sim 2000 - 16000$ km s^{-1}. The resulting spectral line data cube has an angular resolution of $23'' \times 16''$ and a velocity resolution of 16.5 km s^{-1} with typical noise levels ~ 0.4 mJy/beam. The survey configuration allowed for an H I-mass detection limit of $M_{HI} = 3 \times 10^8 M_\odot$ at the 6σ noise level assuming a line-width (w_{50}) of 150 km s^{-1} at the median distance of the PPS ($cz \approx 6000$ km s^{-1}).

Semi-automated methods based on Gipsy software tasks were used to search for the H I-emission from galaxies. The search resulted in 211 H I detections in the entire survey volume. Various H I properties of these galaxies were produced including integrated fluxes, line-widths, H I-column density maps and velocity field maps. The average measured line-widths (w_{50}) and H I-masses (M_{HI}) are about 132 km s^{-1} and $\log(M_{HI}/M_\odot) = 9.1$. Only 62% of the H I detected galaxies in our survey volume were found to have a stellar counterpart at near-infrared wavelengths as identified in the deep and high resolution UKIDSS Galactic Plane Survey (GPS) images, which is a testament to the challenges presented by extinction in the ZoA.

5.1.2 Linking large-scale structures across the ZoA

A total of four distinct overdensities were identified in redshift space in the survey volume. Of these, the two minor overdensities were located at the radial velocities of $cz \sim 2000-4000$ km s^{-1} (Aur 1; 15 H I-detections) and $cz \sim 12000-16000$ km s^{-1} (Aur 4; 37 H I-detections). The other two were major overdensities located at the velocity of the PPS of $cz \sim 4000-8000$ km s^{-1} (Aur 2; 87 H I-detections) and in the background of the PPS within the velocity range of $cz \sim 8000-12000$ km s^{-1} (Aur 3; 72 H I-detections). H I-detected galaxies located in these two major overdensities have H I-masses and line-widths in the range of $\log(M_{HI}/M_\odot) = 7.8-10.3$ and $w_{50} = 25-526$ km s^{-1} for Aur 2, and $\log(M_{HI}/M_\odot) = 8.6-10.3$ and $w_{50} = 28-322$km s^{-1} for Aur 3. Galaxies in the radial velocity range of the PPS were used to demonstrate that the Persues-Pisces Supercluster does indeed connect across the ZoA, thus confirming earlier indications (e.g., Focardi, Marano & Vettolani 1984, Chamaraux et al. 1990) of a PPS filamentary connection between the Perseus, the Pisces and the A569 clusters across the ZoA in this region of the sky. In fact, the large-scale structure maps by Jarrett (2004) have shown that the PPS may even connect all the way up to the A634 cluster which would make the PSS one of the largest filamentary chains ($>$ 100 Mpc) in the nearby Universe. Galaxies in the background of the PPS were shown to be part of a structure only known as CID15 in the reconstructed density and velocity maps from the 2MRS (Erdoğdu et al. 2006) and thus validates the accuracy of these reconstructed maps above and below the ZoA in this region on the sky.

5.1.3 The galaxy composition of the 3C 129 cluster.

Given that the only properties that were known about the 3C 129 cluster were based on its X-ray emission and its two embedded radio galaxies, a more detailed exploration requires information on its galaxy population. For this purpose a census of the galaxies within this cluster was conducted. This was carried out by combining the H I-detected galaxies with the galaxies identified in the near-infrared (NIR) taking advantage of the high resolution ($0.2''$/pix, seeing $\approx 0.8''$) images from the UKIDSS Galactic Plane Survey (UKIDSS-GPS). Photometry in the NIR J, H and K bands was obtained for about $\sim$ 9700 galaxies within the WSRT H I surveyed area. Cluster members were selected by fitting the red sequence in the $(J-K)$ vs K colour-magnitude diagram. The resulting fitted slope of the 3C 129 cluster was found to be $\alpha = -0.023 \pm 0.002$ mag, similar to the Coma cluster ($\alpha = -0.017 \pm 0.009$), which lies at a similar recession velocity of $cz \sim 6000$ km s^{-1}. The cluster's spatial extent was defined to be within a radius of $\sim$ 1.7 Mpc ($1.34R_{200}$) motivated by where the galaxies became sparsely distributed. Within this radius 261 galaxies were identified in the UKIDSS-GPS images and visually confirmed. This process demonstrated the efficiency of fitting the red-sequence to identify cluster galaxies in the absence of redshift data. The high resolution of the UKIDSS-GPS images made it possible to estimate the morphologies of these galaxies. More than half of the galaxies seen in projection against the cluster region were found to be early-type galaxies (E and E/S0) and bulge-dominated spirals.

The velocity and spatial distributions of the gas-rich, H I-detected galaxies and the gas-poor red-sequence galaxies are different in this cluster. Specifically, the early-type population that comprises the E and E/S0 galaxies dominates the inner regions of the cluster while the population of gas-rich galaxies that constitutes for 83% of late-type spirals, is found in the cluster outskirts. An obvious radial morphological segregation is seen within a radius of $\sim$ 0.9 Mpc from the centre of the cluster where an increase of the early-type galaxies is balanced by a decrease of the late-type galaxies. Moreover, the H I-detected galaxies seem to strongly avoid the inner region within a radius of $\sim$ 0.5 Mpc, thus pointing to a strong effect of the cluster's environment on the gas content of galaxies.

The richness of the cluster was examined by comparing its K-band luminosity function to those of two well-known clusters at similar redshifts. One being a massive cluster in the Great Attractor region, namely the Norma cluster ($M_K^* = -25.4 \pm 0.8, \alpha = -1.26 \pm 0.10, \phi^* = 27.8 \pm 2.4$

h_{70}^2 Mpc^{-2}), also located in the ZoA but in the South, and the other being the Coma cluster ($M_K^* = -24.0, \alpha = -0.98, \phi^* = 76.0 \pm 3.0$ h_{70}^2 Mpc^{-2}). The comparison showed that the 3C 129 cluster is quite rich as was suspected. The galaxy density in the core of the 3C 129 cluster is similar to that in the Norma cluster and slightly less than in the Coma cluster. This finding is consistent with the relative X-ray luminosities of these three clusters.

Additionally, the spatial distribution of galaxies in the core of the cluster showed a slight asymmetry aligned with the irregular distribution of the X-ray emission. This is consistent with the results from the X-ray analysis by Leahy & Yin (2000) who surmised that the 3C 129 cluster seems to have undergone a merger and has not reached a dynamically relaxed state yet. Furthermore, a large substructure dominated by gas-rich galaxies was found North of the main cluster at a slightly higher recession velocity. These observations seem to point to a scenario where the 3C 129 cluster might still be growing through the accretion of galaxies falling in along the PPS filament.

Overall, the examination of this cluster points to a diverse and dynamic environment that is relatively nearby from which studies of the environmental effects on galaxy properties would benefit.

5.1.4 Effects of the environment on H I-properties

The wealth of H I data from the WSRT PPZoA survey revealed a myriad of cosmic environments ranging from major galaxy overdensities, an X-ray emitting galaxy cluster to voids. This offered a unique laboratory in which H I-properties of the galaxies in these various environments could be examined under the same observational conditions.

The main environments of interest in the volume were the two major galaxy overdensities, one containing the 3C 129 cluster at the recession velocities of the PPS of $cz \sim 4000 - 8000$ km s^{-1} (Aur 2), and the other in the background of the PPS at $cz \sim 8000 - 12000$ km s^{-1} (Aur 3). Substructures in these galaxy systems were identified by performing the Dressler-Shectman test for the gas-rich H I-detected galaxies and by assessing the 2-dimensional galaxy distribution of the gas-poor galaxies using the adaptive kernel smoothing based technique applied in smoothed particle hydrodynamics. Both overdensities exhibit substructure and are unique in their galaxy composition and thus represent different environments. Galaxies in substructures located in the Aur 2 system were mostly found to be early-type galaxies while in Aur 3, substructures mostly con-

tained late-type galaxies.

The H I-morphologies of galaxies in these substructures were examined by assessing asymmetries in their global H I profiles, integrated H I maps and kinematics. The well-known H I-morphology density relation is found, such that more disturbed H I morphologies are frequent in the larger and more densely populated galaxy groups, while in the less populated groups the H I is distributed more in regular disks. The result is thought to be due to the higher incidence of tidal interactions in denser environments.

An investigation of the H I-content of galaxies within the 3C 129 cluster revealed an H I-gas deficiency in the core of the cluster as indicated by the lack of H I-detections in this region. The cause of this gas-deficiency was examined by modelling the impact of the intra-cluster medium on the galaxies in the cluster. The ram-pressure stripping mechanism was found to be the dominant gas removal process in the core of the cluster. However, galaxies with significantly low H I-content were also found in the cluster outskirts. Most of these galaxies are located within galaxy groups inside the cluster radius and are falling into the cluster for the first time. Additionally, a similarly low H I-content was measured in the Aur 3 galaxy system in which no X-ray emission or galaxy cluster is known, thus confirming the importance of gas-removal processes occurring in galaxy-groups/filaments in the transformation of galaxies.

5.2 Future work

5.2.1 Perseus-Pisces Supercluster ZoA flow-fields

The H I observations conducted in the hidden region of the Perseus-Pisces filament have revealed overdensities that could contribute to ongoing studies aimed at fully understanding the dynamics of the Local Universe. The next natural step is to construct cosmic flow-fields in this region of the ZoA. This requires a decomposition of the detected galaxy velocities into their two components; the recession velocity which is caused by the expansion of the Universe and the peculiar velocity which arises due to the gravitational force caused by the non-uniform mass density distribution. Disentangling the two requires a distance indicator such as the Tully-Fisher (TF; Tully & Fisher 1977) relation, which is a correlation between the rotational velocities and absolute magnitudes. The rotational velocities of the galaxies will be acquired from the H I global profiles of the detected galaxies, and the apparent magnitude from the NIR photometry. With these parameters, the peculiar velocities using the

TF relation can be derived. This is possible using a new re-calibration of the TF relation for isophotal magnitudes (Said, Kraan-Korteweg & Jarrett 2015). This re-calibrated TF was customised especially for the ZoA where the derived total magnitudes are unreliable. The measured peculiar velocity field maps will provide information on the relevance of this overdensity and its immediate surrounding PPS.

5.2.2 Spectroscopic follow-up

For the work presented in this thesis the gas-poor galaxies that belong to the 3C 129 cluster were selected mainly based on their red-sequence using the NIR colour-magnitude relation. This method is effective at finding cluster galaxy candidates in the absence of optical spectroscopy since it has been shown to have a low contamination rate of about 5% at both near-infrared and optical wavelengths (Gladders & Yee 2000). Moreover, the slope of the red-sequence is similar for clusters at the same redshift while evolving with redshift (Gladders et al. 1998, López-Cruz, Barkhouse & Yee 2004). This is advantageous since the slope of the red-sequence can provide an estimate for the cluster redshift. However, the uncertainty on the redshift estimate has been found to be around 10% (Gilbank et al. 2007) as a result, structures that are close to each other in distance may be inseparable along the line-of-sight. It is therefore possible that some galaxies from the background overdensity at $cz \sim 10000$ km s^{-1} (Aur 3) could have entered the 3C 129 cluster sample. For this reason it is important to confirm the validity of this colour selection and verify that the selected galaxies are indeed cluster members and not interlopers from the background. This can only be achieved through optical or near-infrared spectroscopic follow-up, preferably with a multi-object spectrograph, such as the new WEAVE instrument on the William Herschel Telescope (Dalton et al. 2012), capable of taking spectra of up to 1000 targets at the same time. Although optical wavelengths might suffer from extinction, the catalogues compiled in this study contain the necessary positional and photometric information for all objects on the red-sequence within the HI survey area. This will make it easier to select only those sources that are likely to provide reliable measurements. Extending the number of redshift measurements will not only be valuable in confirming the members of the 3C 129 cluster spectroscopically, but it will also allow for detailed studies of the overdensity in the background. Examining the state of this structure will be useful in determining flow-fields in this region and compare these to those predicted from the 2MRS reconstructed maps by Erdoğdu et al. (2006).

5.2.3 The Cluster Dynamics

Obtaining additional spectroscopic redshifts for the 3C 129 cluster will improve membership designation of galaxies to this cluster. This is vital in determining the gravitational potential of the cluster, which generally is obtained from the dispersion of the line-of-sight velocities. Additionally, better redshift statistics will help avoid biases in the velocity dispersion and cluster mass measurements (Beers, Flynn & Gebhardt 1990, Ruel et al. 2014).

The velocity dispersion of the 3C 129 cluster is currently only estimated from the galaxies detected in H I or from the X-ray data. However, there are issues with both these measurements. First, the cluster velocity dispersion based on the H I detections is highly uncertain given that almost all of the H I detected galaxies lie outside the core of the cluster, which means that the velocity dispersion measured this way does not properly represent the densest regions of the cluster. Secondly, the X-ray analyses are hampered by the lack of redshifts, which means that the velocity dispersion had to be determined from the β-model of the 3C 129 cluster surface brightness profile (Leahy & Yin 2000). However, it is well-known that the β values derived from the X-ray surface brightness profiles are less than those computed from the actual galaxy velocity dispersions (Forman, Jones & Tucker 1984). As a result, not only is the dispersion uncertain but it would have likely translated into large relative uncertainties that dominate the derived density and temperature profiles of the 3C 129 cluster (Leahy & Yin 2000). Obtaining better redshift statistics will allow for more accurate measurements of these important X-ray parameters of the cluster.

With a larger redshift sample a more robust dynamical analysis can be conducted and the dynamical mass of the cluster computed. This is important in determining the cluster's role in, and the mass contribution to the PPS.

5.2.4 Radio Continuum and Star-Formation

The sensitivity of the data in the observed WSRT volume is excellent for examining the radio continuum emission of galaxies. This is useful for studying star formation rates of galaxies in the 3C 129 cluster environment. These galaxies produce radio synchroton emission through relativistic electrons in supernova remnants. The radio and far-infrared correlation shows a connection between the rate of supernovae and the dust heating produced by massive stars in these galaxies (Condon, An-

derson & Helou 1991, Murphy et al. 2008). The radio continuum data will also provide a complementary diagnostic tool for studying the interactions of the late-type galaxies with the cluster environment. Recent studies have shown that gas stripping of the galaxies have local effects on the radio continuum in the core of clusters where ram-pressure is strong (Murphy et al. 2009, Vollmer et al. 2013). With the acquired WSRT data, investigations of this phenomenon are possible. Furthermore, the ram-pressure effect on star-formation rates can be studied in combination with data from the Wide-field Infrared Survey Explorer (WISE; Wright et al. 2010) and the Galactic Legacy Infrared Mid-Plane Survey Extraordinaire (GLIMPSE; Churchwell et al. 2009) from the Spitzer program. Moreover, radio continuum data will provide an optimal data sample for studies of AGN in galaxy clusters, particularly in the infalling regions. This will give insights in AGN feedback on the surrounding gas at the galaxy-group scale where a mix of X-ray emission, HI and radio continuum has been shown to exist.

Nederlandse Samenvatting

Objecten die zich buiten de Melkweg bevinden, worden in het optisch golflengtegebied aan het zicht onttrokken als gevolg van verduistering door stofwolken tussen de sterren en door de hoge dichtheid aan sterren in het vlak van de Melkweg. Het ontbreken van objecten of *nebulae* aan de hemel in de richting van de Melkweg werd voor het eerst opgemerkt door Proctor (1878) in de *General Catalogue of Nebulae* (Herschel 1864). Rond die tijd was nog niet bekend dat deze *nebulae* feitelijk extragalactische objecten zijn. De extragalactische oorsprong van deze objecten bleek pas met het waarnemen van variabele Cepheïde sterren in de *nebulae* en vervolgens werden deze objecten ook aangeduid als sterrenstelsels. Gezien de geringe kennis in die tijd omtrent stofwolken in de Melkweg, kon men de schijnbare afwezigheid van sterrenstelsels in dit gebied aan de hemel niet verklaren. Pas later toonde Trumpler (1930) aan dat interstellair stof in de Melkweg deze objecten verduisterde, waardoor ze kleiner en minder helder leken, en er zodoende sprake was van een schijnbaar lagere dichtheid aan sterrenstelsels. Dit gebied werd in de Lick en Harvard Surveys (Shapley 1961) aanvankelijk gedefinieerd als een gebied aan de hemel dat ongeveer 5 sterrenstelsels/graad^2 bevatte. De typische dichtheid aan sterrenstelsels buiten het Galactische vlak daarentegen was, gemeten met instrumenten uit die tijd, ongeveer $\sim$54 sterrenstelsels/graad^2. Gezien de opvallende afwezigheid van sterrenstelsels en de moeilijkheid om hier objecten te detecteren, werd dit gebied de "vermijdingszone" genoemd (*Zone of Avoidance*- ZoA; zie Kraan-Korteweg & Lahav 2000a voor een gedetailleerde review).

De verduistering door stof is afhankelijk van de golflengte en hierdoor hangt de omvang van de ZoA af van de golflengte waarop waarnemingen worden uitgevoerd. Het gebied aan de hemel dat de ZoA in beslag neemt, is groter voor kortere golflengtes en kleiner voor langere golflengtes. Zo beslaat de ZoA bijvoorbeeld ongeveer 20% van de hemel voor optische golflengtes (bv., B-band, 445 nm) (Kraan-Korteweg 2005) terwijl dit slechts 10% is voor het nabij-infrarode (NIR) golflengtegebied (bv., K-band, 2.2μm) (Jarrett et al. 2000). In het NIR wordt de ZoA bepaald door de hoge stellaire dichtheid waardoor het lastig is om diffuse sterrenstelsels te onderscheiden.

Motivatie voor het bestuderen van sterrenstelsels in de ZoA

Wat is de reden voor het bestuderen van sterrenstelsels in de ZoA, gezien de observationele uitdagingen die hiermee samenhangen? Waarom bestuderen we niet gewoon sterrenstelsels buiten de ZoA, aangezien er geen reden is om aan te nemen dat sterrenstelsels in de ZoA verschillen van sterrenstelsels daarbuiten? Het bestaan van de ZoA verandert niet onze kennis van de populatie van sterrenstelsels. Evenwel is gebleken dat de ZoA wel onzekerheden veroorzaakt in ons begrip van de bewegingen van nabijgelegen sterrenstelsels (Rowan-Robinson et al. 2000, Loeb & Narayan 2008, Springob et al. 2016).

Een groot aantal studies en waarnemingen zijn gewijd aan het onderzoeken van de verdeling en de bewegingen van sterrenstelsels in het universum. Het beeld dat hieruit naar voren komt is dat sterrenstelsels zijn gelegen langs filamenten, in gekromde vlakken en in clusters met daartussen grote lege ruimtes waar vrijwel geen sterrenstelsels worden aangetroffen (Proust et al. 2006, Jones et al. 2009, Tempel et al. 2014). De afmetingen van deze grootschalige structuren (*Large Scale Structure* - LSS) leggen limieten op aan theorieën die de vorming van deze structuren en de bewegingen van sterrenstelsels in het heelal proberen te verklaren (Ouchi et al. 2005, Springel et al. 2005). De twee dominante conglomeraties van clusters van sterrenstelsels die de beweging van de nabijgelegen sterrenstelsels beïnvloeden, zijn de *Great Attractor* (Lynden-Bell et al. 1988) en de *Perseus-Pisces Supercluster* (Giovanelli et al. 1986, Haynes et al. 1988, Wegner, Haynes & Giovanelli 1993). Het is een toeval dat deze beide super-structuren op ongeveer gelijke afstand maar aan tegenovergestelde zijden van de hemel te vinden zijn, en dat beide in zekere

mate worden verduisterd door stofwolken in de Melkweg (Pomarède et al. 2015). Het in kaart brengen van de groot-schalige structuren gevormd door clusters van sterrenstelsels, gekromde vlakken en filamenten, heeft plaats gevonden aan de hand van surveys van roodverschuivingen op verschillende golflengtes, zoals de *Center for Astrophysics Redshift Survey* (CfA; Huchra et al. 1983), de *Two degree-Field Galaxy Redshift Survey* (2dFGRS; Colless et al. 2001), en de meer recente *2MRS* (Huchra et al. 2012) en *Sloan Digital Sky Survey* (SDSS; Alam et al. 2015). De ZoA strekt zich echter uit over grote gebieden aan de hemel. Dit beperkt onze kennis van de daadwerkelijke verdeling en omvang van de kosmische structuren achter de Melkweg. Veel studies van grootschalige structuren nemen hun toevlucht tot het voorspellen van de LSS achter de Melkweg door extrapolatie van in kaart gebrachte structuren boven en onder het Galactische vlak (Kolatt, Dekel & Lahav 1995, Erdoğdu et al. 2006, Sorce, Hoffman & Gottlöber 2017). Een risico van deze methode is evenwel dat aannames met betrekking tot de verdeling van grootschalige structuren in de ZoA incorrect zijn en dit zou kunnen leiden tot voorspellingen waarin structuren misplaatst zijn of niet bestaan. Het in kaart brengen van de daadwerkelijke verdeling van sterrenstelsels door surveys van roodverschuivingen in het vlak van de Melkweg is belangrijk om de onzekerheden in de verdeling van de grootschalige structuren te verminderen. Surveys van roodverschuivingen in de ZoA bieden in het bijzonder de mogelijkheid om de verdeling van grootschalige structuren volledig in kaart te brengen, om de voorspelde dichtheidskaarten te controleren, en om de geometrie van de lege ruimtes achter de Melkweg te begrijpen. Dit laatste is van belang om limieten te kunnen stellen aan kosmologische parameters (Lavaux et al. 2010).

HI-waarnemingen

De meest effectieve methode voor het in kaart brengen van sterrenstelsels in de verduisterde gebieden van de ZoA is het waarnemen van neutraal atomair waterstof (H I). Galactisch stof is doorzichtig voor de lange 21 cm lijnemissie van H I. Er is daarom veel tijd geïnvesteerd in het in kaart brengen van de verdeling van sterrenstelsels achter de Melkweg door middel van HI-surveys. Een van de eerste HI-surveys in de ZoA was de blinde HI-survey uitgevoerd door Kerr & Henning (1987) in de noordelijke ZoA met de 91-m Green Bank radiotelescoop tot snelheden van $cz = 7500$ km s^{-1}. De andere belangrijke survey de *Dwingeloo Obscured Galaxy Survey* (DOGS; Kraan-Korteweg et al. 1994, Henning et al. 1998), een systema-

tische survey tot cz = 4000 km s^{-1} van de meest verduisterde gebieden in het noorden. Recentelijk is de systematische HI Zone of Avoidance survey (HIZOA; Henning et al. 2000, Staveley-Smith et al. 2016) uitgevoerd in de zuidelijke ZoA, die zich ook uitstrekte tot de noordelijke ZoA (HIZOA-N; Donley et al. 2005) met behulp van de Parkes *multi-beam* ontvanger. Deze survey dekt snelheden tot $cz = 12700$ km s^{-1}. Daarnaast is er ook een veel diepere HI-survey uitgevoerd in roodverschuivingsruimte in de noordelijke ZoA tot een diepte van $cz = 18000$ km s^{-1}, de *Arecibo L-Band Array Zone of Avoidance survey* (ALFA ZoA; Henning et al. 2010, McIntyre et al. 2015). De meest recente blinde HI-survey voor de gehele noordelijke hemel ($\delta > -5°$) is de Effelsberg-Bonn HI Survey (EBHIS; Kerp et al. 2011, Winkel et al. 2016) die een gebied van meer dan 8000 vierkante graden in kaart brengt tot een diepte van $cz \approx 20000$ km s^{-1} met de 100-m Effelsberg Telescope. Deze grote HI-surveys hebbem, samen met andere kleinere surveys die hier niet genoemd worden, een belangrijke rol gespeeld in het aantonen van de effectiviteit van het zoeken naar sterrenstelsels in de ZoA met behulp van H I-waarnemingen, hetgeen heeft geleid tot een verkleining van de ZoA.

Naast de mogelijkheid die HI-gas biedt voor het goed in kaart brengen van sterrenstelsels in de meest verduisterde gebieden van de ZoA, biedt emissie van het HI-gas de mogelijkheid om de evolutionaire eigenschappen van sterrenstelsels in clusters, filamenten en groepen gesitueerd op de knooppunten van de grootschalige structuren te bestuderen. Clusters van sterrenstelsels groeien continue door accretie van sterrenstelsels en groepen van sterrenstelsels uit de nabijgelegen filamenten (Ebeling, Barrett & Donovan 2004, Braglia, Pierini & Böhringer 2007, Fadda et al. 2008, Coppin et al. 2012). Aangetoond is dat gasrijke laat-type sterrenstelsels uit de buitengebieden zich transformeren in gasarme vroeg-type sterrenstelsels tegen de tijd dat ze het centrum van een cluster bereiken. Door te bepalen of en hoe deze transformatie plaatsvindt, kan belangrijke informatie worden verkregen over de processen die verantwoordelijk zijn voor de evolutie van sterrenstelsels. De omgeving van een sterrenstelsel is één van de belangrijke factoren die deze evolutie beïnvloedt. Clusters van sterrenstelsels zijn een ideale omgeving voor het bestuderen en begrijpen van de omgevingseffecten op de oorsprong van sterrenstelsels. Voorbeelden van een aantal van deze omgevingsspecifieke mechanismen die verantwoordelijk zijn voor de transformatie van sterrenstelsels zijn *ram-pressure stripping*, morfologische verstoringen en botsingen tussen sterrenstelsels. Deze processen laten duidelijke afdrukken achter op de fragiele en diffuse H I-schijven van sterrenstelsels. Hierdoor is HI een

ideaal middel om de mechanismes die de evolutie van sterrenstelsels beïnvloeden te bestuderen (Poggianti & van Gorkom 2001, Bravo-Alfaro et al. 2000a, Bravo-Alfaro et al. 2009, Chung et al. 2009, Gavazzi et al. 2013, Jaffé et al. 2015, Yoon et al. 2017). Deze taak vereist een uitgebreid overzicht van de verschillende omgevingen, waarbij de HI-surveys geen *bias* mogen vertonen en het volume groot genoeg moet zijn om niet alleen de dichtste omgevingen te omvatten (d.w.z. clusters van sterrenstelsels) maar ook de filamenten waarmee deze omgeven zijn.

Deze thesis

Ten grondslag aan het werk dat gepresenteerd wordt in deze dissertatie liggen recentelijk uitgevoerde, doelgerichte 21 cm-waarnemingen van de 2MASS sterrenstelsels helderder dan $K < 11.25$ mag in de ZoA tussen $80° \leq \ell \leq 180°$ en $|b| < 5°$ met de 94-m Nancay Radio Telescope (NRT). De resultaten van dit onderzoek wijzen op een gebied met een zeer hoge dichtheid aan sterrenstelsels dat het vlak van de Melkweg doorkruist op ongeveer $\ell \approx 160°$ en $cz \sim 6500$ km s^{-1} (Ramatsoku et al. 2014). De locatie en afstand van deze structuur valt samen met de uitgebreide *Perseus-Pisces Supercluster* (PPS; Giovanelli et al. 1986, Haynes et al. 1988). Over het bestaan van een verbinding van filamenten van het PPS boven en onder de ZoA is reeds in eerdere studies gespeculeerd (Focardi, Marano & Vettolani 1984, Chamaraux et al. 1990). Er zijn prominente aanwijzingen voor deze verbinding in de 2MASS *all-sky distribution* (Jarrett 2004) en deze verbinding was ook voorspeld door de 2MRS gereconstrueerde dichtheidsvelden (Erdoğdu et al. 2006). Het bestaan ervan was tot op heden echter nog nooit spectroscopisch bevestigd als gevolg van de grote verduistering op optische golflengtes. In dit PPS filament is een Röntgen-cluster van sterrenstelsels te vinden waarin zich twee heldere kop-staart radiosterrenstelsels bevinden met een gebogen morfologie, 3C 129 en 3C 129.1, (Spinrad 1975, Jaegers & de Grijp 1983, Lane et al. 2002, Lal & Rao 2004, Murgia et al. 2016). Hoewel deze cluster uitgebreid is bestudeerd in het Röntgen deel van het spectrum (Leahy & Yin 2000, Harris, Krawczynski & Taylor 2002, Krawczynski et al. 2003) is er ondanks dat het mogelijkerwijs een massieve, evoluerende cluster betreft binnen de PPS, erg weinig bekend over de populatie van sterrenstelsels. Gezien het feit dat clusters van sterrenstelsels een goed proeflaboratorium vormen om onze kennis te vergroten van omgevingseffecten op de oorsprong van sterrenstelsels en de schaarste van grote nabije clusters van sterrenstelsels, blijft het nuttig om clusters en hun omgeving indi-

vidueel te analyseren. Dit is met name nuttig wanneer blijkt dat deze clusters voldoende dichtbij zijn om met grote precisie waargenomen en geanalyseerd te kunnen worden met onze huidige instrumenten.

Methodologie

Er is een blinde HI-imaging survey uitgevoerd met als doel een muurachtige structuur in kaart te brengen die een onbekende maar mogelijk veelbelovende cluster omvat. Deze cluster, voornamelijk bekend vanwege de Röntgenstraling als de 3C 129 cluster, maakt deel uit van het *Perseus-Pisces Supercluster* filament dat zicht uitstrekt vanaf de ZoA rond $(\ell, b, cz) \approx (160.5°, 0.27°, 6000 \text{ km s}^{-1})$. De waarnemingen zijn uitgevoerd met de Westerbork Synthese Radio Telescoop (WSRT) en bestaan uit 35 individuele *pointings* die elk 12 uur zijn waargenomen. De *pointings* vormen een hexagonaal mozaïek, vergelijkbaar met een enkele Apertif *pointing*. De waarnemingen beslaan een oppervlakte van ongeveer 9.6 vierkante graden, gecentreerd op $(\ell, b) \approx (160.8°, 0.9°)$ en hebben een afstandsbereik van ongeveer $cz \sim 2000 - 16000$ km s^{-1}. De resulterende datakubus heeft een hoekresolutie van $23'' \times 16''$ en een snelheidsresolutie van 16.5 km s^{-1} met een ruisniveau van typisch ~ 0.4 mJy/beam. De configuratie van de survey staat een 6σ-detectielimiet van $M_{HI} = 3 \times 10^8 M_\odot$ toe voor de HI-massa, onder de aanname van een lijnbreedte (w_{50}) van 150 km s^{-1} op de afstand van het PPS ($cz \approx 6000$ km s^{-1}).

Samenvatting van de belangrijkste resultaten

De resultaten van het onderzoek uitgevoerd in deze dissertatie kunnen worden samengevat in drie hoofdpunten zoals hieronder beschreven:

Inzicht in de samenhang van grootschalige structuren achter de ZoA: Er zijn in totaal vier verschillende concentraties van sterrenstelsels geïdentificeerd in roodverschuivingsruimte in het volume van de survey. Van deze concentraties bevinden twee kleine zich op $cz \sim 2000 - 4000$ km s^{-1} (Aur 1; 15 H I-detecties) en $cz \sim 12000 - 16000$ km s^{-1} (Aur 4; 37 H I-detecties). De andere twee zijn grote concentraties die zich bevinden op een afstand van het PPS van $cz \sim 4000 - 8000$ km s^{-1} (Aur 2; 87 H I-detecties) en achter het PPS met $cz \sim 8000 - 12000$ km s^{-1} (Aur 3; 72 H I-detecties). De in H I gedetecteerde sterrenstelsels in deze twee grote concentraties hebben HI-massa's en lijnbreedtes tussen $\log(M_{HI}/M_\odot) = 7.8 - 10.3$ en $w_{50} = 25 - 526$ km s^{-1} voor Aur 2, en $\log(M_{HI}/M_\odot) =$

$8.6 - 10.3$ en $w_{50} = 28 - 322$km s^{-1} voor Aur 3. Sterrenstelsels op een afstand gelijk aan die van het PPS zijn gebruikt om aan te tonen dat er verbindingen zijn in het PPS achter de ZoA, hetgeen eerdere indicaties (bijv., Focardi, Marano & Vettolani 1984, Chamaraux et al. 1990) van een samenhang van filamenten tussen de Perseus, de Pisces en de A569 clusters aan weerszijden van de ZoA bevestigt. Kaarten van de grootschalige structuur Jarrett (2004) tonen zelfs aan dat het PPS volledig in verbinding zou kunnen staan met de A634 cluster, wat het PPS één van de grootste filamenten (> 100 Mpc) in het nabije universum zou maken. Van sterrenstelsels achter het PPS filament is met behulp van gereconstrueerde dichtheids- en snelheidskaarten van 2MRS (Erdoğdu et al. 2006) aangetoond dat deze deel uitmaken van de CID15 structuur. Dit bevestigt de nauwkeurigheid van de gereconstrueerde kaarten boven en onder de ZoA in dit gebied aan de hemel.

De populatie van sterrenstelsels in de 3C 129 cluster: Aangezien de enige eigenschappen die bekend waren van de 3C 129 cluster gebaseerd waren op de Röntgen-emissie en de twee radiosterrenstelsels die het bevat, vereist een meer gedetailleerde studie aanvullende informatie met betrekking tot de populatie van sterrenstelsels. Met dit doel voor ogen is een inventaris opgemaakt van de sterrenstelsels in deze cluster. Dit is gedaan door de in HI gedetecteerde populatie van sterrenstelsels te combineren met de sterrenstelsels die geïdentificeerd zijn in het nabij-infrarood (NIR) met behulp van afbeeldingen van de UKIDSS *Galactic Plane Survey* (UKIDSS-GPS). Metingen in de NIR J, H en K banden zijn verkregen voor ongeveer ~ 9700 sterrenstelsels binnen het waargenomen WSRT gebied. Sterrenstelsels die deel uit maken van de cluster zijn geselecteerd door de *red sequence* te bepalen in het $(J - K)$ vs K kleur-magnitude diagram. De resulterende helling voor de 3C 129 cluster is $\alpha = -0.023 \pm 0.002$ mag, vergelijkbaar met de Coma cluster ($\alpha = -0.017 \pm 0.009$) die op een vergelijkbare afstand ligt van $cz \sim 6000$ km s^{-1}. De ruimtelijke omvang van de cluster is zo gedefinieerd dat het een straal van ~ 1.7 Mpc ($1.34R_{200}$) heeft, op grond van de sterk afnemende dichtheid van sterrenstelsels. Binnen deze straal zijn 261 sterrenstelsels automatisch geïdentificeerd en visueel bevestigd aan de hand van de UKIDSS-GPS afbeeldingen. Dit proces toont aan hoe efficiënt het bepalen van de *red sequence* is wanneer roodverschuivingsdata ontbreken. De verdelingen van de gas-rijke, HI-gedetecteerde sterrenstelsels en de gasarme sterrenstelsels zijn verschillend in de cluster. De gasarme populatie van sterrenstelsels domineert de binnenste gebieden van de cluster, terwijl de populatie van gasrijke sterrenstelsels de binnenste

gebieden binnen een straal van ~ 0.5 Mpc van het centrum van het cluster lijken te vermijden. Dit wijst op een sterk effect van de omgeving op de hoeveelheid gas in een sterrenstelsel.

De effecten van de omgeving op HI-eigenschappen: De schat aan HI-data van de WSRT PPZoA survey heeft een breed scala aan omgevingen blootgelegd, uiteenlopend van grote concentraties van sterrenstelsels, een Röntgen-straling uitzendende cluster van sterrenstelsels, tot gebieden waar bijna geen sterrenstelsels te vinden zijn. Dit biedt een uniek laboratorium om de H I-eigenschappen van sterrenstelsels in deze verschillende omgevingen te bestuderen onder dezelfde waarneemcondities.

De meest interessante omgevingen in het door de WSRT waargenomen gebied zijn de twee grote concentraties van sterrenstelsels, waarvan één de 3C 129 cluster bevat op een afstand van $cz \sim 4000 - 8000$ km s^{-1} van het PPS (Aur 2) en de andere achter het PPS ligt, op een afstand van $cz \sim 8000 - 12000$ km s^{-1} (Aur 3). Beide concentraties vertonen substructuur en zijn uniek in hun samenstelling van sterrenstelsels en representeren dan ook verschillende omgevingen. Sterrenstelsels in substructuren in het Aur 2-systeem blijken voornamelijk vroeg-type sterrenstelsels te zijn terwijl de sterrenstelsels in Aur 3 voornamelijk laat-type sterrenstelsels zijn.

De asymmetrie in de HI-verdeling binnen de sterrenstelsels in deze substructuren is onderzocht. Sterrenstelsels met meer verstoorde H I-verdelingen blijken vaker gevonden te worden in de grotere en dichter bevolkte groepen van sterrenstelsels, terwijl in de dunner bevolkte groepen de H I gelijkmatiger is verdeeld. Van de grote verstoringen in de distributie van HI wordt verondersteld dat deze worden veroorzaakt door het vaker voorkomen van getijde-interacties in de dichter bevolkte omgevingen.

Onderzoek naar de HI-inhoud van sterrenstelsels in de 3C 129 cluster heeft vanwege het ontbreken van H I-detecties in dit gebied een tekort aan H I-gas in het centrum van het cluster aangetoond. De oorzaak van dit tekort aan gas is onderzocht door het effect van het intra-cluster medium op de sterrenstelsels in de cluster te onderzoeken. Het principe van *ram-pressure stripping* schijnt het dominante proces te zijn om gas uit sterrenstelsels in het centrum van de cluster te verwijderen. Sterrenstelsels met een significant lage H I-inhoud van $\mathrm{Log}(\mathrm{M_{HI}/L_K}) < 1.0$ $\mathrm{M_\odot/L_\odot}$ worden echter ook in de buitengebieden van groepen van sterrenstelsels gevonden. Het merendeel van deze sterrenstelsels bevindt zich in groepen van sterrenstelsels binnen de straal van de cluster en verkeren in het proces dat ze voor het eerst in de cluster vallen. In het Aur 3-systeem is een

vergelijkbare lage H I-inhoud gevonden waarbij geen Röntgen-straling of clustering van sterrenstelsels bekend is. Dit toont aan dat processen waarbij gas wordt verwijderd uit groepen van sterrenstelsels ook een rol spelen in de transformatie van sterrenstelsels.

Kakaretso ka Sesotho

Dintho tse dutseng sebakeng se ka morao ho Molalatladi (Milky Way) ha di bonahale hantle ka baka la lerotho le bakwang ke maru a lerole le ho teteana ha dinaledi tse ka hare ho ona Molalatladi. Ho se bonahale hona hwa "*nebulae*" tse sebakeng sena ho sibolotswe ke Proctor (1878) lesedinyaneng le bitswang *General Catalogue of Nebulae* (Herschel 1864). Ka nako tseo ho ne ho sa lemohwe hore *nebulae* tsena hantle ke melalatladi (*galaxies*) e meng e dibakeng tse hole haholo le Molalatladi wa rona. Semelo le bohole ba tsona se tlisitswe ke ho lemoha *cepheids* ka hara *nebulae* tsena, empa ka nako eo ho ne ho sena tlhaloso kapa kutlwisiso ya ho ka hlalosa lebaka le etsang hore melalatladi ena e se bonahale. Ho ile hwa tholwa ka morao hore maru a lerole a baka hore melalatladi e se hlake hantle kapa e se bonahale. Ka labaka lena sebaka seo se ile sa rehwa "sebaka sa lerotho" (*Zone of Avoidance*-ZoA; bona lesedinyana la Kraan-Korteweg & Lahav 2000a bakeng sa tlhaloso e felletseng).

Boithuto ba melalatladi e ka hare ho ZoA

Ha re tadima sebaka sa lerotho (ZoA) re fumana diphephetso tse re fang thahasello ya ho ka fumana se hlileng se etsahalang ho sona. Ha re sheba melalatladi e ka hare ho ZoA ha re a labella letho le ka fapanang le melalatladi e dibakeng tse ding tse senang lerotho lena. Boteng ba sebaka sena ha bo fetole kutlwisiso ya rona ya hore melalatladi e bopilwe jwang. Le ha ho le jwalo, ho ya ka dithuto tse hlaloswang ditokomaneng tsa Rowan-Robinson et al. (2000) le Loeb & Narayan (2008), sebaka sena se lerotho se etsa hore re se utlwisise ka ho phetahala hore melalatladi e ka hare ho Bokahohle (Universe) bo haufi le rona e tsamaya ka tsela e

jwang.

Se fumanehang ka (HI)

Mokgwa o motle wa tshebetso wa ho ba tseba hore semelo sa melalatladi tse ka hara sebaka sa lerotho (ZoA) ke ho tadima kgase e bitswang (*neutral hydrogen*-H I) e tswang ka hare ho tsona. Boputswa ba Molalatladi bo a hlaka ha re sheba sebaka sena re sebidisa H I, ka lebaka lena dithuto tse ngata tse shebaneng le ho utliwisisa melalatladi e ka hare ho ZoA di sebedisa mokgwa ona wa ho sheba H I. Ka ho etsa diphuhutso, le ho ithuta ka H I, re ka kgona ho thola lesedi la hore melalatladi ena e bopilwe jwang le hore e fetoha ka mokgwa o jwang. Le ha hole jwalo, dingata tseo re sa ditsebeng ka boemo ba melalatladi, ka lebaka lena diphuphutso tse tebileng le tse hlokolosi di ntse di hlokahala.

Mosebetsi ona

Mosebetsi o tekwang mona o qholoditswe ke diketsahalo tsa morao-rao tse neng di shebane le diponahalo tsa H I tsa melalatladi e kganyang e neng di hlahlojwe ka hare ho ZoA ka *telescope* e bitswang *Nancay Radio Telescope*-NRT. Sephetho se tswileng boithuting ba NRT se bontshitse hore ho ka nna ha ba le sebopeho se nang le malatladi e mengata, se teteaneng, se tshelang Molalatladi. Tsena di hlalositswe tokomaneng ya Ramatsoku et al. (2014). Sebaka le bohole ba sebaka sena se teteaneng bo hokahantswe le sebopeho se seholo-hadi sa kgwele ya dihlopha tsa melalatladi (*supercluster*) se bitswang *Perseus-Pisces Supercluster*-PPS (Giovanelli et al. 1986, Haynes et al. 1988). Bo teng ba sebopeho sena se teteaneng bo ne bo ile ba belaellwa bo le teng boithutong bo ileng ba etswa kgajana (Focardi, Marano & Vettolani 1984, Chamaraux et al. 1990), empa leha ha ho le jwalo sena se so netefatswe. Ka hare ho sebopeho sena ho fumanehile kgobokano ya melalatladi eo e neng e sa tsejwe ka botlalo o bitswang 3C 129 *cluster*. Ha ho letho le neng le tsejwa ka melalatladi e ka hare ho kgobokano ena.

Ho bohlokwa ho fuputsa melalatladi e kgobokaneng ka tsela ena hobane e re fa tsebo e pharaletseng ya hore Bokahohle bo bupuwe jwang.

Mokgwa wa tshebetso

Boithuto ba H I bo ile ba etswa bo tobile lebota le akaretsang kgobokano e na ya 3C 129 *cluster*, le dibaka tse haufi le yona tse amanang le *Perseus-*

Pisces Supercluster. Re ile ra sebedisa *telescope* e bitswang *Westerbork Synthesis Radio Telescope*-WSRT ho hlahloba lebota lena. Sebaka sena se ile sa sejwa ka ditshupo tse mashome a mararo a metso e mehlano (35), mme e nngwe le e nngwe ya ditshupo tsena ya sejwa bolele ba hora tse leshome le metso e mmedi (12) ka WSRT.

Kakaretso ya diphetho sa Mantlha

Sephetho sa mosebetsi o fihletsweng boithutong bona se ka akaretswa ka dintlha tse tharo tse hlalositsweng ka tlase:

Kopantshong ya dibopeho tse kgolo hara ZoA: Kakaretso ya ditereke tse nne tsa tshubehlellano ya melalatladi di ile tsa fumanwa. Ho tsena, tse pedi tse kgolohadi di fumaneha boleleleng ba PPS le ka morao ho PPS. Dihlopha tsena tsa melalatladi di ile tsa sebediswa ho bontsha hore ruri kgobokano e kgolohadi ya PPS e kopana ka hara ZoA, mme ya netefatsa dipono tsa pele tsa Focardi, Marano & Vettolani (1984) le Chamaraux et al. (1990). E bile di bontsha hore kgwele e na e tletseng kgobokano tsa melalatladi e leng PPS ke yona e kgolohadi ka hara Bokahohle bo haufi le rona.

Sebopeho sa Kgobokano ya melalatladi ya 3C 129 *cluster*: Ka hobane semelo sa 3C 129 *cluster* se ne se sa tsebahale hantle, le hore kgobokano e na e na le melalatladi e kae ka palo. Re ile ra nka diphuphutso tsa ho hlahloba hore e boholo bo bokae. Re sebedisitse melalatladi e ileng ya fumanwa ka HI le e fumanweng ka mokgwa o mong wa *near-infared*. Sephetho sa diphuphutso tsena se ile sa fumana hore kgobokano e na ya 3C 129 *cluster* e na le melalatladi e ka bang 261, ka hoo e kgolohadi ha re e bapisa le kgobokano tse ding tsa melalatladi tse bohole bo tshwanang le yona.

Ditlamorao tsa tikoloho ho HI: Bongata ba pokello ya HI ho tswa boithutong ba WSRT bo hlahisitse phapano e kgolo ya dibaka, ho tloha ho ditokoloho tse kgolohadi tse nang le dihlopha tse ngata tsa melalatladi ho ya ho tikiloho tse nyane. Ho na ho ile hwa re fa monyetla wa ho fuputsa hore tikoloho e ama HI ka hare melalatladi ka tsela e jwang. Re fumane hore ka hare ho tikoloho tse teteaneng, HI ea tloswa ka labaka la ho thulana ha melalatladi, mme sena se fetola sebopeho sa melalatladi ena.

Bibliography

Abramson A., Kenney J. D. P., Crowl H. H., Chung A., van Gorkom J. H., Vollmer B., Schiminovich D., 2011, AJ , 141, 164

Alam S. et al., 2015, ApJS , 219, 12

Allen S. W., Schmidt R. W., Ebeling H., Fabian A. C., van Speybroeck L., 2004, MNRAS , 353, 457

Andreon S., 1996, A&A, 314, 763

Baldry I. K., Glazebrook K., Brinkmann J., Ivezić Ž., Lupton R. H., Nichol R. C., Szalay A. S., 2004, ApJ , 600, 681

Balogh M. L. et al., 2009, MNRAS , 398, 754

Barnes D. G. et al., 2001, MNRAS , 322, 486

Beers T. C., Flynn K., Gebhardt K., 1990, AJ , 100, 32

Bell E. F. et al., 2004, ApJ , 608, 752

Bennett C. L. et al., 2003, ApJS , 148, 1

Bertin E., Arnouts S., 1996, A&AS, 117, 393

Bilicki M., Chodorowski M., Jarrett T., Mamon G. A., 2011, ApJ , 741, 31

Bilicki M., Jarrett T. H., Peacock J. A., Cluver M. E., Steward L., 2014, ApJS , 210, 9

Booth R. S., Jonas J. L., 2012, African Skies, 16, 101

Borgani S. et al., 2001, ApJ , 561, 13

Bower R. G., Lucey J. R., Ellis R. S., 1992, MNRAS , 254, 589

Braglia F., Pierini D., Böhringer H., 2007, A&A, 470, 425

Branchini E., Plionis M., 1996, ApJ , 460, 569

Bravo-Alfaro H., Cayatte V., van Gorkom J. H., Balkowski C., 2000a, AJ , 119, 580

—, 2000b, AJ , 119, 580

Bravo-Alfaro H., van Gorkom J. H., Caretta C., Islas J. M., 2009, ArXiv e-prints

Buta R. J., McCall M. L., 1999, ApJS , 124, 33

Cardelli J. A., Clayton G. C., Mathis J. S., 1989, ApJ , 345, 245

Carrick J., Turnbull S. J., Lavaux G., Hudson M. J., 2015, MNRAS , 450, 317

Casali M. et al., 2007, A&A, 467, 777

Cattaneo A., 2015, Nature , 521, 164

Cavaliere A., Fusco-Femiano R., 1976, A&A, 49, 137

Cayatte V., Kotanyi C., Balkowski C., van Gorkom J. H., 1994, AJ , 107, 1003

Cayatte V., van Gorkom J. H., Balkowski C., Kotanyi C., 1990, AJ , 100, 604

Chamaraux P., Cayatte V., Balkowski C., Fontanelli P., 1990, A&A, 229, 340

Chilingarian I. V., Melchior A.-L., Zolotukhin I. Y., 2010, MNRAS , 405, 1409

Chung A., van Gorkom J. H., Kenney J. D. P., Crowl H., Vollmer B., 2009, AJ , 138, 1741

Churchwell E. et al., 2009, PASP , 121, 213

Cluver M. E., Jarrett T. H., Kraan-Korteweg R. C., Koribalski B. S., Appleton P. N., Melbourne J., Emonts B., Woudt P. A., 2010, ApJ , 725, 1550

Cohen M., Wheaton W. A., Megeath S. T., 2003, AJ , 126, 1090

Colless M. et al., 2001, MNRAS , 328, 1039

Condon J. J., Anderson M. L., Helou G., 1991, ApJ , 376, 95

Condon J. J., Cotton W. D., Greisen E. W., Yin Q. F., Perley R. A., Taylor G. B., Broderick J. J., 1998, AJ , 115, 1693

Conselice C. J., Gallagher, III J. S., Wyse R. F. G., 2003, AJ , 125, 66

Coppin K. E. K. et al., 2012, ApJL , 749, L43

Crowl H. H., Kenney J. D. P., van Gorkom J. H., Vollmer B., 2005, AJ , 130, 65

Dalton G. et al., 2012, in Proc. SPIE, Vol. 8446, Ground-based and Airborne Instrumentation for Astronomy IV, p. 84460P

de Blok W. J. G., 2011, in IAU Symposium, Vol. 277, IAU Symposium, Carignan C., Combes F., Freeman K. C., eds., pp. 96–99

De Lucia G., Blaizot J., 2007, MNRAS , 375, 2

De Lucia G., Weinmann S., Poggianti B. M., Aragón-Salamanca A., Zaritsky D., 2012, MNRAS , 423, 1277

De Propris R., 2017, MNRAS , 465, 4035

De Propris R., Eisenhardt P. R., Stanford S. A., Dickinson M., 1998, ApJL , 503, L45

Dénes H., Kilborn V. A., Koribalski B. S., 2014, MNRAS , 444, 667

Donley J. L. et al., 2005, AJ , 129, 220

Dressler A., 1980, ApJ , 236, 351

Dressler A., Faber S. M., Burstein D., Davies R. L., Lynden-Bell D., Terlevich R. J., Wegner G., 1987, ApJL , 313, L37

Dressler A. et al., 1997, ApJ , 490, 577

Dressler A., Oemler, Jr. A., Poggianti B. M., Gladders M. D., Abramson L., Vulcani B., 2013, ApJ , 770, 62

Dressler A., Shectman S. A., 1988, AJ , 95, 985

Drinkwater M. J., Gregg M. D., Colless M., 2001, ApJL , 548, L139

Duc P.-A., Bournaud F., 2008, ApJ , 673, 787

Duffy A. R., Meyer M. J., Staveley-Smith L., Bernyk M., Croton D. J., Koribalski B. S., Gerstmann D., Westerlund S., 2012, MNRAS , 426, 3385

Dye S. et al., 2006, MNRAS , 372, 1227

Ebeling H., Barrett E., Donovan D., 2004, ApJL , 609, L49

Ebeling H., Edge A. C., Bohringer H., Allen S. W., Crawford C. S., Fabian A. C., Voges W., Huchra J. P., 1998a, MNRAS , 301, 881

—, 1998b, MNRAS , 301, 881

Ebeling H., Mullis C. R., Tully R. B., 2002, ApJ , 580, 774

Eisenhardt P. R., De Propris R., Gonzalez A. H., Stanford S. A., Wang M., Dickinson M., 2007, ApJS , 169, 225

Eisenstein D. J. et al., 2011, AJ , 142, 72

Ellingson E., Lin H., Yee H. K. C., Carlberg R. G., 2001, ApJ , 547, 609

Erdoğdu P. et al., 2006, MNRAS , 373, 45

Espada D., Verdes-Montenegro L., Huchtmeier W. K., Sulentic J., Verley S., Leon S., Sabater J., 2011, A&A, 532, A117

Fadda D., Biviano A., Marleau F. R., Storrie-Lombardi L. J., Durret F., 2008, ApJL , 672, L9

Feigelson E. D., Babu G. J., 2012, Modern Statistical Methods for Astronomy

Feldman H. A., Watkins R., Hudson M. J., 2010, MNRAS , 407, 2328

Fitzpatrick E. L., 1999, PASP , 111, 63

Fixsen D. J., Cheng E. S., Gales J. M., Mather J. C., Shafer R. A.,

Wright E. L., 1996, ApJ , 473, 576

Fixsen D. J., Kashlinsky A., 2011, ApJ , 734, 61

Focardi P., Marano B., Vettolani G., 1984, A&A, 136, 178

—, 1986, A&A, 161, 217

Forman W., Jones C., Cominsky L., Julien P., Murray S., Peters G., Tananbaum H., Giacconi R., 1978, ApJS , 38, 357

Forman W., Jones C., Tucker W., 1984, ApJ , 277, 19

Fujita Y., 2004, PASJ , 56, 29

Gavazzi G., Fumagalli M., Fossati M., Galardo V., Grossetti F., Boselli A., Giovanelli R., Haynes M. P., 2013, A&A, 553, A89

Gavazzi G. et al., 2008, A&A, 482, 43

Gavazzi G., O'Neil K., Boselli A., van Driel W., 2006, A&A, 449, 929

Genel S. et al., 2014, MNRAS , 445, 175

Giese N., van der Hulst T., Serra P., Oosterloo T., 2016, MNRAS , 461, 1656

Gilbank D. G., Yee H. K. C., Ellingson E., Gladders M. D., Barrientos L. F., Blindert K., 2007, AJ , 134, 282

Giovanelli R., Haynes M. P., 1985a, AJ , 90, 2445

—, 1985b, ApJ , 292, 404

Giovanelli R., Haynes M. P., Chincarini G. L., 1986, ApJ , 300, 77

Giovanelli R., Myers S. T., Roth J., Haynes M. P., 1986, AJ , 92, 250

Gladders M. D., López-Cruz O., Yee H. K. C., Kodama T., 1998, ApJ , 501, 571

Gladders M. D., Yee H. K. C., 2000, AJ , 120, 2148

Goto T., Yamauchi C., Fujita Y., Okamura S., Sekiguchi M., Smail I., Bernardi M., Gomez P. L., 2003, MNRAS , 346, 601

Gregory S. A., Thompson L. A., Tifft W. G., 1981, ApJ , 243, 411

Greisen E. W., 1990, in Acquisition, Processing and Archiving of Astronomical Images, Longo G., Sedmak G., eds., pp. 125–142

Gunn J. E., Gott, III J. R., 1972, ApJ , 176, 1

Haines C. P., Gargiulo A., La Barbera F., Mercurio A., Merluzzi P., Busarello G., 2007, MNRAS , 381, 7

Hambly N. C. et al., 2008, MNRAS , 384, 637

Hammer D. et al., 2010, ApJS , 191, 143

Hanski M. O., Theureau G., Ekholm T., Teerikorpi P., 2001, A&A, 378, 345

Harris D. E., Krawczynski H., Taylor G. B., 2002, ApJ , 578, 60

Haynes M. P., Giovanelli R., 1986, ApJL , 306, L55

Haynes M. P., Giovanelli R., Chincarini G. L., 1984, ARA&A , 22, 445

Haynes M. P. et al., 2011, AJ , 142, 170

Haynes M. P., Magri C., Giovanelli R., Starosta B. M., 1988, AJ , 95, 607

Henning P. A., Kraan-Korteweg R. C., Rivers A. J., Loan A. J., Lahav O., Burton W. B., 1998, AJ , 115, 584

Henning P. A. et al., 2010, AJ , 139, 2130

—, 2000, AJ , 119, 2686

Hernández-Fernández J. D., Haines C. P., Diaferio A., Iglesias-Páramo J., Mendes de Oliveira C., Vilchez J. M., 2014, MNRAS , 438, 2186

Herschel J. F. W., 1864, Philosophical Transactions of the Royal Society of London Series I, 154, 1

Hess K. M., Cluver M. E., Yahya S., Leisman L., Serra P., Lucero D. M., Passmoor S. S., Carignan C., 2017, MNRAS , 464, 957

Hewett P. C., Warren S. J., Leggett S. K., Hodgkin S. T., 2006, MNRAS , 367, 454

Hodgkin S. T., Irwin M. J., Hewett P. C., Warren S. J., 2009, MNRAS , 394, 675

Hou A. et al., 2012, MNRAS , 421, 3594

Huchra J., Davis M., Latham D., Tonry J., 1983, ApJS , 52, 89

Huchra J. P. et al., 2012, ApJS , 199, 26

Hudson M. J., 1993, MNRAS , 265, 43

Hudson M. J., Lucey J. R., Smith R. J., Steel J., 1997, MNRAS , 291, 488

Hudson M. J., Smith R. J., Lucey J. R., Branchini E., 2004, MNRAS , 352, 61

Hughes J. P., 1989, ApJ , 337, 21

Jaegers W. J., de Grijp M. H. K., 1983, A&A, 127, 235

Jaffé Y. L. et al., 2011, MNRAS , 417, 1996

Jaffé Y. L., Smith R., Candlish G. N., Poggianti B. M., Sheen Y.-K., Verheijen M. A. W., 2015, MNRAS , 448, 1715

Jaffé Y. L. et al., 2016, MNRAS , 461, 1202

Jarrett T., 2004, PASA , 21, 396

Jarrett T. H., 2000, PASP , 112, 1008

Jarrett T.-H., Chester T., Cutri R., Schneider S., Rosenberg J., Huchra J. P., Mader J., 2000, AJ , 120, 298

Jarrett T. H. et al., 2012, AJ , 144, 68

Johnston S., Feain I. J., Gupta N., 2009, in Astronomical Society of the Pacific Conference Series, Vol. 407, The Low-Frequency Radio Universe, Saikia D. J., Green D. A., Gupta Y., Venturi T., eds., p. 446

Jones C., Forman W., 1984, ApJ , 276, 38

Jones D. H. et al., 2009, MNRAS , 399, 683

—, 2004, MNRAS , 355, 747

Kapferer W., Sluka C., Schindler S., Ferrari C., Ziegler B., 2009, A&A, 499, 87

Karachentsev I. D., Tully R. B., Wu P.-F., Shaya E. J., Dolphin A. E., 2014, ApJ , 782, 4

Kerp J., Winkel B., Ben Bekhti N., Flöer L., Kalberla P. M. W., 2011, Astronomische Nachrichten, 332, 637

Kerr F. J., Henning P. A., 1987, ApJL , 320, L99

Kocevski D. D., Ebeling H., 2006, ApJ , 645, 1043

Kogut A. et al., 1993, ApJ , 419, 1

Kolatt T., Dekel A., Lahav O., 1995, MNRAS , 275, 797

Koribalski B. S. et al., 2004, AJ , 128, 16

Kraan-Korteweg R. C., 2005, in Reviews in Modern Astronomy, Vol. 18, Reviews in Modern Astronomy, S. Röser, ed., pp. 48–75

Kraan-Korteweg R. C., Lahav O., 2000a, A&A Rev., 10, 211

—, 2000b, A&A Rev., 10, 211

Kraan-Korteweg R. C., Loan A. J., Burton W. B., Lahav O., Ferguson H. C., Henning P. A., Lynden-Bell D., 1994, Nature , 372, 77

Kraan-Korteweg R. C., Woudt P. A., Cayatte V., Fairall A. P., Balkowski C., Henning P. A., 1996, Nature , 379, 519

Krawczynski H., Harris D. E., Grossman R., Lane W., Kassim N., Willis A. G., 2003, MNRAS , 345, 1255

Lal D. V., Rao A. P., 2004, A&A, 420, 491

Lane W. M., Kassim N. E., Ensslin T. A., Harris D. E., Perley R. A., 2002, AJ , 123, 2985

Lavaux G., Hudson M. J., 2011, MNRAS , 416, 2840

Lavaux G., Tully R. B., Mohayaee R., Colombi S., 2010, ApJ , 709, 483

Lawrence A. et al., 2007, MNRAS , 379, 1599

Leahy D. A., Yin D., 2000, MNRAS , 313, 617

Lewis I. et al., 2002, MNRAS , 334, 673

Loeb A., Narayan R., 2008, MNRAS , 386, 2221

López-Cruz O., Barkhouse W. A., Yee H. K. C., 2004, ApJ , 614, 679

Lu N. Y., Freudling W., 1995, ApJ , 449, 527

Lucas P. W. et al., 2008, MNRAS , 391, 136

Lynden-Bell D., Faber S. M., Burstein D., Davies R. L., Dressler A., Terlevich R. J., Wegner G., 1988, ApJ , 326, 19

Macaulay E., Feldman H., Ferreira P. G., Hudson M. J., Watkins R.,

2011, MNRAS , 414, 621
Mahajan S., Mamon G. A., Raychaudhury S., 2011, MNRAS , 416, 2882
Mamon G. A., Biviano A., Murante G., 2010, A&A, 520, A30
Mantz A., Allen S. W., Rapetti D., Ebeling H., 2010, MNRAS , 406, 1759
Marasco A., Crain R. A., Schaye J., Bahé Y. M., van der Hulst T., Theuns T., Bower R. G., 2016, MNRAS , 461, 2630
Masters K. L., Springob C. M., Huchra J. P., 2008, AJ , 135, 1738
McGee S. L., Balogh M. L., Bower R. G., Font A. S., McCarthy I. G., 2009, MNRAS , 400, 937
McIntyre T. P., Henning P. A., Minchin R. F., Momjian E., Butcher Z., 2015, AJ , 150, 28
Merighi R., Focardi P., Marano B., Vettolani G., 1986, A&A, 160, 398
Mieske S., Hilker M., Infante L., 2005, A&A, 438, 103
Miller N. A., Hornschemeier A. E., Mobasher B., Bridges T. J., Hudson M. J., Marzke R. O., Smith R. J., 2009, AJ , 137, 4450
Mobasher B. et al., 2003, ApJ , 587, 605
Monaghan J. J., 2005, Reports on Progress in Physics, 68, 1703
Monaghan J. J., Lattanzio J. C., 1985, A&A, 149, 135
Moore B., Katz N., Lake G., Dressler A., Oemler A., 1996, Nature , 379, 613
Moran S. M., Ellis R. S., Treu T., Smith G. P., Rich R. M., Smail I., 2007, ApJ , 671, 1503
Muldrew S. I., Hatch N. A., Cooke E. A., 2015, MNRAS , 452, 2528
Murgia M. et al., 2016, MNRAS , 461, 3516
Murphy E. J., Helou G., Kenney J. D. P., Armus L., Braun R., 2008, ApJ , 678, 828
Murphy E. J., Kenney J. D. P., Helou G., Chung A., Howell J. H., 2009, ApJ , 694, 1435
Mutabazi T., Blyth S. L., Woudt P. A., Lucey J. R., Jarrett T. H., Bilicki M., Schröder A. C., Moore S. A. W., 2014, MNRAS , 439, 3666
Navarro J. F., Frenk C. S., White S. D. M., 1996, ApJ , 462, 563
Nulsen P. E. J., Stewart G. C., Fabian A. C., Mushotzky R. F., Holt S. S., Ku W. H.-M., Malin D. F., 1982, MNRAS , 199, 1089
Obreschkow D., Croton D., De Lucia G., Khochfar S., Rawlings S., 2009a, ApJ , 698, 1467
Obreschkow D., Klöckner H.-R., Heywood I., Levrier F., Rawlings S., 2009b, ApJ , 703, 1890
Oman K. A., Hudson M. J., Behroozi P. S., 2013, MNRAS , 431, 2307
Oosterloo T., Verheijen M., van Cappellen W., 2010, in ISKAF2010 Sci-

ence Meeting, p. 43

Ouchi M. et al., 2005, ApJL , 620, L1

Owen F. N., Burns J. O., Rudnick L., Greisen E. W., 1979, ApJL , 229, L59

Pantoja C. A., Altschuler D. R., Giovanardi C., Giovanelli R., 1997, AJ , 113, 905

Park C., Choi Y.-Y., Vogeley M. S., Gott, III J. R., Blanton M. R., SDSS Collaboration, 2007, ApJ , 658, 898

Paturel G., Theureau G., Bottinelli L., Gouguenheim L., Coudreau-Durand N., Hallet N., Petit C., 2003, A&A, 412, 57

Peng Y., Maiolino R., Cochrane R., 2015, Nature , 521, 192

Piffaretti R., Arnaud M., Pratt G. W., Pointecouteau E., Melin J.-B., 2011, A&A, 534, A109

Pinkney J., Roettiger K., Burns J. O., Bird C. M., 1996, ApJS , 104, 1

Plionis M., Kolokotronis V., 1998, ApJ , 500, 1

Poggianti B. M., van Gorkom J. H., 2001, in Astronomical Society of the Pacific Conference Series, Vol. 240, Gas and Galaxy Evolution, Hibbard J. E., Rupen M., van Gorkom J. H., eds., p. 599

Pomarède D., Tully R. B., Hoffman Y., Courtois H. M., 2015, ApJ , 812, 17

Porter S. C., Raychaudhury S., Pimbblet K. A., Drinkwater M. J., 2008, MNRAS , 388, 1152

Proctor R., 1878, The Universe of Stars, Proctor, R., ed.

Proust D. et al., 2006, The Messenger, 124

Ramatsoku M., Kraan-Korteweg R., Schröder A., van Driel W., 2014, ArXiv e-prints

Ramatsoku M. et al., 2016, MNRAS , 460, 923

Riad I. F., Kraan-Korteweg R. C., Woudt P. A., 2010, MNRAS , 401, 924

Roediger E., 2009, Astronomische Nachrichten, 330, 888

Roediger E., Brüggen M., 2007, MNRAS , 380, 1399

Roman A. T., Iwata I., Saitō M., 2000, ApJS , 127, 27

Rowan-Robinson M. et al., 1990, MNRAS , 247, 1

—, 2000, MNRAS , 314, 375

Roychowdhury S., Chengalur J. N., Chiboucas K., Karachentsev I. D., Tully R. B., Kaisin S. S., 2012, MNRAS , 426, 665

Ruel J. et al., 2014, ApJ , 792, 45

Safonova E. S., 2011, Astronomy Reports, 55, 1016

Said K., Kraan-Korteweg R. C., Jarrett T. H., 2015, MNRAS , 447, 1618

Saunders W. et al., 2000a, in Astronomical Society of the Pacific Conference Series, Vol. 218, Mapping the Hidden Universe: The Universe behind the Mily Way - The Universe in HI, Kraan-Korteweg R. C., Henning P. A., Andernach H., eds., p. 153

Saunders W., Frenk C., Rowan-Robinson M., Lawrence A., Efstathiou G., 1991, Nature , 349, 32

Saunders W. et al., 2000b, MNRAS , 317, 55

Saurer W., Seeberger R., Weinberger R., 1997, A&AS, 126, 247

Schlafly E. F., Finkbeiner D. P., 2011, ApJ , 737, 103

Schlegel D. J., Finkbeiner D. P., Davis M., 1998, ApJ , 500, 525

Schmoldt I. M. et al., 1999, AJ , 118, 1146

Schröder A., Drinkwater M. J., Richter O.-G., 2001, A&A, 376, 98

Scrimgeour M. I. et al., 2016, MNRAS , 455, 386

Seeberger R., Huchtmeier W. K., Weinberger R., 1994, A&A, 286, 17

Shapley H., 1961, JRASC, 55, 273

Shaya E. J., Tully R. B., 2013, MNRAS , 436, 2096

Skelton R. E., Woudt P. A., Kraan-Korteweg R. C., 2009, MNRAS , 396, 2367

Skrutskie M. F. et al., 2006, AJ , 131, 1163

Smith R. et al., 2015, MNRAS , 454, 2502

Solanes J. M., Manrique A., García-Gómez C., González-Casado G., Giovanelli R., Haynes M. P., 2001, ApJ , 548, 97

Solanes J. M., Sanchis T., Salvador-Solé E., Giovanelli R., Haynes M. P., 2002, AJ , 124, 2440

Sorce J. G., Hoffman Y., Gottlöber S., 2017, MNRAS , 468, 1812

Spinrad H., 1975, ApJL , 199, L1

Springel V. et al., 2005, Nature , 435, 629

Springob C. M. et al., 2016, MNRAS , 456, 1886

Stark A. A., Gammie C. F., Wilson R. W., Bally J., Linke R. A., Heiles C., Hurwitz M., 1992, ApJS , 79, 77

Staveley-Smith L., Kraan-Korteweg R. C., Schröder A. C., Henning P. A., Koribalski B. S., Stewart I. M., Heald G., 2016, AJ , 151, 52

Stetson P. B., 1987, PASP , 99, 191

Stott J. P., Pimbblet K. A., Edge A. C., Smith G. P., Wardlow J. L., 2009, MNRAS , 394, 2098

Strauss M. A., Willick J. A., 1995, Phys. Rep., 261, 271

Swaters R. A., van Albada T. S., van der Hulst J. M., Sancisi R., 2002, A&A, 390, 829

Takata T., Yamada T., Saito M., Chamaraux P., Kazes I., 1994, A&AS,

104

Taylor G. B., Govoni F., Allen S. W., Fabian A. C., 2001, MNRAS , 326, 2

Tempel E., Stoica R. S., Martínez V. J., Liivamägi L. J., Castellan G., Saar E., 2014, MNRAS , 438, 3465

Thomas T., Katgert P., 2006, A&A, 446, 31

Tonnesen S., Bryan G. L., 2009, ApJ , 694, 789

Tonnesen S., Bryan G. L., van Gorkom J. H., 2007, ApJ , 671, 1434

Toomre A., Toomre J., 1972, ApJ , 178, 623

Treu T., Ellis R. S., Kneib J.-P., Dressler A., Smail I., Czoske O., Oemler A., Natarajan P., 2003, ApJ , 591, 53

Truemper J., 1982, Advances in Space Research, 2, 241

Trumpler R. J., 1930, PASP , 42, 214

Tully R. B., Fisher J. R., 1977, A&A, 54, 661

Valentinuzzi T. et al., 2011, A&A, 536, A34

van de Weygaert R., Schaap W., 2009, in Lecture Notes in Physics, Berlin Springer Verlag, Vol. 665, Data Analysis in Cosmology, Martínez V. J., Saar E., Martínez-González E., Pons-Bordería M.-J., eds., pp. 291–413

van der Hulst J. M., Terlouw J. P., Begeman K. G., Zwitser W., Roelfsema P. R., 1992, in Astronomical Society of the Pacific Conference Series, Vol. 25, Astronomical Data Analysis Software and Systems I, Worrall D. M., Biemesderfer C., Barnes J., eds., p. 131

van Dokkum P. G., Franx M., Fabricant D., Illingworth G. D., Kelson D. D., 2000, ApJ , 541, 95

van Driel W., Schneider S. E., Kraan-Korteweg R. C., Monnier Ragaigne D., 2009, A&A, 505, 29

van Moorsel G., Kemball A., Greisen E., 1996, in Astronomical Society of the Pacific Conference Series, Vol. 101, Astronomical Data Analysis Software and Systems V, Jacoby G. H., Barnes J., eds., p. 37

Verdes-Montenegro L., Yun M. S., Williams B. A., Huchtmeier W. K., Del Olmo A., Perea J., 2001, A&A, 377, 812

Verheijen M. A. W., Oosterloo T. A., van Cappellen W. A., Bakker L., Ivashina M. V., van der Hulst J. M., 2008, in American Institute of Physics Conference Series, Vol. 1035, The Evolution of Galaxies Through the Neutral Hydrogen Window, Minchin R., Momjian E., eds., pp. 265–271

Vijayaraghavan R., Ricker P. M., 2013, MNRAS , 435, 2713

Vikhlinin A. et al., 2009, ApJ , 692, 1060

Visvanathan N., Sandage A., 1977, ApJ , 216, 214

Vollmer B., 2003, A&A, 398, 525

Vollmer B., Cayatte V., Balkowski C., Duschl W. J., 2001, ApJ , 561, 708

Vollmer B., Soida M., Beck R., Chung A., Urbanik M., Chyży K. T., Otmianowska-Mazur K., Kenney J. D. P., 2013, A&A, 553, A116

Walker I. R., Mihos J. C., Hernquist L., 1996, ApJ , 460, 121

Wegner G., Colless M., Baggley G., Davies R. L., Bertschinger E., Burstein D., McMahan, Jr. R. K., Saglia R. P., 1996, ApJS , 106, 1

Wegner G., Haynes M. P., Giovanelli R., 1993, AJ , 105, 1251

Weinberger R., 1980, A&AS, 40, 123

Weinzirl T. et al., 2014, MNRAS , 441, 3083

White R. L., Becker R. H., 1992, ApJS , 79, 331

Willick J. A., 1990, ApJL , 351, L5

Winkel B., Kerp J., Flöer L., Kalberla P. M. W., Ben Bekhti N., Keller R., Lenz D., 2016, A&A, 585, A41

Woudt P. A., Fairall A., Kraan-Korteweg R. C., Lucey J., Schröder A., Burstein D., McCall M. L., 2005, in Astronomical Society of the Pacific Conference Series, Vol. 329, Nearby Large-Scale Structures and the Zone of Avoidance, Fairall A. P., Woudt P. A., eds., p. Fairall

Wright E. L. et al., 2010, AJ , 140, 1868

Yoon H., Chung A., Smith R., Jaffé Y. L., 2017, ApJ , 838, 81

Zabludoff A. I., Mulchaey J. S., 1998, ApJ , 496, 39

Acknowledgments

Working on this PhD has been an incredible experience. I have changed in many different ways and have discovered parts of myself I did not know existed. I certainly would not have made it here if it were not for all the people who supervised, helped, supported and inspired me through this journey.

Marc, It is not possible to express my gratitude in this short paragraph. Thank you for taking me on as one of your students and for sharing your immense scientific and technical knowledge with me. Your patience is admirable, I learned a lot from your lengthy descriptions of the concepts of radio astronomy and from spending hours guiding me through the immense data reduction process. I am a better scientist for it. I greatly enjoyed the stimulating discussions we had on all other non-astronomy related topics as well, your worldly view on current events was striking. Thank you for your advise, for always listening and valuing my opinions, for your great support and for believing in my ability to produce this piece of work even when I did not believe it myself at times. I am very grateful that you and Marti welcomed me into your home and treated us to all those delicious home-cooked dinners, particularly given my not so great relationship with proper food.

Renee, I am so glad I walked into your office at UCT 10 years ago. No number of words could ever express my sincere and deep gratitude for the tutelage I have received from you over the years. You have always been there to teach, encourage and listen. Thank you for your supervision and enthusiasm for science which you also imparted on me. You shared your

knowledge with me and patiently guided me through the complexities and challenges of the Zone of Avoidance, I developed a thick skin working in this area. Your detailed input and feedback on every material I have ever written and presented has made a researcher out of me. You opened doors for me and believed in my abilities in ways that I cannot describe. Thank you for your mentorship, for your unwavering support through the hardships and for celebrating the achievements with me.

Anja, I highly appreciate all the input you have had in all the work I have done over for the many years ($\sim$7 years) that I have known you. Thank you for your patience in explaining many many times what Galactic extinction was about and how to correct for it. I missed some of our deadlines or failed to deliver on some of the things we would discuss, yet you never gave up on me. Your input and feedback on all the data analyses and written text I have done has helped me grow into a better researcher. You always paid great attention to every detail of my work and taught me to do the same. I am taking these lessons with me moving forward.

Tom, I am grateful that you adopted me into your research group. I highly appreciate all the knowledge you have shared with me as well as your input and feedback on my work. I found it easy to talk to you and come to you with any questions I had regarding infrared data. Thank you for always making the time for me and for being available to address any and all of my issues even at 1am! That is incredible!.

Thank you to my co-supervisor Erwin, for being my contact person at ASTRON and for always reacting quickly to all of my travel needs, particularly during my work visits to UCT.

A very special thanks to Josh, for organising all the observations and HI-data that made this project possible and for patiently talking me through how to even begin handling interferometric radio data.

A special thanks to Khaled for the useful discussions we had on the near-infrared photometry and for offering a lot of his time to help me greatly with it. A special thanks to Wendy for also helping with the photometry by addressing the technical questions regarding star-subtraction.

Many thanks to Ed for teaching me new and innovative methods of assessing completeness in blind HI-surveys and for spending many many hours helping me through the process.

I would like to thank the members of the reading committee, C. Carignan, M.J. Drinkwater, J.H. van Gorkom and J.M. van der Hulst for carefully

reading and assessing my thesis and for their useful comments.

Thank you to Mathjis and Marti for their quick reactions in helping me with the Dutch translation. I would also like to thank Litsi'itso Pule for helping me with the Sesotho translation. I learned words I did not even know existed in my language.

Many thanks to Patrick Bos for allowing me to use this beautiful thesis template. I am told that it has been floating around the Kapteyn Institute for at least a decade. Its family tree consists of the PhD theses of Bruno Letarte (2006), Matias Arrigoni (2010), Thomas Martinsson (2011), Stephan Peters (2014) and Patrick Bos (2016). Cool!.

I highly appreciate all the great help I received with all the administrative things. Many many thanks to Lucia, Hennie, Christa and Martine at the Kapteyn Institute, and to Roslyn and Carol at the UCT astronomy department for taking care of the incredible amount of paperwork that was involved in making my stay and work life at both institutes possible. You all keep these places running.

Thank you to the computer group at Kapteyn and UCT for providing me with robust IT facilities to enable my work. Special thanks to Wim and Martin for going above and beyond to ensure that I had the best machine and right softwares to handle all the data I had to work with and for always being available to address all of my IT problems. Thank you to Bianca and Siphelo for providing me with the necessary support whenever I was UCT, particularly installing those seemingly impossible softwares I needed.

I have had the privilege of being part of two vibrant, dynamic and international institutes. I am very grateful to every single person I have interacted with at both these places, some of whom I mentioned here. I am certain that everyone of them influenced me in one way or another even if they are not mentioned in this text.

The office ("266 vibes!!!") was always a lovely place to work in because of the people I shared it with. Eva, I am thankful for the times I spent with you in that office. Navigating our trip together in India was a breeze because you are so organised.

Enrico, I am thankful you joined our office and brought awesome vibes with you. I have enjoyed our stimulating conversations on neuroscience, food, health and fitness, machine learning, what did we not talk about?. I quietly admired your chilled approach to life during these discussions, the office was never boring when you were around.

Katya, our honorary officemate. Thank you for all the lovely conversations we have had, you are an amazing person. You might have singlehandedly kept me healthy at some point with all the fruits you provided. I am very thankful for that.

Anastasia, I am so grateful I was put in the same office as you. Knowing has been a fun adventure from the moment I met you on that dark-supercold night in January. You were there, through the best and the worst times of this journey, always willing to lend a helping hand or just listen. You are probably the one person who knows me better than anybody else in the whole of Netherlands. Your positive and engaging energy kept me sane at some points :). Words cannot express how thankful I am to you for not only being an officemate but for being a dear friend as well.

Elaheh, without saying too much, your calm energy and positive spirit kept me going especially when the going got tough and I started panicking as I do sometimes (okay.. a lot of the times:)). Going to your office to see you or you walking into my office to ask how I was doing was always a welcomed sight. Thank you for all the delicious treats you would bring from Iran, for being a friend and my yoga partner at the back of the class at ACLO :).

Davide, thank you for your help in visualising my data cubes. Your visualisation stuff have made for great impressions whenever I was giving talks on this work.

Thank you to Maciej in Leiden for the insightful conversations we had whenever you came to Groningen, they really helped with my work.

To the UCT and Kapteyn crew including those who have left; Zolile, Sam, Nagres, Iniyan, Hannes, Liz, Mariam, Marc, Marie, Brenda, Kerry, Amadou, Toky, Seyda, Dorota, Nadine, Robin, Ming, Mustafa, Avanti, Jan, Pooja, Crescenzo, Khine, Rajin, Itumeleng, Blaise, Leon, Julia, Jamie, Marisa, Francesco, Fillipo, Sarrvesh, Antonino, Laura, Khan, Pece. The Cape-Town and/or Cape-Town North people: Brad, Danielle, Kelley, Natasha. The various interactions, conversations and fun times I have had with you all made both institutes pleasant places to work in.

Many thanks to Hugo at Kapteyn for sharing the amazing stories of your travel experiences in South Africa many years ago before I was born. They made for great lunch conversations.

I have had the good fortune of being surrounded by a large group of people who have all steadfastly stood in my corner.

Moeketsi, skim sa ka!! :), thank you for being a constant source of support in my life, for being an amazing friend from the day I met you and for keeping me going and encouraging me through this work and everything I have ever tried to do.

Mpheng my awesome friend, we have had amazing road trips and shared our not so great taste in pop music. Our lengthy discussions on the latest Taylor Swift songs :) were always a nice distraction from stressful thesis situations. Thank for your friendship even when I was too occupied at times.

Velile, duuude, we spent so many nights on campus together, thank you for the "good" frozen food cooked in your lab's microwave, they made those long nights of writing text and data reduction go much easier. Thank you for being there with me in the great and not so great moments and for always willing to go for a drink whenever there was a need for it. I learned a lot from watching go through your research work and life with graceful chill vibes.

Sahba, you are one of a kind lady. I have admired your fearless and easy approach to all things and you have encouraged me to do the same (something we both know is not easy for me). Your friendship has meant a lot to me and was instrumental in the completion of this thesis. Thank you thank you thank you.

Gopolang, many thanks for always being available to talk and for the awesome Groningen adventures. The road trip through the Midwest was particularly interesting :). I was always baffled by how passionate you were about particle physics and by how much you were trying to get me excited about being at Fermilab. I am very happy to see your advancements over the years.

Priscilla, thank you for being a friend and my travel companion. The trips we took were a lovely and welcomed break. I particularly enjoyed our wine "tasting" adventures. I cannot wait for Cuba.

Nikki, you got me through the worst of times. I can never thank you enough. I will always be grateful that you are in my life and that you introduced me to the red espresso, I love that stuff. Thank you for being one of my people.

Zwido, thank you for the fun evenings, the drinks and the very much needed laughter. I still cannot believe how much you guys sucked at football, really? How is it even possible?.

Songo, you are a force to be reckoned with. I have been inspired by your passion for green energy and for "saving the planet". I am so glad I met you on that camping trip. Thanks for introducing me to your great taste in food and wine, and for being there whenever I needed to talk or just missed home.

Ojwang, thank you for the many many Skype chats. I appreciated your ability to help me through the most chaotic moments with your organised way of thinking which helped me prioritise the important things. Thank you for always being there for me, to talk or just to hangout and for insisting that I remember to eat during the busiest times.

I know there are so many other people I forgot to mention. For all that you all have done and for the interactions I have had with you, thank you, thank you, thank you, thank you.

My parents have always encouraged me to fearlessly follow my dreams wherever they may take me. I would not have made it this far without them. I do not have the chance to thank my mother but I am sure she would be happiest to see me finish my PhD. I know my father is overjoyed to see me make it this far. Ntatepula, I cannot thank you enough for always being in my corner every step of the way. I know you would move mountains to see me happy, make it through and succeed at all things. Many thanks to my brother for being there when I needed him even though I had to (he would let me) use my "big-sister" card sometimes.

Ho malapa a heso kaofela, Basia le Bafokeng. BoMangwane, BoRangwane, BoRakgadi, BoMalome, ke leboha ho menahane ka ho ba teng ha lona bophelo ba ka. Ha ho mokgwa o lekaneng oo nka le lebohang ka hona ka tsohle tseo le nthusitseng ka tsona le tseo le nketseditseng tsona. Ho mme Mamoratoe le ntatemoholo Mohapi, le nkgodisitse ho tloha bonyaneng ka lerato, la nkgothalletsa thuto, la nketsa motho eo ke leng yena kajeno. Ha ho mantswe ao nka a buang a ho le leboha. Ke moo ke le teng kajeno ka lebaka la lona.